

Recent Advances in Modeling, Analysis, and Synchronization of Chaotic Systems

Lead Guest Editor: Christos Volos

Guest Editors: Lazaros Moysis, Mahendra K. Gupta, Serdar Çiçek, and Viet-Thanh Pham





Recent Advances in Modeling, Analysis, and Synchronization of Chaotic Systems

Complexity

Recent Advances in Modeling, Analysis, and Synchronization of Chaotic Systems

Lead Guest Editor: Christos Volos


Guest Editors: Lazaros Moysis, Mahendra K. Gupta,
Serdar Çiçek, and Viet-Thanh Pham



Copyright © 2020 Hindawi Limited. All rights reserved.

This is a special issue published in "Complexity." All articles are open access articles distributed under the Creative Commons Attribution License, which permits unrestricted use, distribution, and reproduction in any medium, provided the original work is properly cited.

Chief Editor

Hiroki Sayama , USA

Associate Editors

Albert Diaz-Guilera , Spain
Carlos Gershenson , Mexico
Sergio Gómez , Spain
Sing Kiong Nguang , New Zealand
Yongping Pan , Singapore
Dimitrios Stamovlasis , Greece
Christos Volos , Greece
Yong Xu , China
Xinggang Yan , United Kingdom

Academic Editors

Andrew Adamatzky, United Kingdom
Marcus Aguiar , Brazil
Tarek Ahmed-Ali, France
Maia Angelova , Australia
David Arroyo, Spain
Tomaso Aste , United Kingdom
Shonak Bansal , India
George Bassel, United Kingdom
Mohamed Boutayeb, France
Dirk Brockmann, Germany
Seth Bullock, United Kingdom
Diyi Chen , China
Alan Dorin , Australia
Guilherme Ferraz de Arruda , Italy
Harish Garg , India
Sarangapani Jagannathan , USA
Mahdi Jalili, Australia
Jeffrey H. Johnson, United Kingdom
Jurgen Kurths, Germany
C. H. Lai , Singapore
Fredrik Liljeros, Sweden
Naoki Masuda, USA
Jose F. Mendes , Portugal
Christopher P. Monterola, Philippines
Marcin Mrugalski , Poland
Vincenzo Nicosia, United Kingdom
Nicola Perra , United Kingdom
Andrea Rapisarda, Italy
Céline Rozenblat, Switzerland
M. San Miguel, Spain
Enzo Pasquale Scilingo , Italy
Ana Teixeira de Melo, Portugal

Shahadat Uddin , Australia
Jose C. Valverde , Spain
Massimiliano Zanin , Spain


Contents

Minimal Diagnosis and Diagnosability of Discrete-Event Systems Modeled by Automata

Xiangfu Zhao , Gianfranco Lamperti , Dantong Ouyang , and Xiangrong Tong 

Research Article (17 pages), Article ID 4306261, Volume 2020 (2020)

Study on Amplitude Modulation Principle of Chaotic System

Jian-Rong Du, Chun-Lai Li , Kun Qian, Zhao-Yu Li, and Wen Li


Research Article (13 pages), Article ID 9106132, Volume 2020 (2020)

Analysis, Stabilization, and DSP-Based Implementation of a Chaotic System with Nonhyperbolic Equilibrium

Xuan-Bing Yang, Yi-Gang He , Chun-Lai Li , and Chang-Qing Liu



Research Article (11 pages), Article ID 6786832, Volume 2020 (2020)

Coexisting Three-Scroll and Four-Scroll Chaotic Attractors in a Fractional-Order System by a Three-Scroll Integer-Order Memristive Chaotic System and Chaos Control

Xikui Hu and Ping Zhou 


Research Article (7 pages), Article ID 5796529, Volume 2020 (2020)

Adaptive Multi-Switching Synchronization of High-Order Memristor-Based Hyperchaotic System with Unknown Parameters and Its Application in Secure Communication

Zhili Xiong , Shaocheng Qu , and Jing Luo

Research Article (18 pages), Article ID 3827201, Volume 2019 (2019)

Enhancing Ikeda Time Delay System by Breaking the Symmetry of Sine Nonlinearity

Xiaojing Gao 


Research Article (14 pages), Article ID 2941835, Volume 2019 (2019)

The Synchronization of N Cascade-Coupled Chaotic Systems

Pengyu Li, Juan Du , Shouliang Li , Yazhao Zheng, and Bowen Jia 




Research Article (10 pages), Article ID 2709820, Volume 2019 (2019)

Bursting and Synchronization of Coupled Neurons under Electromagnetic Radiation

Xiaoyu Hu  and Chongxin Liu






Research Article (10 pages), Article ID 4835379, Volume 2019 (2019)

Degradation Analysis of Chaotic Systems and their Digital Implementation in Embedded Systems

Rodrigo Méndez-Ramírez , Adrian Arellano-Delgado, Miguel Murillo-Escobar , and César Cruz-Hernández 


Research Article (22 pages), Article ID 9863982, Volume 2019 (2019)

Analysis and FPGA Realization of a Novel 5D Hyperchaotic Four-Wing Memristive System, Active Control Synchronization, and Secure Communication Application





Fei Yu , Li Liu , Binyong He , Yuanyuan Huang , Changqiong Shi, Shuo Cai , Yun Song , Sichun Du , and Qiuzhen Wan 

Research Article (18 pages), Article ID 4047957, Volume 2019 (2019)

Research on Grid Scroll Chaotic Extended Sequence Algorithm and Its Circuit Implementation for F-OFDM System

Yingjie Ma, Ya Li , Geng Zhao, Ping Zeng, and Yatao Yang
Research Article (7 pages), Article ID 5904801, Volume 2019 (2019)



Dimensionality Reduction Reconstitution for Extreme Multistability in Memristor-Based Colpitts System

Yunzhen Zhang, Zhong Liu , Mo Chen , Huagan Wu , Shengyao Chen, and Bocheng Bao 
Research Article (12 pages), Article ID 4308549, Volume 2019 (2019)


Complex Dynamical Behaviors of a Fractional-Order System Based on a Locally Active Memristor

Yajuan Yu, Han Bao , Min Shi , Bocheng Bao , Yangquan Chen , and Mo Chen 
Research Article (13 pages), Article ID 2051053, Volume 2019 (2019)

A Fractional-Order Model for Zika Virus Infection with Multiple Delays

R. Rakkiyappan , V. Preethi Latha, and Fathalla A. Rihan 
Research Article (20 pages), Article ID 4178073, Volume 2019 (2019)


Combination Synchronization of Three Different Fractional-Order Delayed Chaotic Systems

Bo Li, Xiaobing Zhou , and Yun Wang
Research Article (9 pages), Article ID 5184032, Volume 2019 (2019)


Robust Control of Disturbed Fractional-Order Economical Chaotic Systems with Uncertain Parameters

Song Xu , Hui Lv , Heng Liu , and Aijing Liu
Research Article (13 pages), Article ID 7567695, Volume 2019 (2019)


Master-Slave Synchronization of Chaotic Φ^6 Duffing Oscillators by Linear State Error Feedback Control

Ke Ding 
Research Article (10 pages), Article ID 3637902, Volume 2019 (2019)


Chaotic Dynamics of an Airfoil with Higher-Order Plunge and Pitch Stiffnesses in Incompressible Flow

Karthikeyan Rajagopal , Yesgat Admassu, Riessom Weldegiorgis, Prakash Duraisamy, and Anitha Karthikeyan
Research Article (10 pages), Article ID 5234382, Volume 2019 (2019)

A New 4D Chaotic System with Two-Wing, Four-Wing, and Coexisting Attractors and Its Circuit Simulation

Lilian Huang , Zefeng Zhang, Jianhong Xiang, and Shiming Wang
Research Article (13 pages), Article ID 5803506, Volume 2019 (2019)

Dynamics and Synchronization of a Memristor-Based Chaotic System with No Equilibrium

Hong-Min Li, Yan-Feng Yang, Yang Zhou, Chun-Lai Li , Kun Qian, Zhao-Yu Li, and Jian-Rong Du
Research Article (11 pages), Article ID 4647608, Volume 2019 (2019)

Contents

Influence of Piezoelectric Performance on Nonlinear Dynamic Characteristics of MFC Shells

Xiangying Guo , Pan Jiang, and Dongxing Cao 

Research Article (15 pages), Article ID 1970248, Volume 2019 (2019)

Research Article

Minimal Diagnosis and Diagnosability of Discrete-Event Systems Modeled by Automata

Xiangfu Zhao ¹, Gianfranco Lamperti ², Dantong Ouyang ³, and Xiangrong Tong ¹

¹School of Computer and Control Engineering, Yantai University, Yantai 264005, China

²Department of Information Engineering, University of Brescia, Brescia 25123, Italy

³College of Computer Science and Technology, Jilin University, Changchun 130012, China

Correspondence should be addressed to Xiangfu Zhao; xiangfuzhao@gmail.com and Xiangrong Tong; txr@ytu.edu.cn

Received 13 September 2019; Revised 13 December 2019; Accepted 7 January 2020; Published 18 February 2020

Guest Editor: Viet-Thanh Pham

Copyright © 2020 Xiangfu Zhao et al. This is an open access article distributed under the Creative Commons Attribution License, which permits unrestricted use, distribution, and reproduction in any medium, provided the original work is properly cited.

In the last several decades, the model-based diagnosis of discrete-event systems (DESs) has increasingly become an active research topic in both control engineering and artificial intelligence. However, in contrast with the widely applied minimal diagnosis of static systems, in most approaches to the diagnosis of DESs, all possible candidate diagnoses are computed, including nonminimal candidates, which may cause intractable complexity when the number of nonminimal diagnoses is very large. According to the principle of parsimony and the principle of joint-probability distribution, generally, the minimal diagnosis of DESs is preferable to a nonminimal diagnosis. To generate more likely diagnoses, the notion of the minimal diagnosis of DESs is presented, which is supported by a minimal diagnoser for the generation of minimal diagnoses. Moreover, to either strongly or weakly decide whether a minimal set of faulty events has definitely occurred or not, two notions of minimal diagnosability are proposed. Necessary and sufficient conditions for determining the minimal diagnosability of DESs are proven. The relationships between the two types of minimal diagnosability and the classical diagnosability are analysed in depth.

1. Introduction

In recent years, several disasters, including the nuclear leakage that occurred in Fukushima (Japan) in 2011 and the blackout that occurred in nearly the entire country of India in 2012, have greatly threatened the safety of society and even the lives of many people. To prevent such disasters, determining faulty events/components is a very important topic. To this end, model-based fault diagnosis techniques may be very effective.

Nonlinear science is a new interdisciplinary subject which studies the common problems proposed by nonlinear interaction widely existing in various disciplines, especially in complex networks [1–4], system control [5–7], secure communication [8–10], chaotic systems [11], random number generators [12, 13], discrete-event systems (DESs) [14], and other fields. The creative work on the diagnosis/diagnosability of DESs, presented in [15, 16], with the originally proposed concept of a diagnoser, model-based diagnosis, and diagnosability have attracted more and more

attention, as indicated by the large number of methods and techniques proposed in the literature, including [17–26]. Because of the intractable complexity of reasoning of the global DES model and the corresponding centralized diagnoser, decentralized approaches were proposed in [27–29]. More recently, fuzzy diagnoser/diagnosability [30, 31] or the stochastic diagnoser/diagnosability/prognosability [32–35] has been studied, with fuzzy or stochastic information being injected into an automaton that models a DES. In addition to diagnoser-based approaches for the diagnosis of DESs, a history-based approach [36, 37] and a consistency-based approach [38] to the diagnosis of DESs have also been presented.

However, as far as we know, one of the current main problems is that, in most approaches to diagnosing DESs, all possible candidate diagnoses are derived, even if many candidates are proper supersets of some other candidates. In other words, nonminimal (redundant) diagnoses are generated.

In this paper, we extend the idea of a minimal diagnosis, first presented in [39], via additional theoretical analyses, formal proofs, examples, and comparisons with related work.

Example 1. Among candidate diagnoses (sets of possible faulty events) $\{f_1\}$, $\{f_2, f_3\}$, $\{f_1, f_2, f_3\}$, $\{f_1, f_3, f_4\}$, and $\{f_2, f_3, f_4\}$, only $\{f_1\}$ and $\{f_2, f_3\}$ are minimal according to the set-inclusion relationship, as all other candidates contain $\{f_1\}$ or $\{f_2, f_3\}$ and include additional faults (f_2 and/or f_3 and/or f_4). Minimal diagnosis differs from minimal-cardinality diagnosis. In our example, the only minimal-cardinality diagnosis is $\{f_1\}$. In this paper, we focus on minimal diagnosis rather than minimal-cardinality diagnosis. In addition, in our example, even if we cannot definitely know whether f_4 has occurred or not, we know that minimal diagnoses $\{f_1\}$ and $\{f_2, f_3\}$ are generally more probable than others.

In theory, all possible fault sets need to be diagnosed. However, considering a scenario like Example 1, although there are a large number of possible candidate diagnoses that can explain the current observation sequence, there may exist set-inclusion relationships among some of them.

The two principles of parsimony and joint-probability distribution, which are briefly described as follows:

- (i) The principle of parsimony: also called ‘‘Occam’s razor’’ [40], parsimony is a principle of succinctness often adopted in logic and problem solving which states that, among competing hypotheses, the hypothesis with the fewest assumptions should be selected. The principle of parsimony has also been introduced for the minimal diagnosis of static systems [41].
- (ii) The principle of joint-probability distribution: a widely used assumption in the literature, in this paper, a joint-probability distribution means that each fault is independent of one another and that the prior probability of each fault is equal.

Minimal diagnoses (based on the set-inclusion relationship (for instance, we assume that there are three candidate diagnoses $\{f_1\}$, $\{f_1, f_2\}$, and $\{f_2, f_3, f_4, f_5\}$. Then, $\{f_1\}$ and $\{f_2, f_3, f_4, f_5\}$ are minimal diagnoses, even if $\{f_2, f_3, f_4, f_5\}$ has a bigger cardinality than $\{f_1, f_2\}$ but without a set-inclusion relationship between them.)) are more likely than the corresponding nonminimal ones. As a result, just like the minimal diagnosis of static systems [41, 42], determining only the minimal diagnoses of DESs is bound to reduce the complexity, as additional nonminimal diagnoses are not considered.

The benefit of a minimal diagnosis is related to both cognition and computation. Cognition is relevant to the human who is responsible for the monitoring of the DES. Consider, for instance, the operator in the control room of a power network, who is responsible for the correct behaviour of the network. When a misbehaviour occurs, such as a short circuit on a transmission line, several actions can be triggered by the protection system to isolate the shorted line,

e.g., opening breakers and reconfiguring the power load to avoid a blackout. If the reaction of the protection system is abnormal, a possibly large number of alarms and messages will be generated. Since the operator is expected to activate specific recovery actions, it is essential that the (possibly overwhelming) stream of information generated by the system, namely, the observation, be interpreted correctly under stringent time constraints. This is why automated diagnosis becomes a key factor in supporting the operator in performing his/her critical job. To this end, the diagnosis engine may generate diagnosis information in a relatively short amount of time. Specifically, a set of candidate diagnoses are presented to the operator, who is expected to make critical decisions regarding the safety of the involved population. However, if the number of candidates is large, the operator may be confused about which diagnoses should deserve more attention. Choosing minimal diagnoses is a good heuristic, as they are more probable and, as such, more worthy of attention.

Computation involves the efficient generation of candidate diagnoses. Since a key factor in real applications of automated diagnosis is the time response, that is, the delay between the occurrence of a faulty event and the generation of candidate diagnoses, it is of paramount importance that the diagnosis engine is not only effective but also efficient. Being free of the burden of nonminimal candidates, minimal diagnosis allows the diagnosis engine to be more efficient compared with nonminimal diagnosis with respect to both processing speed and memory space.

In summary, the main contribution of the paper is that the theoretical concepts of minimal diagnosis and minimal diagnosability of DESs are proposed, and meanwhile, the minimal diagnosis of DESs is not a purely academic exercise; it may drive attention to the actual cause of a misbehaviour effectively (cognition) and efficiently (computation).

The rest of the paper is organized as follows. The terminology and preliminary concepts related to the model-based diagnosis of DESs are given in Section 2. Several novel concepts, including minimal diagnosis, minimal diagnoser, and minimal diagnosability of DESs, are presented in Section 3. Related work is discussed in Section 4. Conclusions and future work are presented in Section 5.

2. Background

In this section, the classical notions of the diagnosis, diagnoser, and diagnosability of DESs [16] are recalled.

2.1. Classical Diagnosis of DESs. A DES is a deterministic finite state machine (FSM), namely, $G = (Q, \Sigma, T, q_0)$, where

Q is the set of states.

Σ is the set of events, including two disjoint sets of observable events (Σ_o) and unobservable events (Σ_{uo}); $\Sigma_f = \{f_1, f_2, \dots, f_m\}$ (for the sake of simplicity, the classification (types) of faults in [16] is disregarded in this paper), with $\Sigma_f \subseteq \Sigma_{uo}$, is the set of faulty events to be inferred, while $(\Sigma_{uo} - \Sigma_f)$ is the set of events that are both unobservable and nonfaulty.

$T \subseteq Q \times \Sigma \times Q$ is the set of transitions, where a transition from state q to state q' , when event e is activated on state q , is equivalently denoted by $(q, e, q') \in T$, $q \xrightarrow{e} q'$, or $T(q, e) = q'$.

$q_0 \in Q$ denotes the initial state of the system.

The behaviour of G consists of all possible traces generated from q_0 to some state in G , which form a prefix-closed language $L(G)$, abbreviated as L , with $L \subseteq \Sigma^*$ (Σ^* is the set of all possible strings composed of events in Σ , including the empty string ε). For simplicity, we assume that language L is live, that is,

For each state $q \in Q$, there exists at least one event $\sigma \in \Sigma$ such that $q \xrightarrow{\sigma} q'$ holds, where $q' \in Q$ (with q' being nonnecessarily different from q).

In addition, similar to [16], we assume that there does not exist any cycle of unobservable events, that is,

For any cycle $q_1 \xrightarrow{\sigma_1} q_2 \xrightarrow{\sigma_2} \dots q_{k-1} \xrightarrow{\sigma_{k-1}} q_k \xrightarrow{\sigma_k} q_1$ ($k \geq 1$, $q_i \in Q$, and $\sigma_i \in \Sigma$ ($i \in [1 \dots k]$)), there exists at least one event σ_j ($j \in [1 \dots k]$) such that $\sigma_j \in \Sigma_o$.

Example 2. Outlined in Figure 1(a) is the diagrammatic representation of a DES model G , where $\Sigma_o = \{\alpha, \beta, \gamma, \theta, \rho\}$, $\Sigma_f = \{f_1, f_2\}$, and $\Sigma_{uo} = \{\sigma_{uo1}, \sigma_{uo2}\} \cup \Sigma_f$.

We denote the empty trace as ε and extend one transition event to a string of transition events as follows:

$q \xrightarrow{\varepsilon} q$ always holds

For $s \in \Sigma^*$ and $\sigma \in \Sigma$, $q \xrightarrow{s} \sigma q'$ holds whenever $q \xrightarrow{s} q''$ and $q'' \xrightarrow{\sigma} q'$ hold for $q'' \in Q$

Denoting a transition in which the entered state is missing, $q \xrightarrow{s}$ indicates that, for $s \in \Sigma^*$, there exists at least one state $q' \in Q$ such that $q \xrightarrow{s} q'$ holds.

The notation L/s represents the postlanguage of L after string $s \in L$, that is, $L/s = \{t \mid t \in \Sigma^*, st \in L\}$.

Two types of projection are given: Prj_{Σ_o} (on observation) and P_{Σ_f} (on faults). Assuming that $\sigma \in \Sigma$ and $s \in \Sigma^*$, $\text{Prj}_{\Sigma_o} : \Sigma^* \rightarrow \Sigma_o^*$ represents how a trace is projected onto a sequence of observable events:

$$\text{Prj}_{\Sigma_o}(s\sigma) = \text{Prj}_{\Sigma_o}(s)\text{Prj}_{\Sigma_o}(\sigma). \quad (1)$$

Conversely, $\text{Prj}_{\Sigma_o}^{-1}(s_o) = \{s \mid s \in L, \text{Prj}_{\Sigma_o}(s) = s_o\}$ denotes the set of traces whose projection equals s_o (note here that $\text{Prj}_{\Sigma_o}^{-1}(\text{Prj}_{\Sigma_o}(s_o))$ may not equal s_o).

$P_{\Sigma_f} : \Sigma^* \rightarrow 2^{\Sigma_f}$ denotes how a (possibly empty) trace $s \in \Sigma^*$ is mapped onto a set of faults:

$$P_{\Sigma_f}(s) = \{f_i \mid f_i \in \Sigma_f, f_i \in s\}. \quad (2)$$

Example 3. Let $s = af_1bcf_2$, $\{f_1, f_2\} \subseteq \Sigma_f$, and $\{a, b, c\} \subseteq \Sigma_o$. We have $\text{Prj}_{\Sigma_o}(s) = abc$ and $P_{\Sigma_f}(s) = \{f_1, f_2\}$.

Let s_e denote the last event of a nonempty trace $s \in \Sigma^+$, where $\Sigma^+ = \Sigma^* - \{\varepsilon\}$, and $F \subseteq \Sigma_f$. Then, $S_F = \{s \mid s \in L, P_{\Sigma_f}(s) = F, s_e \in F\}$ denotes the set of all traces ending with one fault of F and containing all the faulty events of F .

We use $L(G, q)$ to denote all traces in G starting from state q . Let $L_o(G, q) = \{s \mid s \in L(G, q), s = u\sigma, u \in \Sigma_{uo}^*, \sigma \in \Sigma_o\}$ denote all traces starting from state q up to the first observable event and $L_\sigma(G, q) = \{s \mid s \in L_o(G, q), s_e = \sigma\}$ denote all traces starting from q up to the first observable event σ .

Based on $G = (Q, \Sigma, T, q_0)$, an FSM $G^o = (Q^o, \Sigma_o, T^o, q_0)$ (in general, nondeterministic (a nondeterministic FSM is a state in G which may reach more than one state via the same transition event. Accordingly, in Figure 1(b), state 1 can reach four different states (2, 7, 14, and 18) via the same observation α)) is defined as follows:

$Q^o = \{q_0\} \cup \{q' \mid q \xrightarrow{\sigma} q' \in T, \sigma \in \Sigma_o\}$ denotes both q_0 and all observable states.

$T^o \subseteq Q^o \times \Sigma_o \times Q^o$ denotes the set of transitions, defined as follows:

$$(q^o, \sigma, q'^o) \in T^o, \quad \text{iff } T(q^o, s) = q'^o, s \in L_\sigma(G, q^o). \quad (3)$$

As such, $L(G^o) = \{t \mid t = \text{Prj}_{\Sigma_o}(s), s \in L\}$.

Example 4. With reference to Example 2, Figure 1(b) presents a diagrammatic representation of G^o , with G being displayed in Figure 1(a).

Based on the abovementioned notions, the notion of the diagnosis of a DES is given in Definition 1.

Definition 1. Let $G = (Q, \Sigma, T, q_0)$ be a DES, L be the corresponding language of G , and $\text{obs} \in \Sigma_o^*$ be the current observation sequence for G . A subset $F \subseteq \Sigma_f$ is called a candidate diagnosis (or just a diagnosis) of a DES for observation sequence obs (written as $F \rightsquigarrow \text{obs}$) iff there is a string of events $s \in L$ with $s_e \in \Sigma_o$ such that $P_{\Sigma_f}(s) = F \wedge \text{Prj}_{\Sigma_o}(s) = \text{obs}$.

In other words, a diagnosis of a DES is a set of faulty events (unlike the diagnosis of static systems (e.g., [41, 42]), where a diagnosis is defined as a set of faulty components.) in a trace whose mapping onto observable events equals only the current observation sequence obs . Note that the condition $s_e \in \Sigma_o$ must be satisfied in the definition, as we generally use the currently received observation sequences immediately after the DES fails to work properly to infer a set of faults to explain observation obs (this is also a fundamental principle of finding the diagnosis of DESs).

Example 5. With reference to Example 2, for the DES G displayed in Figure 1(a), if we get the current observation sequence $\text{obs} = \alpha\beta\theta$, then all candidate diagnoses are \emptyset , $\{f_1\}$, and $\{f_1, f_2\}$, with $\alpha\beta\theta$, $f_1\alpha\beta\theta$, and $f_1\alpha\beta f_2\theta$ being the corresponding traces of events, respectively.

2.2. Classical Diagnoser for DESs. To generate candidate diagnoses, the diagnoser-based approach introduced in [16] is used.

Let $\Delta = 2^{\Sigma_f \cup \{A\}}$ be all possible fault labels, with each label being a set of faulty events. N is used as an alias for the empty fault set (to indicate a normal state). A is interpreted as

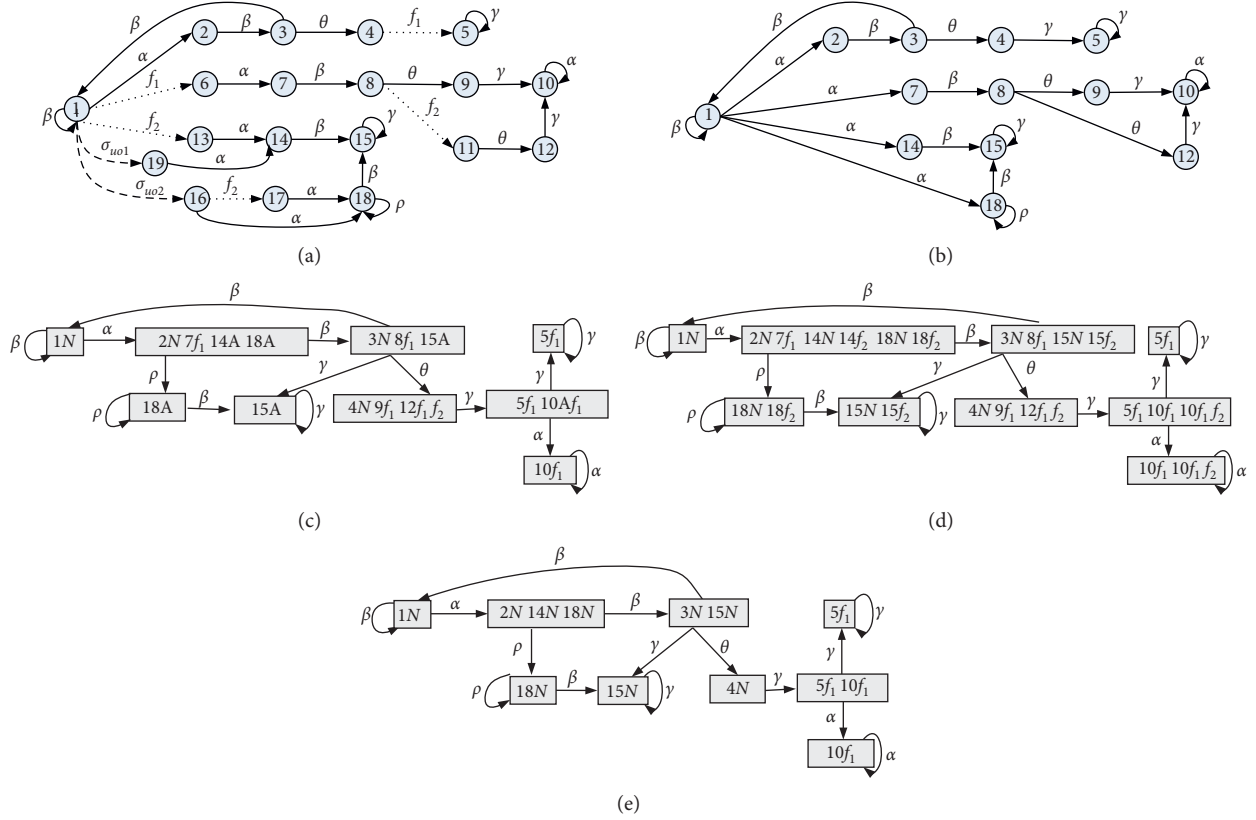


FIGURE 1: A DES and its related variant diagnosers: (a) DES model G . (b) Nondeterministic FSM G^o for G . (c) Classical diagnoser G_d for G . (d) Revised diagnoser G^d for G . (e) Minimal diagnoser G^m for G .

“ambiguous” (that is, we cannot be sure that some faults have definitely occurred).

Starting from $G^o = (Q^o, \Sigma_o, T^o, q_0)$, the classical diagnoser G_d for G is a deterministic FSM:

$$G_d = (q_d, \Sigma_o, T_d, q_d^0), \quad (4)$$

where

$q_d \subseteq 2^{(Q^o \times \Delta)}$ is the set of states.

$q_d^0 = \{(q_0, N)\}$ (since the fault label associated with q_0 is N , G is assumed to be normal at the initial state.) Any state $q_d \in q_d$ is reachable from q_d^0 via transitions in T_d , written as $q_d = \{(q_1^o, l_1), \dots, (q_n^o, l_n)\}$, where $q_i^o \in Q^o$ and $l_i \in \Delta$ (that is, l_i is in the form of either N or a nonempty subset of $\Sigma_f \cup \{A\}$). In subsequent set-theoretic operations in the minimal diagnoser, we replace N with the empty set \emptyset .

The range function $R: q_d \times \Sigma_o \rightarrow q_d$ is defined as follows:

$$R(q_d, \sigma) = \bigcup_{(q^o, l) \in q_d} \left(\bigcup_{s \in L_o(G, q^o)} \{(T(q^o, s), LP(q^o, l, s))\} \right), \quad (5)$$

where $LP: Q^o \times \Delta \times \Sigma^* \rightarrow \Delta$ denotes the fault label propagation function. Given $q^o \in Q^o$, $l \in \Delta$, and $s \in L_o(G, q^o)$, fault label l is propagated by LP over string s from q^o in the following way:

$$LP(q^o, l, s) = \{f_i \mid f_i \in l \vee f_i \in s\}. \quad (6)$$

Then, the label correction function $LC: q_d \rightarrow q_d$ is defined as follows:

$$LC(q_d) = \{(q^o, l) \mid (q^o, l) \in q_d, \text{ and } \nexists (q^o, l') \in q_d \text{ with } l' \neq l\} \cup \{(q^o, \{A\} \cup (l_i \cap \dots \cap l_k)) \mid (q^o, l_i), \dots, (q^o, l_k) \in q_d, l_v \neq l_w, v, w \in \{i_1, \dots, i_k\}, v \neq w, k \geq 2\}. \quad (7)$$

The label correction function LC and the label A can be explained as follows. When the system moves along trace s

and transitions from some state into a state q^o with at least two different fault labels, we cannot be sure that some faults

have definitely occurred; therefore, we use label A to refer to this scenario.

The transition function $T_d: q_d \times \Sigma_o \longrightarrow q_d$ is defined as follows:

$$q_d^2 = T_d(q_d^1, \sigma) \iff q_d^2 = LC(R(q_d^1, \sigma)). \quad (8)$$

In other words, assuming that the current state in diagnoser G_d is q_d^1 , while the next observable event is σ , we generate the new state q_d^2 of G_d in the following way:

- (1) For each $(q^o, l) \in q_d^1$, compute the set $S(q^o, \sigma)$ of reachable states of G from q^o using observation σ :

$S(q^o, \sigma) = \{T(q^o, u\sigma) \mid u \in \Sigma_{uo}^*, \text{ and } \sigma \in \Sigma_o\}$ (note here that $S(q^o, \sigma)$ is a finite set of observable states, as we have made an assumption (in Section 2.1) that there does not exist any cycle of unobservable events [16]).

- (2) Given $q^{o'} \in S(q^o, \sigma)$ with $T(q^o, u\sigma) = q^{o'}$, propagate label l associated with q^o to label l' associated with $q^{o'}$ according to the following rules:
 - (a) If $l = N$ and s contains no faulty events, then label l' is kept as N .
 - (b) If $l = \{A\}$ and s contains no faulty events, then label l' is kept as $\{A\}$.
 - (c) If $l = \{A\} \cup F$ with $F \subseteq \Sigma_f$ and s contains no faulty events, then label l' is updated to F .
 - (d) If $l = N$ or $\{A\}$ and s contains a set F of faulty events, then label l' is updated to F .
 - (e) If either $l = F$ or $\{A\} \cup F$ with $F \subseteq \Sigma_f$ and s contains a set F' of faulty events, then label l' is updated to $F \cup F'$ (in cases (c), (d), and (e) above, we do not propagate label A from one state to the next. As noted in [16], while this leads to a reduction in the state space of the diagnoser, no information necessary for either determining the diagnosability properties of a language or for implementing diagnostics is lost).
- (3) Let q_d^2 be the set of all pairs $(q^{o'} l')$ generated by (1) and (2) above for each $(q^o, l) \in q_d^1$. Replace all $(q^{o'}, l')$, $(q^{o'}, l'')$ $\in q_d^2$ ($l' \neq l''$) with $(q^{o'}, \{A\} \cup l' \cup l'')$. That is, if the same state $q^{o'}$ appears more than once in q_d^2 with different labels, then associate all the common faults with $q^{o'}$ as well as the ambiguous label A with $q^{o'}$.

Example 6. With reference to Example 2 and Example 4, Figure 1(c) presents the classical diagnoser G_d relevant to DES G displayed in Figure 1(a) (where pairs (q, l) are written as ql , while “ $\{\}$ ” is omitted for each nonempty fault label l for simplicity). According to G_d in Figure 1(c), we can easily obtain the definite diagnosis $\{f_1\}$, for a given observation sequence $\alpha\beta\theta\gamma\gamma$, online by synchronizing diagnoser G_d with the sequence.

2.3. Classical Diagnosability of DESs. To decide whether or not a faulty event in a DES has definitely occurred, the classical notion of diagnosability presented by [16] is

rephrased in Definition 2 (Definition 2 is slightly different from the original definition of diagnosability in [16]. Specifically, “ $\exists n_i (n_i \in \mathbb{N})$ ” is placed after “ $\forall s (s \in L, s_e = f_i)$ ”, while n_i in [16] becomes the greatest n_i for all s in Definition 2. This adjustment, while not affecting the virtual meaning of diagnosability, allows us to provide a formalization that is more consistent with the notions of minimal diagnosability introduced below).

Definition 2. A prefix-closed and live language L is said to be diagnosable iff, for any fault $f_i \in \Sigma_f$, we have

$$\begin{aligned} &\forall s (s \in L, s_e = f_i) \exists n_i (n_i \in \mathbb{N}), \\ &\forall t (t \in L/s, t_e \in \Sigma_o), \\ &(\|t\| \geq n_i \implies D), \end{aligned} \quad (9)$$

where the diagnosability condition D is defined as follows:

$$\omega \in \text{Prj}_{\Sigma_o}^{-1}(\text{Prj}_{\Sigma_o}(st)) \implies f_i \in \omega. \quad (10)$$

In other words, if a DES G is diagnosable, then any faulty event f_i of G will definitely be detected after its occurrence, provided that the observation sequence after f_i is long enough.

Example 7. From Definition 2, we know that DES G in Figure 1(a) is not diagnosable, since for observation sequences $\alpha\rho^k$, $k \in \mathbb{N}$, we cannot decide whether fault f_2 has definitely occurred or not.

3. Minimal Diagnosis of DESs

In this section, in a way similar to the minimal diagnosis of static systems [41, 42], a notion of the “minimal diagnosis” of DESs is proposed. Then, the related “minimal diagnoser” for DESs is presented to generate all minimal diagnoses. Finally, the relevant “minimal diagnosability” is put forward and compared with classical diagnosability.

3.1. Minimal Diagnosis of DESs. Based on Definition 1 and Example 5, for a given observation sequence, there are three possible candidate diagnoses. Generally, given a DES G with language L , there is usually more than one string in L , with each string having a projection on the set of observable events equal to the current observation sequence obs . Hence, there may be more than one candidate diagnosis set according to the different strings. However, as noted above, minimal diagnoses are very valuable. For example, for a batch of new products from a factory, the qualification rate is usually very high (generally required to be more than 95%). The probability of a product with a fault is very low (less than 5%). According to the principles of joint probability distribution (usually, in the literature, it is assumed that faults are independent of one another and have equal probability of occurrence), the probability of a product with two or more faults is significantly lower.

To obtain more likely candidates and to reduce the space complexity (with less space to store diagnoses with fewer faults), we provide a definition below to formalize the

concept of the minimal diagnosis of DESs based on set-inclusion relationship.

Let F_1 and F_2 be two candidate diagnoses for an observation sequence obs , namely, $(F_1 \rightsquigarrow \text{obs}) \wedge (F_2 \rightsquigarrow \text{obs})$. The following notation is defined:

$$F_1 \leq F_2 \text{ if } F_1 \subseteq F_2$$

$$F_1 < F_{2ss} \text{ if } F_1 \subset F_2$$

$$F_1 < > F_2 \text{ if } (F_1 \not\subseteq F_2) \wedge (F_2 \not\subseteq F_1)$$

Definition 3. Let $G = (Q, \Sigma, T, q_0)$ be a DES, obs be a relevant observation sequence, and F be a candidate diagnosis for obs . Candidate F is called a minimal diagnosis of G for obs , also written as $F \rightsquigarrow_{\min} \text{obs}$, if there is no other candidate diagnosis F' for obs such that $F' < F$. The family of all minimal candidate diagnoses for obs is $\{F \mid F \rightsquigarrow_{\min} \text{obs}\}$.

In other words, if a fault set F is a minimal diagnosis of G , then none of its proper subsets is a diagnosis. Furthermore, according to the principle of joint-probability distribution, a minimal diagnosis (with fewer number of faults) is more probable than the corresponding nonminimal diagnosis (with additional faults). As a result, some faulty events may not appear in the minimal diagnosis, although they can also be used to explain the current observation sequence. The following example explicitly verifies this conclusion.

Example 8. With reference to Example 5, for the DES G displayed in Figure 1(a), when the current observation sequence is $\text{obs} = \alpha\beta\theta$, we find that all the possible candidate diagnoses are \emptyset (or N), $\{f_1\}$, and $\{f_1, f_2\}$. Then, we get the minimal diagnosis N , i.e., the system is probably working normally. Although two fault sets $\{f_1\}$ and $\{f_1, f_2\}$ can also be used to explain the current observation sequence, they are not minimal diagnoses.

3.2. Minimal Diagnoser for DESs. In this section, we propose a type of minimal diagnoser based on a revised diagnoser.

3.2.1. Revised Diagnoser. In order to properly and briefly define the concept of a minimal diagnoser, we first introduce a revised diagnoser G^d based on the classical notion of diagnoser G_d presented in [16].

Starting from $G^o = (Q^o, \Sigma_o, T^o, q_0)$, a revised diagnoser G^d for G is a deterministic FSM:

$$G^d = (Q^d, \Sigma_o, T^d, q_0^d), \quad (11)$$

where

$Q^d \subseteq 2^{(Q^o \times \Delta)}$ is the set of states.

$q_0^d = \{(q_0, N)\}$. Any state $Q^d \in Q^d$ is reachable from q_0^d via transitions in T^d , written as $Q^d = \{(q_1^o, l_1), \dots, (q_n^o, l_n)\}$, where $q_i^o \in Q^o$ and $l_i \in \Delta$ (that is, l_i is in the form of either N or a nonempty subset of Σ_f).

The transition function $T^d: Q^d \times \Sigma_o \rightarrow Q^d$ is defined as follows:

$$T^d(Q^d, \sigma) = \bigcup_{(q^o, l) \in Q^d} \left(\bigcup_{s \in L_\sigma(G, q^o)} \{(T(q^o, s), LP(q^o, l, s))\} \right). \quad (12)$$

In other words, assume that q_1^d is the current state in the revised diagnoser G^d and that σ is the next observable event. The new state q_2^d of G^d is generated in the following way (the revised diagnoser can also be computed by performing a parallel composition between G and the label automaton Al , as suggested in the book by Cassandras and Lafortune [14], where Al is an automaton whose initial state is N , whose remaining (2^{p-1}) states are nonempty subsets of $\{f_1, f_2, \dots, f_p\}$, with p being the number of faulty events, and whose transition events are f_1, f_2, \dots, f_p when appropriate):

- (1) For each $(q^o, l) \in q_1^d$, compute the set $S(q^o, \sigma)$ of reachable states of G from q^o over observable event σ :

$$S(q^o, \sigma) = \{T(q^o, u\sigma) \mid u \in \Sigma_{uo}^*, \text{ and } \sigma \in \Sigma_o\}. \quad (13)$$

- (2) Given $q^{o'} \in S(q^o, \sigma)$ with $T(q^o, u\sigma) = q^{o'}$, propagate fault label l related to q^o to fault label l' related to $q^{o'}$ as follows: $l' = l \cup \{f_i \mid f_i \in u\}$.
- (3) Let q_2^d be the set of all pairs $(q^{o'}, l')$, generated by the above steps (1) and (2), for each $(q^o, l) \in q_1^d$.

According to the definitions of G^d and G_d , we can find that for each state in G^d , there is a corresponding state in G_d ; the contrary, however, is not always the case. In addition, an important difference between G^d and G_d is that the symbol A is not introduced in G^d . Hence, we can retain more relevant fault information (for obtaining the minimal diagnosis). For example, if one state $Q^d \in G^d$ is $\{(q_i, f_i), (q_j, f_j)\}$, then the two minimal diagnoses $\{f_i\}$ and $\{f_j\}$ are both kept, that is, clearer fault information is provided compared with G_d . In fact, the fault information in G_d is denoted only as A in this situation, and the necessary fault information is missing (e.g., states $\{(18, \{A\})\}$ and $\{(15, \{A\})\}$ in Figure 1(c)). Additionally, some relevant fault information is again missing for all possible diagnoses, according to rules (c), (d), and (e) when propagating fault label l , including A , into l' because the ambiguous symbol A is omitted (see Section 2.2 and the transition from state $\{(5, \{f_1\}), (10, \{A, f_1\})\}$ to state $\{(10, \{f_1\})\}$ in Figure 1(c)). In contrast, all possible fault information is preserved in the revised diagnoser G^d .

Example 9. With reference to Example 2 and Example 4, Figure 1(d) presents the revised diagnoser G^d relevant to the DES G displayed in Figure 1(a) (similar to Example 6, each pair (q, l) is written as ql , while, for the sake of simplicity, “ $\{\}$ ” is omitted for each nonempty fault label l).

Notice how all possible fault information is maintained in G^d , which can be conveniently exploited by a minimal diagnoser for the minimization of fault sets.

3.2.2. *Minimal Diagnoser.* To efficiently generate all minimal diagnoses of a DES online, we propose a novel notion of minimal diagnoser, which can be generated offline.

Definition 4. Given a DES $G = (Q, \Sigma, T, q_0)$, the related $G^o = (Q^o, \Sigma_o, T^o, q_0)$, and the revised diagnoser $G^d = (Q^d, \Sigma_o, T^d, q_0^d)$, a minimal diagnoser for G is an FSM:

$$G^m = (Q^m, \Sigma_o, T^m, q_0^m), \quad (14)$$

where

$Q^m \subseteq 2^{(Q^o \times \Delta)}$ is the set of states.

$q_0^m = \{(q_0, N)\}$. Any state $q^m \in Q^m$ is reachable from q_0^m via transitions in T^m , written as $q^m = \{(q_1^o, l_1), \dots, (q_n^o, l_n)\}$, where $q_i^o \in Q^o$ and $l_i \in \Delta$ (that is, l_i is in the form of either N or a nonempty subset of Σ_f).

$T^m: Q^m \times \Sigma_o \rightarrow Q^m$ is the transition function.

More specifically, T^m and Q^m are generated as follows:

- (1) For each $q_i^d \in Q^d$, there exists a corresponding minimized state $q_i^m \in Q^m$, obtained as follows: initially, $q_i^m = q_i^d$; then, for each $(q^o, l) \in q_i^d$, any other $(q^{o'}, l') \in q_i^d$ with $l < l'$ will be removed from q_i^m (in particular, state $q^{o'}$ may equal q^o). In other words, all the pairs labelled with nonminimal fault labels will be dropped.
- (2) For each transition $(q_i^d \xrightarrow{\sigma} q_j^d) \in T^d$ (where $\sigma \in \Sigma_o$ and $q_i^d, q_j^d \in Q^d$), there is a corresponding transition $(q_i^m \xrightarrow{\sigma} q_j^m) \in T^m$ (where $q_i^m, q_j^m \in Q^m$).
- (3) All states and transitions in G^m are generated by the abovementioned steps (1) and (2).
- (4) Trim operation: if any two minimal states share not only the same contents but also the same transitions from them (to the same states), they will be seen as the same state and be merged into one state. Otherwise, they will not be merged even if they have the same contents.

From the definition of minimal diagnoser, any state in the revised G^d is transformed into a state in the minimal diagnoser G^m , though generally with the same or fewer labels (there may be several different states in G^d that have been transformed into one state in G^m).

In other words, the minimal diagnoser G^m , with the same number of states and the same isomorphic transition structure as those of the classical diagnoser G_d , is a deterministic (and trim) FSM, where each state is generally smaller than the corresponding state in G_d (although the space complexity of G^m is still exponential regarding the number of states of the system model, since only the minimal fault labels are retained, less space is required. Although, for simplicity, the theoretical definition of minimal diagnoser is based on that of the revised diagnoser G^d , we would actually like to consider some algorithms that generate a minimal diagnoser based only on the DES G in some special situations, without the need to generate G^d again. This is an interesting topic that should be analysed in future research).

Remark 1. Based on the definition of a “minimal diagnoser,” it seems that some nonminimal diagnoses will be lost as well as the diagnosis completeness of the requirement in model-based diagnosis. As a matter of fact, the property of minimal-diagnosis completeness is indeed preserved by the minimal diagnoser, that is, most probable diagnoses are retained in the diagnosis results.

Remark 2. Like the classical diagnoser, the minimal diagnoser can generally be built offline and used for online efficient diagnosis.

Example 10. Figures 2(a) and 2(b) show two different DESs and their different diagnosers G_d , G^d , and G^m . We can see that G^m is isomorphic to the corresponding G_d . Also, note that in Figure 2(a), two states of G^d , namely, $(3N \ 3f_1)$ and $(3N \ 3f_2)$, are merged into one state $(3N)$ in G^m after minimization. By contrast, in Figure 2(b), two states of G^d , namely, $(4N \ 5f_1)$ and $(4N \ 6f_2)$, are not merged into one state $(4N)$ in G^m , as they have different transitions from themselves (to different states).

According to Definition 4, a number of relevant properties of minimal diagnoser G^m are given below (which will be used to prove the subsequent related lemmas/propositions):

(P₁) Let $q_i^m \in Q^m$. For each $(q_i^o, l_i) \in q_i^m$, there is at least a state $q_i^d \in Q^d$ in G^d such that $(q_i^o, l_i) \in q_i^d$.

(P₂) Let $q^m \in Q^m$. If $(q^o, l), (q^{o'}, l') \in q^m$, then there exist $s, s' \in L$ with $s_e, s'_e \in \Sigma_o$ such that $T(q_0, s) = q^o$, $T(q_0, s') = q^{o'}$, $\text{Prj}_{\Sigma_o}(s) = \text{Prj}_{\Sigma_o}(s')$, $P_{\Sigma_f}(s) = l$, $P_{\Sigma_f}(s') = l'$, and either $l = l'$ or $l < l'$.

(P₃) Let $q^m \in Q^m$. There may exist $(q^o, l), (q^{o'}, l') \in q^m$, that is, the system might reach the same observable state q^o with different minimal fault labels ($l \neq l'$).

(P₄) For each $q^m \in Q^m$ and for each $(q^o, l), (q^{o'}, l') \in q^m$, we have

$$\begin{aligned} l = l' &\iff l \subseteq l' \\ l \neq l' &\iff l < l' \end{aligned}$$

(P₅) Let $(q_i^m \xrightarrow{\sigma} q_j^m) \in T^m$. For each $(q_j^o, l_j) \in q_j^m$, there exists $(q_i^o, l_i) \in q_i^m$ such that $l_i \subseteq l_j$.

After (offline) building the minimal diagnoser G^m for DES G and assuming that the current observation is obs , we can (online) synchronize obs with G^m to reach the corresponding state in G^m to directly obtain the minimal diagnoses within the state.

Example 11. Consider the DES G outlined in Figure 1(a) and assume $\text{obs} = \alpha\beta\theta$. According to the minimal diagnoser G^m outlined in Figure 1(e), we obtain the current minimal diagnosis N , that is, no fault is produced by $(4, N)$. In addition, when we receive the additional observation γ , we obtain the new minimal diagnosis $\{f_1\}$ (while the non-minimal diagnosis $\{f_1, f_2\}$ in label $(10, \{f_1, f_2\})$ of G^d is avoided).

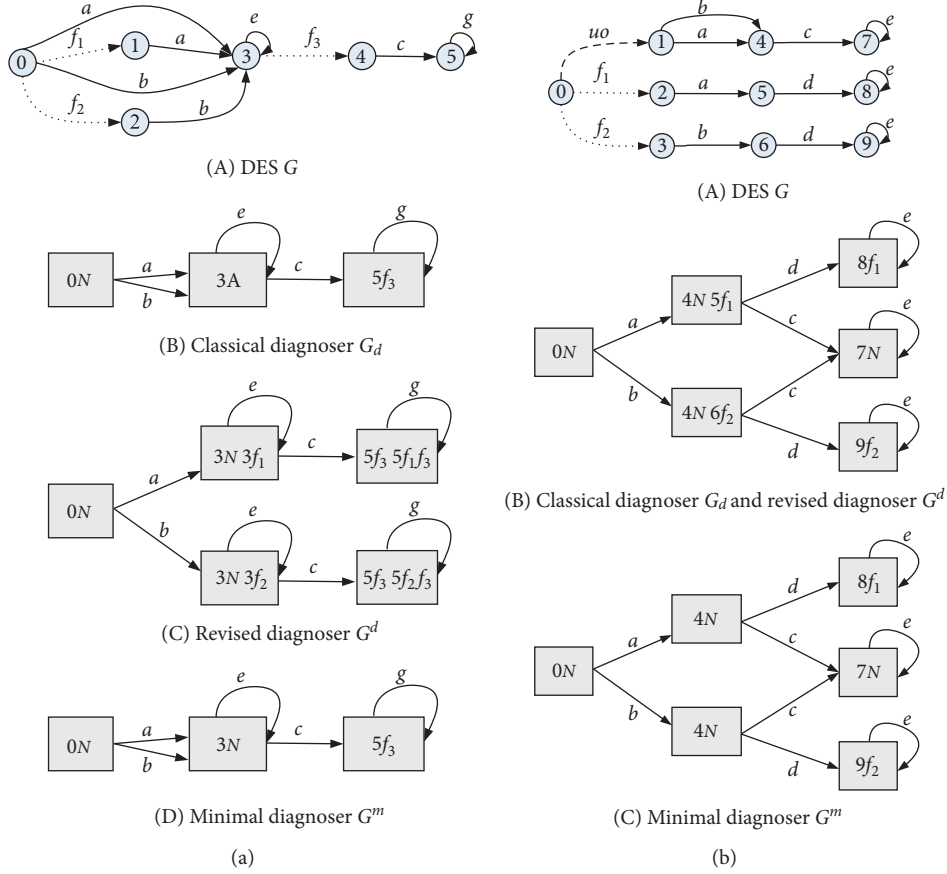


FIGURE 2: Two DESs and their minimal diagnosers: (a) the first DES and (b) the second DES.

3.3. Minimal Diagnosability of DESs. Just as the classical diagnosability was defined to determine whether a classical diagnosis has definitely occurred or not, it is natural to define minimal diagnosability to determine whether a set of faults has definitely occurred or not.

In this section, to either strongly or weakly determine whether a set of faults has definitely occurred or not, two notions (strong and weak) of the minimal diagnosability of DESs are proposed.

To introduce the formalizations for the minimal diagnosability of a DES G , we define the domain \mathcal{F}_L to denote the collection of all possible fault sets of G (with behaviour L) as follows:

$$\mathcal{F}_L = \bigcup_{s \in L \wedge s_e \in \Sigma_o} \{ \{f_i \mid f_i \in s\} \}. \quad (15)$$

Obviously, $\mathcal{F}_L = \bigcup_{s \in L \wedge s_e \in \Sigma_o} \{ P_{\Sigma_f}(s) \}$.

3.3.1. Strong Minimal Diagnosability of DESs

Definition 5. A prefix-closed and live language L is said to be strongly minimally diagnosable if, for any fault set $F \in \mathcal{F}_L$ and for any string $s \in S_F$, the following properties hold:

$$(i) \forall t (t \in L/s, t_e \in \Sigma_o, P_{\Sigma_f}(t) \subseteq F) \exists t' (t' \in L/(st), (tt')_e \in \Sigma_o, P_{\Sigma_f}(t') \subseteq F) ((F \rightsquigarrow_{\min} \text{Prj}_{\Sigma_o}(st)) \implies D_m^1)$$

$$(ii) \exists n (n \in \mathbb{N}) \forall t (t \in L/s, t_e \in \Sigma_o) (\|t\| \geq n \implies ((F \rightsquigarrow_{\min} \text{Prj}_{\Sigma_o}(st)) \implies D_m^2))$$

where the strong minimal diagnosability conditions D_m^1 and D_m^2 are defined as follows:

$$D_m^1: (\omega \in \text{Prj}_{\Sigma_o}^{-1}(\text{Prj}_{\Sigma_o}(stt'))) \implies (F \preceq P_{\Sigma_f}(\omega)), \quad (16)$$

$$D_m^2: (\omega \in \text{Prj}_{\Sigma_o}^{-1}(\text{Prj}_{\Sigma_o}(st))) \implies (F \preceq P_{\Sigma_f}(\omega)).$$

In other words, assume that s is a trace in G ending with one fault of F and containing exactly the faulty events of F :

- (i) For any continuation t of string s without any new fault, the DES will always reach an observable state after a continuation t' of t (i.e., $(tt')_e \in \Sigma_o$), also without any new fault, such that if F is a minimal fault set for st , then F will be the unique minimal diagnosis for any trace with the same observation sequence in stt' (here, we make an implicit assumption that a faulty event may be triggered by a string many times. In other words, if all faulty events in F have been triggered by string s , then some faults in F may still be triggered again in a suffix string t after s).
- (ii) In addition, it is required that there is always a natural number n such that when any continuation t

of s is long enough (i.e., the length of t is not less than n), if F is a minimal fault set for st , then F will be the unique minimal diagnosis for any trace with the same observation sequence in st .

Note: in contrast with the notion of classical diagnosability (Definition 2), here, we add two additional conditions, namely, $P_{\Sigma_f}(t) \subseteq F$ and $P_{\Sigma_f}(t') \subseteq F$, to restrict later subsequences, after the complete occurrence of F , such that they do not contain any new fault, except those in F , to ensure that F is still retained as a candidate diagnosis.

In [16], the notion of classical diagnosability is proposed for checking any single fault f_i of G (Definition 2), whereas our notion of minimal diagnosability is proposed for a set F of faulty events of G , which must be minimal (compared to other related candidates). Both require that any fault f_i or any minimal fault set F must be definitely detected after their occurrences (within a finite delay).

However, there is no logic entailment between the classical diagnosability and our strong minimal diagnosability, as shown in the following example.

Example 12. According to Definition 2 and Definition 5, DES G in Figure 1(a) is strongly minimally diagnosable yet not diagnosable (we can verify the strong minimal diagnosability of the DES in Figure 1(a) based on Proposition 1 below. That is, we can check the minimal diagnoser in Figure 1(e). It is much easier to find that the minimal diagnoser satisfies the following two conditions in Proposition 1: (1) there is no F -indeterminate cycle and (2) there is no F -incomparable state. Thus, the DES in Figure 1(a) is strongly minimally diagnosable). By contrast, DES G_3 in Figure 3(e) is diagnosable yet not strongly minimally diagnosable.

Before introducing the necessary and sufficient conditions for the strong minimal diagnosability of DESs, a number of related definitions and relevant lemmas are provided below.

Definition 6. A state $q^m \in Q^m$ is said to be F -certain if, for any two pairs $(q^o, l), (q^{o'}, l') \in q^m$ (where $q^{o'}$ can possibly equal q^o), we always have $l' = l$.

A state $q^m \in Q^m$ is said to be F -incomparable if there exist two pairs $(q^o, l), (q^{o'}, l') \in q^m$ (where $q^{o'}$ can possibly equal q^o) such that $l < > l'$.

For instance, the state exactly labelled with $\{4f_1, 5f_2\}$ in Figure 3 is F -incomparable, whereas other states of minimal diagnosers in Figure 3 are all F -certain. The basic properties of the two types of states are described by the following lemma.

Lemma 1. *For the minimal diagnoser G^m of DES G , the following properties hold.*

Let $T^m(q_0^m, s) = q^m, s \in \Sigma_o^*$. If state q^m with fault label l is F -certain, then for each $\omega \in \text{Prj}_{\Sigma_o}^{-1}(s)$, we have $l \preceq P_{\Sigma_f}(\omega)$.

If a state $q^m \in Q^m$ is F -incomparable, then for any two pairs $(q^o, l), (q^{o'}, l') \in q^m$ with $l \neq l'$, there exist two strings $t, t' \in L$ with $t_e, t'_e \in \Sigma_o$ such that $T(q_0, t) = q^o$,

$$T(q_0, t') = q^{o'}, \text{Prj}_{\Sigma_o}(t) = \text{Prj}_{\Sigma_o}(t'), T^m(q_0^m, \text{Prj}_{\Sigma_o}(t)) = q^m, l = P_{\Sigma_f}(t), l' = P_{\Sigma_f}(t'), \text{ and } l < > l'.$$

In other words, if a state q^m is F -certain, then any trace ω with the same observation projection as observation sequence s will necessarily contain fault set l . Otherwise, if a state q^m is F -incomparable, then there exist at least two different traces t and t' having the same observation projection but with two incomparable fault sets l and l' .

Definition 7. A set of F -incomparable states $q_1^m, q_2^m, \dots, q_n^m \in Q^m$ is said to form an F -indeterminate cycle if $T^m(q_i^m, \sigma_i) = q_{(i+1) \bmod n}^m$ (here, " $(i+1) \bmod n$ " represents the modulus of $(i+1)$ divided by n), where $\sigma_i \in \Sigma_o, i \in [1 \dots n]$.

Based on Definition 7, an interesting lemma is given below.

Lemma 2. *Assume that $q_1^m, q_2^m, \dots, q_n^m \in Q^m$ are a set of F -incomparable states forming an F -indeterminate cycle, where*

$$q_i^m = \{(q_{i_1}^o, l_{i_1}), (q_{i_2}^o, l_{i_2}), \dots, (q_{i_{\text{len}_i}}^o, l_{i_{\text{len}_i}})\},$$

$$q_j^m = \{(q_{j_1}^o, l_{j_1}), (q_{j_2}^o, l_{j_2}), \dots, (q_{j_{\text{len}_j}}^o, l_{j_{\text{len}_j}})\},$$
(17)

with $i, j \in [1 \dots n]$ and $\text{len}_i, \text{len}_j$ denoting the number of pairs in q_i^m and q_j^m , respectively. Then, we have

$$\{l_{i_1}, l_{i_2}, \dots, l_{i_{\text{len}_i}}\} = \{l_{j_1}, l_{j_2}, \dots, l_{j_{\text{len}_j}}\}.$$
(18)

In other words, in an F -indeterminate cycle, any state has the same set of different fault labels. Intuitively, on the one hand, a fault in the current state will stay in the next state (we assume that the faults are persistent); on the other hand, since all states form a cycle, the previous state of the current one can also be seen as the next state. Therefore, all states share the same faults (in fact, Lemma 2 is true for all kinds of cycles. That is, the conclusion is much clearer when all states in the cycle are F -certain).

Lemma 3. *Given a prefix-closed language L , if $F \rightsquigarrow_{\min} \text{Prj}_{\Sigma_o}(s)$ holds for a fault set $F \in \mathcal{F}_L$ and a string $s \in L$ with $s_e \in \Sigma_o$ and $P_{\Sigma_f}(s) = F$, then for any string $t \in L/s$ with $t_e \in \Sigma_o$ and $P_{\Sigma_f}(t) \subseteq F$, we have $F \rightsquigarrow_{\min} \text{Prj}_{\Sigma_o}(st)$.*

In other words, if a fault set F of a trace s is a minimal diagnosis for the observation projection of s , then F is still a minimal diagnosis for any subsequent longer trace from s , provided there is no new fault in the subsequent trace.

Lemma 4. *Given a prefix-closed language L , $F \rightsquigarrow_{\min} \text{Prj}_{\Sigma_o}(s)$ holds for a fault set $F \in \mathcal{F}_L$ and a string $s \in L$ with $s_e \in \Sigma_o$ and $P_{\Sigma_f}(s) = F$. If F is the unique minimal diagnosis for observation $\text{Prj}_{\Sigma_o}(s)$, i.e.,*

$$\omega \in \text{Prj}_{\Sigma_o}^{-1}(\text{Prj}_{\Sigma_o}(s)) \implies F \preceq P_{\Sigma_f}(\omega),$$
(19)

then for each string $t \in L/s$ with $t_e \in \Sigma_o$, the following holds:

$$\omega' \in \text{Prj}_{\Sigma_o}^{-1}(\text{Prj}_{\Sigma_o}(st)) \implies F \preceq P_{\Sigma_f}(\omega').$$
(20)

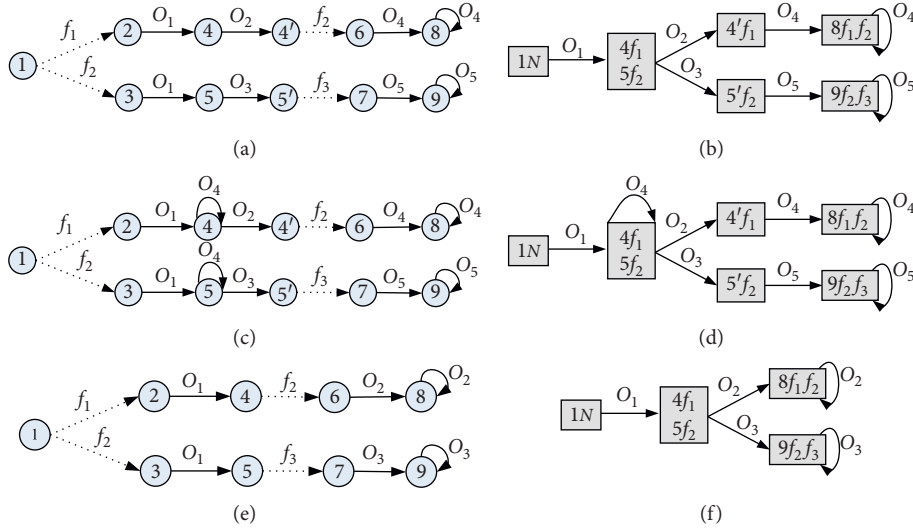


FIGURE 3: DES models and minimal diagnosers. (a) DES model G_1 . (b) Minimal diagnoser G_m^1 for G_1 . (c) DES model G_2 . (d) Minimal diagnoser G_m^2 for G_2 . (e) DES model G_3 . (f) Minimal diagnoser G_m^3 for G_3 .

In other words, if F is the unique minimal diagnosis for a string s (and its projection on the observation is $\text{Prj}_{\Sigma_o}(s)$), then any trace with the same observation $\text{Prj}_{\Sigma_o}(st)$ will still contain all the faults in F .

Given the definitions and lemmas introduced above, we now present the necessary and sufficient conditions for the strong minimal diagnosability of a DES G in Proposition 1, based on its minimal diagnoser G^m .

Proposition 1. *A language L generated by an FSM G is strongly minimally diagnosable iff its minimal diagnoser G^m satisfies the following two conditions:*

(C₁) *There is no F -indeterminate cycle in G^m*

(C₂) *For each F -incomparable state $q^m \in Q^m$ and for each pair $(q^o, l) \in q^m$, there exist a state $q^{m'}$ and a nonempty observation sequence $s_o \in \Sigma_o^+$ such that $T^m(q^m, s_o) = q^{m'}$, and for each pair (q^o, l') , we have $l' = l$, that is, $q^{m'}$ (after q^m) is an F -certain state with the unique minimal fault label l*

Remark 3. Condition (C₁) is almost identical to the first condition for checking the classical diagnosability in [16], with the exception that “ F_i -indeterminate cycle” is replaced by “ F -indeterminate cycle”. However, Condition (C₂) is more complex than the corresponding one for checking the classical diagnosability (where only one statement is needed, namely, “No state $q \in q_d$ is ambiguous”), as the strong minimal diagnosability is conceptually more complex.

Example 13. Consider the three DES models G_1 , G_2 , and G_3 in Figure 3, where f_1 , f_2 , and f_3 are faults, while the other events are observable. Their minimal diagnosers G_m^1 , G_m^2 , and G_m^3 are also depicted in Figure 3. According to the three minimal diagnosers, we can find that only G_1 is strongly minimally diagnosable. G_2 is not strongly minimally diagnosable because it does not fulfil Condition (C₁): there does

exist an F -indeterminate cycle including state $\{(4, \{f_1\}), (5, \{f_2\})\}$ and the cyclic transition event o_4 in G_2^m . G_3 is also not strongly minimally diagnosable because it does not fulfil Condition (C₂): there does exist an F -incomparable state $q^m = \{(4, \{f_1\}), (5, \{f_2\})\}$ in G_3^m , but there are no states such as $\{(4', \{f_1\})\}$ or $\{(5', \{f_2\})\}$ after q^m in G_3^m .

3.3.2. Weak Minimal Diagnosability of DESs. As mentioned above, according to Definition 5, it is required that any minimal fault set F be the unique minimal diagnosis after a finite delay but before a new faulty event (not in F) occurs. In theory, the condition is very strong. Therefore, we provide the following notion of the weak minimal diagnosability of a DES.

Definition 8. A prefix-closed and live language L is weakly minimally diagnosable if the following condition holds:

$$\begin{aligned} & \forall F (F \in \mathcal{F}_L), \\ & \forall s (s \in S_F), \\ & \exists n (n \in \mathbb{N}), \\ & \forall t (t \in L/s, t_e \in \Sigma_o), \\ & (t \geq n \implies D_m), \end{aligned} \quad (21)$$

where the minimal diagnosability condition D_m is defined in the following way:

$$(F \rightsquigarrow_{\min} \text{Prj}_{\Sigma_o}(st)) \implies (\omega \in \text{Prj}_{\Sigma_o}^{-1}(\text{Prj}_{\Sigma_o}(st)) \implies F \preceq P_{\Sigma_f}(\omega)). \quad (22)$$

In other words, assume that s is a trace of G ending with a set F of faulty events. For each continuation trace t of s , there always exists a natural number n such that when the length of trace t is greater than or equal to n , and if F is still the minimal fault set for st , then fault set F will be the unique minimal diagnosis for any trace with the same observation projection on st .

If the language of a DES has the property of weakly minimal diagnosability, when a trace is long enough (i.e., the length of its continuation t is not less than a given integer n), and if the set of faulty events in the trace is still minimal, then it will definitely be the unique minimal diagnosis. According to the above analysis, the condition of Definition 8 is weaker than that provided in Definition 5 and Definition 2. The following proposition shows the relations between the representation of classical diagnosability and our two representations of minimal diagnosability.

Proposition 2. *Let G be a DES with language L . If L is strongly minimally diagnosable, then L is also weakly minimally diagnosable. If L is diagnosable, then L is also weakly minimally diagnosable.*

However, based on the following example, we can show that the contrary of Proposition 2 does not hold.

Example 14. According to our definitions, we can see that DES G_3 in Figure 3(e) is weakly minimally diagnosable yet not strongly diagnosable. In contrast, the DES G in Figure 1(a) is weakly minimally diagnosable yet not diagnosable.

Remark 4. The notion of minimal diagnosability allows missed detection. That is, it is possible that some of the failures are not detected by a minimal diagnoser. For example, the occurrence of f_2 cannot be detected in the DES model shown in Figure 1(a), although the DES is also weakly minimally diagnosable. After all, only subset-minimal diagnoses are taken into account in our framework.

In the following, we give the necessary and sufficient conditions for the weak minimal diagnosability of a DES.

Proposition 3. *A language L generated by an FSM G is weakly minimally diagnosable iff its minimal diagnoser G^m does not include any F -indeterminate cycle.*

Remark 5. Compared with the necessary and sufficient conditions for the strong minimal diagnosability of DESs in Proposition 1, the conditions for weak minimal diagnosability for the DESs in Proposition 3 are much weaker.

Example 15. Consider the three DESs and the related minimal diagnosers shown in Figure 3. Based on the three minimal diagnosers, we conclude that both G_1 and G_3 are weakly minimally diagnosable. Instead, G_2 is not weakly minimally diagnosable, as there is an F -indeterminate cycle that includes the only state $\{(4, \{f_1\}), (5, \{f_2\})\}$ and the corresponding cyclic transition event o_4 in G_2^m .

4. Related Work and Comparison

Several works aimed at finding only the minimal diagnosis of DESs are based on either AI planning [43, 44] or SAT approaches [45]. Significantly, they require first to transform a diagnosis problem description into the corresponding knowledge representation, generally with the bottleneck of quickly solving planning or SAT problems for online

diagnosis. However, we generate minimal diagnoses by minimal diagnoser only, which is the main advantage of our approach.

In addition, we compared our method with many other related approaches for diagnosis in different views:

- (1) Minimal diagnosis of static systems vs. minimal diagnosis of DESs: Similarity: Like the minimal diagnosis of static systems [41, 42], the minimal diagnosis of DESs is also quite valuable.
 - (a) First, a diagnosis with fewer faults is more probable than one with more faults
 - (b) Second, some space is saved by a minimal diagnosis than corresponding superset diagnoses with very large sizes

Difference: a superset diagnosis of the static system is still a diagnosis, but a superset may not be a diagnosis for a given observation sequence of a DES.

- (2) Minimal diagnosis vs. diagnosis with probability:
 - (a) Minimal diagnosis does not need probability information, which sometimes cannot present quite precise diagnoses.
 - (b) Diagnosis with explicit fault probability based on Bayesian/probabilistic reasoning [32–35] can offer precise diagnoses in a mathematically rigorous way. However, the shortcomings of these approaches may be twofold.
 - (i) First, the prior probability of each faulty event is required, which may be difficult to obtain in practice
 - (ii) Second, adding the probability of each faulty event will possibly make the diagnosis process more complex

5. Conclusions

In this paper, to focus on the more likely diagnoses, a notion of minimal diagnosis of DESs is proposed, where only subset-minimal fault sets are considered as the most probable explanations for the given observation sequences. Then, the notion of a minimal diagnoser is proposed for the online minimal diagnosis of DESs. Moreover, two sorts of minimal diagnosability are presented for deciding whether a DES is strongly/weakly minimally diagnosable or not, along with necessary and sufficient conditions for testing the minimal diagnosability, which are based on the notion of a minimal diagnoser. Finally, the basic relationships among the three types of diagnosability (classical diagnosability and the two novel notions of minimal diagnosability) are presented.

However, since the generation of the minimal diagnoser requires the availability of the whole DES model, a problem of complexity may arise if the DES is large (which is normal for real, possibly distributed systems). To cope with this problem, as in previous approaches to developing decentralized diagnosers, a challenging goal for future research is the decentralization/distribution of minimal diagnoses.

The paper is conceived to provide a theoretical/formal foundation for the minimal diagnosis and minimal diagnosability of DESs. Unfortunately, as far as we know, although there are several real case studies on the diagnosis of DESs (e.g., the hydraulic circuit case [46]), there are still no widely used artificially well-designed or widely used real-application benchmarks for the diagnosis of DESs to be applied for testing the diagnosis approaches. Accordingly, practical applications are one interesting subject for future research as well as an effective/efficient algorithm for constructing a minimal diagnoser of a DES with a sound space complexity.

A polynomial “twin-plant” approach has been proposed in [47, 48] for efficiently testing the diagnosability of DESs. Designing similar polynomial approaches to check the minimal diagnosability of DESs is also an interesting future topic.

Still, a number of important issues must be considered in future research. An essential assumption of this paper is the independence of faults. Although this may be reasonable in a wide variety of contexts, the question remains: how will the notion of the minimal diagnosis of DESs change when fault dependence actually occurs? Another challenging task is the injection of minimal diagnosis into other approaches for the diagnosis of DESs, including those that do not require the generation of a diagnoser (which may be impractical in real-application domains), such as the diagnosis of active systems [21]. Like our model-based distributed minimal diagnosis of static systems [49] or the decentralized/distributed diagnosis of DESs [27–29, 50], the decentralized/distributed minimal diagnosis of DESs is also an interesting and challenging topic. Eventually, only the application of minimal diagnosis to real DESs will provide evidence of its practical utility.

Appendix

Proofs for Properties, Lemmas, and Propositions

Properties of minimal diagnoser G^m :

(P₁) Let $q_i^m \in Q^m$. For each $(q_i^o, l_i) \in q_i^m$, there is at least a state $q_i^d \in Q^d$ in G^d such that $(q_i^o, l_i) \in q_i^d$.

(P₂) Let $q^m \in Q^m$. If $(q^o, l), (q^{o'}, l') \in q^m$, then there exist $s, s' \in L$ with $s_e, s'_e \in \Sigma_o$ such that $T(q_0, s) = q^o$, $T(q_0, s') = q^{o'}$, $\text{Prj}_{\Sigma_o}(s) = \text{Prj}_{\Sigma_o}(s')$, $P_{\Sigma_f}(s) = l$, $P_{\Sigma_f}(s') = l'$, and either $l = l'$ or $l < > l'$.

(P₃) Let $q^m \in Q^m$. There may exist $(q^o, l), (q^{o'}, l') \in q^m$, that is, the system might reach the same observable state q^o while having different minimal fault labels ($l \neq l'$).

(P₄) For each $q^m \in Q^m$ and for each $(q^o, l), (q^{o'}, l') \in q^m$, we have

(i) $l = l' \iff l \subseteq l'$

(ii) $l \neq l' \iff l < > l'$

(P₅) Let $\left(q_i^m \xrightarrow{\sigma} q_j^m \right) \in T^m$. For each $(q_i^o, l_i) \in q_i^m$, there exists $(q_j^o, l_j) \in q_j^m$ such that $l_i \subseteq l_j$.

Proof.

(P₁) According to case (1) of the definition (Definition 4) of a minimal diagnoser, for each $q_i^d \in Q^d$, there exists a state $q_i^m \in Q^m$ with $(q^o, l) \in q_i^d$, with l being the minimal fault label in q_i^d . On the contrary, for each $q_i^m \in Q^m$, we can apply a backward process to G^d to find at least a state q_i^d with $(q^o, l_i) \in q_i^d$, as well as for any other $(q^{o'}, l'_i) \in q_i^d$ (if they exist), such that $l_i < l'_i$.

(P₂) According to the definitions of the revised diagnoser (especially the two functions S and T^d) and the minimal diagnoser, for $(q^o, l), (q^{o'}, l') \in q^m$, we can find two corresponding traces $s, s' \in L$, with $s_e, s'_e \in \Sigma_o$, such that $T(q_0, s) = q^o$ (i.e., to reach the observable state q^o), $T(q_0, s') = q^{o'}$, $\text{Prj}_{\Sigma_o}(s) = \text{Prj}_{\Sigma_o}(s')$ (since s and s' reach the same state q^m , they may have the same observation sequence), and $P_{\Sigma_f}(s) = l$ and $P_{\Sigma_f}(s') = l'$. Because q^o may equal $q^{o'}$, then $l = l'$ may hold; otherwise, $l \not\subseteq l'$ and $l' \not\subseteq l$ (i.e., $l < > l'$). If, for example, $l \subset l'$, then l' will not be a minimal diagnosis. Hence we get the conclusion.

(P₃) As in (P₂), when $q^o = q^{o'}$, i.e., s and s' reach the same observable state, but with $l = P_{\Sigma_f}(s) \neq P_{\Sigma_f}(s') = l'$ and $l < > l'$, then $l \neq l'$.

(P₄) Because q^m is a minimal state, any two fault labels l and l' in q^m are minimal. Then,

- (a) If $l \subseteq l'$, then $l = l'$, since otherwise, if, for instance, $l \subset l'$ but $l \neq l'$, then $l \subset l'$, that is, l is the minimal fault set. However, l' is not, which contradicts the idea that l' is in q^m . On the contrary, if $l = l'$, then obviously $l \subseteq l'$. Thus, $l = l' \iff l \subseteq l'$ holds.
- (b) If $l \neq l'$, then suppose that $l \subset l'$ or $l' \subset l$. In the former case, l' is not minimal, which contradicts the idea that l' is in q^m ; in the latter case, l is not minimal, which also contradicts the idea that l is in q^m . Thus, $l < > l'$ holds. On the contrary, if $l < > l'$, then according to the definition of $< >$, obviously $l \neq l'$. Therefore, $l \neq l' \iff l < > l'$ holds.

(P₅) According to the method for the propagation of labels using T^d (i.e., case (2) of the definition of T^d , where $l' = l \cup \{f_i \mid f_i \in u\}$), l' in the next state is a superset of the label l in the previous state. Accordingly, l_j in q_j^m is a superset of the label l_i in the previous state q_i^m . Thus, $l_i \subseteq l_j$ holds. \square

Lemma A.1. For the minimal diagnoser G^m of DES G , the following properties hold:

- (i) Let $T^m(q_0^m, s) = q^m$, $s \in \Sigma_o^*$. If state q^m with fault label l is F -certain, then for each $\omega \in \text{Prj}_{\Sigma_o}^{-1}(s)$, we have $l \leq P_{\Sigma_f}(\omega)$.
- (ii) If a state $q^m \in Q^m$ is F -incomparable, then for any two pairs $(q^o, l), (q^{o'}, l') \in q^m$ with $l \neq l'$, there exist two strings $t, t' \in L$ with $t_e, t'_e \in \Sigma_o$ such that $T(q_0, t) = q^o$, $T(q_0, t') = q^{o'}$, $\text{Prj}_{\Sigma_o}(t) = \text{Prj}_{\Sigma_o}(t')$, $T^m(q_0^m, \text{Prj}_{\Sigma_o}(t)) = q^m$, $l = P_{\Sigma_f}(t)$, $l' = P_{\Sigma_f}(t')$, and $l < > l'$.

Proof.

(i) For property (i)

In the revised diagnoser G^d for DES G , consider any pair $(q^o, P_{\Sigma_f} | \omega)$ with $Q^d \in Q^d$ and $T^d(q_0, s) = Q^d$.

(a) On the one hand, if $(q^o, P_{\Sigma_f}(\omega))$, then either $l = P_{\Sigma_f}(\omega)$ or $l < > P_{\Sigma_f}(\omega)$ holds. However, if $l < > P_{\Sigma_f}(\omega)$ holds, that is, there exist at least two different fault labels in q^m , then it contradicts the idea that q^m is F -certain. Therefore, only $l = P_{\Sigma_f}(\omega)$ holds, which is also consistent with property (P_1) of a “minimal diagnoser”.

(b) On the other hand, if $(q^o, P_{\Sigma_f}(\omega))$, according to the first condition in Definition 4, we obtain $l < P_{\Sigma_f}(\omega)$. In other words, $P_{\Sigma_f}(\omega)$ is not a minimal diagnosis for observation $\text{Prj}_{\Sigma_o}(s)$.

Based on the above analysis, we have $l < P_{\Sigma_f}(\omega)$.

(b) For property (ii)

It is easy to draw a conclusion from property (P_2) of a “minimal diagnoser.” \square

Lemma A.2. Assume that $q_1^m, q_2^m, \dots, q_n^m \in Q^m$ are a set of F -incomparable states forming an F -indeterminate cycle, where

$$\begin{aligned} q_i^m &= \{(q_{i_1}^o, l_{i_1}), (q_{i_2}^o, l_{i_2}), \dots, (q_{i_{\text{len}_i}}^o, l_{i_{\text{len}_i}})\}, \\ q_j^m &= \{(q_{j_1}^o, l_{j_1}), (q_{j_2}^o, l_{j_2}), \dots, (q_{j_{\text{len}_j}}^o, l_{j_{\text{len}_j}})\}, \end{aligned} \quad (\text{A.1})$$

with $i, j \in [1 \dots n]$ and len_i and len_j denotes the number of pairs in q_i^m and q_j^m , respectively. Then, we have

$$\{l_{i_1}, l_{i_2}, \dots, l_{i_{\text{len}_i}}\} = \{l_{j_1}, l_{j_2}, \dots, l_{j_{\text{len}_j}}\}. \quad (\text{A.2})$$

Proof. For any two adjacent states q_i^m and $q_{(i+1)}^m$ in the F -indeterminate cycle, according to property (P_5) of a “minimal diagnoser,” we have the following.

For any pair $(q_{(i+1)j_{(i+1)}}^o, l_{(i+1)j_{(i+1)}}) \in q_{(i+1)}^m$ ($1 \leq j_{(i+1)} \leq \text{len}_-(i+1)$), there exists $(q_{ij_i}^o, l_{ij_i}) \in q_i^m$ such that $l_{ij_i} \subseteq l_{(i+1)j_{(i+1)}}$.

Then, we have

$$l_{1j_1} \subseteq l_{2j_2}, l_{2j_2} \subseteq l_{3j_3}, \dots, l_{(n-1)j_{(n-1)}} \subseteq l_{nj_n}, \quad (\text{A.3})$$

and then we obtain

$$l_{1j_1} \subseteq l_{2j_2} \subseteq \dots \subseteq l_{(n-1)j_{(n-1)}} \subseteq l_{nj_n}. \quad (\text{A.4})$$

Because $q_1^m, q_2^m, \dots, q_n^m$ form a cycle, then for a pair $(q_{1j_1}^o, l_{1j_1}) \in q_1^m$, according to property (P_5) of a “minimal diagnoser,” there exists a pair $(q_{nkn}^o, l_{nkn}) \in q_n^m$ such that

$$l_{nkn} \subseteq l_{1j_1}. \quad (\text{A.5})$$

From formula (A.4), we obtain

$$l_{1j_1} \subseteq l_{nj_n}. \quad (\text{A.6})$$

From formulas (A.5) and (A.6), we obtain

$$l_{nkn} \subseteq l_{nj_n}. \quad (\text{A.7})$$

From property (P_4) of a “minimal diagnoser,” we have

$$l_{nkn} = l_{nj_n}. \quad (\text{A.8})$$

From formulas (A.5), (A.6), and (A.8), we obtain

$$l_{1j_1} = l_{nj_n}. \quad (\text{A.9})$$

From formulas (A.4) and (A.8), we obtain

$$l_{1j_1} = l_{2j_2} = \dots = l_{nj_n}. \quad (\text{A.10})$$

That is, for any pair with label l_i in any state q_i^m , there exists the same label in each of the other states. Therefore, we have the following conclusion:

$$\{l_{i_1}, l_{i_2}, \dots, l_{i_{\text{len}_i}}\} = \{l_{j_1}, l_{j_2}, \dots, l_{j_{\text{len}_j}}\}. \quad (\text{A.11})$$

\square

Lemma A.3. Given a prefix-closed language L , if $F \rightsquigarrow_{\min} \text{Prj}_{\Sigma_o}(s)$ holds for a fault set $F \in \mathcal{F}_L$ and a string $s \in L$ with $s_e \in \Sigma_o$ and $P_{\Sigma_f}(s) = F$, then for any string $t \in L/s$ with $t_e \in \Sigma_o$ and $P_{\Sigma_f}(t) \subseteq F$, we have $F \rightsquigarrow_{\min} \text{Prj}_{\Sigma_o}(st)$.

Proof. According to the definition of a “minimal diagnosis” (Definition 1 and Definition 3), to prove that $F \rightsquigarrow_{\min} \text{Prj}_{\Sigma_o}(st)$, we have to prove the following two statements:

(i) $F \rightsquigarrow \text{Prj}_{\Sigma_o}(st)$

(ii) $\nexists F'' \subseteq \Sigma_f$ such that $F'' \rightsquigarrow \text{Prj}_{\Sigma_o}(st) \wedge F'' < F$

For the first statement, because $P_{\Sigma_f}(s) = F$ and $P_{\Sigma_f}(t) \subseteq F$, then $F = \text{Prj}_{\Sigma_f}(st)$, that is, $F \rightsquigarrow \text{Prj}_{\Sigma_o}(st)$.

For the second statement, by contradiction, assume that there exists $F'' \subseteq \Sigma_f$ such that $F'' \rightsquigarrow \text{Prj}_{\Sigma_o}(st) \wedge F'' < F$ (i.e., $F'' \subset F$). That is, there exists a string $s'' \in L$ with $\text{Prj}_{\Sigma_o}(s'') = \text{Prj}_{\Sigma_o}(st)$ and $F'' = P_{\Sigma_f}(s'')$.

Let $s'' = s't'$ such that $s' \in S_F$, that is, $s'_e \in \Sigma_o \wedge \text{Prj}_{\Sigma_o}(s') = \text{Prj}_{\Sigma_o}(s)$.

Since $F \rightsquigarrow_{\min} \text{Prj}_{\Sigma_o}(s)$, we have $F \rightsquigarrow_{\min} \text{Prj}_{\Sigma_o}(s')$.

Then, we have two possible cases regarding the relations between F and $P_{\Sigma_f}(s')$:

(A) $F \leq P_{\Sigma_f}(s')$ (also $F \subseteq P_{\Sigma_f}(s')$)

(B) $F < > P_{\Sigma_f}(s')$

For case (A), since $F \subseteq P_{\Sigma_f}(s') \subseteq P_{\Sigma_f}(s't') = P_{\Sigma_f}(s'') = F''$, we get $F \subseteq F''$, which contradicts the assumption that $F'' \subset F$.

For case (B), from $F < > P_{\Sigma_f}(s')$, we get $P_{\Sigma_f}(s') \not\subseteq F$, and then $P_{\Sigma_f}(s't') \not\subseteq F$, that is, $P_{\Sigma_f}(s'') \not\subseteq F$; thus, we get $F'' \not\subseteq F$, which also contradicts the assumption that $F'' \subset F$.

Therefore, the second statement also holds.

Hence, we get the conclusion. \square

Lemma A.4. Given a prefix-closed language L , $F \rightsquigarrow_{\min} \text{Prj}_{\Sigma_o}(s)$ holds for a fault set $F \in \mathcal{F}_L$ and a string $s \in L$ with $s_e \in \Sigma_o$ and $P_{\Sigma_f}(s) = F$. If F is the unique minimal diagnosis for observation $\text{Prj}_{\Sigma_o}(s)$, i.e.,

$$\omega \in \text{Prj}_{\Sigma_o}^{-1}(\text{Prj}_{\Sigma_o}(s)) \implies F \preceq P_{\Sigma_f}(\omega), \quad (\text{A.12})$$

then for each string $t \in L/s$ with $t_e \in \Sigma_o$, and the following holds:

$$\omega' \in \text{Prj}_{\Sigma_o}^{-1}(\text{Prj}_{\Sigma_o}(st)) \implies F \preceq P_{\Sigma_f}(\omega'). \quad (\text{A.13})$$

Proof. For each $\omega' \in \text{Prj}_{\Sigma_o}^{-1}(\text{Prj}_{\Sigma_o}(st))$, we have $\text{Prj}_{\Sigma_o}(\omega') = \text{Prj}_{\Sigma_o}(st)$.

Let $\omega' = s't'$ with $\text{Prj}_{\Sigma_o}(t') = \text{Prj}_{\Sigma_o}(t)$ and $\text{Prj}_{\Sigma_o}(s') = \text{Prj}_{\Sigma_o}(s)$ with $s'_e \in \Sigma_o$; thus, $s' \in \text{Prj}_{\Sigma_o}^{-1}(\text{Prj}_{\Sigma_o}(s))$, and then $F \preceq P_{\Sigma_f}(s')$ (i.e., $F \subseteq P_{\Sigma_f}(s')$).

Then, $F \subseteq P_{\Sigma_f}(s') \subseteq P_{\Sigma_f}(s't') = P_{\Sigma_f}(\omega')$; thus, we get $F \preceq P_{\Sigma_f}(\omega')$.

Therefore, we obtain the following conclusion: $\omega' \in \text{Prj}_{\Sigma_o}^{-1}(\text{Prj}_{\Sigma_o}(st)) \implies F \preceq P_{\Sigma_f}(\omega')$. \square

Proposition A.1. *A language L generated by an FSM G is strongly minimally diagnosable iff its minimal diagnoser G^m satisfies the following two conditions:*

(C₁) *There is no F -indeterminate cycle in G^m*

(C₂) *For each F -incomparable state $q^m \in Q^m$ and for each pair $(q^o, l) \in q^m$, there exist a state $q^{m'} \in Q^m$ and a nonempty observation sequence $s_o \in \Sigma_o^+$ such that $T^m(q^m, s_o) = q^{m'}$, and for each pair (q^o, l') , we have $l' = l$, that is, $q^{m'}$ (after q^m) is an F -certain state with the unique minimal fault label l .*

Proof. Necessity: firstly, we prove that if L is strongly minimally diagnosable, then it satisfies condition (C₁). By contradiction, assume there exist $q_1^m, q_2^m, \dots, q_n^m \in Q^m$ such that they form an F -indeterminate cycle, and let $T^m(q_i^m, \sigma_i) = q_{(i+1) \bmod n}^m$, $\sigma_i \in \Sigma_o$. According to Lemma A.2, let $q_i^m = \{(q_{i_1}^{o_1}, l_{i_1}^1), (q_{i_2}^{o_2}, l_{i_2}^2), \dots, (q_{i_{\text{len}-i_1}}^{o_{\text{len}-i_1}}, l_{i_{\text{len}-i_1}}^{\text{len}-i_1}), \dots, (q_{i_k}^{o_1}, l_{i_k}^1), (q_{i_k}^{o_2}, l_{i_k}^2), \dots, (q_{i_k}^{o_{\text{len}-i_k}}, l_{i_k}^{\text{len}-i_k})\}$, ($1 \leq i \leq n$), where k is the number of different fault labels in q_i^m , and

$$\begin{aligned} l_{i_j}^1 &= l_{i_j}^2 = \dots = l_{i_j}^{\text{len}-i_j} \quad (1 \leq j \leq k), \\ l_{i_r}^1 &> l_{i_s}^1 \quad (1 \leq r, s \leq k, r \neq s), \\ l_{i_x}^1 &= l_{i_y}^1 \quad (1 \leq x, y \leq n, 1 \leq j \leq k). \end{aligned} \quad (\text{A.14})$$

For any two pairs $(q_{1_j}^{o_1}, l_{1_j}^1), (q_{1_m}^{o_1}, l_{1_m}^1) \in q_1^m$ ($1 \leq j, m \leq k$) with $l_{1_j}^1 < l_{1_m}^1$, since q_1^m is F -incomparable, according to Lemma A.1-(ii), there exist two strings $s, s' \in L$ with $s_e, s'_e \in \Sigma_o$ such that $l_{1_j}^1 = P_{\Sigma_f}(s)$, $l_{1_m}^1 = P_{\Sigma_f}(s')$, $T(q_0, s) = q_{1_j}^{o_1}$, $T(q_0, s') = q_{1_m}^{o_1}$, and $T^m(q_0^m, \text{Prj}_{\Sigma_o}(s)) = q_1^m$. Then, $l_{1_j}^1 \rightsquigarrow_{\min} \text{Prj}_{\Sigma_o}(s)$ and $l_{1_m}^1 \rightsquigarrow_{\min} \text{Prj}_{\Sigma_o}(s')$.

Consider the following two traces:

$$\begin{aligned} \omega &= s(s_1\sigma_1s_2\sigma_2 \cdots s_z\sigma_z)^p; \\ \omega' &= s'(s'_1\sigma_1s'_2\sigma_2 \cdots s'_z\sigma_z)^p; \end{aligned} \quad (\text{A.15})$$

with $p \in \mathbb{N}$ and $p \geq 1$ being arbitrarily large, $s_q, s'_q \in \Sigma_{uo}^*$, and $\sigma_q \in \Sigma_o$ ($q \in [1 \cdots z]$).

Let $P_{\Sigma_f}(s_q) \subseteq l_{1_j}^1$ and $P_{\Sigma_f}(s'_q) \subseteq l_{1_m}^1$ for each q ($q \in [1 \cdots z]$). Then, we have

$$\text{Prj}_{\Sigma_o}(\omega) = \text{Prj}_{\Sigma_o}(\omega'),$$

$$P_{\Sigma_f}(\omega) = l_{1_j}^1, \quad (\text{A.16})$$

$$P_{\Sigma_f}(\omega') = l_{1_m}^1.$$

Let $F = l_{1_j}^1$ and $t \in L/s$ such that $\omega = st$; then, $t = (s_1\sigma_1s_2\sigma_2 \cdots s_z\sigma_z)^p$, $t_e \in \Sigma_o$, and $P_{\Sigma_f}(t) \subseteq F$. By choosing p to be arbitrarily large, we can obtain $\|t\| \geq n$ for any given $n \in \mathbb{N}$, and then we have: $\omega' \in \text{Prj}_{\Sigma_o}^{-1}(\text{Prj}_{\Sigma_o}(st))$ and $l_{1_j}^1 \rightsquigarrow_{\min} \text{Prj}_{\Sigma_o}(st)$ (according to Lemma A.3 $l_{1_j}^1 \rightsquigarrow_{\min} \text{Prj}_{\Sigma_o}(s)$, $l_{1_j}^1 = P_{\Sigma_f}(s)$, and $P_{\Sigma_f}(t) \subseteq l_{1_j}^1$.) but $l_{1_j}^1 \not\preceq P_{\Sigma_f}(\omega') = l_{1_m}^1$ (because $l_{1_j}^1 < l_{1_m}^1$), which contradicts condition D_m^2 of the definition of a “strong minimal diagnosability” (Definition 5).

Thus, for two such traces, according to Definition 5, L is not strongly minimally diagnosable.

Therefore, condition (C₁) must be satisfied.

Then, we prove that if L is strongly minimally diagnosable, then it satisfies condition (C₂). By contradiction, assume that there exists an F -incomparable state $q^m \in Q^m$ and that there also exists a pair $(q^o, l) \in q^m$ but there does not exist a state $q^{m'} \in Q^m$ such that $T^m(q^m, s_o) = q^{m'}$ (where $s_o \in \Sigma_o^+$), and for each $(q^o, l') \in q^{m'}$, $l' = l$. Then, for each $q^{m'}$, there exist only two possible distinct cases:

- (1) For each $(q^o, l') \in q^{m'}$, $l' \neq l$
- (2) There exist $(q_1^o, l_1'), (q_2^o, l_2') \in q^{m'}$ such that $l_1' = l$ and $l_2' \neq l$

For case (1), because $(q^o, l) \in q^m$, according to property (P₂) of a “minimal diagnoser,” there exists $s' \in \Sigma^*$ with $s'_e \in \Sigma_o$ such that $T(q_0, s') = q^o$ and $P_{\Sigma_f}(s') = l$.

Let $s' = st$ with $s_e \in \Sigma_f$, $P_{\Sigma_f}(s) = l$ (i.e., $s \in S_l$), $t_e = s'_e \in \Sigma_o$, and $P_{\Sigma_f}(t) = \emptyset$ ($\subseteq l$).

Then, for condition (i) of Definition 5, we cannot find a trace $t' \in L/(st)$, $(tt')_e \in \Sigma_o$, and $P_{\Sigma_f}(t') \subseteq l$ such that $(l \rightsquigarrow_{\min} \text{Prj}_{\Sigma_o}(st)) \implies D_m^1$.

By contradiction, assume that there exist $t' \in L/(st)$, $(tt')_e \in \Sigma_o$, and $P_{\Sigma_f}(t') \subseteq l$ (then, according to Lemma A.3, $l \rightsquigarrow_{\min} \text{Prj}_{\Sigma_o}(s't')$). Let $s_o = \text{Prj}_{\Sigma_o}(t')$ and $T^m(q^m, s_o) = q^{m'}$; then, there must exist a pair $(q^o, l') \in q^{m'}$ with $l' = l$ (because $l \rightsquigarrow_{\min} \text{Prj}_{\Sigma_o}(s't')$), which contradicts case (1), in which $\forall (q^o, l') \in q^{m'}$, $l' \neq l$. Even if s_o (i.e., $\text{Prj}_{\Sigma_o}(t')$) is ε , the condition D_m^1 of Definition 5 will not be satisfied, or else q^m will be F -certain with the unique fault label l , which contradicts the assumption that q^m is F -incomparable.

For case (2), as in case (1), there also exists $s' \in \Sigma^*$ with $s'_e \in \Sigma_o$ such that $T(q_0, s') = q^o$ and $P_{\Sigma_f}(s') = l$.

Let $s' = st$ with $s_e \in \Sigma_f$, $P_{\Sigma_f}(s) = l$ (i.e., $s \in S_l$), $t_e = s'_e \in \Sigma_o$, and $P_{\Sigma_f}(t) = \emptyset$ ($\subseteq l$).

For each $t' \in L/(st)$ with $P_{\Sigma_f}(t') \subseteq l$ (and subsequently $P_{\Sigma_f}(stt') \subseteq l$) and $\text{Prj}_{\Sigma_o}(t') = s_o$, according to Case (2), we have $T(q_0, stt') = q_1^o$, $l_1' (= l) \rightsquigarrow_{\min} \text{Prj}_{\Sigma_o}(stt')$, and $l_2' \rightsquigarrow_{\min} \text{Prj}_{\Sigma_o}(stt')$, but $l_1' \neq l_2'$, which contradicts the definition of a “strong minimal diagnosability” (condition D_m^1). Even if s_o (i.e., $\text{Prj}_{\Sigma_o}(t')$) is ε , as in case (1), condition D_m^1 of Definition 5 is not satisfied.

Therefore, condition (C₂) must be satisfied.

Sufficiency: assume that the minimal diagnoser G^m satisfies conditions (C₁) and (C₂). For any fault set $F \in \mathcal{F}_L$, pick any $s \in L$ with $s \in S_F$. Pick any $t \in L/s$ with $t_e \in \Sigma_o$ (based on the assumption that there is no infinite sequence of unobservable events in L , we let a natural number n_0 denote the maximum length of any sequence of unobservable events; thus, $t \leq (n_0 + 1)$).

Let $T(q_0, st) = q_i^o$, and then we get the corresponding state $q_j^m = T^m(q_0^m, \text{Prj}_{\Sigma_o}(st))$ in G^m . Since $P_{\Sigma_f}(st) = F$, according to the conditions of Definition 5, we suppose that $F \rightsquigarrow_{\min} \text{Prj}_{\Sigma_o}(st)$, and then we get $(q_i^o, F) \in q_j^m$. Then, we have two distinct cases to consider:

- (a) q_j^m is F -certain
- (b) q_j^m is F -incomparable

For case (a), in which q_j^m is F -certain, according to Lemma A.1-(i), we have

$$\omega \in \text{Prj}_{\Sigma_o}^{-1}(\text{Prj}_{\Sigma_o}(st)) \implies F \preceq P_{\Sigma_f}(\omega). \quad (\text{A.17})$$

Thus, there exists $t' = \varepsilon$ such that $t' \in L/(st)$, $(tt')_e \in \Sigma_o$ (because $tt' = t$ and $t_e \in \Sigma_o$), and $P_{\Sigma_f}(t') \subseteq F$. If $F \rightsquigarrow_{\min} \text{Prj}_{\Sigma_o}(st)$, then D_m^1 of Definition 5 holds:

$$\omega \in \text{Prj}_{\Sigma_o}^{-1}(\text{Prj}_{\Sigma_o}(stt')) \implies F \preceq P_{\Sigma_f}(\omega). \quad (\text{A.18})$$

Thus, the first condition (i) of Definition 5 holds ($F \rightsquigarrow_{\min} \text{Prj}_{\Sigma_o}(st) \implies D_m^1$).

According to Lemma A.4, for each $t'' \in L/(st)$ with $t''_e \in \Sigma_o$,

$$\omega \in \text{Prj}_{\Sigma_o}^{-1}(\text{Prj}_{\Sigma_o}(stt'')) \implies F \preceq P_{\Sigma_f}(\omega). \quad (\text{A.19})$$

Then, for the second condition (ii) of Definition 5, let $n = t$; for each string u with $u \in L/s$ and $u_e \in \Sigma_o$, when $u \geq n$, we have the following:

If $F \rightsquigarrow_{\min} \text{Prj}_{\Sigma_o}(su)$, then

$$\omega \in \text{Prj}_{\Sigma_o}^{-1}(\text{Prj}_{\Sigma_o}(su)) \implies F \preceq P_{\Sigma_f}(\omega), \quad (\text{i.e., } D_m^2 \text{ holds}). \quad (\text{A.20})$$

Thus, the second condition (ii) of Definition 5 holds.

For case (a), since the conclusion is true for any $F \in \mathcal{F}_L$, L is strongly minimally diagnosable.

For case (b), if q_j^m is F -incomparable, according to condition (C₁) (there is no F -indeterminate cycle), there must exist $m \in \mathbb{N}$ and $r \in \Sigma_o^+$. When $r \geq m$, the diagnoser will reach the first F -certain state $q_j^{m'}$ with the unique fault label F' via observation sequence r only in two possible distinct scenarios:

- (b1) $F \subset F'$ for each $(q_i^o, F') \in q_j^{m'}$
- (b2) $F = F'$ for each $(q_i^o, F') \in q_j^{m'}$

For scenario (b1), because F is no longer a minimal diagnosis, we do not care about this scenario.

Scenario (b2) is just condition (C2). According to (C2), there exists $s_o \in \Sigma_o^+$ such that $T^m(q_j^m, s_o) = q_j^{m'}$; then, there exists $t' \in L/(st)$ with $\text{Prj}_{\Sigma_o}(t') = s_o$, $P_{\Sigma_f}(t') \subseteq F$, and $t'_e \in \Sigma_o$ (also $(tt')_e \in \Sigma_o$) such that $T(q_0, stt') = q_i^o$ and $(q_i^o, F) \in q_j^{m'}$. By Lemma A.1-(i), we have

$$\omega \in \text{Prj}_{\Sigma_o}^{-1}(\text{Prj}_{\Sigma_o}(stt')) \implies F \preceq P_{\Sigma_f}(\omega). \quad (\text{A.21})$$

That is, D_m^1 of Definition 5 holds.

Thus, the first condition (i) of Definition 5 holds.

For any $t'' \in L/(stt')$ with $t''_e \in \Sigma_o$, according to Lemma A.4, we have

$$\omega \in \text{Prj}_{\Sigma_o}^{-1}(\text{Prj}_{\Sigma_o}(stt't'')) \implies F \preceq P_{\Sigma_f}(\omega). \quad (\text{A.22})$$

In other words, $\exists n = tt'$, $\forall u (u \in L/s, u_e \in \Sigma_o)$. When $u \geq n$, we have the following. If $F \rightsquigarrow_{\min} \text{Prj}_{\Sigma_o}(su)$, then

$$\omega \in \text{Prj}_{\Sigma_o}^{-1}(\text{Prj}_{\Sigma_o}(su)) \implies F \preceq P_{\Sigma_f}(\omega). \quad (\text{A.23})$$

That is, the second condition (ii) of Definition 5 holds.

Hence, L is strongly minimally diagnosable. \square

Proposition 3.18. *Let G be a DES with language L . If L is strongly minimally diagnosable, then L is also weakly minimally diagnosable. If L is diagnosable, then L is also weakly minimally diagnosable.*

Proof.

- (1) From the second condition (ii) of Definition 5 (“strong minimal diagnosability”) and the condition of Definition 8 (“weak minimal diagnosability”), we can clearly see that the former condition is just the latter one. Therefore, if G is strongly minimally diagnosable, then G is necessarily weakly minimally diagnosable.
- (2) Let a DES G with language L be diagnosable. Pick any fault set $F \in \mathcal{F}_L$, with $F = \{f_1, f_2, \dots, f_p\}$. According to Definition 2, for each $f_i \in F$ and for each $s \in L, s_e = f_i$, there exists $n \in \mathbb{N}$ such that

$$\forall t (t \in L/s, t_e \in \Sigma_o), \quad (\|t\| \geq n \implies D), \quad (\text{A.24})$$

where the diagnosability condition D is defined as follows:

$$\omega \in \text{Prj}_{\Sigma_o}^{-1}(\text{Prj}_{\Sigma_o}(st)) \implies f_i \in \omega. \quad (\text{A.25})$$

Hence,

$$\omega \in \text{Prj}_{\Sigma_o}^{-1}(\text{Prj}_{\Sigma_o}(st)) \implies f_i \in \omega \implies f_i \in P_{\Sigma_f}(\omega). \quad (\text{A.26})$$

Thus, we obtain

$$\omega \in \text{Prj}_{\Sigma_o}^{-1}(\text{Prj}_{\Sigma_o}(st)) \implies F \subseteq P_{\Sigma_f}(\omega) \implies F \preceq P_{\Sigma_f}(\omega). \quad (\text{A.27})$$

Thus,

$$(F \rightsquigarrow_{\min} \text{Prj}_{\Sigma_o}(st)) \implies \left(\omega \in \text{Prj}_{\Sigma_o}^{-1}(\text{Prj}_{\Sigma_o}(st)) \implies F \preceq P_{\Sigma_f}(\omega) \right). \quad (\text{A.28})$$

Therefore, if G is diagnosable, then G is also weakly minimally diagnosable. \square

Proposition 3.20. *A language L generated by an FSM G is weakly minimally diagnosable iff its minimal diagnoser G^m does not include any F -indeterminate cycle.*

Proof. (sketch)Based on the proof of Proposition 3.15, we can see that condition (C_1) is only required by the second case (ii) of “strong minimal diagnosability” (Definition 5), which is the same as “weak minimal diagnosability” (Definition 8). Therefore, only condition (C_1) of Proposition 3.15 is required for the current proposition. That is, a language L generated by an FSM G is weakly minimally diagnosable iff its minimal diagnoser G^m does not include any F -indeterminate cycle. \square

Data Availability

The data used to support the findings of this study are included within the article.

Conflicts of Interest

The authors declare that they have no conflicts of interest.

Acknowledgments

This work was supported by the National Natural Science Foundation of China (Grant no. 61972360).

References

- [1] F. Yu, L. Li, B. He et al., “Design and FPGA implementation of a pseudorandom number generator based on a four-wing memristive hyperchaotic system and bernoulli map,” *IEEE Access*, vol. 7, pp. 181884–181898, 2019.
- [2] L. Zhou, F. Tan, and F. Yu, “A robust synchronization-based chaotic secure communication scheme with double-layered and multiple hybrid networks,” *IEEE Systems Journal*, pp. 1–12, 2019.
- [3] X. Yang, Q. Zhu, and C. Huang, “Lag stochastic synchronization of chaotic mixed time-delayed neural networks with uncertain parameters or perturbations,” *Neurocomputing*, vol. 74, no. 10, pp. 1617–1625, 2011.
- [4] J. Jin, L. Zhao, M. Li, F. Yu, and Z. Xi, “Improved zeroing neural networks for finite time solving nonlinear equations,” *Neural Computing and Applications*, pp. 1–10, 2019.
- [5] Q. Xie, X. Wang, Z. Han, Y. Zuo, and M. Tang, “Immersion and invariance control of a class of nonlinear cascaded discrete systems,” *Neurocomputing*, vol. 171, pp. 1661–1665, 2016.
- [6] Y.-S. Huang and Z.-Y. Wang, “Decentralized adaptive fuzzy control for a class of large-scale MIMO nonlinear systems with strong interconnection and its application to automated highway systems,” *Information Sciences*, vol. 274, no. 8, pp. 210–224, 2014.
- [7] Y.-S. Huang and M. Wu, “Robust decentralized direct adaptive output feedback fuzzy control for a class of large-sale nonaffine nonlinear systems,” *Information Sciences*, vol. 181, no. 11, pp. 2392–2404, 2011.
- [8] M. Long, Y. Chen, and F. Peng, “Simple and accurate analysis of BER performance for DCSK chaotic communication,” *IEEE Communications Letters*, vol. 15, no. 11, pp. 1175–1177, 2011.
- [9] L. Zhou, F. Tan, F. Yu, and W. Liu, “Cluster synchronization of two-layer nonlinearly coupled multiplex networks with multi-links and time-delays,” *Neurocomputing*, vol. 359, pp. 264–275, 2019b.
- [10] F. Peng, X. W. Zhu, and M. Long, “An ROI privacy protection scheme for H.264 video based on FMO and chaos,” *IEEE Transactions on Information Forensics and Security*, vol. 8, no. 10, pp. 1688–1699, 2013.
- [11] F. Yu, L. Li, Q. Tang, S. Cai, Y. Song, and Q. Xu, “A survey on true random number generators based on chaos,” *Discrete Dynamics in Nature and Society*, vol. 2019, Article ID 2545123, 10 pages, 2019.
- [12] F. Yu, L. Liu, B. He et al., “Analysis and FPGA realization of a novel 5D hyperchaotic four-wing memristive system, active control synchronization, and secure communication application,” *Complexity*, vol. 2019, Article ID 4047957, 18 pages, 2019.
- [13] F. Yu, L. Liu, L. Xiao, K. Li, and S. Cai, “A robust and fixed-time zeroing neural dynamics for computing time-variant nonlinear equation using a novel nonlinear activation function,” *Neurocomputing*, vol. 350, pp. 108–116, 2019.
- [14] C. G. Cassandras and S. Lafortune, *Introduction to Discrete Event Systems*, Springer-Verlag New York, Inc., Secaucus, NJ, USA, 2008.
- [15] F. Lin, “Diagnosability of discrete event systems and its applications,” *Discrete Event Dynamic Systems: Theory and Applications*, vol. 4, no. 2, pp. 197–212, 1994.
- [16] M. Sampath, R. Sengupta, S. Lafortune, K. Sinnamohideen, and D. Teneketzis, “Diagnosability of discrete-event systems,” *IEEE Transactions on Automatic Control*, vol. 40, no. 9, pp. 1555–1575, 1995.
- [17] X. Zhao and D. Ouyang, “Model-based diagnosis of discrete event systems with an incomplete system model,” in *Proceedings of the 18th European Conference on Artificial Intelligence (ECAI-08)*, pp. 189–193, IOS Press, Patras, Greece, July 2008.
- [18] R. H. Kwong and D. L. Yonge-Mallo, “Fault diagnosis in discrete-event systems with incomplete models: learnability and diagnosability,” *IEEE Transactions on Cybernetics*, vol. 45, no. 7, pp. 1236–1249, 2015.
- [19] S. Takai and R. Kumar, “A generalized framework for inference-based diagnosis of discrete event systems capturing both disjunctive and conjunctive decision-making,” *IEEE Transactions on Automatic Control*, vol. 62, no. 6, pp. 2778–2793, 2017.
- [20] X. Yin, J. Chen, Z. Li, and S. Li, “Robust fault diagnosis of stochastic discrete event systems,” *IEEE Transactions on Automatic Control*, vol. 64, no. 10, pp. 4237–4244, 2019.
- [21] G. Lamperti, M. Zanella, and X. Zhao, *Introduction to Diagnosis of Active Systems*, Springer, Basel, Switzerland, 2018.
- [22] N. Kanagawa and S. Takai, “Diagnosability of discrete event systems subject to permanent sensor failures,” *International Journal of Control*, vol. 88, no. 12, pp. 2598–2610, 2015.
- [23] C. Keroglou and C. N. Hadjicostis, “Distributed fault diagnosis in discrete event systems via set intersection refinements,” *IEEE Transactions on Automatic Control*, vol. 63, no. 10, pp. 3601–3607, 2018.
- [24] F. Liu, “Predictability of failure event occurrences in decentralized discrete-event systems and polynomial-time verification,” *IEEE Transactions on Automation Science and Engineering*, vol. 16, no. 1, pp. 498–504, 2019.
- [25] G. S. Viana, M. V. Moreira, and J. C. Basilio, “Codiagnosability analysis of discrete-event systems modeled by weighted automata,” *IEEE Transactions on Automatic Control*, vol. 64, no. 10, pp. 4361–4368, 2019.
- [26] G. Zhu, Z. Li, and N. Wu, “Model-based fault identification of discrete event systems using partially observed petri nets,” *Automatica*, vol. 96, pp. 201–212, 2018.
- [27] R. Debouk, S. Lafortune, and D. Teneketzis, “On the effect of communication delays in failure diagnosis of decentralized

- discrete event systems,” *Discrete Event Dynamic Systems*, vol. 13, no. 3, pp. 263–289, 2003.
- [28] Y. Pencolé and M.-O. Cordier, “A formal framework for the decentralised diagnosis of large scale discrete event systems and its application to telecommunication networks,” *Artificial Intelligence*, vol. 164, no. 1-2, pp. 121–170, 2005.
- [29] W. Qiu and R. Kumar, “Decentralized failure diagnosis of discrete event systems,” *IEEE Transactions on Systems, Man, and Cybernetics-Part A: Systems and Humans*, vol. 36, no. 2, pp. 384–395, 2006.
- [30] F. Liu and D. Qiu, “Diagnosability of fuzzy discrete-event systems: a fuzzy approach,” *IEEE Transactions on Fuzzy Systems*, vol. 17, no. 2, pp. 372–384, 2009.
- [31] M. Luo, Y. Li, F. Sun, and H. Liu, “A new algorithm for testing diagnosability of fuzzy discrete event systems,” *Information Sciences*, vol. 185, no. 1, pp. 100–113, 2012.
- [32] D. Thorsley and D. Teneketzis, “Diagnosability of stochastic discrete-event systems,” *IEEE Transactions on Automatic Control*, vol. 50, no. 4, pp. 476–492, 2005.
- [33] J. Chen and R. Kumar, “Failure detection framework for stochastic discrete event systems with guaranteed error bounds,” *IEEE Transactions on Automatic Control*, vol. 60, no. 6, pp. 1542–1553, 2015.
- [34] J. Chen, C. Keroglou, C. N. Hadjicostis, and R. Kumar, “Revised test for stochastic diagnosability of discrete-event systems,” *IEEE Transactions on Automation Science and Engineering*, vol. 15, no. 1, pp. 404–408, 2018.
- [35] X. Geng, D. Ouyang, X. Zhao, and S. Hao, “Probabilistic logical approach for testing diagnosability of stochastic discrete event systems,” *Engineering Applications of Artificial Intelligence*, vol. 53, pp. 53–61, 2016.
- [36] G. Lamperti and M. Zanella, “Flexible diagnosis of discrete-event systems by similarity-based reasoning techniques,” *Artificial Intelligence*, vol. 170, no. 3, pp. 232–297, 2006.
- [37] G. Lamperti and X. Zhao, “Diagnosis of active systems by semantic patterns,” *IEEE Transactions on Systems, Man, and Cybernetics: Systems*, vol. 44, no. 8, pp. 1028–1043, 2014.
- [38] A. Grastien, P. Haslum, and S. Thiébaux, “Conflict-based diagnosis of discrete event systems: theory and practice,” in *Proceedings of the 13th International Conference on the Principles of Knowledge Representation and Reasoning (KR-12)*, pp. 489–499, AAAI Press, Rome, Italy, June 2012.
- [39] X. Zhao, G. Lamperti, and D. Ouyang, “Minimal diagnosis of discrete-event systems,” in *Proceedings of the 24th International Workshop on Principles of Diagnosis (DX-13)*, pp. 154–159, Jerusalem, Israel, October 2013.
- [40] Wikipedia, “Occam’s razor,” 2016, https://en.wikipedia.org/wiki/Occam%27s_razor.
- [41] R. Reiter, “A theory of diagnosis from first principles,” *Artificial Intelligence*, vol. 32, no. 1, pp. 57–95, 1987.
- [42] J. de Kleer and B. C. Williams, “Diagnosing multiple faults,” *Artificial Intelligence*, vol. 32, no. 1, pp. 97–130, 1987.
- [43] S. Sohrabi, J. Baier, and S. McIlraith, “Diagnosis as planning revisited,” in *Proceedings of the 12th International Conference on the Principles of Knowledge Representation and Reasoning (KR-10)*, pp. 26–36, AAAI Press, Toronto, Canada, May 2010.
- [44] P. Haslum and A. Grastien, “Diagnosis as planning: two case studies,” in *Proceedings of the 5th Scheduling and Planning Applications Workshop (SPARK-11)*, pp. 37–44, Cambridge, UK, December 2011.
- [45] A. Grastien, A. Anbulagan, J. Rintanen, and E. Kelareva, “Diagnosis of discrete-event systems using satisfiability algorithms,” in *Proceedings of the 22nd AAAI Conference on Artificial Intelligence (AAAI-07)*, pp. 305–310, AAAI Press, Vancouver, Canada, July 2007.
- [46] M. Cerrada, L. Ferarini, and A. Dedè, “Modular fault diagnosis using temporized analysis for a class of discrete event systems,” in *Proceedings of the 12th IFAC Symposium on Large Scale Systems: Theory and Applications*, pp. 180–185, Ville-neuve-d’Ascq, France, July 2010.
- [47] S. Jiang, Z. Huang, V. Chandra, and R. Kumar, “A polynomial algorithm for testing diagnosability of discrete-event systems,” *IEEE Transactions on Automatic Control*, vol. 46, no. 8, pp. 1318–1321, 2001.
- [48] T.-S. Yoo and S. Lafortune, “Polynomial-time verification of diagnosability of partially observed discrete-event systems,” *IEEE Transactions on Automatic Control*, vol. 47, no. 9, pp. 1491–1495, 2002.
- [49] X. Zhao and D. Ouyang, “Deriving all minimal hitting sets based on join relation,” *IEEE Transactions on Systems, Man, and Cybernetics: Systems*, vol. 45, no. 7, pp. 1063–1076, 2015.
- [50] R. Su and W. M. Wonham, “Global and local consistencies in distributed fault diagnosis for discrete-event systems,” *IEEE Transactions on Automatic Control*, vol. 50, no. 12, pp. 1923–1935, 2005.

Research Article

Study on Amplitude Modulation Principle of Chaotic System

Jian-Rong Du, Chun-Lai Li , Kun Qian, Zhao-Yu Li, and Wen Li

College of Physics and Electronics, Hunan Institute of Science and Technology, Yueyang 414006, China

Correspondence should be addressed to Chun-Lai Li; hnistlichl@163.com

Received 2 July 2019; Revised 16 November 2019; Accepted 3 December 2019; Published 11 February 2020

Guest Editor: Mahendra K. Gupta

Copyright © 2020 Jian-Rong Du et al. This is an open access article distributed under the Creative Commons Attribution License, which permits unrestricted use, distribution, and reproduction in any medium, provided the original work is properly cited.

Exploring the amplitude modulation phenomenon of chaotic signal has become a subject of great concern in recent years. This paper mainly concentrates on the preliminary study on amplitude modulation principle of a chaotic system. First, two 3D chaotic systems with quadratic product terms are introduced for studying the amplitude modulation phenomenon of chaotic signal. It is found that the signal amplitude of the first system can be controlled by partial quadratic coefficient. But for the second system, none of nonlinear coefficient can be employed to control the signal amplitude. Then, the amplitude modulation principle of chaotic system is preliminarily studied by exploring the intrinsic relationship between nonzero equilibrium point and phase space trajectory, and it is further validated by introducing unified parameter to the two 3D chaotic systems. As a necessary condition, the principle provides a feasible and simple method for constructing and analyzing an amplitude modulation chaotic system.

1. Introduction

Chaos has evoked much attention in many scientific fields due to its unique characteristics, such as sensitivity to initial conditions and parameter deviations, strange attractor with locally unbounded but globally bounded trajectory, unpredictability of future behavior, and so on [1–4]. In the past few decades, the issue of construction, analysis, and application of chaotic systems has become a very active topic [5–10].

The signal amplitude of a chaotic system can be often modulated by controlling one or more coefficients in the dynamical equations, while the Lyapunov exponents and power spectral density remain invariable [11–14]. Since the variables can be rescaled by directly controlling the amplitude parameter to avoid the exceeding limitations of bandwidth and amplitude, this kind of system can resolve the contradiction of signal processing and information retention in practical amplification circuit, so it is a promising type of system for the reality of chaotic encryption, chaotic radar, chaotic communication, and chaotic signal processing.

Generally, for the presented amplitude modulation systems with quadratic nonlinearity, the amplitude parameters are the coefficients of quadratic terms, which can

nonlinearly modulate the signal amplitude of partial or total state variables [11–15]. In fact, while chaotic system holds the only nonlinear term, the corresponding coefficient can control the signal amplitude since it uniquely determines the scale of the variables [16–18]. As an example, a simple chaotic system with a single nonlinearity x_1^3 is recalled as $\dot{x}_1 = x_2, \dot{x}_2 = x_3, \dot{x}_3 = bx_1 - x_2 - ax_3 - bx_1^3$ [16]. Accordingly, it holds the resulting system $\dot{x}_1 = x_2, \dot{x}_2 = x_3, \dot{x}_3 = bx_1 - x_2 - ax_3 - bpx_1^3$ with the substitution $x_1 \rightarrow \sqrt{p}x_1, x_2 \rightarrow \sqrt{p}x_2, x_3 \rightarrow \sqrt{p}x_3$. Thereby, the coefficient of the nonlinear term x_1^3 can control the amplitude of x_1, x_2, x_3 according to $1/\sqrt{p}$. However, it is found in the recent work that for the dynamical system with exponential nonlinearity, the coefficient of quadratic term cannot provide amplitude modulation [19]. Thus, naturally, an interesting question is raised as “whether each coefficient of nonlinear term in chaotic system can control the signal amplitude.” Another more important question is “what is the principle of constructing and analyzing amplitude modulation chaotic system.” However, as far as we know, there is little information about this kind of system in the literature so far, so it still remains open and challenging.

This paper attempts to provide some answers to these questions by introducing two carefully screened chaotic systems. Differing from the system with a single linear or a

single nonlinear term, the present systems have nonunique linear terms and three quadratic cross-product terms. Basic dynamics of these two nonlinear systems are analyzed theoretically and numerically. Somewhat surprisingly, only one coefficient of the quadratic nonlinearity in the first system can be employed to control the amplitude of chaotic signal. But for the second system, none of the coefficient of quadratic nonlinearity can be employed to control the amplitude of chaotic signal. The discovery that not all coefficients of nonlinear term can provide amplitude control is of interest and inspiration. As a further concern in this work, the amplitude modulation principle of chaotic system is addressed, based on the analysis of the intrinsic relationship between nonzero equilibrium point and phase space trajectory. Although it is not a sufficient and necessary condition for amplitude modulation, the proposed principle provides a feasible method for constructing and analyzing amplitude modulation chaotic system. Furthermore, this method is simple in actual operation and will hopefully enlighten for revealing the amplitude modulation mechanism of chaotic system.

This paper is organized as follows. Following the introduction, we propose a chaotic system with partial coefficient of nonlinearity employed to control amplitude. In

Section 3, we introduce another chaotic system with no coefficient of nonlinearity employed to control amplitude. The principle of amplitude modulation is addressed in Section 4. Finally, some concluding remarks are drawn in Section 5.

2. Chaotic System with Partial Coefficient of Nonlinearity for Amplitude Control

2.1. System Description. The reported system possesses four linear terms and three quadratic cross-product terms, which is given by the following ordinary differential equations:

$$\begin{cases} \dot{x}_1 = a(x_2 - x_1) + dx_2x_3, \\ \dot{x}_2 = bx_2 - ex_1x_3, \\ \dot{x}_3 = -cx_3 + fx_1x_2. \end{cases} \quad (1)$$

It is easy to know that the proposed system is symmetric with respect to the x_3 -axis, as shown by the coordinate transformation $(x_1, x_2, x_3) \rightarrow (-x_1, -x_2, x_3)$.

By considering the equilibrium condition $a(x_2 - x_1) + dx_2x_3 = 0$, $bx_2 - ex_1x_3 = 0$, $-cx_3 + fx_1x_2 = 0$, five equilibrium points of system (1) are determined as

$$\begin{aligned} &P_0(0, 0, 0), \\ &P_1\left(\sqrt{\frac{bc}{ef}}, \frac{-a\sqrt{ce} + \sqrt{ce}\sqrt{a^2 + (4abd/e)}}{2d\sqrt{bf}}, \frac{-a + \sqrt{a^2 + (4abd/e)}}{2d}\right), \\ &P_2\left(\sqrt{\frac{bc}{ef}}, \frac{-a\sqrt{ce} - \sqrt{ce}\sqrt{a^2 + (4abd/e)}}{2d\sqrt{bf}}, \frac{-a - \sqrt{a^2 + (4abd/e)}}{2d}\right), \\ &P_3\left(-\sqrt{\frac{bc}{ef}}, \frac{a\sqrt{ce} + \sqrt{ce}\sqrt{a^2 + (4abd/e)}}{2d\sqrt{bf}}, \frac{a + \sqrt{a^2 + (4abd/e)}}{2d\sqrt{bf}}\right), \\ &P_4\left(-\sqrt{\frac{bc}{ef}}, \frac{a\sqrt{ce} - \sqrt{ce}\sqrt{a^2 + (4abd/e)}}{2d\sqrt{bf}}, \frac{a - \sqrt{a^2 + (4abd/e)}}{2d\sqrt{bf}}\right). \end{aligned} \quad (2)$$

And the characteristic equation is deduced as

$$\begin{aligned} \varphi(\lambda) = &-\lambda^3 + (-a + b - c)\lambda^2 + [ab + bc - ac + dfx_2^2 - aex_3 - dex_3^2 - efx_1^2]\lambda \\ &+ [abc - aefx_1x_2 - bdfx_2^2 - acex_3 - cdex_3^2 - aefx_1^2]. \end{aligned} \quad (3)$$

When selecting the parameter set $a = 28$, $b = 20$, $c = 3$, $d = 1$, $e = 5$, and $f = 1$, the four nonzero equilibrium points are calculated as $P_1(3.4641, 3.0743, 3.5499)$, $P_2(3.4641, -27.3230, -31.5499)$, $P_3(-3.4641, 27.3230, -31.5499)$, and $P_4(-3.4641, -3.0743, 3.5499)$. And the corresponding characteristic roots are

$$\begin{aligned} &P_0: \lambda_1 = -28, \lambda_2 = 20, \lambda_3 = -3, \\ &P_{1,4}: \lambda_1 = -18.1945, \lambda_2 = 3.5973 + 13.8748i, \\ &\lambda_3 = 3.5973 - 13.8748i, \\ &P_{2,3}: \lambda_1 = -43.6337, \lambda_2 = 16.3169 + 22.2518i, \\ &\lambda_3 = 16.3169 - 22.2518i. \end{aligned} \quad (4)$$

Obviously, equilibrium point P_0 is a saddle-node with two-dimensional stable manifold and one-dimensional unstable manifold. But for the remaining nonzero equilibrium points P_1 to P_4 , λ_1 is a negative real number and λ_2 and λ_3 become a pair of complex conjugate roots with positive real parts. Accordingly, the four equilibrium points are saddle-focus points with two-dimensional unstable manifold and one-dimensional stable manifold.

When selecting $a = 28$, $b = 20$, $c = 3$, $d = 1$, $e = 5$, and $f = 1$ and computing time 5000 s, the three finite time Lyapunov exponents of system (1) are calculated by orthogonal method as $3.29613 > 0$, 0.01355 , $-19.34679 < 0$. And the Kaplan–Yorke dimension is obtained as $D_{KY} = 2 + (3.29613 + 0.01355)/19.34679 = 2.1711$, revealing a fractional feature. Therefore, system (1) is chaotic. The corresponding chaotic phase diagrams and Poincare mapping on plane $x_2 = 0$ are depicted in Figure 1.

2.2. Analysis of Amplitude Modulation

Theorem 1. *The parameter f in cross-product term x_1x_2 is a local parameter of nonlinear amplitude modulation, which can control the signal amplitude of x_1 , x_2 by the power function of index $-1/2$ respectively, but the amplitude of*

variable x_3 remains in the same range; besides, the Lyapunov exponent spectrum remains unchanged with the variation of parameter f .

Proof. Considering the variable substitution $x_1 = u_1/\sqrt{h}$, $x_2 = u_2/\sqrt{h}$, $x_3 = u_3$ ($h > 0$), system (1) is turned to

$$\begin{cases} \dot{u}_1 = a(u_2 - u_1) + du_2u_3, \\ \dot{u}_2 = bu_2 - eu_1u_3, \\ \dot{u}_3 = -cu_3 + (f/h)u_1u_2. \end{cases} \quad (5)$$

Therefore, when parameter f increases linearly, the signal amplitude of system variables x_1 , x_2 change according to the power function of index $-1/2$, respectively, but the amplitude of variable x_3 is in the same range.

When substituting the equilibrium point P_0 into characteristic equation (3), it holds

$$\varphi(\lambda) = -\lambda^3 + (-a + b - c)\lambda^2 + (ab + bc - ac)\lambda + abc. \quad (6)$$

In equation (6), the influence of parameter f is eliminated. We can draw a similar conclusion for the other equilibrium points. As an illustration, we insert the equilibrium P_1 into expression (3) obtaining

$$\begin{aligned} \varphi(\lambda) = & -\lambda^3 + (-a + b - c)\lambda^2 + \left\{ ab + bc - ac + \frac{ce[2a^2 + (4abd/e) - 2a\sqrt{a^2 + (4abd/e)}]}{4bd} \right. \\ & \left. - ae \frac{-a + \sqrt{a^2 + (4abd/e)}}{2d} - \frac{2a^2e + 4abd - 2ae\sqrt{a^2 + (4abd/e)}}{4d} - bc \right\} \lambda \\ & + \left\{ abc - ae \frac{c\sqrt{be}(-a + \sqrt{a^2 + (4abd/e)})}{2d\sqrt{be}} - \frac{ce[2a^2 + (4abd/e) - 2a\sqrt{a^2 + (4abd/e)}]}{4d} \right. \\ & \left. - ace \frac{-a + \sqrt{a^2 + (4abd/e)}}{2d} - cde \frac{2a^2 + (4abd/e) - 2a\sqrt{a^2 + (4abd/e)}}{4d^2} - abc \right\}. \end{aligned} \quad (7)$$

That is, parameter f does not produce effect on the characteristic root of equation (7). Therefore, when parameter f varies in field of real number, the Lyapunov exponent spectrum remains constant. This completes the proof.

The corresponding bifurcation diagram and Lyapunov exponent spectrum versus f are shown in Figure 2, which authenticates the theoretical results.

It is generally accepted that for the quadratic chaotic systems, the coefficients of nonlinear terms can modulate the signal amplitude of partial or total state variables [11–14]. The bifurcation diagram for $e \in [0, 20]$ is shown in Figure 3(a). Superficially, the coefficient e can modulate the signal amplitude nonlinearly. But from the enlarged view, one can see that there emerges a visible periodic window, and the Lyapunov exponent spectrum further verifies the

observation, as depicted in Figures 3(b) and 3(c). The concrete bifurcation diagram and Lyapunov exponent spectrum versus d also show that not all coefficients of quadratic terms can modulate the signal amplitude, which is illustrated in Figure 4. In spite of this, the chaos of the reported system is still robust in a large range of parameters d and e . Consequently, the system can be recommended as an important candidate in secure communication. \square

3. Chaotic System with Noncoefficient of Nonlinearity for Amplitude Control

3.1. System Description. We consider another three-dimensional autonomous system with five linear terms and three quadratic cross-product terms, as follows:

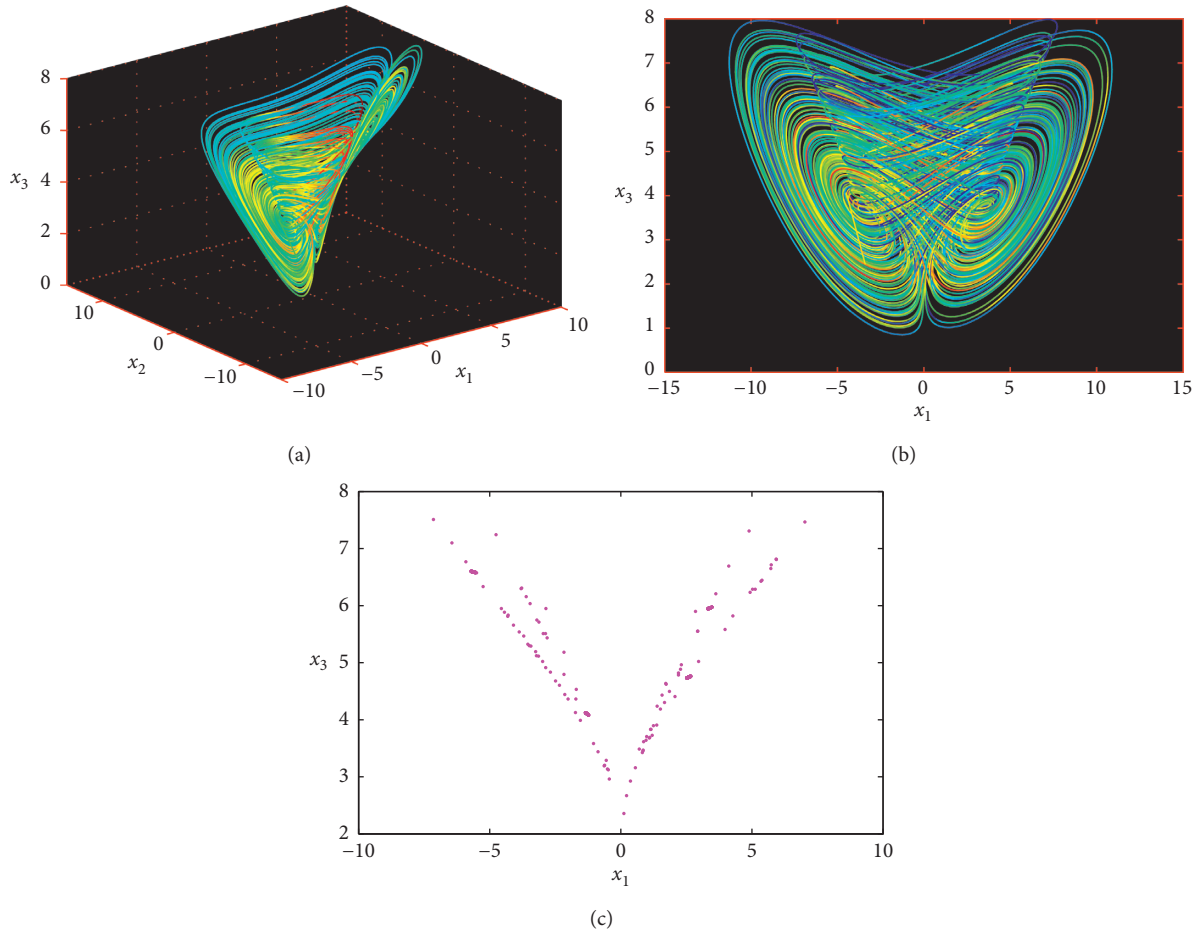


FIGURE 1: (a) x_1 - x_2 - x_3 phase portrait; (b) x_1 - x_3 phase portrait; (c) Poincaré mapping.

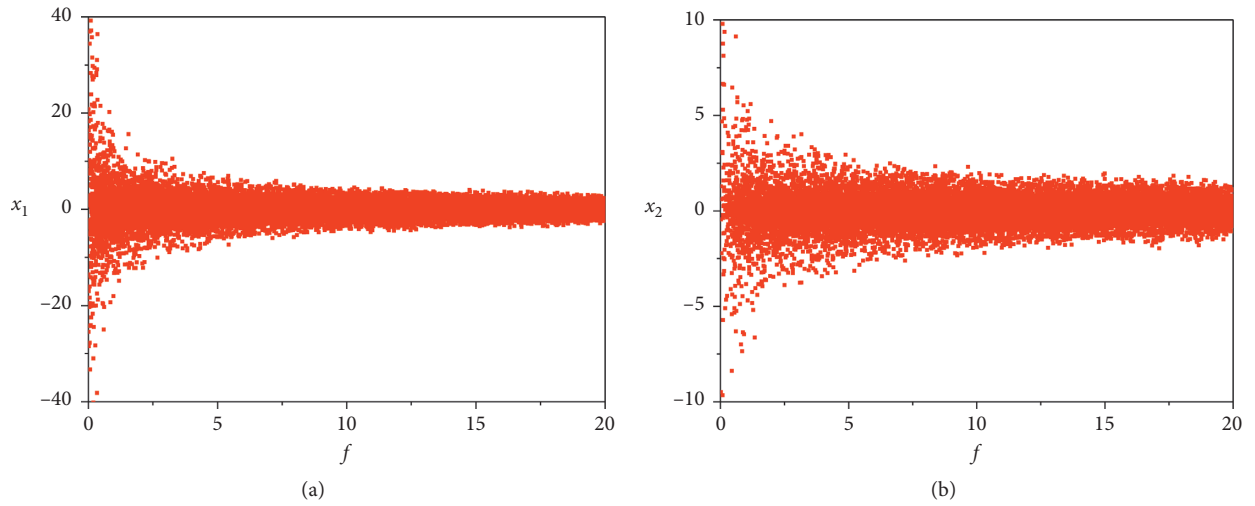


FIGURE 2: Continued.

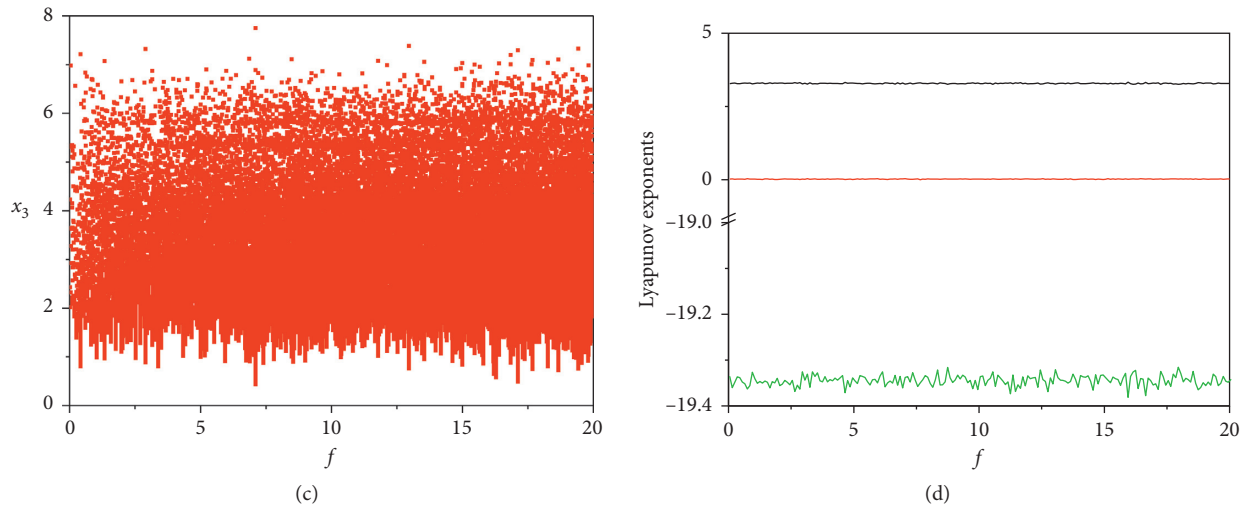


FIGURE 2: (a, b, c) Bifurcation diagram versus f ; (d) finite time Lyapunov exponent spectrum versus f .

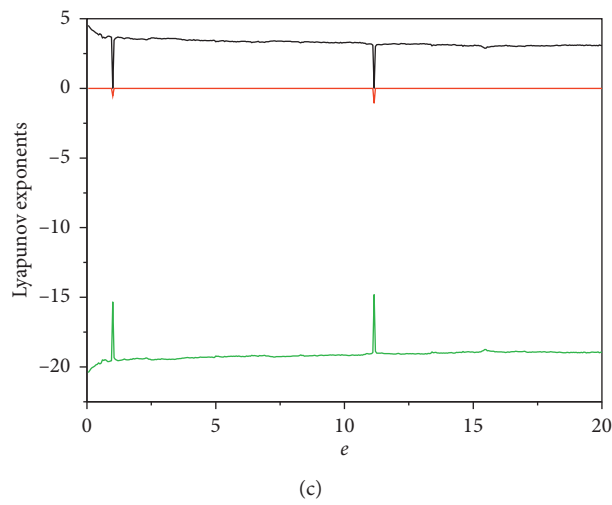
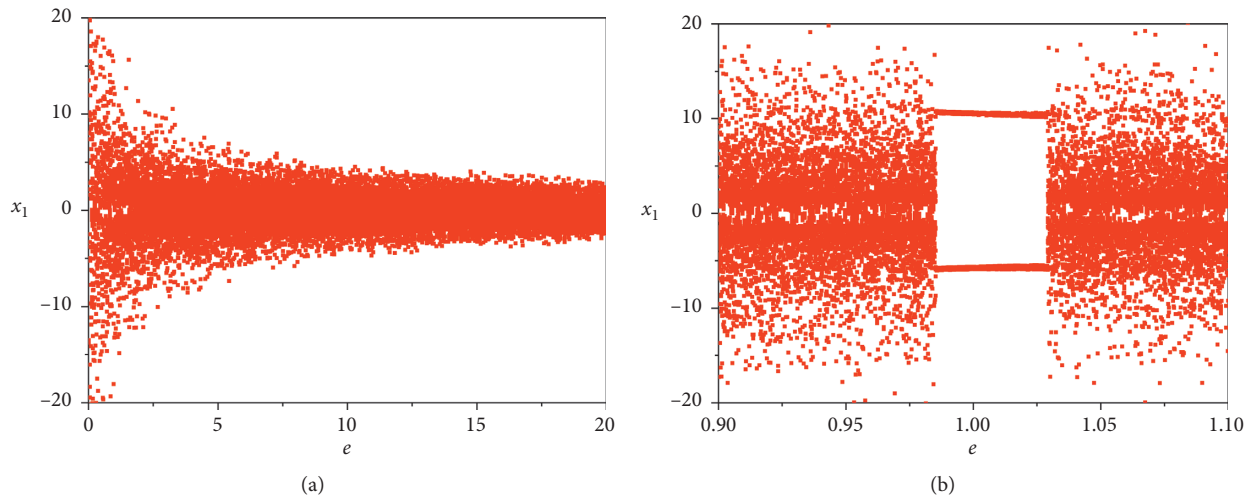


FIGURE 3: (a, b) Bifurcation diagram versus e ; (c) finite time Lyapunov exponent spectrum versus e .

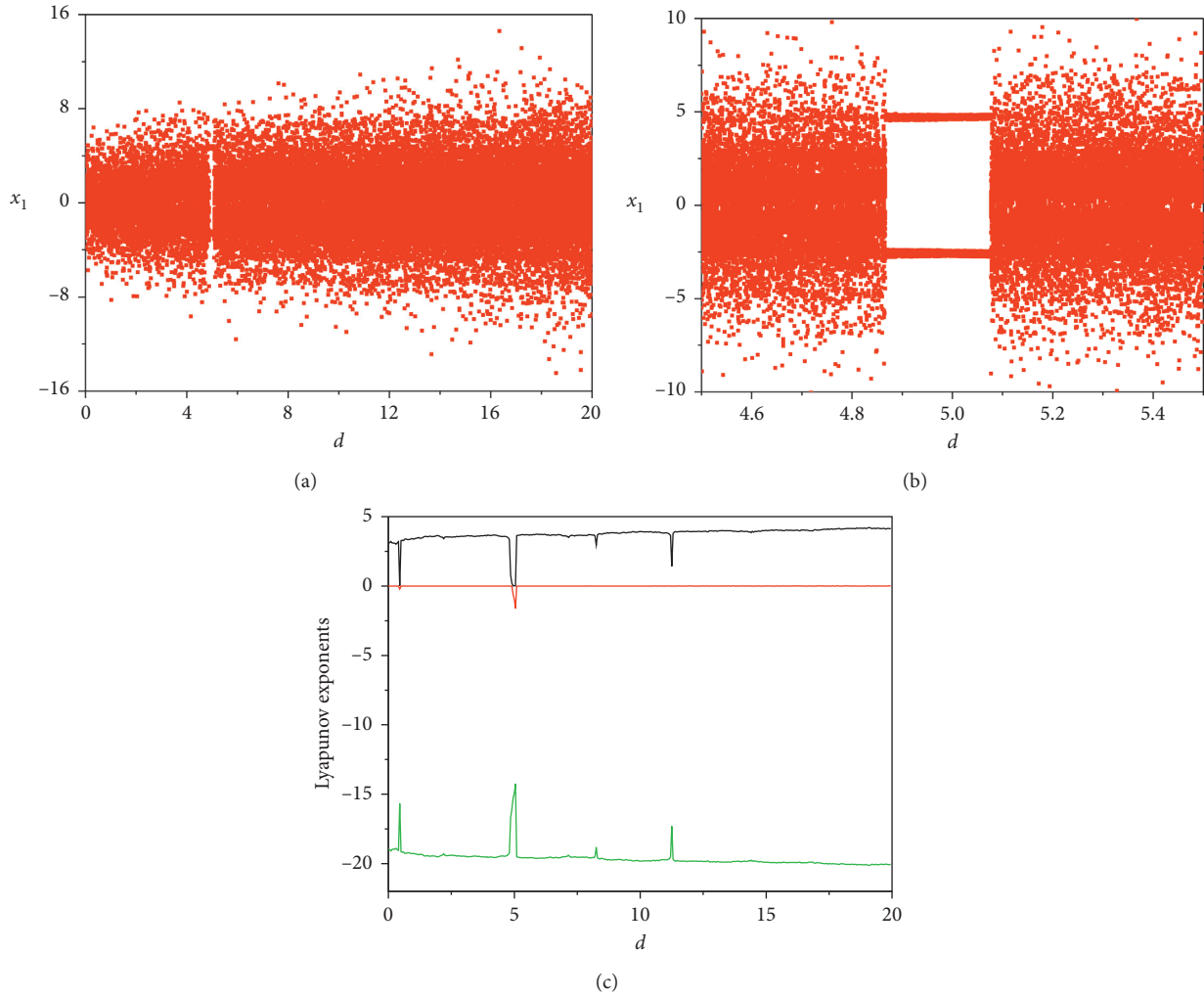


FIGURE 4: (a, b) Bifurcation diagram versus d ; (c) finite time Lyapunov exponent spectrum versus d .

$$\begin{cases} \dot{x}_1 = ax_2 - gx_1 + dx_2x_3, \\ \dot{x}_2 = bx_1 - ex_1x_3, \\ \dot{x}_3 = kx_1 - cx_3 + fx_1x_2. \end{cases} \quad (8)$$

System (8) possesses three equilibrium points, which are, respectively, described by

$$\begin{aligned} &P_0(0, 0, 0), \\ &P_1\left((ae + bd)\frac{-k + \sqrt{k^2 + (4bcgf/(ae + bd))}}{2gef}, \frac{-k + \sqrt{k^2 + (4bcgf/(ae + bd))}}{2f}, \frac{b}{e}\right), \\ &P_2\left((ae + bd)\frac{-k - \sqrt{k^2 + (4bcgf/(ae + bd))}}{2gef}, \frac{-k - \sqrt{k^2 + (4bcgf/(ae + bd))}}{2f}, \frac{b}{e}\right). \end{aligned} \quad (9)$$

When selecting the parameter set $a=24$, $b=12$, $c=1$, $d=1$, $e=1$, $f=1$, $k=1$, and $g=6$, the two nonzero

equilibrium points are obtained as $P_1(6, 1, 12)$ and $P_2(-12, -2, 12)$. The corresponding characteristic roots are

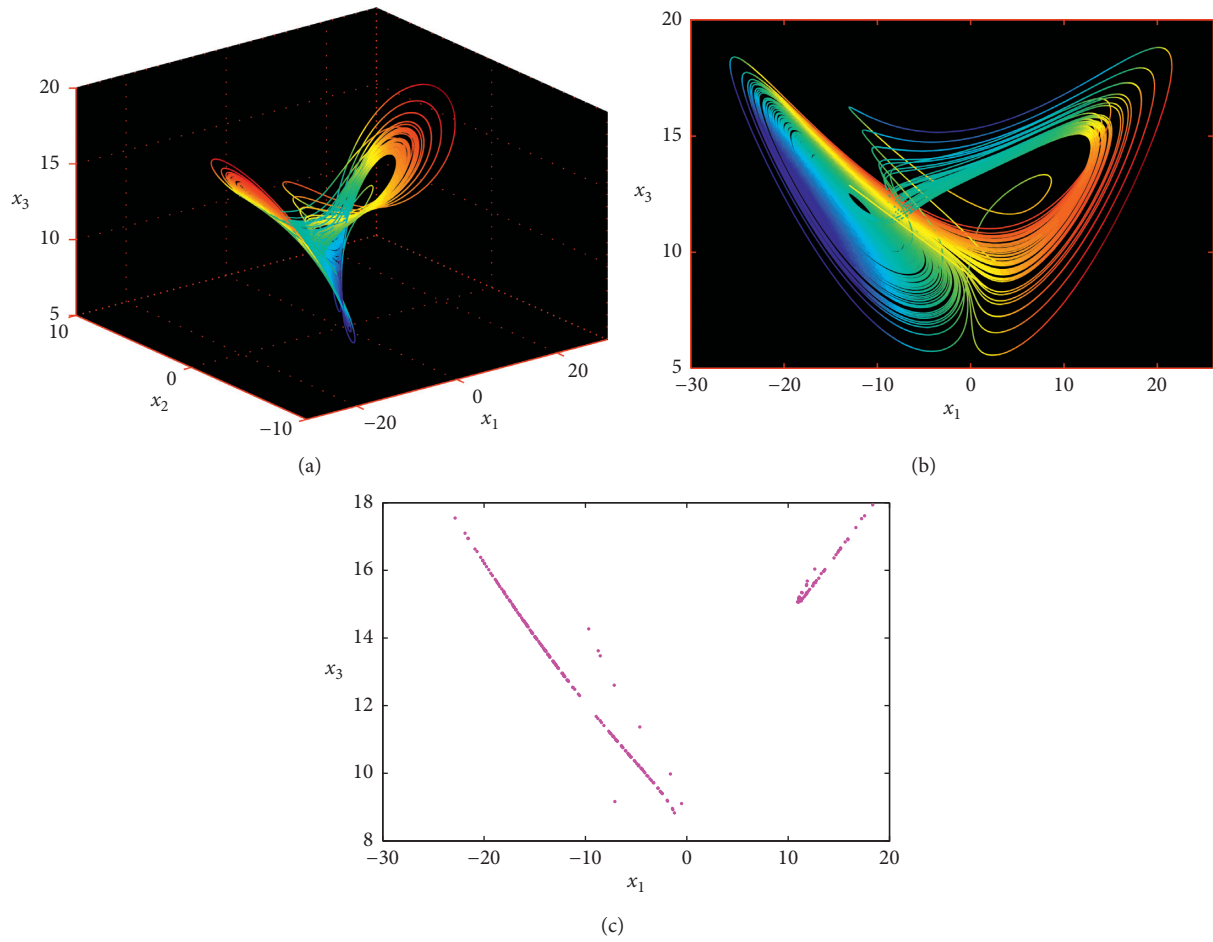


FIGURE 5: (a) x_1 - x_2 - x_3 phase portrait; (b) x_1 - x_3 phase portrait; (c) Poincaré mapping.

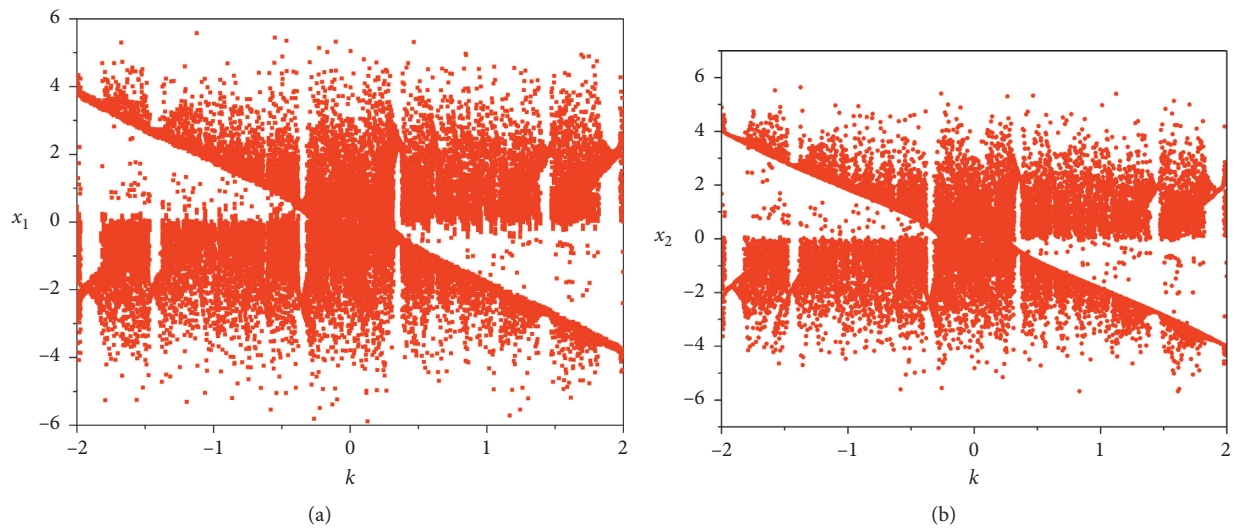


FIGURE 6: Continued.

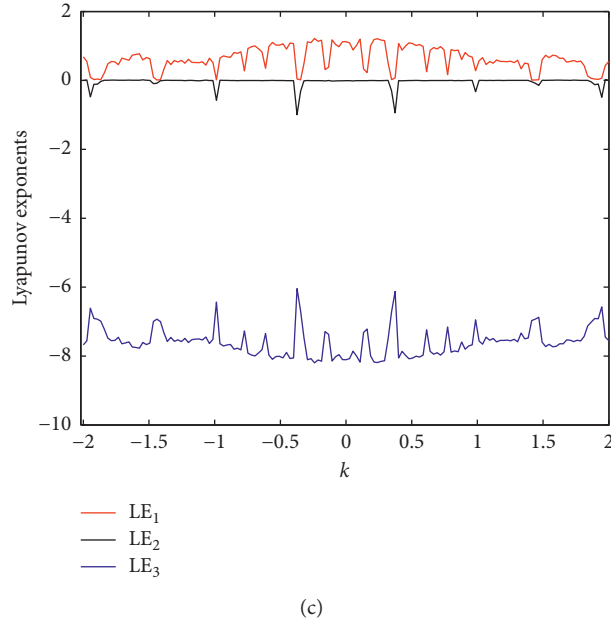


FIGURE 6: (a, b) Bifurcation diagram versus k ; (c) finite time Lyapunov exponent spectrum versus k .

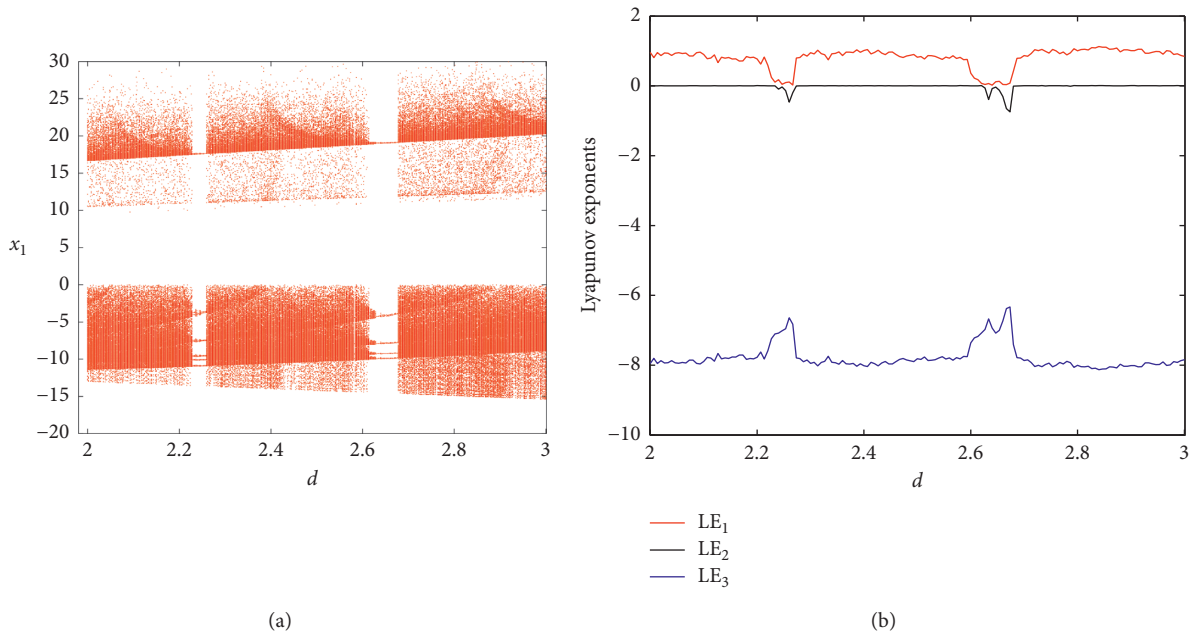


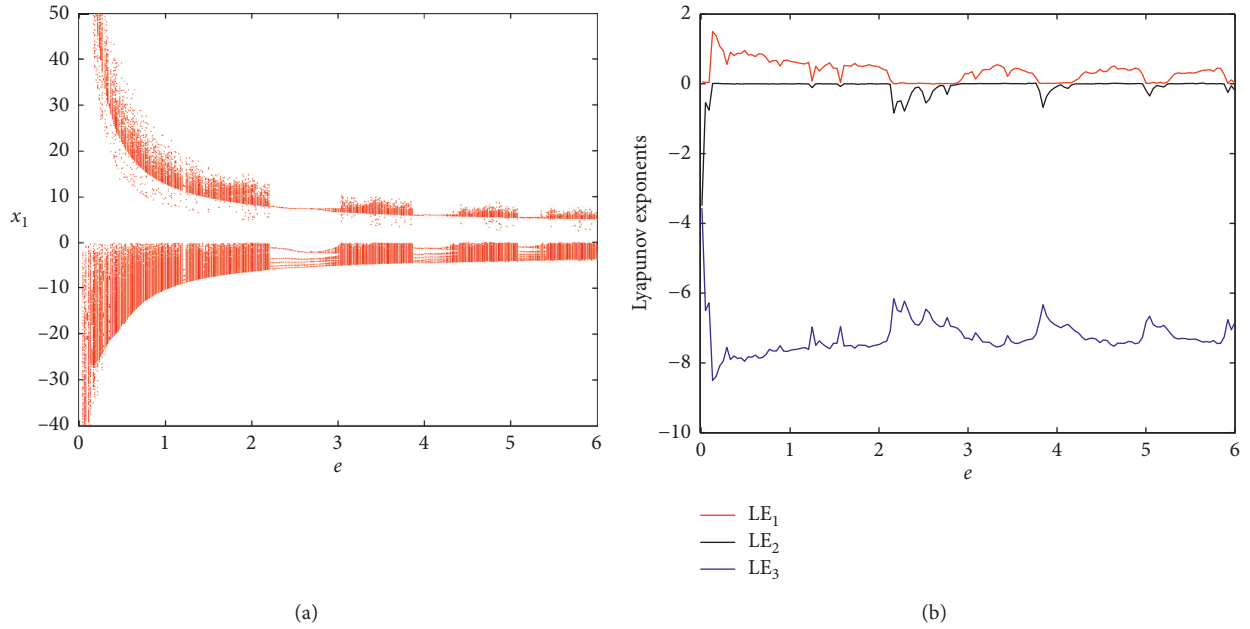
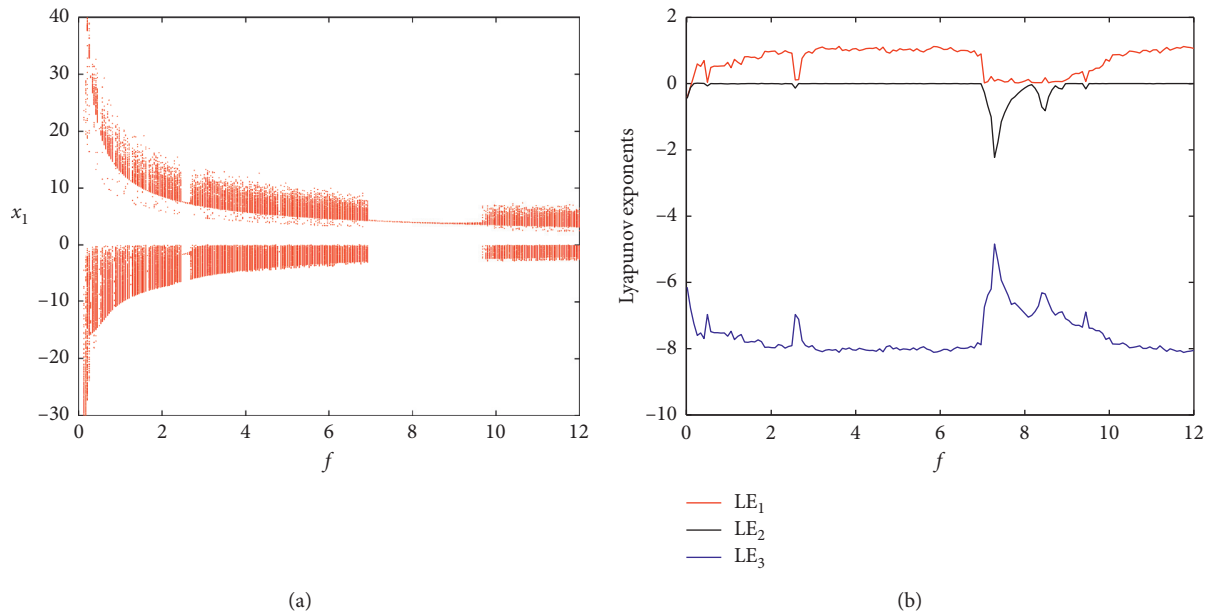
FIGURE 7: (a) Bifurcation diagram and (b) finite time Lyapunov exponent spectrum versus d .

$$\begin{aligned}
 P_0: \lambda_1 &= -1, \lambda_2 = 14.2337, \lambda_3 = -20.2337, \\
 P_1: \lambda_1 &= -9.7318, \lambda_2 = 1.3659 + 8.0449i, \\
 &\lambda_3 = 1.3659 - 8.0449i, \\
 P_2: \lambda_1 &= -8.2073, \lambda_2 = 0.6036 + 12.5517i, \\
 &\lambda_3 = 0.6036 - 12.5517i.
 \end{aligned} \tag{10}$$

Obviously, equilibrium point P_0 is a saddle-node with two-dimensional stable manifold and one-dimensional

unstable manifold. And the equilibrium points P_1 and P_2 are saddle-focus points with two-dimensional unstable manifold and one-dimensional stable manifold.

The corresponding finite time Lyapunov exponents by orthogonal method are calculated as 0.926059, 0.051479, and -10.972296 . And the Kaplan–Yorke dimension is obtained as $D_{KY} = 2 + (0.926059 + 0.051479)/10.972296 = 2.0891$, revealing a fractional feature. Therefore, system (8) is chaotic. The typical chaotic phase diagrams and Poincare mapping on plane $x_2 = 0$ are depicted in Figure 5.

FIGURE 8: (a) Bifurcation diagram and (b) finite time Lyapunov exponent spectrum versus e .FIGURE 9: (a) Bifurcation diagram and (b) finite time Lyapunov exponent spectrum versus f .

3.2. Analysis of Phase Modulation. In system (8), coefficient k is a phase parameter, which can control the signal phase of x_1 , x_2 simultaneously. The phase reversal can be verified by the invariance of the transformation $(x_1, x_2, x_3, a, b, c, d, e, f, g, k) \rightarrow (-x_1, -x_2, x_3, a, b, c, d, e, f, g, -k)$. The bifurcation diagrams for x_1 and x_2 are reverse symmetrical, and the Lyapunov exponent spectrum is symmetrical about $k=0$, as depicted in Figure 6. This further demonstrates that the sign of k can control the polarity of x_1 and x_2 , independent of the dynamics behavior.

3.3. Analysis of Amplitude Modulation. In the search for the property of amplitude modulation, it is surprising to find that for the presented system (8), there is no coefficient of nonlinearity employed to control the signal amplitude. The obtained result is different from the existing quadratic system [11–14] and the reported system (1). The most intuitive interpretation is the numerical simulations of bifurcation diagram and Lyapunov exponent spectrum versus the nonlinear parameter, as shown in Figures 7–9. Theoretically, according to the proposed method in [19], we cannot access appropriate variable

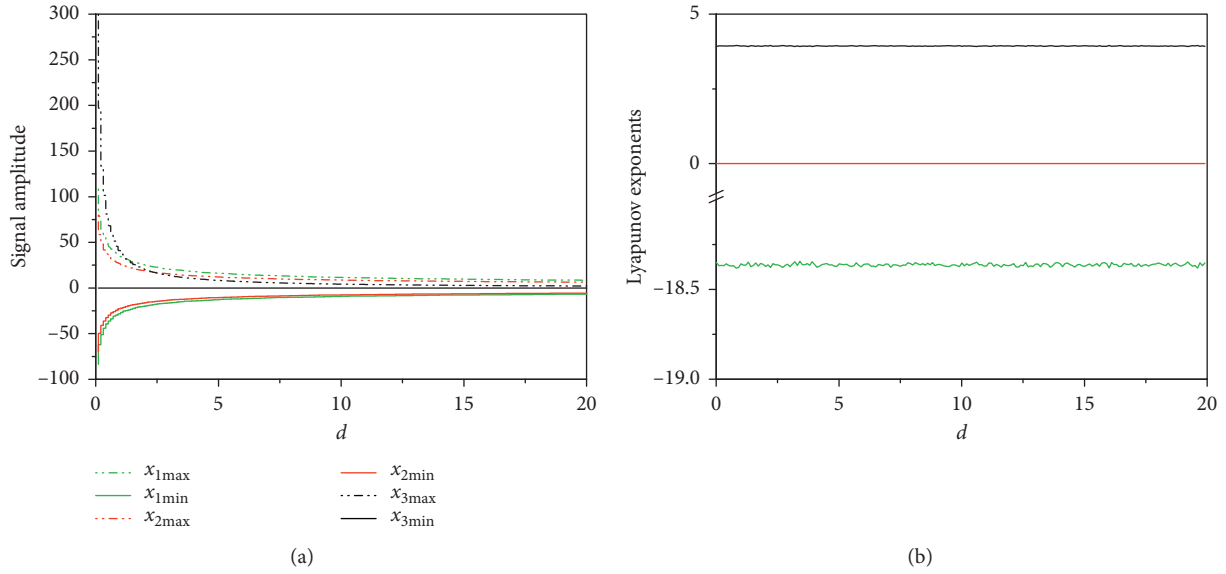


FIGURE 10: (a) Signal amplitude and (b) finite time Lyapunov exponent spectrum versus d .

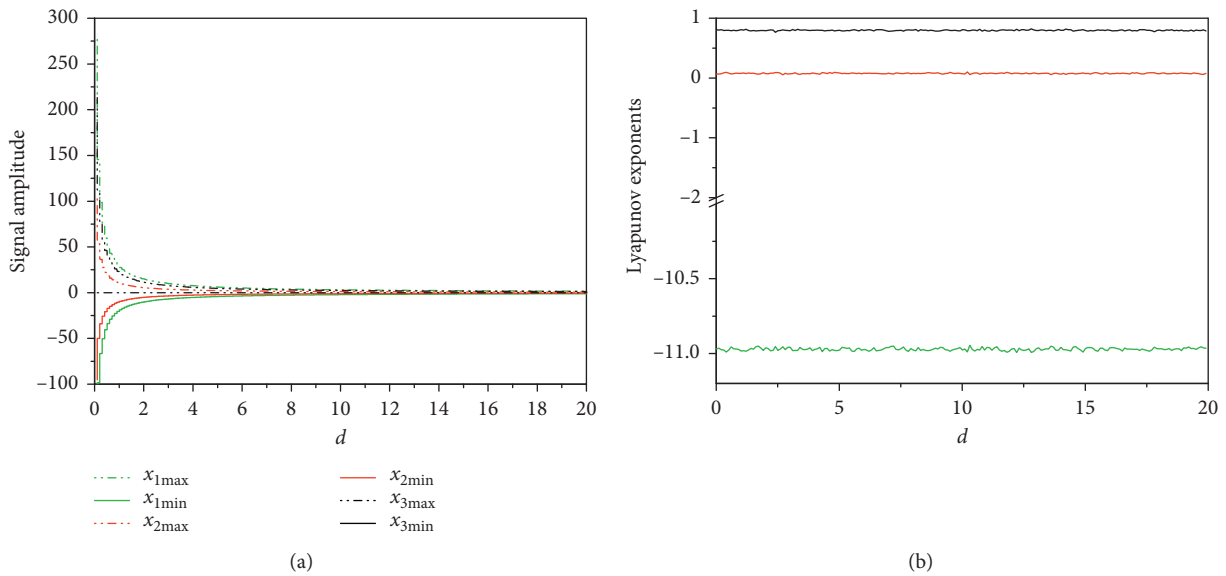


FIGURE 11: (a) Signal amplitude and (b) finite time Lyapunov exponent spectrum versus d .

substitution to realize the normalization of the system equation and characteristic equation [19].

4. Amplitude Modulation Principle of Chaotic System

As shown in the previous literatures [11–15], the coefficients of quadratic terms in smooth chaotic systems can modulate the signal amplitude of partial or total state variables. However, for systems (1) and (8) reported in this study, it is found that not all quadratic nonlinearity coefficients can be used to modulate the amplitude of signals. Therefore, when investigating dynamic properties of a chaotic system, we propose a

naturally confusing but worthwhile question: “what is the possible principle for modulating the amplitude of chaotic signals?”

The physical significance of equilibrium point of dynamic system can be explained as zero velocity point. When the trajectory of a chaotic attractor is rescaled, the nonzero equilibrium point will deviate from the initial position. On the contrary, when the nonzero equilibrium point deviates from the initial position, the signal amplitude of the phase space trajectory can be rescaled. Therefore, the amplitude modulation principle of chaotic system with multiple equilibrium points can be described as follows: (1) in the mathematical representation of nonzero equilibrium point, the amplitude parameter is axisymmetric and (2) the location of the nonzero

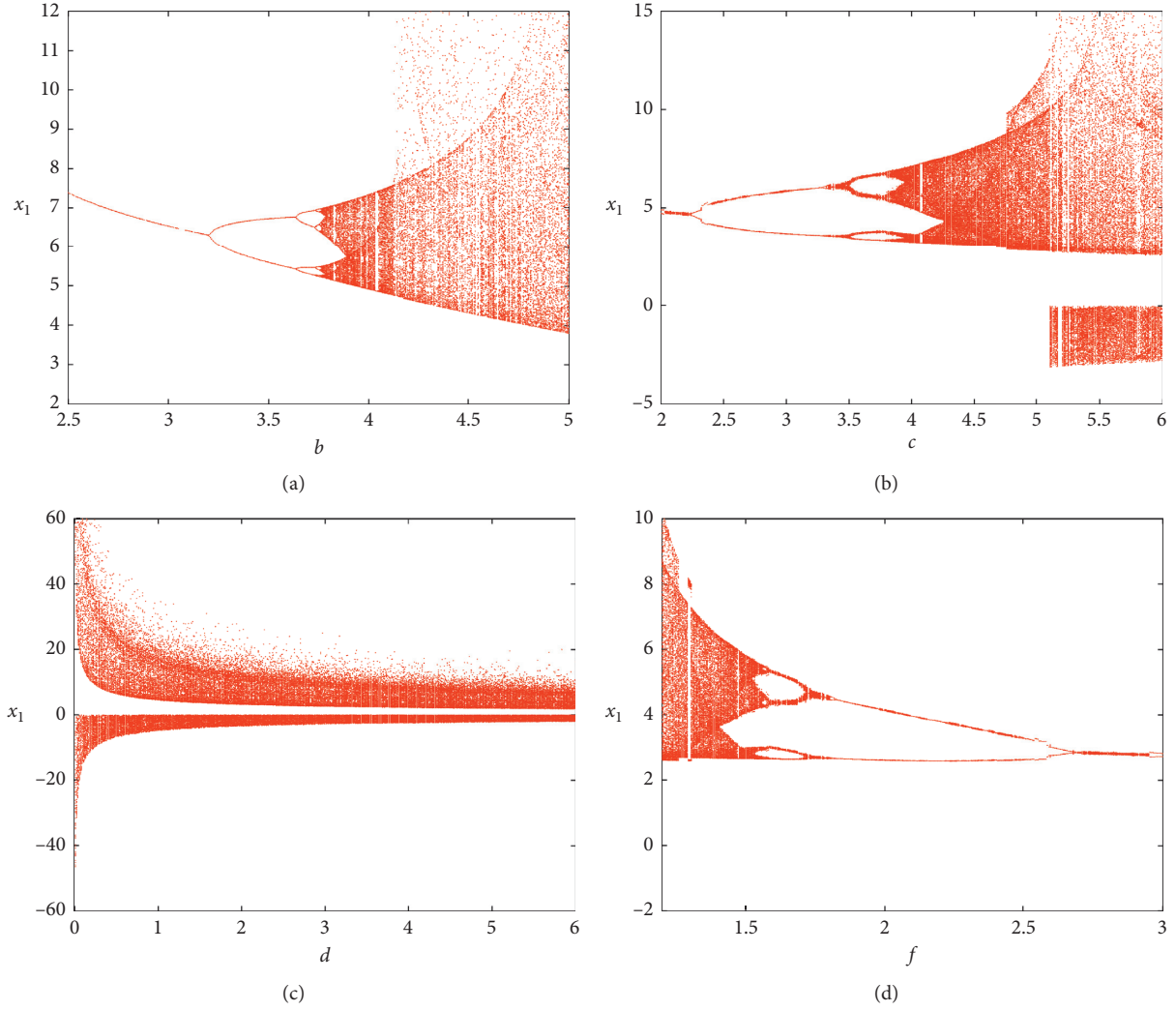


FIGURE 12: Modulation property of signal amplitude for system (15).

equilibrium point in phase space can be controlled by the amplitude parameter.

From the expression of nonzero equilibrium points of system (1), it can be seen that the parameters d and e of nonlinear term cannot modulate the location of equilibrium point P_1 , P_2 , P_3 , or P_4 . Accordingly, parameter d or e cannot modulate the signal amplitude. When we introduce a unified parameter d in x_2x_3 and x_1x_3 , system (1) is deduced to

$$\begin{cases} \dot{x}_1 = a(x_2 - x_1) + dx_2x_3, \\ \dot{x}_2 = bx_2 - dx_1x_3, \\ \dot{x}_3 = -cx_3 + fx_1x_2, \end{cases} \quad (11)$$

and the four nonzero equilibrium points are

$$\begin{aligned} P_1 & \left(\sqrt{\frac{bc}{df}}, \frac{-a\sqrt{c} + \sqrt{c}\sqrt{a^2 + 4ab}}{2\sqrt{bdf}}, \frac{-a + \sqrt{a^2 + 4ab}}{2d} \right), \\ P_2 & \left(\sqrt{\frac{bc}{df}}, \frac{-a\sqrt{c} - \sqrt{c}\sqrt{a^2 + 4ab}}{2\sqrt{bdf}}, \frac{-a - \sqrt{a^2 + 4ab}}{2d} \right), \\ P_3 & \left(-\sqrt{\frac{bc}{df}}, \frac{a\sqrt{c} + \sqrt{c}\sqrt{a^2 + 4ab}}{2\sqrt{bdf}}, \frac{a + \sqrt{a^2 + 4ab}}{2d\sqrt{bf}} \right), \\ P_4 & \left(-\sqrt{\frac{bc}{df}}, \frac{a\sqrt{c} - \sqrt{c}\sqrt{a^2 + 4ab}}{2\sqrt{bdf}}, \frac{a - \sqrt{a^2 + 4ab}}{2d\sqrt{bf}} \right). \end{aligned} \quad (12)$$

It is known that for equilibrium points P_1 and P_2 , the set of symmetrical axis is $(0, -a\sqrt{c}/2\sqrt{bdf}, -a/2d)$, and the set of symmetrical axis for equilibrium points P_3 and P_4 is $(0, a\sqrt{c}/2\sqrt{bdf}, -a/2d\sqrt{bf})$. In addition, the parameter d can modulate the location of the nonzero equilibrium points according to $\sqrt{1/d}$, $\sqrt{1/d}$, and $1/d$, respectively. As a result, the parameter d can modulate the amplitude of signal x_1 , x_2 , and x_3 according to $\sqrt{1/d}$, $\sqrt{1/d}$, and $1/d$, respectively. The signal amplitude and Lyapunov exponent spectrum versus d are depicted in Figure 10.

For the expression of nonzero equilibrium points of system (8), parameters d , e , and f of quadratic terms cannot

modulate the location of equilibrium point P_1 or P_2 . Accordingly, parameter d , e , or f cannot modulate the signal amplitude. To realize amplitude modulation in system (8), we introduce a unified parameter d in each nonlinear term yielding

$$\begin{cases} \dot{x}_1 = ax_2 - gx_1 + dx_2x_3, \\ \dot{x}_2 = bx_1 - dx_1x_3, \\ \dot{x}_3 = kx_1 - cx_3 + dx_1x_2, \end{cases} \quad (13)$$

and the two nonzero equilibrium points are deduced as

$$\begin{aligned} P_1 & \left((a+b) \frac{-k + \sqrt{k^2 + (4bcg)/(a+b)}}{2gd}, \frac{-k + \sqrt{k^2 + (4bcg)/(a+b)}}{2d}, \frac{b}{d} \right), \\ P_2 & \left((a+b) \frac{-k - \sqrt{k^2 + (4bcg)/(a+b)}}{2gd}, \frac{-k - \sqrt{k^2 + (4bcg)/(a+b)}}{2d}, \frac{b}{d} \right). \end{aligned} \quad (14)$$

We know that for equilibrium points P_1 and P_2 , the set of symmetrical axis is $(-k(a+b)/2gd, -k/2d, 0)$. In addition, the parameter d can modulate the location of the nonzero equilibrium points according to $1/d$, respectively. Similarly, parameter d can modulate the amplitude of x_1 , x_2 , and x_3 according to $1/d$, respectively. The signal amplitude and Lyapunov exponent spectrum versus d are shown in Figure 11.

5. Discussion and Conclusion

Exploring the amplitude modulation phenomenon of chaotic signal is attractive yet recent topic of interest. This paper reported two chaotic systems with three quadratic cross-product terms and analyzed the property of amplitude modulation. By making an exhaustive study on the characteristics of nonzero equilibrium points, we attempt to address the possible principle for amplitude modulation. That is to say, the amplitude parameter in the expression of nonzero equilibrium point is symmetrical about some axis and can modulate the location of the nonzero equilibrium point in phase space.

The addressed principle can be popularized to high-dimensional chaotic system and other chaotic systems except with quadratic nonlinearity [19–22], not relying on the type of nonzero equilibrium point. However, for the dynamical system with none, single, or an infinite number of equilibrium points [23–26], the principle is out of our consideration and deserves an in-depth study.

It must be reiterated that the proposed principle is just a prerequisite, but not a sufficient and necessary condition for amplitude modulation. As an interpretation, we consider the following system with cubic nonlinearity:

$$\begin{cases} \dot{x}_1 = -ax_1 + bx_2x_3, \\ \dot{x}_2 = -cx_2^3 + dx_1x_3, \\ \dot{x}_3 = ex_3 - fx_1x_2. \end{cases} \quad (15)$$

System (15) holds five equilibrium points, and the nonzero equilibrium points are described by

$$\begin{aligned} P_1 & \left(\frac{e}{f} \sqrt{\frac{ac}{bd}}, \sqrt{\frac{ae}{bf}}, \frac{a}{b} \sqrt{\frac{ce}{df}} \right), \\ P_2 & \left(-\frac{e}{f} \sqrt{\frac{ac}{bd}}, \sqrt{\frac{ae}{bf}}, -\frac{a}{b} \sqrt{\frac{ce}{df}} \right), \\ P_3 & \left(\frac{e}{f} \sqrt{\frac{ac}{bd}}, -\sqrt{\frac{ae}{bf}}, \frac{a}{b} \sqrt{\frac{ce}{df}} \right), \\ P_4 & \left(\frac{e}{f} \sqrt{\frac{ac}{bd}}, -\sqrt{\frac{ae}{bf}}, -\frac{a}{b} \sqrt{\frac{ce}{df}} \right). \end{aligned} \quad (16)$$

Clearly, the set of symmetrical axis for equilibrium points P_1 , P_2 , P_3 , and P_4 is $(0, 0, 0)$. In addition, the parameter b can modulate the location of the nonzero equilibrium points according to $\sqrt{1/b}$, $\sqrt{1/b}$, and $1/b$; the parameter c can modulate the location of the nonzero equilibrium points according to \sqrt{c} , 1 , and \sqrt{c} ; the parameter d can modulate the location of the nonzero equilibrium points according to $\sqrt{1/d}$, 1 , and $\sqrt{1/d}$; and the parameter f can modulate the location of the nonzero equilibrium points according to $1/f$, $\sqrt{1/f}$, and $\sqrt{1/f}$. However, it is found from the numerical experiment that only the nonlinear parameter d can modulate the amplitude of x_1 , x_2 , and x_3 according to $\sqrt{1/d}$, 1 , and $\sqrt{1/d}$, respectively, as plotted in Figure 12.

In spite of this, the principle provides a feasible mentality for analyzing amplitude modulation of chaotic signal, which can be briefly summarized from theoretical analysis to numerical confirmation. We hope that our work can

constitute a stimulus and afford a subservient reference for further exploring the intrinsic amplitude modulation mechanism of chaotic systems.

Data Availability

The data used to support the findings of this study are included within the article.

Conflicts of Interest

The authors declare that there are no conflicts of interest regarding the publication of this paper.

Acknowledgments



This work was supported in part by the Hunan Provincial Natural Science Foundation of China (no. 2019JJ40109), the Research Foundation of Education Bureau of Hunan Province of China (nos. 18A314, 19C0864 and 16K037), Science and Technology Program of Hunan Province (nos. 2016TP1021 and 2019TP1014), the research and innovation project of the graduate students of Hunan Institute of technology (no. YCX2019A13), and the Science and Research Creative Team of Hunan Institute of Science and Technology (no. 2019-TD-10).

References

- [1] M. Siewe, C. Tchawoua, and P. Woafu, "Melnikov chaos in a periodically driven Rayleigh-Duffing oscillator," *Mechanics Research Communications*, vol. 37, no. 4, pp. 363–368, 2010.
- [2] A. Zarei, "Complex dynamics in a 5-D hyper-chaotic attractor with four-wing, one equilibrium and multiple chaotic attractors," *Nonlinear Dynamics*, vol. 81, no. 1-2, pp. 585–605, 2015.
- [3] F. Peng, Q. Long, Z.-X. Lin, and M. Long, "A reversible watermarking for authenticating 2D CAD engineering graphics based on iterative embedding and virtual coordinates," *Multimedia Tools and Applications*, vol. 78, no. 19, pp. 26885–26905, 2019.
- [4] E. Bilotta, F. Chiaravalloti, and P. Pantano, "Complexity and emergence of wave dynamics in a chain of sequentially interconnected Chua circuits," *Mechanics Research Communications*, vol. 68, pp. 9–17, 2015.
- [5] C. Li, B. Feng, S. Li, J. Kurths, and G. Chen, "Dynamic analysis of digital chaotic maps via state-mapping networks," *IEEE Transactions on Circuits and Systems I: Regular Papers*, vol. 66, no. 6, pp. 2322–2335, 2019.
- [6] Q. Zhao, C. Wang, and X. Zhang, "A universal emulator for memristor, memcapacitor, and meminductor and its chaotic circuit," *Chaos*, vol. 29, Article ID 013141, 2019.
- [7] C. Li, K. Qian, S. He, H. Li, and W. Feng, "Dynamics and optimization control of a robust chaotic map," *IEEE Access*, vol. 7, pp. 160072–160081, 2019.
- [8] A. Jimenez-Triana, G. Chen, and A. Gauthier, "A parameter-perturbation method for chaos control to stabilizing UPOs," *IEEE Transactions on Circuits and Systems II: Express Briefs*, vol. 62, no. 4, pp. 407–411, 2015.
- [9] X. Wang, J. Yu, C. Jin, H. H. C. Iu, and S. Yu, "Chaotic oscillator based on memcapacitor and meminductor," *Nonlinear Dynamics*, vol. 96, no. 1, pp. 161–173, 2019.
- [10] Q. Lai, B. Norouzi, and F. Liu, "Dynamic analysis, circuit realization, control design and image encryption application of an extended Lü system with coexisting attractors," *Chaos, Solitons & Fractals*, vol. 114, pp. 230–245, 2018.
- [11] C. Li, L. Wu, H. Li, and Y. Tong, "A novel chaotic system and its topological horseshoe," *Nonlinear Analysis: Modelling and Control*, vol. 18, no. 1, pp. 66–77, 2013.
- [12] C. Li, K. Su, and L. Wu, "Adaptive sliding mode control for synchronization of a fractional-order chaotic system," *Journal of Computational and Nonlinear Dynamics*, vol. 8, pp. 0310051–0310057, 2013.
- [13] C. Li and J. Zhang, "Synchronisation of a fractional-order chaotic system using finite-time input-to-state stability," *International Journal of Systems Science*, vol. 47, no. 10, pp. 2440–2448, 2016.
- [14] C. Li, Y. Tong, Y. Tong, and Y. Zeng, "Adaptive control and synchronization of a fractional-order chaotic system," *Pramana*, vol. 80, no. 4, pp. 583–592, 2013.
- [15] X. Zhou, "A chaotic system with invariable Lyapunov exponent and its circuit simulation," *Acta Physica Sinica*, vol. 60, p. 100503, 2011.
- [16] M.-S. Abdelouahab and N.-E. Hamri, "A new chaotic attractor from hybrid optical bistable system," *Nonlinear Dynamics*, vol. 67, no. 1, pp. 457–463, 2012.
- [17] M.-F. Danca, N. Kuznetsov, and G. Chen, "Unusual dynamics and hidden attractors of the Rabinovich-Fabrikant system," *Nonlinear Dynamics*, vol. 88, no. 1, pp. 791–805, 2017.
- [18] A. E. Matouk and H. N. Agiza, "Bifurcations, chaos and synchronization in ADVP circuit with parallel resistor," *Journal of Mathematical Analysis and Applications*, vol. 341, no. 1, pp. 259–269, 2008.
- [19] C. Li, K. Su, and J. Zhang, "Amplitude control and projective synchronization of a dynamical system with exponential nonlinearity," *Applied Mathematical Modelling*, vol. 39, no. 18, pp. 5392–5398, 2015.
- [20] Q. Yang and C. Chen, "A 5D hyperchaotic system with three positive Lyapunov exponents coined," *International Journal of Bifurcation and Chaos*, vol. 23, no. 6, p. 1350109, 2013.
- [21] A. Sahab, M. Ziabari, and M. Modabbernia, "A novel fractional order hyperchaotic system with a quadratic exponential nonlinear term and its synchronization," *Advances in Difference Equations*, vol. 2012, no. 194, pp. 393–444, 2012.
- [22] M.-F. Danca, "Attractors synthesis for a Lotka-Volterra like system," *Applied Mathematics and Computation*, vol. 216, no. 7, pp. 2107–2117, 2010.
- [23] Z. Wei, "Dynamical behaviors of a chaotic system with no equilibria," *Physics Letters A*, vol. 376, no. 2, pp. 102–108, 2011.
- [24] D. Cafagna and G. Grassi, "Chaos in a new fractional-order system without equilibrium points," *Communications in Nonlinear Science and Numerical Simulation*, vol. 19, no. 9, pp. 2919–2927, 2014.
- [25] X. Wang and G. Chen, "A chaotic system with only one stable equilibrium," *Communications in Nonlinear Science and Numerical Simulation*, vol. 17, no. 3, pp. 1264–1272, 2012.
- [26] P. Zhou and F. Yang, "Hyperchaos, chaos, and horseshoe in a 4D nonlinear system with an infinite number of equilibrium points," *Nonlinear Dynamics*, vol. 76, no. 1, pp. 473–480, 2014.

Research Article

Analysis, Stabilization, and DSP-Based Implementation of a Chaotic System with Nonhyperbolic Equilibrium

Xuan-Bing Yang,^{1,2} Yi-Gang He ,^{1,3} Chun-Lai Li ,² and Chang-Qing Liu¹

¹School of Electrical Engineering and Automation, Hefei University of Technology, Hefei 230009, China

²School of Information Science and Engineering, Hunan Institute of Science and Technology, Yueyang 414006, China

³School of Electrical Engineering and Automation, Wuhan University, Wuhan 430072, China

Correspondence should be addressed to Yi-Gang He; 18655136887@163.com and Chun-Lai Li; hnistlichl@163.com

Received 31 August 2019; Revised 21 October 2019; Accepted 13 November 2019; Published 8 January 2020

Guest Editor: Viet-Thanh Pham

Copyright © 2020 Xuan-Bing Yang et al. This is an open access article distributed under the Creative Commons Attribution License, which permits unrestricted use, distribution, and reproduction in any medium, provided the original work is properly cited.

This paper reports an autonomous dynamical system, and it finds that one nonhyperbolic zero equilibrium and two hyperbolic nonzero equilibria coexist in this system. Thus, it is difficult to demonstrate the existence of chaos by Šil'nikov theorem. Consequently, the topological horseshoe theory is adopted to rigorously prove the chaotic behaviors of the system in the phase space of Poincaré map. Then, a single control scheme is designed to stabilize the dynamical system to its zero-equilibrium point. Besides, to verify the theoretical analyses physically, the attractor and stabilization scheme are further realized via DSP-based technique.

1. Introduction

Chaotic behaviors exist widely in biology, engineering, economy, and many other scientific disciplines [1–4]. Chaotic systems have the properties of unpredictability, topological mixing, ergodicity, and sensitivity to their initial values and control parameters. Owing to the noise-like spectrum and broad-band, chaotic signals are potentially applicable in engineering such as random sequence generation [5], secure communication [6], image encryption [7, 8], signal detection [9], radar and sonar systems [10], and so on. Therefore, it is significant to design and analyze new chaotic systems. In 1963, Lorenz proposed the first three-dimensional chaotic system when studying earth's atmospheric convection [11]. Then, many low-dimensional mathematical models with positive Lyapunov exponents have been introduced, along with the analysis of a rich class of dynamical behaviors. New examples continue to be reported for publication in nonlinear dynamics journals for the physical applications. Nevertheless, it is necessary to develop chaotic systems with simple structure and rich dynamical behaviors from the perspective of application.

As a striking chaos theory with symbolic dynamics obtained by Kennedy in continuous map [12], the topological horseshoe can provide an impactful tool for proving chaotic dynamics in hyperbolic or nonhyperbolic system. Up to present, many noteworthy theoretical progresses have been extended in finding the existence of horseshoe. For example, Yang introduced the remarkable criteria for finding the topological horseshoe in noncontinuous map [13, 14], which has been successfully applied to some practical systems for verifying chaos [15, 16]. Li presented a new method with three steps for finding horseshoes in dynamical systems by using several simple results on topological horseshoes [17]. However, it is still a tough work to find a topological horseshoe in a practical chaotic system [18].

It is impossible to chronically predict the future behavior of chaotic system, but one can stabilize the future behavior into a certain range by using control technology. The seminal attempt of controlling chaos is the well-known OGY method, which applies small perturbations to system parameter to keep the system close to the target periodic orbit [19]. However, the experimental implementation of this

method is restricted by the level of noise in the experimental data for the sake of the discrete nature of the control signal. Then, a continuous delayed feedback scheme is proposed consequently [20]. The control signal is the perturbations of the difference between the states of the current system and one period of the target orbit in the past. Therefore, the intensity of the perturbations will vanish when the system evolves to the desired orbit. Since then, a wide variety of control approaches emerged for different applications, such as backstepping control [21], sliding mode control [22], sampled-data control [23], and multiswitching combination control [24], just to name a few. However, the present schemes focused on the control problem need several controllers. From the points of both practical application and theoretical research, it is significant to design simple yet executable control technique.

In this paper, an autonomous chaotic system with a simple algebraic structure of six terms is proposed. Basic dynamical properties of the system, including equilibrium point, phase portrait, Poincaré map, parameter bifurcation, and Lyapunov exponent, are studied in theory and numerical simulation. It is found that this system exhibits fruitful dynamic behaviors of dense periodic windows and coexistence of nonhyperbolic and hyperbolic equilibrium points. And to rigorously verify the emergence of chaos of this system in theory, the topological horseshoe is investigated in the phase space of Poincaré map. Then, based on the Lyapunov stability criterion, a single control scheme is designed to stabilize the chaotic system to its zero-equilibrium point. The implementation scheme of attractors and control scheme are discussed in detail and realized via DSP-based technique, confirming the validity and enforceability of the theoretical scheme.

2. The Proposed Dynamical System

The autonomous dynamical system considered here is given by

$$\begin{cases} \dot{x}_1 = -ax_1 + bx_2, \\ \dot{x}_2 = ex_2 - fx_1x_3, \\ \dot{x}_3 = -cx_3^3 + dx_1x_2. \end{cases} \quad (1)$$

Differential equations of system (1) are simple with a cubic term and two quadratic cross-product terms. The system parameters a , b , c , d , e , and f are all positive constants.

2.1. Dissipativity and Existence of Attractor. We first consider the general condition of dissipativity to ensure the chaotic property:

$$\nabla V = \frac{\partial \dot{x}_1}{x_1} + \frac{\partial \dot{x}_2}{x_2} + \frac{\partial \dot{x}_3}{x_3} = -a + e - 3cx_3^2. \quad (2)$$

Therefore, system (1) would be dissipative and will converge to a subset of measure zero volume according to $dV/dt = e^{(-a+e-3cx_3^2)t}$, when satisfying $-a + e - 3cx_3^2 < 0$. This means that the volume will become $V(0)e^{(-a+e-3cx_3^2)t}$ at time

t through the flow generated by the system for an initial volume $V(0)$. Therefore, there exists an attractor in system (1) with $-a + e - 3cx_3^2 < 0$.

2.2. Equilibrium Points and Stability. Considering the condition of equilibrium point $\dot{x}_1 = 0$, $\dot{x}_2 = 0$, and $\dot{x}_3 = 0$, we obtain three equilibrium points of system (1), as follows:

$$\begin{aligned} P_0 & (0, 0, 0), \\ P_1 & \left(\frac{a}{b} \sqrt{\frac{ce^3}{df^3}}, \frac{a^2}{b^2} \sqrt{\frac{ce^3}{df^3}}, \frac{ae}{bf} \right), \\ P_2 & \left(-\frac{a}{b} \sqrt{\frac{ce^3}{df^3}}, -\frac{a^2}{b^2} \sqrt{\frac{ce^3}{df^3}}, \frac{ae}{bf} \right). \end{aligned} \quad (3)$$

When selecting $a = 1$, $b = 6$, $c = 5$, $d = 1$, $e = 3$, and $f = 2$, the equilibrium points and the corresponding eigenvalues are shown in Table 1, including the type of equilibrium points.

From Table 1, it is known that the three equilibrium points are all unstable with stable manifold and unstable manifold. According to [25], since the characteristic value λ_3 of equilibrium point P_0 equals to zero, the equilibrium point is nonhyperbolic type. However, equilibrium points P_1 and P_2 are hyperbolic since all the real parts of the corresponding eigenvalues of these two equilibrium points are nonzero. Therefore, this is a chaotic system in which hyperbolic and nonhyperbolic equilibrium points coexist. And, this kind of chaotic system does not belong to Šil'nikov sense of the chaotic system, and it is difficult to prove the existence of chaos by Šil'nikov theorem. At present, chaotic systems with special features, such as chaotic systems with nonequilibrium, with multistability and with hyperbolic and nonhyperbolic equilibrium coexisting, have attracted extensive attention by researchers [26, 27].

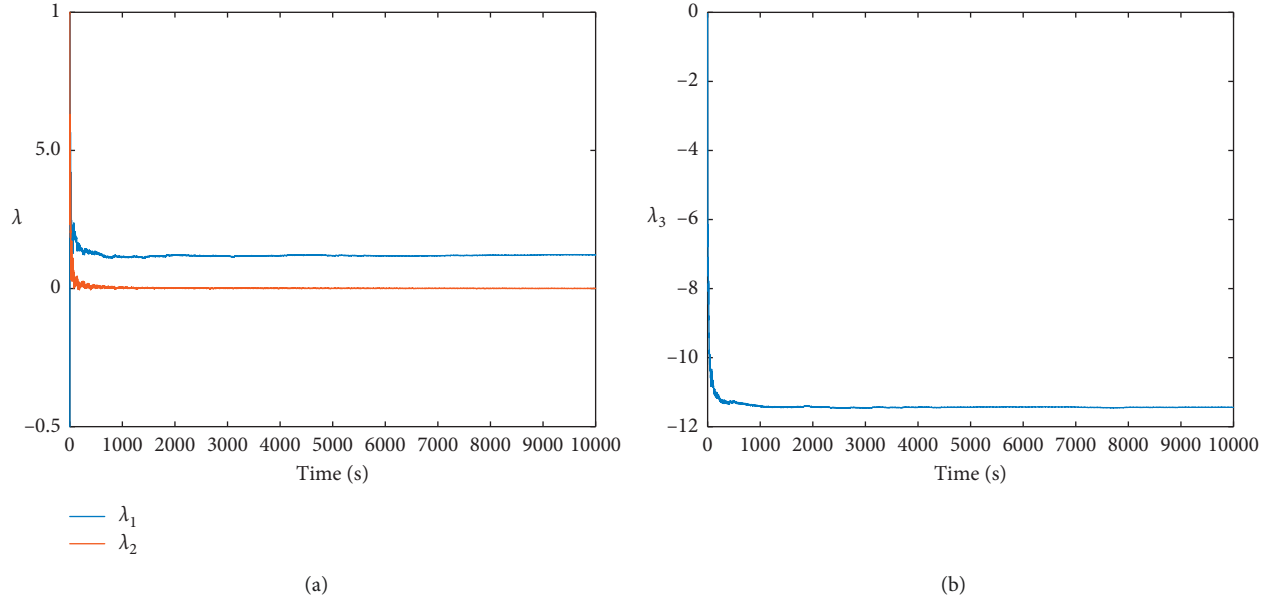
2.3. Phase Portrait and Chaotic Properties. When selecting $a = 1$, $b = 6$, $c = 5$, $d = 1$, $e = 3$, $f = 2$, and initial values $x(0) = (0.01, 0.01, 0.05)$, the Lyapunov exponents of system (1) are depicted in Figures 1(a) and 1(b) with the values as 0.123017, 0.000029, and -11.414797 . According to the three Lyapunov exponents, the Kaplan–Yorke dimension is $D_{KY} = 2 + (0.123017 + 0.000029)/11.414797 = 2.0108$. Therefore, the Kaplan–Yorke dimension is fractional. The corresponding chaotic phase diagrams further reveal that the proposed system displays complicated chaotic behaviors, as depicted in Figure 2.

As an important analytical technique, Poincaré map can reflect the bifurcation and folding properties of chaos. Selecting the parameter values $a = 1$, $b = 6$, $c = 5$, $d = 1$, $e = 3$, and $f = 2$ and taking the crossing planes $x_3 = 0$, $x_1 = 0$, and $x_2 = 0$, we obtain the corresponding Poincaré maps illustrated in Figure 3. We can see the attractor structure from the dense dots.

2.4. Influence of Parameter Variation. It is found that system (1) exhibits complicated dynamical behaviors with the

TABLE 1: Equilibrium points and eigenvalues of system (1).

Equilibrium point	Eigenvalues	Type of equilibrium point
$P_0 (0, 0, 0)$	$\lambda_1 = -1, \lambda_2 = 3, \lambda_3 = 0$	Nonhyperbolic
$P_1 (0.6847, 0.1141, 0.25)$	$\lambda_1 = 1.1087 + 0.6279i,$ $\lambda_2 = 1.1087 - 0.6279i,$ $\lambda_3 = -1.1549$	Hyperbolic
$P_2 (-0.6847, -0.1141, 0.25)$	$\lambda_1 = 1.1087 + 0.6279i,$ $\lambda_2 = 1.1087 - 0.6279i,$ $\lambda_3 = -1.1549$	Hyperbolic

FIGURE 1: Lyapunov exponents of system (1) when $a = 1, b = 6, c = 5, d = 1, e = 3,$ and $f = 2.$

variation of system parameters. As explication, we only consider the variation of parameters c and f in this section.

When fixing parameters $\{a = 1, b = 6, d = 1, e = 3, f = 2\}$ and letting c vary from 2 to 8, the corresponding bifurcation diagram of state variable x_3 and the maximum Lyapunov exponent of system (1) versus c of numerical calculation are shown in Figures 4(a) and 4(b), respectively. As we know that system (1) shows rich dynamical behaviors, ranging from stable equilibrium points, periodic orbits to chaotic oscillations, depending on the parameter values. Furthermore, there emerge many visible periodic windows in the chaotic region. Then, we fix parameters $a = 1, b = 6, c = 5, d = 1,$ and $e = 3,$ while letting f vary from 1 to 3. Figures 5(a) and 5(b) depict the bifurcation diagram of state variable x_3 and the maximum Lyapunov exponent of system (1) versus parameter $f,$ respectively. It is known that with the variation of parameter $f,$ system (1) ranges from stable equilibrium points, periodic orbits to chaotic oscillations, and there emerges many densely distributed periodic windows in the chaotic region, also showing the rich dynamics. The variation of the properties of system (1) with system parameters c and f is of great importance in image encryption.

3. Topological Horseshoe in the Dynamical System

3.1. Review of Topological Horseshoe Theorems. It is still a challenge to find topological horseshoes in a concrete system, especially to select a suitable quadrilateral in the cross section. Before studying the horseshoe embedded in the dynamical system, some theorems on topological horseshoe are reviewed below [12–14, 17].

Let D be a compact subset of $S,$ which is a metric space, and there exists m mutually disjoint compact subsets D_1, D_2, \dots, D_m of $D.$

Definition 1. Let $D_i^1, D_i^2 \subset D_i$ be two fixed disjoint compact subsets with $1 \leq i \leq m.$ If $\gamma \cap D_i^1$ and $\gamma \cap D_i^2$ are compact and nonempty, we say that the connected subset γ of D_i connects D_i^1 and $D_i^2,$ and denote this by $D_i^1 \xrightarrow{\gamma} D_i^2.$

Definition 2. Let γ be a connected subset of $D_i,$ we say that $f(\gamma)$ is suitably across D_i with respect to D_i^1 and $D_i^2,$ if there is a connected subset $\gamma_i \subset \gamma$ satisfying $f(\gamma_i) \subset D_i,$ and $f(\gamma_i) \cap D_i^1$ and $f(\gamma_i) \cap D_i^2$ are nonempty. In this case, it is denoted by $f(\gamma) \mapsto D_i.$

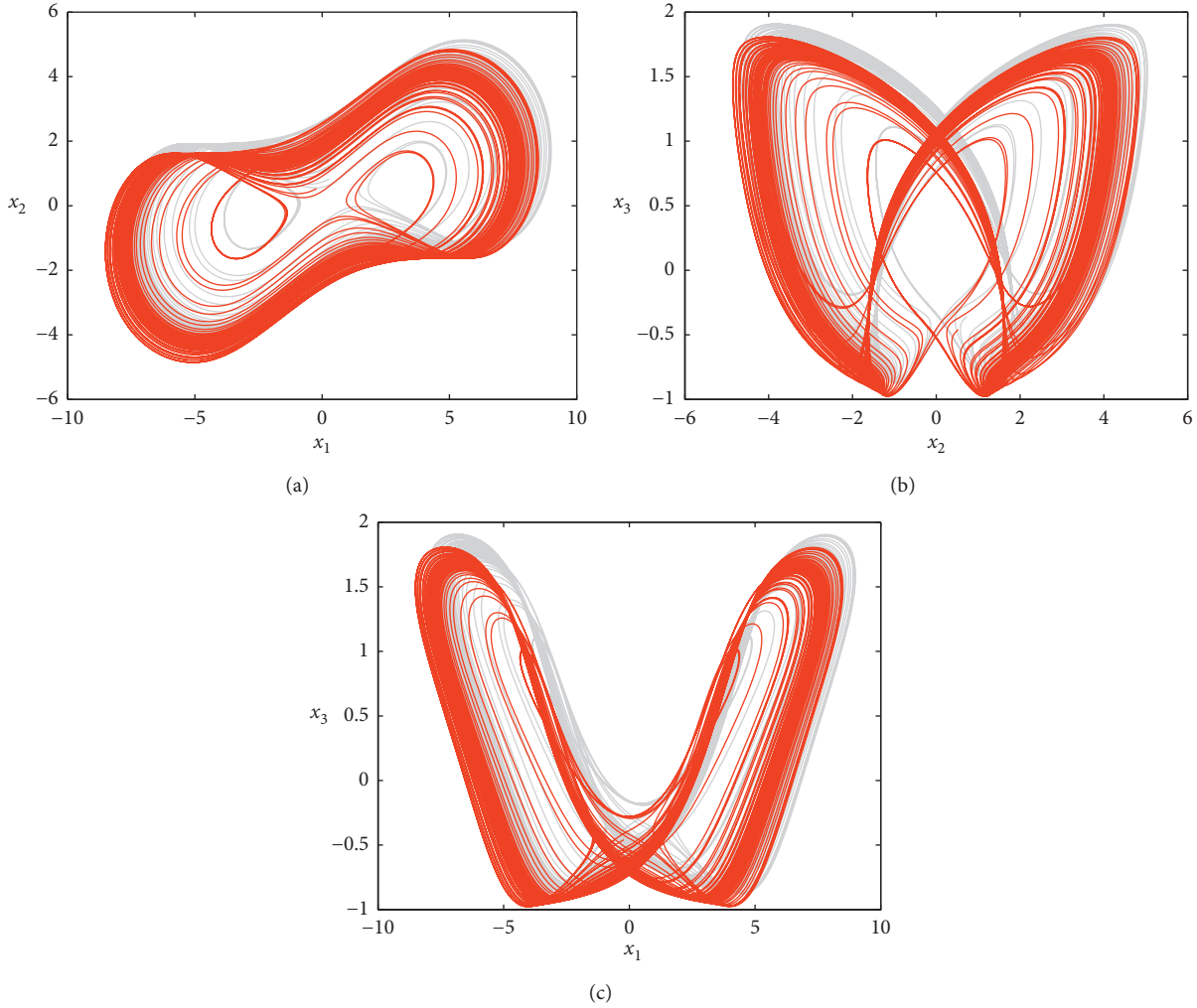


FIGURE 2: Chaotic phase diagrams of the proposed system.

Definition 3. Suppose that $\sigma: \Sigma m \rightarrow \Sigma m$ and $f: S \rightarrow S$ are both continuous functions with topological spaces Σm and S , respectively. If there exists a continuous surjection $h: \Sigma m \rightarrow S$ confirming to $f \circ h = h \circ \sigma$, it is said that f is topologically semiconjugate to function σ .

Lemma 1. If $f^p(D_i) \mapsto D_i$, then we have $f^{mp}(D_i) \mapsto D_i$, where m is a positive integer.

Lemma 2. If $f^p(D_1) \mapsto D_1$, $f^p(D_1) \mapsto D_2$, $f^q(D_2) \mapsto D_1$, and $f^q(D_2) \mapsto D_2$, then there would exist a compact invariant set $M \subset D$, such that $f^{p+q}|_M$ is semi-conjugate to 2-shift dynamics and the topological entropy of f will satisfy $\text{ent}(f) \geq [1/(p+q)] \log 2$.

3.2. Finding Topological Horseshoe in the Dynamical System. According to the theory above, a horseshoe will be found in the dynamical system by three steps [17]. In this process, we set the parameters of system (1) as $a = 1$, $b = 6$, $c = 5$, $d = 1$, $e = 3$, $f = 2$, and initial condition $x(0) = (0.01, 0.01, 0.05)$.

Step 1. As shown in Figure 6, we first select four vertices of the Poincaré section P on the plane $\Theta = \{(x_1, x_2, x_3) \in \mathbb{R}^3: x_2 = 0\}$ as $(-8, 0, -0.5)$, $(-8, 0, 1.5)$, $(8, 0, 1.5)$, and $(8, 0, -0.5)$.

Step 2. Then, after many trial-and-error numerical simulations, we carefully pick a quadrilateral D_1 of quadrangle P , with the four vertices being

$$\begin{aligned} &(-7.618610595, 0, 1.062250623) \\ &(-7.643703532, 0, 1.049345387) \\ &(-7.239428439, 0, 1.018765586) \\ &(-7.215729554, 0, 1.031951372). \end{aligned} \quad (4)$$

Let us suppose that D_1^1 denotes the left side while D_1^2 denotes the right side of quadrilateral D_1 . It is known from the numerical result that the third return map $H^3(D_1^1)$ lies on the left side of D_1 , but the third return map $H^3(D_1^2)$ lies on the right side of D_1 . Thereby, under this return map, the image $H^3(x)$ ($x \in D_1$) lies wholly across the quadrangle D_1 with respect to the sides D_1^1 and D_1^2 , seen in Figure 7(a).

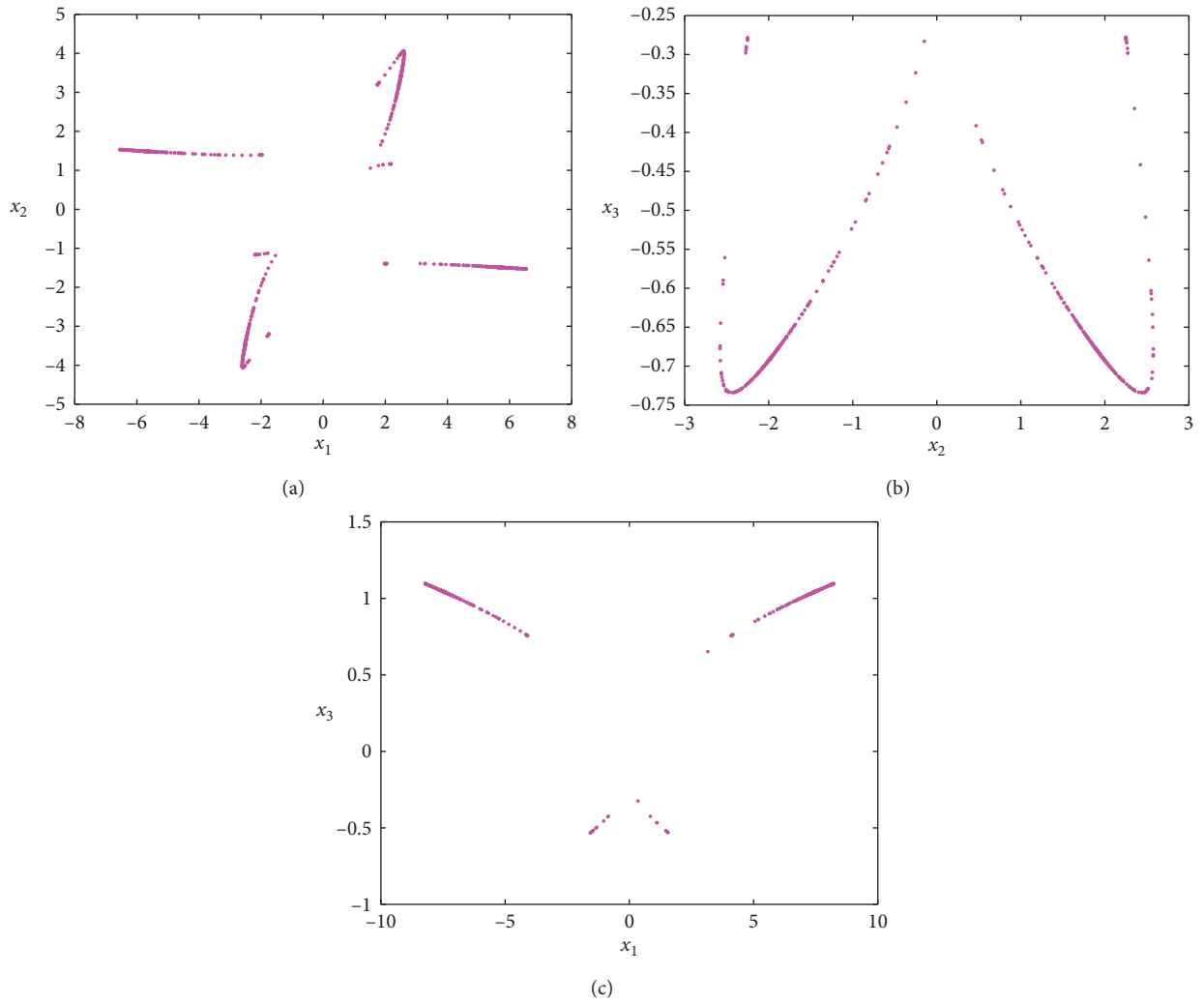


FIGURE 3: Poincaré maps on the plane of (a) $x_3=0$, (b) $x_1=0$, and (c) $x_2=0$.

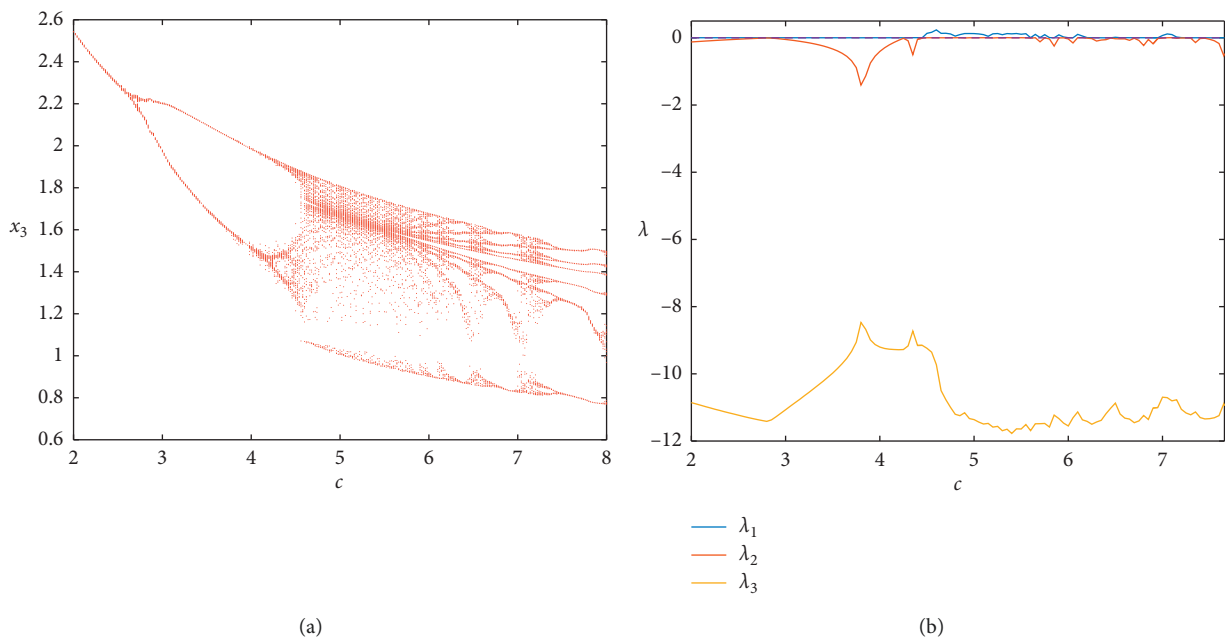


FIGURE 4: (a) Bifurcation diagram and (b) Lyapunov exponents of system (1) versus parameter c .

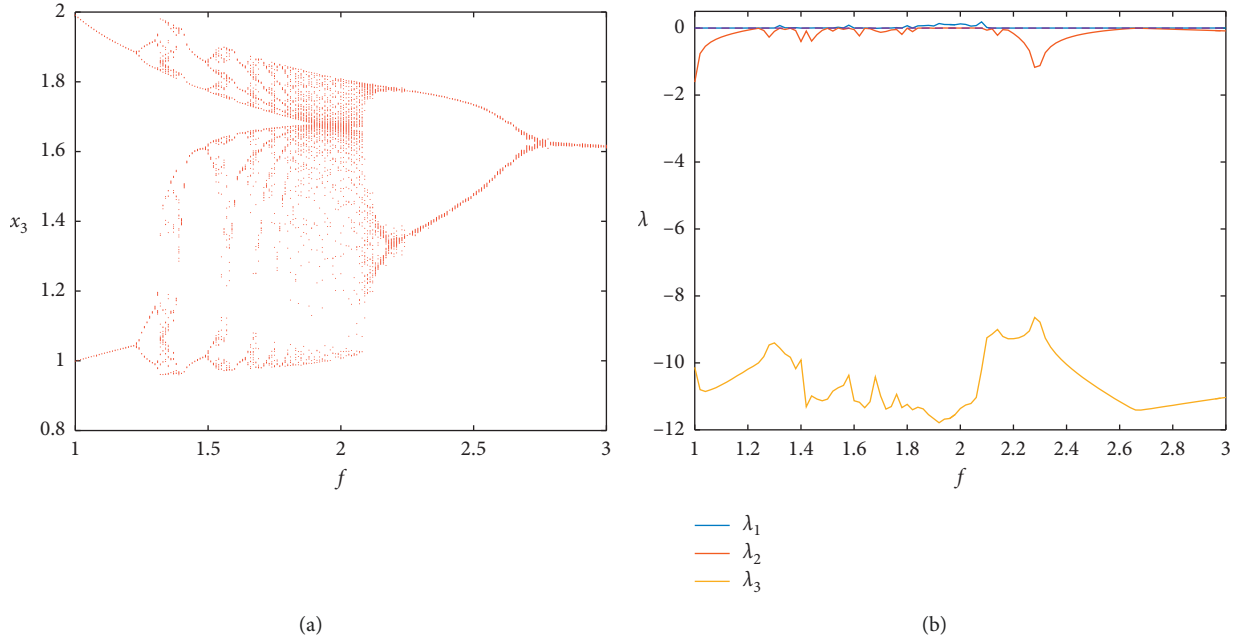


FIGURE 5: (a) Bifurcation diagram and (b) Lyapunov exponents of system (1) versus parameter f .

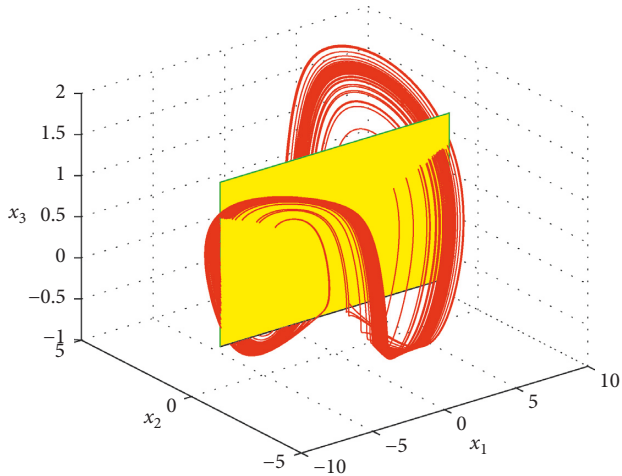


FIGURE 6: Poincaré cross section of the proposed system.

Step 3. Finally, we will take another quadrilateral D_2 of P such that $H(D_1) \mapsto D_2$, $H(D_2) \mapsto D_2$ and $H(D_2) \mapsto D_1$. By a great deal of attempts, the four vertices of D_2 are picked as follows:

$$\begin{aligned} &(-7.865357807, 0, 1.082029302) \\ &(-7.896026952, 0, 1.066318579) \\ &(-7.661826208, 0, 1.048363466) \\ &(-7.633945167, 0, 1.063232544). \end{aligned} \quad (5)$$

Analogously, D_1^2 and D_2^2 indicate the left and right sides of quadrilateral D_2 , respectively. The numerical simulations of the third return Poincaré map $H^3(D_2)$ and the enlarged view are depicted in Figures 7(b) and 7(c), respectively. It is shown from the figures that the return map $H^3(x)$ ($x \in D_2$) suitably across the quadrangles D_1 and D_2 , with $H^3(D_1^2)$ lying on the right side of D_1 and $H^3(D_2^2)$ lying on the left side of D_2 .

Therefore, we conclude by virtue of Lemma 2 that there would exist a compact invariant set $M \subset D$, such that $H^6|_M$ is semiconjugate to 2-shift dynamics, and we obtain $\text{ent}(H) \geq (\log 2)/6 > 0$. Thus, system (1) is proved to be chaotic in theory, with the parameters of $a=1$, $b=6$, $c=5$, $d=1$, $e=3$, $f=2$, and the initial condition of $x(0) = (0.01, 0.01, 0.05)$.

4. Stabilization for the Dynamical System

4.1. Control Scheme. In order to stabilize the proposed dynamical system, we add the single controller u on the second equation. Thus, the controlled dynamical system is depicted as follows:

$$\begin{cases} \dot{x}_1 = -ax_1 + bx_2, \\ \dot{x}_2 = ex_2 - fx_1x_3 + u, \\ \dot{x}_3 = -cx_3^3 + dx_1x_2. \end{cases} \quad (6)$$

The purpose of our design is to propose suitable control scheme u such that all the output variables of system (6) converge to the zero equilibrium point asymptotically.

Theorem 1. For the controlled system (6), we design the single controller u as

$$u = K \text{sign}(x_2). \quad (7)$$

If the control gain satisfies $K \leq -((b^2/4a) + e)B_2$ with $B_2 \geq \|x_2\|$, then the output variables of the controlled system (6) converges to the zero equilibrium point asymptotically.

Proof. We choose the candidate Lyapunov function as

$$V = 0.5 \left(\frac{x_1^2 + x_2^2 + fx_3^2}{d} \right). \quad (8)$$

The corresponding time derivative of $V(x)$ is deduced by

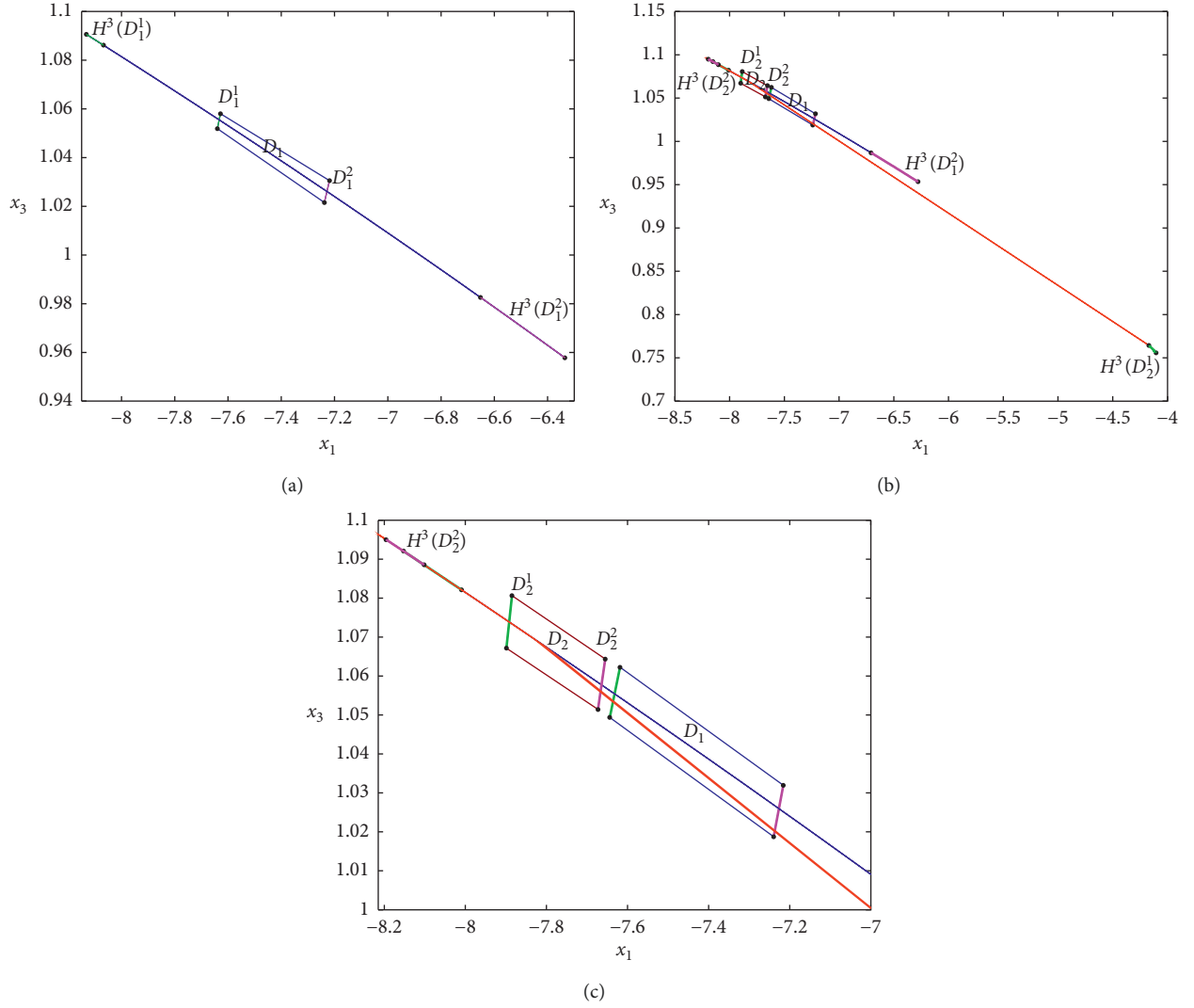


FIGURE 7: (a) The subset D_1 and its image; (b) and (c) the subset D_2 and its image.

$$\begin{aligned}
 \dot{V} &= \frac{x_1 \dot{x}_1 + x_2 \dot{x}_2 + f x_3 \dot{x}_3}{d} \\
 &= -ax_1^2 + bx_1 x_2 + ex_2^2 - fx_1 x_2 x_3 \\
 &\quad + Kx_2 \text{sign}(x_2) - \frac{cfx_3^4}{d} + fx_1 x_2 x_3 \\
 &= -ax_1^2 + bx_1 x_2 + ex_2^2 + K|x_2| - \frac{cfx_3^4}{d} \\
 &= -\left[ax_1^2 - bx_1 x_2 + \left(\frac{b}{2\sqrt{a}} x_2 \right)^2 \right] + \left(\frac{b}{2\sqrt{a}} x_2 \right)^2 \\
 &\quad + ex_2^2 + K|x_2| - \frac{cfx_3^4}{d} \\
 &= -\left[\sqrt{a} x_1 - \frac{b}{2\sqrt{a}} x_2 \right]^2 + \left[\left(\frac{b^2}{4a} + e \right) |x_2| + K \right] |x_2| - \frac{cfx_3^4}{d}.
 \end{aligned} \tag{9}$$

Thus, when $K \leq -((b^2/4a) + e)B_2$, we find that

$$\begin{aligned}
 \dot{V} &\leq -\left[\sqrt{a} x_1 - \frac{b}{2\sqrt{a}} x_2 \right]^2 + \left[\left(\frac{b^2}{4a} + e \right) B_2 + K \right] |x_2| - \frac{cfx_3^4}{d} \\
 &\leq -\left[\sqrt{a} x_1 - \frac{b}{2\sqrt{a}} x_2 \right]^2 - \frac{cfx_3^4}{d} \leq 0.
 \end{aligned} \tag{10}$$

Therefore, the output variables of the controlled system (6) will converge to the zero equilibrium point asymptotically. \square

4.2. Numerical Verification. In this section, numerical simulations are executed by adopting the ODE45 method to verify the availability of the proposed control scheme. For comparing conveniently, we choose the system parameters as $a = 1$, $b = 6$, $c = 5$, $d = 1$, $e = 3$, and $f = 2$, and the initial states are set as $x(0) = (0.01, 0.01, 0.01)$. With the parameter set, system (6) is chaotic before the controller is put into effect.

The controller u is exerted at 60th second, and the control gain is taken as $K = -2$ and $K = -16$. Figures 8(a) and 8(b) depict the control results, from which one can see that we can obtain good control effect with only taking a short time for the system to be stabilized at the fixed point. And, as we can also know only small control energy is needed to reach our control purpose.

5. DSP-Based Realization of the Attractors and Stabilization Scheme

The implementation of continuous chaotic systems with electronic circuit has been widely adopted. The parameter tolerance of the components of analog electronic circuit will cause the trajectory change of the chaotic system, which restricts its practical engineering application. Therefore, DSP-based implement of continuous chaotic system can overcome these problems effectively. In this section, the attractors of system (1) and stabilization scheme for system (6) are implemented based on the DSP platform. In our experiments, the Texas Instrument DSP TMS320F28335 is employed to calculate the state variable and the control variable, which can run at 150 MHz and interfaces with a 12-bit quad-channel digital-to-analog converter DAC7724 by parallel bus (PB) mode. Control signals required by DAC7724 are generated by DSP and CPLD chips. The block diagram of hardware platform is shown in Figure 9.

In practice, we discretize the continuous system by the classical fourth-order Runge–Kutta algorithm with the sampling period ΔT . From Figure 2, we know that the amplitude of variable x_3 ($|x_3| < 2$) is too small to affect the computational precision. Therefore, we proposed a general method to rescale the system variables by scaling factors k_i , where $i = 1, 2, 3$.

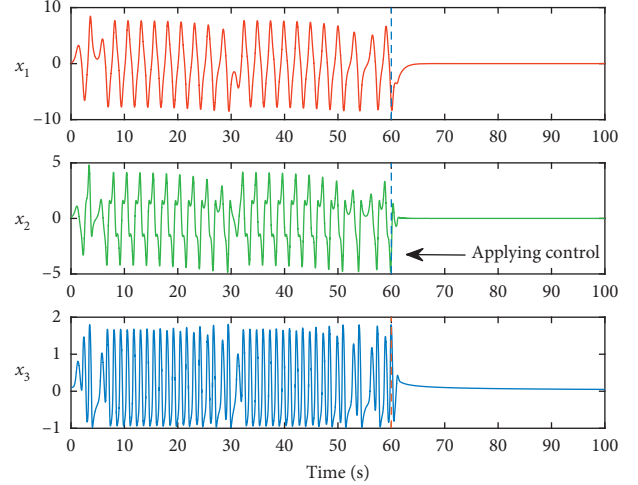
Setting $u_i = k_i x_i, i = 1, 2, 3$, system (1) can be transformed to

$$\dot{u}_i = f_i(a, b, c, d, e, f, k_1, k_2, k_3, u_1, u_2, u_3), \quad (11)$$

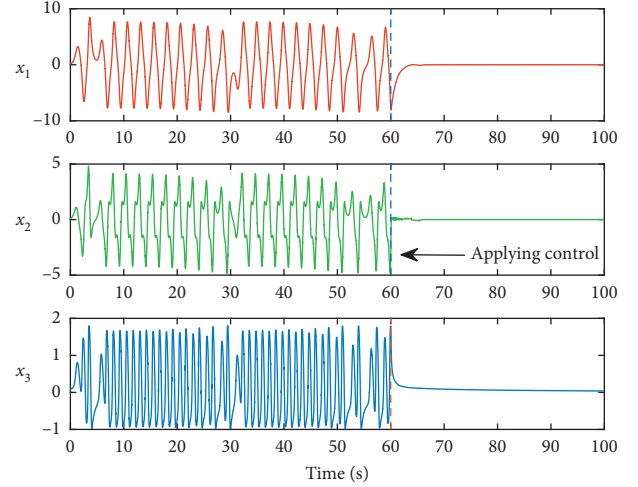
where $i = 1, 2, 3$.

When introducing the linear transformation of $u_i \rightarrow x_i$, the corresponding differential equation of system (11) can be expressed as

$$\begin{cases} \dot{x}_1 = -ax_1 + \frac{bk_1}{k_2}x_2, \\ \dot{x}_2 = ex_2 - \frac{fk_2}{k_1k_3}x_1x_3, \\ \dot{x}_3 = -\frac{c}{k_3^2}x_3^3 + \frac{dk_3}{k_1k_2}x_1x_2. \end{cases} \quad (12)$$



(a)



(b)

FIGURE 8: Control results of state variables with (a) $K = -2$ and (b) $K = -16$.

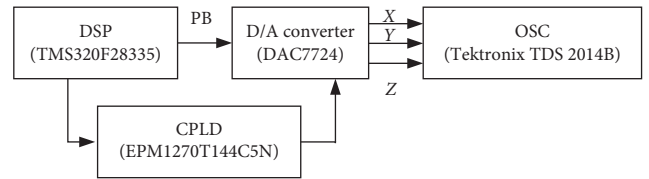


FIGURE 9: Block diagram for DSP implementation of chaotic attractors and its stabilization.

Discretizing system (12) using the classical fourth-order Runge–Kutta algorithm, the following difference equations can be obtained:

$$x_i(n+1) = x_i(n) + \Delta T \frac{(K_{i,1} + 2K_{i,2} + 2K_{i,3} + K_{i,4})}{6}, \quad (13)$$

where $i = 1, 2, 3$ and

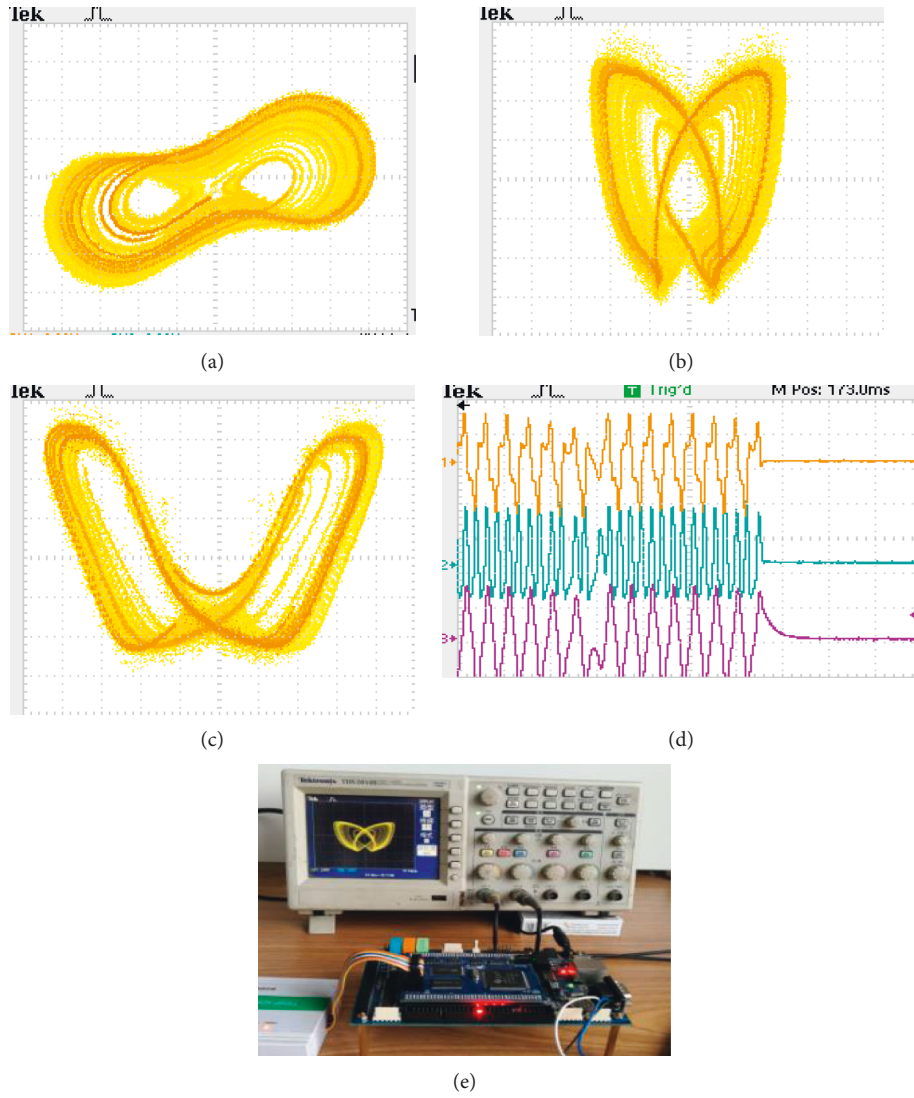


FIGURE 10: DSP-based realization for (a)–(c) chaotic attractors; (d) stabilization process; (e) experiment platform.

$$\begin{cases} K_{1,1} = -ax_1(n) + \frac{bk_1}{k_2}x_2(n), \\ K_{2,1} = ex_2(n) - \frac{fk_2}{k_1k_3}x_1(n)x_3(n), \\ K_{3,1} = \frac{c}{k_3^2}x_3^3(n) + \frac{dk_3}{k_1k_2}x_1(n)x_2(n), \end{cases} \quad (14)$$

$$\begin{cases} K_{1,j} = -a[x_1(n) + mK_{1,j-1}] + \frac{bk_1}{k_2}[x_2(n) + mK_{2,j-1}], \\ K_{2,j} = e[x_2(n) + mK_{2,j-1}] - \frac{fk_2}{k_1k_3}[x_1(n) + mK_{1,j-1}][x_3(n) + mK_{3,j-1}], \\ K_{3,j} = \frac{c}{k_3^2}[x_3(n) + mK_{3,j-1}]^3 + \frac{dk_3}{k_1k_2}[x_1(n) + mK_{1,j-1}][x_2(n) + mK_{2,j-1}]. \end{cases} \quad (15)$$

When $j = 2, 3$, $m = 0.5$, and when $j = 4$, $m = 1$.

The digital sequences $x_1(n)$, $x_2(n)$, $x_3(n)$ are produced by DSP according to (13)–(15) and converted into the corresponding analog sequences by the DAC7724 and then transmitted to oscilloscope. With the set $a = 1$, $b = 6$, $c = 5$, $d = 1$, $e = 3$, $f = 2$, $k_1 = 1$, $k_2 = 1$, $k_3 = 2$, $x(0) = (0.01, 0.01, 0.01)$, and the control gain $K = -6$, the results of DSP-based realization of the attractor and stabilization scheme are depicted in Figure 10. By comparing with the attractors in Figure 2 and stabilization process in Figure 7 simulated by Matlab, it can be concluded that they have a good qualitative agreement.

6. Conclusion

In this paper, we presented a three-dimensional dynamical system with a simple algebraic structure. Basic dynamical properties of the system, including equilibrium point, phase portrait, Poincaré map, parameter bifurcation, and Lyapunov exponent, are studied through theoretical analysis and numerical simulation. And, the theory of topological horseshoe is adopted to rigorously prove the chaotic emergence of the system theoretically. Then, based on the Lyapunov stability criterion, we designed a single control scheme to stabilize the chaotic system to its zero-equilibrium point. The attractor and stabilization process are realized via DSP-based technology, which have a good qualitative agreement to the Matlab simulation; thus it well confirmed the validity and enforceability of the theoretical scheme.

Data Availability

The figure data and table data used to support the findings of this study are included within the article.

Conflicts of Interest

The authors declare that there are no conflicts of interest regarding the publication of this paper.

Acknowledgments

This work was supported by the National Natural Science Foundation of China under Grant nos. 51977153 and 51577046, the State Key Program of National Natural Science Foundation of China under Grant no. 51637004, the National Key Research and Development Plan “Important Scientific Instruments and Equipment Development” under Grant no. 2016YFF0102200, the Equipment Research Project in Advance under Grant no. 41402040301, the Research Foundation of Education Bureau of Hunan Province of China under Grant no. 18A314, Hunan Provincial Natural Science Foundation of China under Grant no. 2019JJ40109, and the Science and Research Creative Team of Hunan Institute of Science and Technology (no. 2019-TD-10).

References

- [1] J. Mou, K. Sun, J. Ruan, and S. He, “A nonlinear circuit with two memcapacitors,” *Nonlinear Dynamics*, vol. 86, no. 3, pp. 1735–1744, 2016.
- [2] J. Zhou, X. Wang, D. Xu, and S. Bishop, “Nonlinear dynamic characteristics of a quasi-zero stiffness vibration isolator with cam-roller-spring mechanisms,” *Journal of Sound and Vibration*, vol. 346, pp. 53–69, 2015.
- [3] F. Peng, Q. Long, Z.-X. Lin, and M. Long, “A reversible watermarking for authenticating 2D CAD engineering graphics based on iterative embedding and virtual coordinates,” *Multimedia Tools and Applications*, vol. 78, no. 19, pp. 26885–26905, 2017.
- [4] Z. Wei, Y. Li, B. Sang, Y. Liu, and W. Zhang, “Complex dynamical behaviors in a 3D simple chaotic flow with 3D stable or 3D unstable manifolds of a single equilibrium,” *International Journal of Bifurcation and Chaos*, vol. 29, no. 7, p. 1950095, 2019.
- [5] Y. Zhou, Z. Hua, C. M. Pun, and C. L. Chen, “Cascade chaotic system with applications,” *IEEE Transactions on Cybernetics*, vol. 45, no. 45, pp. 2001–2012, 2015.
- [6] M. Zapateiro, Y. Vidal, and L. Acho, “A secure communication scheme based on chaotic Duffing oscillators and frequency estimation for the transmission of binary-coded messages,” *Communications in Nonlinear Science and Numerical Simulation*, vol. 19, no. 4, pp. 991–1003, 2014.
- [7] C. Zhu, S. Xu, Y. Hu, and K. Sun, “Breaking a novel image encryption scheme based on Brownian motion and PWLCM chaotic system,” *Nonlinear Dynamics*, vol. 79, no. 2, pp. 1511–1518, 2015.
- [8] G. Ye, C. Pan, X. Huang, Z. Zhao, and J. He, “A chaotic image encryption algorithm based on information entropy,” *International Journal of Bifurcation and Chaos*, vol. 28, no. 1, Article ID 1850010, 2018.
- [9] X. Xiang and B. Shi, “Weak signal detection based on the information fusion and chaotic oscillator,” *Chaos*, vol. 20, no. 1, Article ID 013104, 2010.
- [10] Y. Ding, K. Sun, and X. Xu, “Hough-MHAF localization algorithm for dual-frequency continuous-wave through-wall radar,” *IEEE Transactions on Aerospace and Electronic Systems*, vol. 52, no. 1, pp. 111–121, 2016.
- [11] E. N. Lorenz, “Deterministic nonperiodic flow,” *Journal of Atmospheric Sciences*, vol. 20, no. 2, pp. 130–141, 1963.
- [12] J. Kennedy, S. Koçak, and J. A. YORKE, “A chaos lemma,” *The American Mathematical Monthly*, vol. 108, no. 5, pp. 411–423, 2001.
- [13] X.-S. Yang and Y. Tang, “Horseshoes in piecewise continuous maps,” *Chaos, Solitons & Fractals*, vol. 19, no. 4, pp. 841–845, 2004.
- [14] X.-S. Yang, “Topological horseshoes and computer assisted verification of chaotic dynamics,” *International Journal of Bifurcation and Chaos*, vol. 19, no. 4, pp. 1127–1145, 2009.
- [15] W.-Z. Huang and Y. Huang, “Chaos, bifurcation and robustness of a class of hopfield neural networks,” *International Journal of Bifurcation and Chaos*, vol. 21, no. 3, pp. 885–895, 2011.
- [16] C. Ma and X. Wang, “Hopf bifurcation and topological horseshoe of a novel finance chaotic system,” *Communications in Nonlinear Science and Numerical Simulation*, vol. 17, no. 2, pp. 721–730, 2012.
- [17] Q. Li and X.-S. Yang, “A simple method for finding topological horseshoes,” *International Journal of Bifurcation and Chaos*, vol. 20, no. 2, pp. 467–478, 2010.
- [18] C. Li, L. Wu, H. Li, and Y. Tong, “A novel chaotic system and its topological horseshoe,” *Nonlinear Analysis: Modelling and Control*, vol. 18, no. 1, pp. 66–77, 2013.

- [19] E. Ott, C. Grebogi, and J. A. Yorke, "Controlling chaos," *Physical Review Letters*, vol. 64, no. 11, pp. 1196–1199, 1990.
- [20] K. Pyragas, "Continuous control of chaos by self-controlling feedback," *Physics Letters A*, vol. 170, no. 6, pp. 421–428, 1992.
- [21] F. Farivar, M. A. Nekoui, M. A. Shoorehdeli, and M. Teshnehlab, "Modified projective synchronization of chaotic dissipative gyroscope systems via backstepping control," *Indian Journal of Physics*, vol. 86, no. 10, pp. 901–906, 2012.
- [22] C. Li, K. Su, and L. Wu, "Adaptive sliding mode control for synchronization of a fractional-order chaotic system," *Journal of Computer Nonlinear Dynamics*, vol. 8, no. 3, Article ID 031005, 2013.
- [23] E. Fridman, "A refined input delay approach to sampled-data control," *Automatica*, vol. 46, no. 2, pp. 421–427, 2010.
- [24] A. B. MUZAFFAR and K. AYUB, "Multiswitching combination synchronization of non-identical fractional-order chaotic systems," *Pramana-J. Phys.* vol. 90, no. 6, 2018.
- [25] Z. Wei, J. C. Sprott, and H. Chen, "Elementary quadratic chaotic flows with a single non-hyperbolic equilibrium," *Physics Letters A*, vol. 379, no. 37, pp. 2184–2187, 2015.
- [26] A. T. Azar, C. Volos, N. A. Gerodimos et al., "A novel chaotic system without equilibrium: dynamics, synchronization, and circuit realization," *Complexity*, vol. 2017, no. 11, Article ID 7871467, 2017.
- [27] G. Y. Peng, F. H. Min, and E. R. Wang, "Circuit implementation, synchronization of multistability, and image encryption of a four-wing memristive chaotic system," *Journal of Electrical and Computer Engineering*, vol. 2018, Article ID 8649294, 13 pages, 2018.

Research Article

Coexisting Three-Scroll and Four-Scroll Chaotic Attractors in a Fractional-Order System by a Three-Scroll Integer-Order Memristive Chaotic System and Chaos Control

Xikui Hu¹ and Ping Zhou ^{1,2}

¹Center of System Theory and Its Applications, Chongqing University of Posts and Telecommunications, Chongqing 400065, China

²Key Laboratory of Network Control and Intelligent Instrument of Ministry of Education, Chongqing University of Posts and Telecommunications, Chongqing 400065, China

Correspondence should be addressed to Ping Zhou; zhouping@cqupt.edu.cn

Received 10 June 2019; Accepted 5 August 2019; Published 8 January 2020

Guest Editor: Viet-Thanh Pham

Copyright © 2020 Xikui Hu and Ping Zhou. This is an open access article distributed under the Creative Commons Attribution License, which permits unrestricted use, distribution, and reproduction in any medium, provided the original work is properly cited.

Based on the integer-order memristive system that can generate two-scroll, three-scroll, and four-scroll chaotic attractors, in this paper, we found other phenomena that two kinds of three-scroll chaotic attractors coexist in this system with different initial conditions. Furthermore, we proposed a coexisting fractional-order system based on the three-scroll chaotic attractors system, in which the three-scroll or four-scroll chaotic attractors emerged with different fractional-orders q . Meanwhile, with fractional-order $q = 0.965$ and different initial conditions, coexistence of two kinds of three-scroll and four-scroll chaotic attractors is found simultaneously. Finally, we discussed controlling chaos for the fractional-order memristive chaotic system.

1. Introduction

Due to the typical characteristics of high irregularity, unpredictability, and complexity of chaotic systems, chaotic systems and its applications have been attracted more and more attentions in the last few decades [1–16], e.g., information processing [11], secure communication [12, 13], image encryption [14, 15], machine learning [16], and so on. Memristor—the missing circuit element—has been discovered by Leon Chua in 1971 [17], and it has been successfully realized in 2008 [18]. Recently, some mathematical models of memristor-based systems were proposed. For example, Muthuswamy and Chua reported a memristor-based chaotic system with single-scroll attractor [19], Bao et al. presented a memristor-based chaotic system with double-scroll attractor [20], Teng et al. reported a memristor-based chaotic system with double-scroll and four-scroll attractors [21], Zhou and Ke gave a memristive-based chaotic system with two-scroll to four-scroll attractors [1], Sun et al. suggested a memristor-based chaotic system with infinite chaotic attractors [22], and so on.

Chaotic attractors have also been reported in many fractional-order nonlinear systems, e.g., the fractional-order Lorenz chaotic system [23], the fractional-order Chen chaotic system [24], the fractional-order Lu chaotic system [24], the fractional-order brushless DC motor chaotic system [25], the fractional-order micro-electro-mechanical chaotic system [26], the fractional order coronary artery chaotic system [27], etc. On the other hand, some memristor-based fractional-order chaotic systems have been proposed. For example, a fractional-order memristor-based simplest chaotic circuit with double-scroll and four-scroll attractors using fourth-degree polynomial [21] was reported by Teng et al. and a fractional-order memristor-based chaotic system with single-scroll attractor and a stable equilibrium point [28] was reported by Prakash et al., and a fractional-order memristor-based chaotic system with coexisting attractors [1] was reported by Zhou and Ke. Moreover, some fractional-order chaotic systems have been implemented by electronic circuit, e.g., a fractional-order Lorenz hyperchaotic system has been implemented by DSP [29], a 4-D nonequilibrium fractional-order chaotic system has been implemented by EWB [30], and the fractional-order

chaotic systems with two equilibriums and no equilibrium have been realized by FPGA [31].

On the other hand, due to the important application of stability and control of chaotic systems in engineering science [9, 10, 24–26, 32–34], the stability and control of chaotic systems have attracted more and more attention in recent years. Many control schemes have been suggested, e.g., linear and nonlinear feedback, scalar and vector controller, single-state variable, and multiple-state variables. However, control cost and control effectiveness must be considered in practice. Therefore, in the process of stability control of chaotic system, single-state variable or scalar controller should be the first choice.

Based on the integer-order memristor-based chaotic system [1] reported by Zhou and Ke, in this paper, we find some new results in the integer-order memristor-based chaotic system [1], i.e., two kinds of three-scroll chaotic attractor coexist with different initial conditions. Furthermore, its fractional-order version is proposed. We find that not only three-scroll chaotic attractors but also four-scroll chaotic attractors are emerged in its fractional-order version. Meanwhile, two kinds of three-scroll and four-scroll chaotic attractors coexist with different initial conditions for fractional order $q = 0.965$. To the best of our knowledge, our results have rarely been reported before. Finally, in order to stabilize the fractional-order version memristive chaotic system via a single-state variable, a control strategy is suggested.

This article is structure as follows: we describe the integer-order memristor-based chaotic system [1] and find some new results in Section 2. In Section 3, based on the integer-order memristor-based chaotic system [1], its fractional-order version is suggested and the four-scroll chaotic attractors are found, and coexisting two kinds of three-scroll and four-scroll chaotic attractors for different initial conditions are found. The Section 4 presents a control strategy via single-state variable. In Section 5, the conclusion is given.

2. Two Kinds of Three-Scroll Chaotic Attractors Coexist in an Integer-Order Memristive System

Recently, an integer-order memristive system reported by Zhou and Ke [1] is as follows:

$$\begin{aligned} \frac{dx_1}{dt} &= x_2, \\ \frac{dx_2}{dt} &= -\frac{[x_1 + (0.5x_3^4 - 2.4)x_2]}{L}, \\ \frac{dx_3}{dt} &= -x_2 - \left(\frac{3}{4} - x_2^2\right)x_3, \end{aligned} \quad (1)$$

where $1 \leq L \leq 8$.

Remark 1. There is only one equilibrium point in (1), i.e., $(x_1, x_2, x_3) = (0, 0, 0)$, and the equilibrium point is unstable. More details are in reference [1].

Zhou and Ke [1] reported that there are two-scroll to four-scroll chaotic attractors in this system (1) with different L . For

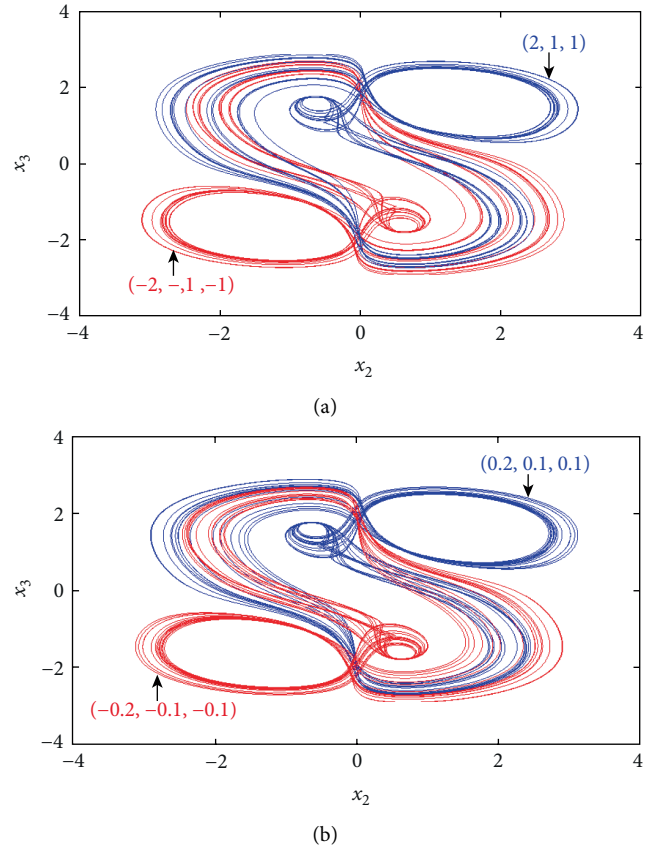


FIGURE 1: Coexistence of two kinds of three-scroll chaotic attractors.

example [1], the two-scroll chaotic attractor is emerged for $L = 4$, the four-scroll chaotic attractor is emerged for $L = 1.4$, the three-scroll chaotic attractors are emerged for $L = 1.734$, and another type of three-scroll chaotic attractor is emerged for $L = 1.8$.

In this paper, the integer-order memristive system is further studied. By numerical calculations, we find that two kinds of three-scroll chaotic attractors coexist in this system (1) for $L = 1.8$ with different initial conditions, which has not been reported by Zhou and Ke [1]. Some results are as follows.

Let $L = 1.8$ and initial conditions be $(2, 1, 1)$ and $(-2, -1, -1)$, respectively, two kinds of three-scroll chaotic attractors coexist as shown in Figure 1(a).

Let $L = 1.8$ and initial conditions be $(0.2, 0.1, 0.1)$ and $(-0.2, -0.1, -0.1)$, respectively, two kinds of three-scroll chaotic attractors also coexist as shown in Figure 1(b).

After a great deal of numerical calculations, we find that there are the same chaotic attractors (blue line) with initial conditions $(2, \pm 1, \pm 1)$ and $(0.2, \pm 0.1, \pm 0.1)$, and the same chaotic attractors (red line) with initial conditions $(-2, \pm 1, \pm 1)$ and $(-0.2, \pm 0.1, \pm 0.1)$. It must be pointed out that only the chaotic attractors described by blue line are reported in Ref. [1] with $L = 1.8$. In this paper, new chaotic attractors (red line) are found and two kinds of three-scroll chaotic attractors coexist in system (1) with $L = 1.8$.

3. Two Kinds of Three-Scroll and Four-Scroll Chaotic Attractors Coexist in Fractional-Order Memristive Chaotic System

Based on memristive chaotic system mentioned above with $L = 1.8$, a fractional-order memristive system is constructed, and coexistence of two kinds of three-scroll and four-scroll chaotic attractors is found. The fractional-order memristive system is described as

$$\begin{aligned} \frac{d^q x_1}{dt^q} &= x_2, \\ \frac{d^q x_2}{dt^q} &= -\frac{[x_1 + (0.5x_3^4 - 2.4)x_2]}{1.8}, \\ \frac{d^q x_3}{dt^q} &= -x_2 - \left(\frac{3}{4} - x_2^2\right)x_3, \end{aligned} \quad (2)$$

where $0 < q \leq 1$ is fractional-order, and $d^q x_i/dt^q = \int_0^t (t-\tau)^{-q} dx_i(\tau)/\Gamma(1-q)$ with $\Gamma(1-q) = \int_0^t t^{-q} e^{-t} dt$.

$$\begin{aligned} x_1(n+1) &= x_1(0) + \frac{m^q}{\Gamma(q+2)} \left[x_2^r(n+1) + \sum_{k=0}^n \alpha_{k,n+1} x_2(k) \right], \\ x_2(n+1) &= x_2(0) + \frac{m^q}{\Gamma(q+2)} \left[-\frac{(x_1^r(n+1) + (0.5(x_3^r(n+1))^4 - 2.4)x_2^r(n+1))}{1.4} + \sum_{k=0}^n a_{k,n+1} \left(-\frac{(x_1(k) + (0.5(x_3(k))^4 - 2.4)x_2(k))}{1.4} \right) \right], \\ x_3(n+1) &= x_3(0) + \frac{m^q}{\Gamma(q+2)} \left[-x_2^r(n+1) - (0.75 - (x_2^r(n+1))^2)x_3^r(n+1) + \sum_{k=0}^n a_{k,n+1} (-x_2(k) - (0.75 - (x_2(k))^2)x_3(k)) \right], \end{aligned} \quad (3)$$

and

$$\begin{aligned} x_1^r(n+1) &= x_1(0) + \frac{1}{\Gamma(q)} \sum_{k=0}^n b_{k,n+1} x_2(k), \\ x_2^r(n+1) &= x_2(0) + \frac{1}{\Gamma(q)} \sum_{k=0}^n b_{k,n+1} \left(-\frac{(x_1(k) + (0.5(x_3(k))^4 - 2.4)x_2(k))}{1.4} \right), \\ x_3^r(n+1) &= x_3(0) + \frac{1}{\Gamma(q)} \sum_{k=0}^n b_{k,n+1} (-x_2(k) - (0.75 - (x_2(k))^2)x_3(k)), \end{aligned} \quad (4)$$

$$a_{k,n+1} = \begin{cases} n^{q+1} - (n-q)(n+1)^q, & k=0, \\ (n-k+2)^{q+1} + (n-k)^{q+1} - 2(n-k+1)^{q+1}, & 1 \leq k \leq n, \\ 1, & k=n+1, \end{cases} \quad (5)$$

$$b_{k,n+1} = m^q \frac{[(n-k+1)^q - (n-k)^q]}{q}, \quad 0 \leq k \leq n. \quad (6)$$

The approximation error is as follows:

$$\begin{aligned} |x_1(t_n) - x_1(n)| &= o(m^{1+q}), \\ |x_2(t_n) - x_2(n)| &= o(m^{1+q}), \\ |x_3(t_n) - x_3(n)| &= o(m^{1+q}), \end{aligned} \quad (7)$$

where $(x_1(0), x_2(0), x_3(0))$ are the initial conditions for fractional-order system (2).

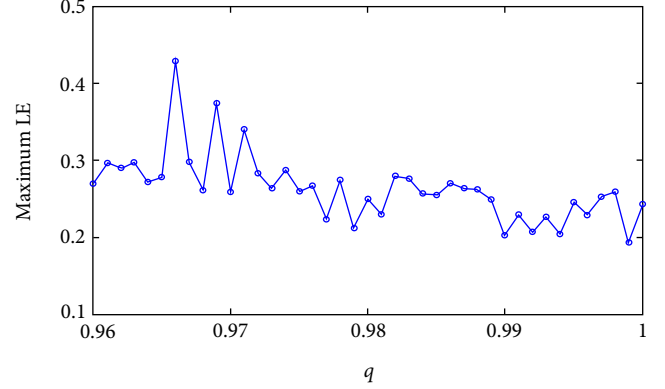


FIGURE 2: The maximum LE varies with fractional-order q .

Now, based on the Adams–Bashforth–Moulton algorithm [1] for fractional-order system, let T be the total time of numerical calculation, N be the iterative times, the step length be $m = T/N$ and $t_n = nm$ ($n = 0, 1, 2, \dots, N$). So, the fractional-order memristive system (2) is discretized as follows:

In order to study the dynamical behaviors of system (2), we calculate the maximum Lyapunov exponents (Maximum LE) of system (2) firstly. The Maximum LE with respect to fractional-order q is displayed in Figure 2.

In Figure 2, the positive Maximum LE indicates that there are chaotic attractors in fractional-order memristive system (2). Now, some results are as follows:

3.1. Four-Scroll Chaotic Attractor Emerges in System (2) with $Q = 0.98$. Let $q = 0.98$, we can obtain that the Maximum LE is 0.2501. It indicates that the fractional-order memristive system (2) has a chaotic attractor. Let initial conditions be $(2, 1, 1)$, it is obtained that four-scroll chaotic attractor emerges in system (2) as shown in Figure 3.

We note that there are only three-scroll chaotic attractors in integer-order memristive system (1). However, the four-scroll chaotic attractors are generated in its fractional-order

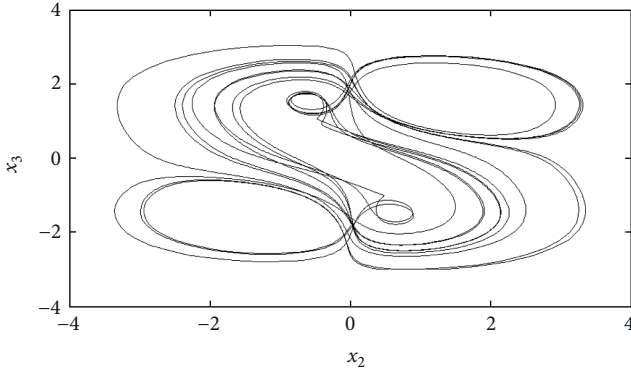


FIGURE 3: Four-scroll chaotic attractors in fractional-order memristive system (2).

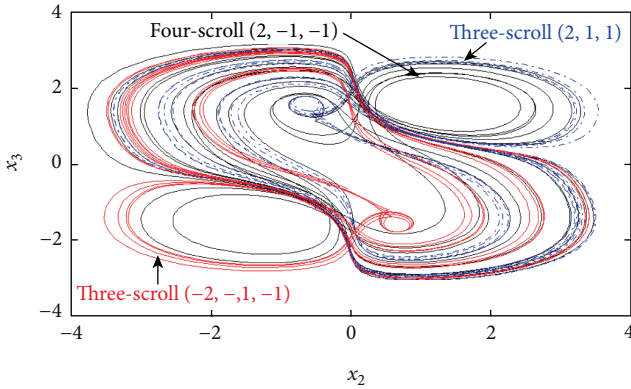


FIGURE 4: Coexisting two kinds of three-scroll, four-scroll chaotic attractors in fractional-order memristive system (2).

version system. By numerical calculation, we find that there are same chaotic attractors (as shown in Figure 3) with initial conditions $(\pm 2, \pm 1, \pm 1)$ or $(\pm 0.2, \pm 0.1, \pm 0.1)$.

3.2. Two Kinds of Three-Scroll, and Four-Scroll Chaotic Attractors Coexist in System (2) with $q = 0.965$. Let $q = 0.965$, we can obtain that the maximum LE is 0.2781. It indicates that the fractional-order memristive system (2) has a chaotic attractor. By numerical calculation, we find that a three-scroll chaotic attractor emerges with initial conditions $(2, 1, 1)$, another type of three-scroll chaotic attractor emerges with initial conditions $(-2, -1, -1)$, and a four-scroll chaotic attractor emerges with initial conditions $(2, -1, -1)$. Therefore, two kinds of three-scroll chaotic attractors coexist with four-scroll chaotic attractor in fractional-order memristive chaotic system (2), as shown in Figure 4.

Please note that only two kinds of three-scroll chaotic attractors coexist in the integer-order memristive system (1), while two kinds of three-scroll chaotic attractors coexist with four-scroll chaotic attractor in the fractional-order memristive system (2).

Remark 2. By numerical calculation, we find that there are only coexisting two kinds of three-scroll chaotic

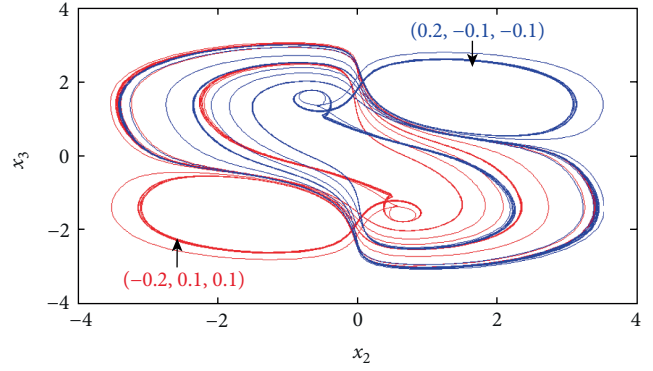


FIGURE 5: Coexisting two kinds of three-scroll chaotic attractors in fractional-order memristive system (2) for $q = 0.965$ with initial conditions $(\pm 0.2, \pm 0.1, \pm 0.1)$.

attractors in system (2) for $q = 0.965$ with initial conditions $(\pm 0.2, \pm 0.1, \pm 0.1)$, i.e., there is no four-scroll chaotic attractor in system (2) with these initial conditions. The coexisting two kinds of three-scroll chaotic attractors are shown in Figure 5.

In summary, two kinds of three-scroll chaotic attractors emerge in the integer-order memristive system (1) for $L = 1.8$. The fractional-order memristive system (2), however, can generate four-scroll chaotic attractors for $q = 0.98$. Moreover, coexisting two kinds of three-scroll and four-scroll chaotic attractors are found in fractional-order memristive system (2) for $q = 0.965$. It indicates that the fractional-order memristive system (2) has richer and more complex chaotic attractors than the integer-order memristive system (1).

4. Control of the Fractional-Order Memristive Chaotic System (2) via a Single State Variable

Firstly, in order to control the fractional-order memristive chaotic system (2), the following lemma for the fractional-order nonlinear system is given. Consider the following fractional-order nonlinear system (8),

$$\frac{d^q z}{dt^q} = Lz + f(z), \quad (8)$$

where $0 < q \leq 1$, $z = [z_1, z_2, \dots, z_n]^T$ is the real state vector, $L \in R^{n \times n}$ is a constant real matrix, Lz and $f(z)$ denote the linear and nonlinear parts in nonlinear system (8).

Lemma 3 (More details are in [35]). *Given the fractional-order nonlinear system (8), if the following conditions are held,*

- $f(z)|_{z=0} = 0$, and $\lim_{z \rightarrow 0} \|f(z)/z\| = 0$,
- $|\arg \lambda_i(L)| \geq 0.5\pi q$ ($i = 1, 2, \dots, n$), and $q\|L\| > 1$, where $\lambda_i(L)$ ($i = 1, 2, \dots, n$) are the eigenvalues of matrix L , and $\|L\|$ is the l_2 -norm of matrix L , then, system (8) is said to be asymptotically stable.

Secondly, in order to stable the fractional-order memristive chaotic system (2) via single-state variable, the following controlled fractional-order memristive system (9) is considered.

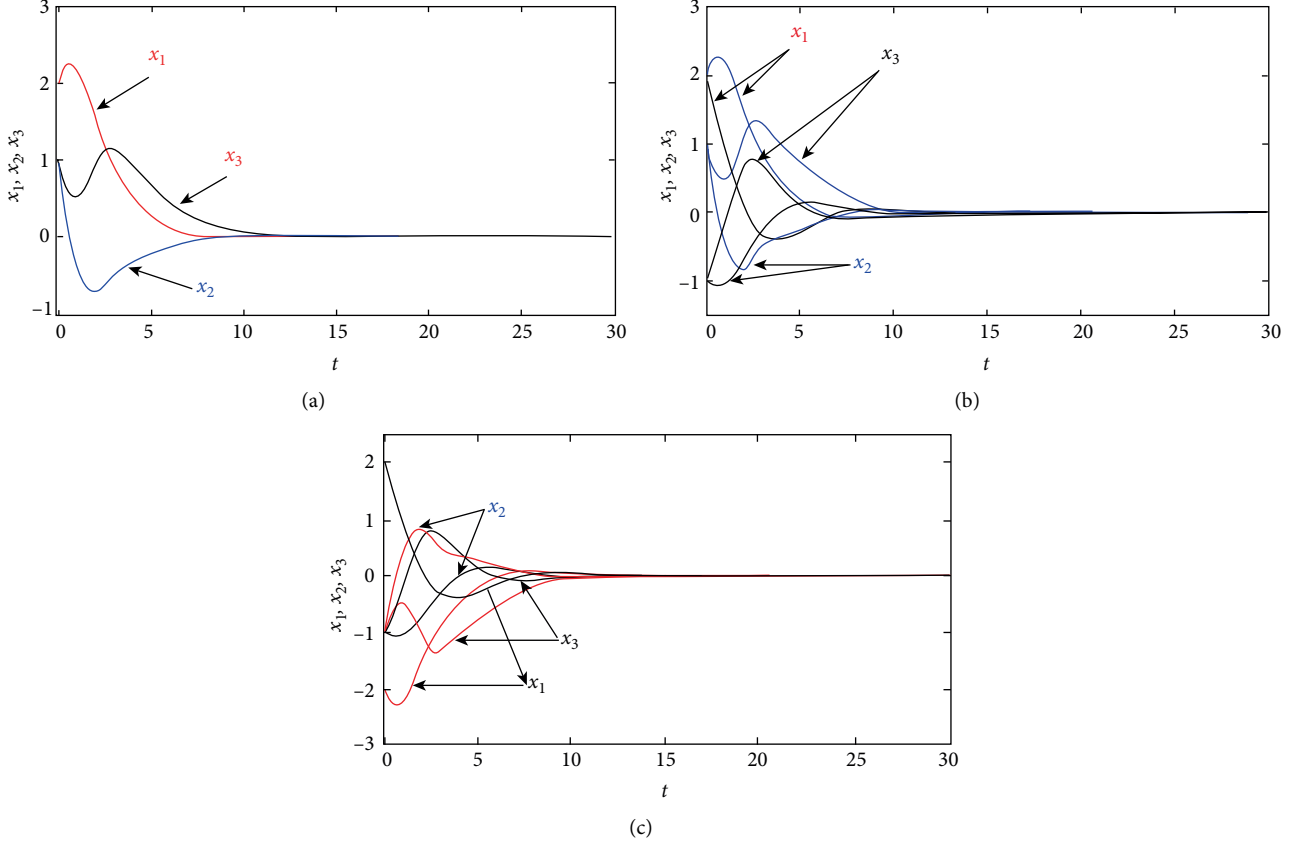


FIGURE 6: The results of state variables vary with time.

$$\begin{aligned}
 \frac{d^q x_1}{dt^q} &= x_2, \\
 \frac{d^q x_2}{dt^q} &= Cx_2 - \frac{[x_1 + (0.5x_3^4 - 2.4)x_2]}{1.8}, \\
 \frac{d^q x_3}{dt^q} &= -x_2 - \left(\frac{3}{4} - x_2^2\right)x_3,
 \end{aligned} \tag{9}$$

where C is a real number. According to system (8), we can write out,

$$\begin{aligned}
 L(C) &= \begin{pmatrix} 0 & 1 & 0 \\ -\frac{1}{1.8} & C + \frac{4}{3} & 0 \\ 0 & -1 & -\frac{3}{4} \end{pmatrix}, \\
 f(x) &= \begin{pmatrix} 0 \\ -\frac{5x_2x_3^4}{18} \\ x_2^2x_3 \end{pmatrix}.
 \end{aligned} \tag{10}$$

Now, one can obtain $f(x)|_{x=0} = 0$ and

$$\begin{aligned}
 \lim_{x \rightarrow 0} \left(\left\| \frac{f(x)}{x} \right\| \right) &= \lim_{x \rightarrow 0} \sqrt{\frac{\{(-5x_2x_3^4/18)^2 + (x_2^2x_3)^2\}}{(x_1^2 + x_2^2 + x_3^2)}} \\
 &\leq \lim_{x \rightarrow 0} \sqrt{x_3^8 + x_2^2x_3^2} = 0.
 \end{aligned} \tag{11}$$

Meanwhile, it is obvious that there will be some real number C , which can meet the needs of both

$|\arg \lambda_i L(C)| \geq 0.5\pi q (i = 1, 2, 3)$ and $q \|L(C)\| > 1$. According to the lemma, the controlled fractional-order memristive system (9) is asymptotically stable. This result indicates that the fractional-order memristive chaotic system (2) can be stability controlled via the single-state variable x_2 .

In addition, some numerical simulations are given to verify the validity of the control strategy.

For example, choosing $q = 0.98$, and $C = -7/3$, thus, the eigenvalues of matrix $L(C)$ are $-0.5 + \sqrt{11}j/6$, $-0.5 - \sqrt{11}j/6$, $-3/4$, and $q \|L(C)\| = 1.7824$, respectively. According to the lemma, the controlled fractional-order memristive system (9) is asymptotically stable. The results of state variables vary with time as shown in Figure 6(a). Here, the initial conditions are $x_{10} = 2$, $x_{20} = 1$, and $x_{30} = 1$, respectively.

For example, choosing $q = 0.965$ and $C = -2$, the eigenvalues of matrix $L(C)$ are thus $(-1 + 2j)/3$, $(-1 - 2j)/3$, and $-3/4$, respectively, as well as $q \|L(C)\| = 1.6023$. According to the lemma, the controlled fractional-order memristive system (9) is still asymptotically stable. The results of state variables vary with time as shown in Figures 6(b) and 6(c). In Figure 6(b), the black curve corresponds to the initial conditions $(x_{10}, x_{20}, x_{30}) = (2, -1, -1)$, and the blue curve corresponds to the initial conditions $(x_{10}, x_{20}, x_{30}) = (2, 1, 1)$. It should be mentioned that there are four-scroll chaotic attractors (the black curve in Figure 4) in fractional-order memristive system (2) with initial conditions $(x_{10}, x_{20}, x_{30}) = (2, -1, -1)$, while there are three-scroll chaotic attractors (the blue curve in Figure 4) in fractional-order memristive system (2) with initial conditions $(x_{10}, x_{20}, x_{30}) = (2, 1, 1)$.

The results in Figure 6(c) indicate that the state variables vary with time for initial conditions $(2, -1, -1)$ and $(-2, -1, -1)$. The black curve corresponds to the initial conditions $(x_{10}, x_{20}, x_{30}) = (2, -1, -1)$, and the red curve corresponds to the initial conditions $(x_{10}, x_{20}, x_{30}) = (-2, -1, -1)$, respectively. It should be mentioned again that there are four-scroll chaotic attractors (the black curve in Figure 4) in fractional-order memristive system (2) with initial conditions $(x_{10}, x_{20}, x_{30}) = (2, -1, -1)$, while there are three-scroll chaotic attractors (the red curve in Figure 4) in fractional-order memristive system (2) with initial conditions $(x_{10}, x_{20}, x_{30}) = (-2, -1, -1)$.

Proposition 4. *Let the controlled fractional-order memristive chaotic system (2) be,*

$$\begin{aligned} \frac{d^q x_1}{dt^q} &= x_2 + Cx_2, \\ \frac{d^q x_2}{dt^q} &= -\frac{[x_1 + (0.5x_3^4 - 2.4)x_2]}{1.8}, \\ \frac{d^q x_3}{dt^q} &= -x_2 - \left(\frac{3}{4} - x_2^2\right)x_3, \end{aligned} \quad (12)$$

if the following conditions are held,

- (a) $20C + 4 > 0$,
 (b) $|\arctan(\sqrt{20C + 4}/4)| \geq 0.5\pi q$, and $q\|L(C)\| > 1$,
 where

$$L(C) = \begin{pmatrix} 0 & 1 + C & 0 \\ -\frac{1}{1.8} & \frac{4}{3} & 0 \\ 0 & -1 & -\frac{3}{4} \end{pmatrix}, \quad (13)$$

and then, system is said to be asymptotically stable.

Proof. By the above Lemma, this Proposition is easy to prove.

As mentioned above, the fractional-order memristive chaotic system (2) can be stability controlled via the single-state variable x_2 .

5. Conclusions

In this paper, some new results for the integer-order memristive system [1] are found. The coexistence of two kinds of three-scroll chaotic tractors emerges in the integer-order memristive system (1) with different initial conditions, which Zhou and Ke have not reported in reference [1]. Furthermore, based on chaotic system (1), a fractional-order memristive system (2) is suggested. The largest Lyapunov exponents are obtained by numerical algorithm, which indicates that there are chaotic attractors in the fractional-order memristive system (2).

By numerical calculation, we find that the four-scroll chaotic attractors emerge in the fractional-order memristive system (2) for $q = 0.98$, which is different from the integer-

order memristive system (1). It indicates that the fractional-order memristive system (2) generates four-scroll chaotic attractors while the integer-order memristive system (1) generates three-scroll chaotic attractors. To the best of our knowledge, this result is rarely reported. Moreover, let fractional-order $q = 0.965$, it is obtained that the coexisting two kinds of three-scroll and four-scroll chaotic attractors emerge for different initial conditions. Therefore, not only three-scroll chaotic attractors but also four-scroll chaotic attractors are found in fractional-order memristive system (2).

Finally, a control strategy for the fractional-order memristive chaotic system (2) is proposed via single-state variable, and numerical simulations are employed to verify the validity of the proposed control strategy.

Data Availability

The data used in our manuscript is obtained by MATLAB program. The data used to support the finding of this study are available from the corresponding author upon request.

Conflicts of Interest

The authors declare that there are no conflicts of interest regarding the publication of this paper.

References

- [1] P. Zhou and M. Ke, "An integer-order memristive system with two-to four-scroll chaotic attractors and its fractional-order version with a coexisting chaotic attractor," *Complexity*, vol. 2018, p. 4970152, 2018.
- [2] V. T. Pham, A. Ouannas, C. Volos, and T. Kapitaniak, "A simple fractional-order chaotic system without equilibrium and its synchronization," *AEU- International Journal of Electronics and Communications (AEÜ)*, vol. 86, pp. 69–76, 2018.
- [3] V. T. Pham, C. Volos, T. Kapitaniak, S. Jafari, and X. Wang, "Dynamics and circuit of a chaotic system with a curve of equilibrium points," *International Journal of Electronics*, vol. 105, no. 3, pp. 385–397, 2018.
- [4] V. T. Pham, S. Jafari, T. Kapitaniak, C. Volos, and S. T. Kingni, "Generating a chaotic system with one stable equilibrium," *International Journal of Bifurcation and Chaos*, vol. 27, no. 4, p. 1750053, 2017.
- [5] P. Zhou and M. Ke, "A new 3D autonomous continuous system with two isolated chaotic attractors and its topological horseshoes," *Complexity*, vol. 2017, Article ID 4037682, 7 pages, 2017.
- [6] V. T. Pham, C. Volos, S. Jafari, S. Vaidyanathan, T. Kapitaniak, and X. Wang, "A chaotic system with different families of hidden attractors," *International Journal of Bifurcation and Chaos*, vol. 26, no. 8, p. 1650139, 2016.
- [7] V. T. Pham, C. Volos, S. Jafari, and T. Kapitaniak, "Coexistence of hidden chaotic attractors in a novel no-equilibrium system," *Nonlinear Dynamics*, vol. 87, no. 3, pp. 2001–2010, 2017.
- [8] J. Kengne, Z. T. Njitacke, and H. B. Fotsin, "Dynamical analysis of a simple autonomous jerk system with multiple attractors," *Nonlinear Dynamics*, vol. 83, no. 1-2, pp. 751–765, 2016.

- [9] J. C. Sprott, *Chaos and Time-Series Analysis*, Oxford University Press, Oxford, 2003.
- [10] G. R. Chen and X. Dong, *From Chaos to Order Perspectives, Methodologies and Applications*, World Scientific, Singapore, 1998.
- [11] C. E. C. Souza, D. P. B. Chaves, and C. Pimentel, "Digital communication systems based on three-dimensional chaotic attractors," *IEEE ACCESS*, vol. 7, pp. 10523–10532, 2019.
- [12] F. Zouad, K. Kemih, and H. Hamiche, "A new secure communication scheme using fractional order delayed chaotic system: design and electronics circuit simulation," *Analog Integrated Circuits and Signal Processing*, vol. 99, no. 3, pp. 619–632, 2019.
- [13] Y. Q. Xiao, J. Cao, Z. Y. Wang, C. X. Long, Y. Liu, and J. He, "Polar coded optical OFDM system with chaotic encryption for physical-layer security," *Optics Communications*, vol. 433, pp. 231–235, 2019.
- [14] Z. Y. Hua, Y. C. Zhou, and H. J. Huang, "Cosine-transform-based chaotic system for image encryption," *Information Sciences*, vol. 480, pp. 403–419, 2019.
- [15] M. Alawida, A. Samsudin, J. Sen Teh, and R. S. Alkhalwaldeh, "A new hybrid digital chaotic system with applications in image encryption," *Signal Processing*, vol. 160, pp. 45–58, 2019.
- [16] T. F. Weng, H. J. Yang, C. G. Gu, J. Zhang, and M. Small, "Synchronization of chaotic systems and their machine-learning models," *Physical Review E*, vol. 99, no. 4, p. 042203, 2019.
- [17] L. O. Chua, "Memristor—the missing circuit element," *IEEE Transactions on Circuit Theory*, vol. 18, no. 5, pp. 507–519, 1971.
- [18] D. B. Strukov, G. S. Snider, G. R. Stewart, and R. S. Williams, "The missing memristor found," *Nature*, vol. 453, no. 7191, pp. 80–83, 2008.
- [19] B. Muthuswamy and L. O. Chua, "Simplest chaotic circuit," *International Journal of Bifurcation and Chaos*, vol. 20, no. 5, pp. 1567–1580, 2010.
- [20] B. C. Bao, Z. H. Ma, J. P. Xu, Z. Liu, and Q. Xu, "A simple memristor chaotic circuit with complex dynamics," *International Journal of Bifurcation and Chaos*, vol. 21, no. 9, pp. 2629–2645, 2011.
- [21] L. Teng, H. H. C. Iu, X. Y. Wang, and X. K. Wang, "Chaotic behavior in fractional-order memristor-based simplest chaotic circuit using fourth degree polynomial," *Nonlinear Dynamics*, vol. 77, no. 1-2, pp. 231–241, 2014.
- [22] J. W. Sun, X. T. Zhao, J. Fang, and Y. F. Wang, "Autonomous memristor chaotic systems of infinite chaotic attractors and circuitry realization," *Nonlinear Dynamics*, vol. 94, no. 4, pp. 2879–2887, 2018.
- [23] I. Grigorenko and E. Grigorenko, "Chaotic dynamics of the fractional Lorenz system," *Physical Review Letters*, vol. 91, no. 3, p. 034101, 2003.
- [24] P. Zhou and W. Zhu, "Function projective synchronization for fractional-order chaotic systems," *Nonlinear Analysis: Real World Applications*, vol. 12, no. 2, pp. 811–816, 2011.
- [25] P. Zhou, R. J. Bai, and J. M. Zheng, "Stabilization of a fractional-order chaotic brushless DC motor via a single input," *Nonlinear Dynamics*, vol. 82, no. 1-2, pp. 519–525, 2015.
- [26] M. P. Aghababa, "Chaos in a fractional-order micro-electro-mechanical resonator and its suppression," *Chinese Physics B*, vol. 21, no. 10, p. 100505, 2012.
- [27] K. Rajagopal, V. T. Pham, F. E. Alsaadi, F. E. Alsaadi, A. Karthikeyan, and P. Duraisamy, "Multistability and coexisting attractors in a fractional order coronary artery system," *The European Physical Journal Special Topics*, vol. 227, no. 7–9, pp. 837–850, 2018.
- [28] P. Prakash, J. P. Singh, and B. K. Roy, "Fractional-order memristor-based chaotic system with a stable equilibrium point, its fractional-order PI-based sliding mode control and switching synchronization," *Pramana-Journal of Physics*, vol. 92, no. 2, p. 19, 2019.
- [29] S. B. He, K. H. Sun, H. H. Wang, X. Y. Mei, and Y. F. Sun, "Generalized synchronization of fractional-order hyperchaotic systems and its DSP implementation," *Nonlinear Dynamics*, vol. 92, no. 1, pp. 85–96, 2018.
- [30] P. Zhou and K. Huang, "A new 4-D non-equilibrium fractional-order chaotic system and its circuit implementation," *Communications in Nonlinear Science and Numerical Simulation*, vol. 19, no. 6, pp. 2005–2011, 2014.
- [31] K. Rajagopal, A. Karthikeyan, and A. K. Srinivasan, "FPGA implementation of novel fractional-order chaotic systems with two equilibriums and no equilibrium and its adaptive sliding mode synchronization," *Nonlinear Dynamics*, vol. 87, no. 4, pp. 2281–2304, 2017.
- [32] H. S. Nik, S. Effati, and J. Saberi-Nadjafi, "Ultimate bound sets of a hyperchaotic system and its application in chaos synchronization," *Complexity*, vol. 20, no. 4, pp. 30–44, 2015.
- [33] H. S. Nik and R. A. Gordor van, "Competitive modes for the Baier-Sahle hyperchaotic ow in arbitrary dimensions," *Nonlinear Dynamics*, vol. 74, no. 3, pp. 581–590, 2013.
- [34] S. Effati, J. Saberi-Nadjafi, and H. S. Nik, "Optimal and adaptive control for a kind of 3D chaotic and 4D hyper-chaotic systems," *Applied Mathematical Modelling*, vol. 38, no. 2, pp. 759–774, 2014.
- [35] L. Chen, Y. Chai, R. Wu, and J. Yang, "Stability and stabilization of a class of nonlinear fractional-order systems with caputo derivative," *IEEE Transactions on Circuits and Systems II Express*, vol. 59, no. 9, pp. 602–606, 2012.

Research Article

Adaptive Multi-Switching Synchronization of High-Order Memristor-Based Hyperchaotic System with Unknown Parameters and Its Application in Secure Communication

Zhili Xiong ^{1,2}, Shaocheng Qu ¹, and Jing Luo¹

¹Department of Electronics and Information Engineering, Central China Normal University, Wuhan 430079, China

²School of Physics and Electric Information, Huanggang Normal University, Huanggang 438000, China

Correspondence should be addressed to Shaocheng Qu; qushaocheng@mail.ccnu.edu.cn

Received 19 May 2019; Revised 24 June 2019; Accepted 4 July 2019; Published 19 December 2019

Guest Editor: Lazaros Moysis

Copyright © 2019 Zhili Xiong et al. This is an open access article distributed under the Creative Commons Attribution License, which permits unrestricted use, distribution, and reproduction in any medium, provided the original work is properly cited.

This article investigates an adaptive multi-switching synchronization for two identical high-order memristor-based hyperchaotic systems with uncertain parameters. Firstly, the dynamic characteristics of two high-order memristor hyperchaotic systems with uncertain parameters are analyzed. Then, an adaptive multi-switching controller is designed to realize the multi-switching synchronization of the two high-order hyperchaotic systems, and the unknown parameters of the systems are identified to their true values. Furthermore, numerical simulation results testify the effectiveness of the proposed strategy. Finally, the proposed algorithm applied in secure communication of masking encryption and image encryption is validated by statistical analysis.

1. Introduction

Chaos is a kind of irregular and unstable motion state existing in nonlinear system. And it has three properties: infinite recurrence, bondedness, and sensitivity to initial conditions. Since the slight change of the initial state value will result in a large error in the chaotic system, chaos was considered to be harmful until Pecora and Carrol proposed the concept of chaos synchronization in 1990, the synchronization of two coupled chaotic oscillators is observed for the first time [1]. Chaos synchronization means that the motion trajectory of one system converges to the trajectory of another system and is always consistent. The synchronization of chaotic systems has drawn attentions in many fields including secure communication [2–4], electrical engineering, and biological system [5]. In practical engineering, there exists partially or fully uncertain parameters in drive or response systems, the conventional control methods can not be applied to synchronize the two chaotic systems with uncertainties. Hence, a number of control methods have been studied to accomplish two chaos synchronization with unknown parameters or uncertain terms, such as sliding mode control method [6–8], impulsive control [9], fuzzy control scheme [10, 11], and adaptive strategies [6,

12–14]. The adaptive synchronization for uncertain chaotic system was proposed by Parlitz firstly, the identification method of the adaptive synchronization was employed to estimation the unknown parameters in Lorenz system [15]. Later, this strategy has been extended to other uncertain chaotic systems. Adaptive synchronization methods for a class of chaotic systems existing in the literature are studied in [16]. However, the linear independence condition for some chaotic systems with unknown parameters is neglected to guarantee the true convergence of the estimated parameters. Reference [17] described the principle of the linear independence, the functions $f_i(t)$ ($i = 1, 2, \dots, n$) are said to be linear independent if there do not exist nonzero constants α_i ($i = 1, 2, \dots, n$), such that $f_1(t)\alpha_1 + f_2(t)\alpha_2 + \dots + f_n(t)\alpha_n = 0$. The adaptive multi-switching synchronization was proven to be effective to solve the identification of the unknown parameters in [18].

Multi-switching synchronization proposed by Ucar can provide more combined error spaces [19], it is beneficial to prevent intruders from gaining useful informations of the chaotic synchronization system. Although multi-switching synchronization is suitable to enhance anti-attack and resistance for secure communication, only a few literatures for it have been proposed [20–24]. Wang and S investigated the

multi-switching synchronization of chaotic systems with unknown parameters by the adaptive control techniques [20]. Ahmad et al. implemented multi-switching combination synchronization for three chaotic systems, and introduced its application in secure communication [21]. Wen et al. addressed adaptive control method to accomplish multi-switching combination synchronization of three nonidentical chaotic systems with unknown parameters [22]. Khan et al. designed a multi-switching synchronization strategy for different switches of three masters and one slave hyperchaotic system [23]. Prajapati et al. completed multi-switching compound synchronization of four different chaotic systems [24]. Above these analysis, these chaotic or hyperchaotic systems are 3D or 4D systems without considering memristors. It will be a challenging task to study chaotic synchronization with memristor. Hence, the adaptive multi-switching synchronization can be extend to the memristor-based systems with unknown parameters.

The memristor is one of three breakthrough inventions of Chua in the nonlinear control systems. In 1971, Chua conceived the notion of memristors based on the principle of symmetry and signal integrity analysis, and considered memristors to be the fourth circuit component following capacitors, resistors, and inductors [25]. The researches on memristor have attract significant attentions only recently after the realization of TiO_2 -based physical memristor by the HP Laboratories in 2008 [26]. Itoh and Chua developed memristor oscillators which was a kind of typical memristor-based chaotic system [27]. In recent years, many researches on memristor have attracted the attention of scholars [10, 11, 13, 14, 28–32]. Wen et al. designed an adaptive controller to solve the synchronization problem of the memristor-based Chua circuit. Wen et al. established a fuzzy modeling and proposed a fuzzy controller to solve the synchronization of different memristor-based chaotic systems [10]. Wang et al. designed and analyzed the adaptive synchronization for two flux-controlled 5D memristor chaotic systems, but the unknown parameters of the systems can not be identified to the true value for the linear independence condition. In [31], the analysis of the linear dependence condition for the parameter identification is followed as

$$\begin{aligned}\dot{e}_1 &= (a - \hat{a}(t))(e_2 - e_1) - k_1 e_1, \\ \dot{e}_2 &= -k_2 e_2, \\ \dot{e}_3 &= (\hat{b}(t) - b)e_3 - k_3 e_3, \\ \dot{e}_4 &= -k_4 e_4, \\ \dot{e}_5 &= -k_5 e_5.\end{aligned}\quad (1)$$

Finally, it is clear that $e_1 = 0|_{t \rightarrow \infty}$, $e_2 = 0|_{t \rightarrow \infty}$, $e_3 = 0|_{t \rightarrow \infty}$, $e_4 = 0|_{t \rightarrow \infty}$, $e_5 = 0|_{t \rightarrow \infty}$ with the realization of synchronization between the drive system and the response system. We know $a - \hat{a}(t) = \text{const}1$ and $\hat{b}(t) - b = \text{const}2$ according to linear independence, where the constant numbers $\text{const}i$ ($i = 1, 2$) can be arbitrary values. Hence, the unknown parameters can not be identified to the true values. Based on the above analysis, memristor-based chaotic system synchronization has been widely studied [2, 8, 13, 33], but there are few literatures on the synchronization of memristor chaotic systems with considering the linear independence of unknown parameters, the unknown parameters can not be identified the true values.

In order to solve the problem of unknown parameter identification, the adaptive multi-switching synchronization is extent to employ in the high-order memristor-based hyperchaotic systems with unknown parameters.

Due to the sensitivity of initial states, unpredictability and the pseudo-random property, memristor-based chaotic systems are suitable for secure communication. The useful signals can be hidden in chaotic signals to prevent being hacked and modified. However, the image encryption process involves a large amount of image data, it is difficult to accomplish image encryption by the traditional encryption techniques, such as RSA algorithm, IDEA, and AES. Therefore, researchers and engineers are committed to the researches of the new image encryption algorithm to enhance the information security. Sun et al. proposed an adaptive controller to realize compound synchronization among 4D chaotic oscillator systems and presented a secure communication method based on Chaotic Synchronization [2]. Li et al. analyzed the dynamic characteristics of memristor-based chaotic system and applied chaotic sequences of the new system to secure communication [34]. However, the literature of multi-switch synchronization for high-order memristor-based hyperchaotic systems with unknown parameters appears less, especially its application in secure communication.

Motivated from the above analysis, the adaptive multi-switching controller is designed to realize the synchronization for high-order memristor hyperchaotic systems with uncertain parameters and its corresponding applications in secure communication. The main contributions of this paper are as follows:

- (1) The principle of linear independence is introduced. By the analysis of the linear independence condition for the system in [31], the unknown parameters can be arbitrary values and failed to be identified to their true values.
- (2) The nonlinear dynamic characteristics of the high-order memristor-based hyperchaotic systems which has two Lyapunov exponents are analyzed.
- (3) In order to solve the problem of the parameter identification in [31], the adaptive multi-switching synchronization scheme is proposed in the paper, the numerical results show that the master-slave system can be synchronized and the unknown parameters can be consistent with the given value simultaneously.
- (4) The adaptive multi-switching synchronization can offer various different dynamic errors of the master-slave hyperchaotic system, which is suitable for secure communication. An encryption algorithm based on multi-switching synchronization hyperchaotic system with memristor is presented, by the gray histogram and correlation analysis, the numerical simulation results reflect that the proposed method improved the security to prevent intruders from cracking and tampering during the process of information transmission.

The organization of this paper lists as follows. Section 2 analyzes the adaptive multi-switching synchronization strategy. Section 3 implements the adaptive multi-switching synchronization for high-order memristor hyperchaotic systems with unknown parameters, and validates the feasibility and effectiveness of the proposed strategy by using numerical simulations. Section 4 proposes a new encryption algorithm based on proposed strategy to improve the security of the useful signals, and introduces the statistical analysis methods of the gray histogram and correlation. Finally, Section 5 draws the conclusion and prospects further works.

2. Problem Formulation

In this section, an adaptive multi-switching synchronization strategy is introduced for master-slave chaotic system with unknown parameters.

Considering three n -dimensional hyperchaotic systems with unknown parameters, the two master hyperchaotic systems are given by

$$\begin{cases} \dot{v}_1(t) = f_{11}(v_1, v_2, \dots, v_n) + F_{11}(v_1, v_2, \dots, v_n)\psi_1, \\ \dot{v}_2(t) = f_{12}(v_1, v_2, \dots, v_n) + F_{12}(v_1, v_2, \dots, v_n)\psi_2, \\ \vdots \\ \dot{v}_n(t) = f_{1n}(v_1, v_2, \dots, v_n) + F_{1n}(v_1, v_2, \dots, v_n)\psi_n, \end{cases} \quad (2)$$

and

$$\begin{cases} \dot{w}_1(t) = f_{21}(w_1, w_2, \dots, w_n) + F_{21}(w_1, w_2, \dots, w_n)\gamma_1, \\ \dot{w}_2(t) = f_{22}(w_1, w_2, \dots, w_n) + F_{22}(w_1, w_2, \dots, w_n)\gamma_2, \\ \vdots \\ \dot{w}_n(t) = f_{2n}(w_1, w_2, \dots, w_n) + F_{2n}(w_1, w_2, \dots, w_n)\gamma_n, \end{cases} \quad (3)$$

where $v(t) = [v_1, v_2, \dots, v_n]^T$, and $w(t) = [w_1, w_2, \dots, w_n]^T$ are the state vectors. $f_{1i}(v) = (f_{11}(v), f_{12}(v), \dots, f_{1n}(v))^T$ and $f_{2i}(w) = (f_{21}(w), f_{22}(w), \dots, f_{2n}(w))^T$ are nonlinear vector terms from $R^n \rightarrow R^n$, $F(v_{1i}) \in R^{n \times n}$ and $F(v_{2i}) \in R^{n \times n}$ are the system matrices, and $\psi, \gamma \in R^n$ are unknown vector parameters.

The slave hyperchaotic system is described by

$$\begin{cases} \dot{z}_1(t) = g_1(z_1, z_2, \dots, z_n) + G_1(z_1, z_2, \dots, z_n)\eta_1 + u_1, \\ \dot{z}_2(t) = g_2(z_1, z_2, \dots, z_n) + G_2(z_1, z_2, \dots, z_n)\eta_2 + u_2, \\ \vdots \\ \dot{z}_n(t) = g_n(z_1, z_2, \dots, z_n) + G_n(z_1, z_2, \dots, z_n)\eta_n + u_n, \end{cases} \quad (4)$$

where $z(t) = [z_1, z_2, \dots, z_n]^T$ is a state vector, $g(z) = (g_1(z), g_2(z), \dots, g_n(z))^T$ is a nonlinear vector function from $R^n \rightarrow R^n$, $G(z) \in R^{n \times n}$ is a system matrix, and $\eta \in R^n$ is an unknown vector parameter, and $U = (u_1, u_2, \dots, u_n)$ is

a controller to be designed for the synchronization of master-slave hyperchaotic systems.

Definition 1. The slave system (3) will realize the synchronization with the two master systems (1) and (2), if there exist diagonal matrices $C, D, H \in R^{n \times n}$, and $H \neq 0$, such that

$$\lim_{t \rightarrow \infty} \|e\| = \lim_{t \rightarrow \infty} \|Cv + Dw - Hz\| = 0, \quad (5)$$

where $\|\cdot\|$ represents the Euclidean norm, and $e = Cv + Dw - Hz$ is the error vector of the synchronization with master-slave systems.

Remark 1. Assume the scaling matrices C, D, H as $C = \text{diag}(c_1, c_2, \dots, c_n)$, $D = \text{diag}(d_1, d_2, \dots, d_n)$, and $H = \text{diag}(h_1, h_2, \dots, h_n)$ respectively. The error vectors are obtained as $e_{ijk} = c_i v_i + d_j w_j - h_k z_k$. In accordance with the Definition 1, $i = j = k$, $i \neq j = k$, $i = j \neq k$, ($i, j, k = 1, 2, \dots, n$). According to (1)–(4), the error dynamics is gain by

$$\begin{aligned} \dot{e} = & Cf_1(v) + CF_1(v)\psi + Df_2(w) + DF_2(w)\gamma \\ & - Hg(z) - HG(z)\eta - HU. \end{aligned} \quad (6)$$

Now, in order to achieve the synchronization of the master-slave systems, an appropriate controller U and the unknown parameters ψ, γ , and η need to design.

$\hat{\psi}, \hat{\gamma}$, and $\hat{\eta}$ are the estimated values of the parameters ψ, γ and η respectively.

Define the estimated error parameters as

$$\tilde{\psi} = \psi - \hat{\psi}, \quad \tilde{\gamma} = \gamma - \hat{\gamma}, \quad \tilde{\eta} = \eta - \hat{\eta}. \quad (7)$$

Then,

$$\dot{\tilde{\psi}} = -\dot{\hat{\psi}}, \quad \dot{\tilde{\gamma}} = -\dot{\hat{\gamma}}, \quad \dot{\tilde{\eta}} = -\dot{\hat{\eta}}. \quad (8)$$

Theorem 1. The controller U is selected as

$$\begin{aligned} U = & H^{-1}Cf_1(v) + H^{-1}CF_1(v)\hat{\psi} + H^{-1}Df_2(w) + H^{-1}DF_2(w)\hat{\gamma} - g(z) \\ & - G(z)\hat{\eta} + H^{-1}e + H^{-1}\text{sgn}(e)|e|^\mu, \end{aligned} \quad (9)$$

where $\text{sgn}(e)$ expresses signum function. The parameter update laws are designed as

$$\dot{\hat{\psi}} = F_1(v)^T Ce, \quad \dot{\hat{\gamma}} = F_2(w)^T De, \quad \dot{\hat{\eta}} = G(z)^T He. \quad (10)$$

Proof. The Lyapunov function is selected as

$$V(t) = \frac{1}{2} (e^T e + \tilde{\psi}^T \tilde{\psi} + \tilde{\gamma}^T \tilde{\gamma} + \tilde{\eta}^T \tilde{\eta}), \quad (11)$$

Then,

$$\dot{V}(t) = \dot{e}^T e - \tilde{\psi}^T \dot{\tilde{\psi}} - \tilde{\gamma}^T \dot{\tilde{\gamma}} - \tilde{\eta}^T \dot{\tilde{\eta}}. \quad (12)$$

Substituting (6)–(10) into (12) gains as

$$\begin{aligned} \dot{V}(t) = & [Cf_1(v) + CF_1(v)\psi + Df_2(w) + DF_2(w)\gamma - Hg(z) - HG(z)\eta - HU]^T e - \tilde{\psi}^T \dot{\tilde{\psi}} - \tilde{\gamma}^T \dot{\tilde{\gamma}} - \tilde{\eta}^T \dot{\tilde{\eta}}, \\ = & [CF_1(v)(\psi - \hat{\psi}) + DF_2(w)(\gamma - \hat{\gamma}) - HG(z)(\eta - \hat{\eta}) - e - \text{sgn}(e)|e|^\mu]^T e - \tilde{\psi}^T \dot{\tilde{\psi}} - \tilde{\gamma}^T \dot{\tilde{\gamma}} - \tilde{\eta}^T \dot{\tilde{\eta}}, \\ = & [CF_1(v)\tilde{\psi} + DF_2(w)\tilde{\gamma} - HG(z)\tilde{\eta} - e - \text{sgn}(e)|e|^\mu]^T e - \tilde{\psi}^T \dot{\tilde{\psi}} - \tilde{\gamma}^T \dot{\tilde{\gamma}} - \tilde{\eta}^T \dot{\tilde{\eta}}, \\ = & \tilde{\psi}^T (F_1(v)^T Ce - \dot{\hat{\psi}}) + \tilde{\gamma}^T (F_2(w)^T De - \dot{\hat{\gamma}}) + \tilde{\eta}^T (G(z)^T He - \dot{\hat{\eta}}) - e^T e - |e|^{\mu+1}, \\ = & -e^T e - |e|^{\mu+1}. \end{aligned} \quad (13)$$

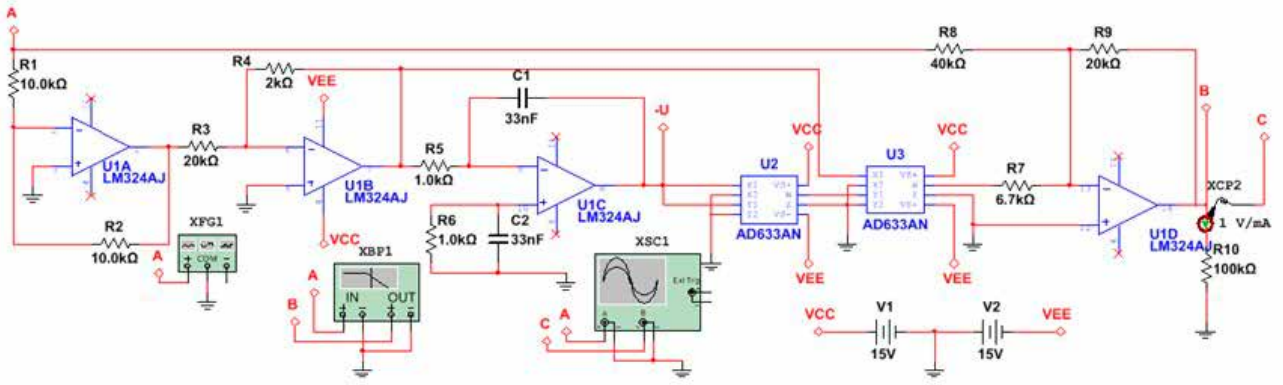


FIGURE 1: The equivalent circuit of the flux-controlled smooth cubic memristor.

Thus, we can know $\dot{V}(t) < 0$. In the light of the Lyapunov stability theory, if $V(t) > 0$ and $\dot{V}(t) < 0$, the master system will synchronize with the slave system.

Remark 2. If $C = 0$ or $D = 0$, the synchronization problem becomes multi-switching modified projective synchronization. If $C = 0$ or $D = 0$ and $H = 1$, the synchronization problem turns into multi-switching synchronization. In order to facilitate the analysis of multi-switch synchronization of complex systems, the parameters $C = 1$, $D = 0$, and $H = 1$ are selected in the following sections.

3. Adaptive Multi-Switching Synchronization of High-Order Memristor-Based Hyperchaotic System

In this section, firstly, the 5D hyperchaotic system with memristor is introduced. Secondly, two identical 5D memristor hyperchaotic systems with unknown parameters are composited a master-slave system. Thirdly, an adaptive multi-switching synchronization strategy is proposed for the system. Finally, the numerical simulation results indicate that the synchronization of the master-slave system can be implemented, and unknown parameters of the system can be identified to their given values.

3.1. High-Order Memristor-Based Hyperchaotic System. Memristors represent the relationship between magnetic flux φ and charge q which is a missing circuit component with memory characteristic conceived by Chua in 1971 [25]. The function between the magnetic flux and the charge passing the memristor is not unique. Select a smooth cubic memristor [35] which can be expressed as

$$q(\varphi) = \alpha\varphi + \beta\varphi^3, \quad (14)$$

and

$$W(\varphi) = \frac{dq(\varphi)}{d\varphi} = \alpha + 3\beta\varphi^2, \quad (15)$$

where α and β are positive parameters.

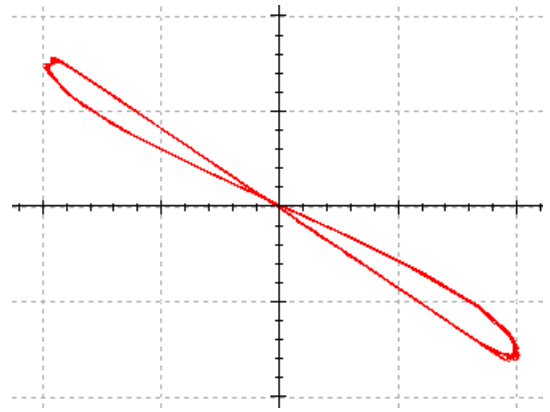


FIGURE 2: Flux-controlled memristors characteristics.

In line with the above defined flux-controlled memristor formula (14), an equivalent circuit with a smooth cubic memristor is shown in Figure 1, where $a = 0.1$, $b = 0.01$ (input is 1 V 100 Hz sinusoidal wave). Circuit diagram of $C1 = C2 = 33$ nF, $R1 = R2 = 10$ k Ω , $R3 = R9 = 20$ k Ω , $R4 = 2$ k Ω , $R5 = R6 = 1$ k Ω , $R7 = 6.7$ k Ω , $R8 = 40$ k Ω , $R10 = 100$ k Ω . The circuit consists of operational amplifiers, multipliers, resistors, and capacitors. The first and second stage operational amplifiers are used for signal reduction. The third pole operational amplifier using differential integrator prevents “zero drift”. Two multipliers perform simulated multiplication. The fourth operational amplifier performs reverse addition.

Memristor is a nonlinear resistor with charge memory function. Applying an arbitrary periodic voltage signal to the ideal memristor, the V-I characteristics of the excitation voltage and the corresponding response current can be depicted as a skewed “8” shaped pinched hysteresis loop in Figure 2.

The model originated from wang’s 5D hyperchaotic system [31] is as follows:

$$\begin{aligned} \dot{x}_1 &= a(x_2 - x_1) + 4x_2x_3 - kx_1W(x_5), \\ \dot{x}_2 &= -x_1 + x_4 + 16x_2 - x_1x_3, \\ \dot{x}_3 &= -bx_3 - x_2x_4 + x_1x_2 - x_1x_5, \\ \dot{x}_4 &= -gx_3x_5 - 10x_2 + 0.15x_1x_3, \\ \dot{x}_5 &= -x_1. \end{aligned} \quad (16)$$

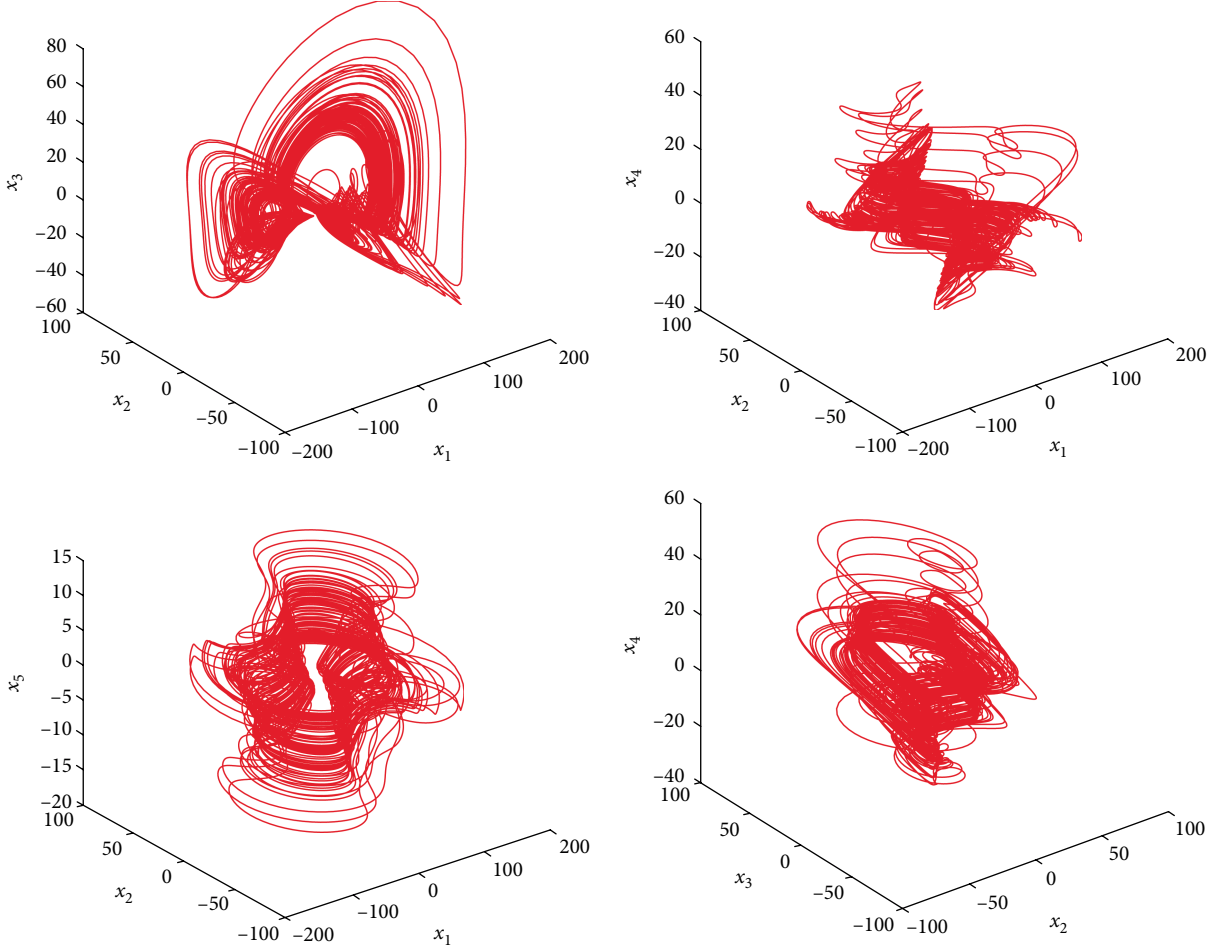


FIGURE 3: 3D phase portraits of the hyperchaotic system.

where $W(x_5)$ is the memristor model, as follows

$$W(x_5) = \alpha + 3\beta x_5^2. \quad (17)$$

Substituting (17) into (16) obtains

$$\begin{aligned} \dot{x}_1 &= a(x_2 - x_1) + 4x_2x_3 - kx_1(\alpha + 3\beta x_5^2), \\ \dot{x}_2 &= -x_1 + 16x_2 - x_1x_3 + x_4, \\ \dot{x}_3 &= -bx_3 + x_1x_2 - x_1x_5 - x_2x_4, \\ \dot{x}_4 &= -10x_2 + 0.15x_1x_3 - gx_3x_5, \\ \dot{x}_5 &= -x_1. \end{aligned} \quad (18)$$

If the parameters are selected as $a = 14$, $b = 78$, $k = 0.02$, $\alpha = 0.1$, $\beta = 0.01$, $g = 0.3$, and the initial states are given as: $x(0) = [4, 1.2, 0.5, -3.6, 6]$, the Lyapunov exponents of system (17) can be calculated as $L_1 = 0.0137$, $L_2 = 1.0241$, $L_3 = -0.1735$, $L_4 = -2.3787$, and $L_5 = -70.3244$. Two positive Lyapunov exponents indicate that the system is a hyperchaotic system. And its 3D phase portraits and hyperchaotic attractors are shown in Figures 3 and 4 respectively.

Remark 3. In [21–23], third-order chaotic system is as the research object without considering memristor. The high-order hyperchaotic systems with memristor has complex dynamic characteristics, which has attracted attention in engineering practice. It has good application potential in many

fields, among them, the research of chaotic synchronization has become a hot spot, especially in secure communication.

3.2. Multi-Switching Synchronization for the 5D Memristor Hyperchaotic System with Unknown Parameters. The multi-switching synchronization process can be extended to several identical schemes or different structures of hyperchaotic system which have unknown parameters.

Here, two identical hyperchaotic systems with uncertain parameters composite the master-slave system.

The master system is represented by

$$\begin{aligned} \dot{x}_1 &= a(x_2 - x_1) + 4x_2x_3 - kx_1(0.1 + 0.03x_5^2), \\ \dot{x}_2 &= -x_1 + x_4 + 16x_2 - x_1x_3, \\ \dot{x}_3 &= -bx_3 + x_1x_2 - x_2x_4 - x_1x_5, \\ \dot{x}_4 &= -10x_2 - gx_3x_5 + 0.15x_1x_3, \\ \dot{x}_5 &= -x_1. \end{aligned} \quad (19)$$

The slave system is expressed as

$$\begin{aligned} \dot{y}_1 &= a(y_2 - y_1) + 4y_2y_3 - ky_1(0.1 + 0.03y_5^2) + U_1, \\ \dot{y}_2 &= -y_1 + y_4 + 16y_2 - y_1y_3 + U_2, \\ \dot{y}_3 &= -by_3 + y_1y_2 - y_2y_4 - y_1y_5 + U_3, \\ \dot{y}_4 &= -10y_2 - gy_3y_5 + 0.15y_1y_3 + U_4, \\ \dot{y}_5 &= -y_1 + U_5. \end{aligned} \quad (20)$$

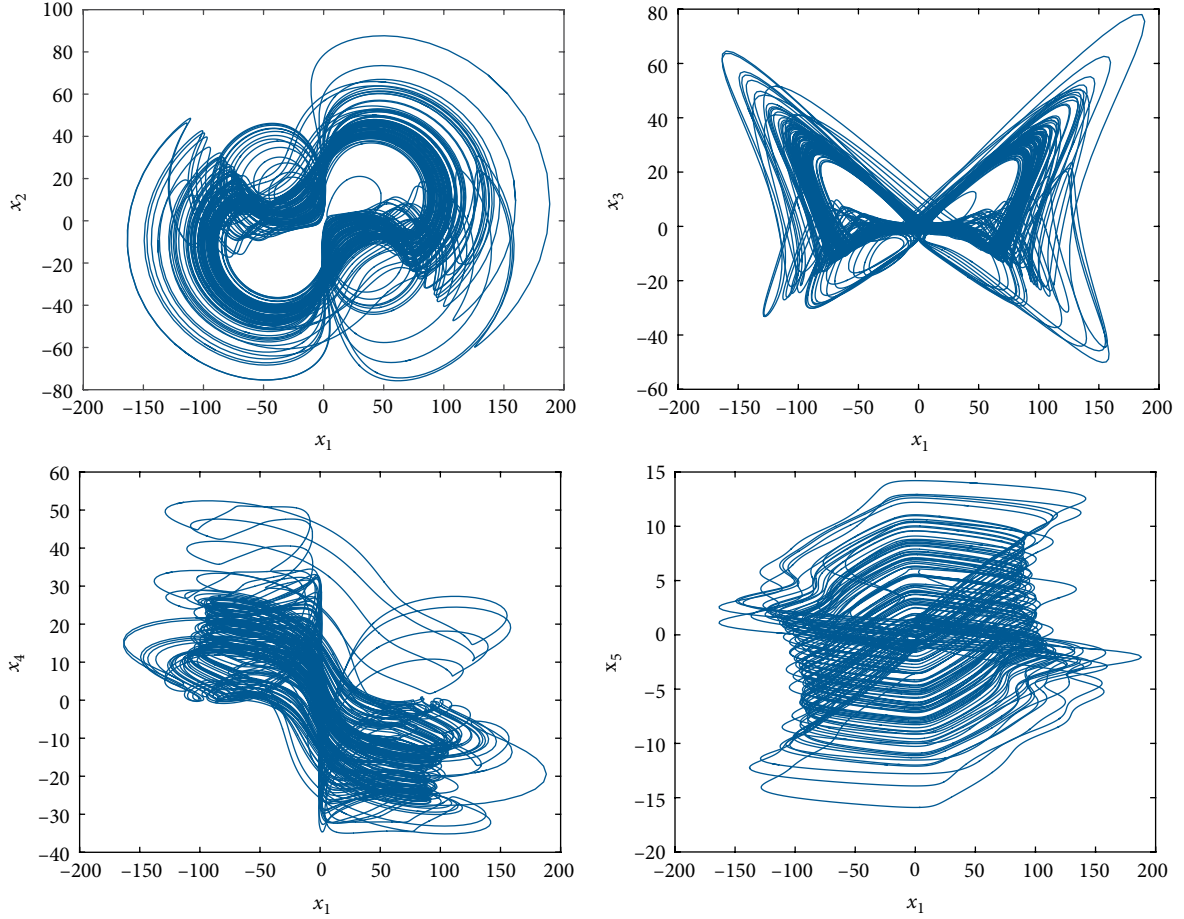


FIGURE 4: 2D projections of the hyperchaotic systems.

According to the Definition 1, the parameters $D = 0$ and $H = 1$ are selected, error system is changed into $e_{ij} = y_j - x_i$, where $i, j = 1, 2, \dots, 5$.

When $i = j$,

$$e_{11} = y_1 - x_1, e_{22} = y_2 - x_2, \dots, e_{nn} = y_n - x_n, \quad (21)$$

When $i \neq j$,

$$\begin{aligned} e_{12} &= y_1 - x_2, e_{13} = y_1 - x_3, \dots, e_{1n} = y_1 - x_n, \\ e_{21} &= y_2 - x_1, e_{23} = y_2 - x_3, \dots, e_{2n} = y_2 - x_n, \\ &\vdots \\ e_{n1} &= y_n - x_1, e_{n2} = y_n - x_2, \dots, e_{nn-1} = y_n - x_{n-1}, \end{aligned} \quad (22)$$

From (21) and (22), multiple error systems are obtained, for example:

$$\begin{aligned} \text{Switch-1} \quad & e_{13} = y_1 - x_3, e_{22} = y_2 - x_2, e_{31} = y_3 - x_1, \\ & e_{44} = y_4 - x_4, e_{55} = y_5 - x_5, \\ \text{Switch-2} \quad & e_{12} = y_1 - x_2, e_{34} = y_3 - x_4, e_{23} = y_2 - x_3, \\ & e_{51} = y_5 - x_1, e_{45} = y_4 - x_5, \\ \text{Switch-3} \quad & e_{12} = y_1 - x_2, e_{13} = y_1 - x_3, e_{14} = y_1 - x_4, \\ & e_{15} = y_1 - x_5, e_{21} = y_2 - x_1, \\ \text{Switch-4} \quad & e_{11} = y_1 - x_1, e_{22} = y_2 - x_2, e_{33} = y_3 - x_3, \\ & e_{44} = y_4 - x_4, e_{55} = y_5 - x_5, \\ & \text{and so on.} \end{aligned}$$

Remark 4. According to the conditions of the two indices $i, j = 1, 2, \dots, 5$, this section selects two out of the several switches,

$$\begin{aligned} \text{Switch-1} \quad & e_{13} = y_1 - x_3, e_{22} = y_2 - x_2, e_{31} = y_3 - x_1, \\ & e_{44} = y_4 - x_4, e_{55} = y_5 - x_5, \\ \text{Switch-2} \quad & e_{12} = y_1 - x_2, e_{34} = y_3 - x_4, e_{23} = y_2 - x_3, \\ & e_{51} = y_5 - x_1, e_{45} = y_4 - x_5. \end{aligned}$$

Corollary 1. For switch-1, the dynamic errors are calculated as

$$\begin{aligned} \dot{e}_{13} &= a(y_2 - y_1) + 4y_2y_3 - ky_1(0.1 + 0.03y_5^2) \\ &\quad + bx_3 - x_1x_2 + x_1x_5 + x_2x_4 + U_1, \\ \dot{e}_{22} &= -y_1 + x_1 + 16e_{22} + e_{24} - y_1y_3 + x_1x_3 + U_2, \\ \dot{e}_{31} &= -by_3 + y_1y_2 - y_1y_5 - y_2y_4 - a(x_2 - x_1) \\ &\quad - 4x_2x_3 - kx_1(0.1 + 0.03x_5^2) + U_3, \\ \dot{e}_{44} &= -10e_{22} + 0.15y_1y_3 - 0.15x_1x_3 - 0.3y_3y_5 + 0.3x_3x_5 + U_4, \\ \dot{e}_{55} &= -y_1 + x_1 + U_5. \end{aligned} \quad (23)$$

Theorem 2. The control laws of (21) in switch-1 are chosen as follows

$$\begin{aligned}
U_1 &= -\tilde{a}(y_2 - y_1) - 4y_2y_3 + ky_1(0.1 + 0.03y_5^2) - \tilde{b}x_3 + x_1x_2 \\
&\quad - x_1x_5 - x_2x_4 - k_1e_{13} - h_1\text{sgn}(e_{13})|e_{13}|^\mu, \\
U_2 &= y_1 - x_1 - 16e_{22} - e_{24} + y_1y_3 - x_1x_3 - k_2e_{22} - h_2\text{sgn}(e_{22})|e_{22}|^\mu, \\
U_3 &= \tilde{b}y_3 - y_1y_2 + y_1y_5 + y_2y_4 + \tilde{a}(x_2 - x_1) + 4x_2x_3 \\
&\quad + kx_1(0.1 + 0.03x_5^2) - k_3e_{31} - h_3\text{sgn}(e_{31})|e_{31}|^\mu, \\
U_4 &= 10e_{22} - 0.15y_1y_3 + 0.15x_1x_3 + 0.3y_3y_5 - 0.3x_3x_5 \\
&\quad - k_4e_{44} - h_4\text{sgn}(e_{44})|e_{44}|^\mu, \\
U_5 &= y_1 - x_1 - k_5e_{25} - h_5\text{sgn}(e_{55})|e_{55}|^\mu. \tag{24}
\end{aligned}$$

where $k_i (i = 1 \dots 5)$ and $h_i (i = 1 \dots 5)$ are the positive constants, $0 < \mu < 1$, $\tilde{a}(t)$ and $\tilde{b}(t)$ are the estimated values of the unknown parameters a and b , respectively.

The parameters update laws are designed as

$$\begin{aligned}
\dot{\tilde{a}}(t) &= e_{13}(y_2 - y_1) - e_{31}(x_2 - x_1), \\
\dot{\tilde{b}}(t) &= e_{13}x_3 - e_{31}y_3. \tag{25}
\end{aligned}$$

Proof. Substituting (23) into (22) yields

$$\begin{aligned}
\dot{e}_{13} &= \tilde{a}(t)(y_2 - y_1) + \tilde{b}(t)x_3 - k_1e_{13} - h_1\text{sgn}(e_{13})|e_{13}|^\mu, \\
\dot{e}_{22} &= -k_2e_{22} - h_2\text{sgn}(e_{22})|e_{22}|^\mu, \\
\dot{e}_{31} &= -\tilde{b}(t)y_3 - \tilde{a}(t)(x_2 - x_1) - k_2e_{31} - h_3\text{sgn}(e_{31})|e_{31}|^\mu, \\
\dot{e}_{44} &= -k_4e_{44} - h_4\text{sgn}(e_{44})|e_{44}|^\mu, \\
\dot{e}_{55} &= -k_5e_{55} - h_5\text{sgn}(e_{55})|e_{55}|^\mu, \tag{26}
\end{aligned}$$

where $\tilde{b}(t) = b - \hat{b}(t)$ and $\tilde{a}(t) = a - \hat{a}(t)$ are parameter errors, correspondingly, $\hat{b}(t) = -\tilde{b}(t)$ and $\hat{a}(t) = -\tilde{a}(t)$.

A candidate Lyapunov function is considered as follows,

$$V = \frac{1}{2}(e_{13}^2 + e_{22}^2 + e_{31}^2 + e_{44}^2 + e_{55}^2 + \tilde{a}^2 + \tilde{b}^2). \tag{27}$$

Then

$$\begin{aligned}
\dot{V} &= e_{13}\dot{e}_{13} + e_{22}\dot{e}_{22} + e_{31}\dot{e}_{31} + e_{44}\dot{e}_{44} + e_{55}\dot{e}_{55} + \tilde{a}\dot{\tilde{a}} + \tilde{b}\dot{\tilde{b}}, \\
&= e_{13}(\tilde{a}(y_2 - y_1) + \tilde{b}x_3 - k_1e_{13} - h_1\text{sgn}(e_{13})|e_{13}|^\mu) - k_2e_{22}^2 - h_2|e_{22}|^{\mu+1} \\
&\quad + e_{31}(-\tilde{b}y_3 - \tilde{a}(x_2 - x_1) - k_2e_{31} - h_3\text{sgn}(e_{31})|e_{31}|^\mu) \\
&\quad - k_4e_{44}^2 - h_4|e_{44}|^{\mu+1} - k_5e_{55}^2 - h_5|e_{55}|^{\mu+1} + \tilde{a}\dot{\tilde{a}} + \tilde{b}\dot{\tilde{b}}, \\
&= -k_1e_{13}^2 - k_2e_{22}^2 - k_3e_{31}^2 - k_4e_{44}^2 - k_5e_{55}^2 \\
&\quad + \tilde{a}(e_{13}(y_2 - y_1) - e_{31}(x_2 - x_1)) \\
&\quad - \tilde{b}(e_{13}x_3 - e_{31}y_3) + \tilde{a}\dot{\tilde{a}} + \tilde{b}\dot{\tilde{b}} - h_1|e_{13}|^{\mu+1} \\
&\quad - h_2|e_{22}|^{\mu+1} - h_3|e_{31}|^{\mu+1} - h_4|e_{44}|^{\mu+1} - h_5|e_{55}|^{\mu+1}, \\
&= -k_1e_{13}^2 - k_2e_{22}^2 - k_3e_{31}^2 - k_4e_{44}^2 - k_5e_{55}^2 \\
&\quad + \tilde{a}(e_{13}(y_2 - y_1) - e_{31}(x_2 - x_1) - \dot{\tilde{a}}) - \tilde{b}(e_{13}x_3 - e_{31}y_3 - \dot{\tilde{b}}) \\
&\quad - h_1|e_{13}|^{\mu+1} - h_2|e_{22}|^{\mu+1} - h_3|e_{31}|^{\mu+1} - h_4|e_{44}|^{\mu+1} - h_5|e_{55}|^{\mu+1}. \tag{28}
\end{aligned}$$

Substituting (23) into (26) gains

$$\begin{aligned}
\dot{V} &= e_{13}\dot{e}_{13} + e_{22}\dot{e}_{22} + e_{31}\dot{e}_{31} + e_{44}\dot{e}_{44} + e_{55}\dot{e}_{55} + \tilde{a}\dot{\tilde{a}} + \tilde{b}\dot{\tilde{b}}, \\
&= -k_1e_{13}^2 - k_2e_{22}^2 - k_3e_{31}^2 - k_4e_{44}^2 - k_5e_{55}^2 - h_1|e_{13}|^{\mu+1} \\
&\quad - h_2|e_{22}|^{\mu+1} - h_3|e_{31}|^{\mu+1} - h_4|e_{44}|^{\mu+1} - h_5|e_{55}|^{\mu+1} \leq -K\|e\|^2 \leq 0, \tag{29}
\end{aligned}$$

where $K = \min\{k_1, k_2, k_3, k_4, k_5\} |k_i| \in \mathbb{R}^+, i = 1, 2, \dots, 5$. Thus, it is obvious that \dot{V} is negative definite. According to the Lyapunov stability theory, $\lim_{t \rightarrow \infty} \|e(t)\| = 0$ which means that

the adaptive multi-switching synchronization of the master-slave hyperchaotic system is implemented. The analysis of the linear dependence condition for the parameter identification is follows as

$$\begin{aligned}
e_{13} &= 0|_{t \rightarrow \infty}, e_{22} = 0|_{t \rightarrow \infty}, e_{31} = 0|_{t \rightarrow \infty}, e_{44} = 0|_{t \rightarrow \infty}, \\
e_{55} &= 0|_{t \rightarrow \infty}, \tag{30}
\end{aligned}$$

$$\begin{aligned}
\dot{e}_{13} &= \tilde{a}(t)(y_2 - y_1) + \tilde{b}(t)x_3 - k_1e_{13} - h_1\text{sgn}(e_{13})|e_{13}|^\mu = 0, \\
\dot{e}_{22} &= -k_2e_{22} - h_2\text{sgn}(e_{22})|e_{22}|^\mu = 0, \\
\dot{e}_{31} &= -\tilde{b}(t)y_3 - \tilde{a}(t)(x_2 - x_1) - k_2e_{31} - h_3\text{sgn}(e_{31})|e_{31}|^\mu = 0, \\
\dot{e}_{44} &= -k_4e_{44} - h_4\text{sgn}(e_{44})|e_{44}|^\mu = 0, \\
\dot{e}_{55} &= -k_5e_{55} - h_5\text{sgn}(e_{55})|e_{55}|^\mu = 0. \tag{31}
\end{aligned}$$

For $y_2 \neq y_1, x_3 \neq 0, y_3 \neq 0, x_2 \neq x_1$ according to the linear independence conditions, $\tilde{a}(t) = 0, \tilde{b}(t) = 0$ hence $\hat{b}(t) = b$ and $\hat{a}(t) = a$, the parameters can be identified to the true values.

Remark 5. Since (24) contains a discontinuous sign function that causes an unwanted chattering. To avoid thrashing, replace sign functions with continuous *tanh* function to eliminate discontinuities. Therefore, the control law (24) is amended as follows:

$$\begin{aligned}
U_1 &= -\tilde{a}(y_2 - y_1) - 4y_2y_3 + ky_1(0.1 + 0.03y_5^2) - \tilde{b}x_3 \\
&\quad + x_1x_2 - x_1x_5 - x_2x_4 - k_1e_{13} - h_1 \tanh(e_{13})|e_{13}|^\mu, \\
U_2 &= y_1 - x_1 - 16e_{22} - e_{24} + y_1y_3 - x_1x_3 - k_2e_{22} - h_2 \tanh(e_{22})|e_{22}|^\mu, \\
U_3 &= \tilde{b}y_3 - y_1y_2 + y_1y_5 + y_2y_4 + \tilde{a}(x_2 - x_1) + 4x_2x_3 \\
&\quad + kx_1(0.1 + 0.03x_5^2) - k_3e_{31} - h_3 \tanh(e_{31})|e_{31}|^\mu, \\
U_4 &= 10e_{22} - 0.15y_1y_3 + 0.15x_1x_3 + 0.3y_3y_5 - 0.3x_3x_5 \\
&\quad - k_4e_{44} - h_4 \tanh(e_{44})|e_{44}|^\mu, \\
U_5 &= y_1 - x_1 - k_5e_{25} - h_5 \tanh(e_{55})|e_{55}|^\mu. \tag{32}
\end{aligned}$$

Corollary 2. For switch-2, the dynamic equation error is represented as

$$\begin{aligned}
\dot{e}_{12} &= a(y_2 - y_1) + 4y_2y_3 - ky_1(0.1 + 0.03y_5^2) + x_1 \\
&\quad - 16x_2 + x_1x_3 - x_4 + U_1, \\
\dot{e}_{23} &= -y_1 + 16y_2 - y_1y_3 + y_4 + bx_3 - x_1x_2 + x_1x_5 + x_2x_4 + U_2, \\
\dot{e}_{34} &= -by_3 + y_1y_2 - y_1y_5 - y_2y_4 + 10x_2 - 0.15x_1x_3 + gx_3x_5 + U_3, \\
\dot{e}_{45} &= -10y_2 + 0.15y_1y_3 - gy_3y_5 + x_1 + U_4, \\
\dot{e}_{51} &= -y_1 - a(x_2 - x_1) - 4x_2x_3 + kx_1(0.1 + 0.03x_5^2) + U_5. \tag{33}
\end{aligned}$$

Theorem 3. The control laws of (32) are chosen as follows:

$$\begin{aligned}
U_1 &= -\tilde{a}(y_2 - y_1) - 4y_2y_3 + ky_1(0.1 + 0.03y_5^2) - x_1 + 16x_2 \\
&\quad - x_1x_3 + x_4 - k_1e_{12} - h_1 \tanh(e_{12})|e_{12}|^\mu, \\
U_2 &= y_1 - 16y_2 + y_1y_3 - y_4 + \tilde{b}x_3 + x_1x_2 - x_1x_5 - x_2x_4 - k_2e_{23} \\
&\quad - h_2 \tanh(e_{23})|e_{23}|^\mu, \\
U_3 &= \tilde{b}y_3 - y_1y_2 + y_1y_5 + y_2y_4 - 10x_2 + 0.15x_1x_3 - gx_3x_5 \\
&\quad - k_3e_{34} - h_3 \tanh(e_{34})|e_{34}|^\mu, \\
U_4 &= 10y_2 - 0.15y_1y_3 + gy_3y_5 - x_1 - k_4e_{45} - h_4 \tanh(e_{45})|e_{45}|^\mu, \\
U_5 &= y_1 + \tilde{a}(x_2 - x_1) + 4x_2x_3 - kx_1(0.1 + 0.03x_5^2) \\
&\quad - k_5e_{51} - h_5 \tanh(e_{51})|e_{51}|^\mu, \tag{34}
\end{aligned}$$

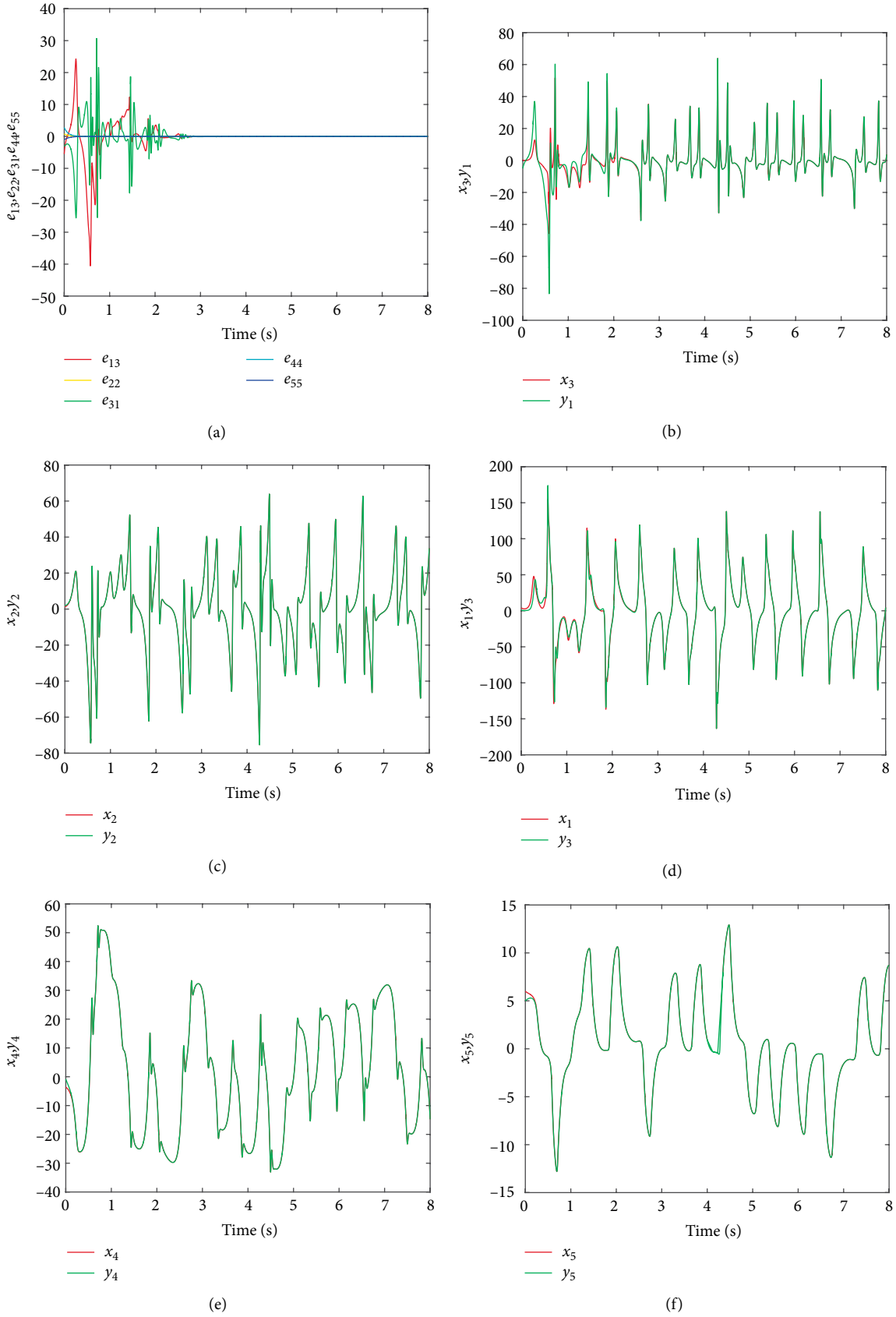


FIGURE 5: Switch-1: (a) the synchronization error, (b) the error of $x_3 - y_1$, (c) the error of $x_2 - y_2$, (d) the error of $x_1 - y_3$, (e) the error of $x_4 - y_4$, (f) the error of $x_5 - y_5$.

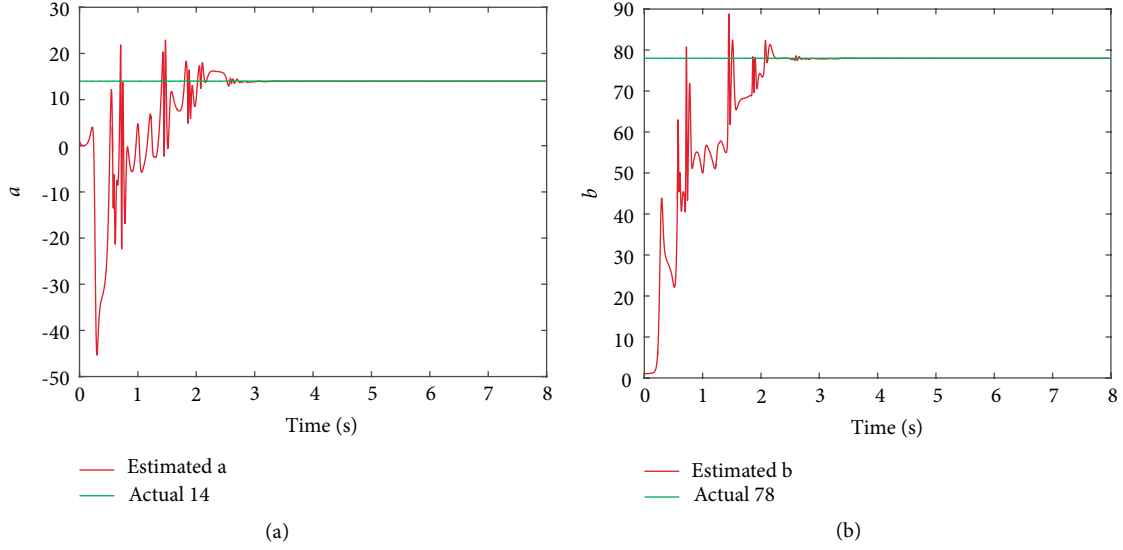


FIGURE 6: Switch-1: (a) unknown term a , (b) unknown term b .

where k_i ($i = 1 \dots 5$) and h_i ($i = 1 \dots 5$) are the positive constant, $0 < \mu < 1$, $\hat{a}(t)$, and $\hat{b}(t)$ are the estimated value of the unknown parameters a and b respectively.

Meanwhile, parameters update laws of the unknown parameters are selected as

$$\begin{aligned} \dot{\hat{a}}(t) &= e_{12}(y_2 - y_1) - e_{51}(x_2 - x_1), \\ \dot{\hat{b}}(t) &= e_{23}x_3 - e_{34}y_3. \end{aligned} \quad (35)$$

Remark 6. The proof of switch-2 is the same as that of switch-1, and finally $e(t) \rightarrow 0$, the adaptive multi-switching synchronization for the master-slave system is implemented.

3.3. Simulation Results. The initial values of (19) and (20) are taken as $x(0) = [4, 1.2, 0.5, -3.6, 6]^T$ and $y(0) = [-5, 2, 1, -0.8, 5]^T$ respectively. The parameters $K = k_i = 10$ ($i = 1 \dots 5$), $h_i = 2$ ($i = 1 \dots 5$), $\mu = 0.5$ are selected simultaneously.

Case 1. For switch-1, the synchronization of two 5D memristor hyperchaotic systems is implemented at 2.8 s in Figure 5. The unknown parameters a and b of the master-slave synchronization system are identified to their given values 14 and 78 respectively in Figure 6.

Case 2. For switch-2, Figure 7 demonstrates the synchronization of two 5D memristor hyperchaotic systems, the dynamic error of the system can reach to zero at 1.4 s. Figure 8 indicates that the uncertain parameters a , b can arrive at 14, 78 respectively when $a = 14$ and $b = 78$.

Remark 7. The above description illustrates that the synchronization of two 5D memristor hyperchaotic systems with unknown parameters is achieved by the adaptive control in each switching form, the uncertain parameters can converge to their given values simultaneously. For multi-switching synchronization can offer various combinations of the dynamics errors, which is very difficult to get or modify useful information for intruders, the adaptive multi-switching

synchronization strategy is suitable for applying in secure communication.

4. Applications in Secure Communication

Due to the importance of information, information confidentiality is particularly important in secure communication. The essence of secure communication is to encrypt the transmitted information in some way. The concealment, unpredictability, high complexity, and easy implementation of hyperchaotic signals are especially suitable for secure communication. Hyperchaotic encryption is a dynamic encryption method, the encrypted information is difficult to decipher and has a high density in this way. In order to recover the original information, the decryption process is very important and can be realized by hyperchaotic synchronization scheme [36].

In the following sections, masking encryption and image encryption are discussed based on adaptive multi-switching synchronization of hyperchaotic systems with memristors.

4.1. Chaotic Masking Encryption and Decryption. The schematic diagram of hyperchaotic masking secure communication [37] is shown in Figure 9. The communication system is consisted by a transmitter which is a master system and a receiver which is a slave system, an output signal of the master system is acted as a masking signal to mask a message signal, the transmitted signal is a mixed output of a useful signal, and a hyperchaotic signal. In the receiver, the corresponding chaotic synchronization signal is employed to decrypt the mixed signals, ultimately, the original message signal is recovered.

In this work, the message signal is selected as a sinusoidal function which can be recovered in the receiver. The chaotic signal x is taken as the masking signal, then the encrypted signal $s_m(t) = s_i(t) + x$. In the receiver, the chaotic signal y is taken as the decrypt signal, the final output signal of the

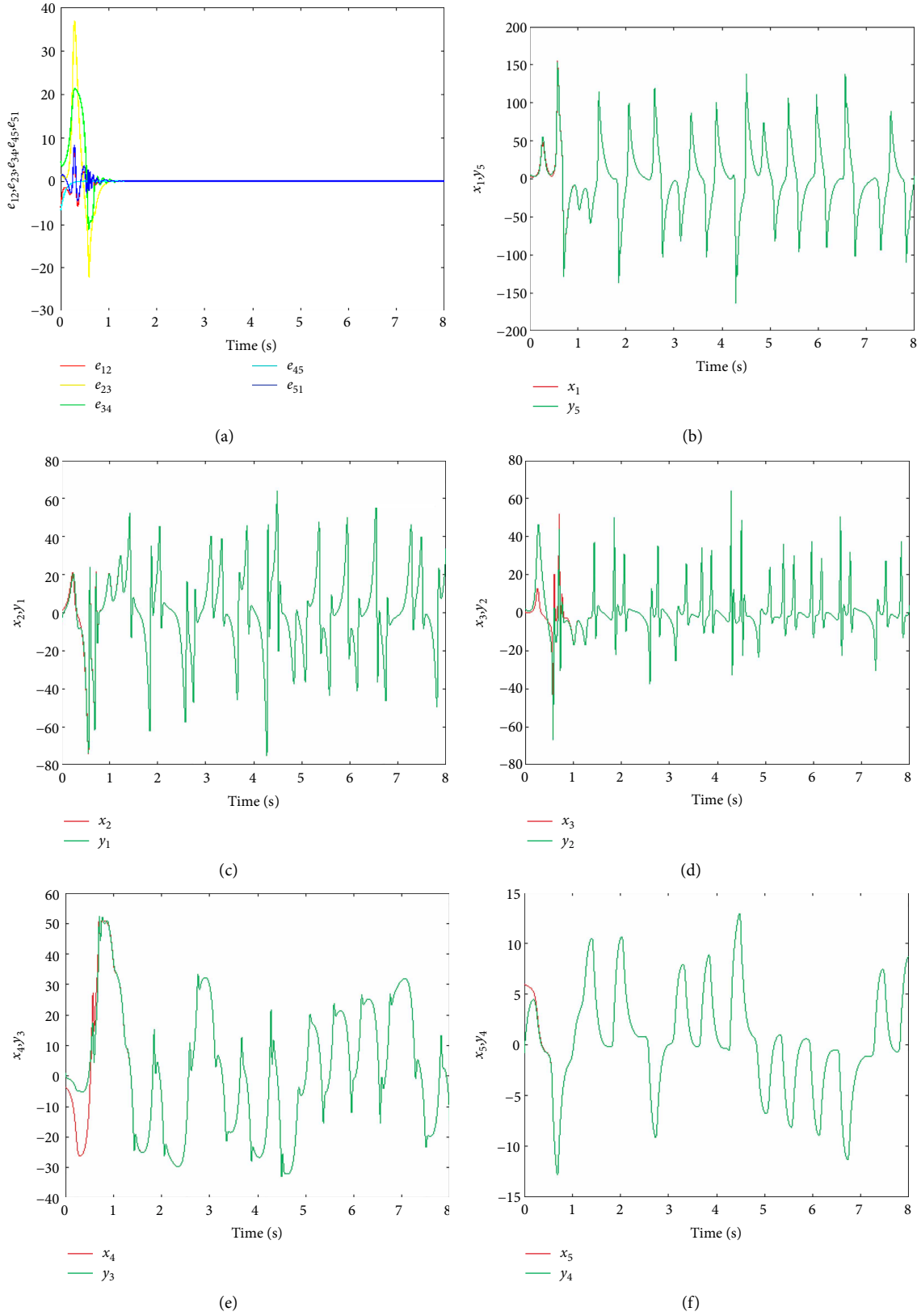


FIGURE 7: Switch-2: (a) the synchronization error, (b) the error of $x_1 - y_5$, (c) the error of $x_2 - y_1$, (d) the error of $x_3 - y_2$, (e) the error of $x_4 - y_3$, (f) the error of $x_5 - y_4$.

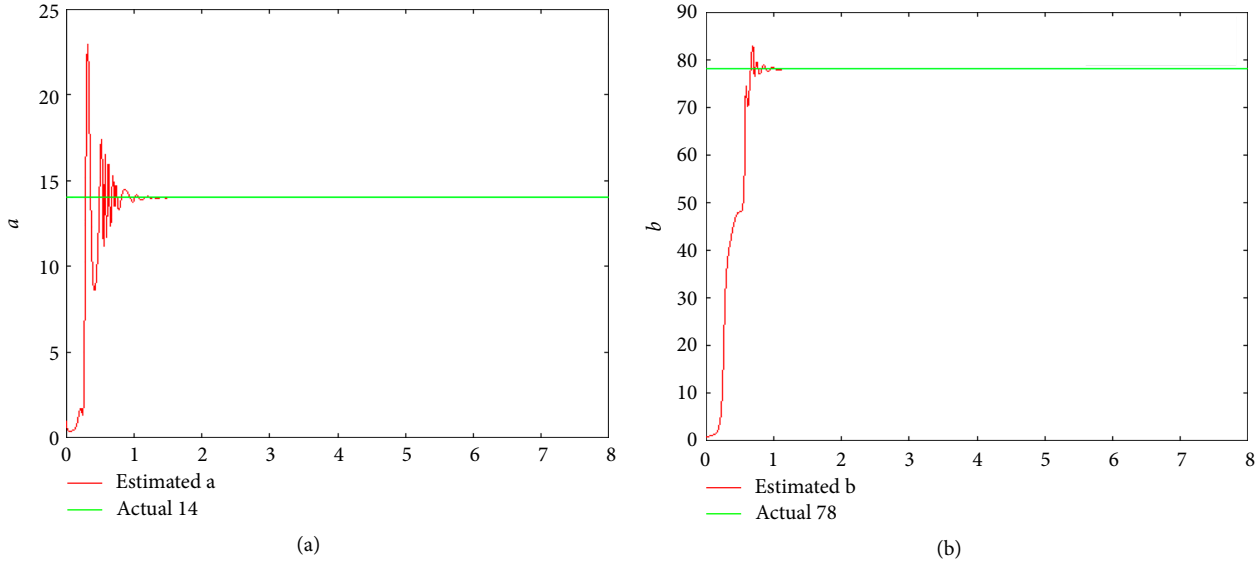
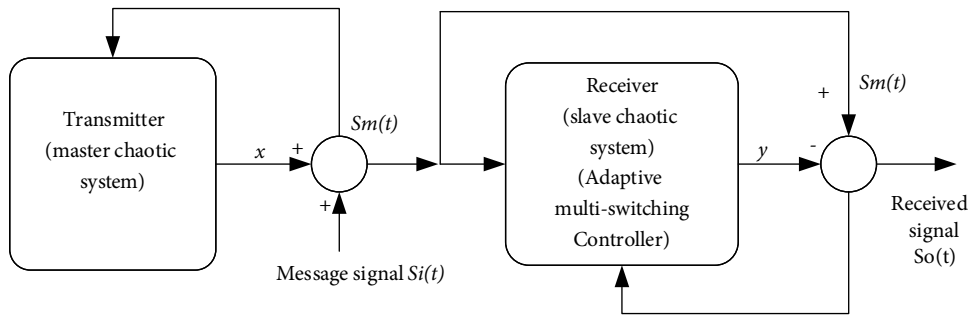
FIGURE 8: Switch-2: (a) unknown term a , (b) unknown term b .

FIGURE 9: The schematic diagram of hyperchaotic masking secure communication.

receiver $s_o(t)$ can be calculated by $s_o(t) = s_m(t) - y$. When system (19) and (20) reach the adaptive synchronization, then $y - x \rightarrow 0$ and $s_o = s_p$, the numerical simulation results are demonstrated in Figures 10 and 11.

4.2. Image Encryption and Decryption. In 1997, Fridrich composited chaos theory and image encryption to propose a chaotic image encryption method for the first time [38]. The potential application value of high order hyperchaotic system in image processing has been deeply studied, because it has more complex dynamics, more positive Lyapunov exponents, larger Kolmogorov entropy, and more sensitive to initial values. This subsection verifies the effectiveness of image encryption algorithm about the adaptive multi-switching hyperchaotic synchronization with memristors. The overall structure of image encryption and decryption process is shown in Figure 12.

4.2.1. The Process of Image Encryption. The detailed steps of the image encryption are as follows:

- (a) Read the 3-color data matrices R , G , B of the original image with $256 \times 256 \times 3$ pixels.

- (b) Gain the 5-dimensional different chaotic sequences from $x = [x_1, x_2, x_3, x_4, x_5]^T$, then convert each chaotic sequence of x_1, x_2, x_3 into a two-dimensional sequence of rows and columns, and confuse them by ascending order or descending order, finally get the cipher text matrices R' , G' , B' of the original image.

- (c) Replace the pixel values by chaotic sequence x_4 . First take two parameters c and d as follows

$$\begin{cases} c_{ij} = \text{abs}(x_4(i, j) - \text{round}(x_4(i, j))) \times 10^2, \\ d_{ij} = \text{abs}(x_4(i, j) - \text{round}(x_4(i, j))) \times 10^3, \end{cases} \quad (36)$$

- (d) The matrix of intermediate variables A is assumed as follows

$$A = (c_{ij} \times i + d_{ij} \times j) \bmod L, \quad (37)$$

where i and j are row and column position of the pixel respectively, L Gray level of the pixel.

Complete the XOR operation between R' , G' , B' , and A .

$$\begin{cases} R'' = R' \oplus A, \\ G'' = G' \oplus A, \\ B'' = B' \oplus A, \end{cases} \quad (38)$$

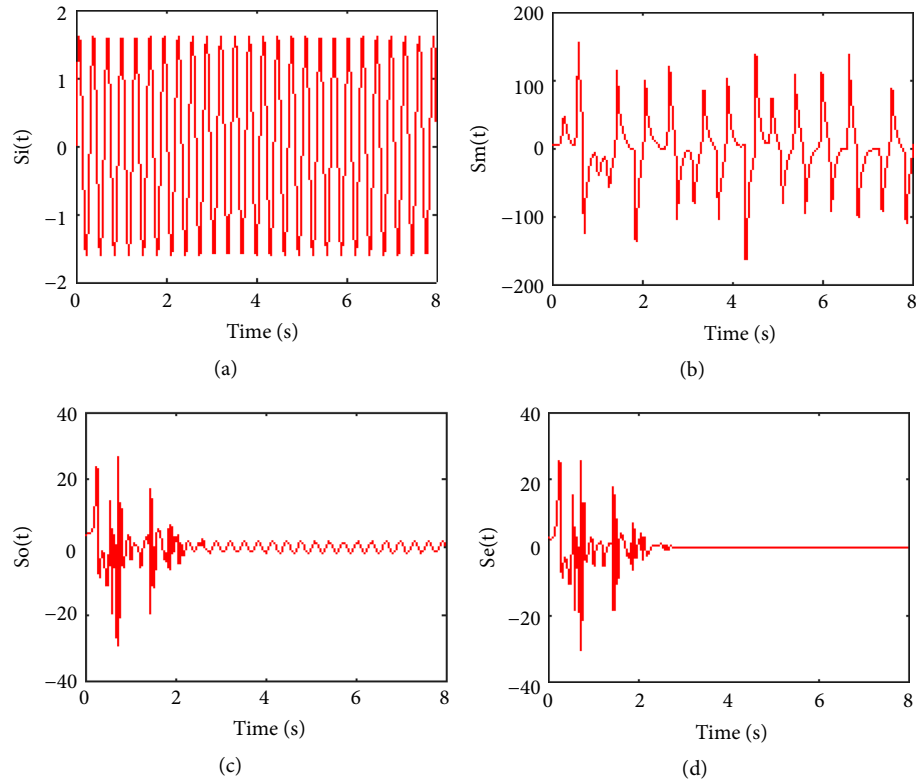


FIGURE 10: Switch-1 (a) the message signal $s_i(t) = 1.6\sin(20t)$, (b) the encrypted signal $s_m(t)$, (c) the recovered signal $s_0(t)$, and (d) the error signal $s_e(t)$.

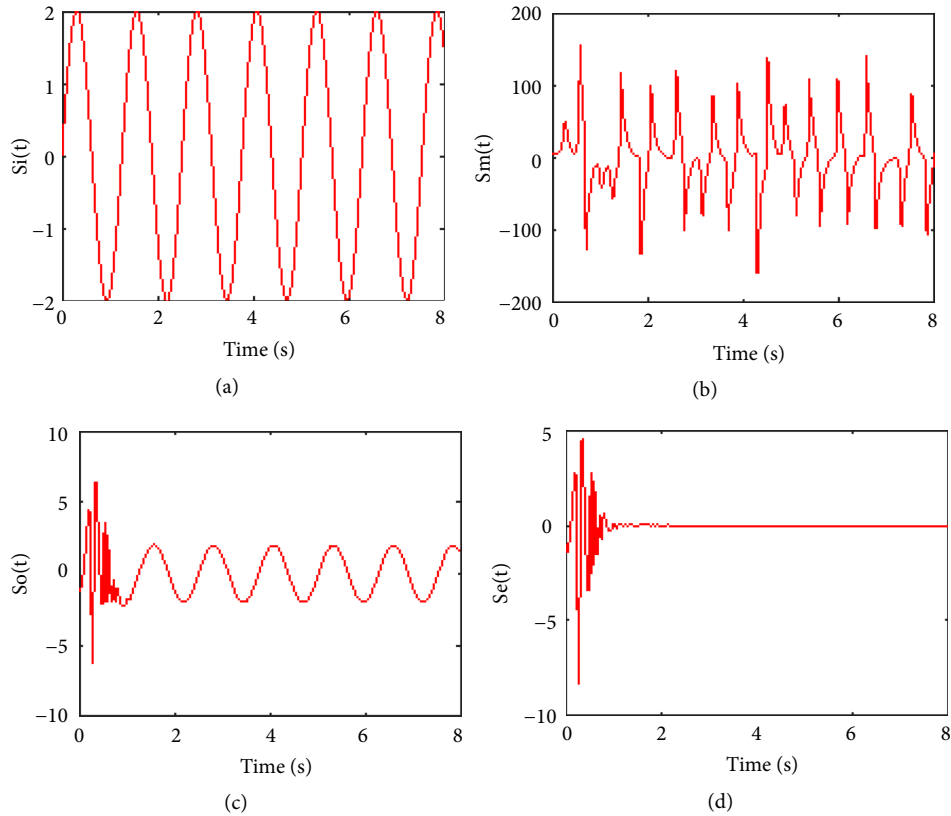


FIGURE 11: For switch-2 (a) The message signal $s_i(t) = 2\sin(5t)$, (b) the encrypted signal $s_m(t)$, (c) the recovered signal $s_0(t)$, and (d) the error signal $s_e(t)$.

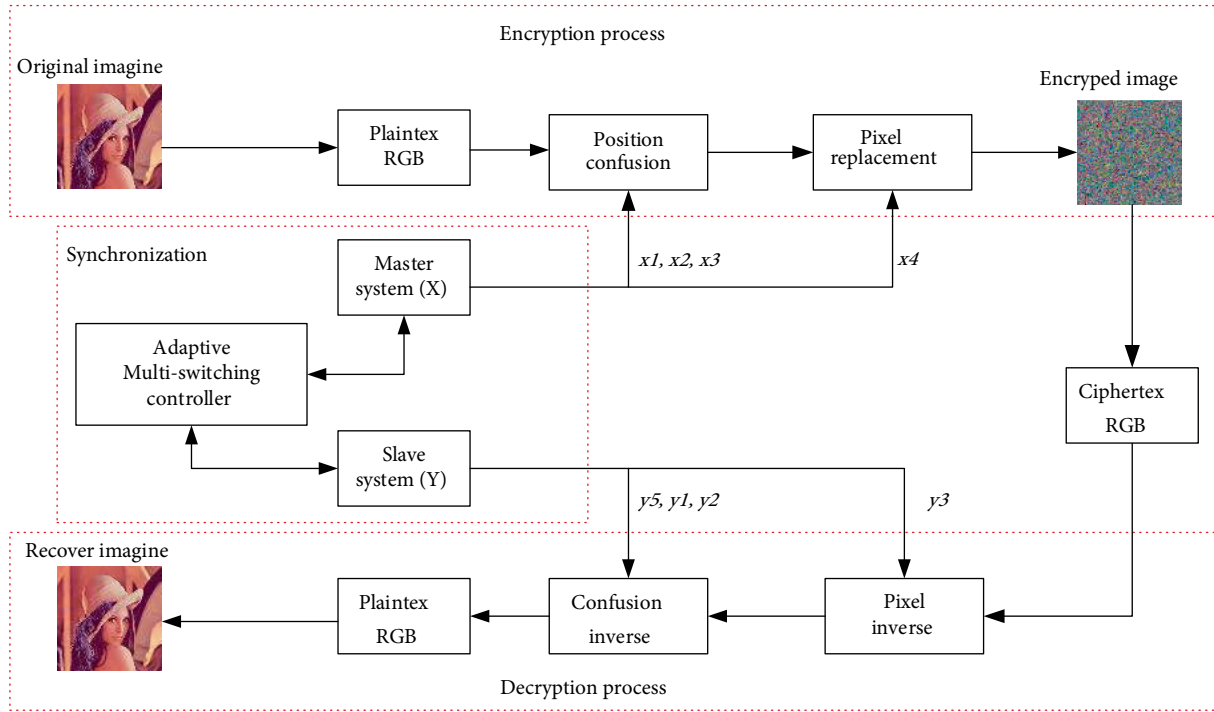


FIGURE 12: The overall structure of image encryption and decryption.

TABLE 1: XOR operation.

R'	G'	B'	A	$R'' = R' \oplus A$	$G'' = G' \oplus A$	$B'' = B' \oplus A$
0	0	0	0	1	1	1
0	0	0	1	0	0	0
1	1	1	0	0	0	0
1	1	1	1	1	1	1

TABLE 2: XOR operation.

R'''	G'''	B'''	A'	$R'' = R''' \oplus A'$	$G'' = G''' \oplus A'$	$B'' = B''' \oplus A'$
0	0	0	0	1	1	1
0	0	0	1	0	0	0
1	1	1	0	0	0	0
1	1	1	1	1	1	1

where R'' , G'' and B'' are 3-color matrices of the encrypted image.

XOR operation results are shown in Table 1.

- (e) Convert the binary sequences into the 2-dimension matrices R''' , G''' , and B''' .
- (f) Finally restructure the 2-dimension matrices R''' , G''' , and B''' , then obtain an encrypted image.

4.2.2. The Process of Image Decryption. Image encryption specific steps are as follows:

- (a) Read the 3-color cipher text matrices R''' , G''' , and B''' of the encrypted image with $256 \times 256 \times 3$ pixels.
- (b) Gain the 5-dimentional different chaotic sequences from $y = [y_1, y_2, y_3, y_4, y_5]^T$, then convert each chaotic sequence of y_3 into a two-dimensional sequence of rows and columns.
- (c) Recover the pixel values by chaotic sequence y_3 . First take two parameters c'_{ij} and d'_{ij} as follows

$$\begin{cases} c'_{ij} = \text{abs}(y_3(i, j) - \text{round}(y_3(i, j))) \times 10^2, \\ d'_{ij} = \text{abs}(y_3(i, j) - \text{round}(y_3(i, j))) \times 10^3, \end{cases} \quad (39)$$

- (d) The matrix of intermediate variables A' is assumed as follows

$$A' = (c'_{ij} \times i + d'_{ij} \times j) \bmod L, \quad (40)$$

where i and j are row and column position of the pixel respectively, L Gray level of the pixel.

Accomplish the XOR operation between R'' , G'' , and B'' and A' .

$$\begin{cases} R'' = R''' \oplus A', \\ G'' = G''' \oplus A', \\ B'' = B''' \oplus A', \end{cases} \quad (41)$$

where R'' , G'' , and B'' are 3-color matrices of the decrypted image.

XOR operation results are shown in Table 2.

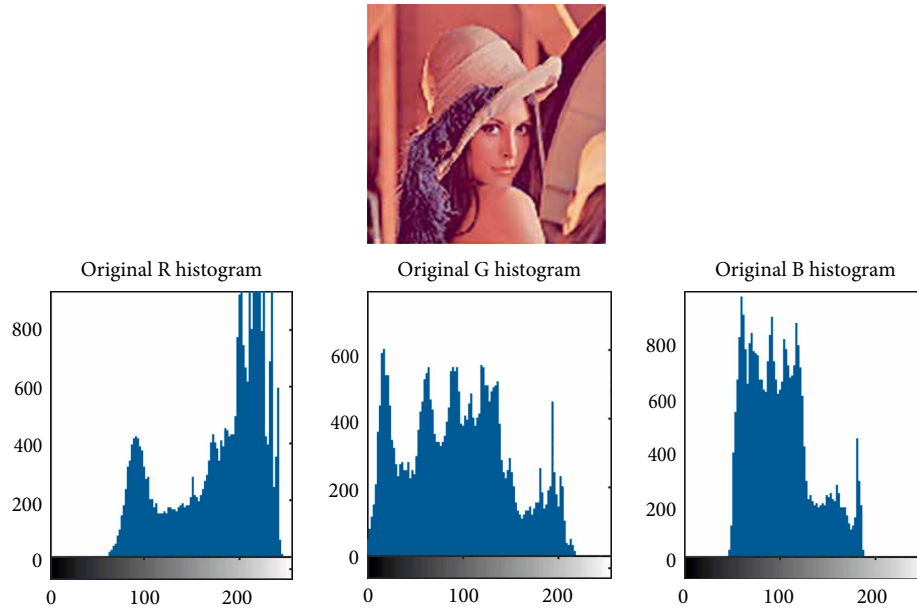


FIGURE 13: The original image with its histograms of color image (reproduced from Jing Luo et al. (2019), (under the Creative Commons Attribution License/public domain)).

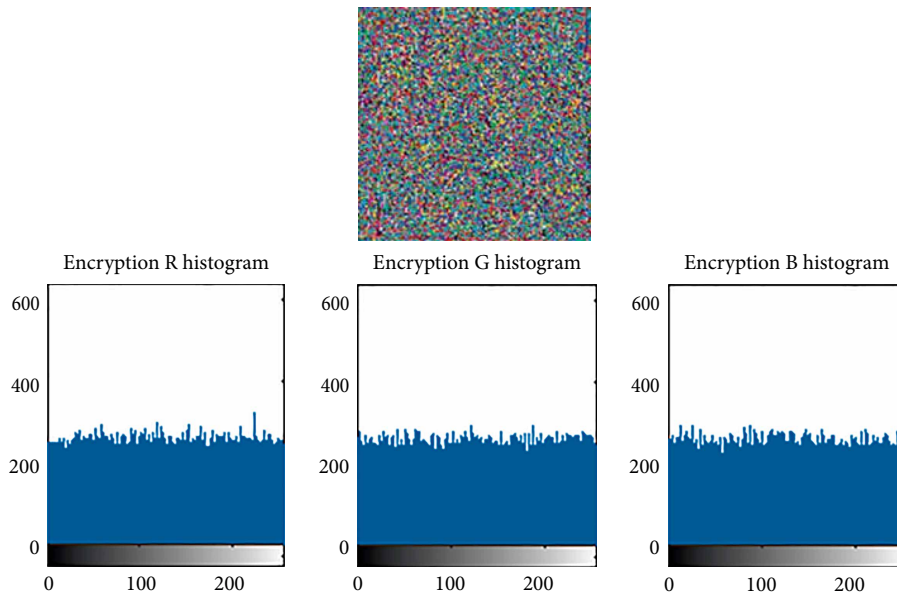


FIGURE 14: The encrypted image with its histograms (reproduced from Jing Luo et al. (2019), (under the Creative Commons Attribution License/public domain)).

- (e) Convert the binary sequences into the 2-dimension matrices R' , G' , and B' .
- (f) Sort the matrices of y_5, y_1, y_2 , in descending order and ascending order as column confusion indexes to recover the cipher text image from $R', G',$ and B' , then gain R, G, B plaintext matrix.
- (g) Finally restructure the 2-dimension matrices R, G, B , then obtain an decrypted image.

4.3. *Analysis of the Image.* Image histogram analysis and correlation coefficient analysis are two important statistical

methods during the process of image encryption and decryption. By image histogram analysis, Figures 13–15 indicated the effects and performance of image encryption and decryption. Among them, Figure 13 demonstrates the histograms of the original image with uneven distribution, but Figure 14 shows uniform distribution of the encrypted image. After recovering the encrypted image, Figure 15 indicates that the decrypted image and its histograms is the same with Figure 13.

For the pixels are concentrated in original image with higher correlation distribution between adjacent pixels, in order to resist external attack, the correlation of adjacent pixels are reduced by image encryption strategy. 2000 pairs of

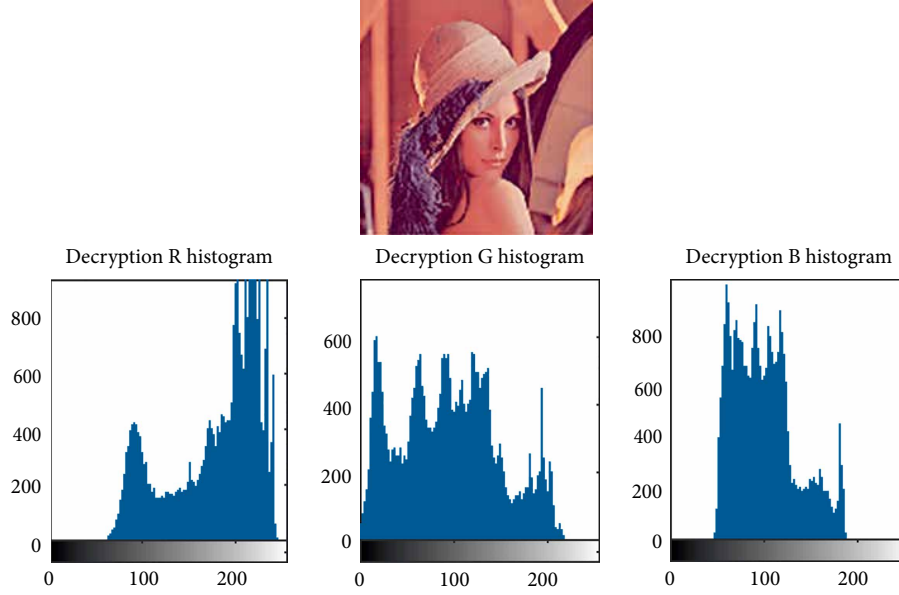


FIGURE 15: The decrypted image with its histograms (reproduced from Jing Luo et al. (2019), (under the Creative Commons Attribution License/public domain)).

TABLE 3: Correlation coefficient results.

Correlation	Original image	Encryption image	Original image [39]	Encryption image [39]
Horizontal	0.9748	0.0230	0.9856	-0.0318
Vertical	0.9511	0.0226	0.9682	0.0965
Diagonal	0.9105	0.0105	0.9669	0.0362

adjacent pixels are chosen from the original image and encrypted image respectively [36], the correlation coefficient can be calculated by (42). An interesting phenomenon is that the correlation coefficient of the original image in Table 3 is approximate to one. However, that of encrypted image is nearly equal to zero. Figures 16(b), 16(d), and 16(f) indicate that adjacent pixels of encrypted image are evenly distributed, Figures 16(a), 16(c), and 16(e) show that those of original image are higher correlation distribution.

$$\begin{aligned}
 E(v) &= \frac{1}{M} \sum_{i=1}^M w_i, \\
 D(v) &= \frac{1}{M} \sum_{i=1}^M (v_i - E(v))^2, \\
 \text{cov}(v, w) &= \frac{1}{M} \sum_{i=1}^M (a_i - E(v))(v_i - E(v)), \\
 R_{vw} &= \frac{\text{cov}(v, w)}{\sqrt{D(v)} \times \sqrt{D(w)}},
 \end{aligned} \tag{42}$$

where v and w are grey values between adjacent pixels, $E(v)$ is mathematical expectation, $\text{cov}(v, w)$ is covariance, $D(v)$ is variance.

Remark 8. Literature [31] only presented adaptive synchronization design and simulation without considering its application. Literature [21] realized signal masking encryption

by multi-switching chaos synchronization, not premeditated image encryption scheme. Compare with literature [39], Table 1 indicates the correlation coefficient in this section is lower. In this section, the adaptive multi-switching memristor-based hyperchaotic system is not only applied to signal masking encryption but also image encryption, which improves the security in signal transmission and resists external attacks.

Remark 9. Image encryption and decryption process in other switches is the same to one in switch-1.

5. Conclusions

Researches of hyperchaotic synchronous with memristor have attracted great attentions in theory and engineering practice. According to the Lyapunov stability theory, this paper presents an adaptive multi-switching synchronization strategy for high-order hyperchaotic systems with uncertain parameters. The numerical simulation results illustrate that the dynamic errors of the systems can quickly converge to zero and the unknown parameters can also be identified to the true values, which validates the feasibility and effectiveness of the proposed method. At last, adaptive multi-switching synchronization for high-order hyperchaotic systems is applied to image encryption, which is more secure than conventional encryption methods.

Unknown parameters, external disturbances, and time-delay are unavoidable in engineering practice, finite-time robust multi-switching synchronization control for memristor hyperchaotic systems with unknown parameters, external disturbances, and time-delay is a challenging study. In the future, our research will focus on designing the complex circuit of hyperchaotic system with memristors to accomplish the multi-switching synchronization and its application in image encryption.

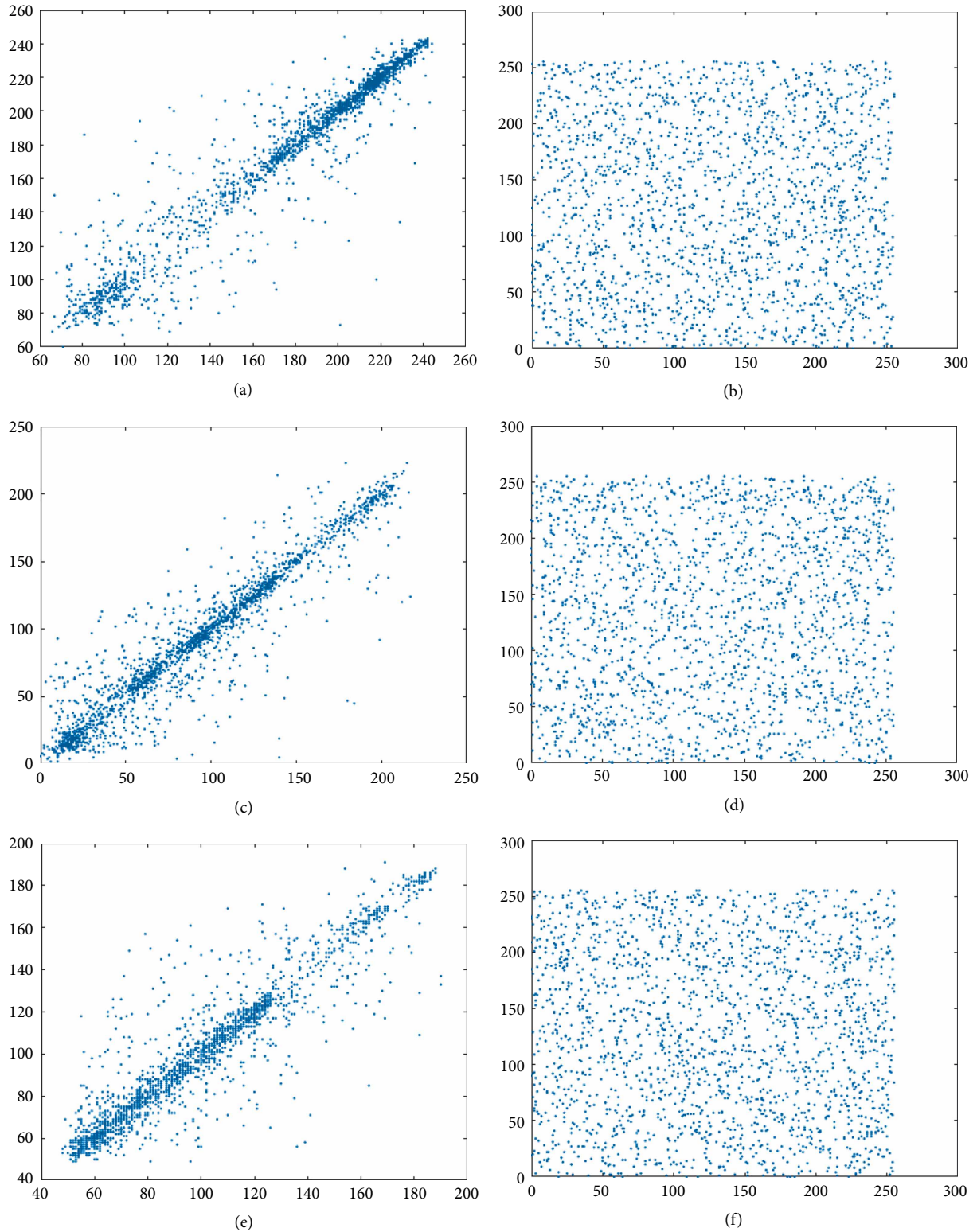


FIGURE 16: Horizontal correlation of original image. (a, c, e) are the correlation of original image in RG , and B , respectively; (b, d, f) are the correlation of encrypted image in RG , and B , respectively.

Data Availability

The data used to support the findings of this study are available from the corresponding author upon request.

Conflicts of Interest

The authors declare that there are no conflicts of interest regarding the publication of this paper.

Acknowledgments

This work was supported by National Natural Science Foundation of China under Grant Nos. 61673190/F03010, self-determined research funds of CCNU from the colleges' basic research and operation of MOE under Grant No. CCNU18TS042.

References

- [1] L. M. Pecora and T. L. Carroll, "Synchronization in chaotic systems," *Controlling Chaos*, vol. 6, Elsevierpp. 142–145, 1996.
- [2] J. Sun, Y. Shen, Q. Yin, and C. Xu, "Compound synchronization of four memristor chaotic oscillator systems and secure communication," *Chaos*, vol. 23, pp. 821–812, 2013.
- [3] B. Lei and I. Y. Soon, "A multipurpose audio watermarking algorithm with synchronization and encryption," *Journal of Zhejiang University Science C Computers & Electronics*, vol. 13, no. 1, pp. 11–19, 2012.
- [4] L. Wang, T. Dong, and M.-F. Ge, "Finite-time synchronization of memristor chaotic systems and its application in image encryption," *Applied Mathematics and Computation*, vol. 347, pp. 293–305, 2019.
- [5] M. G. Rosenblum, A. S. Pikovsky, and J. Kurths, "Synchronization approach to analysis of biological systems," *Fluctuation & Noise Letters*, vol. 4, no. 1, pp. L53–L62, 2004.
- [6] X. Xi, S. Mobayen, H. Ren, and S. Jafari, "Robust finite-time synchronization of a class of chaotic systems via adaptive global sliding mode control," *Journal of Vibration and Control*, vol. 24, pp. 3842–3854, 2017.
- [7] J. Sun, W. Yan, Y. Wang, and S. Yi, "Finite-time synchronization between two complex-variable chaotic systems with unknown parameters via nonsingular terminal sliding mode control," *Nonlinear Dynamics*, vol. 85, no. 2, pp. 1105–1117, 2016.
- [8] F. Min, C. Li, L. Zhang, and C. Li, "Initial value-related dynamical analysis of the memristor-based system with reduced dimensions and its chaotic synchronization via adaptive sliding mode control method," *Chinese Journal of Physics*, vol. 58, pp. 117–131, 2019.
- [9] C. Li, X. Liao, and X. Zhang, "Impulsive synchronization of chaotic systems," *Chaos An Interdisciplinary Journal of Nonlinear Science*, vol. 15, no. 2, pp. 3031–382, 2006.
- [10] S. Wen, Z. Zeng, T. Huang, and Y. Chen, "Fuzzy modeling and synchronization of different memristor-based chaotic circuits," *Physics Letters A*, vol. 377, no. 34–36, pp. 2016–2021, 2013.
- [11] S. Wen, S. Xiao, Y. Yang, Z. Yan, Z. Zeng, and T. Huang, "Adjusting learning rate of memristor-based multilayer neural networks via fuzzy method," *IEEE Transactions on Computer-Aided Design of Integrated Circuits and Systems*, vol. 38, no. 6, pp. 1084–1094, 2019.
- [12] A. Khan, D. Khattar, and N. Prajapati, "Adaptive multi switching combination synchronization of chaotic systems with unknown parameters," *International Journal of Dynamics and Control*, vol. 6, no. 2, pp. 621–629, 2018.
- [13] S. Wen, Z. Zeng, and T. Huang, "Adaptive synchronization of memristor-based chua's circuits," *Physics Letters A*, vol. 376, pp. 2775–2780, 2012.
- [14] C. Li, F. Min, and C. Li, "Multiple coexisting attractors of the serial-parallel memristor-based chaotic system and its adaptive generalized synchronization," *Nonlinear Dynamics*, vol. 94, no. 4, pp. 2785–2806, 2018.
- [15] U. Parlitz, "Estimating model parameters from time series by autosynchronization," *Physical Review Letters*, vol. 76, no. 8, pp. 1232–1235, 1996.
- [16] H. Adloo and M. Roopaei, "Review article on adaptive synchronization of chaotic systems with unknown parameters," *Nonlinear Dynamics*, vol. 65, no. 1–2, pp. 141–159, 2011.
- [17] W. Yu, G. Chen, J. Cao, J. Lu, and U. Parlitz, "Parameter identification of dynamical systems from time series," *Physical Review E Statistical, Nonlinear, biological, and Soft Matter Physics*, vol. 75, no. 6, p. 067201, 2007.
- [18] Z. Sun, W. Zhu, G. Si, Y. Ge, and Y. Zhang, "Adaptive synchronization design for uncertain chaotic systems in the presence of unknown system parameters: a revisit," *Nonlinear Dynamics*, vol. 72, no. 4, pp. 729–749, 2013.
- [19] A. Uçar, K. E. Lonngren, and E. W. Bai, "Multi-switching synchronization of chaotic systems with active controllers," *Chaos, Solitons & Fractals*, vol. 38, no. 1, pp. 254–262, 2008.
- [20] X.-Y. Wang and P. Sun, "Multi-switching synchronization of chaotic system with adaptive controllers and unknown parameters," *Nonlinear Dynamics*, vol. 63, no. 4, pp. 599–609, 2011.
- [21] I. Ahmad, M. Shafiq, and M. M. Al-Sawalha, "Globally exponential multi switching-combination synchronization control of chaotic systems for secure communications," *Chinese Journal of Physics*, vol. 56, no. 3, pp. 974–987, 2018.
- [22] Y. Wen, X. Chen, J. Qiu, Z. Li, and C. Yang, "Multi-switching network transmission synchronization behavior for three uncertain chaotic systems with unknown parameters," in *Conference of the IEEE Industrial Electronics Society, IEEEBeijing, China, 2017*.
- [23] A. Khan, M. Budhreja, and A. Ibraheem, "Multi-switching synchronization of four non-identical hyperchaotic systems," *International Journal of Applied & Computational Mathematics*, vol. 4, no. 2, p. 71, 2018.
- [24] N. Prajapati, A. Khan, and D. Khattar, "On multi switching compound synchronization of non identical chaotic systems," *Chinese Journal of Physics*, vol. 56, no. 4, pp. 1656–1666, 2018.
- [25] L. O. Chua, "Memristor-the missing circuit element," *IEEE Trans Circuit Theory*, vol. 18, no. 5, pp. 507–519, 1971.
- [26] D. B. Strukov, G. S. Snider, D. R. Stewart, and R. S. Williams, "The missing memristor found," *Nature*, vol. 453, no. 7191, pp. 80–83, 2008.
- [27] M. Itoh and L. O. Chua, "Memristor oscillators," *International Journal of Bifurcation & Chaos*, vol. 18, no. 11, pp. 3183–3206, 2008.
- [28] S. Wen, R. Hu, Y. Yang, T. Huang, Z. Zeng, and Y.-D. Song, "Memristor-based echo state network with online least mean square," *IEEE Transactions on Systems, Man, and Cybernetics: Systems*, pp. 1–10, 2018.
- [29] S. Wen, X. Xie, Z. Yan, T. Huang, and Z. Zeng, "General memristor with applications in multilayer neural networks," *Neural Networks*, vol. 103, pp. 142–149, 2018.
- [30] J. Sun, X. Zhao, J. Fang, and Y. Wang, "Autonomous memristor chaotic systems of infinite chaotic attractors and circuitry realization," *Nonlinear Dynamics*, vol. 94, no. 4, pp. 2879–2887, 2018.
- [31] R. Wang, M. Li, Z. Gao, and H. Sun, "A new memristor-based 5D chaotic system and circuit implementation," *Complexity*, vol. 2018, Article ID 6069401, 12 pages, 2018.

- [32] S. Wen, S. Xiao, and Y. Yang, "Passivity and passification of memristive neural networks with leakage term and time-varying delays," *Applied Mathematics and Computation*, vol. 361, pp. 294–310, 2019, In press.
- [33] J. Sun, S. Yi, Y. Quan, and C. Xu, "Compound synchronization of four memristor chaotic oscillator systems and secure communication," *Chaos: An Interdisciplinary Journal of Nonlinear Science*, vol. 23, no. 1, p. 013140, 2013.
- [34] C. Li, F. Min, Q. Jin, and H. Ma, "Extreme multistability analysis of memristor-based chaotic system and its application in image decryption," *AIP Advances*, vol. 7, no. 12, p. 125204, 2017.
- [35] J. Ma, Z. Chen, Z. Wang, and Q. Zhang, "A four-wing hyperchaotic attractor generated from a 4-D memristive system with a line equilibrium," *Nonlinear Dynamics*, vol. 81, pp. 1275–1288, 2015.
- [36] M. A. Murillo-Escobar, C. Cruz-Hernández, F. Abundiz-Pérez, R. M. López-Gutiérrez, and O. R. A. D. Campo, "A RGB image encryption algorithm based on total plain image characteristics and chaos," *Signal Processing*, vol. 109, pp. 119–131, 2015.
- [37] Y. Fei and C. Wang, "Secure communication based on a four-wing chaotic system subject to disturbance inputs," *Optik-International Journal for Light and Electron Optics*, vol. 125, no. 20, pp. 5920–5925, 2014.
- [38] J. Fridrich, "Symmetric ciphers based on two-dimensional chaotic maps," *International Journal of Bifurcation & Chaos*, vol. 8, no. 6, pp. 1259–1284, 1998.
- [39] H. Liu and X. Wang, "Color image encryption based on one-time keys and robust chaotic maps," *Computers & Mathematics with Applications*, vol. 59, pp. 3320–3327, 2010.

Research Article

Enhancing Ikeda Time Delay System by Breaking the Symmetry of Sine Nonlinearity

Xiaojing Gao 

School of Computer Science, China University of Geosciences, Building No. 1, North Campus, CUG Lumo Road 388, Wuhan 430074, China

Correspondence should be addressed to Xiaojing Gao; gaoxj@cug.edu.cn

Received 23 August 2019; Accepted 25 November 2019; Published 16 December 2019

Guest Editor: Serdar Çiçek

Copyright © 2019 Xiaojing Gao. This is an open access article distributed under the Creative Commons Attribution License, which permits unrestricted use, distribution, and reproduction in any medium, provided the original work is properly cited.

In the present contribution, an asymmetric central contraction mutation (ACCM) model is proposed to enhance the Ikeda time delay system. The modified Ikeda system model is designed by introducing a superimposed tanh function term into the sine nonlinearity term. Stability and Hopf bifurcation characteristics of the system are analyzed theoretically. Numerical simulations, carried out in terms of bifurcation diagrams, Lyapunov exponents spectrum, phase portraits, and two-parameter (2D) largest Lyapunov exponent diagrams are employed to highlight the complex dynamical behaviors exhibited by the enhanced system. The results indicate that the modified system has rich dynamical behaviors including limit cycle, multiscroll hyperchaos, chaos, and hyperchaos. Moreover, as a major outcome of this paper, considering the fragile chaos phenomenon, the ACCM-Ikeda time delay system has better dynamical complexity and larger connected chaotic parameter spaces (connectedness means that there is no stripe corresponding to nonchaotic dynamics embedded in the chaos regions).

1. Introduction

Chaotic system has many specific properties, such as initial state and parameters sensitivity, unpredictability, and topological mixing [1–3]. Although the equation model of a chaotic system is deterministic, it is impossible to predict its long-term behavior. These meaningful properties make chaotic systems widely studied and applied in many disciplines [4–10]. Specially, with the rapid development of information society chaos, secure communication has already been established to be a good candidate for transmission of confidential message [11–13]. In addition, chaotic systems have important applications in chaos-based random number generation [14] and sensors [15].

In recent years, time delay (TD) systems have become the subject of active research, which stems from the following reasons: (i) the existence of TD in nonlinear systems makes systems more complex. It has been found that communication systems based on low-dimensional chaotic systems (having a single positive LE) are insecure because their dynamics can be easily reconstructed by

Takens' embedding theorem [16]. TD chaotic systems modelled by nonlinear delay differential equations (DDEs) exhibit infinite dimensional phase space that cannot be anticipated by a low-dimensional system. As such, time delay systems can provide a higher level of computational security against embedding reconstruction. (ii) TD systems provide hyperchaos with multiple positive Lyapunov exponents (LEs) [17]. Due to these reasons, a number of simple and well characterized TD systems have been designed to produce chaos and hyperchaos [18–20]. Dynamics of nonlinear time-delay systems have been studied [19, 21].

In this paper, we focus our attention towards the simple and well characterized first-order Ikeda TD system:

$$\dot{x}(t) = -ax(t) + b \sin(x_\tau), \quad (1)$$

where $a \in R$ and $b \in R$ are positive parameters, $\tau \in R^+$ is the time delay constant, and $x_\tau \equiv x(t - \tau)$. From the theoretical point of view, some works have been carried out with the aim of inherent dynamics of the Ikeda TD system. In [22], the chaotic dynamics of first-order scalar

delay differential equations, including Ikeda equations, have been investigated. An analytical framework for study of dynamics of breathers in slow-fast Ikeda optoelectronic systems was proposed in [23]. A study on the biorhythmic behavior and its control in an optoelectronic oscillator was presented in [24]. From the viewpoint of engineering, some research studies have focused on the performance enhancement of the system for random number generation, optical chaotic secure communication, chaotic image encryption, optical secret communication, and so on [25–31].

It is noted that chaotic dynamical properties such as high complexity and wide chaotic parameter range are strongly required in some scenarios, including secure communication and random number generation. But researchers found that existing chaotic systems have certain limitations in different aspects. One concern is that many systems suffered from the fragile chaos phenomenon [32]. Fragile chaos means that a system has small chaotic parameter regions or has some nonchaotic structures embedded in the chaotic parameter zone. Small perturbation modulation of a parameter of the system is possible to destroy the chaotic attractors and transform the chaotic oscillator to period oscillations, as the parameter will fall into a nonchaotic region easily. Moreover, due to the limitation of physical devices, the range of physical parameters is always restricted, which will cause performance degradation in many cases. A typical scenario is chaotic secure communication. The security level of a chaos-based scheme is significantly dependent on the chaotic parameter range [33].

Considering the fragile chaos phenomenon, this paper proposes an asymmetric central contraction mutation (ACCM) model to enhance the Ikeda TD system. The modified TD system with ACCM is studied. We carry out stability analysis to identify the parameter zone for which the system shows a stable equilibrium response. And we simulate the system model numerically to show that with the variation of delay and other system parameters, the system exhibits stable limit cycle, chaos, hyperchaos, and multiscroll hyperchaos over the whole three-dimensional (3D) parameter space (given by a , b , and τ). Single parameter bifurcation diagrams, phase plots, and two-parameter (2D) Lyapunov exponent diagrams [34] are employed to explore the dynamics of the system. The ACCM model not only can enhance the dynamical complexity of the original Ikeda TD system in the chaotic range, but also can produce chaos in the nonchaotic range. It is worth mentioning that the improved system has larger chaotic parameter zones with good connectivity.

The rest of the paper is arranged in the following order. Section 2 presents the related mathematical model of the proposed ACCM-Ikeda time delay system. Analysis of stability and Hopf bifurcation are shown in Section 3. Simulation results of the ACCM-Ikeda time delay system and discussions are presented in Section 4, followed by performance comparison in Section 5. Section 6 draws conclusion.

2. System Description

We propose the following Ikeda TD system with Asymmetric Central Contraction Mutation (ACCM):

$$\dot{x}(t) = -ax(t) + b \sin[x_\tau + \tanh(x_\tau) + \tanh(x_\tau - 2)], \quad (2)$$

where $a > 0$ and $b > 0$ are real positive system parameters. $x_\tau \equiv x(t - \tau)$, and $\tau \in R^+$ is the intrinsic time delay of the system.

Sketches of the nonlinearities $\sin(x_\tau)$, $\tanh(x_\tau)$, and $g(x_\tau) = \sin[x_\tau + \tanh(x_\tau) + \tanh(x_\tau - 2)]$ are depicted in Figures 1(a)–1(c), respectively. It can be found from Figure 1(c) that the sketch of nonlinearity $g(x_\tau)$ showing a variation law similar to that of the $\sin(x_\tau)$ function, but with asymmetric central contraction, emerging more humps and valleys in the curve within the same parameter range. Therefore, we named the modified model as the ACCM-Ikeda TD system, which will have expected dynamic characteristics, such as better complexity, more larger and connected (meaning that there is no transient nonchaotic window interspersed in the chaotic parameter zone) chaotic parameter zone than the seed Ikeda time delay system (will be discussed in Section 5).

3. Stability and Hopf Bifurcation Analysis

Consider the TD system (2) expressed as

$$\begin{aligned} \dot{x}(t) &= f(x, x_\tau) \\ &= -ax(t) + bg(x_\tau). \end{aligned} \quad (3)$$

Equilibrium points x^* of (3) are obtained by solving

$$f(x^*, x^*) = 0. \quad (4)$$

3.1. Linearization near Equilibrium. Defining a small perturbation $\delta = x - x^*$ in equilibrium solution and using first-order Taylor's approximation, we get a linearized equation of (3) as

$$\begin{aligned} \frac{d\delta}{dt} &= \frac{dx}{dt} \\ &= f(x, x_\tau) \\ &= f(x + \delta, x_\tau + \delta_\tau) \\ &= f(x^*, x^*) + \partial_1 f(x^*, x^*)\delta + \partial_2 f(x^*, x^*)\delta_\tau \\ &= p\delta + q\delta_\tau, \end{aligned} \quad (5)$$

where $x_\tau \equiv x(t - \tau)$, $\delta_\tau \equiv \delta(t - \tau)$, $p = \partial_1 f(x^*, x^*) = -a$, and $q = \partial_2 f(x^*, x^*) = bg'(x^*)$ are partial derivatives of $f(x, x_\tau)$ with respect to variables x and x_τ evaluated at (x^*, x^*) , respectively. We can get the characteristic equation as

$$\lambda = -a + qe^{-\lambda\tau}. \quad (6)$$

3.2. Stability of Equilibrium. For the stability analysis, we use the methodology discussed in [22]. An equilibrium point x^*

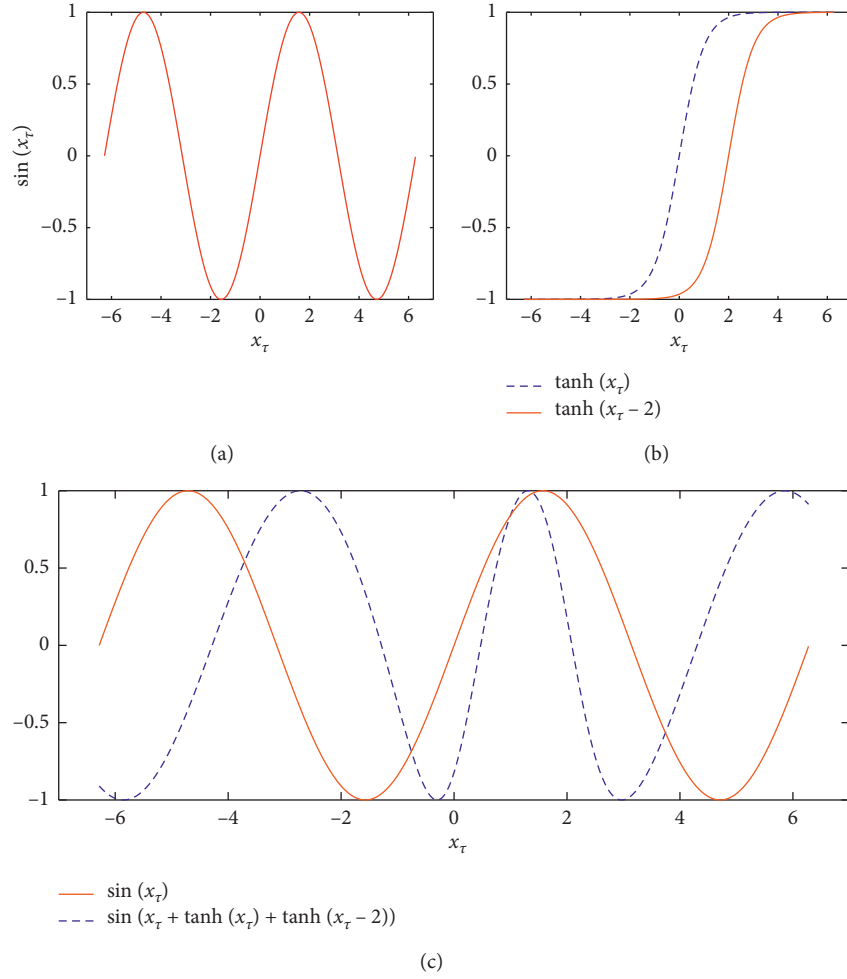


FIGURE 1: Sketches of (a) $\sin(x_\tau)$, (b) $\tanh(x_\tau)$ and $\tanh(x_\tau - 2)$, and (c) $g(x_\tau)$ (dotted line).

is asymptotically stable if all the roots λ_i of characteristic equation (6) satisfy

$$\operatorname{Re}(\lambda_i) < 0, \quad \text{for } \forall i. \quad (7)$$

If $\tau = 0$, then condition (7) takes the form

$$-a + q < 0. \quad (8)$$

Write $\lambda = u + i\omega$, $u, \omega \in \mathbb{R}$. Stability of equilibrium will change if λ crosses imaginary axis at $\lambda = i\omega$. The characteristic equation in this case becomes

$$i\omega = -a + qe^{-i\omega\tau}. \quad (9)$$

Using $e^{-i\omega\tau} = \cos(\omega\tau) - i\sin(\omega\tau)$ and separating real and imaginary parts in (9), we get

$$\begin{cases} q \cos(\omega\tau) = a, \\ q \sin(\omega\tau) = -\omega. \end{cases} \quad (10)$$

This gives

$$q^2 = a^2 + \omega^2. \quad (11)$$

Then, we can get

$$\omega = \sqrt{q^2 - a^2}. \quad (12)$$

This is possible if and only if

$$|q| > a. \quad (13)$$

3.3. Critical Surfaces. For $|b| > a$, from (10) we can obtain the critical surfaces expressed as

$$\tau_k = \begin{cases} \frac{\cos^{-1}(a/bg'(x^*)) + 2k\pi}{\sqrt{q^2 - a^2}}, & \text{for } g'(x^*) < 0, \\ \frac{2\pi - \cos^{-1}(a/bg'(x^*)) + 2k\pi}{\sqrt{q^2 - a^2}}, & \text{for } g'(x^*) > 0. \end{cases} \quad (14)$$

Differentiating characteristic equation (6) with respect to τ , we get

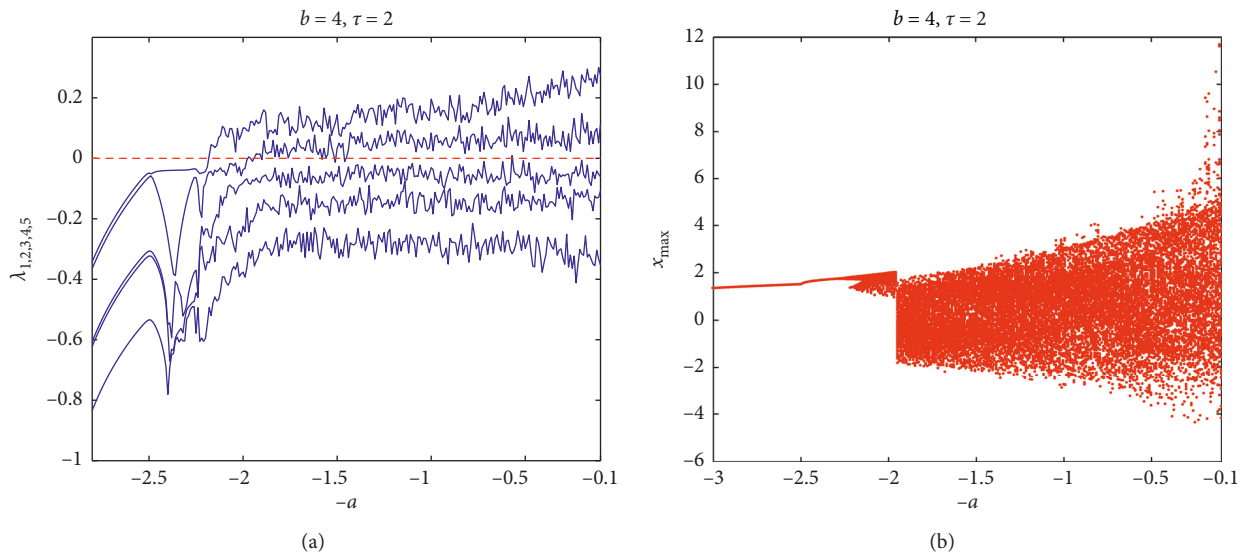


FIGURE 2: (a) The five largest Lyapunov exponents $\lambda_{1,2,3,4,5}$ plotted versus the bifurcation parameter $-3 \leq -a \leq -0.1$ for parameter $b = 4$ and time delay $\tau = 2$. (b) The bifurcation diagram for the same parameter as in case (a).

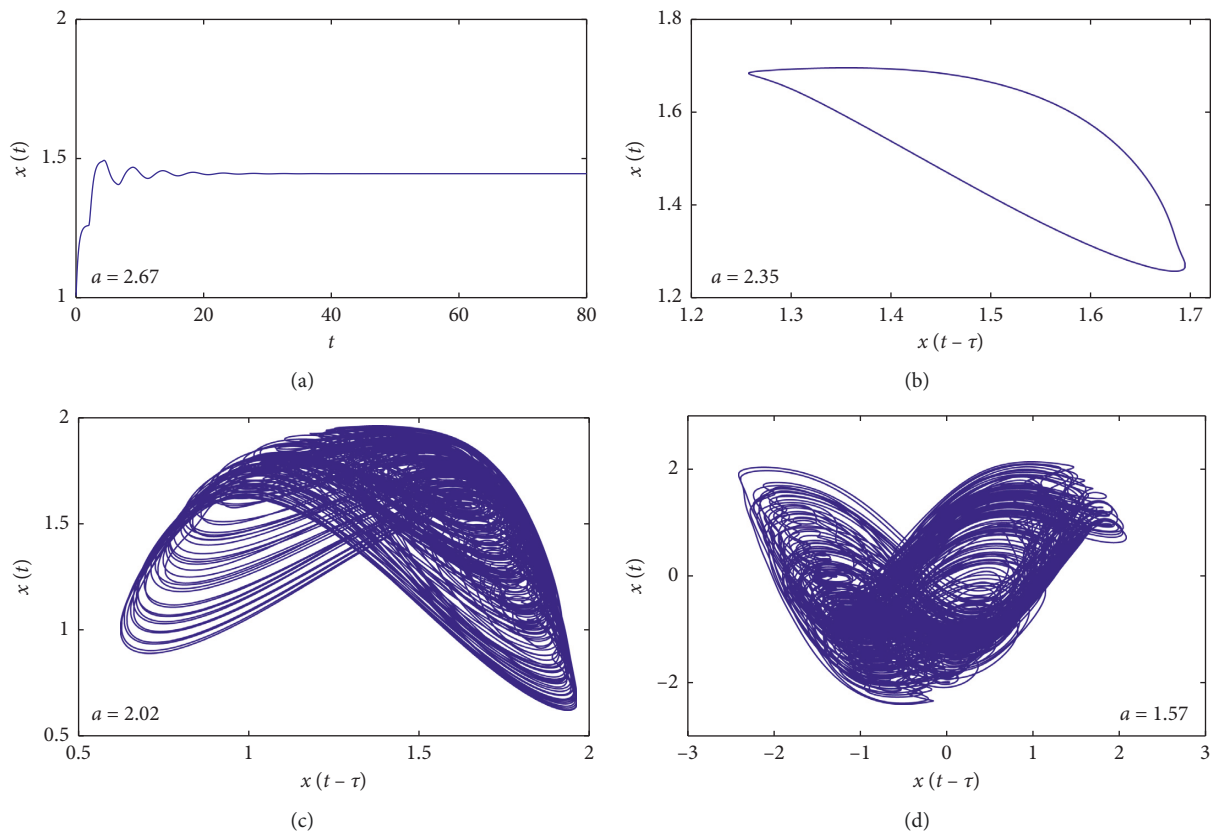


FIGURE 3: Continued.

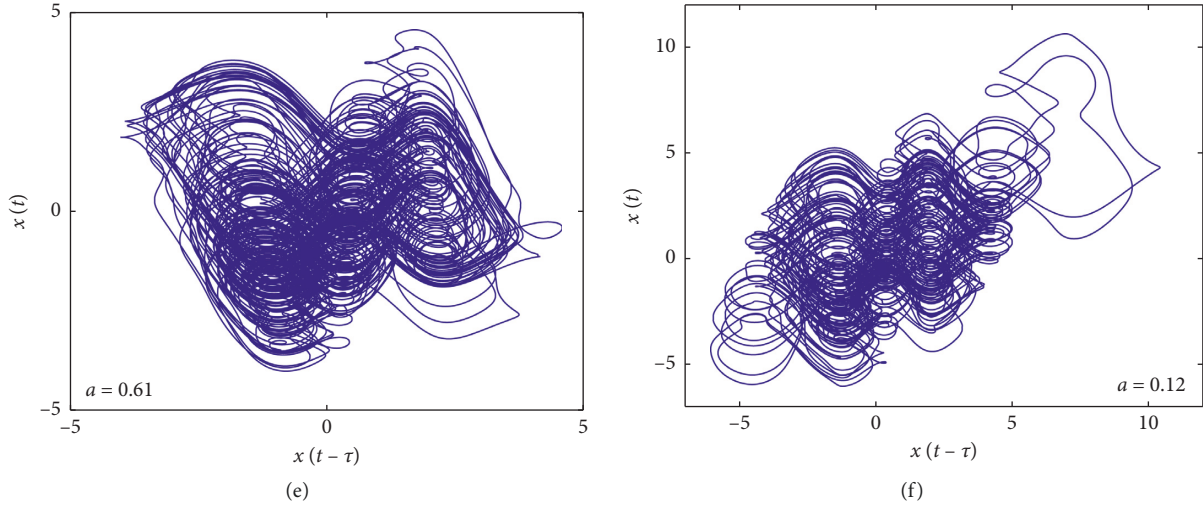


FIGURE 3: The initial condition is $\phi(t) = 1$ for $t \in [-\tau, 0]$ throughout the investigation. Parameter $b = 4$, and time delay $\tau = 2$. (a) Time series for $a = 2.67$, the fixed point is stable. Phase plane plots in $(x(t-\tau) - x(t))$ plane for variable a , (b) period limit cycle for $a = 2.35$, (c) chaotic attractor for $a = 2.02$, (d and e) hyperchaotic attractor for $a = 1.57$ and $a = 0.61$, (f) multiscroll hyperchaotic attractor for $a = 0.12$.

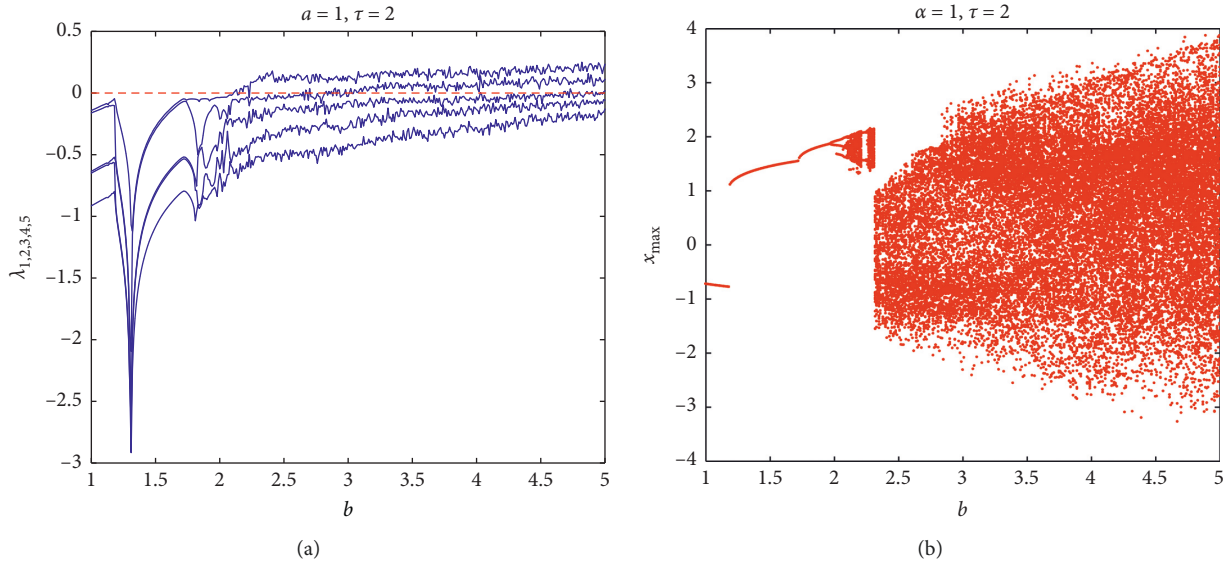


FIGURE 4: (a) The five largest Lyapunov exponents $\lambda_{1,2,3,4,5}$ plotted versus the bifurcation parameter $1 \leq b \leq 5$ for parameter $a = 1$ and time delay $\tau = 2$. (b) The bifurcation diagram for the same parameter as in case (a).

$$\frac{d\lambda}{d\tau} = qe^{-\lambda\tau} \left[-\lambda - \tau \frac{d\lambda}{d\tau} \right]. \quad (15)$$

Noting that $qe^{-\lambda\tau} = \lambda + a$, we can have

$$\frac{d\lambda}{d\tau} = -\frac{\lambda(\lambda + a)}{1 + \tau(\lambda + a)}, \quad (16)$$

and hence

$$\left. \frac{d\lambda}{d\tau} \right|_{u=0} = \frac{\omega^2 - ia\omega}{1 + a\tau + i\omega\tau}. \quad (17)$$

On critical surfaces (14),

$$\left. \frac{d\lambda}{d\tau} \right|_{u=0} = \frac{\omega^2}{(1 + a\tau)^2 + (\omega\tau)^2}, \quad (18)$$

$du/d\tau > 0$ on each of the critical surfaces τ_k . This implies that there does not exist any eigenvalue with negative real part across the critical surfaces (14). Thus, there is only one possible stability region (under condition (8)) enclosed by $\tau = 0$ and the critical surface τ_0 closest to it.

For $a > 0$, we have following main results:

Theorem 1. Suppose x^* is an equilibrium solution of the ACCM-Ikeda TD system (3) and $q = \partial_2 f(x^*, x^*) = bg'(x^*)$, then we can get the following:

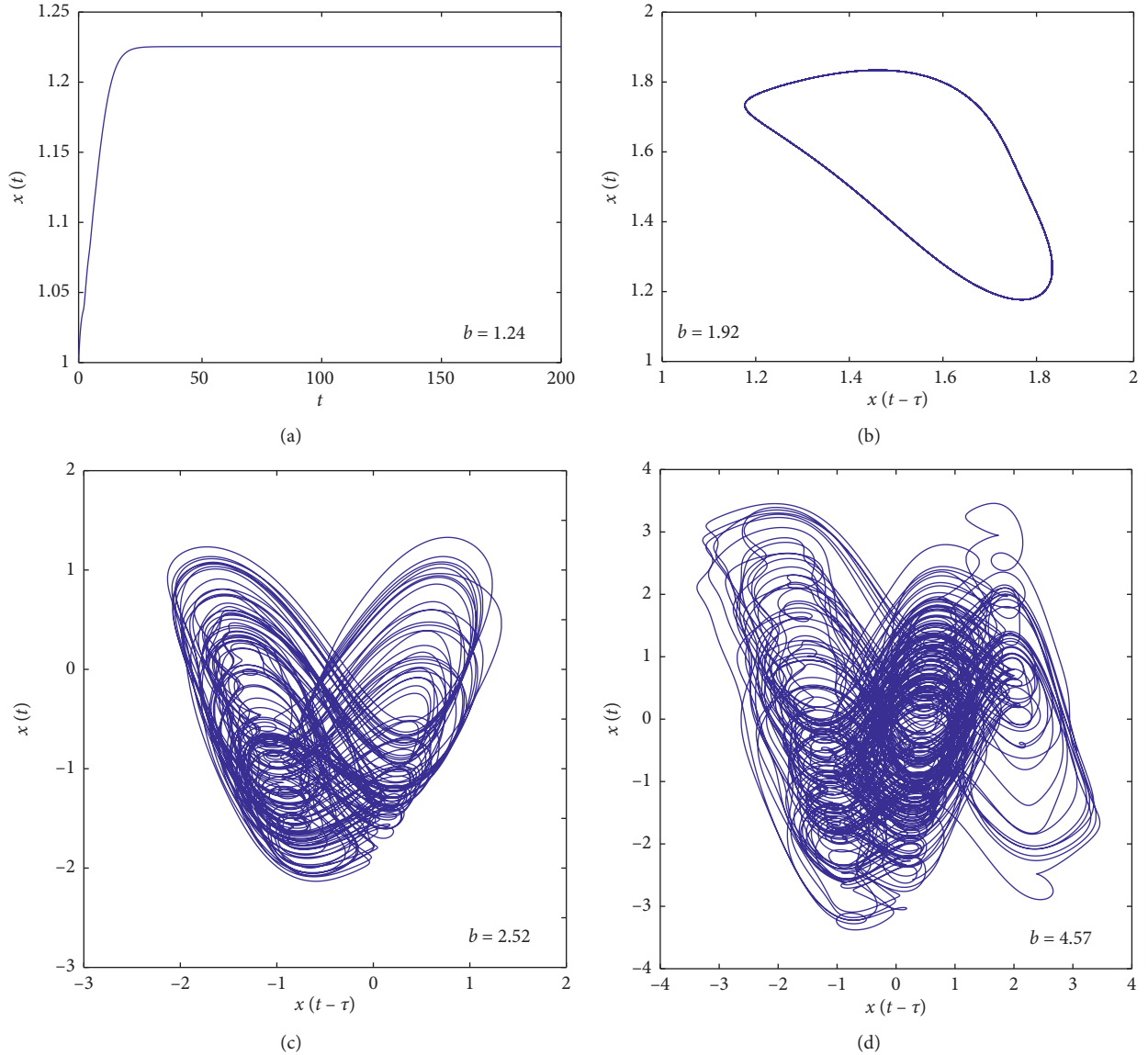


FIGURE 5: The initial condition is $\phi(t) = 1$ for $t \in [-\tau, 0]$ throughout the investigation. Parameter $a = 1$, and time delay $\tau = 2$. (a) Time series for $b = 1.24$, the fixed point is stable, (b) period limit cycles for $b = 1.92$, (c) chaotic attractors for $b = 2.52$, and (d) hyperchaotic attractors for $b = 4.57$.

- (1) If $q \in (-\infty, -a)$, then the stability region of x^* in (τ, a, q) parameter space is located between the plane $\tau = 0$ and τ_0 , i.e. equation undergoes Hopf bifurcation at this value.
- (2) If $q \in (a, \infty)$, then x^* is unstable for any $\tau \geq 0$.
- (3) If $q \in (-a, a)$, then x^* is stable for any $\tau \geq 0$.

4. Numerical Studies

In this section, the system equation (2) is solved numerically using the fourth-order Runge–Kutta algorithm with a step size $h = 0.01$. The initial condition is $\phi(t) = 1$ for $t \in [-\tau, 0]$ throughout the investigation. Then, the dynamics of the ACCM-Ikeda TD system is investigated

through bifurcation diagram, phase plots, and Lyapunov exponent spectrum (LES) considered from different perspectives. The LES is calculated using the method proposed in [35].

4.1. Varying a for $b = 4$ and Time Delay $\tau = 2$. System (2) with parameter $b = 4$ and the time delay $\tau = 2$ is numerically examined for the single bifurcation parameter a . The bifurcation parameter a varies in the range $0.1 \leq a \leq 3$. Five largest Lyapunov exponents $\lambda_{1,2,3,4,5}$ of all the spectrum versus the bifurcation parameter a is shown in Figure 2(a), which reveals that,

- (1) in the region $a \in [2.18, 3]$, the equilibrium point x^* is stable

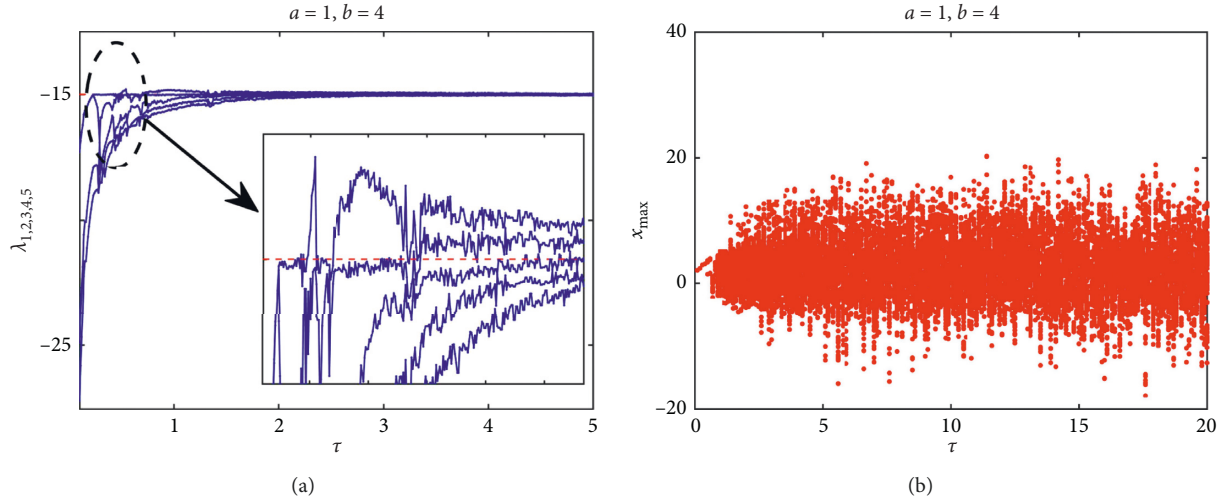


FIGURE 6: (a) The five largest Lyapunov exponents $\lambda_{1,2,3,4,5}$ plotted versus the time delay $0.1 \leq \tau \leq 20$ for parameters $a = 1$ and $b = 4$. (b) The bifurcation diagram for the same parameter as in case (a).

- (2) in the region $a \in [1.9, 2.17]$, there is one positive LE ($\lambda_1 > 0$) meaning that chaos appears
- (3) in the region $a \in [1.44, 1.89]$, chaotic and hyperchaotic regime appears alternately
- (4) in the region $a \in [0.1, 1.43]$, there are two positive LE ($\lambda_1 > 0$ and $\lambda_2 > 0$) meaning that hyperchaos appears

These regions of nonchaos and chaos observed in Figure 2(a) are best visualized in the bifurcation diagram, where we plot the maxima of $x(t)$ versus the bifurcation parameter a , as shown in Figure 2(b). A good consistency can be noted between the bifurcation diagram and the LES. The outcomes of this variation are shown in Figure 3.

- (i) For $a = 2.67$, we get equilibrium point $x^* = 1.44555$ and $q = bg'(x^*) = -2.0435$. By Case 3 of Theorem 1, the time series $x(t)$ converges to x^* , as shown in Figure 3(a).
- (ii) For $a = 2.35$, we get equilibrium point $x^* = 1.53665$ and $q = bg'(x^*) = -3.4094$. Therefore, in view of Case 1 of Theorem 1, the stability region is located between $\tau = 0$ and $\tau_0 = 0.7564$. By setting $\tau = 2$, the equilibrium is found unstable leading to a limit cycle, as depicted in Figure 3(b).
- (iii) For $a = 2.02$, we get $q = bg'(x^*) = -4.6290$. Therefore, in view of Case 1 of Theorem 1, the stability region is located between $\tau = 0$ and $\tau_0 = 0.4294$. By setting $\tau = 2$, the equilibrium is found unstable leading to a chaotic attractor, as depicted in Figure 3(c).
- (iv) For $a = 1.57$, $a = 0.61$, and $a = 0.12$, we get $q = 7.5144$, $q = 7.8277$, and $q = 7.9023$. In view of Case 2 of Theorem 1, x^* is unstable for any $\tau \geq 0$. We can obtain hyperchaotic attractors (shown in Figures 3(d) and 3(e)) and a multiscroll hyperchaotic attractor (Figure 3(f)), respectively.

4.2. *Varying b for $a = 1$ and Time Delay $\tau = 2$.* System (2) with the parameter $a = 1$ and the time delay $\tau = 2$ is numerically examined for the single bifurcation parameter b . The bifurcation parameter b varies in the range $1 \leq b \leq 5$. Five largest Lyapunov exponents $\lambda_{1,2,3,4,5}$ of all the spectrum versus the bifurcation parameter b is shown in Figure 4(a), which reveals that,

- (1) in the region $1 \leq b \leq 2.1$, the equilibrium x^* is stable
- (2) in the region $2.11 \leq b \leq 2.23$, chaotic and hyperchaotic regime appears alternately
- (3) in the region $2.24 \leq b \leq 3$, there is one positive LE ($\lambda_1 > 0$) meaning that the chaos has appeared
- (4) in the region $3.1 \leq b \leq 5$, there are two positive LE ($\lambda_1 > 0$ and $\lambda_2 > 0$) meaning that hyperchaos appears

These regions of nonchaos and chaos observed in Figure 4(a) are best visualized in the bifurcation diagram, where we plot the maxima of $x(t)$ versus the bifurcation parameter b , as shown in Figure 4(b). The outcomes of this variation are shown in Figure 5.

- (i) For $b = 1.24$, we get $q = 0.3554$. x^* is stable in view of Case 3 of Theorem 1. And the solution converges to $x^* = 1.22535$, as shown in Figure 5(a).
- (ii) For $b = 1.92$, we get $q = -2.1159$. In view of Case 1 of Theorem 1, the stability region is located between $\tau = 0$ and $\tau_0 = 1.1064$. By setting $\tau = 2$, the equilibrium is found unstable leading to a limit cycle, as depicted in Figure 5(b).
- (iii) For $b = 2.52$ and $b = 4.57$, we get $q = 4.7286$ and $q = 8.8743$. By Case 2 of Theorem 1, we observe a chaotic attractor in Figure 5(c) and a hyperchaotic attractor in Figure 5(d), respectively.

4.3. *Varying Time Delay τ for $a = 1$ and $b = 4$.* System (2) with the parameter $a = 1$ and $b = 4$ is numerically examined for

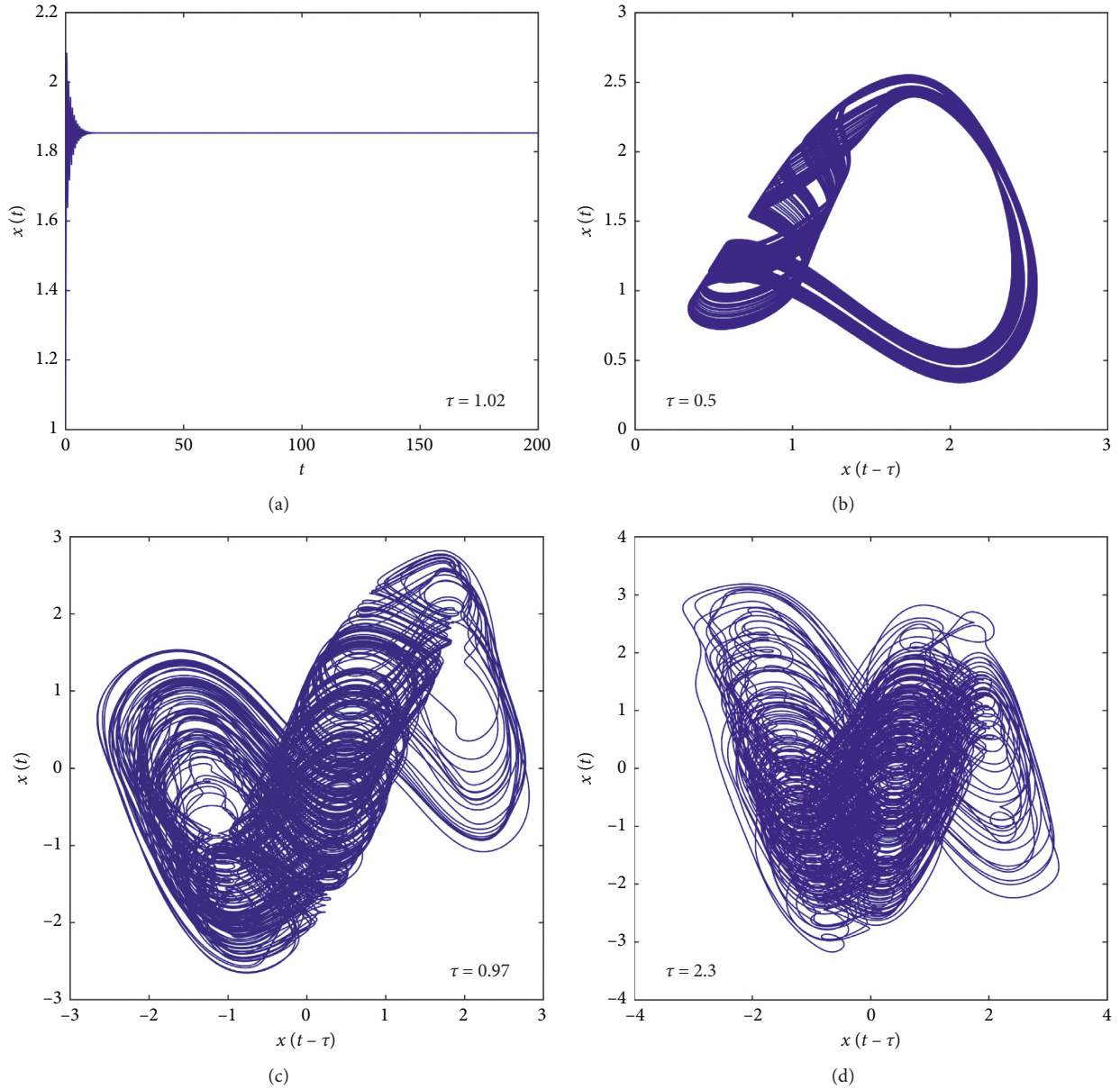


FIGURE 7: The initial condition is $\phi(t) = 1$ for $t \in [-\tau, 0]$ throughout the investigation. Parameters $a = 1$ and $b = 4$. (a) Period limit cycle for $\tau = 0.2$, (b and c) chaos attractors for $\tau = 0.5$ and $\tau = 0.97$, and (d) multiscroll hyperchaotic attractors for $\tau = 2.3$.

the time delay τ . The time delay τ varies in the range $0.1 \leq \tau \leq 20$. Five largest Lyapunov exponents $\lambda_{1,2,3,4,5}$ of all the spectrum versus the time delay τ is shown in Figure 6(a), which reveals that there is a narrow region of chaos ($\lambda_1 > 0$) between $0.48 \leq \tau \leq 0.54$ and $0.7 \leq \tau \leq 1.33$. When τ is starting at about 1.45, there is already a permanent hyperchaos ($\lambda_1, \lambda_2 > 0$) range.

These regions of nonchaos and chaos observed in Figure 6(a) are best visualized in the bifurcation diagram, where we plot the maxima of $x(t)$ versus the time delay τ , as shown in Figure 6(b).

For $a = 1$ and $b = 4$, we get $x^* = 1.853$ and $q = bg'(x^*) = -7.3430$, then x^* is stable in view of Case 1 of Theorem 1 and the stability region is located between $0 \leq \tau \leq 0.2347$. The outcomes of this variation are shown in Figure 7.

- (i) For $\tau = 0.2 < \tau_0$, x^* is stable and the solution converges to $x^* = 1.853$, as shown in Figure 7(a)
- (ii) Chaos attractors for $\tau = 0.5$ and $\tau = 0.97$ are shown in Figures 7(b) and 7(c)
- (iii) At $\tau = 2.3$ a hyperchaotic attractor is exhibited in Figure 7(d)

5. Performance Evaluations

To exhibit the effect of the ACCM in enhancing the chaotic dynamic characteristics of the Ikeda TD system, we compare the chaos and hyperchaos characteristics of the improved system with that of the seed Ikeda TD system. The systems are integrated with a fourth-order Runge–Kutta algorithm,

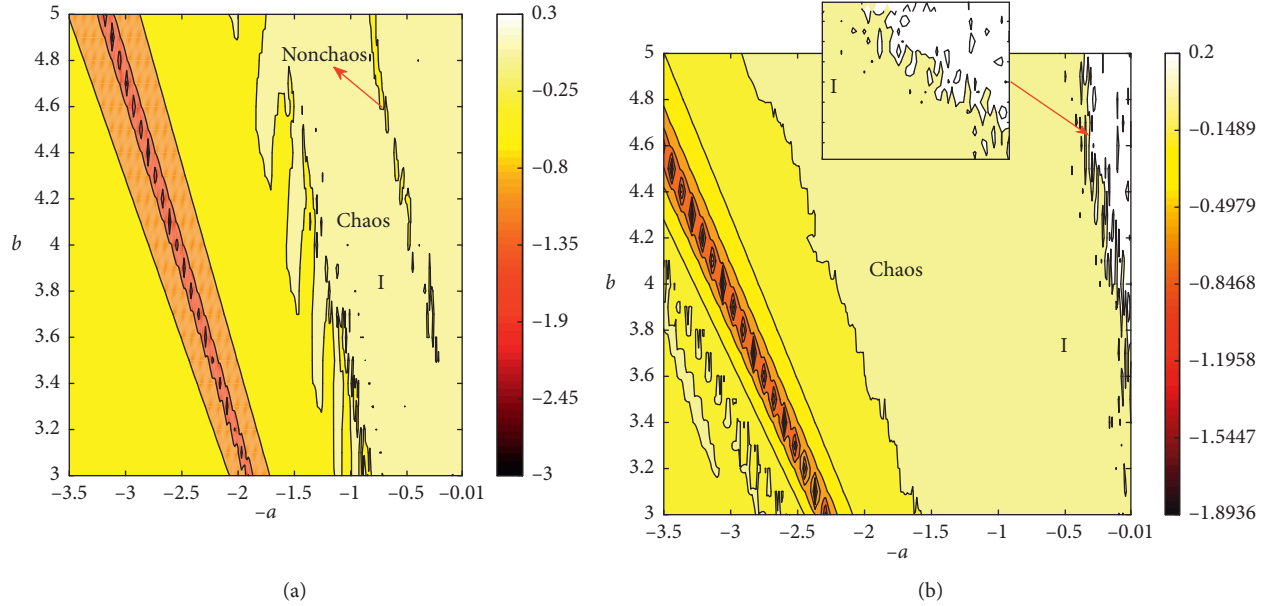


FIGURE 8: (a) The 2D LE diagram showing the largest Lyapunov exponent (λ_1) of the Ikeda TD system in the $(a - b)$ space. (b) The 2D LE diagram showing the largest Lyapunov exponent of the ACCM-Ikeda TD system in the $(a - b)$ space.

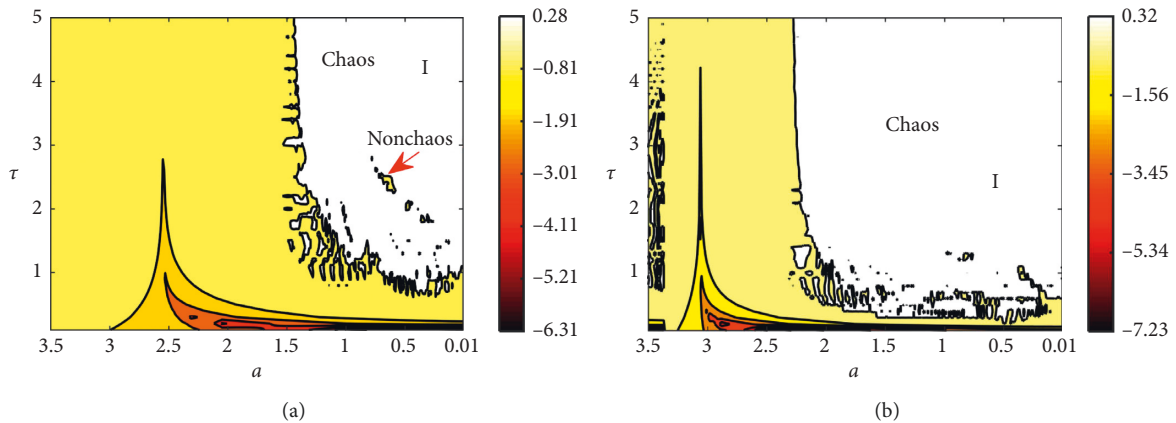


FIGURE 9: (a) The 2D LE diagram showing the largest Lyapunov exponent (λ_1) of the Ikeda TD system in the $(a - \tau)$ space. (b) The 2D LE diagram showing the largest Lyapunov exponent of the ACCM-Ikeda TD system in the $(a - \tau)$ space.

with a fixed time step size equal to $h = 0.01$. Two-parameter (2D) Lyapunov exponent diagrams are employed to explore the dynamics of the systems over the whole three-dimensional (3D) parameter space (given by a , b , and τ).

5.1. 2D Largest Lyapunov Exponent Diagrams. The chaotic dynamical behaviors of the ACCM-Ikeda and seed Ikeda TD systems over the whole (a, b) , (a, τ) , and (b, τ) parameter space are presented in this section. All of these 2D parameter space diagrams are obtained by considering the LLE value. The results for a cut of this 3D space at $\tau = 2$, $b = 4$, and $a = 1$ are shown in Figures 8–10. The white and faint yellow zones (noted by I) indicate the chaotic dynamics of the system ($\lambda_1 > 0$). In Figure 8(a), some stripes corresponding to nonchaotic regions embedded in the chaos

region can be found. In Figure 8(b), we can find a larger connected chaos region. The ACCM-Ikeda TD system has larger connected chaos region in the (a, b) space. And from Figures 9 and 10, we can get the same results. The ACCM-Ikeda TD system has larger connected chaos region over the whole (a, b) , (a, τ) , and (b, τ) parameter space. Moreover, it is noteworthy that with increasing b smaller time delay of the ACCM-Ikeda TD system is required to produce chaos (Figure 10(b)).

5.2. 2D Second Largest Lyapunov Exponent. The hyperchaotic dynamical behaviors of the ACCM-Ikeda and seed Ikeda TD systems over the whole (a, b) , (a, τ) , and (b, τ) parameter space are presented in this section. Hyperchaotic dynamical behavior is studied by using the second largest

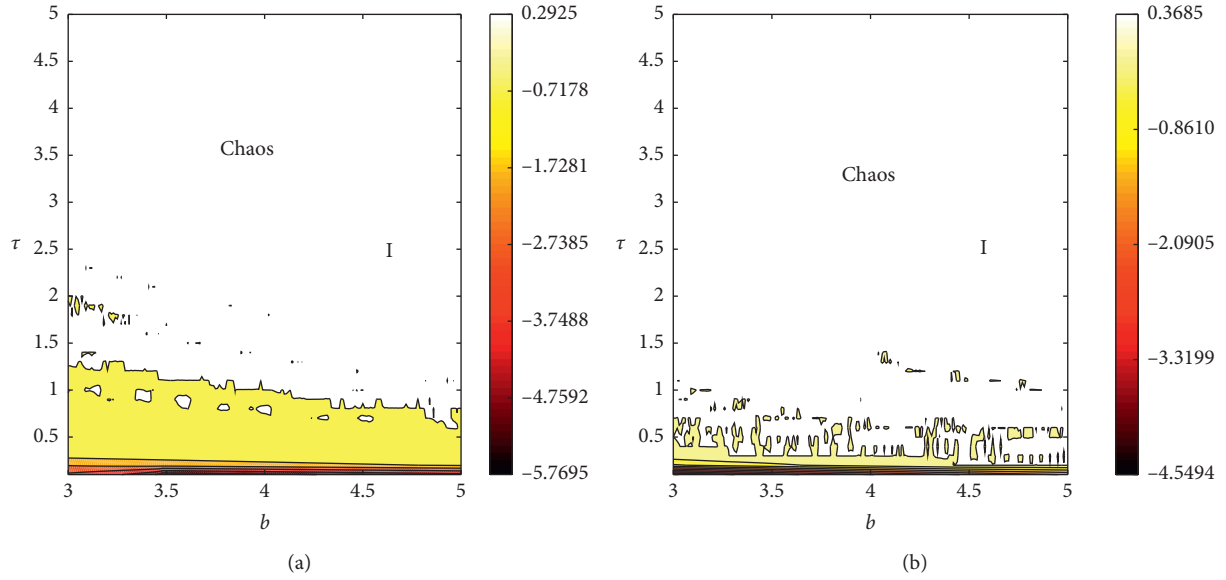


FIGURE 10: (a) The 2D LE diagram showing the largest Lyapunov exponent (λ_1) of the Ikeda TD system in the $(b - \tau)$ space. (b) The 2D LE diagram showing the largest Lyapunov exponent of the ACCM-Ikeda TD system in the $(b - \tau)$ space.

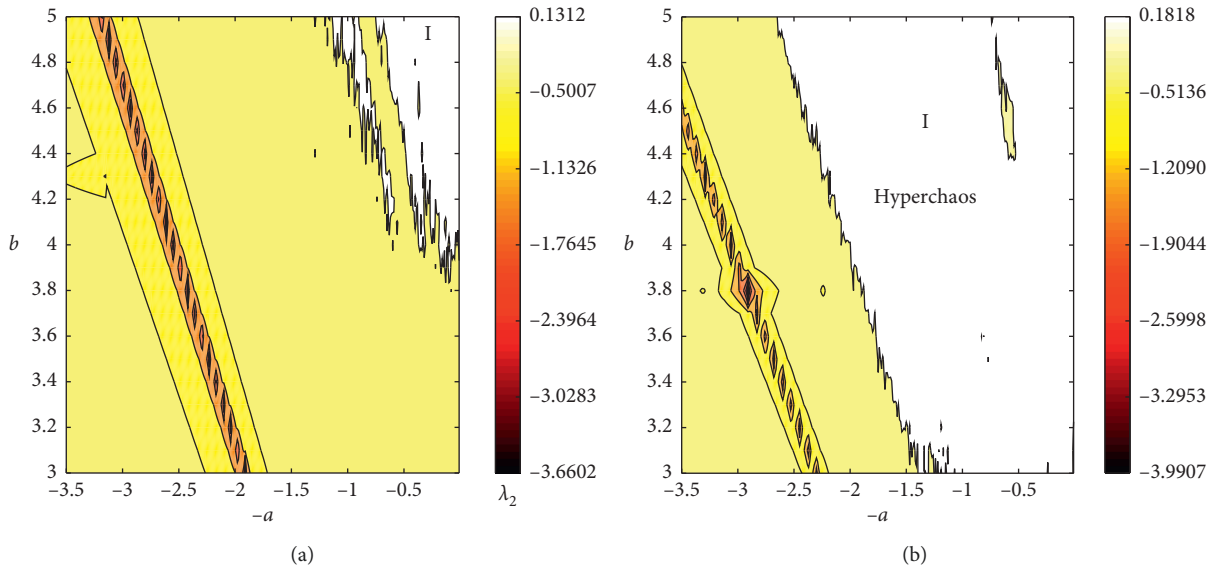


FIGURE 11: (a) The 2D LE diagram showing the second largest Lyapunov exponent (λ_2) of the Ikeda TD system in the $(a - b)$ space. (b) The 2D LE diagram showing the second largest Lyapunov exponent of the ACCM-Ikeda TD system in the $(a - b)$ space.

Lyapunov exponent (LE_2) as indicators. As shown in Figures 11–13, the white and faint yellow zones (noted by I) indicate the hyperchaotic states of the system ($\lambda_2 > 0$ and $\lambda_1 > 0$, in Figures 8–10). Clearly in Figures 11–13, the ACCM-Ikeda TD system has larger connected hyperchaotic regions in 2D parameter spaces (a, b) , (a, τ) , and (b, τ) . With parameters $-a$, b , and time delay τ increase, λ_2 of the enhanced ACCM-Ikeda TD system become larger and positive when λ_2 of the original Ikeda system is still negative. As such, the ACCM model can transform the chaotic oscillator to hyperchaotic oscillations.

5.3. Largest Lyapunov Exponent. Moreover, the complexity of the two systems is compared by calculating the single parameter Largest Lyapunov Exponent. Lyapunov Exponent can describe the average separation rate of trajectories starting from two extremely close initial states. A positive LE means that the two adjacent trajectories of a dynamical system exponentially separate in each iteration. A dynamical system with a positive LE is regarded as chaotic, and larger LE represents higher dynamical complexity. Figures 14(a)–14(c) compare the largest Lyapunov exponents (LLEs) of the ACCM-Ikeda TD system and its associated seed Ikeda

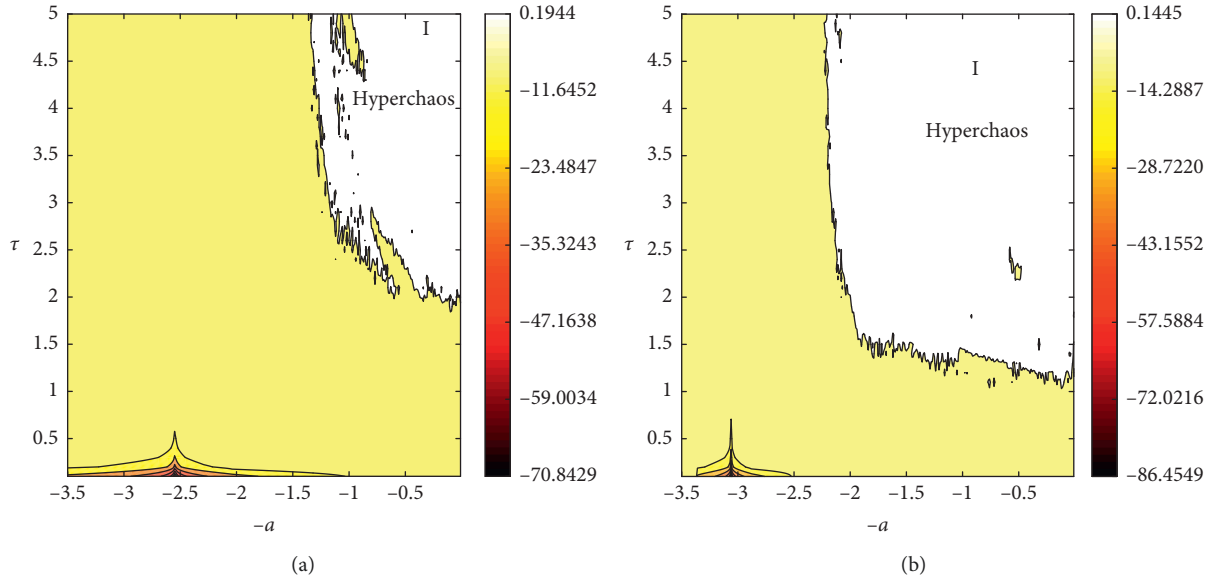


FIGURE 12: (a) The 2D LE diagram showing the second largest Lyapunov exponent (λ_2) of the Ikeda TD system in the $(a - \tau)$ space. (b) The 2D LE diagram showing the second largest Lyapunov exponent of the ACCM-Ikeda TD system in the $(a - \tau)$ space.

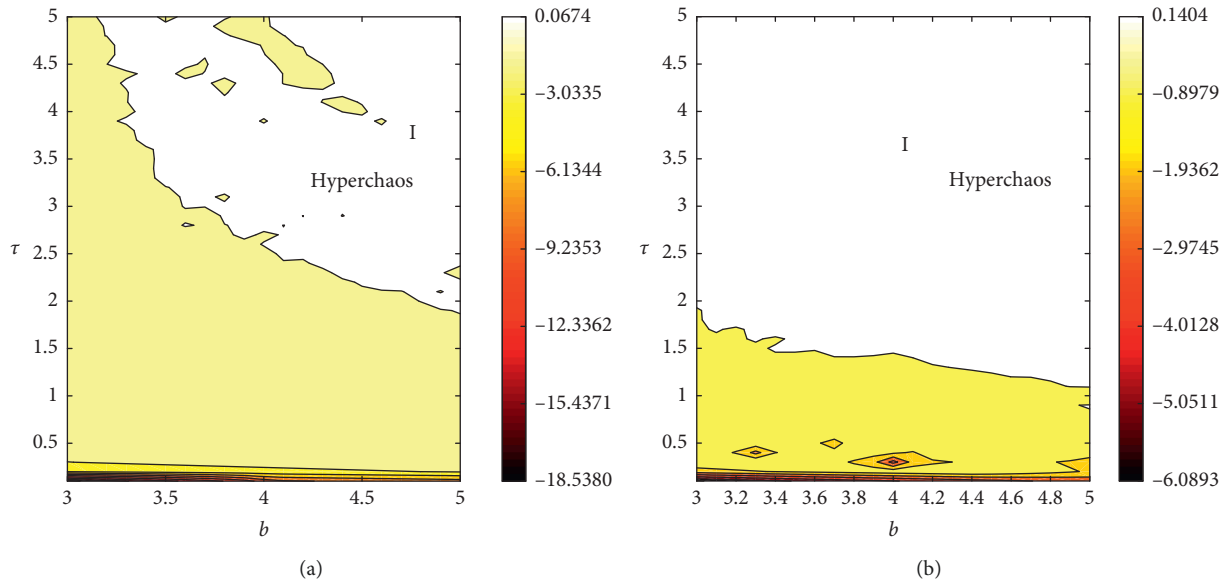


FIGURE 13: (a) The 2D LE diagram showing the second largest Lyapunov exponent (λ_2) of the Ikeda TD system in the $(b - \tau)$ space. (b) The 2D LE diagram showing the second largest Lyapunov exponent of the ACCM-Ikeda TD system in the $(b - \tau)$ space.

system. The largest Lyapunov exponents (LLEs) curve with the change of parameters a , b , and time delay τ , as shown in Figures 11(a) and 11(b), respectively. As can be observed from these figures that the ACCM-Ikeda TD system has larger LLEs, it proves that ACCM can enhance the chaos complexity of the original Ikeda system.

6. Conclusion

In this paper, a new Ikeda time delay system with asymmetric central contraction mutation (ACCM) is proposed and examined. First, we have analyzed the stability and Hopf

bifurcation of the system. The results for different types of stability regions are derived. The conditions on the partial derivatives of function f at equilibrium points are provided theoretically. The Hopf bifurcation value of delay τ is also mentioned. Next, the dynamical analysis of the system is carried out by visualizing the bifurcation diagram and spectrum of the first five LEs as a function of system parameters a , b , and the time delay τ . In a large range of parameters, rich dynamical behaviors including asymptotic stability, limit cycles, chaos, hyperchaos, and multiscroll chaos are observed. Finally, we have compared the chaotic dynamics of the ACCM-Ikeda TD system and those of the

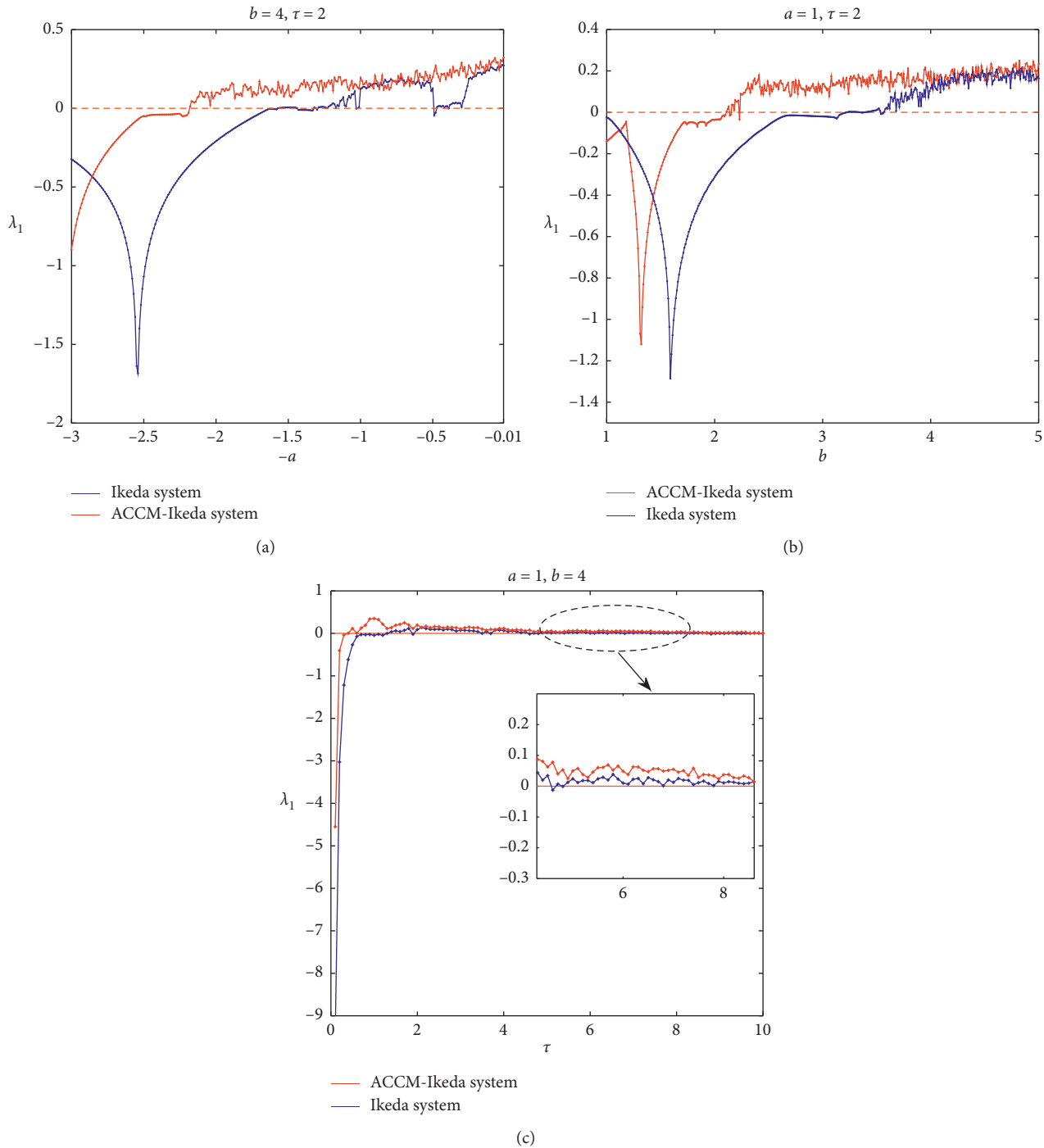


FIGURE 14: The first largest LEs comparisons of the ACCM-Ikeda TD system (2) and the seed Ikeda TD system (1): (a) LLE (λ_1) comparison for bifurcation parameter a ; (b) LLE (λ_1) comparison for bifurcation parameter b ; (c) LLE (λ_1) comparison for bifurcation parameter τ .

seed Ikeda TD system. Two-parameter (2D) LE diagrams are employed to explore the chaotic dynamics of the system over the whole parameter space. Complexity of the systems is characterized by LLE as a function of single parameter. The simulation results show that the ACCM-Ikeda TD system has higher complexity and larger chaotic and hyperchaotic parameter zones. There is no transient nonchaos window, and the fragile chaos phenomenon is successfully

suppressed. Moreover, chaotic regime can be transformed to hyperchaotic regime by introducing the ACCM strategy. As a theoretical extension of the Ikeda TD system, the proposed scheme could be realized by the combination of electrical and optical devices according to some existing research studies [28, 36], and the ACCM-Ikeda TD system has the potential to be used in real world applications such as secure communications and random number generation.

Data Availability

The data used to support the findings of this study are available from the corresponding author upon request.

Conflicts of Interest

The author declares that there are no conflicts of interest.

References

- [1] J. Chen, F. Min, Q. Jin, and B. Ye, "Coexistence, bifurcation and chaos of a periodically forced duffing system with absolute nonlinearity," *The European Physical Journal Special Topics*, vol. 228, no. 6, pp. 1405–1419, 2019.
- [2] M. Inubushi, "Unpredictability and robustness of chaotic dynamics for physical random number generation," *Chaos: An Interdisciplinary Journal of Nonlinear Science*, vol. 29, no. 3, Article ID 033133, 2019.
- [3] H. Wang and G. Dong, "New dynamics coined in a 4-d quadratic autonomous hyper-chaotic system," *Applied Mathematics and Computation*, vol. 346, pp. 272–286, 2019.
- [4] H. Liu, Y. Zhang, A. Kadir, and Y. Xu, "Image encryption using complex hyper chaotic system by injecting impulse into parameters," *Applied Mathematics and Computation*, vol. 360, pp. 83–93, 2019.
- [5] L. Wang, T. Dong, and M.-F. Ge, "Finite-time synchronization of memristor chaotic systems and its application in image encryption," *Applied Mathematics and Computation*, vol. 347, pp. 293–305, 2019.
- [6] S. Vaidyanathan, A. Akgul, S. Kaçar, and U. Çavuşoğlu, "A new 4-d chaotic hyperjerk system, its synchronization, circuit design and applications in RNG, image encryption and chaos-based steganography," *The European Physical Journal Plus*, vol. 133, no. 2, p. 46, 2018.
- [7] M. Li, Y. Hong, Y. Song, and X. Zhang, "Effect of controllable parameter synchronization on the ensemble average bit error rate of space-to-ground downlink chaos laser communication system," *Optics Express*, vol. 26, no. 3, pp. 2954–2964, 2018.
- [8] L. Liu and S. Miao, "An image encryption algorithm based on baker map with varying parameter," *Multimedia Tools & Applications*, vol. 76, no. 15, pp. 16511–16527, 2017.
- [9] H. Hu, L. Liu, Y. Deng, and S. Miao, "Pseudorandom bit generator based on non-stationary logistic maps," *IET Information Security*, vol. 10, no. 2, pp. 87–94, 2016.
- [10] Ü. Çavuşoğlu, S. Kaçar, A. Zengin, and I. Pehlivan, "A novel hybrid encryption algorithm based on chaos and S-AES algorithm," *Nonlinear Dynamics*, vol. 92, no. 4, pp. 1745–1759, 2018.
- [11] D. M. Wang, L. S. Wang, Y. Y. Guo, Y. C. Wang, and A. B. Wang, "Key space enhancement of optical chaos secure communication: chirped FBG feedback semiconductor laser," *Optics Express*, vol. 27, no. 3, pp. 3065–3073, 2019.
- [12] H. Yin, Q. Zhao, D. Xu et al., "1.25 Gbits/s-message experimental transmission utilising chaos-based fibre-optic secure communications over 143 km," *International Journal of High Performance Computing and Networking*, vol. 14, no. 1, pp. 42–51, 2019.
- [13] L. Wang, Y. Guo, D. Wang, Y. Wang, and A. Wang, "Experiment on 10-Gb/s message transmission using an all-optical chaotic secure communication system," *Optics Communications*, vol. 453, Article ID 124350, 2019.
- [14] S. Ergun, "Vulnerability analysis of a chaos-based random number generator," in *Proceedings of the 2018 IEEE International Conference on Systems, Man, and Cybernetics (SMC)*, pp. 3331–3334, IEEE, Miyazaki, Japan, February 2018.
- [15] H. Natiq, M. R. K. Ariffin, M. R. M. Said, and S. Banerjee, "Enhancing the sensitivity of a chaos sensor for internet of things," *Internet of Things*, vol. 7, Article ID 100083, 2019.
- [16] T. Banerjee, D. Biswas, and B. C. Sarkar, "Design and analysis of a first order time-delayed chaotic system," *Nonlinear Dynamics*, vol. 70, no. 1, pp. 721–734, 2012.
- [17] H. Wernecke, B. Sándor, and C. Gros, "Chaos in time delay systems, an educational review," *Physics Reports*, vol. 824, pp. 1–40, 2019.
- [18] D. V. Senthilkumar, K. Srinivasan, K. Murali, M. Lakshmanan, and J. Kurths, "Experimental confirmation of chaotic phase synchronization in coupled time-delayed electronic circuits," *Physical Review E*, vol. 82, Article ID 065201, 2010.
- [19] K. Srinivasan, I. Raja Mohamed, K. Murali, M. Lakshmanan, and S. Sinha, "Design of time delayed chaotic circuit with threshold controller," *International Journal of Bifurcation and Chaos*, vol. 21, no. 3, pp. 725–735, 2011.
- [20] D. Biswas and T. Banerjee, "Chaotic time-delayed system with hard nonlinearity: design and characterization," in *Time-Delayed Chaotic Dynamical Systems*, Springer, Berlin, Germany, 2018.
- [21] M. Lakshmanan and D. V. Senthilkumar, *Dynamics of Nonlinear Time-Delay Systems*, Springer Science & Business Media, Berlin, Germany, 2011.
- [22] J. Wei, "Bifurcation analysis in a scalar delay differential equation," *Nonlinearity*, vol. 20, no. 11, pp. 2483–2498, 2007.
- [23] J. H. T. Mbé, A. F. Talla, G. R. G. Chengui et al., "Mixed-mode oscillations in slow-fast delayed optoelectronic systems," *Physical Review E*, vol. 91, no. 1, Article ID 012902, 2015.
- [24] D. Ghosh, A. Mukherjee, N. R. Das, and B. Biswas, "Control of coexisting periodic oscillations in an optoelectronic oscillator," *Optical Engineering*, vol. 57, no. 12, Article ID 126108, 2018.
- [25] M. Li, H. Fan, Y. Xiang, Y. Li, and Y. Zhang, "Cryptanalysis and improvement of a chaotic image encryption by first-order time-delay system," *IEEE MultiMedia*, vol. 25, no. 3, pp. 92–101, 2018.
- [26] W. Shao, M. Cheng, C. Luo et al., "An image encryption scheme based on hybrid electro-optic chaotic sources and compressive sensing," *IEEE Access*, vol. 7, pp. 156582–156591, 2019.
- [27] Z. Zhao, M. Cheng, C. Luo et al., "Semiconductor-laser-based hybrid chaos source and its application in secure key distribution," *Optics Letters*, vol. 44, no. 10, pp. 2605–2608, 2019.
- [28] Y. Fu, M. Cheng, X. Jiang et al., "High-speed optical secure communication with an external noise source and an internal time-delayed feedback loop," *Photonics Research*, vol. 7, no. 11, pp. 1306–1313, 2019.
- [29] Z. Zhao, M. Cheng, C. Luo et al., "Synchronized random bit sequences generation based on analog-digital hybrid electro-optic chaotic sources," *Journal of Lightwave Technology*, vol. 36, no. 20, pp. 4995–5002, 2018.
- [30] R. M. Nguimdo, P. Colet, L. Larger, and L. Pesquera, "Digital key for chaos communication performing time delay concealment," *Physical Review Letters*, vol. 107, no. 3, Article ID 034103, 2011.
- [31] S. Miao and L. Liu, "Two-dimensional electro-optic delayed feedback system with electrical and optical coupling," *IET Optoelectronics*, vol. 12, no. 3, pp. 156–160, 2018.
- [32] Z. Hua, B. Zhou, and Y. Zhou, "Sine chaotification model for enhancing chaos and its hardware implementation," *IEEE*

- Transactions on Industrial Electronics*, vol. 66, no. 2, pp. 1273–1284, 2019.
- [33] X. Gao, F. Xie, and H. Hu, “Enhancing the security of electro-optic delayed chaotic system with intermittent time-delay modulation and digital chaos,” *Optics Communications*, vol. 352, pp. 77–83, 2015.
- [34] T. F. Fozin, P. M. Ezhilarasu, Z. N. Tabekoueng et al., “On the dynamics of a simplified canonical chua’s oscillator with smooth hyperbolic sine nonlinearity: hyperchaos, multistability and multistability control,” *Chaos: An Interdisciplinary Journal of Nonlinear Science*, vol. 29, no. 11, Article ID 113105, 2019.
- [35] J. D. Farmer, “Chaotic attractors of an infinite-dimensional dynamical system,” *Physica D Nonlinear Phenomena*, vol. 4, no. 3, pp. 366–393, 1982.
- [36] D. Biswas, B. Karmakar, and T. Banerjee, “A hyperchaotic time-delayed system with single-humped nonlinearity: theory and experiment,” *Nonlinear Dynamics*, vol. 89, no. 58, pp. 1733–1743, 2017.

Research Article

The Synchronization of N Cascade-Coupled Chaotic Systems

Pengyu Li, Juan Du , Shouliang Li , Yazhao Zheng, and Bowen Jia 

School of Information Science and Engineering, Lanzhou University, Lanzhou 730000, China

Correspondence should be addressed to Juan Du; duj@lzu.edu.cn

Received 12 September 2019; Accepted 27 November 2019; Published 12 December 2019

Guest Editor: Mahendra K. Gupta

Copyright © 2019 Pengyu Li et al. This is an open access article distributed under the Creative Commons Attribution License, which permits unrestricted use, distribution, and reproduction in any medium, provided the original work is properly cited.

In this paper, we investigate a novel synchronization method, which consists of n ($n \geq 2$) cascade-coupled chaotic systems. Furthermore, as the number of chaotic systems decreases from n to 2, the proposed synchronization will transform into bidirectional coupling synchronization. Based on Lyapunov stability theory, a general criterion is proposed for choosing the appropriate coupling parameters to ensure cascading synchronization. Moreover, 4 Lü systems are taken as an example and the corresponding numerical simulations demonstrate the effectiveness of our idea.

1. Introduction

Since Pecora and Carrol reported the discovery of synchronization for two chaotic systems by circuits implementation [1], the exciting phenomenon has gained much attention. In various fields, such as secure communication, signal processing, and life sciences, many types of chaotic synchronization are proving to be increasingly useful [2–5]. The design of novel synchronization models is necessary in such applications and thus motivating researchers to develop it, such as phase synchronization [6], projective synchronization [7], generalized synchronization [8], complex synchronization [9], modulus synchronization [10], and hybrid dislocated synchronization [11].

It is known that chaotic systems are extremely sensitive to initial values [12]. For two chaotic systems with the same structure, minor deviations in their initial values will lead to significantly different chaotic state [13]. After the transmission through the cascade-coupled systems, the difference becomes more difficult to be analyzed. In these cases, when a signal to be transmitted is loaded into a cascade of chaotic systems, the security of the transmitted information and the difficulty of being deciphered will be greatly enhanced. However, the existing synchronization has been acquired for two chaotic systems, and the synchronization problems of n chaotic systems are yet to be investigated.

In fact, the synchronization for two chaotic systems can be defined as the following two types: unidirectional coupling synchronization and bidirectional coupling synchronization [14]. Unidirectional coupling synchronization includes a drive system and a response system. The two systems are synchronized by introducing the state of the drive system on the response system [15–17]. However, bidirectional coupling synchronization, also known as mutual coupling synchronization, can be obtained by introducing the state of a system to that of another system, in which each system can be considered as drive system or response system [18–20]. When compared with unidirectional coupling synchronization, bidirectional (or mutual) coupling synchronization is more attractive due to the fact that it is ready to implement in practice. Recently, Sivagnesh et al. proposed the synchronization of a network of mutually coupled chaotic systems, in which the synchronization behaviour changes as the coupling parameters change [21].

Interestingly, Carroll and Pecora not only discovered chaos synchronization phenomenon but also studied cascading synchronized chaotic systems [22]. Their model consists of a 3D drive system and two 2-D subresponse systems, where the subresponse systems can be constructed by copying two of the expressions of the drive systems. By combining the cascading synchronized chaotic system with projective synchronization schemes, An and Chen reported

the function cascade synchronization method [23, 24], which presented 3 chaotic systems. Indeed, the two 2-D response systems are not chaotic systems. And, the status signal of the response system is not fed back to the drive system.

By the motivation of the above discussion, a novel synchronization method is investigated in this paper, which consists of n ($n \geq 2$) cascade-coupled chaotic systems. This implies that the chaotic systems are in linear topology and cascade-coupled with each other. For example, the i -th system will be synchronized with the $(i-1)$ -th and $(i+1)$ -th systems ($2 \leq i \leq (n-1)$). Further, as the number of chaotic systems decreases from n to 2, the proposed synchronization will transform into bidirectional coupling synchronization. Based on global control strategy, the synchronization scheme can be realized by choosing the appropriate coupling parameters, and the corresponding numerical simulations are presented to verify the effectiveness of our idea. In short, the proposed synchronization of n cascade-coupled chaotic systems can provide a novel choice for secure communication and signal processing.

The remainder of this paper is organized as follows. In Section 2, the principle of the synchronization for n cascade-coupled chaotic systems is introduced. And 4 Lü systems are chosen as an example to illustrate the effectiveness of our idea in Section 3. Conclusions are drawn in Section 4.

2. Model Description of the Synchronization of N Cascade-Coupled Chaotic Systems

This section mainly introduces the principle of the synchronization of N cascade-coupled chaotic systems.

We consider the following n chaotic systems.

The first system can be depicted as

$$\dot{X}_1 = AX_1 + f(X_1) - D_1(X_1 - X_2). \quad (1)$$

The second system can be depicted as

$$\dot{X}_2 = AX_2 + f(X_2) - D'_1(X_1 - X_2) - D_2(X_2 - X_3). \quad (2)$$

The third system can be depicted as

$$\begin{aligned} \dot{X}_3 &= AX_3 + f(X_3) - D'_2(X_2 - X_3) - D_3(X_3 - X_4), \\ &\vdots \end{aligned} \quad (3)$$

The $(n-1)$ -th system can be depicted as

$$\begin{aligned} \dot{X}_{n-1} &= AX_{n-1} + f(X_{n-1}) - D'_{n-2}(X_{n-2} - X_{n-1}) \\ &\quad - D_{n-1}(X_{n-1} - X_n). \end{aligned} \quad (4)$$

The n -th system can be depicted as

$$\dot{X}_n = AX_n + f(X_n) - D'_{n-1}(X_{n-1} - X_n), \quad (5)$$

where X_1, X_2, \dots, X_n denote m -dimensional state vectors of the chaotic systems. A denotes an $m \times m$ parameters matrix. $f(X_1), f(X_2), \dots, f(X_{n-1})$, and $f(X_n)$ denote $m \times 1$ continuous vector functions. $D_1, D'_1, D_2, D'_2, D_3, D'_3, \dots, D_{n-1}$ and D'_{n-1} are diagonal matrices which rule the feedback gain.

Definition 1. For the n chaotic systems, our goal is that the trajectory of X_1 synchronizes with that of X_2 , and the trajectory of X_2 synchronizes with that of X_3, \dots , finally the trajectory of X_{n-1} synchronizes with that of X_n . Then

$$\lim_{t \rightarrow \infty} \|e(t)\| = 0, \quad (6)$$

where $e(t)$ is a $(m \times (n-1))$ -dimensional column vector and $e(t) = (e_1(t), e_2(t), \dots, e_{n-1}(t))^T$, with $e_1(t) = X_1 - X_2, e_2(t) = X_2 - X_3, \dots, e_{n-1}(t) = X_{n-1} - X_n$, and $\|\cdot\|$ represents the Euclidean norm.

Remark 1. The error dynamical system can be acquired from equations (1)–(6):

$$\begin{aligned} \dot{e}_1(t) &= \dot{X}_1 - \dot{X}_2 = [A + H_{X_1, X_2} - (D_1 - D'_1)]e_1(t) + D_2e_2(t), \\ \dot{e}_2(t) &= \dot{X}_2 - \dot{X}_3 = [A + H_{X_2, X_3} - (D_2 - D'_2)]e_2(t) - D'_1e_1(t) + D_3e_3(t), \\ &\vdots \\ \dot{e}_{n-2}(t) &= \dot{X}_{n-2} - \dot{X}_{n-1} = [A + H_{X_{n-2}, X_{n-1}} - (D_{n-2} - D'_{n-2})]e_{n-2}(t) - D'_{n-3}e_{n-3}(t) + D_{n-1}e_{n-1}(t), \\ \dot{e}_{n-1}(t) &= \dot{X}_{n-1} - \dot{X}_n = [A + H_{X_{n-1}, X_n} - (D_{n-1} - D'_{n-1})]e_{n-1}(t) - D'_{n-2}e_{n-2}(t), \end{aligned} \quad (7)$$

where $f(X_1) - f(X_2) = H_{X_1, X_2} \cdot e_1(t)$, $f(X_2) - f(X_3) = H_{X_2, X_3} \cdot e_2(t), \dots$, and $f(X_{n-1}) - f(X_n) = H_{X_{n-1}, X_n} \cdot e_{n-1}(t)$. It is clear that $f(X_1), f(X_2), f(X_3), \dots, f(X_{n-1}), f(X_n)$ are bounded matrices, and thus $H_{X_1, X_2}, H_{X_2, X_3}, \dots, H_{X_{n-1}, X_n}$ are also bounded matrices. A general condition for achieving

the synchronization of n cascade-coupled chaotic systems is given in the following theorem.

Theorem 1. *If there exists a positive definite symmetric matrix P , and $n-1$ constants $\lambda_1 > 0, \lambda_2 > 0, \dots, \lambda_{n-1} > 0$, we have that*

$$\begin{cases} \left(A + H_{X_1, X_2} - (D_1 - D'_1) \right)^T P + P \left(A + H_{X_1, X_2} - (D_1 - D'_1) \right) \leq -\lambda_1 I, \\ \left(A + H_{X_2, X_3} - (D_2 - D'_2) \right)^T P + P \left(A + H_{X_2, X_3} - (D_2 - D'_2) \right) \leq -\lambda_2 I, \\ \vdots \\ \left(A + H_{X_{n-1}, X_n} - (D_{n-1} - D'_{n-1}) \right)^T P + P \left(A + H_{X_{n-1}, X_n} - (D_{n-1} - D'_{n-1}) \right) \leq -\lambda_{n-1} I, \end{cases} \quad (8)$$

where I is the identity matrix. Then the synchronization for the cascade-coupled systems (1)–(5) is realized.

$$V(t) = e^T(t) P_{n-1} e(t), \quad (9)$$

where $P_{n-1} = \text{diag}(P, P, \dots, P)$, with the total is $n-1$. Then it is easily known that $V(t) \geq 0$. And the time derivative of $V(t)$ is given as

Proof. Construct a Lyapunov function as

$$\begin{aligned} \dot{V}(t) &= \dot{e}_1^T(t) P e_1(t) + e_1^T(t) P \dot{e}_1(t) + e_2^T(t) P \dot{e}_2(t) + \dot{e}_2^T(t) P e_2(t) + \dots + \dot{e}_{n-1}^T(t) P e_{n-1}(t) + e_{n-1}^T(t) P \dot{e}_{n-1}(t) \\ &= e_1^T(t) \left(A + H_{X_1, X_2} - (D_1 - D'_1) \right)^T P e_1(t) + e_1^T(t) P \left(A + H_{X_1, X_2} - (D_1 - D'_1) \right) e_1(t) + e_2^T(t) D_2^T P e_1(t) + e_1^T(t) P D_2 e_2(t) \\ &\quad + e_2^T(t) \left(A + H_{X_2, X_3} - (D_2 - D'_2) \right)^T P e_2(t) + e_2^T(t) P \left(A + H_{X_2, X_3} - (D_2 - D'_2) \right) e_2(t) - e_1^T(t) (D'_1)^T P e_2(t) \\ &\quad + e_3^T(t) D_3^T P e_2(t) - e_2^T(t) P D'_1 e_1(t) + e_2^T(t) P D_3 e_3(t) + \dots + e_{n-1}^T(t) \left(A + H_{X_{n-1}, X_n} - (D_{n-1} - D'_{n-1}) \right)^T P e_{n-1}(t) \\ &\quad + e_{n-1}^T(t) P \left(A + H_{X_{n-1}, X_n} - (D_{n-1} - D'_{n-1}) \right) e_{n-1}(t) - e_{n-2}^T(t) (D'_{n-2})^T P e_{n-1}(t) - e_{n-1}^T(t) P D'_{n-2} e_{n-2}(t) \\ &= e_1^T(t) \left[\left(A + H_{X_1, X_2} - (D_1 - D_2) \right)^T P + P \left(A + H_{X_1, X_2} - (D_1 - D_2) \right) \right] e_1(t) + e_2^T(t) \left[\left(A + H_{X_2, X_3} - (D_2 - D_3) \right)^T P \right. \\ &\quad \left. + P \left(A + H_{X_2, X_3} - (D_2 - D_3) \right) \right] e_2(t) + \dots + e_{n-1}^T(t) \left[\left(A + H_{X_{n-1}, X_n} - (D_{n-1} - D_n) \right)^T P + P \left(A + H_{X_{n-1}, X_n} - (D_{n-1} - D_n) \right) \right] \\ &\quad \cdot e_{n-1}(t) + e_1^T(t) \left[P(D_2 - D'_1) + (D_2 - D'_1)^T P \right] e_2 + e_2^T(t) \left[P(D_3 - D'_2) + (D_3 - D'_2)^T P \right] e_3 + \dots \\ &\quad + e_{n-2}^T(t) \left[P(D_{n-1} - D'_{n-2}) + (D_{n-1} - D'_{n-2})^T P \right] e_{n-1}. \end{aligned} \quad (10)$$

As long as

$$\begin{cases} D'_1 = D_2, \\ D'_2 = D_3, \\ \vdots \\ D'_{n-2} = D_{n-1}. \end{cases} \quad (11)$$

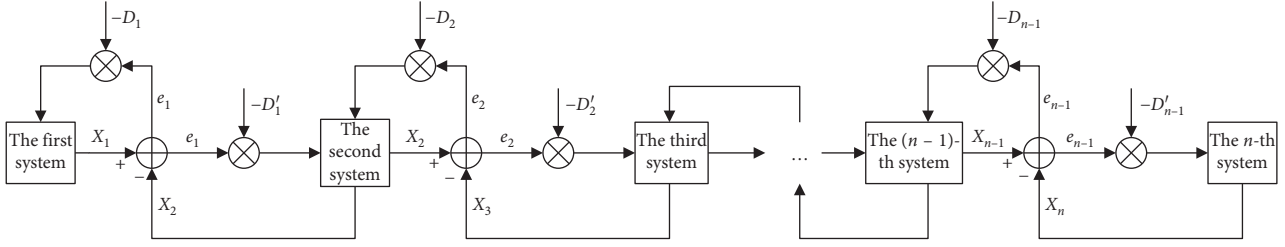
Then, equation (12) can be represented as

$$\begin{aligned} \dot{V}(t) &= \dot{e}_1^T(t) P e_1(t) + e_1^T(t) P \dot{e}_1(t) + e_2^T(t) P \dot{e}_2(t) + \dot{e}_2^T(t) P e_2(t) \\ &\quad + \dots + \dot{e}_{n-1}^T(t) P e_{n-1}(t) + e_{n-1}^T(t) P \dot{e}_{n-1}(t) \\ &= e_1^T(t) \left[\left(A + H_{X_1, X_2} - (D_1 - D_2) \right)^T P \right. \\ &\quad \left. + P \left(A + H_{X_1, X_2} - (D_1 - D_2) \right) \right] e_1(t) \\ &\quad + e_2^T(t) \left[\left(A + H_{X_2, X_3} - (D_2 - D_3) \right)^T P \right. \\ &\quad \left. + P \left(A + H_{X_2, X_3} - (D_2 - D_3) \right) \right] e_2(t) + \dots \\ &\quad + e_{n-1}^T(t) \left[\left(A + H_{X_{n-1}, X_n} - (D_{n-1} - D_n) \right)^T P \right. \\ &\quad \left. + P \left(A + H_{X_{n-1}, X_n} - (D_{n-1} - D_n) \right) \right] e_{n-1}(t) \\ &\leq \left(-\lambda_1 e_1^T(t) e_1(t) \right) + \left(-\lambda_2 e_2^T(t) e_2(t) \right) + \dots \\ &\quad + \left(-\lambda_{n-1} e_{n-1}^T(t) e_{n-1}(t) \right) < 0. \end{aligned} \quad (12)$$

Equation (12) holds if and only if $e(t) \neq 0$. Based on Lyapunov stability theory, system (7) is globally asymptotically stable. This implies that the synchronization of n cascade-coupled chaotic systems is achieved. The proof is completed. \square

Remark 2. From Theorem 1, we obtain that $e_1(t) = X_1 - X_2 = 0$, $e_2(t) = X_2 - X_3 = 0$, \dots , and $e_{n-1}(t) = X_{n-1} - X_n = 0$ as $t \rightarrow \infty$, i.e., $X_1 = X_2 = \dots = X_n$. This implies that any two systems in the n chaotic systems can be synchronized with each other. The interesting phenomenon is demonstrated in Figure 1. Take the first and second system in Figure 1 as an example. Firstly, we get the error signal $e_1(t) = X_1 - X_2$ through an adder. Then, $e_1(t)$ is injected into the first system via multiplier $-D_1$, while being injected into the second system via multiplier $-D'_1$. The coupling cases between the subsequent systems are similar.

Remark 3. If the n chaotic systems are degraded to 2 chaotic systems, then synchronization problem in this paper will change into bidirectional coupling synchronization problem, which has been intensively revealed in previous researches.

FIGURE 1: The schematic representation of (n) cascade-coupled chaotic systems.

3. Synchronization of 4 Cascade-Coupled Lü Systems

This section demonstrates the effectiveness and flexibility of the model by adopting 4 Lü systems as an example.

The first system can be presented as

$$\begin{cases} \dot{x}_{11} = a(x_{12} - x_{11}) - d_{11}(x_{11} - x_{21}), \\ \dot{x}_{12} = cx_{12} - x_{11}x_{13} - d'_{12}(x_{12} - x_{22}), \\ \dot{x}_{13} = x_{11}x_{12} - bx_{13} - d'_{13}(x_{13} - x_{23}). \end{cases} \quad (13)$$

The second system can be presented as

$$\begin{cases} \dot{x}_{21} = a(x_{22} - x_{21}) - d'_{11}(x_{11} - x_{21}) - d_{21}(x_{21} - x_{31}), \\ \dot{x}_{22} = cx_{22} - x_{21}x_{23} - d'_{12}(x_{12} - x_{22}) - d_{22}(x_{22} - x_{32}), \\ \dot{x}_{23} = x_{21}x_{22} - bx_{23} - d'_{13}(x_{13} - x_{23}) - d_{23}(x_{23} - x_{33}). \end{cases} \quad (14)$$

The third system can be presented as

$$\begin{cases} \dot{x}_{31} = a(x_{32} - x_{31}) - d'_{21}(x_{21} - x_{31}) - d_{31}(x_{31} - x_{41}), \\ \dot{x}_{32} = cx_{32} - x_{31}x_{33} - d'_{22}(x_{22} - x_{32}) - d_{32}(x_{32} - x_{42}), \\ \dot{x}_{33} = x_{31}x_{32} - bx_{33} - d'_{23}(x_{23} - x_{33}) - d_{33}(x_{33} - x_{43}). \end{cases} \quad (15)$$

The fourth system can be presented as

$$\begin{cases} \dot{x}_{41} = a(x_{42} - x_{41}) - d'_{31}(x_{31} - x_{41}), \\ \dot{x}_{42} = cx_{42} - x_{41}x_{43} - d'_{32}(x_{32} - x_{42}), \\ \dot{x}_{43} = x_{41}x_{42} - bx_{43} - d'_{33}(x_{33} - x_{43}), \end{cases} \quad (16)$$

where $X_1 = (x_{11}, x_{12}, x_{13})^T$, $X_2 = (x_{21}, x_{22}, x_{23})^T$, $X_3 = (x_{31}, x_{32}, x_{33})^T$, and $X_4 = (x_{41}, x_{42}, x_{43})^T$ are the state vectors of 4 Lü systems; d_{ij} and d'_{ij} ($i = 1, 2, 3; j = 1, 2, 3$) are coupling parameters.

Let $e_{1i} = x_{1i} - x_{2i}$, $e_{2i} = x_{2i} - x_{3i}$, and $e_{3i} = x_{3i} - x_{4i}$, with $i = 1, 2, 3$. From Remark 1, the error dynamical system can be described as

$$\begin{aligned} \dot{e}_1(t) &= \dot{X}_1 - \dot{X}_2 = [A + H_{X_1, X_2} - (D_1 - D'_1)]e_1 + D_2e_2, \\ \dot{e}_2(t) &= \dot{X}_2 - \dot{X}_3 = [A + H_{X_2, X_3} - (D_2 - D'_2)]e_2 - D'_1e_1 + D_3e_3, \\ \dot{e}_3(t) &= \dot{X}_3 - \dot{X}_4 = [A + H_{X_3, X_4} - (D_3 - D'_3)]e_3 - D'_2e_2, \end{aligned} \quad (17)$$

where $e_1 = (e_{11}, e_{12}, e_{13})^T$, $e_2 = (e_{21}, e_{22}, e_{23})^T$, and $e_3 = (e_{31}, e_{32}, e_{33})^T$.

The n systems model, which was presented in Section 2, illustrates that A , $f(X_1)$, $f(X_2)$, $f(X_3)$, $f(X_4)$, H_{X_1, X_2} , H_{X_2, X_3} , H_{X_3, X_4} , D_1 , D_2 , D_3 , and D_4 can be described as

$$\begin{aligned} A &= \begin{pmatrix} -a & a & 0 \\ 0 & c & 0 \\ 0 & 0 & -b \end{pmatrix}, \\ f(X_1) &= \begin{pmatrix} 0 \\ -x_{11}x_{13} \\ x_{11}x_{12} \end{pmatrix}, \\ f(X_2) &= \begin{pmatrix} 0 \\ -x_{21}x_{23} \\ x_{21}x_{22} \end{pmatrix}, \\ f(X_3) &= \begin{pmatrix} 0 \\ -x_{31}x_{33} \\ x_{31}x_{32} \end{pmatrix}, \\ f(X_4) &= \begin{pmatrix} 0 \\ -x_{41}x_{43} \\ x_{41}x_{42} \end{pmatrix}, \\ H_{X_1, X_2} &= \begin{pmatrix} 0 & 0 & 0 \\ -x_{13} & 0 & -x_{21} \\ x_{12} & x_{21} & 0 \end{pmatrix}, \\ H_{X_2, X_3} &= \begin{pmatrix} 0 & 0 & 0 \\ -x_{23} & 0 & -x_{31} \\ x_{22} & x_{31} & 0 \end{pmatrix}, \\ H_{X_3, X_4} &= \begin{pmatrix} 0 & 0 & 0 \\ -x_{33} & 0 & -x_{41} \\ x_{32} & x_{41} & 0 \end{pmatrix}, \end{aligned} \quad (18)$$

$$D_1 = \text{diag}\{d_{11}, d_{12}, d_{13}\},$$

$$D'_1 = \text{diag}\{d'_{11}, d'_{12}, d'_{13}\},$$

$$D_2 = \text{diag}\{d_{21}, d_{22}, d_{23}\},$$

$$D'_2 = \text{diag}\{d'_{21}, d'_{22}, d'_{23}\},$$

$$D_3 = \text{diag}\{d_{31}, d_{32}, d_{33}\},$$

$$D'_3 = \text{diag}\{d'_{31}, d'_{32}, d'_{33}\}.$$

When the coupling parameter matrices are set as $D_1 = D'_1 = D_2 = D'_2 = D_3 = D'_3 = 0$ and the initial condition of systems (13)–(16) are chosen as $(x_{11}, x_{12}, x_{13}) = (1, 1, 1)$, $(x_{21}, x_{22}, x_{23}) = (5, 5, 5)$, $(x_{31}, x_{32}, x_{33}) = (10, 10, 10)$, $(x_{41}, x_{42}, x_{43}) = (20, 20, 20)$. Figure 2 indicates that systems (13)–(16) do not synchronize with each other.

Based on global control strategy, we choose the positive definite symmetric constant matrix $P = \text{diag}(p_1, p_2, p_3)$, with $p_i > 0$ ($i = 1, 2, 3$), and positive constants $\lambda_1 > 0$, $\lambda_2 > 0$, $\lambda_3 > 0$, then we have

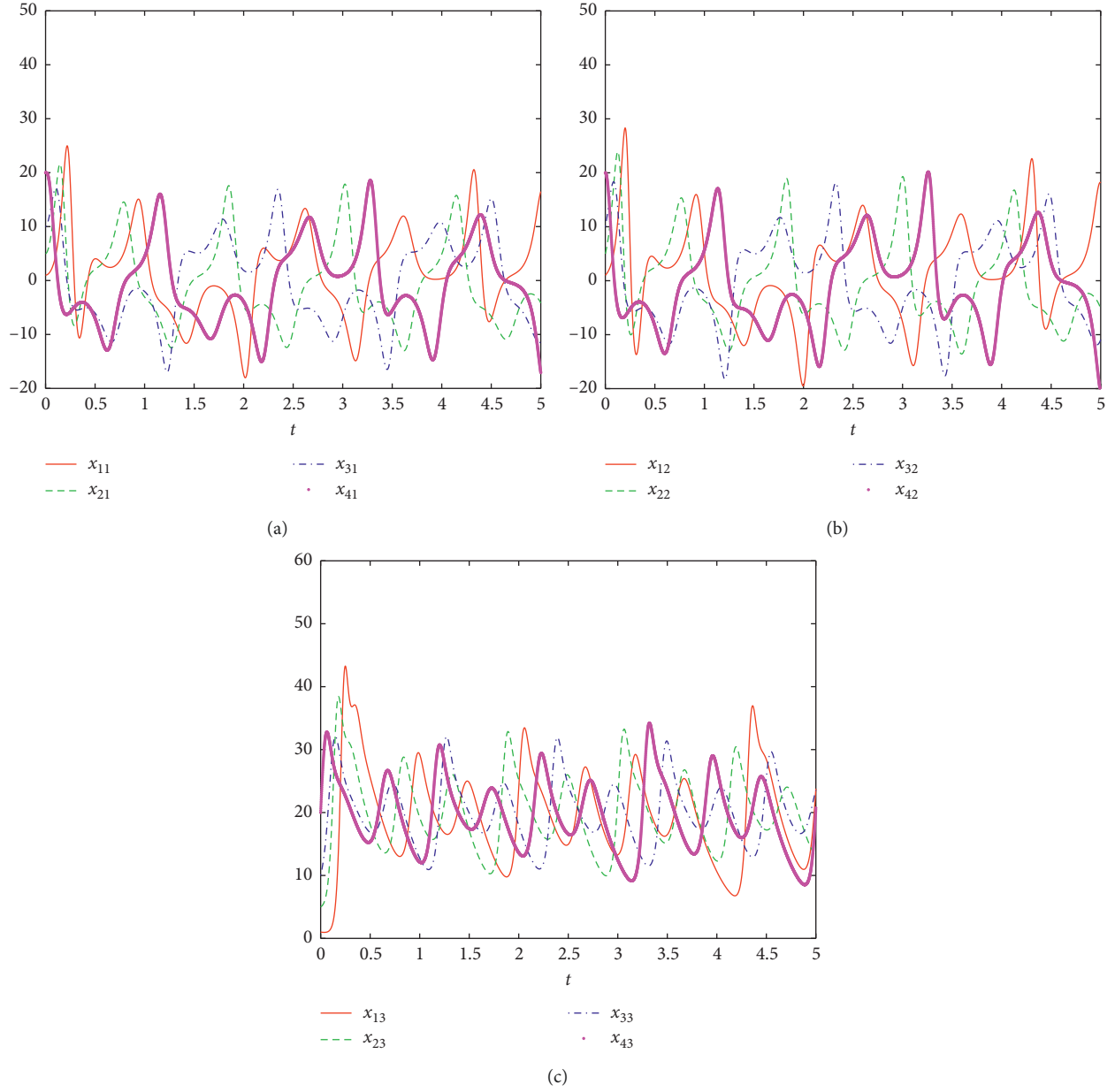


FIGURE 2: The graph of synchronization when the coupling parameters are all zero. (a) x_{11} , x_{21} , x_{31} and x_{41} vs. t . (b) x_{12} , x_{22} , x_{32} and x_{42} vs. t . (c) x_{13} , x_{23} , x_{33} and x_{43} vs. t .

$$\begin{aligned}
 & (A + H_{x_1, x_2} - (D_1 - D'_1))^T P + P(A + H_{x_1, x_2} - (D_1 - D'_1)) + \lambda_1 I \\
 & = \begin{pmatrix} -2p_1 \left(a + d_{11} - d'_{11} - \frac{\lambda_1}{2p_1} \right) & p_1 a - p_2 x_{13} & p_3 x_{12} \\ p_1 a - p_2 x_{13} & 2p_2 \left(c - d_{12} + d'_{12} + \frac{\lambda_1}{2p_2} \right) & (p_3 - p_2) x_{21} \\ p_3 x_{12} & (p_3 - p_2) x_{21} & -2p_3 \left(b + d_{13} - d'_{13} - \frac{\lambda_1}{2p_3} \right) \end{pmatrix}. \tag{19}
 \end{aligned}$$

According to the basic algebraic theory, the matrix (19) is negative definite as long as

$$\Delta_1 = -2p_1 \left(a + d_{11} - d'_{11} - \frac{\lambda_1}{2p_1} \right) < 0, \quad (20)$$

$$\Delta_2 = \begin{vmatrix} -2p_1 \left(a + d_{11} - d'_{11} - \frac{\lambda_1}{2p_1} \right) & p_1 a - p_2 x_{13} \\ p_1 a - p_2 x_{13} & 2p_2 \left(c - d_{12} + d'_{12} + \frac{\lambda_1}{2p_2} \right) \end{vmatrix} \quad (21)$$

$$= -4p_1 p_2 \cdot \left(a + d_{11} - d'_{11} - \frac{\lambda_1}{2p_1} \right) \left(c - d_{12} + d'_{12} + \frac{\lambda_1}{2p_2} \right) - (p_1 a - p_2 x_{13})^2 > 0,$$

$$\Delta_3 = \begin{vmatrix} -2p_1 \left(a + d_{11} - d'_{11} - \frac{\lambda_1}{2p_1} \right) & p_1 a - p_2 x_{13} & p_3 x_{12} \\ p_1 a - p_2 x_{13} & 2p_2 \left(c - d_{12} + d'_{12} + \frac{\lambda_1}{2p_2} \right) & (p_3 - p_2) x_{21} \\ p_3 x_{12} & (p_3 - p_2) x_{21} & -2p_3 \left(b + d_{13} - d'_{13} - \frac{\lambda_1}{2p_3} \right) \end{vmatrix}$$

$$= -2p_3 \cdot \left(b + d_{13} - d'_{13} - \frac{\lambda_1}{2p_3} \right) \Delta_2 - (p_3 x_{12})^2 \cdot [2p_2 (c - d_{12} + d'_{12} + \lambda_1)] + (p_3 - p_2) x_{21} \cdot [(2p_1 (a + d_{11} - d'_{11}) - \lambda_1) \cdot (p_3 - p_2) x_{21} + 2p_3 x_{12} (p_1 a - p_2 x_{13})] < 0. \quad (22)$$

From equations (20)–(22), we can get

$$\begin{cases} d_{11} - d'_{11} > -a + \frac{\lambda_1}{2p_1}, \\ d_{12} - d'_{12} > \frac{-(p_1 a - p_2 x_{13})^2}{4p_1 p_2 \cdot (a + d_{11} - d'_{11} - (\lambda_1/2p_1))} + c + \frac{\lambda_1}{2p_2}, \\ d_{13} - d'_{13} > -b + \frac{\lambda_1}{2p_3} - \frac{p_3 x_{12}^2 \cdot [2p_2 (c - d_{12} + d'_{12}) + \lambda_1]}{2\Delta_2} \\ \quad + \frac{(p_3 - p_2) x_{21} \cdot [(2p_1 (a + d_{11} - d'_{11}) - \lambda_1) (p_3 - p_2) x_{21} + 2p_3 x_{12} (p_1 a - p_2 x_{13})]}{2p_3 \Delta_2}. \end{cases} \quad (23)$$

The synchronization can be achieved easily as long as the inequalities (23) holds, i.e., we need to choose the appropriate

coupling parameters d_{ij} and d'_{ij} , with $i = 1, 2, 3$ and $j = 1, 2, 3$.

For convenience, let the matrix $p_2 = p_3$, then we have

$$\begin{cases} d_{11} - d'_{11} > -a + \frac{\lambda_1}{2p_1}, \\ d_{12} - d'_{12} > \frac{-(p_1 a - p_2 x_{13})^2}{4p_1 p_2 \cdot (a + d_{11} - d'_{11} - (\lambda_1/2p_1))} + c + \frac{\lambda_1}{2p_2}, \\ d_{13} - d'_{13} > -b + \frac{\lambda_1}{2p_3} - \frac{p_3 x_{12}^2 \cdot [2p_2 (c - d_{12} + d'_{12}) + \lambda_1]}{2\Delta_2}. \end{cases} \quad (24)$$

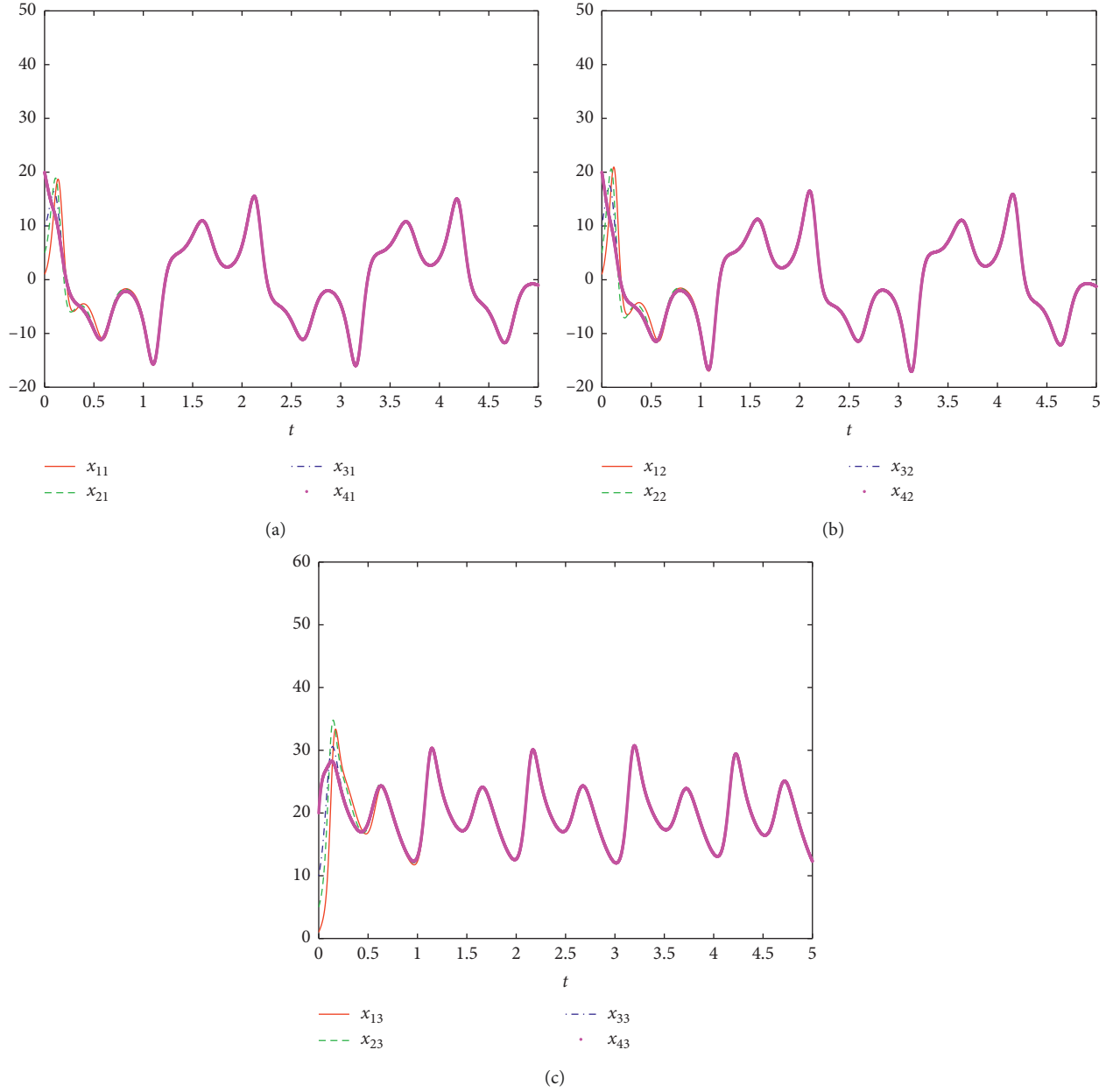


FIGURE 3: The graph of synchronization. (a) x_{11} , x_{21} , x_{31} and x_{41} vs. t . (b) x_{12} , x_{22} , x_{32} and x_{42} vs. t . (c) x_{13} , x_{23} , x_{33} and x_{43} vs. t .

In a similar way, we can get the following two inequalities:

$$\begin{cases} d_{21} - d'_{21} > -a + \frac{\lambda_2}{2p_1}, \\ d_{22} - d'_{22} > \frac{-(p_1 a - p_2 x_{23})^2}{4p_1 p_2 \cdot (a + d_{21} - d'_{21} - (\lambda_2/2p_1))} + c + \frac{\lambda_2}{2p_2}, \\ d_{23} - d'_{23} > -b + \frac{\lambda_2}{2p_3} - \frac{p_3 x_{22}^2 \cdot [2p_2(c - d_{22} + d'_{22}) + \lambda_2]}{2\Delta_2'} \end{cases} \quad (25)$$

$$\begin{cases} d_{31} - d'_{31} > -a + \frac{\lambda_3}{2p_1}, \\ d_{32} - d'_{32} > \frac{-(p_1 a - p_2 x_{33})^2}{4p_1 p_2 \cdot (a + d_{31} - d'_{31} - (\lambda_3/2p_1))} + c + \frac{\lambda_3}{2p_2}, \\ d_{33} - d'_{33} > -b + \frac{\lambda_3}{2p_3} - \frac{p_3 x_{32}^2 \cdot [2p_2(c - d_{32} + d'_{32}) + \lambda_3]}{2\Delta_2''} \end{cases} \quad (26)$$

where $\Delta_2' = -4p_1 p_2 \cdot (a + d_{21} - d'_{21} - (\lambda_2/2p_1))(c - d_{22} + d'_{22} + (\lambda_2/2p_2)) - (p_1 a - p_2 x_{23})^2$, and $\Delta_2'' = -4p_1 p_2 \cdot (a + d_{31} - d'_{31} - (\lambda_3/2p_1))(c - d_{32} + d'_{32} + (\lambda_3/2p_2)) - (p_1 a - p_2 x_{33})^2$.

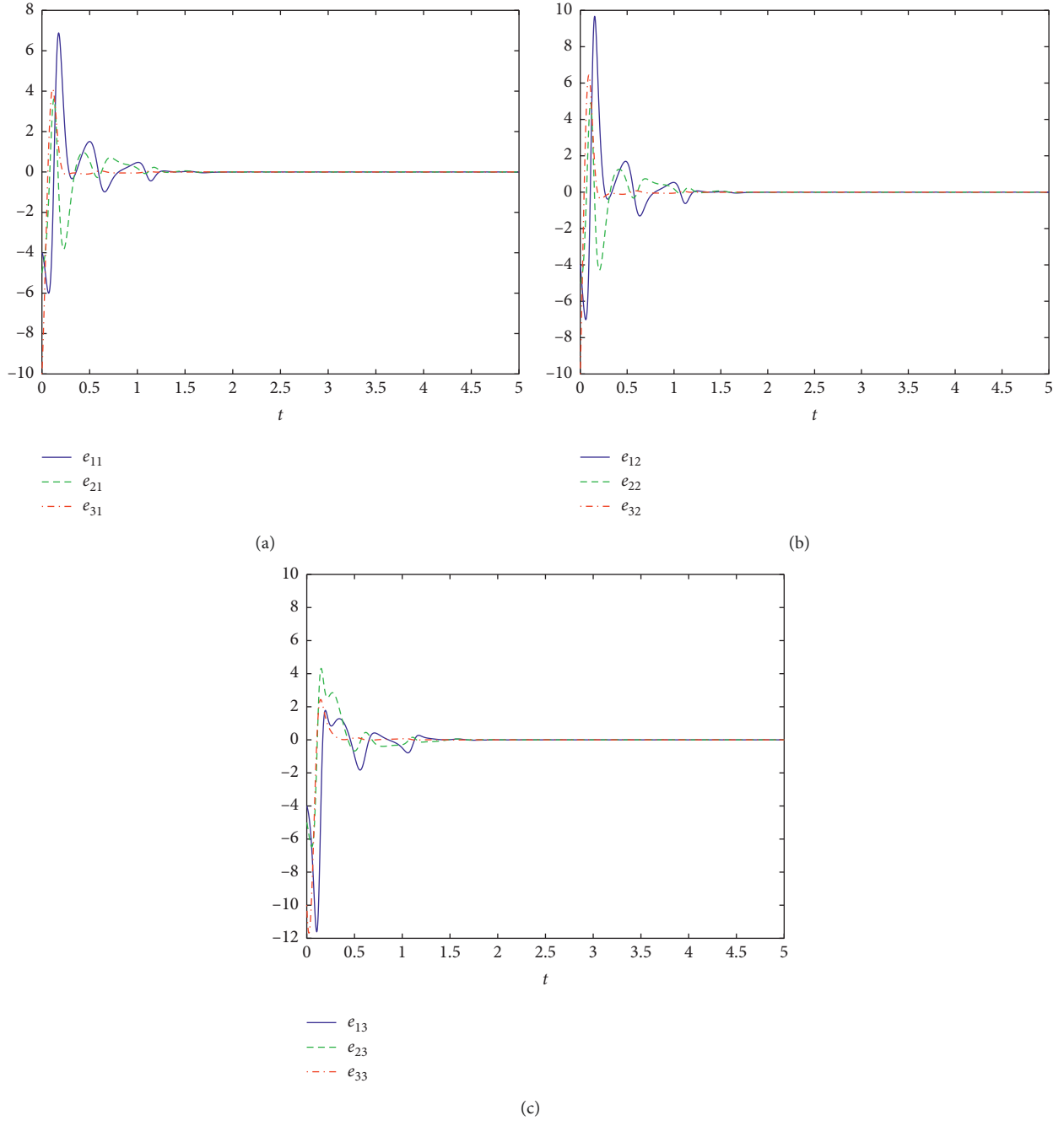


FIGURE 4: The errors of synchronization. (a) e_{11} , e_{21} and e_{31} vs. t . (b) e_{12} , e_{22} and e_{32} vs. t . (c) e_{13} , e_{23} and e_{33} vs. t .

The following numerical simulations are presented to demonstrate the effectiveness of our idea. Let $a = 36$, $b = 3$, $c = 20$, $P = \text{diag}\{1, 1, 1\}$. $\lambda_j = 60$, with $j = 1, 2, 3$. For the purpose of satisfying above inequalities (24)–(26), the coupling parameters are set as $d_{11} = d_{12} = d_{13} = 10$, $d'_{11} = d'_{12} = d'_{13} = 5$, $d_{21} = d_{22} = d_{23} = 5$, $d'_{21} = d'_{22} = d'_{23} = 5$, $d_{31} = d_{32} = d_{33} = 1$, $d'_{31} = d'_{32} = d'_{33} = -10$. The corresponding numerical results are illustrated in Figures 3 and 4. Figure 3 indicates that the trajectory of 4 Lü systems can be synchronized with each other. Figure 4 illustrates that the errors $e_1 = (e_{11}, e_{12}, e_{13})^T$, $e_2 = (e_{21}, e_{22}, e_{23})^T$, $e_3 = (e_{31}, e_{32},$

$e_{33})^T$ are finally stabilized to 0 as $t \rightarrow \infty$, i.e., the synchronization for 4 cascade-coupled Lü systems is realized.

Remark 4. When fixing the above coupling parameters except d_{11} , then we obtain $d_{11} > -1$. Further, we select $d_{11} \in (-10, 40)$ to observe the nature of the dynamical state of system (13) before and after synchronization. Here, we note that the largest Lyapunov exponent of system (13) is always greater than zero, which demonstrates that system (13) operates in chaotic state within a large range of coupling parameters (Figure 5).

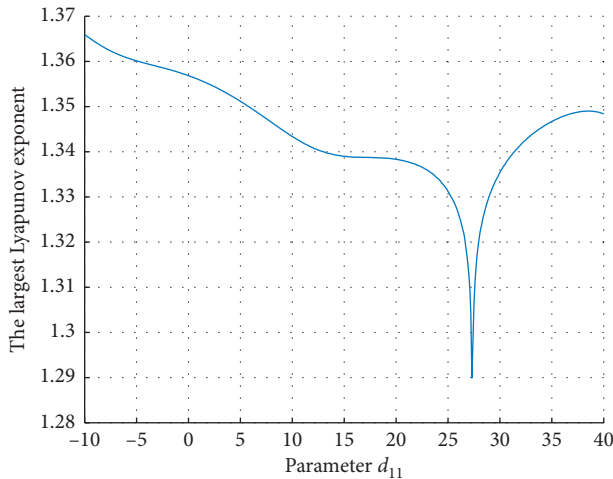


FIGURE 5: The largest Lyapunov exponent of system (13).

4. Conclusions

Recently, the chaos synchronization has been a subject of increasing research interest due to its potential application in fields of secure communication, signal processing, and life sciences. Numerous researchers have extensively explored the synchronization of two chaotic systems. This paper firstly proposes cascade-coupled synchronization of n ($n \geq 2$) chaotic systems, which is proved by rigorous mathematical analysis. Based on Lyapunov stability theory, a general condition is presented and applied to 4 Lü systems. This validates the effectiveness of our idea and then motivates us to develop cascade synchronization in different cases, such as complex chaotic systems, fractional-order chaotic systems, and time-delayed chaotic systems. Moreover, the other coupling parameter types are also worthy of further investigation.

Data Availability

The data used to support the findings of this study are available from the corresponding author upon request.

Conflicts of Interest

The authors declare that there are no conflicts of interest regarding the publication of this paper.

Acknowledgments

This work was supported by the Fundamental Research Funds for the Central Universities (lzujbky-2019-91).

References

- [1] L. M. Pecora and T. L. Carroll, "Synchronization in chaotic systems," *Physical Review Letters*, vol. 64, no. 8, pp. 821–824, 1990.
- [2] J. Liu, Z. Wang, M. Shu, F. Zhang, S. Leng, and X. Sun, "Secure communication of fractional complex chaotic systems based on fractional difference function synchronization," *Complexity*, vol. 2019, Article ID 7242791, 10 pages, 2019.
- [3] S. A. Rahman, M. Zribi, and N. Smaoui, "Secure communications based on the projective synchronization of four-dimensional hyperchaotic systems," *Mathematical Problems in Engineering*, vol. 2019, Article ID 2491850, 16 pages, 2019.
- [4] W. Tan, F. Jiang, C. Huang, and L. Zhou, "Synchronization for a class of fractional-order hyperchaotic system and its application," *Complexity*, vol. 2012, Article ID 974639, 11 pages, 2012.
- [5] H. Yau, Y. Pu, and S. Li, "An FPGA-based PID controller design for chaos synchronization by evolutionary programming," *Discrete Dynamics in Nature and Society*, vol. 2011, Article ID 516031, 11 pages, 2011.
- [6] A. S. Pikovsky, M. G. Rosenblum, G. V. Osipov, and J. Kurths, "Phase synchronization of chaotic oscillators by external driving," *Physica D: Nonlinear Phenomena*, vol. 104, no. 3–4, pp. 219–238, 1997.
- [7] D. Xu and Z. Li, "Controlled projective synchronization in nonpartially-linear chaotic systems," *International Journal of Bifurcation and Chaos*, vol. 12, no. 6, pp. 1395–1402, 2002.
- [8] X.-S. Yang, "On the existence of generalized synchronizer in unidirectionally coupled systems," *Applied Mathematics and Computation*, vol. 122, no. 1, pp. 71–79, 2001.
- [9] A. Ouannas, X. Wang, V. T. Wang, and T. Ziar, "Dynamic analysis of complex synchronization schemes between integer order and fractional order chaotic systems with different dimensions," *Complexity*, vol. 2017, Article ID 4948392, 12 pages, 2017.
- [10] P. Li, J. Du, S. Li, and Y. Zheng, "Modulus synchronization of a novel hyperchaotic real system and its corresponding complex system," *IEEE Access*, vol. 7, pp. 109577–109584, 2019.
- [11] J. Chen, J. Sun, M. Chi, and X.-M. Cheng, "A novel scheme adaptive hybrid dislocated synchronization for two identical and different memristor chaotic oscillator systems with uncertain parameters," *Abstract and Applied Analysis*, vol. 2014, Article ID 675840, 10 pages, 2014.
- [12] J. Sun, Y. Shen, and X. Zhang, "Modified projective and modified function projective synchronization of a class of real nonlinear systems and a class of complex nonlinear systems," *Nonlinear Dynamics*, vol. 78, no. 3, pp. 1755–1764, 2014.
- [13] W. Kinzel, A. Englert, and I. Kanter, "On chaos synchronization and secure communication," *Philosophical Transactions of the Royal Society A—Mathematical Physical and Engineering Sciences*, vol. 368, no. 1911, pp. 379–389, 2010.
- [14] F. Liu, X. Zang, and J. Song, "Anti-synchronism of the bidirectional coupled chaotic system," *Acta Physica Sinica*, vol. 58, no. 6, pp. 3765–3771, 2009.
- [15] S. Kuntanapreeda, "Synchronization of uncertain fractional-order hyperchaotic systems via unidirectional linear error feedback coupling scheme," *Journal of Chaos*, vol. 2013, Article ID 512403, 6 pages, 2013.
- [16] Z.-M. Ge and Y.-S. Chen, "Adaptive synchronization of unidirectional and mutual coupled chaotic systems," *Chaos, Solitons & Fractals*, vol. 26, no. 3, pp. 881–888, 2005.
- [17] J. M. Cruz, M. Rivera, and P. Parmananda, "Chaotic synchronization under unidirectional coupling: numerics and experiments," *The Journal of Physical Chemistry A*, vol. 113, no. 32, pp. 9051–9056, 2009.
- [18] Y. Yu and S. Zhang, "The synchronization of linearly bidirectional coupled chaotic systems," *Chaos, Solitons & Fractals*, vol. 22, no. 1, pp. 189–197, 2004.
- [19] M. A. Khan and S. Poria, "Projective synchronization of chaotic systems with bidirectional nonlinear coupling," *Pramana*, vol. 81, no. 3, pp. 395–406, 2013.

- [20] Y. Yu, "The synchronization for time-delay of linearly bi-directional coupled chaotic system," *Chaos, Solitons & Fractals*, vol. 33, no. 4, pp. 1197–1203, 2007.
- [21] G. Sivaganesh, A. Arulgnanam, and A. N. Seethalakshmi, "Numerical studies on the synchronization of a network of mutually coupled simple chaotic systems," in *Proceedings of the Conference on Nonlinear Systems and Dynamics, (CNSD)*, pp. 95–99, Kanpur, India, September 2019.
- [22] T. L. Carroll and L. M. Pecora, "Cascading synchronized chaotic systems," *Physica D: Nonlinear Phenomena*, vol. 67, no. 1–3, pp. 126–140, 1993.
- [23] H.-L. An and Y. Chen, "A function cascade synchronization method with unknown parameters and applications," *Chinese Physics B*, vol. 17, no. 1, pp. 98–104, 2008.
- [24] H.-L. An and Y. Chen, "The function cascade synchronization method and applications," *Communications in Nonlinear Science and Numerical Simulation*, vol. 13, no. 10, pp. 2246–2255, 2008.

Research Article

Bursting and Synchronization of Coupled Neurons under Electromagnetic Radiation

Xiaoyu Hu ¹ and Chongxin Liu²

¹*School of Electronics and Information, Northwestern Polytechnical University, Xi'an 710072, China*

²*School of Electrical Engineering, Xi'an Jiaotong University, Xi'an 710049, China*

Correspondence should be addressed to Xiaoyu Hu; huxiaoyucool@163.com

Received 12 May 2019; Revised 11 July 2019; Accepted 6 August 2019; Published 4 December 2019

Guest Editor: Lazaros Moysis

Copyright © 2019 Xiaoyu Hu and Chongxin Liu. This is an open access article distributed under the Creative Commons Attribution License, which permits unrestricted use, distribution, and reproduction in any medium, provided the original work is properly cited.

Bursting is an important firing activity of neurons, which is caused by a slow process that modulates fast spiking activity. Based on the original second-order Morris-Lecar neuron model, an improved third-order Morris-Lecar neuron model can produce bursting activity is proposed, in which the effect of electromagnetic radiation is considered as a slow process and the original equation of Morris-Lecar neuron model as a fast process. Extensive numerical simulation results show that the improved neuron model can produce different types of bursting, and bursting activity shows a deep dependence on system parameters and electromagnetic radiation parameters. In addition, synchronization transitions of identical as well as no-identical coupled third-order Morris-Lecar neurons are studied, the results show that identical coupled neurons experience a complex synchronization process and reach complete synchronization finally with the increase of coupling intensity. For no-identical coupled neurons, only anti-phase synchronization and in-phase synchronization can be reached. The studies of bursting activity of single neuron and synchronization transition of coupled neurons have important guiding significance for further understanding the information processing of neurons and collective behaviors in neuronal network under electromagnetic radiation environment.

1. Introduction

The biological or human neural system is usually composed of millions of neurons, which can generate, transmit, receive, and process information by firing various types of electrical activities. Since the pioneering work of Hodgkin and Huxley [1], many models have been proposed for modelling and simulating the electrical activities of a neuron [2–9]. For a neuron, spiking and bursting are two major categories, and they may be periodic motion or chaotic motion. Indeed, bursting is considered as neuron activity alternates between a quiescent state and repetitive spiking, and it is a dynamical consequence of fast/slow dynamics. Bursting is an important firing pattern, and it has been confirmed that neurons in different regions of brain produce bursting activities [10].

Neurons are sensitivity to many external factors, and electrical activities of a neuron and collective behaviours in neuronal network will be changed under certain conditions. Time delay [11–17], noise [18, 19], and network topology [20–23] are common factors being considered to investigate firing

behaviours of neuron and collective behaviours in neuronal network. It is worth noting that electromagnetic radiation is another one cannot be ignored. With the development of modern industry, wide utilizations of electric equipment make neural system are exposed to an environment full of electromagnetic radiation, which has a great influence on the dynamics of a single neuron and network of neurons. In Ref. [24], Wang et al. suggested that the strong external electromagnetic field facilitates the neuron firing action potentials and enhances the mean firing rate of the network, but disrupts the synchronicity of the activities of the neural network. In Ref. [25], Li et al. developed a mathematical model to describe the effect of electromagnetic radiation, the results show that electrical activities of a single neuron can be suppressed by electromagnetic radiation, and spatiotemporal patterns in neuronal network are also suppressed from the stable propagating wave state to a homogeneous resting state. Rebertson et al. [26] argued that low-frequency pulsed electromagnetic field exposure can alter neuroprocessing in humans. In Ref. [27], a small Hopfield neural network with the electromagnetic radiation

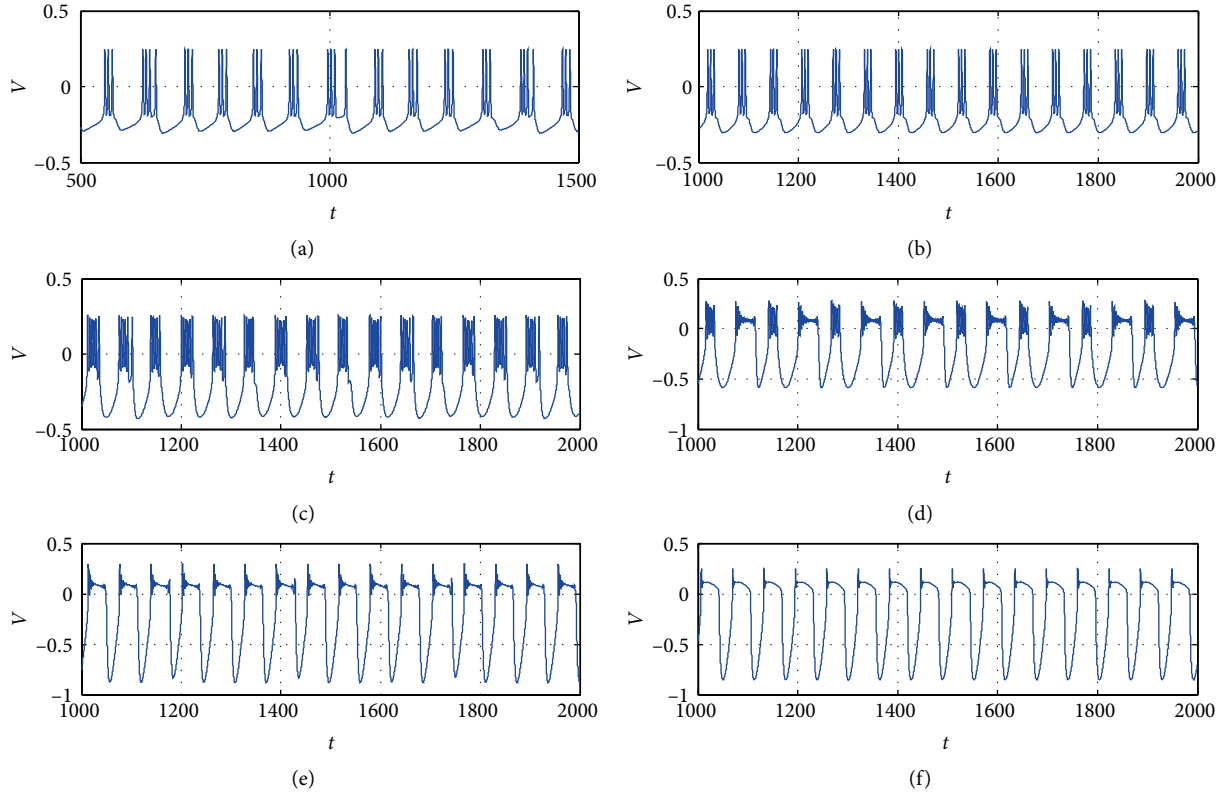


FIGURE 1: Sampled time series for membrane potential when the intensity of external forcing currents is chosen as different values with fixed angular frequency $\omega = 0.1$. (a) $I = 0.001$, (b) $I = 0.005$, (c) $I = 0.05$, (d) $I = 0.1$, (e) $I = 0.2$, and (f) $I = 0.5$. The effect of electromagnetic radiation is considered by setting $k_1 = 0.2$, $k_2 = 0.15$, and $k_3 = 0.15$.

being considered is constructed, in which the previous steady neural network can present abundant chaotic dynamics, and hidden attractors can be observed.

Memory is a natural characteristic of neuron, and it has been considered in studies from neuron models to collective behaviours in neuronal network recently. For example, references [28–30] have proved that the ionic channels of neuron models, e.g., Hodgkin–Huxley and Morris-Lecar neuron model, have memory effect and they can be substituted by first-order or second-order memristors. Moreover, memristive relation is also used to stress the memory effect in some memristor-based neural network [31–33]. Indeed, memristor is an effective element to characteristic the memory effect in neuron and network of neurons. From this point of view, the effect of electromagnetic radiation on neuron can be considered as a variation of magnetic flux, and the flux-controlled memristor is available to represent the memory effect of magnetic flux. As a result, Ma et al. [34–36] proposed several models to describe the effect of electromagnetic radiation on the electrical activities of neuron by using magnetic flux, in which a memristor-like feedback is employed to realize coupling between magnetic flux and membrane potential. It is found that multiple modes of spiking activities can be observed. Moreover, synchronization, noise effect, and spatiotemporal dynamics in neuron and neural networks under electromagnetic radiation were also investigated [37–41]. The effect of electromagnetic radiation can be described by time-varying magnetic flux, the coupling of electromagnetic field between

neurons can be described by exchange of magnetic flux as well, which results in another effective way for coupling between neurons, i.e., field coupling. In Refs. [42–44], field coupling rather than synaptic coupling is considered as a coupling mode between neurons and neural networks, it is found that multiple modes of synchronization can be observed from coupled neurons or neural networks.

In this paper, we propose an improved Morris-Lecar neuron model with electromagnetic radiation being considered, in which the fluctuation of electromagnetic radiation is described by using magnetic flux and considered as a slow subsystem. Unlike previous models, multiple modes of bursting activities are observed. Furthermore, synchronization transitions in coupled identical bursting neurons as well as no-identical bursting neurons are studied. The organization of this paper is as follows. In Section 2, the model setting and description is introduced. In Section 3, numerical results are discussed and analysed carefully. Section 4 summarizes and concludes this paper.

2. Model Setting and Description

Bursting activities are results of fast/slow dynamics, and they cannot be observed in original two-dimensional Morris-Lecar neuron model under constant external forcing current. Researchers [5, 45–47] have explored several improved Morris-Lecar neuron model, in which external forcing current

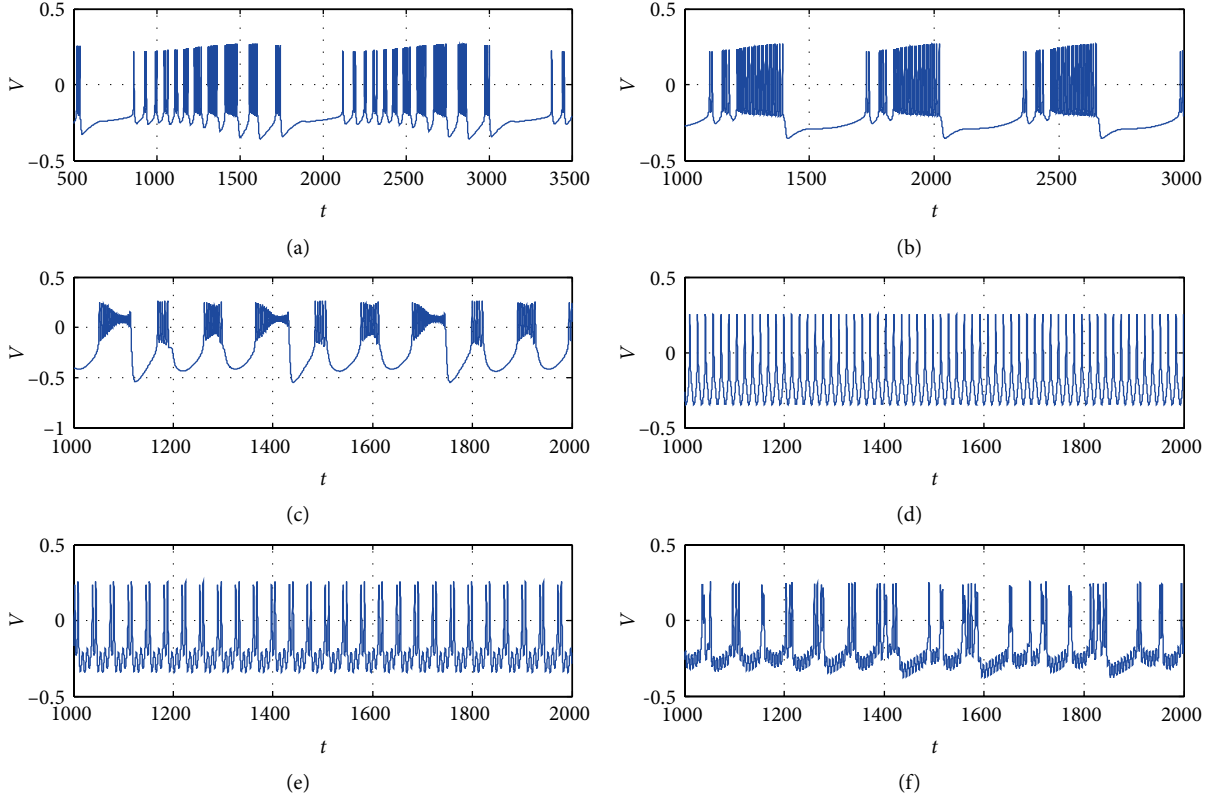


FIGURE 2: Sampled time series for membrane potential when the angular frequency of external forcing currents is chosen as different values with fixed intensity $I = 0.05$. (a) $\omega = 0.005$, (b) $\omega = 0.01$, (c) $\omega = 0.06$, (d) $\omega = 0.4$, (e) $\omega = 0.7$, and (f) $\omega = 1.0$. The effect of electromagnetic radiation is considered by setting $k_1 = 0.2$, $k_2 = 0.15$, and $k_3 = 0.15$.

is considered as a varied state variable with a very slow rate, and several types of bursting are obtained. Inspired by Refs. [35, 48–50], electromagnetic radiation is considered when improved Morris-Lecar neuron model is constructed, in which the effect of electromagnetic radiation is regarded as a slow subsystem and two-dimensional Morris-Lecar neuron model as a fast subsystem. As a result, the improved Morris-Lecar neuron model is described as follows.

$$\begin{aligned} \dot{V} &= -g_{Ca}M_{\infty}(V)(V - V_{Ca}) - g_KW(V - V_K) \\ &\quad - g_l(V - V_l) - I_{st} + k_1(\alpha + \beta\varphi^2)V, \\ \dot{W} &= \lambda(V)(W_{\infty}(V) - W), \\ \dot{\varphi} &= k_2V + k_3\varphi_{ext}, \end{aligned} \quad (1)$$

where

$$\begin{aligned} M_{\infty}(V) &= \frac{1}{2} \left(1 + \tanh \frac{V - V_1}{V_2} \right), \\ W_{\infty}(V) &= \frac{1}{2} \left(1 + \tanh \frac{V - V_3}{V_4} \right), \\ \lambda(V) &= \frac{1}{3} \cosh \left(\frac{V - V_3}{2V_4} \right). \end{aligned} \quad (2)$$

In this model, V represents membrane potential, W represents recovery variable, φ is magnetic flux which is a slower variable than V and W . V_{Ca} , V_K , and V_l are steady state potentials for calcium, potassium, and leak ion channels, respectively. $M_{\infty}(V)$ and $W_{\infty}(V)$ define the stable values of opening probability for calcium and potassium, where V_1 , V_2 , V_3 , and V_4 are

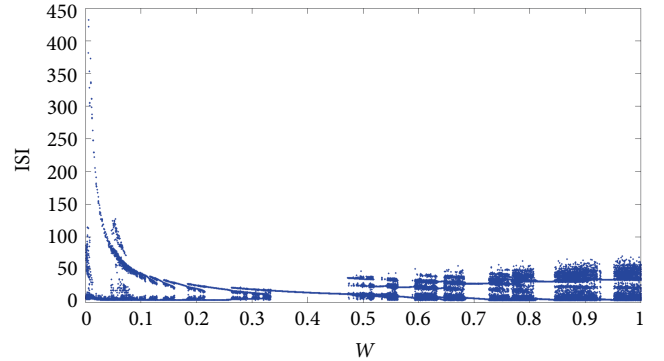


FIGURE 3: Bifurcation diagram of ISI by setting angular frequency ω as the bifurcation parameter with $I = 0.05$. The effect of electromagnetic radiation is considered by setting $k_1 = 0.2$, $k_2 = 0.15$, and $k_3 = 0.15$.

parameters of steady states. I_{st} is external forcing current and $I_{st} = I \sin(\omega t)$. The term $k_1(\alpha + \beta\varphi^2)V$ defines the feedback current on membrane potential when magnet flux is changed in media, and k_1 is the feedback gain. k_2 is a factor which describes the contribution of varied magnetic flux on the formation of membrane potential. $k_3\varphi_{ext}$ is considered as leakage magnet flux, and φ_{ext} is chosen as a constant value 0.2. The rest system parameter are selected as $g_{Ca} = 1.2$, $g_K = 2$, $g_l = 0.5$, $V_{Ca} = 1$, $V_l = -0.5$, $V_K = -0.7$, $V_1 = -0.01$, $V_2 = 0.15$, $V_3 = 0.1$, $V_4 = 0.05$, $\alpha = 0.1$, and $\beta = -0.09$.

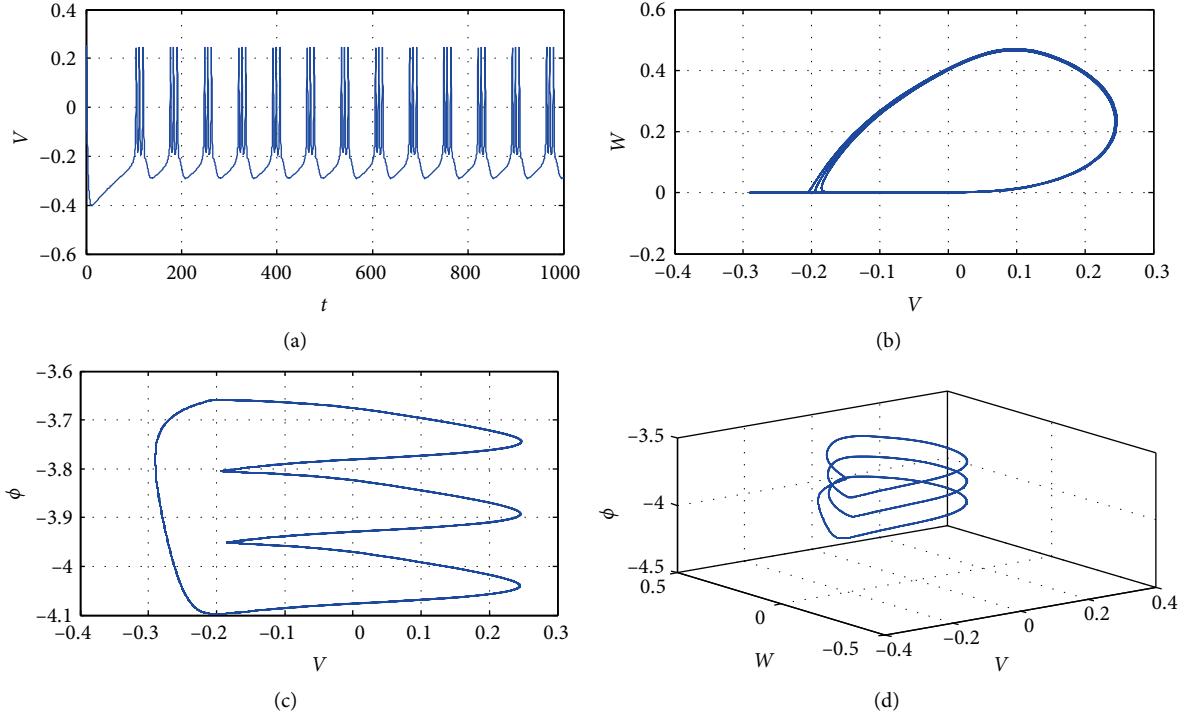


FIGURE 4: Sampled time series for membrane potential and phase diagrams when the system parameters are selected as $I = 0$, $k_1 = 0.2$, $k_2 = 0.15$, and $k_3 = 0.15$.

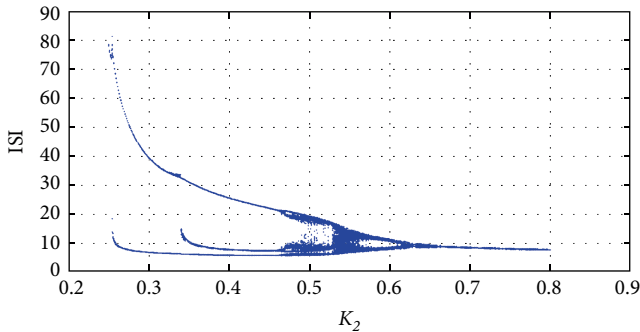


FIGURE 5: Bifurcation diagram of ISI by setting k_2 as the bifurcation parameter with $I = 0$, $k_1 = 0.2$, and $k_3 = 0.3$.

3. Numerical Results and Discussion

3.1 Bursting in Improved ML Neuron Model under Electromagnetic Radiation. In this section, fourth order Runge–Kutta algorithm is used with time step $h = 0.01$. The initial values are set as $(V_0, W_0, \phi_0) = (-0.1, 0, -2.5)$. At first, sampled time series for membrane potential are detected with different intensity of external forcing current, and system parameters and angular frequency are selected as $k_1 = 0.2$, $k_2 = 0.15$, $k_3 = 0.15$, and $\omega = 0.1$. The results are shown in Figure 1.

It is found that even a very small intensity of external forcing current can trigger bursting activities of neuron, and they can be either chaotic or periodic, as show in Figures 1(a)–1(c). Particularly, the model can present two types of burst alternately with appropriate intensity of external forcing current,

as shown in Figure 1(d). With the increase of external current intensity, the emerging type of bursting is stay behind. Furthermore, sampled time series for membrane potential are calculated with different angular frequency of external forcing currents being used, and the results are shown in Figure 2.

In numerical simulations, the intensity of external forcing current is fixed at $I = 0.05$, and the effect of electromagnetic radiation is considered by setting $k_1 = 0.2$, $k_2 = 0.15$, and $k_3 = 0.15$. When small angular frequency is used, the model presents a kind of cluster bursting, i.e., each cluster consist of several bursts which have different number of spikes, as shown in Figures 2(a) and 2(b). In Figure 2(c) it is worth noting that three types of burst emerge alternately when the angular frequency is selected as $\omega = 0.06$. Moreover, spiking, periodic bursting, and chaotic bursting can be also observed when angular frequency is chosen appropriately, as shown in Figures 2(d)–2(f), respectively. To better understand the effect of angular frequency on electrical activities of neurons, bifurcation analysis is carried out by calculating the interspike interval (ISI), and the results are shown in Figure 3. It is found that the neuron can present bursting behaviours in a large parameter region, and chaotic bursting, and periodic bursting emerge alternately with the increase of angular frequency.

In order to discern the effect of electromagnetic radiation, external forcing current is set as $I = 0$, and sampled time series for membrane potential and phase diagrams when the system parameters are selected $k_1 = 0.2$, $k_2 = 0.15$, and $k_3 = 0.15$ are shown in Figure 4. In Figure 4, period-3 bursting is obtained, and it belongs to a type of “Flod/Homoclinic bursting” according to the classification methods in Ref. [45]. To better understand the effect of system parameters on firing activities of

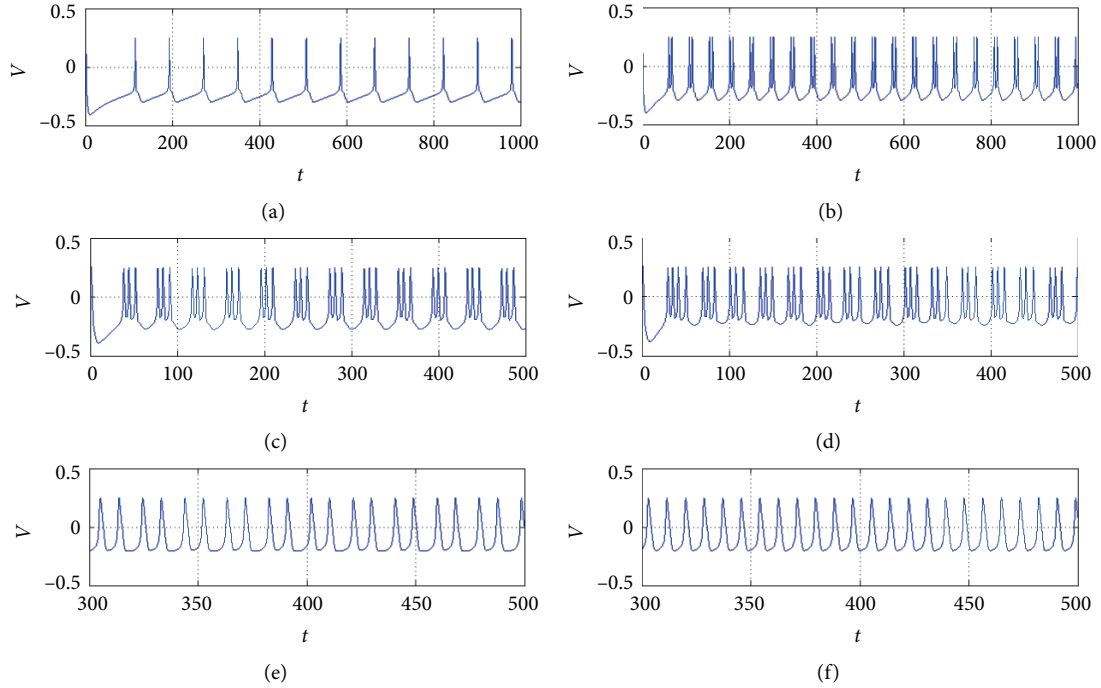


FIGURE 6: Sampled time series for membrane potential when k_2 are chosen as different values with $I = 0, k_1 = 0.2,$ and $k_3 = 0.3.$ (a) Spiking with $k_2 = 0.25,$ (b) period-2 bursting with $k_2 = 0.3,$ (c) period-3 bursting with $k_2 = 0.4,$ (d) chaotic bursting with $k_2 = 0.5,$ (e) period-2 bursting with $k_2 = 0.6,$ and (f) spiking with $k_2 = 0.7.$

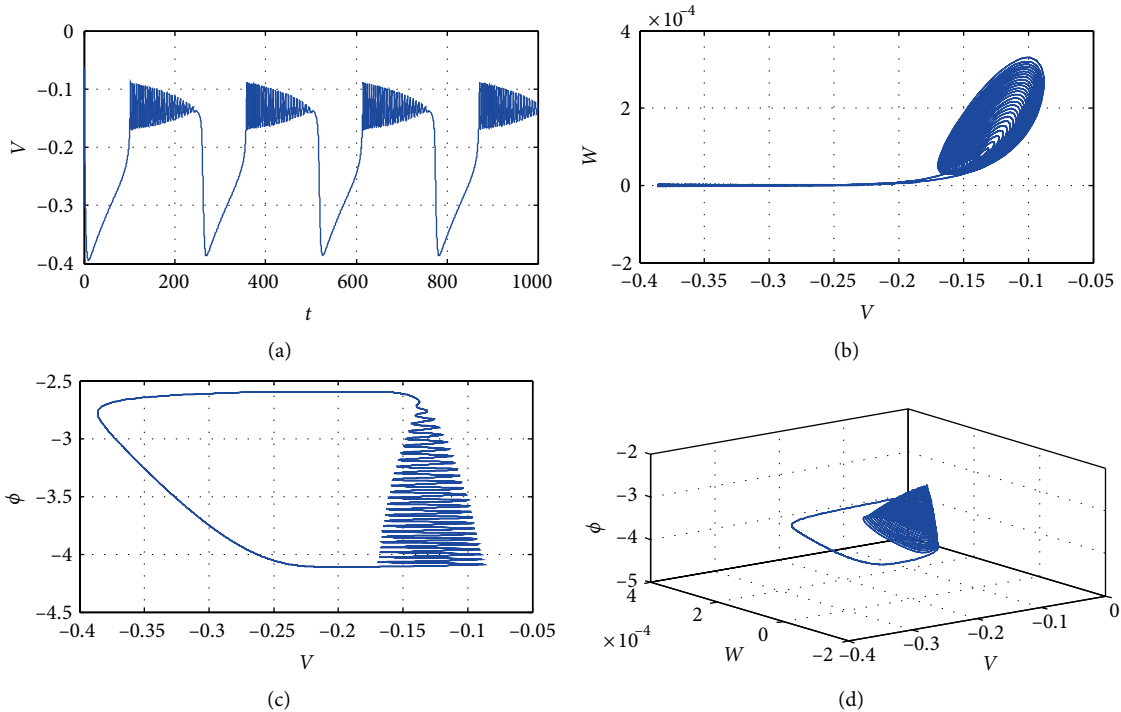


FIGURE 7: Sampled time series for membrane potential and phase diagrams when the system parameters are selected as $I = 0, k_1 = 0.2,$ $k_2 = 0.15, k_3 = 0.15,$ and $V_K = -300$ mV.

neuron, k_2 is selected as bifurcation parameter and bifurcation diagram is calculated, and the results are shown in Figure 5.

In Figure 5, it is found that each burst can have more spikes when k_2 is less than 0.46, and increased k_2 is accompanied by

a chaotic bursting activity. When parameter k_2 exceeds 0.63, only spiking activities can be observed. Particularly, the change of spike number in each burst with the increase of k_2 experiences a parameter region that chaotic bursting emerges.

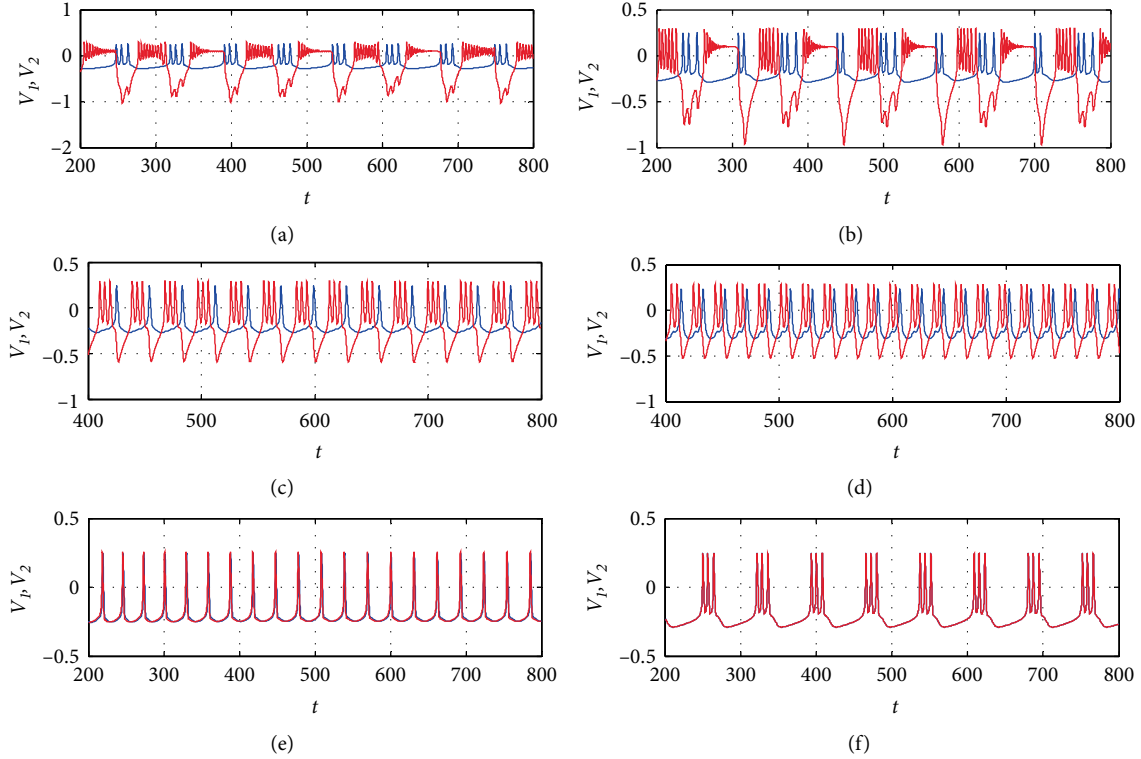


FIGURE 8: Synchronization transition of two identical coupled neurons with different coupling intensity values. (a) $g_s = 0.001$, (b) $g_s = 0.004$, (c) $g_s = 0.025$, (d) $g_s = 0.09$, (e) $g_s = 0.31$, and (f) $g_s = 1.0$. Initial conditions are selected as $(-0.1, 0, -2.5)$ and $(-0.2, 0, -2.5)$, respectively.

Sampled time series for membrane potential are calculated when k_2 are chosen as different values with $I = 0, k_1 = 0.2$, and $k_3 = 0.3$, and results are shown in Figure 6. In Figure 6, multiple period bursting and chaotic bursting are obtained with k_2 being selected carefully.

In addition, extensive numerical simulations have confirmed that different modes of bursting can be obtained when system parameters are chosen appropriately. For example, when $V_K = -300$ is selected, and the rest parameters are the same as that in Figure 4, a type of “Fold/Hopf bursting” [45] is observed. Sampled time series for membrane potential and phase diagrams are shown in Figure 7, it is obvious that the bursting is significantly different from that in Figure 4.

3.2 Synchronization in Coupled Bursting Neurons. In this subsection, synchronization problems are studied, and two electrically coupled bursting neurons are defined by

$$\begin{aligned}
 \dot{V}_1 &= -g_{Ca}M_\infty(V_1)(V_1 - V_{Ca}) - g_KW_1(V_1 - V_{K1}) \\
 &\quad - g_l(V_1 - V_l) - I_{st} + k_1(\alpha + \beta\varphi_1^2)V_1 + g_s(V_2 - V_1), \\
 \dot{W}_1 &= \lambda(V_1)(W_\infty(V_1) - W_1), \\
 \dot{\varphi}_1 &= k_2V_1 + k_3\varphi_{ext}, \\
 \dot{V}_2 &= -g_{Ca}M_\infty(V_2)(V_2 - V_{Ca}) - g_KW_2(V_2 - V_{K2}) \\
 &\quad - g_l(V_2 - V_l) - I_{st} + k_1(\alpha + \beta\varphi_2^2)V_2 + g_s(V_1 - V_2), \\
 \dot{W}_2 &= \lambda(V_2)(W_\infty(V_2) - W_2), \\
 \dot{\varphi}_2 &= k_2V_2 + k_3\varphi_{ext},
 \end{aligned} \tag{3}$$

where g_s is coupling strength, and the rest parameters are the same as that in Figures 4 and 7 except for V_{K1} and V_{K2} . The values of V_{K1} and V_{K2} determine the types of bursting of two neurons.

At first, synchronization transition of two identical coupled neurons is studied with $V_{K1} = V_{K2} = -0.7$, i.e., two coupled “Fold/Homoclinic bursting” neurons. The path to synchronization is shown in Figure 8 for different coupling strength. In Figure 8(a), two neurons present anti-phase bursting synchronization, in which neuron 1 shows period-3 bursting and neuron 2 shows two burst patterns alternately. For $g_s = 0.004$ in Figure 8(b), two neurons present anti-phase bursting synchronization, while neuron 1 shows chaotic bursting which is different from that in Figure 8(a). As g_s increases, such as in Figures 8(c) and 8(d), the two neurons show a phase-locked bursting synchronization, i.e., 1:3 and 1:2, respectively. As g_s further increases, nearly synchronization occurs with only one spike in a burst, as shown in Figure 8(e). When the coupling strength is large enough as in Figure 8(f), the two neurons have a complete bursting synchronization. Moreover, phase diagrams of membrane potentials for two identical coupled neurons with different coupling intensity values are detected in Figure 9.

Let $V_{K1} = -0.7$ and $V_{K2} = -300$, the two uncoupled neurons have different bursting types, i.e., “Fold/Homoclinic bursting” and “Fold/Homoclinic bursting” respectively, and the path to synchronization for two no-identical neurons is shown in Figure 10. When the values of coupling strength are small, the two neurons show anti-phase bursting

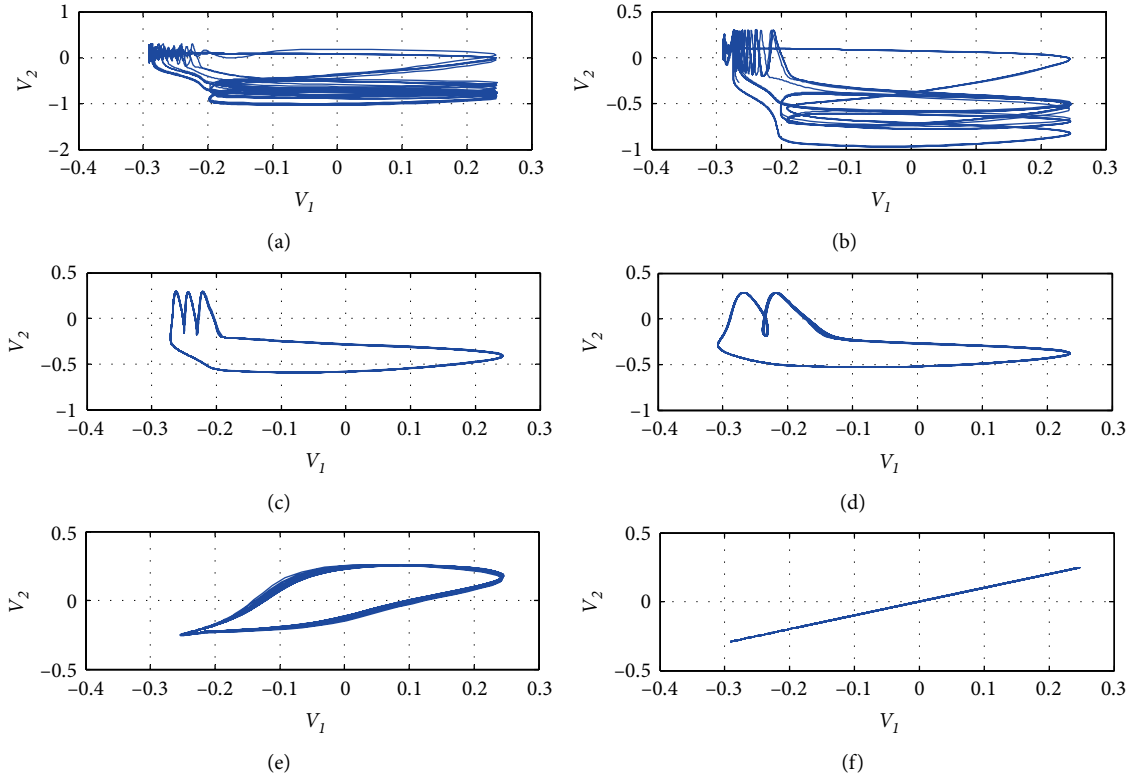


FIGURE 9: Phase diagrams of membrane potentials for two identical coupled neurons with different coupling intensity values. (a) $g_s = 0.001$, (b) $g_s = 0.004$, (c) $g_s = 0.025$, (d) $g_s = 0.09$, (e) $g_s = 0.31$, and (f) $g_s = 1.0$. Initial conditions are selected as $(-0.1, 0, -2.5)$ and $(-0.2, 0, -2.5)$, respectively.

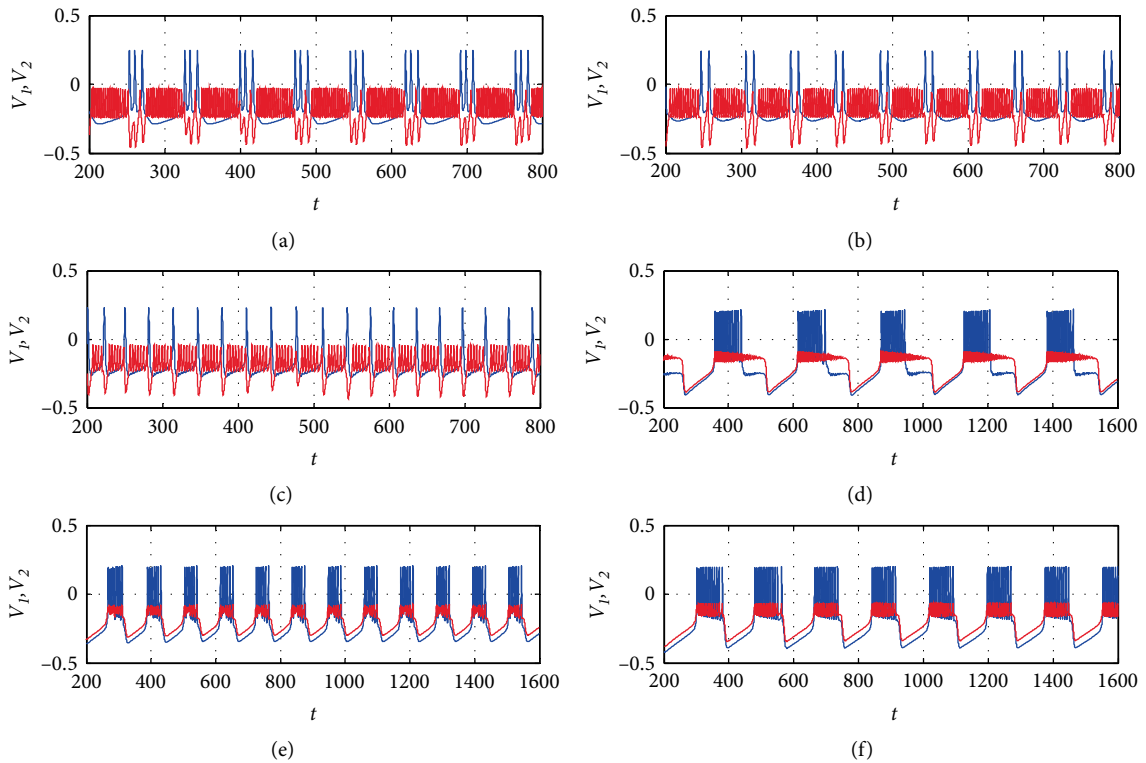


FIGURE 10: Synchronization transition of two nonidentical coupled neurons with different coupling intensity values. (a) $g_s = 0.01$, (b) $g_s = 0.03$, (c) $g_s = 0.15$, (d) $g_s = 0.5$, (e) $g_s = 0.7$, and (f) $g_s = 0.9$. Initial conditions are selected as $(-0.1, 0, -2.5)$ and $(-0.2, 0, -2.5)$, respectively.

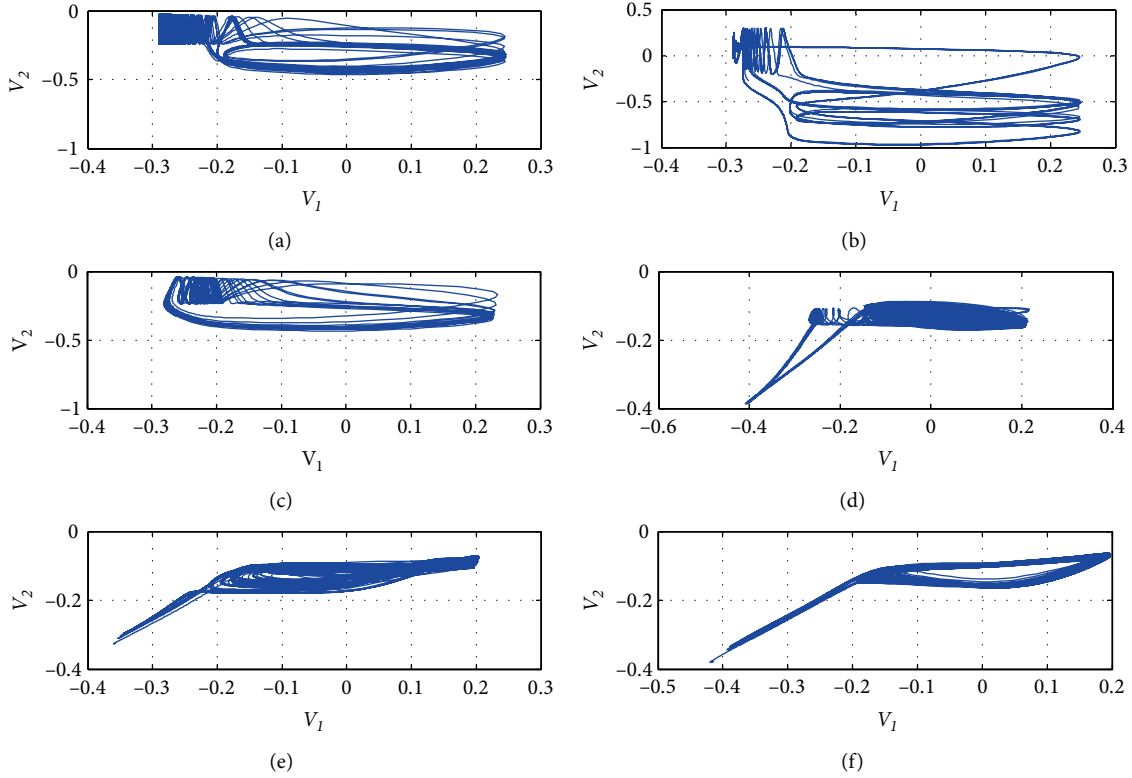


FIGURE 11: Phase diagrams of membrane potentials of two nonidentical coupled neurons with different coupling intensity values. (a) $g_s = 0.01$, (b) $g_s = 0.03$, (c) $g_s = 0.15$, (d) $g_s = 0.5$, (e) $g_s = 0.7$, and (f) $g_s = 0.9$. Initial conditions are selected as $(-0.1, 0, -2.5)$ and $(-0.2, 0, -2.5)$, respectively.

synchronization as shown in Figures 10(a)–10(c), respectively. It is worth noting that spikes in each burst for two neurons decrease as the values of coupling strength increase. When the coupling strength increases to $g_s = 0.5$ in Figure 10(d) the two neurons have an in-phase synchrony with their own natural bursting types. As the coupling strength further increases, the waveform for neuron 2 distorts as shown in Figure 10(e), and the two neurons reach in-phase bursting synchronization, in which the two neurons have different burst amplitude. Extensive numerical simulations have confirmed that the two non-identical coupled neurons cannot attain complete synchronization whatever the values of coupling strength are selected. Furthermore, synchronization transition of phase diagrams for two nonidentical coupled neurons with different coupling intensity values are detected, and the results are shown in Figure 11.

4. Conclusions

In this paper, an improved third-order Morris-Lecar neuron model is proposed with the effect of electromagnetic radiation being considered, in which the bursting activities can be produced. Extensive numerical simulation results show that bursting activities of the neuron shows a deep dependence on system parameters, external forcing current and electromagnetic radiation parameters. For certain parameters, the improved Morris-Lecar neuron model can present two typical modes of bursting, i.e., “Fold/Homoclinic

bursting” and “Fold/Hopf bursting”, which are studied through time series and phase diagrams. Furthermore, Synchronization transitions in two electrically coupled identical as well as non-identical neurons are studied. For the identical coupled neurons, the two neurons experience a complex path to synchronization, for example, anti-phase bursting synchronization, phase-locked bursting synchronization, and complete synchronization. For non-identical coupled neurons, the two neurons only can reach anti-phase synchronization and in-phase synchronization with appropriate coupling strengths.

Bursting is an important firing category of a neuron, which occurs in different regions of neural system in the brain. It has been observed experimentally that the synchronized firing modes during sleeping of human are a kind of bursting activities of neurons [10]. Researchers [51] also argued that some neurological disorders are associate with abnormal bursting firing activity of some specified neurons. In addition, human body is imposed into the environment full of electromagnetic field, and the electromagnetic radiation is getting stronger in modern society. It has been reported that electromagnetic radiation is highly related to neuronal pathological functions, e.g., heart disease, Alzheimer’s disease, and Parkinson’s disease [52, 53]. Therefore, it is very significant to study the effect of electromagnetic radiation on firing activities of neuron and collective behaviours in neuronal network, which will help us deepen the understanding of response mechanism of neural system to external environment.

Data Availability

The data used to support the findings of this study are available from the corresponding author upon request.

Conflicts of Interest

The authors declare that they have no conflicts of interest.

Acknowledgments

This work is partially supported by the Fundamental Research Funds for the Central Universities (Grant No. 3102018KY0308) and the National Nature Science Foundation of China (Grant No. 51877162).

References

- [1] A. L. Hodgkin, and A. F. Huxley, "A quantitative description of membrane current and its application to conduction and excitation in nerve," *The Journal of Physiology*, vol. 117, no. 4, pp. 500–544, 1952.
- [2] J. L. Hindmarsh, R. M. Rose, "A model of neural bursting using three couple first order differential equations," *Proceedings of the Royal Society B. Biological Sciences*, vol. 221, no. 1222, pp. 87–102, 1984.
- [3] C. Morris and H. Lecar, "Voltage oscillations in the barnacle giant muscle fiber," *Biophysical Journal*, vol. 35, no. 1, pp. 193–213, 1981.
- [4] J. Nagumo and S. Sato, "On a response characteristic of a mathematical neuron model," *Kybernetik*, vol. 10, no. 3, pp. 155–164, 1972.
- [5] E. M. Izhikevich, "Which model to use for cortical spiking neurons?," *IEEE Transactions on Neural Networks*, vol. 15, no. 5, pp. 1063–1070, 2004.
- [6] A. V. M. Herz, T. Gollisch, C. K. Machens, and D. Jaeger, "Modeling single-neuron dynamics and computations: a balance of detail and abstraction," *Science*, vol. 314, no. 5796, pp. 80–85, 2006.
- [7] H. Gu, B. Pan, G. Chen, and L. Duan, "Biological experimental demonstration of bifurcations from bursting to spiking predicted by theoretical models," *Nonlinear Dynamics*, vol. 78, no. 1, pp. 391–407, 2014.
- [8] J. L. Hindmarsh and R. M. Rose, "A model of the nerve impulse using two first-order differential equations," *Nature*, vol. 296, no. 5853, pp. 162–164, 1982.
- [9] H. Gu and B. Pan, "A four-dimensional neuronal model to describe the complex nonlinear dynamics observed in the firing patterns of a sciatic nerve chronic constriction injury model," *Nonlinear Dynamics*, vol. 81, no. 4, pp. 2107–2126, 2015.
- [10] D. A. McCormick and H. R. Feese, "Functional implications of burst firing and single spike activity in lateral geniculate relay neurons," *Neuroscience*, vol. 39, no. 1, pp. 103–113, 1990.
- [11] H. Wang, J. Ma, Y. Chen, and Y. Chen, "Effect of an autapse on the firing pattern transition in a bursting neuron," *Communications in Nonlinear Science and Numerical Simulation*, vol. 19, no. 9, pp. 3242–3254, 2014.
- [12] H. Wang, L. Wang, Y. Chen, and Y. Chen, "Effect of autaptic activity on the response of a Hodgkin-Huxley neuron," *Chaos: An Interdisciplinary Journal of Nonlinear Science*, vol. 24, no. 3, p. 033122, 2014.
- [13] Q. Wang, M. Perc, Z. Duan, and G. Chen, "Synchronization transitions on scale-free neuronal networks due to finite information transmission delays," *Physical Review E*, vol. 80, no. 2, 2009.
- [14] Q. Wang, Z. Duan, M. Perc, and G. Chen, "Synchronization transitions on small-world neuronal networks: Effects of information transmission delay and rewiring probability," *EPL (Europhysics Letters)*, vol. 83, no. 5, p. 50008, 2008.
- [15] X. L. Song, C. N. Wang, J. Ma, and J. Tang, "Transition of electric activity of neurons induced by chemical and electric autapses," *Science China Technological Sciences*, vol. 58, no. 6, pp. 1007–1014, 2015.
- [16] H. Gu and Z. Zhao, "Dynamics of time delay-induced multiple synchronous behaviors in inhibitory coupled neurons," *PLoS One*, vol. 10, no. 9, p. e0138593, 2015.
- [17] B. Jia, Y. Wu, D. He, B. Guo, and L. Xue, "Dynamics of transitions from anti-phase to multiple in-phase synchronizations in inhibitory coupled bursting neurons," *Nonlinear Dynamics*, vol. 93, no. 3, pp. 1599–1618, 2018.
- [18] Y. Gong, Y. Xie, X. Lin, and Y. Hao, "Non-Gaussian noise-optimized intracellular cytosolic calcium oscillations," *Biosystems*, vol. 103, no. 1, pp. 13–17, 2011.
- [19] B. Lindner, "Effects of noise in excitable systems," *Physics Reports*, vol. 392, no. 6, pp. 321–424, 2004.
- [20] A. Bogaard, J. Parent, M. Zochowski, and V. Booth, "Interaction of cellular and network mechanisms in spatiotemporal pattern formation in neuronal networks," *Journal of Neuroscience*, vol. 29, no. 6, pp. 1677–1687, 2009.
- [21] Q. Wang, G. Chen, and M. Perc, "Synchronous bursts on scale-free neuronal networks with attractive and repulsive coupling," *PLoS One*, vol. 6, no. 1, p. e15851, 2011.
- [22] Z. Zhao and H. Gu, "The influence of single neuron dynamics and network topology on time delay-induced multiple synchronous behaviors in inhibitory coupled network," *Chaos, Solitons & Fractals*, vol. 80, pp. 96–108, 2015.
- [23] J. Best, A. Borisjuk, J. Rubin, D. Terman, and M. Wechselberger, "The dynamic range of bursting in a model respiratory pacemaker network," *SIAM Journal on Applied Dynamical Systems*, vol. 4, no. 4, pp. 1107–1139, 2005.
- [24] H. Wang and Y. Chen, "Spatiotemporal activities of neural network exposed to external electric fields," *Nonlinear Dynamics*, vol. 85, no. 2, pp. 881–891, 2016.
- [25] J. Li, S. Liu, W. Liu, Y. Yu, and Y. Wu, "Suppression of firing activities in neuron and neurons of network induced by electromagnetic radiation," *Nonlinear Dynamics*, vol. 83, no. 1–2, pp. 801–810, 2015.
- [26] J. A. Robertson, J. Théberge, J. Weller, D. J. Drost, F. S. Prato, and A. W. Thomas, "Low-frequency pulsed electromagnetic field exposure can alter neuroprocessing in humans," *Journal of the Royal Society Interface*, vol. 7, no. 44, pp. 467–473, 2010.
- [27] X. Hu, C. Liu, L. Liu, J. Ni, and Y. Yao, "Chaotic dynamics in a neural network under electromagnetic radiation," *Nonlinear Dynamics*, vol. 91, no. 3, 1, pp. 1541–1554, 2017.
- [28] L. Chua, V. Sbitnev, and H. Kim, "Hodgkin-Huxley axon is made of memristors," *International Journal of Bifurcation & Chaos*, vol. 22, no. 3, p. 1230011, 2012.

- [29] A. M. Hegab, N. M. Salem, A. G. Radwan, and L. Chua, "Neuron model with simplified memristive ionic channels," *International Journal of Bifurcation and Chaos*, vol. 25, no. 6, p. 1530017, 2015.
- [30] M. P. Sah, H. Kim, A. Eroglu, and L. Chua, "Memristive model of the barnacle giant muscle fibers," *International Journal of Bifurcation and Chaos*, vol. 26, no. 1, 1630001 pages, 2016.
- [31] N. Axmacher, F. Mormann, G. Fernandez, C. E. Elger, and J. Fell, "Memory formation by neuronal synchronization," *Brain Research Reviews*, vol. 52, no. 1, pp. 170–182, 2006.
- [32] Q. Li, S. Tang, H. Zeng, and T. Zhou, "On hyperchaos in a small memristive neural network," *Nonlinear Dynamics*, vol. 78, no. 2, pp. 1087–1099, 2014.
- [33] V. T. Pham, S. Jafari, S. Vaidyanathan, C. Volos, and X. Wang, "A novel memristive neural network with hidden attractors and its circuitry implementation," *Science China Technological Sciences*, vol. 59, no. 3, pp. 358–363, 2015.
- [34] M. Lv and J. Ma, "Multiple modes of electrical activities in a new neuron model under electromagnetic radiation," *Neurocomputing*, vol. 205, pp. 375–381, 2016.
- [35] M. Lv, C. Wang, G. Ren, J. Ma, and X. Song, "Model of electrical activity in a neuron under magnetic flow effect," *Nonlinear Dynamics*, vol. 85, no. 3, pp. 1479–1490, 2016.
- [36] F. Wu, C. Wang, Y. Xu, and J. Ma, "Model of electrical activity in cardiac tissue under electromagnetic induction," *Scientific Reports*, vol. 6, no. 1, 2016.
- [37] J. Ma, F. Wu, and C. Wang, "Synchronization behaviors of coupled neurons under electromagnetic radiation," *International Journal of Modern Physics B*, vol. 31, no. 2, p. 1650251, 2017.
- [38] Y. Wang, J. Ma, Y. Xu, F. Wu, and P. Zhou, "The electrical activity of neurons subject to electromagnetic induction and gaussian white noise," *International Journal of Bifurcation and Chaos*, vol. 27, no. 2, p. 1750030, 2017.
- [39] F. Wu, C. Wang, W. Jin, and J. Ma, "Dynamical responses in a new neuron model subjected to electromagnetic induction and phase noise," *Physica A: Statistical Mechanics and its Applications*, vol. 469, pp. 81–88, 2017.
- [40] J. Wu, Y. Xu, and J. Ma, "Lévy noise improves the electrical activity in a neuron under electromagnetic radiation," *PLoS One*, vol. 12, no. 3, p. e0174330, 2017.
- [41] G. Ren, Y. Xu, and C. Wang, "Synchronization behavior of coupled neuron circuits composed of memristors," *Nonlinear Dynamics*, vol. 88, no. 2, pp. 893–901, 2017.
- [42] Y. Xu, Y. Jia, J. Ma, T. Hayat, and A. Alsaedi, "Collective responses in electrical activities of neurons under field coupling," *Scientific Reports*, vol. 8, no. 1, Article ID 1349, 2018.
- [43] J. Ma, L. Mi, P. Zhou, Y. Xu, and T. Hayat, "Phase synchronization between two neurons induced by coupling of electromagnetic field," *Applied Mathematics and Computation*, vol. 307, pp. 321–328, 2017.
- [44] M. Lv, J. Ma, Y. G. Yao, and F. Alzahrani, "Synchronization and wave propagation in neuronal network under field coupling," *Science China Technological Sciences*, vol. 62, no. 3, pp. 448–457, 2019.
- [45] E. M. Izhikevich, "Neural excitability, spiking and bursting," *International Journal of Bifurcation & Chaos*, vol. 10, no. 06, pp. 1171–1266, 2000.
- [46] R. K. Upadhyay and A. Mondal, "Synchronization of bursting neurons with a slowly varying d. c. current," *Chaos, Solitons & Fractals*, vol. 99, pp. 195–208, 2017.
- [47] H. Wang, Q. Lu, and Q. Wang, "Bursting and synchronization transition in the coupled modified ML neurons," *Communications in Nonlinear Science and Numerical Simulation*, vol. 13, no. 8, pp. 1668–1675, 2008.
- [48] J. Ma, Y. Wang, C. Wang, Y. Xu, and G. Ren, "Mode selection in electrical activities of myocardial cell exposed to electromagnetic radiation," *Chaos, Solitons & Fractals*, vol. 99, pp. 219–225, 2017.
- [49] F. Zhan and S. Liu, "Response of Electrical Activity in an Improved Neuron Model under Electromagnetic Radiation and Noise," *Front Computational Neuroscience*, vol. 11, p. 107, 2017.
- [50] Y. Zhang, F. Wu, C. Wang, and J. Ma, "Stability of target waves in excitable media under electromagnetic induction and radiation," *Physica A: Statistical Mechanics and its Applications*, vol. 521, pp. 519–530, 2019.
- [51] T. Ljungberg, P. Apicella, and W. Schultz, "Responses of monkey dopamine neurons during learning of behavioral reactions," *Journal of Neurophysiology*, vol. 67, no. 1, pp. 145–163, 1992.
- [52] K. K. Kesari, M. H. Siddiqui, R. Meena, H. N. Vema, and S. Kumar, "Cell phone radiation exposure on brain and associated biological systems," *Indian Journal of Experimental Biology*, vol. 51, no. 3, pp. 187–200, 2013.
- [53] C. Johansen, "Electromagnetic fields and health effects—epidemiologic studies of cancer, diseases of the central nervous system and arrhythmia-related heart disease," *Scandinavian Journal of Work Environment & Health*, vol. 30, no. 1, pp. 1–30, 2004.

Research Article

Degradation Analysis of Chaotic Systems and their Digital Implementation in Embedded Systems

Rodrigo Méndez-Ramírez ¹, Adrian Arellano-Delgado,² Miguel Murillo-Escobar ¹,
and César Cruz-Hernández ¹

¹Scientific Research and Advanced Studies Center of Ensenada, B. C. (CICESE), 22080 Ensenada, Mexico

²Engineering, Architecture and Design Faculty, Autonomous Baja California University (CONACYT-UABC), Ensenada, BC, Mexico

Correspondence should be addressed to César Cruz-Hernández; ccruz@cicese.mx

Received 8 September 2019; Accepted 14 October 2019; Published 4 December 2019

Guest Editor: Serdar Çiçek

Copyright © 2019 Rodrigo Méndez-Ramírez et al. This is an open access article distributed under the Creative Commons Attribution License, which permits unrestricted use, distribution, and reproduction in any medium, provided the original work is properly cited.

Digital implementation of chaotic systems (CSs) has attracted increasing attention from researchers due to several applications in engineering, e.g., in areas as cryptography and autonomous mobile robots, where the properties of chaotic systems are strongly related. The CSs in the continuous version (CV) need to be discretized where chaotic degradation must be analyzed to guarantee preservation of chaos. In this paper, we present a degradation analysis of five three-dimensional CSs and the necessary conditions to implement the discretized versions (DVs) of Lorenz, Rössler, Chen, Liu and Chen, and Méndez-Arellano-Cruz-Martínez (MACM) CSs. Analytical and numerical analyses of chaos degradation are conducted by using the time series method; the maximum discrete step size and the Lyapunov Exponents (LEs) are computed by using the Euler, Heun, and fourth-order Runge-Kutta (RK4) numerical algorithms (NAs). We conducted comparative studies of performance based on time complexity of the five proposed CSs in their DVs by using four embedded systems (ESs) based on three families of Microchip microcontrollers 8-bit PIC16F, 16-bit dsPIC33FJ, and 32-bit PIC32MZ (of low-cost electronic implementation) and a Field Programmable Gate Array (FPGA). Based on the results, the intervals at control parameters to guarantee chaos are proposed, which improves the performance characteristics of the five proposed CSs in their DVs based on digital applications.

1. Introduction

In recent years, scientific community has become interested in chaotic systems (CSs) due to their potential application in several areas of engineering, where the properties of chaos are desired, such as high sensitivity to initial conditions, high entropy, topology complexity, ergodicity, among others [1–6]. Electronic implementations based on chaos have been developed for digital applications, e.g., as pseudorandom sequence generator [7], synchronization of optical networks [8], image encryption [9], chaotic trajectories for autonomous mobile robot [10], chaotic radar [11], among others [12–17]. Lorenz is the first 3D CS reported in the literature [18]. Since then, many CSs in 3D and 4D with different features and properties have been reported [19–29]. Moreover, literature

reports chaotic maps (discrete by nature) desirable properties at such applications, e.g., the logistic map in 1D [5], Hénon map in 2D [30], among others.

The 3D CSs can be implemented electronically in their continuous or discretized versions; their continuous versions (CVs) can be implemented using operational amplifiers [27–29, 31]. On the other hand, distinct numerical algorithms (NAs) are used to implement the discretized versions (DVs) of the 3D CSs [32–34]. Software tools, such as Matlab or Labview, allow to simulate and reproduce the CSs in their DVs using NAs as Euler, Heun, and RK4 [35], where a small step size is considered to compare their DV versus their CV [32–34].

The literature reports digital implementations of CSs in their DVs for different applications by using embedded

systems (ESs) such as microcontrollers where the main cores are 8-bit PIC18F microcontroller [36]; 16-bit dsPIC microcontroller [37]; 32-bit microcontrollers such as PIC32 [29, 38], ARM Cortex-M3 [39], DSP [40], and Altera and Xilinx FPGAs [7, 32–34, 41, 42]; system on chip (SoC) that contains fast processors as NanoPC-T3 Plus [43]; and Raspberry Pi 3 [44], among others.

Recently, the literature reports degradation studies of 3D CSs in their DVs by using the NA of Euler; a robustness diagram for control parameters guarantee chaos is presented, and its digital implementation is conducted in a microcontroller PIC32 [29].

The methods equivalent used to conduct arithmetic and logical calculations inside of a microprocessor—or its equivalent microcontroller as main core of an ES—are based on numerical standards. Microchip Technology Inc. is the manufacturer of PIC, dsPIC, and PIC32 microcontrollers; their numerical results are based by the IEEE-754 Compliant Floating Point Routines [45]. On the other hand, Altera-Intel is an FPGA manufacturer, and their numerical results of simulations are represented in IEEE-754 (2008) [46, 47]. The NAs are simulated by using Matlab, and its results are similar in comparison with the compilers used by Microchip microcontrollers and software for design used by Altera-Intel FPGA because both are based on IEEE-754 [35, 46, 47].

The FPGA has powerful simulation tools to reproduce chaotic dynamics of CSs in their DVs by using digital signal processing (DSP) modules as a complementary tool for Matlab/Simulink software, e.g., Altera Simulink/DSP Builder and Xilinx System Generator BlockSet [48, 49].

In this paper, we present a degradation analysis of the five 3D CSs in their DVs to determine the performance of implementation in four versions of an ES, the time complexity, and the intervals of control parameters to guarantee chaos are obtained. The results of this paper can be of great interest for digital applications of chaos in engineering. To our knowledge, the literature does not report comparative studies of digital degradation of five 3D CSs in their DVs by using the NAs of Euler, Heun, and RK4, where its performance is conducted in microcontrollers of 8, 16, and 32 bits, and FPGA.

The paper is organized as follows: In Section 2, the normalized version of five three-dimensional CSs are presented, numerical analyses calculating the Lyapunov exponents are conducted to verify the chaotic behavior using the Euler, Heun, and RK4 NAs where a Root-Mean-Square Error (RMSE) analysis is conducted to compare their continuous and DVs. Section 3 presents the digital implementation on ES with 8-bit PIC16F, 16-bit dsPIC33, 32-bit PIC32MZ microcontrollers, and the Altera FPGA Cyclone IV GX, where the performance and the robustness digital diagram to guarantee the chaos is proposed. Finally, conclusions of this work are reported in Section 4.

2. Degradation Analysis

In this section, we describe the normalized equations of the 3D Lorenz, Rössler, Chen, Liu and Chen, and MACM CSs to obtain their DVs by using the NAs of E, H, and RK4. The

time series method is used to obtain the degradation limits by calculating the LEs of the five 3D CSs in their continuous and DVs [50, 51]. We analyzed the accuracy of the trajectories of state variable x of the 3D Lorenz, Rössler, Chen, Liu and Chen, and MACM CSs by calculating the RMSE. All the numerical results and methods described in this section are conducted by using Matlab [35].

2.1. Normalized 3D CSs. This subsection briefly describes the normalized version of the Lorenz, Rössler, Chen, Liu and Chen, and MACM CSs, and the difference between them is given by the complexity of their dynamics, the representation of their nonlinear functions, and parameters.

First, we consider the Lorenz system, which is a well-known example of a CS. Lorenz's three-variable model provides a practical test case with qualitatively realistic properties [18]; it is represented by the nonlinear state equations described as

$$\begin{aligned}\dot{x} &= \sigma(y - x), \\ \dot{y} &= rx - xz - y, \\ \dot{z} &= xy - bz,\end{aligned}\tag{1}$$

where x , y , and z are the state variables and the standard parameter values for Lorenz's chaotic attractor are $\sigma = 10$, $r = 28$, and $b = 8/3$. We also consider the Rössler system introduced by Rössler in 1976 [19], which is described by

$$\begin{aligned}\dot{x} &= -y - z, \\ \dot{y} &= x + ay, \\ \dot{z} &= b + z(x - c),\end{aligned}\tag{2}$$

where x , y , and z are the state variables, the Rössler system presents chaotic behavior for the following parameter values: $a = 0.2$, $b = 0.2$, and $c = 5.7$. Similarly, the Chen system is introduced as a dual system of the Lorenz system in 1999 [23] and is described by

$$\begin{aligned}\dot{x} &= a(y - x), \\ \dot{y} &= (c - a)x - xz + cy, \\ \dot{z} &= xy - bz,\end{aligned}\tag{3}$$

where x , y , and z are the state variables and the Chen system presents chaotic behavior for the following parameter values: $a = 35$, $b = 3$, and $c = 28$. Moreover, the Liu and Chen system was introduced in 2002, and its description is given by [24]

$$\begin{aligned}\dot{x} &= ax + d_1 yz, \\ \dot{y} &= cy + d_2 xz, \\ \dot{z} &= bz + d_3 xy,\end{aligned}\tag{4}$$

where x , y , and z are the state variables, this nonlinear system presents a chaotic behavior when the following condition $ab + ac + bc \neq 0$ is met. It can create a complex 2-scrolls attractor from the following parameter values: $d_1 = -1$, $d_2 = d_3 = 1$, $a = 5$, $c = -10$, and $b = -3.4$. Recently, the MACM CS was proposed in 2017 [29], which is described by

$$\begin{aligned}\dot{x} &= -ax - byz, \\ \dot{y} &= -x + cy, \\ \dot{z} &= d - y^2 - z,\end{aligned}\quad (5)$$

where x , y , and z are the state variables and the MACM system presents chaotic behavior for the following parameter values: $a = b = 2$, $c = 0.5$, and $d = 4$.

In this study, we use the same initial conditions (ICs) $x_0 = y_0 = z_0 = 1$ for the CSs (1)–(5). Table 1 shows the summary of control parameters, critical parameters, nonlinearities, and ICs of the five 3D CSs (1)–(5) [29].

The literature reports the validation of chaos calculating the limits of the LEs by using the time series method by Wolf and Briggs [50, 51], and the LEs and fractal dimension, commonly known as Kaplan–Yorke dimension D_{KY} , of the five 3D CSs (1)–(5) in their CVs are computed by using the proposed time series method. Table 2 shows the LEs and the fractal dimension results of CSs (1)–(5) in their CVs.

2.2. Numerical Algorithms. NAs of Euler, Heun, and RK4 are used to obtain the DV of the CSs (1)–(5), the step size as referred to as τ , and n is the iteration number that represents the time in DV. The nonlinear functions f , g , and h of the five 3D CSs of Lorenz, Rössler, Chen, Liu and Chen, and MACM in their DVs describe the states x , y , and z , respectively.

Euler algorithm presents just one step, and it is easy to implement because it requires less arithmetic operations [35]. The Euler NA is described by

$$\begin{aligned}x_{(n+1)} &= x_{(n)} + \tau f(x_{(n)}, y_{(n)}, z_{(n)}), \\ y_{(n+1)} &= y_{(n)} + \tau g(x_{(n)}, y_{(n)}, z_{(n)}), \\ z_{(n+1)} &= z_{(n)} + \tau h(x_{(n)}, y_{(n)}, z_{(n)}).\end{aligned}\quad (6)$$

The Heun is the second NA implemented [35]; this method is known as trapezoidal in two steps where the first step predicts and the second step corrects. The NA of Heun is described as follows:

$$\begin{aligned}x_{(n+1)}^* &= x_{(n)} + \tau f(x_{(n)}, y_{(n)}, z_{(n)}), \\ y_{(n+1)}^* &= y_{(n)} + \tau g(x_{(n)}, y_{(n)}, z_{(n)}), \\ z_{(n+1)}^* &= z_{(n)} + \tau h(x_{(n)}, y_{(n)}, z_{(n)}),\end{aligned}\quad (7)$$

where

$$\begin{aligned}x_{(n+1)} &= x_{(n)} + \frac{\tau}{2} \left(f(x_{(n)}, y_{(n)}, z_{(n)}) + x_{(n+1)}^* \right), \\ y_{(n+1)} &= y_{(n)} + \frac{\tau}{2} \left(g(x_{(n)}, y_{(n)}, z_{(n)}) + y_{(n+1)}^* \right), \\ z_{(n+1)} &= z_{(n)} + \frac{\tau}{2} \left(h(x_{(n)}, y_{(n)}, z_{(n)}) + z_{(n+1)}^* \right).\end{aligned}\quad (8)$$

The third NA is the RK4; this algorithm is one of the most widely used methods for solving differential equations [35]. The NA of RK4 is given by

$$\begin{aligned}x_{(n+1)} &= x_{(n)} + \frac{\tau}{6} (k_1 + 2k_2 + 2k_3 + k_4), \\ y_{(n+1)} &= y_{(n)} + \frac{\tau}{6} (l_1 + 2l_2 + 2l_3 + l_4), \\ z_{(n+1)} &= z_{(n)} + \frac{\tau}{6} (m_1 + 2m_2 + 2m_3 + m_4),\end{aligned}\quad (9)$$

where k_1, k_2, k_3 , and k_4 are referred to as coefficients of the first equation, similarly, the parameters l_1, l_2, l_3 , and l_4 are referred to as coefficients of the second equation, and the parameters m_1, m_2, m_3 , and m_4 are referred to as coefficients of the third equation. The coefficients described in system (9) are given by

$$\begin{aligned}k_1 &= f(x_{(n)}, y_{(n)}, z_{(n)}), \\ l_1 &= g(x_{(n)}, y_{(n)}, z_{(n)}), \\ m_1 &= h(x_{(n)}, y_{(n)}, z_{(n)}),\end{aligned}\quad (10)$$

$$\begin{aligned}k_2 &= f\left(x_{(n)} + \frac{\tau}{2}k_1, y_{(n)} + \frac{\tau}{2}l_1, z_{(n)} + \frac{\tau}{2}m_1\right), \\ l_2 &= g\left(x_{(n)} + \frac{\tau}{2}k_1, y_{(n)} + \frac{\tau}{2}l_1, z_{(n)} + \frac{\tau}{2}m_1\right), \\ m_2 &= h\left(x_{(n)} + \frac{\tau}{2}k_1, y_{(n)} + \frac{\tau}{2}l_1, z_{(n)} + \frac{\tau}{2}m_1\right),\end{aligned}\quad (11)$$

$$\begin{aligned}k_3 &= f\left(x_{(n)} + \frac{\tau}{2}k_2, y_{(n)} + \frac{\tau}{2}l_2, z_{(n)} + \frac{\tau}{2}m_2\right), \\ l_3 &= g\left(x_{(n)} + \frac{\tau}{2}k_2, y_{(n)} + \frac{\tau}{2}l_2, z_{(n)} + \frac{\tau}{2}m_2\right), \\ m_3 &= h\left(x_{(n)} + \frac{\tau}{2}k_2, y_{(n)} + \frac{\tau}{2}l_2, z_{(n)} + \frac{\tau}{2}m_2\right),\end{aligned}\quad (12)$$

$$\begin{aligned}k_4 &= f(x_{(n)} + \tau k_3, y_{(n)} + \tau l_3, z_{(n)} + \tau m_3), \\ l_4 &= g(x_{(n)} + \tau k_3, y_{(n)} + \tau l_3, z_{(n)} + \tau m_3), \\ m_4 &= h(x_{(n)} + \tau k_3, y_{(n)} + \tau l_3, z_{(n)} + \tau m_3).\end{aligned}\quad (13)$$

Finally, the coefficients described in (10)–(13) are placed in (9); they as whole represent the NA of RK4 (9)–(13).

2.3. Degradation Analysis of the 3D CSs in Their DVs. In this subsection, the maximum step size is referred to as τ_{\max} , and it is computed by using the time series method considering one positive LE as the condition to guarantee chaos in the DV of the five 3D CSs [50, 51]. LEs to obtain the chaotic degradation of the five CSs in their DVs are computed by using the NAs of Euler (6), only the τ_{\max} were reported in [29]; in this study, the LEs and D_{KY} are added, and their results are presented in Table 3. In addition, we computed LEs, τ_{\max} , and D_{KY} of the five CSs in their DVs by using the NAs of Heun (7) and (8) and RK4 (9)–(13), and their results are presented in Tables 4 and 5, respectively.

The results obtained in Tables 3–5 show that MACM CS presents the higher τ_{\max} , and Chen and Liu and Chen CSs

TABLE 1: Parameters, characteristics, and ICs of the five 3D CSs (1)–(5).

CS	Control parameter	Critical parameter	Nonlinearities	Initial condition (x_0, y_0, z_0)
Lorenz (1)	$\sigma = 10,$ $r = 8/3,$ $b = 28$	σ	2	(1, 1, 1)
Rössler (2)	$a = 0.2,$ $b = 0.2,$ $c = 5.7$	c	1	(1, 1, 1)
Chen (3)	$a = 35,$ $b = 3,$ $c = 28$	a	2	(1, 1, 1)
Liu and Chen (4)	$a = 5,$ $c = -10,$ $b = -3.4,$ $d_1 = -1,$ $d_2 = d_3 = 1.$	c	3	(1, 1, 1)
MACM (5)	$a = b = 2,$ $c = 0.5,$ $d = 4.$	c, d	2	(1, 1, 1)

TABLE 2: LEs of the CSs (1)–(5) in their CVs.

CS	LE ₁	LE ₂	LE ₃	D_{KY}
Lorenz (1)	0.91	0	-14.47	2.062
Rössler (2)	0.07	0	-5.39	2.012
Chen (3)	2.02	0	-12.02	2.168
Liu and Chen (4)	0.87	0	-9.27	2.093
MACM (5)	0.24	0	-2.74	2.087

TABLE 3: Analysis of chaos degradation for DV of 3D CSs by using the NA of Euler (6).

CS	τ_{\max}	LE ₁	LE ₂	LE ₃	D_{KY}
Lorenz	≤ 0.024	0.039	-62.8 μ	-0.389	2.101
Rössler	≤ 0.005	49 μ	34.9 μ	-5.53	2.0142
Chen	≤ 0.002	3.8 m	0.11 m	-23.1 m	2.169
Liu and Chen	≤ 0.002	197 μ	-53.21 μ	-18.72 m	2.1029
MACM	≤ 0.085	0.05	-64.58 μ	-0.243	2.099

TABLE 4: Analysis of chaos degradation for DV of 3D CSs by using the NA of Heun (7) and (8).

CS	τ_{\max}	LE ₁	LE ₂	LE ₃	D_{KY}
Lorenz	≤ 0.068	86.6 m	-2.016 m	-0.6231	2.1358
Rössler	≤ 0.191	0.0273	196 μ	-0.24122	2.1141
Chen	≤ 0.017	38.7 m	23.67 μ	-0.19558	2.1984
Liu and Chen	≤ 0.017	17.41 m	-17.88 μ	-0.15542	2.112
MACM	≤ 0.228	95.29 m	315.64 μ	-0.476	2.2006

TABLE 5: Analysis of chaos degradation for DV of 3D CSs by using the NA of RK4 (9)–(13).

CS	τ_{\max}	LE ₁	LE ₂	LE ₃	D_{KY}
Lorenz	≤ 0.1076	64.17 m	-4.03 m	-1.1924	2.0504
Rössler	≤ 0.251	35.53 m	339.62 μ	-0.402	2.0891
Chen	≤ 0.057	97.48 m	-2.949 m	-0.6509	2.1452
Liu and Chen	≤ 0.057	55.52 m	-1.83 m	-0.389	2.0974
MACM	≤ 0.547	0.23081	-48.55 m	-1.0098	2.1805

present the smallest τ_{\max} in comparison with Lorenz. In the case of Rössler system, we recommend to use $\tau_{\max} = 0.005$ because, for higher values, the dynamical chaotic behavior is lost and dynamic behavior of limit cycle for step sizes within the intervals $0.006 \leq \tau \leq 0.091$ is shown; for higher values of $\tau = 0.091$, the LEs cannot be computed using the time series method with the NA (6). Rössler system supports an interval small of τ_{\max} because the chaotic dynamics diverges. Nevertheless, Rössler system presents a high interval in comparison Lorenz system by using the NAs of Heun (7) and (8) and RK4 (9)–(13), and their results are described in Tables 4 and 5.

Figure 1 illustrates the comparison of τ_{\max} obtained with the results of the NAs described in Tables 3–5. NA of RK4 presents higher τ_{\max} in comparison of the NAs of Euler, and Heun. The DV of MACM system presents a higher τ_{\max} than the DV of the CSs of Lorenz, Rössler, Chen, and Liu and Chen systems.

2.4. Performance of Chaotic Behavior. We use RMSE to compare the performance and accuracy of the trajectory of state x of the CSs (1)–(5) in their CVs respect to their DVs by using the NAs of Euler (6), Heun (7) and (8), and RK4 (9)–(13). The RMSE is defined as follows:

$$\text{RMSE} = \sqrt{\frac{1}{n} \sum_{i=1}^n (x_{e(n)} - x_{(n)})^2}, \quad (14)$$

where the state variable $x_{e(n)}$ is referred to as the estimator value of the CV of CSs (1)–(5), the state variable $x_{(n)}$ is referred to as the predicted estimated value of DV of CSs (1)–(5), and n is referred to as the total number samples. The Ordinary Differential Equation (ODE) function number 45 (ODE45) of MATLAB is considered to reproduce the CV of the CSs (1)–(5), although strictly it is also a discretized representation, this algorithm is based on an explicit Runge–Kutta

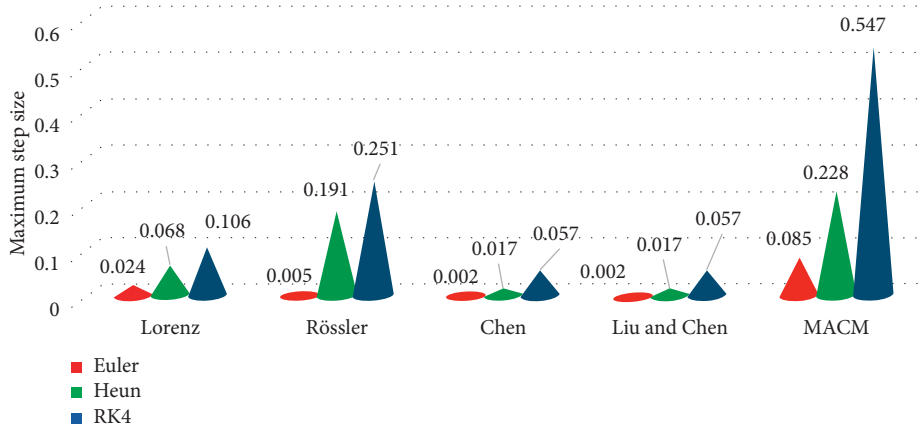


FIGURE 1: τ_{\max} summary of chaotic degradation of the five 3D CSs in their DVs.

4-5 formula, it is a single-step solver and needs only the solution at the immediately preceding point time [52, 53].

Numerical tests of the 3D Lorenz, Rössler, Chen, Liu and Chen, and MACM CSs in their DVs are conducted for each Euler (6), Heun (7) and (8), and RK4 (9)–(13) NA, respectively; we considered $n = 30000$ samples, a small step size $\tau = 0.001$, and same parameters and initial conditions are shown in Table 1.

The error calculation is compared with respect to state variable $x_{(n)}$ of the five 3D CSs in their DVs, and their trajectory errors are referred to as follow: e_1 represents the difference between ODE45 and Euler algorithm (6), e_2 represents the difference between ODE45 and Heun algorithm (7) and (8), and e_3 represents the difference between ODE45 and RK4 algorithm (9)–(13).

Figure 2 shows the comparison of the evolution of the state variable $x_{(n)}$ of the Lorenz, Rössler, Chen, Liu and Chen, and MACM CSs in their continuous version using ODE45 and DVs using the NAs of (6)–(13). Figure 3 shows the trajectory errors e_1 – e_3 of the trajectories of set of CSs shown in Figure 2. Figure 2(b) shows that the trajectories of the Rössler system (2) have no changes; they are practically the same trajectories for the DVs with respect to the continuous version (2), and Figure 3(b) shows that the Rössler system has minimal errors for e_1 – e_3 . Considering the numerical results of the trajectories of state x of the set of five 3D CSs shown in Figures 2 and 3, the RMSE comparison is obtained by using (14), and its result is shown in Figure 4. Chen and Liu and Chen systems show high RMSE, and to a lesser extent in the Lorenz system, followed by this value, the MACM system exhibits a low RMSE value, but the Rössler system exhibits the lowest RMSE (see Figure 4).

Rössler system guarantees a better conservation of the chaos considering the proposed n samples and τ step size by using the NAs of Euler (6), Heun (7)–(8), and RK4 (9)–(13).

3. Digital Implementation

In this section, we present the necessary conditions to implement the NAs of the five 3D CSs in their DVs considering the described studies in Section 2.

The digital implementation is carried out in an ES which main core is represented in four different hardware versions: 8-bit PIC16F, 16-bit dsPIC33, and 32-bit PIC32MZ microcontrollers, and one Cyclone IV GX FPGA. Table 6 shows the hardware description of the four versions of the ES.

Microcontrollers U1–U3, FPGA U4, and DACs U5–U7 are configured according to the performance recommended by their manufacturers—the SPI protocol was configured in the master mode from specification of U1–U4 by using 12 bits of resolution. The DAC U5, U6, and U7 represent the state variables $x_{(t)}$, $y_{(t)}$, and $z_{(t)}$, respectively, and its software configuration is given from U1–U4. Figure 5 shows the hardware description for the four versions of ES. Version 1 (V1) represents the hardware implementation by using U1, Version 2 (V2) represents the hardware implementation by using U2, Version 3 (V3) represents the hardware implementation by using U3, and Version 4 (V4) represents the hardware implementation by using U4.

Initially, the NAs Euler (6), Heun (7) and (8), and RK4 (9)–(13) of the 3D Lorenz, Rössler, Chen, Liu and Chen, and MACM CSs in their DVs are simulated by using Matlab, the numerical standard of Matlab is based on IEEE-754 standard for floating point representation [35]. The compilers used to program and implement the NAs Euler (6), Heun (7) and (8), and RK4 (9)–(13) of the 3D Lorenz, Rössler, Chen, Liu and Chen, and MACM CSs in their DVs inside of U1–U4 are based on C language, the microcontrollers U1–U3 have similar standard IEEE-754 which is referred to as Compliant Floating Point Routines AN575 [45]. According to the Altera-Intel manufacturer, the FPGA U4 is based on the IEEE-754 standard (2008) [46, 47]. The compilers of the manufacturer Mikroelektronika are used to program U1–U3 [54]. The FPGA U4 is programmed by using the set tools of Quartus II to design the hardware, and Eclipse compiler is used to design the software. Therefore, the numerical results conducted in the proposed four versions V1–V4 of the ES are similar because Matlab and the C compilers to program U1–U3 and U4 have the IEEE-754 standard [35, 44–46].

In order to conduct the simulations of the NA, we used the Proteus Virtual System Modeling (VSM) Software, in special, the VSM for Microchip version that contains the device libraries of some families of 8-bit PIC and 16-bit

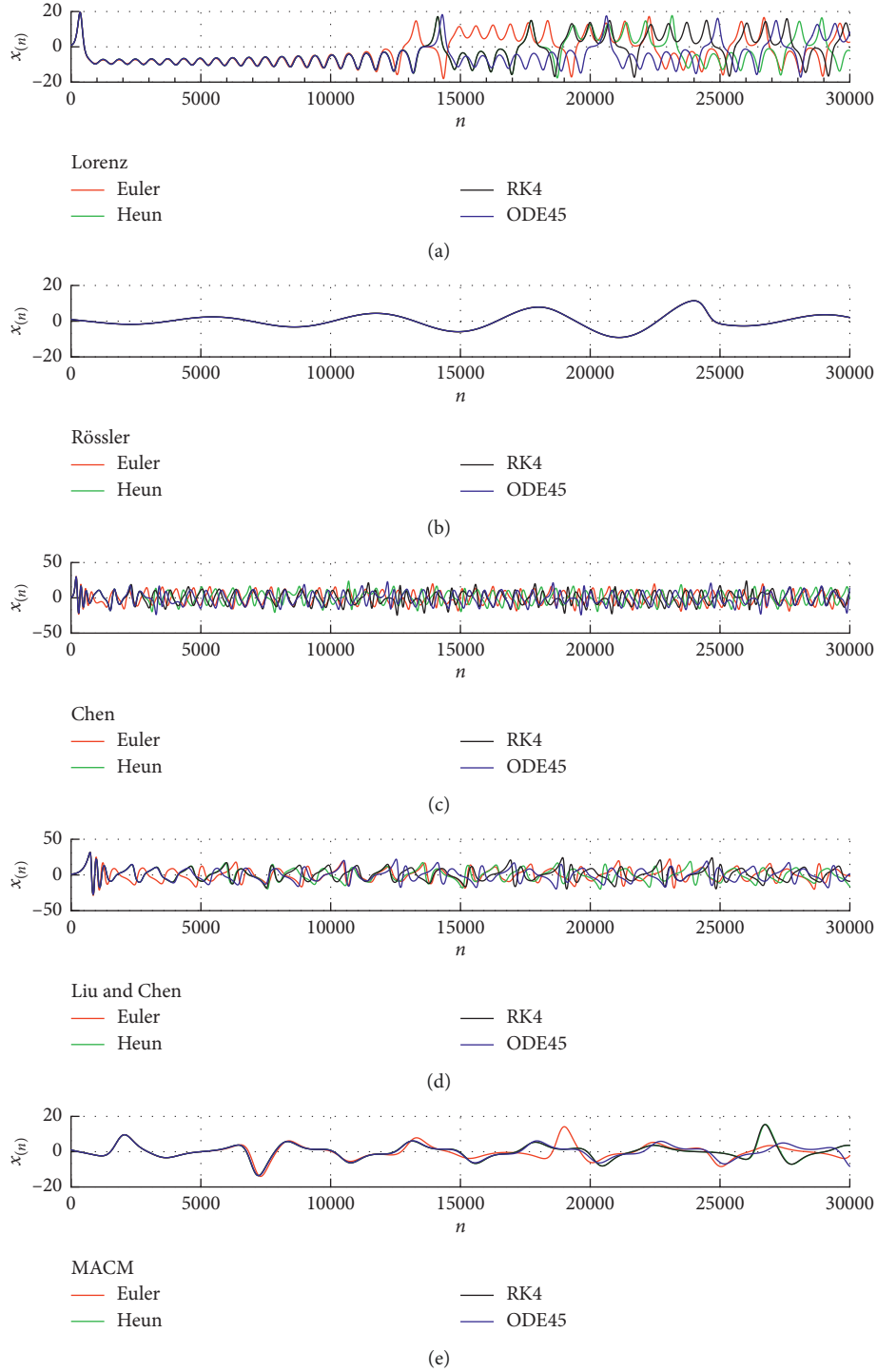


FIGURE 2: Evolution of state variable $x(n)$ of the CSs: (a) Lorenz (2), (b) Rössler (2), (c) Chen (3), (d) Liu and Chen (4), and (e) MACM (5) in their CVs with respect to their DVs by using the NAs of Euler (6), Heun (7)–(8), and RK4 (9)–(13).

dsPIC33 microcontrollers, and the schematic capture tool was used to simulate the complete V1 and V2 ESs [55]. The numerical results of V1–V4 proposed and their equivalences between simulation and implementation are carried out by using the methods described in [29, 37, 38].

The total quantity of iterations Q_T is referred to as the maximum number of n iterations generated in 1 second,

and it is represented in time units (tu), and the CSs (2)–(6) are represented in three dimensions, i.e., we are considering $N=3$ dimensions, and the Q_T representation is given by

$$Q_T = \tau \frac{1}{T_{Td}} = \tau f_{Td} = \tau \frac{1}{t_c + t_{Tg}} = \tau \frac{1}{t_c + \sum_{j=1}^N t_{Tdac(j)}}, \quad (15)$$

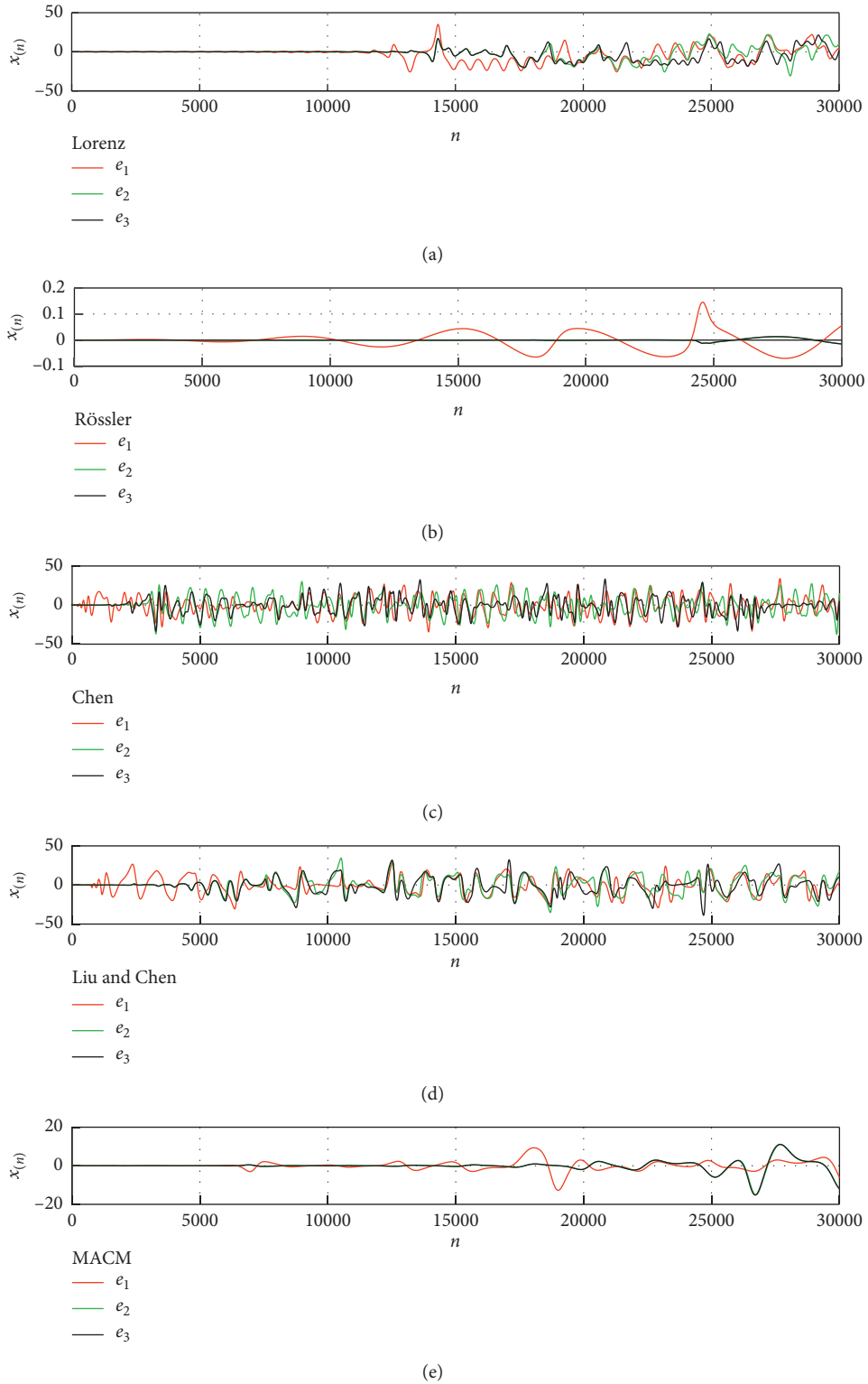


FIGURE 3: Errors e_1 , e_2 , and e_3 shown in Figure 2 for the CSs: (a) Lorenz (1), (b) Rössler (2), (c) Chen (3), (d) Liu and Chen (4), and (e) MACM (5).

where the time period T_{Td} is considered as the total-decoding-time that the algorithm needs to reproduce an iteration n , and f_{Td} represents the maximum number of

iterations n that the ES generates in 1 second (ips); the frequency f_{Td} is the reciprocal of T_{Td} . The time complexity t_c is the time that NA need to reproduce one iteration n by

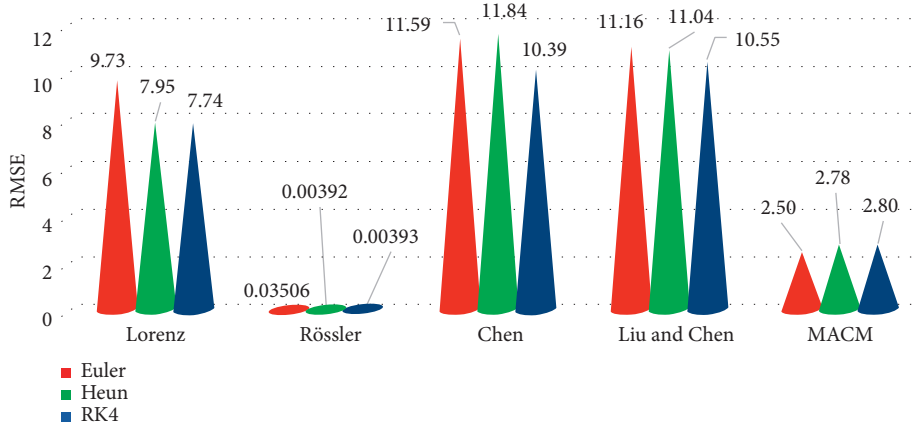


FIGURE 4: RMSE comparison of trajectory performance of state x of five 3D CSs (1)–(5) in their CVs with respect to their DVs using the NAs (6)–(13).

TABLE 6: Hardware description of the ES for V1–V4.

Peripheral number	SPI mode, hardware description
U1	Master, 8-bit PIC16F874A microcontroller
U2	Master, 16-bit dsPIC33FJ32MC204 microcontroller
U3	Master, 32-bit PIC32MZ2048ECM064 microcontroller
U4	Master, EP4CGX150DF31C7 Cyclone IV GX FPGA
U5	Slave 1, DAC MCP4921 shows $x_{(t)}$
U6	Slave 2, DAC MCP4921 shows $y_{(t)}$
U7	Slave 3, DAC MCP4921 shows $z_{(t)}$

using the main core of U1, U2, U3, or U4; the total-graphic time t_{Tg} is the time that the three DACs U5–U7 need to represent the state variables $x_{(t)}$, $y_{(t)}$, and $z_{(t)}$, and the time required for each DAC (U5–U7) is referred by $t_{Tdac(1-3)}$, respectively.

The measurement of the iterations f_{Tg} and the time T_{Td} are obtained experimentally when the program of NA used is executed in the 4 versions of the ES. Only t_c depends on the size of the NA used. The size of t_{Tg} depends of the configuration of SPI protocol used in U1–U4.

The equation (15) is a reference to determine the performance of the proposed ES in their four versions V1–V4. In this study, we need to obtain a smaller period of time to determine a greater number of iterations n and a higher step size to guarantee the chaos proposed in Tables 3–5; their values depend on the NA of the CSs proposed and the version of the ES that will be implemented. Given these considerations, we will obtain a higher Q_T . This means that the state variables of the 3D Lorenz, Rössler, Chen, Liu and Chen, and MACM CSs in their DVs by using the NAs (6)–(13) have a better representation of f_{Td} , which is very attractive for applications based in chaos such as: master key definition, encryption, and secure communications [9, 37, 43, 56].

3.1. Embedded System with 8-Bit PIC Microcontroller. First, we implemented the ES in the V1 by using the microcontroller PIC16F874A U1. We used Proteus to conduct the electronic simulations of the NAs of the CSs

proposed, and the schematic diagram is shown in Figure 6.

Euler algorithm (6) is used to obtain the DV of the Lorenz system and its corresponding system is given by

$$\begin{aligned}
 x_{(n+1)} &= x_{(n)} + \tau(\sigma(y_{(n)} - x_{(n)})), \\
 y_{(n+1)} &= y_{(n)} + \tau(rx_{(n)} - x_{(n)}z_{(n)} - y_{(n)}), \\
 z_{(n+1)} &= z_{(n)} + \tau(x_{(n)}y_{(n)} - bz_{(n)}).
 \end{aligned} \tag{16}$$

Figure 7 shows the results of the Lorenz system simulation in its DV (16), we considered the higher step size $\tau_{max} = 0.024$ according to the results shown in Table 3. The voltage supplied for the ES in V1 is $V_{dd} = +5V$ and $V_{ss} = 0V$, and an external crystal of 16 MHz is used according to the datasheet of U1. The test in the version 1 on the ES is conducted, and we obtained $T_{Td} = 2046 \mu s$ and $f_{Td} = 488.7$ ips; this means that we can obtain $Q_T = 11.7$ tu in 1 second by using V1 in the Proteus simulator.

To conduct the hardware implementation on V1 of ES, we used the same electrical parameters used in the simulation of CS (16). Figure 8 illustrates the implementation results of the algorithm (16) by using the 8-bit PIC microcontroller U1. Figure 8(b) shows the time evolution of the state variables $x_{(n)}$ and $z_{(n)}$ of Lorenz system (16) for 1 second. We experimentally obtained $t_c = 1989 \mu s$, $t_{Tg} = 57 \mu s$, $T_{Td} = 2046 \mu s$, and $f_{Td} = 488.7$ ips considering the same $\tau_{max} = 0.024$; this means that the simulation conducted by using Proteus and the hardware implementation in the version 1 is consistent, because both have the same units of $Q_T = 11.7$ time in 1 second.

The NAs of Euler (6), Heun (7) and (8), and RK4 (9)–(13) of the 3D Lorenz, Rössler, Chen, Liu and Chen, and MACM CSs in their DVs are executed in the V1 of the ES; the NA of RK4 (9)–(13) cannot be executed using U1 because the size of its program flash memory is small and it only supports 4K bytes. We obtained the performance of the ES in the V1, and the time complexity and the iterations per second are detailed in Table 7.

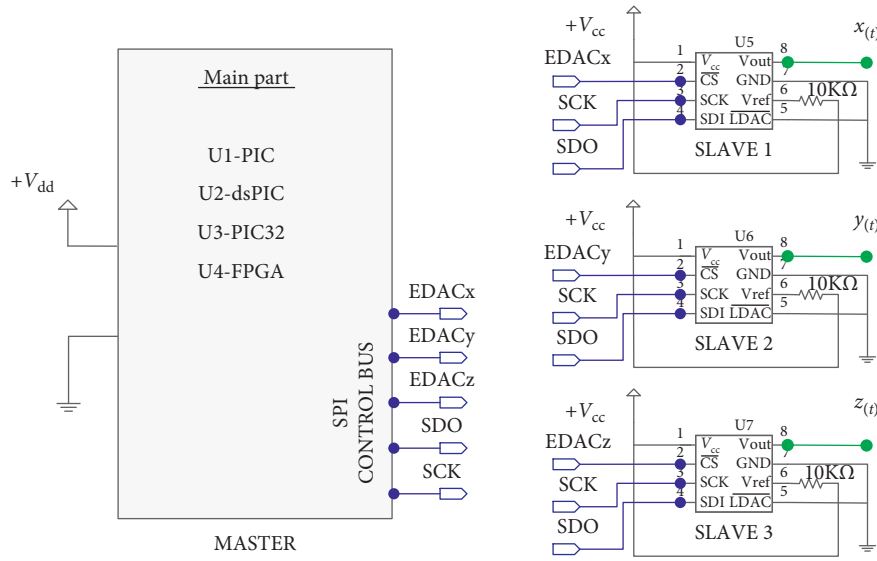


FIGURE 5: Schematic circuit of ES for V1-V4.

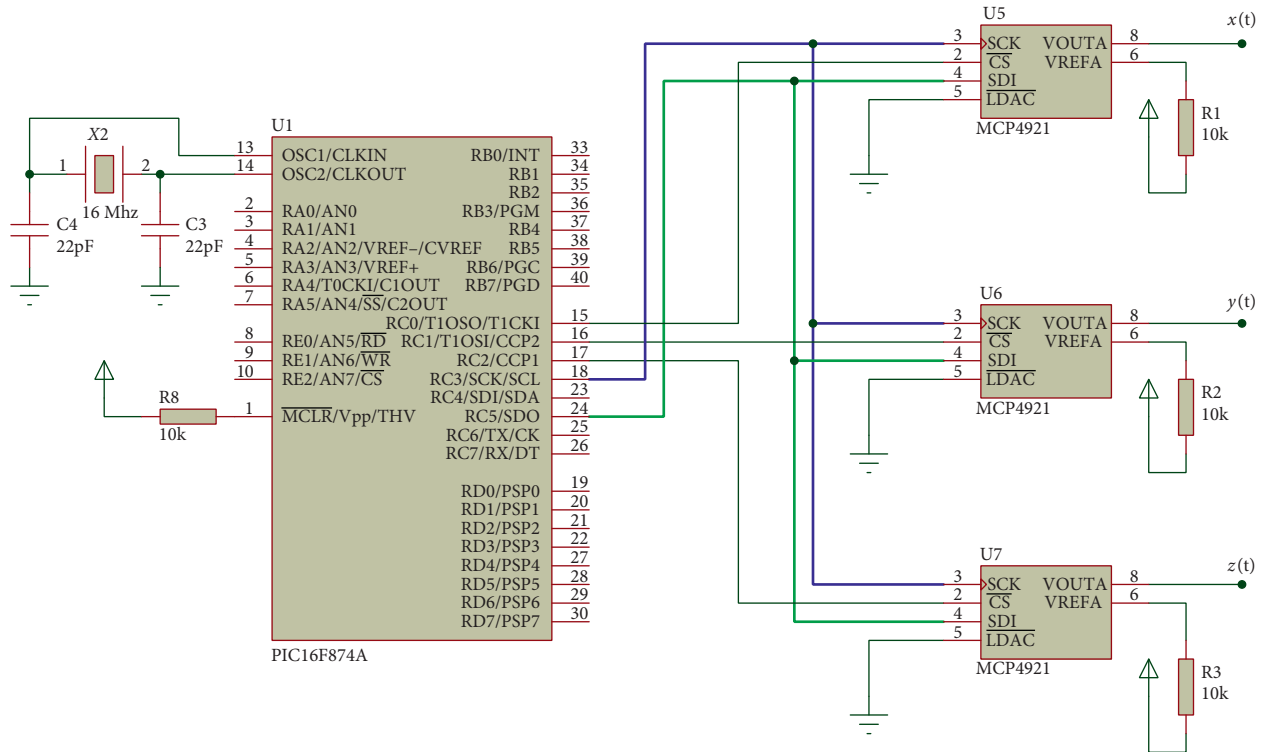


FIGURE 6: Schematic of the simulation of ES in V1 with the Proteus software.

3.2. *Embedded System with dsPIC Microcontroller.* Second implementation is conducted; the NAs of Euler (6), Heun (7) and (8), and RK4 (9)–(13) of the 3D Lorenz, Rössler, Chen, Liu and Chen, and MACM CSs in their DVs are implemented by using the ES in its version 2. Figure 9 illustrates the simulation and implementation of dsPIC33 U2 in Proteus by using the V2 of the ES. The voltage supplied for the ES in V2 is $V_{dd} = +3.3\text{ V}$ and $V_{ss} = 0\text{ V}$, and an external crystal of 10 MHz is used according to the datasheet of U2. We conducted an example to implement the Liu and Chen

CS in its DV by using the Euler algorithm (6), and its algorithm is described as follows:

$$\begin{aligned} x_{(n+1)} &= x_{(n)} + \tau(ax_{4(n)} + d_1y_{(n)}z_{(n)}), \\ y_{(n+1)} &= y_{(n)} + \tau(cy_{4(n)} + d_2x_{(n)}z_{(n)}), \\ z_{(n+1)} &= z_{(n)} + \tau(bz_{(n)} + d_3x_{(n)}y_{(n)}). \end{aligned} \quad (17)$$

Figure 10 shows the simulation results conducted in Proteus of the DV of Liu and Chen CS (17) by using dsPIC33

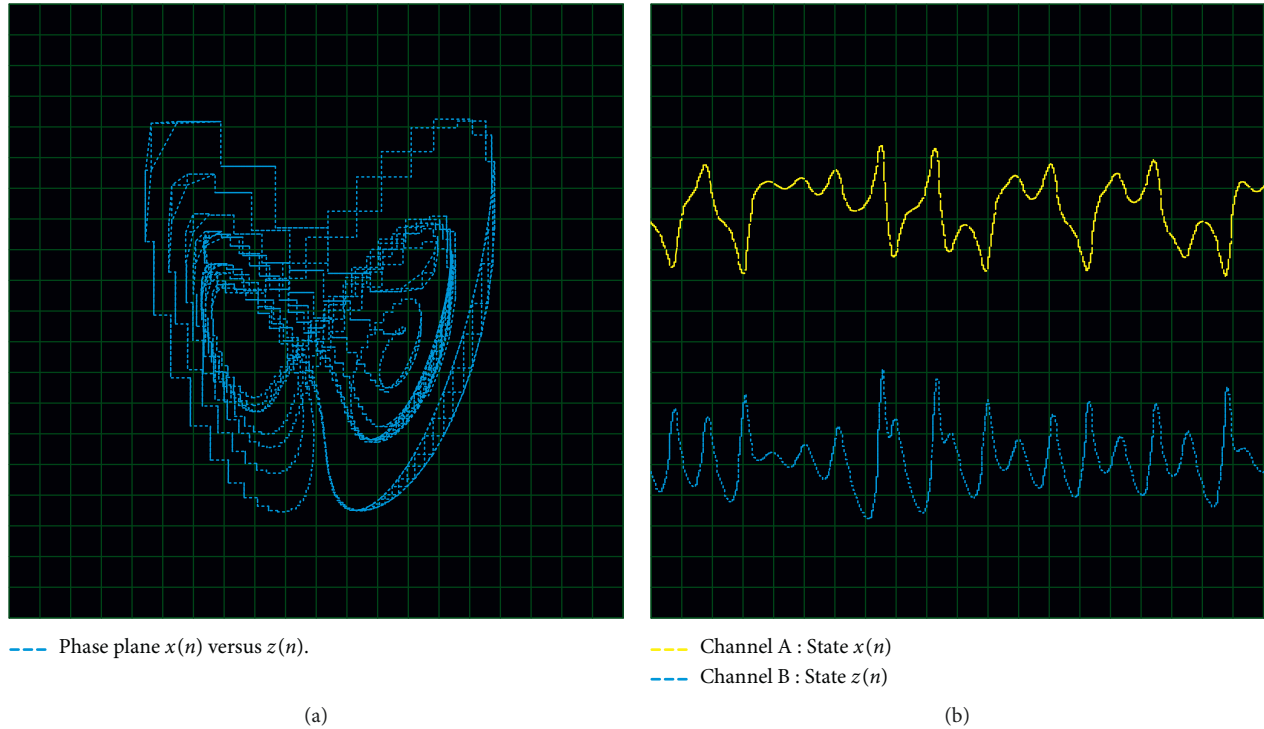


FIGURE 7: Simulation of ES in the V1 of Lorenz system in its DV by using $\tau_{\max} = 0.024$. (a) Phase plane $x(n)$ versus $z(n)$ and (b) evolution of state variables $x(n)$ and $z(n)$.

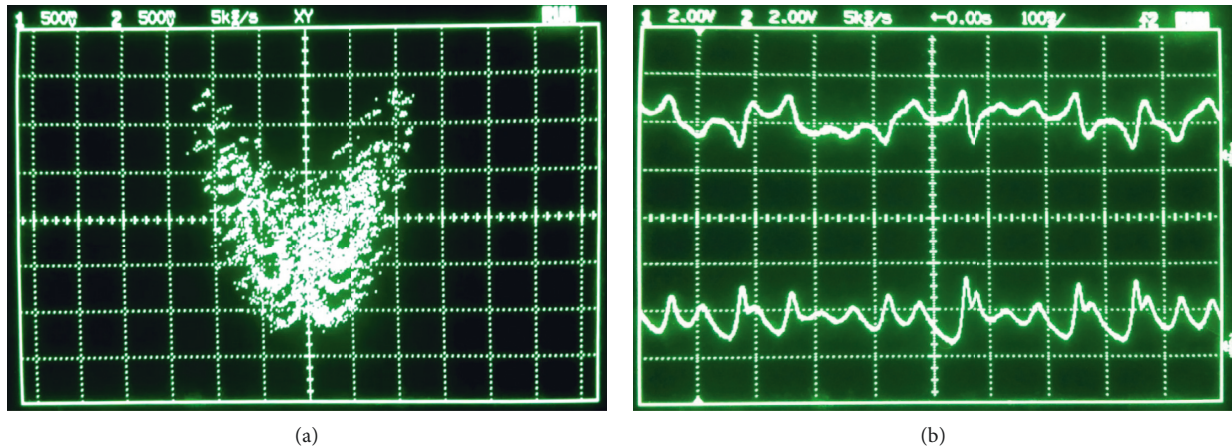


FIGURE 8: Implementation of Lorenz CS (15) in its DV by using the V1 of ES: (a) Phase plane $x(n)$ versus $z(n)$ and (b) evolution of state variables $x(n)$ and $z(n)$.

TABLE 7: Performance of ES in the V1 of the 3D Lorenz, Rössler, Chen, Liu and Chen, and MACM CSs in their DVs by using Euler (6), and Heun (7) and (8) NAs.

CS	Euler		Heun	
	T_{Td} (μs)	f_{Td} (ips)	T_{Td} (μs)	f_{Td} (ips)
Lorenz	2046	488.7	3450	289.8
Rössler	1720	581.3	2760	362.3
Chen	2046	488.7	3450	289.8
Liu and Chen	2480	403.2	4420	226.2
MACM	2046	488.7	3450	289.8

U2. According to the results shown in Table 3, the higher step size $\tau_{\max} = 0.002$ was chosen, we obtained $t_c = 237 \mu s$, $t_{Tg} = 8 \mu s$, $T_{Td} = 245 \mu s$, and $f_{Td} = 4082$ ips; this means that we can reproduce $Q_T = 8.164$ tu in 1 second. Figure 11(a) illustrates the digital oscilloscope of Proteus simulator, it only allows a reduced quantity of samples to show the plane phase $x(n)$ versus $z(n)$.

Figure 11 shows the implementation results of the algorithm (17) of the ES in its V2 considering the same $\tau_{\max} = 0.002$, we obtained $t_c = 86 \mu s$, $t_{Tg} = 3 \mu s$, $T_{Td} = 89 \mu s$,

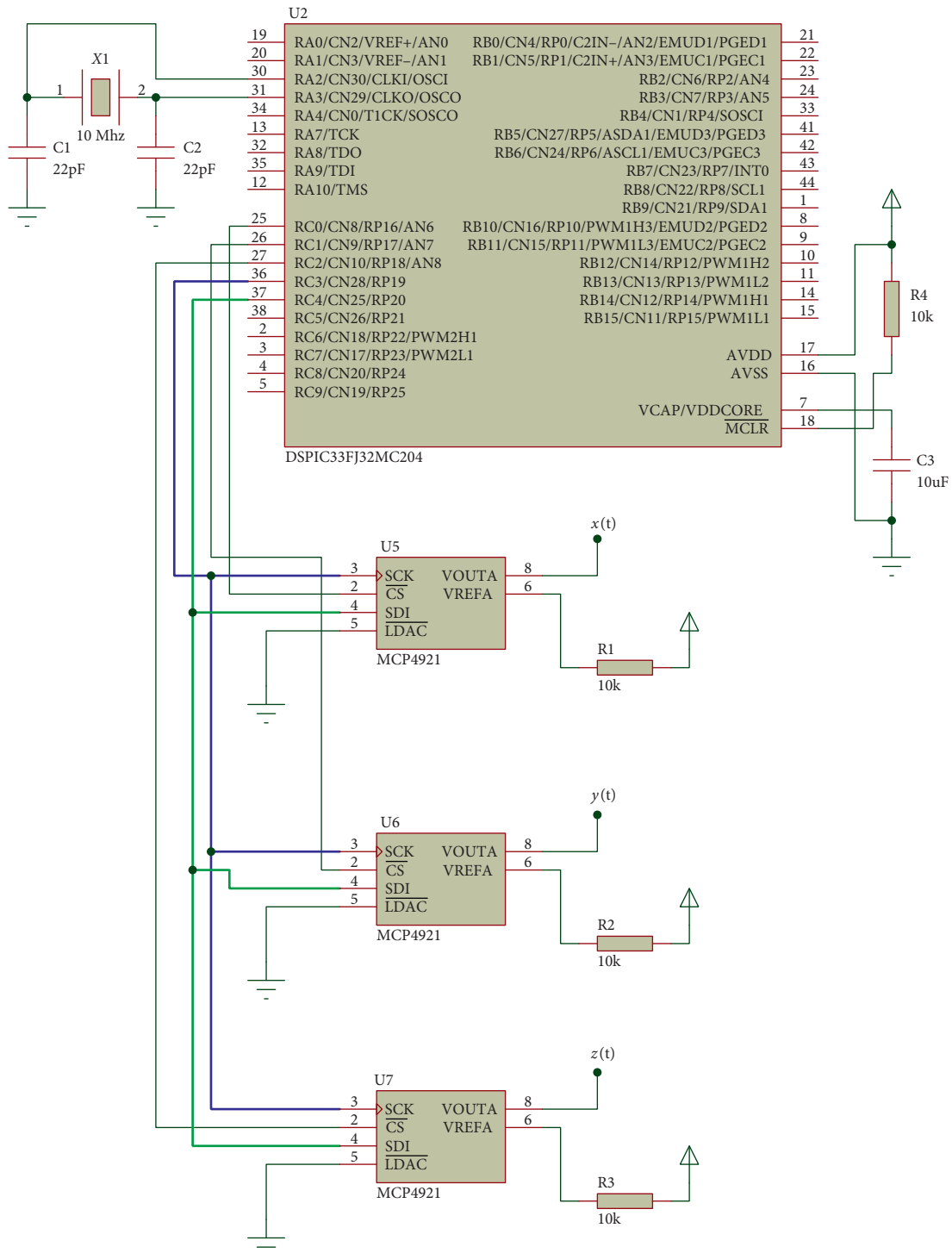


FIGURE 9: Schematic of the simulation of ES in V2 by using Proteus.

and $f_{Td} = 11236$ ips; this means that the hardware implementation in the V2 shows better performance because we obtained $Q_T = 22.5$ tu in 1 second.

Table 8 shows the summarized performance of the 3D Lorenz, Rössler, Chen, Liu and Chen, and MACM CSs in their DV by using the NAs of Euler (6), Heun (7) and (8), and RK4 (9)–(13)—the values of time complexity and its

equivalence are defined in ips. All the NAs can be executed by using dsPIC33 U2 because its program flash memory is 32 Kbytes, and it allows to execute large NAs.

3.3. *Embedded System with PIC32 Microcontroller.* A novel family of PIC32MZ microcontrollers is used to implement the

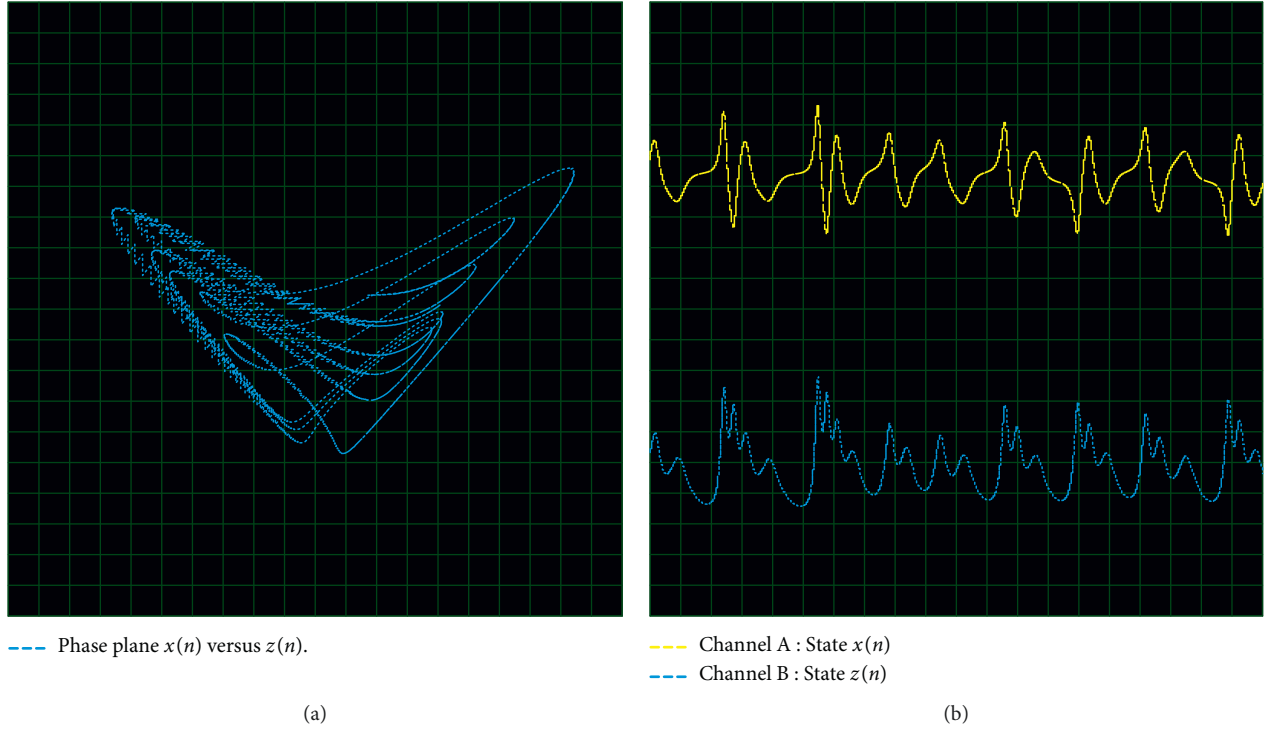


FIGURE 10: Simulation of ES in V2 of Liu and Chen in its DV by using $\tau_{\max} = 0.002$. (a) Phase plane $x(n)$ versus $z(n)$ and (b) evolution of state variables $x(n)$ and $z(n)$.

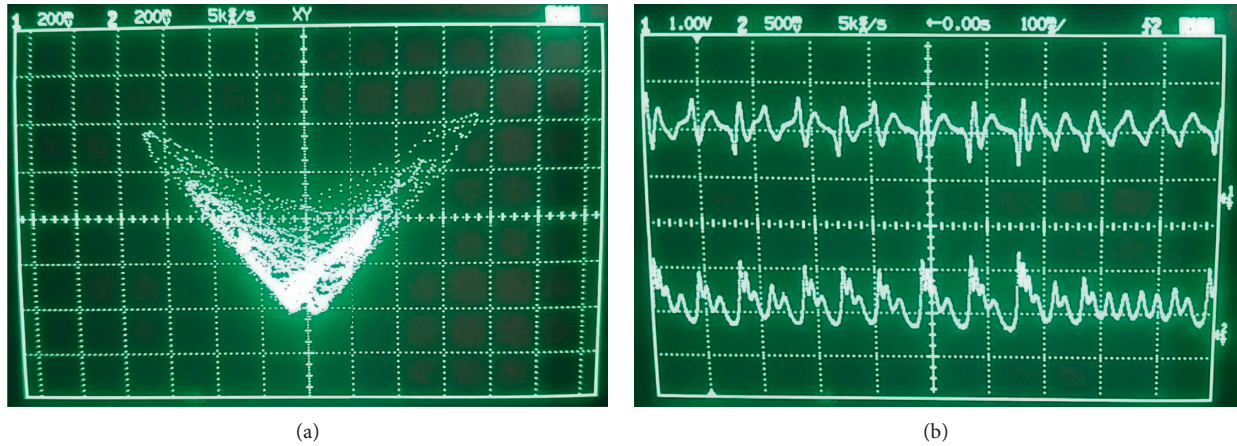


FIGURE 11: Implementation of ES in V2 of Liu and Chen CS (16) in its DV. (a) Phase plane $x(n)$ versus $z(n)$ and (b) evolution of state variables $x(n)$ and $z(n)$.

V3 of ES. The PIC32MZ is not supported by the Proteus simulator; only Mikro C for PIC32 compiler was used to simulate and execute the NAs. Chen CS in its DV was chosen to carry out the test in the V3 of the ES by using Heun algorithm (7) and (8), and its algorithm is given by

$$\begin{aligned} x_{(n+1)}^* &= x_{(n)} + \tau(a(y_{(n)} - x_{(n)})), \\ y_{(n+1)}^* &= y_{(n)} + \tau((c - a)x_{(n)} - x_{(n)}z_{(n)} + cy_{(n)}), \\ z_{(n+1)}^* &= z_{(n)} + \tau(x_{(n)}y_{(n)} - bz_{(n)}), \end{aligned} \quad (18)$$

where

$$\begin{aligned} x_{(n+1)} &= x_{(n)} + \frac{\tau}{2}(a(y_{(n)} - x_{(n)}) + x_{(n+1)}^*), \\ y_{(n+1)} &= y_{(n)} + \frac{\tau}{2}((c - a)x_{(n)} - x_{(n)}z_{(n)} + cy_{(n)} + y_{(n+1)}^*), \\ z_{(n+1)} &= z_{(n)} + \frac{\tau}{2}(x_{(n)}y_{(n)} - bz_{(n)} + z_{(n+1)}^*). \end{aligned} \quad (19)$$

The performance of the algorithm (18) and (19) in the version 3 is $t_c = 13.3 \mu\text{s}$, $t_{Tg} = 3 \mu\text{s}$, $T_{Td} = 16.3 \mu\text{s}$, and

TABLE 8: Performance of ES in the V2 of the 3D Lorenz, Rössler, Chen, Liu and Chen, and MACM CSs in their DVs by using Euler (6), Heun (7) and (8), and RK4 (9)–(13) NAs.

CS	Euler		Heun		RK4	
	T_{Td} (μ s)	f_{Td} (ips)	T_{Td} (μ s)	f_{Td} (ips)	T_{Td} (μ s)	f_{Td} (ips)
Lorenz	84	11905	138	7246	245	4082
Rössler	81	12345	132	7575	233	4291
Chen	84	11905	138	7246	245	4082
Liu and Chen	89	11236	143	6993	271	3690
MACM	84	11905	138	7246	245	4082

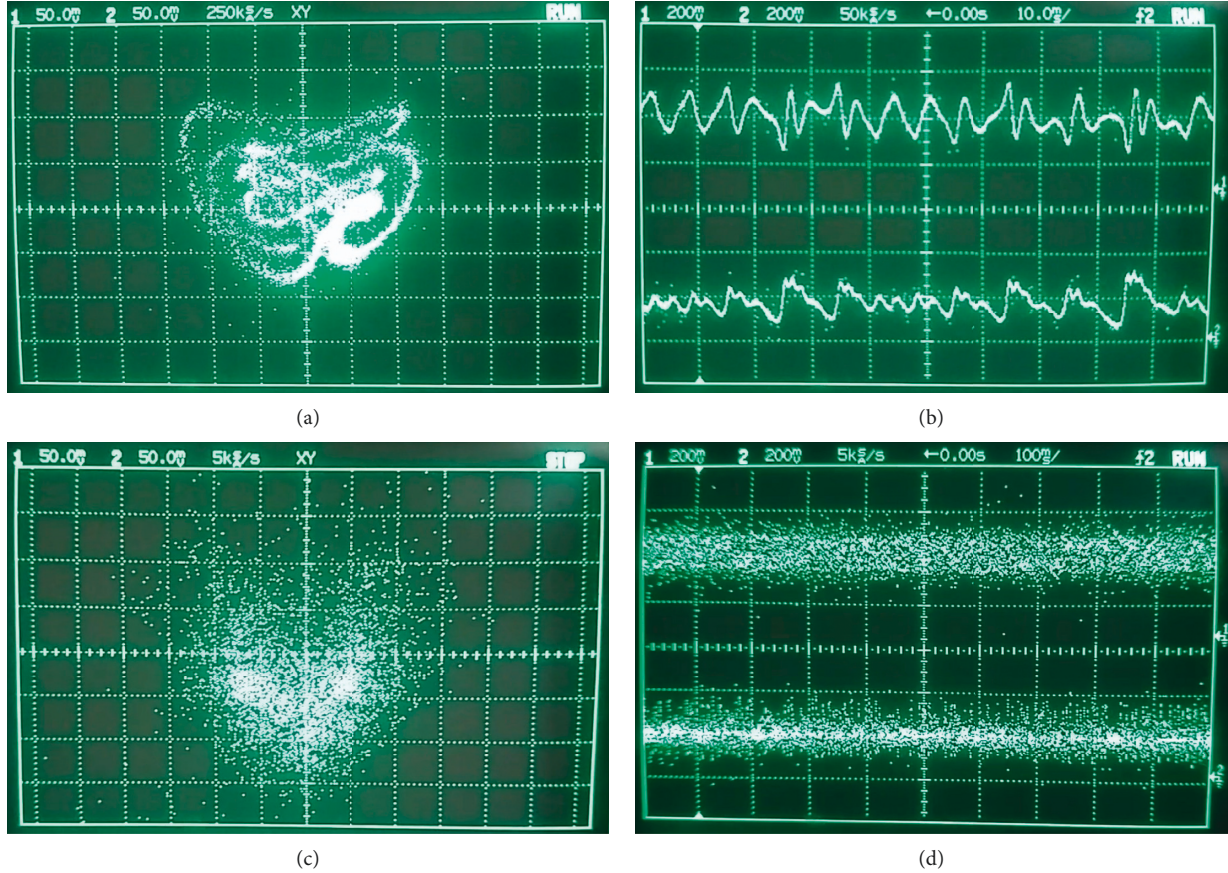


FIGURE 12: Implementation of ES in the V3 of Chen CS (18) and (19) in its DV. (a) Phase plane $x_{(n)}$ versus $z_{(n)}$, (b) evolution of state variables $x_{(n)}$ and $z_{(n)}$ by using $\tau = 0.001$, (c) phase plane $x_{(n)}$ versus $z_{(n)}$, and (d) evolution of state variables $x_{(n)}$ and $z_{(n)}$ by using $\tau_{\max} = 0.017$.

$f_{Td} = 61349$ ips. In order to obtain a comparison between the step sizes obtained, Figure 12 shows two implementations of the algorithm (18) and (19). For the first test, we considered a small step size $\tau = 0.001$; this means that we obtained $Q_T = 20$ time units in 1 second as is shown in Figure 12(b). For the second test, we used the higher step size $\tau_{\max} = 0.017$ as it was described in Table 4. The maximum chaotic degradation is obtained for $Q_T = 340$ time units in 1 second, as is shown in Figure 12(d).

Table 9 shows the time complexity and frequency, expressed in ips, and the performance of ES in V3 by using the NAs of Euler (6), Heun (7) and (8), and RK4 (9)–(13).

TABLE 9: Performance of ES in the V3 of the 3D Lorenz, Rössler, Chen, Liu and Chen, and MACM CSs in their DVs by using Euler (6), Heun (7) and (8), and RK4 (9)–(13) NAs.

CS	Euler		Heun		RK4	
	T_{Td} (μ s)	f_{Td} (ips)	T_{Td} (μ s)	f_{Td} (ips)	T_{Td} (μ s)	f_{Td} (ips)
Lorenz	10.6	94339	16.3	61349	30	33333
Rössler	9.7	103092	12.5	80000	25.8	38759
Chen	10.6	94339	16.3	61349	30	33333
L. and Ch.	10.9	91743	17.1	58479	31.5	31746
MACM	10.6	94339	16.3	61349	30	33333

3.4. *Embedded System Implemented with FPGA by Using Nios Microcontroller.* We introduce a novel method to design an embedded microcontroller in FPGA U4 considering the

similar software and hardware conditions used in the previous implementations of ESs. We create a project in Quartus II (version 12.1) by using the Q_{sys} tool to obtain the hardware design in FPGA U4. The Q_{sys} tool is used to define the specifications of hardware described in a complex arrangement of modules inside FPGA U4; this hardware specification is named Entity, and it can be conducted using the block diagram of Quartus II, e.g., the hardware design of Entity U4 includes a microcontroller as the main processor (its fast version is referred to as Nios II/f which internal clock is configured to 150 MHz), one program memory, peripherals of control, and external ports, among others; to carry out the implementation of the Entity in an FPGA using the Nios II microcontroller, control modules, and other Q_{sys} tools, we recommend reviewing [47]. The hardware implementation is based on the specifications of the FPGA U4 that is included in the hardware of the Terasic DE2i-150 board.

Once the Entity is defined on the FPGA U4, the pins of the SPI control-bus are configured and addressing using the expansion header of the DE2i-150 board where the global peripheral input-output (GPIO) port is configured to write the DACs U4–U6 because the DE2i-150 board does not contain internal DACs. Figure 13 shows the block diagram and the result of the Entity design using Q_{sys} of Quartus II.

Once the hardware structure on FPGA U4 is finished, the Eclipse compiler (version IDE for C/C++ developers) is used to program and implement the NAs of the DV of the 3D Lorenz, Rössler, Chen, Liu and Chen, and MACM CSs in the V4 of the ES. For this example, we used the RK4 algorithm (9)–(13) to obtain the DV of the MACM CS; the algorithm is given by

$$\begin{aligned} k_1 &= -ax_{(n)} - by_{(n)}z_{(n)}, \\ l_1 &= -x_{(n)} + cy_{(n)}, \\ m_1 &= d - y_{(n)}^2 - z_{(n)}, \end{aligned} \quad (20)$$

where

$$\begin{aligned} k_2 &= -a\left(x_{(n)} + \frac{\tau}{2}k_1\right) - b\left(y_{(n)} + \frac{\tau}{2}l_1\right)\left(z_{(n)} + \frac{\tau}{2}m_1\right), \\ l_2 &= -\left(x_{5(n)} + \frac{\tau}{2}k_{15}\right) + c\left(y_{5(n)} + \frac{\tau}{2}l_{15}\right), \\ m_2 &= d - \left(y_{(n)} + \frac{\tau}{2}l_1\right)^2 - \left(z_{(n)} + \frac{\tau}{2}m_1\right), \\ k_3 &= -a\left(x_{(n)} + \frac{\tau}{2}k_2\right) - b\left(y_{(n)} + \frac{\tau}{2}l_2\right)\left(z_{(n)} + \frac{\tau}{2}m_2\right), \\ l_3 &= -\left(x_{(n)} + \frac{\tau}{2}k_2\right) + c\left(y_{(n)} + \frac{\tau}{2}l_2\right), \\ m_3 &= d - \left(y_{(n)} + \frac{\tau}{2}l_2\right)^2 - \left(z_{(n)} + \frac{\tau}{2}m_2\right), \end{aligned} \quad (21)$$

$$\begin{aligned} k_4 &= -a\left(x_{(n)} + \tau k_3\right) - b\left(y_{5(n)} + \tau l_3\right)\left(z_{(n)} + \tau m_3\right), \\ l_4 &= -\left(x_{(n)} + \tau k_3\right) + c\left(y_{(n)} + \tau l_3\right), \\ m_4 &= d - \left(y_{(n)} + \tau l_3\right)^2 - \left(z_{(n)} + \tau m_3\right), \end{aligned} \quad (23)$$

$$\begin{aligned} x_{(n+1)} &= x_{(n)} + \frac{\tau}{6}(k_1 + 2k_2 + 2k_3 + k_4), \\ y_{(n+1)} &= y_{(n)} + \frac{\tau}{6}(l_1 + 2l_2 + 2l_3 + l_4), \\ z_{(n+1)} &= z_{(n)} + \frac{\tau}{6}(m_1 + 2m_2 + 2m_3 + m_4). \end{aligned} \quad (24)$$

The performance of the algorithm (20)–(24) in the V4 is $t_c = 156 \mu\text{s}$, $t_{\text{Tg}} = 3 \mu\text{s}$, $T_{\text{Td}} = 159 \mu\text{s}$, and $f_{\text{Td}} = 6289 \text{ ips}$. As in the previous case, we conduct a comparison between the step sizes obtained. Figure 14 shows the result of two implementations of the algorithms (20)–(24) in the V4. For the first test, we considered a small step size $\tau = 0.01$; Figure 14(b) shows a fewer number of $Q_T = 62.89$ time units generated in 1 second. For the second test, we used the higher step size $\tau_{\text{max}} = 0.547$ described in Table 5, a large number of time units are obtained $Q_T = 3440.1$ in one second, and the maximum chaotic degradation is illustrated in Figure 14(d).

Table 10 shows the results of the ES in the V4; the time complexity and frequency, expressed in ips, were obtained by using the NAs of Euler (6), Heun (7) and (8), and RK4 (9)–(13).

3.5. Results of Embedded System for V1–V4. In order to summarise the studies presented in the previous section, we conducted a comparison considering the performance of the 4 versions in the ES of the 3D Lorenz, Rössler, Chen, Liu and Chen, and MACM CSs in their DVs. We used (15) to obtain the time units Q_T generated in 1 second considering the results obtained of τ_{max} shown in Tables 3–5, and the results of T_{Td} and f_{Td} shown in Tables 7–10. We obtained the best performance of Q_T considering τ_{max} of the 3D Lorenz, Rössler, Chen, Liu and Chen, and MACM CSs in their DVs using the NA of Euler, Heun, and RK4, and the summarized results are presented in Tables 11 and 12.

For a better understanding, Figure 15 illustrates the trajectories of the first state $x_{(n)}$ of the 3D Lorenz, Rössler, Chen, Liu and Chen, and MACM CSs in their DVs by using the NA of Euler (8); the performance of each state $x_{(n)}$ is implemented in the V1-PIC of ES—the results are expressed in the time-units quantity Q_T that the ES in the V1 generates in 1 second, and the t axe is included to compare the performance of CSs used. Figures 15(a), 15(d), and 15(e) show chaotic dynamics more compactly in the trajectories of state $x_{(n)}$. Otherwise, Figures 15(b) and 15(c) show trajectories of the state $x_{(n)}$ less compact.

Figure 16 shows the same trajectories of the first state $x_{(n)}$ of the 3D Lorenz, Rössler, Chen, Liu and Chen, and MACM CSs in their DVs by using the same Euler algorithm (8); now the performance is conducted in the V2-dsPIC of the ES—the results also are expressed in the time-units quantity

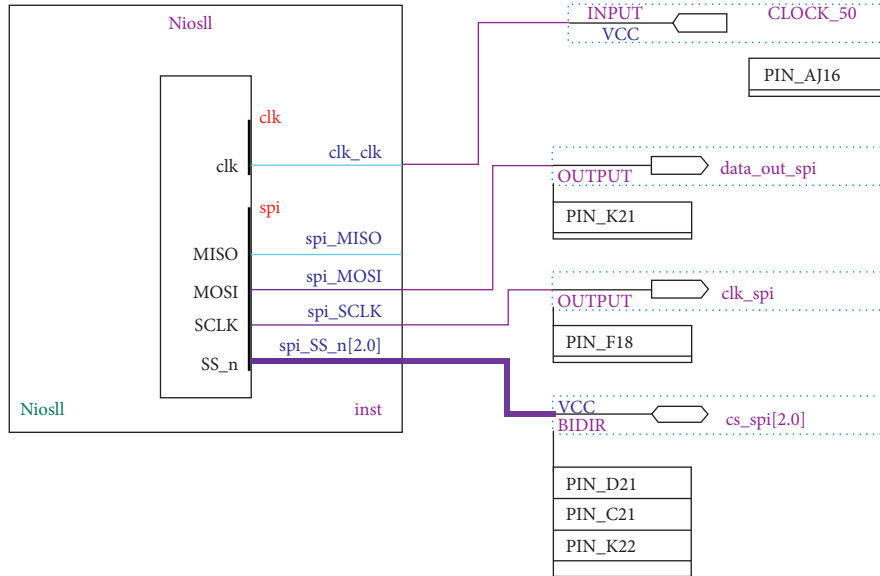


FIGURE 13: Schematic diagram of ES in V4 to implement the Nios II Entity and pins distribution on the FPGA U4.

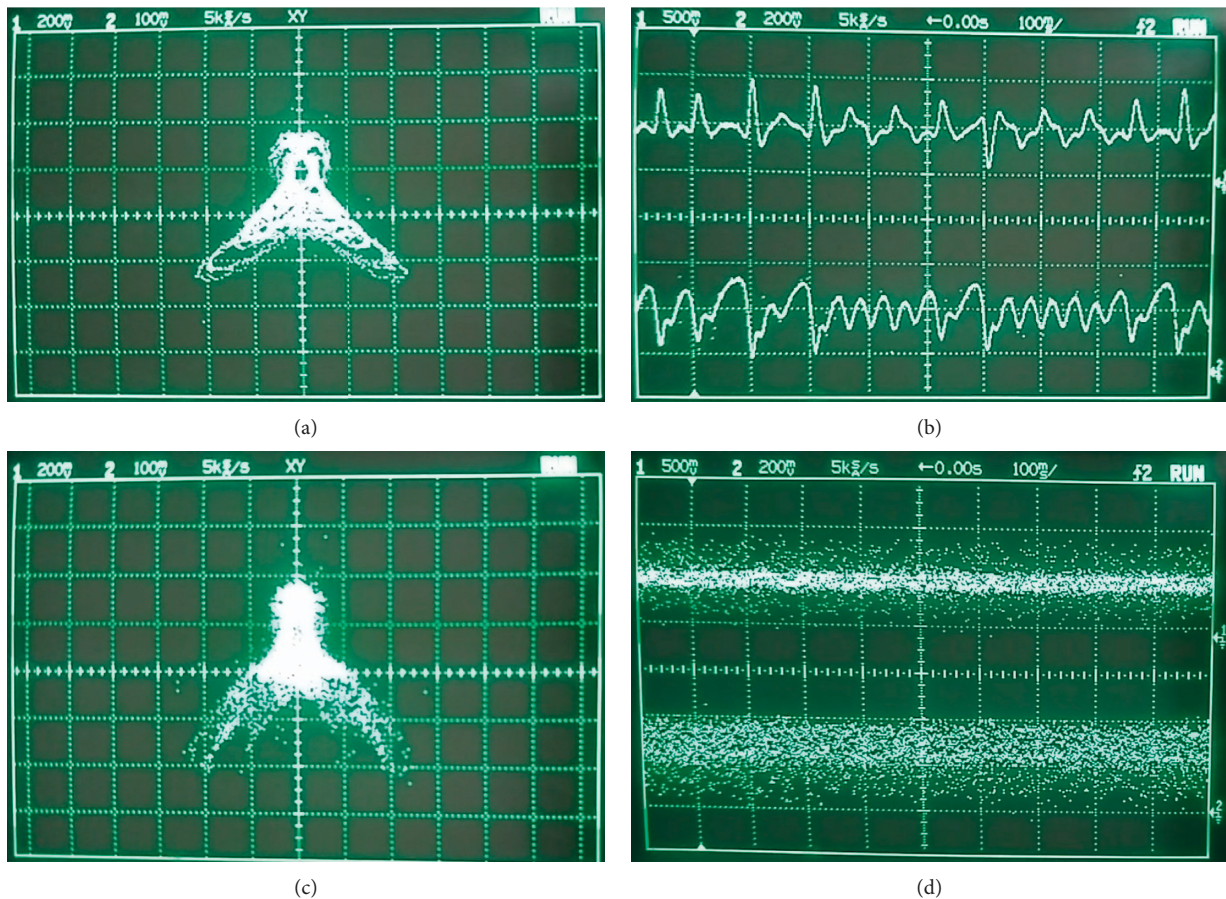


FIGURE 14: Implementation of ES in V4 of the MACM CS (20)–(24) in its DV. (a) Phase plane $x_{(n)}$ versus $z_{(n)}$, (b) evolution of state variables $x_{(n)}$ and $z_{(n)}$ using $\tau = 0.01$, (c) phase plane $x_{(n)}$ versus $z_{(n)}$, and (d) evolution of state variables $x_{(n)}$ and $z_{(n)}$ using $\tau_{\max} = 0.057$.

Q_T that the ES in its version 2 generates in $t = 1$ second. Rössler system presents only one nonlinearity, Figures 15(b) and 16(b) illustrate slow changes in their chaotic dynamics, which means that Rössler system is not tempting to be

implemented in ESs slower like the 8-bit microcontrollers. Figures 15(e) and 16(e) show that MACM CS (represented by (5) in its CV) is most rich in chaos, i.e., it is verified that this CS in its DV presents more rich chaotic dynamics than

TABLE 10: Performance of ES in the V4 of the 3D Lorenz, Rössler, Chen, Liu and Chen, and MACM CSs in their DVs by using Euler (6), Heun (7) and (8), and RK4 (9)–(13) NAs.

CS	Euler		Heun		RK4	
	T_{Td} (μ s)	f_{Td} (ips)	T_{Td} (μ s)	f_{Td} (ips)	T_{Td} (μ s)	f_{Td} (ips)
Lorenz	40	25000	70	14286	159	6289
Rössler	37	27027	53	18868	135	7407
Chen	40	25000	70	14286	159	6289
L. and Ch.	45	22222	83	12048	167	5988
MACM	40	25000	70	14286	159	6289

TABLE 11: Performance of the ES expressed in Q_T of the 3D Lorenz, Rössler, Chen, Liu and Chen, and MACM CSs in their DVs using (6)–(8) for V1, and (6)–(13) for V2.

CS	Q_T for V1-PIC		Q_T for V2-dsPIC		
	Euler	Heun	Euler	Heun	RK4
Lorenz	11.729	6.9552	285.7	492.7	432.7
Rössler	2.9065	1.8115	61.7	1446.8	1077
Chen	0.977	0.5796	23.8	123.2	232.7
L. and Ch.	0.8064	0.4524	22.5	118.9	210.3
MACM	41.05	24.3432	1011.9	1652.1	2232.9

TABLE 12: Performance of the ES expressed in Q_T of V3-V4 for 3D Lorenz, Rössler, Chen, Liu and Chen, and MACM CSs in their DVs using (6)–(13).

CS	Q_T for V3—PIC32			Q_T for V4—FPGA		
	Euler	Heun	RK4	Euler	Heun	RK4
Lorenz	2264	4172	3533	600	971.4	666.6
Rössler	515	15280	9729	135	3603.8	1859.2
Chen	189	1043	1900	50	242.9	358.5
L. and Ch.	183	994	1810	44	204.8	341.3
MACM	8019	13988	18233	2125	3257.2	3440.1

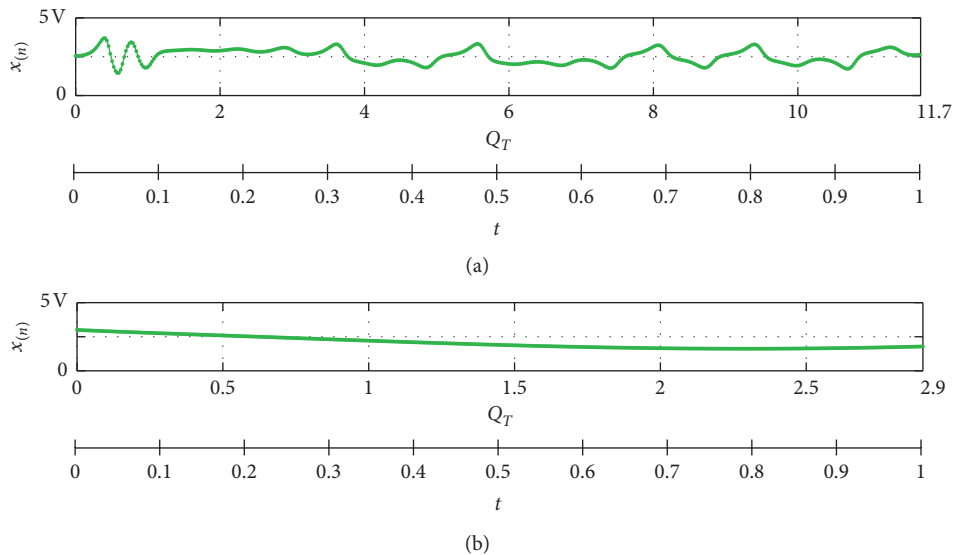


FIGURE 15: Continued.

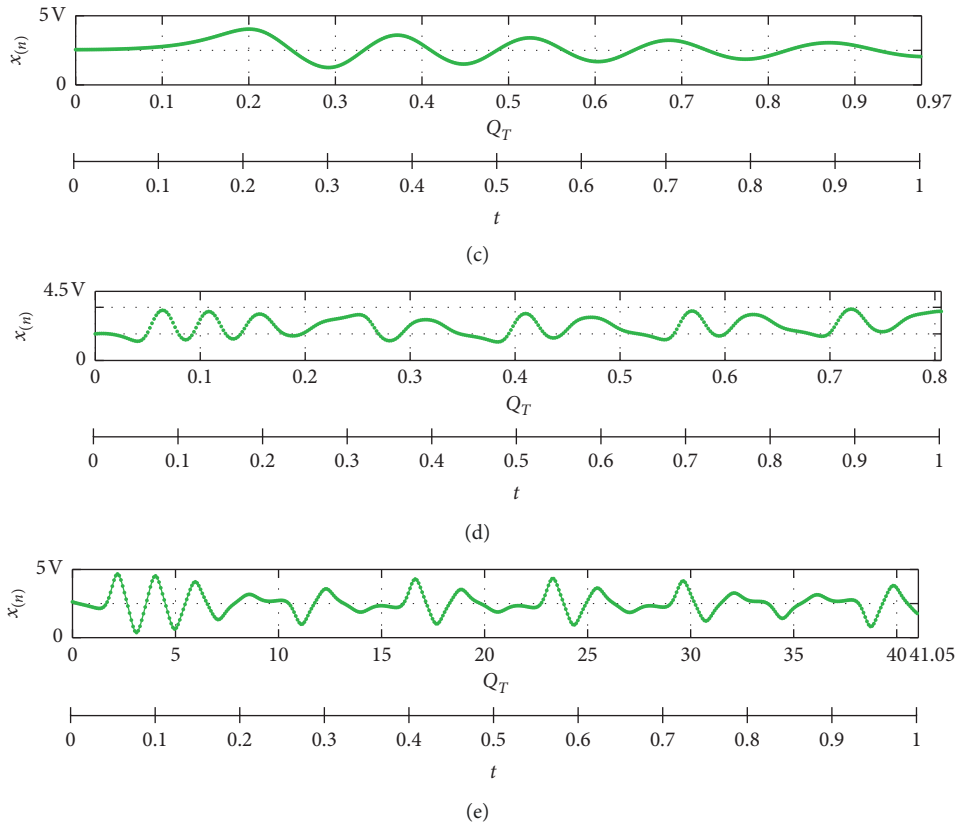


FIGURE 15: Time series of the five CSs of Lorenz, Rössler, Chen, Liu and Chen, and MACM in their DVs by using the Euler NA to compare the performance of version 1 PIC of ES expressed Q_T for $t = 1$ second: (a) $x_{(n)}$ of Lorenz, (b) $x_{(n)}$ of Rössler, (c) $x_{(n)}$ of Chen, (d) $x_{(n)}$ of Liu and Chen, and (e) $x_{(n)}$ of MACM.

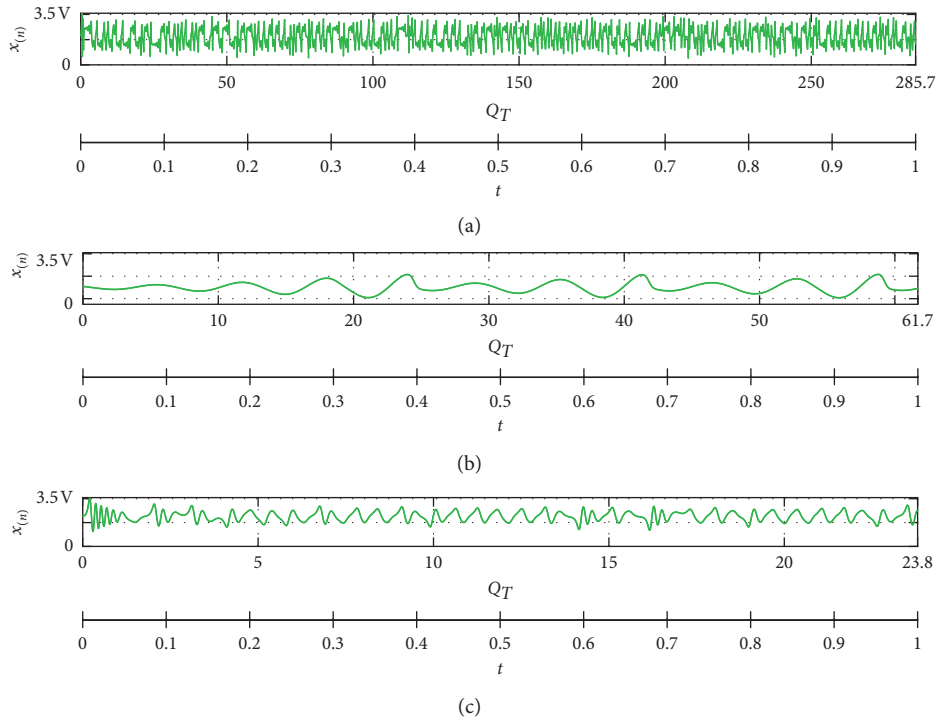


FIGURE 16: Continued.

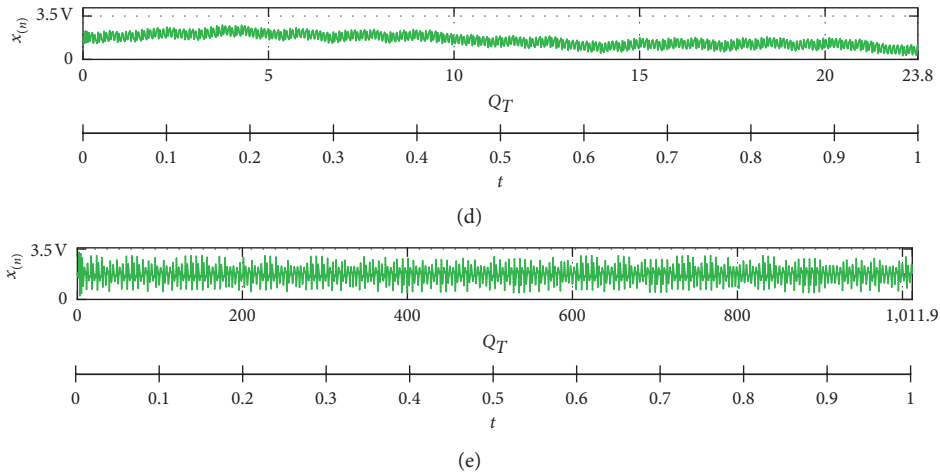


FIGURE 16: Time series of the five CSs of Lorenz, Rössler, Chen, Liu and Chen, and MACM in their DVs by using the Euler NA to compare the performance of version 2 dsPIC of ES expressed Q_T for $t = 1$ second: (a) $x_{(n)}$ of Lorenz, (b) $x_{(n)}$ of Rössler, (c) $x_{(n)}$ of Chen, (d) $x_{(n)}$ of Liu and Chen, and (e) $x_{(n)}$ of MACM.

the others, Lorenz, Rössler, Chen, and Liu and Chen CSs, in their DVs [29].

4. Robustness in Digital Implementation of CSs in DV

The literature reports robustness in ESs considering the characteristics of software and hardware [57]. Regarding the hardware used in the 4 versions of the ES, it has two ways of powering: the first way is through the USB port connected to a laptop or desktop PC, e.g., for the V4 of FPGA device; the second way is using an external power supply for the V1–V3. The ESs V1–V4 energized using an external battery makes them portable, which allows the autonomy of each of them.

On the other hand, a robustness diagram based on the variation of two critical parameters in the five 3D CSs in their DVs using the NAs (6)–(13) was conducted. Figure 17 shows the diagram that determines the regions for two parameters which the existence of chaos is guaranteed for a specific step size obtained in Tables 3–5, each point in the diagram represents the maximum Lyapunov exponent (LE_{\max}). If we have $LE_{\max} > 0$, the dynamics are chaotic denoted in yellow color; otherwise, the blue color is used, previous work was reported in [29]. Figures 17(a)–17(c) represent the variation of the parameters σ versus r of the Lorenz system in its DV, the parameter b was fixed in $8/3$. Figures 17(d)–17(f) represent the variation of the parameters b versus c of the Rössler system in its DV (the parameter a was fixed in 0.2). Figures 17(g)–17(i) represent the variation of the parameters b versus c of the Chen CS in its DV (the parameter a was fixed in 35). Figures 17(j)–17(l) represent the variation of the parameters b versus c of the Liu and Chen CS in its DV (the parameters were fixed with $a = 5$, $d_1 = -1$, and $d_2 = d_3 = 1$). Finally, Figures 17(m)–17(o) represent the variation of the parameters b versus d of the MACM CS in its DV (the parameters were fixed with $a = 2$ and $c = 0.5$). To generate Figures 17(a), 17(d), 17(g), 17(j), and 17(m), we use the Euler NA (6), for Figures 17(b), 17(e), 17(h), 17(k), and 17(n), we use the Heun algorithm (7) and

(8), and for Figures 17(c), 17(f), 17(i), 17(l), and 17(o), we used the NA of RK4 (9)–(13).

Furthermore, it is easy to note that if a value of step size τ less than that considered in yellow color is used, then the chaos regions increase. Taking into account the fact that the preservation of chaos in the DV of the set of 5 CSs in their DVs is robust for the variation of two parameters, considering the characteristics of software and hardware the proposed ES in V1–V4, and the benefits of digital systems, as the elimination of the typical wear of the analog systems, it is stated that the electronical/digital implementation presented in this work is robust.

5. Conclusions

In this paper, we have presented analytical, numerical, and experimental studies of chaos degradation of the Lorenz, Rössler, Chen, Liu and Chen, and MACM three-dimensional chaotic systems (CSs) in their discretized versions (DV) by using the numerical algorithms (NAs) of Euler, Heun, and fourth-order Runge–Kutta (RK4). We obtained a novel robustness diagram with the variation of two parameters of the five CSs in their DVs to guarantee the chaos existence where the maximum step size was found by using Euler, Heun, and fourth-order Runge–Kutta (RK4) NAs, the degradation studies showed that the DV of MACM CS exhibits higher chaotic degradation, while the Chen and Liu Chen presented a lower degradation. The step-size values founded can be used, e.g., for encryption applications, as one more parameter, considering the intervals shown in this paper to guarantee chaos. In addition, the step size obtained can be used in others families of 8-, 16-, and 32-bit microcontrollers, DSP, or FPGA where the DVs of these five 3D CSs studied are desired for general purposes.

The numerical studies of Root-Mean-Square Error (RMSE) have shown better performance in the Rössler system, it provided interesting and attractive results with respect to the DVs of the Lorenz, Chen, Liu and

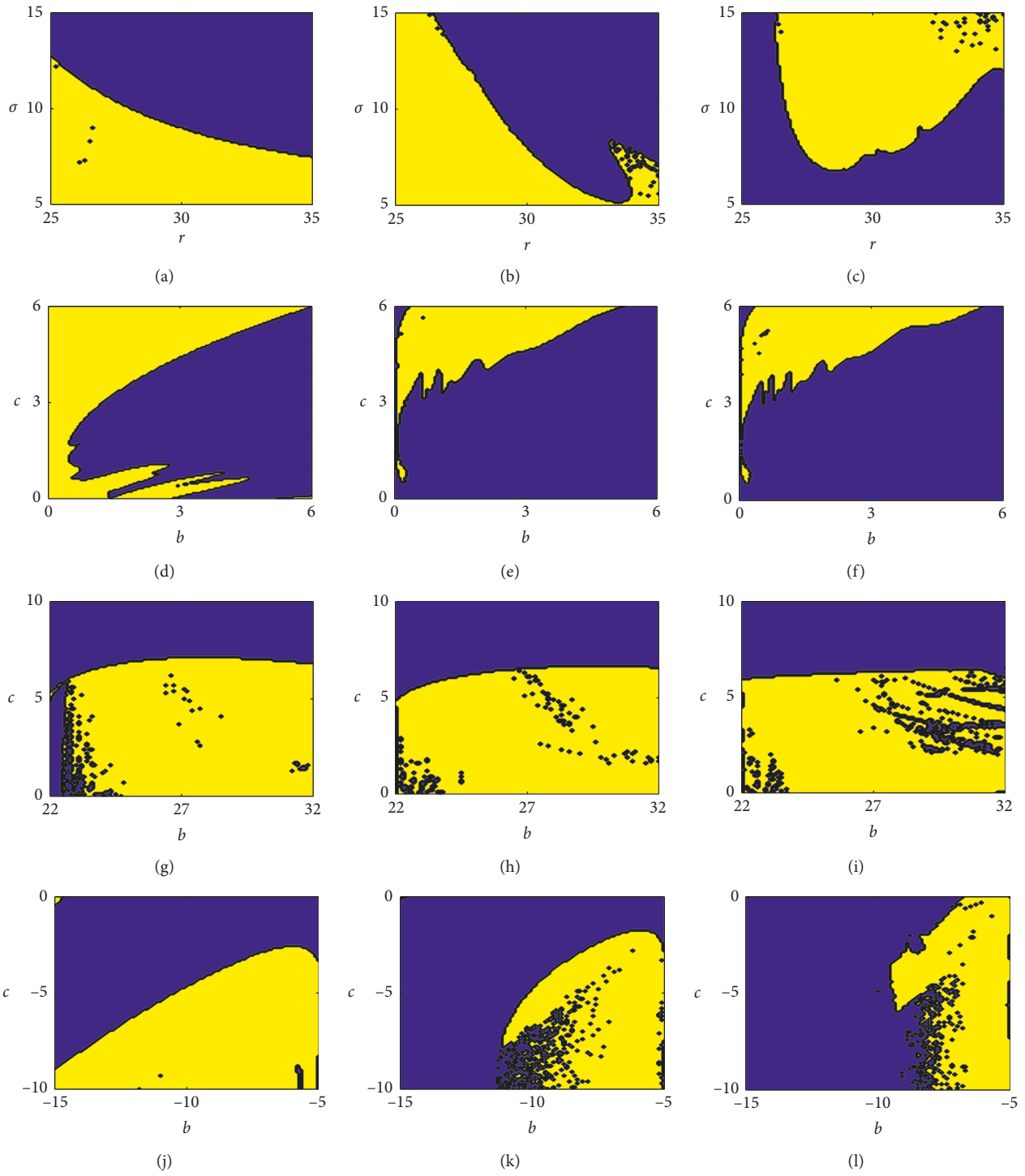


FIGURE 17: Continued.

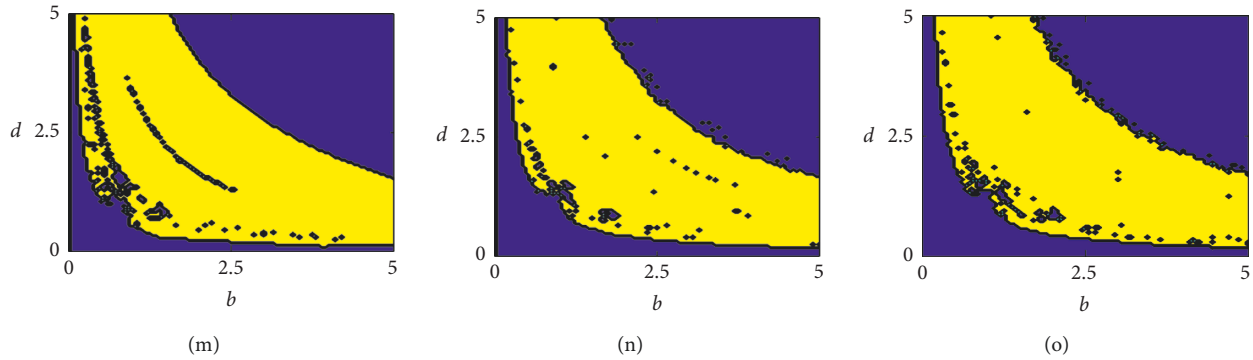


FIGURE 17: Robustness diagram of chaos existence varying two parameters at intervals of 0.05 and with τ according to five 3D CSs in their DVs using the NA (6)–(13): chaos (yellow); no chaos (blue).

Chen, and MACM CSs using the numerical algorithms Euler, Heun, and RK4; it had slow changes in their dynamics and showed small variations in their trajectories to same initial conditions considering 30000 samples. Similar results of RMSE and step sizes were obtained from Chen and Liu and Chen systems although the Liu and Chen system has 3 nonlinearities, one more than Chen system.

All the results of the three-dimensional five chaotic systems in their discretized versions were implemented by using four versions of the embedded system (ES) where the 16-bit dsPIC33 showed better alternative to simulate, reproduce, and implement the numerical algorithms of Euler, Heun, and RK4. The 32-bit PIC32MZ presented the best performance in time complexity and is an interesting alternative to implement and obtain good performance for applications where iteration speed is desirable such as synchronization and multimedia encryption, among others.

As future work, complementary degradation studies of 4D hyperchaotic systems will be conducted for encryption and synchronization applications and their implementation in other families of the ESs.

Data Availability

The data used to support the findings of this study are included within the article.

Conflicts of Interest

The authors declare that there are no conflicts of interest regarding the publication of this paper.

Acknowledgments

This work was supported by the CONACYT, México, under Research Grant 166654 (A1-S-31628).

References

- [1] S. H. Strogatz, *Nonlinear Dynamics and Chaos: With Applications to Physics, Biology, Chemistry, and Engineering*, Perseus Books, Massachusetts, MA, USA, 1994.
- [2] J.-P. Eckmann and D. Ruelle, "Ergodic theory of chaos and strange attractors," *Reviews of Modern Physics*, vol. 57, no. 3, pp. 617–656, 1985.
- [3] A. Argyris, D. Syvridis, L. Larger et al., "Chaos-based communications at high bit rates using commercial fibre-optic links," *Nature*, vol. 438, no. 7066, pp. 343–346, 2005.
- [4] L. Gámez-Guzmán, C. Cruz-Hernández, R. M. López-Gutiérrez, and E. E. García-Guerrero, "Synchronization of Chua's circuits with multi-scroll attractors: application to communication," *Communications in Nonlinear Science and Numerical Simulation*, vol. 14, no. 6, pp. 2765–2775, 2009.
- [5] R. M. May, "Simple mathematical models with very complicated dynamics," *Nature*, vol. 261, no. 5560, pp. 459–467, 1976.
- [6] S. Boccaletti, C. Grebogi, Y.-C. Lai, H. Mancini, and D. Maza, "The control of chaos: theory and applications," *Physics Reports*, vol. 329, no. 3, pp. 103–197, 2000.
- [7] Ch. Wang, Ch. Fan, K. Feng, X. Huang, and Q. Ding, "Analysis of the time series generated by a new high-dimensional discrete chaotic system," *Complexity*, vol. 2018, Article ID 9818520, 11 pages, 2018.
- [8] A. Arellano-Delgado, R. López-Gutiérrez, C. Cruz-Hernández, C. Posadas-Castillo, L. Cardoza-Avenidaño, and H. Serrano-Guerrero, "Experimental network synchronization via plastic optical fiber," *Optical Fiber Technology*, vol. 19, no. 93, pp. 93–98, 2016.
- [9] M. Murillo-Escobar, C. Cruz-Hernández, F. Abundiz-Pérez, R. López-Gutiérrez, and O. Acosta Del Campo, "A RGB image encryption algorithm based on total plain image characteristics and chaos," *Signal Processing*, vol. 109, pp. 109–161, 2015.
- [10] Y. Nakamura and A. Sekiguchi, "The chaotic mobile robot," *IEEE Transactions on Robotics and Automation*, vol. 17, no. 6, pp. 898–904, 2001.
- [11] L. Fan-Yi and L. Jia-Ming, "Chaotic radar using nonlinear laser dynamics," *IEEE Journal of Quantum Electronics*, vol. 40, no. 6, pp. 815–820, 2004.
- [12] K. Junxiang, Y. Lilin, H. Tongtong, H. Ye, X. Guangqiong, and H. Weisheng, "Time delay concealment in feedback chaotic systems with dispersion in loop," *IEEE Photonics Journal*, vol. 9, no. 2, Article ID 7200808, 2017.
- [13] M. Chen, S.-Y. Shao, P. Shi, and Y. Shi, "Disturbance-observer-based robust synchronization control for a class of fractional-order chaotic systems," *IEEE Transactions on Circuits and Systems II: Express Briefs*, vol. 64, no. 4, pp. 417–421, 2017.

- [14] C.-H. Huang, C.-H. Lin, and C.-L. Kuo, "Chaos synchronization-based detector for power-quality disturbances classification in a power system," *IEEE Transactions on Power Delivery*, vol. 26, no. 2, pp. 944–953, 2011.
- [15] G. Doménech, T. J. Kazmierski, R. Ruiz, and J. D. Ruiz, "Architectural synthesis of high level analogue VHDL-AMS descriptions using netlist extraction from parse trees," *Electronic Letters*, vol. 36, no. 20, pp. 1680–1682, 2000.
- [16] S. Sahin and C. Guzelis, "'Chaotification' of real systems by dynamic state feedback," *IEEE Antennas and Propagation Magazine*, vol. 52, no. 6, pp. 222–233, 2010.
- [17] A. Veeraraghavan, A. Srivastava, A. K. Roy-Chowdhury, and R. Chellappa, "Rate-invariant recognition of humans and their activities," *IEEE Transactions on Image Processing*, vol. 18, no. 6, pp. 1626–1639, 2009.
- [18] E. N. Lorenz, "Deterministic nonperiodic flow," *Journal of the Atmospheric Sciences*, vol. 20, no. 2, pp. 160–141, 1963.
- [19] O. E. Röessler, "An equation for continuous chaos," *Physics Letters A*, vol. 57, no. 5, pp. 397–398, 1976.
- [20] J. Lü and G. Chen, "A new chaotic attractor coined," *International Journal of Bifurcation and Chaos*, vol. 12, no. 3, pp. 659–661, 2002.
- [21] L. O. Chua, M. Komuro, and T. Matsumoto, "The double scroll family," *IEEE Transactions on Circuits and Systems*, vol. 33, no. 11, pp. 1073–1118.
- [22] Ch. Liu, T. Liu, L. Liu, and K. Liu, "A new chaotic attractor," *Chaos, Solitons & Fractals*, vol. 22, no. 5, pp. 1031–1038, 2005.
- [23] G. Chen and T. Ueta, "Yet another chaotic attractor," *International Journal of Bifurcation and Chaos*, vol. 9, no. 7, pp. 1465–1466, 1999.
- [24] W. B. Liu and G. Chen, "A new chaotic system and its generation," *International Journal of Bifurcation and Chaos*, vol. 12, pp. 261–267, 2002.
- [25] J. C. Sprott, "Some simple chaotic jerk functions," *American Journal of Physics*, vol. 65, no. 6, pp. 537–543, 1997.
- [26] J. C. Sprott, "Some simple chaotic flows," *Physical Review E*, vol. 50, no. 2, pp. R647–R650, 1994.
- [27] L. Xiong, Y. Lu, Y. Zhang, and X. Zhang, "A novel memductor-based chaotic system and its applications in circuit design and experimental validation," *Complexity*, vol. 2019, Article ID 3870327, 23 pages, 2019.
- [28] V.-T. Pham, S. Jafari, C. Volos, A. Giakoumis, S. Vaidyanathan, and T. Kapitaniak, "A chaotic system with equilibria located on the rounded square loop and its circuit implementation," *IEEE Transactions on Circuits and Systems II: Express Briefs*, vol. 63, no. 9, pp. 878–882, 2016.
- [29] R. Méndez-Ramírez, C. Cruz-Hernández, A. Arellano-Delgado, and R. Martínez-Clark, "A new simple chaotic Lorenz-type system and its digital realization using a TFT touch-screen display embedded system," *Complexity*, vol. 2017, Article ID 6820492, 16 pages, 2017.
- [30] M. Hénon, "A two-dimensional mapping with a strange attractor," *Communications in Mathematical Physics*, vol. 50, no. 1, pp. 69–77, 1976.
- [31] C. Cruz-Hernández and A. A. Martynyuk, "Advances in chaotic dynamics with applications," *Series: Stability, Oscillations, and Optimization of Systems*, Cambridge Scientific Publishers, vol. 4, p. 432, Cambridge, UK, 2010.
- [32] I. Koyuncu, A. T. Ozcerit, and I. Pehlivan, "Implementation of FPGA-based real time novel chaotic oscillator," *Nonlinear Dynamics*, vol. 77, no. 1-2, pp. 49–59, 2014.
- [33] M. S. Azzaz, C. Tanougast, S. Sadoudi, R. Fellah, and A. Dandache, "A new auto-switched chaotic system and its FPGA implementation," *Communications in Nonlinear Science and Numerical Simulation*, vol. 18, no. 7, pp. 1792–1804, 2016.
- [34] L. Cong and W. Xiaofu, "Design and realization of an FPGA-based generator for chaotic frequency hopping sequences," *IEEE Transactions on Circuits and Systems I*, vol. 48, no. 5, pp. 521–532, 2001.
- [35] W. Yang, W. Cao, T.-S. Chung, and J. Morris, *Applied Numerical Methods Using Matlab*, John Wiley & Sons, Hoboken, NJ, USA, 2005.
- [36] E. Köse and A. Mühürçü, "Realization of a digital chaotic oscillator by using a low cost microcontroller," *Engineering Review*, vol. 37, no. 3, pp. 341–348, 2017.
- [37] R. Méndez-Ramírez, A. Arellano-Delgado, C. Cruz-Hernández, F. Abundiz-Perez, and R. Martínez-Clark, "Chaotic digital cryptosystem by using SPI protocol and its dsPICs implementation," *Frontiers of Information Technology & Electronic Engineering*, vol. 19, no. 2, pp. 165–179, 2018.
- [38] R. Mendez-Ramirez, A. Arellano-Delgado, C. Cruz-Hernandez, and R. M. Lopez-Gutierrez, "Degradation analysis of generalized Chua's circuit generator of multi-scroll chaotic attractors and its implementation on PIC32," in *Proceedings of the Future Technologies Conference (FTC)*, pp. 1034–1039, San Francisco, CA, USA, December 2016.
- [39] G. S. Thenge, S. S. Mulla, and A. B. Patki, "System identification using chaos theory on ARM cortex M3 processor development board," in *Proceedings of the 2015 IEEE International Advance Computing Conference (IACC)*, pp. 768–771, Bangalore, India, June 2015.
- [40] B. Cai, G. Wang, and F. Yuan, "Pseudo random sequence generation from a new chaotic system," in *Proceedings of the 2015 IEEE 16th International Conference on Communication Technology (ICCT)*, pp. 863–867, Hangzhou, China, October 2015.
- [41] M. L. Barakat, A. S. Mansingka, A. G. Radwan, and K. N. Salama, "Hardware stream cipher with controllable chaos generator for colour image encryption," *IET Image Processing*, vol. 8, no. 1, pp. 33–43, 2014.
- [42] E. Tlelo-Cuautle, J. J. Rangel-Magdaleno, A. D. Pano-Azucena, P. J. Obeso-Rodelo, and J. C. Nunez-Perez, "FPGA realization of multi-scroll chaotic oscillators," *Communications in Nonlinear Science and Numerical Simulation*, vol. 27, no. 1–3, pp. 66–80, 2015.
- [43] Z. Lin, J. Liu, J. Lian, Y. Ma, and X. Zhang, "A novel fast image encryption algorithm for embedded systems," *Multimedia Tools and Applications*, vol. 78, pp. 6969–6987, 2019.
- [44] A. Flores-Vergara, E. E. García-Guerrero, E. Inzunza-González et al., "Implementing a chaotic cryptosystem in a 64-bit embedded system by using multiple-precision arithmetic," *Nonlinear Dynamics*, vol. 95, no. 1, pp. 497–516, 2019.
- [45] Microchip Technology Inc., AN575. *IEEE-754 Compliant Floating Point Routines, DS00575B*, Microchip Technology Inc., Chandler, AZ, USA, 1997.
- [46] IEEE Computer Society, *IEEE Standard for Floating-point Arithmetic-Redline. IEEE Std 754-2008—Redline*, IEEE Computer Society, New York, NY, USA, 2008.
- [47] J. M. McNichols, E. J. Balster, W. F. Turri, and K. L. Hill, "Design and implementation of an embedded NIOS II system for JPEG2000 tier II encoding," *International Journal of Reconfigurable Computing*, vol. 2013, Article ID 140234, 9 pages, 2013.
- [48] S. Chernyi and A. Zhilenkov, "Modeling of complex structures for the ship's power complex using Xilinx system," *Transport and Telecommunication Journal*, vol. 16, no. 1, pp. 73–82, 2015.

- [49] B. Muthuswamy and S. Banerjee, "A route to chaos using FPGAs," *Experimental Observations*, Vol. 1, Springer, Berlin, Germany, 2014.
- [50] A. Wolf, J. B. Swift, H. L. Swinney, and J. A. Vastano, "Determining Lyapunov exponents from a time series," *Physica D: Nonlinear Phenomena*, vol. 16, no. 3, pp. 285–317, 1985.
- [51] K. Briggs, "An improved method for estimating Liapunov exponents of chaotic time series," *Physics Letters A*, vol. 151, no. 1-2, pp. 27–32, 1990.
- [52] J. R. Dormand and P. J. Prince, "A family of embedded Runge-Kutta formulae," *Journal of Computational and Applied Mathematics*, vol. 6, no. 1, pp. 19–26, 1980.
- [53] L. F. Shampine and M. W. Reichelt, "The MATLAB ODE suite," *SIAM Journal on Scientific Computing*, vol. 18, no. 1, pp. 1–22, 1997.
- [54] Mikroelektronika, *Programing dsPIC MCUs in C*, Mikroelektronika, Belgrade, Serbia, 2018.
- [55] A. Datta, D. Mukherjee, and H. Saha, "A dsPIC based novel digital sinusoidal pulse-width modulation technique for voltage source inverter applications," *Microprocessors and Microsystems*, vol. 38, no. 7, pp. 649–658, 2014.
- [56] M. A. Murillo-Escobar, C. Cruz-Hernández, L. Cardoza-Avenidaño, and R. Méndez-Ramírez, "A novel pseudorandom number generator based on pseudo randomly enhanced logistic map," *Nonlinear Dynamics*, vol. 86, no. 1, pp. 407–425, 2017.
- [57] S. Fraser, D. Campara, C. Chilly et al., "Fostering software robustness in an increasingly hostile world," in *Proceedings of the Companion to the 20th Annual ACM SIGPLAN Conference*, San Diego, CA, USA, October 2005.

Research Article

Analysis and FPGA Realization of a Novel 5D Hyperchaotic Four-Wing Memristive System, Active Control Synchronization, and Secure Communication Application

Fei Yu ¹, Li Liu ¹, Binyong He ¹, Yuanyuan Huang ¹, Changqiong Shi, ¹ Shuo Cai ¹, Yun Song ¹, Sichun Du ², and Qiuzhen Wan ³

¹School of Computer and Communication Engineering, Changsha University of Science and Technology, Changsha 410114, China

²College of Computer Science and Electronic Engineering, Hunan University, Changsha 410082, China

³College of Information Science and Engineering, Hunan Normal University, Changsha 410081, China

Correspondence should be addressed to Fei Yu; yufeiyf@csust.edu.cn and Yuanyuan Huang; snailhyy@126.com

Received 1 September 2019; Revised 26 October 2019; Accepted 29 October 2019; Published 28 November 2019

Guest Editor: Viet-Thanh Pham

Copyright © 2019 Fei Yu et al. This is an open access article distributed under the Creative Commons Attribution License, which permits unrestricted use, distribution, and reproduction in any medium, provided the original work is properly cited.

By introducing a flux-controlled memristor with quadratic nonlinearity into a 4D hyperchaotic system as a feedback term, a novel 5D hyperchaotic four-wing memristive system (HFWMS) is derived in this paper. The HFWMS with multiline equilibrium and three positive Lyapunov exponents presented very complex dynamic characteristics, such as the existence of chaos, hyperchaos, limit cycles, and periods. The dynamic characteristics of the HFWMS are analyzed by using equilibria, phase portraits, Poincaré map, Lyapunov exponential spectrum, bifurcation diagram, and spectral entropy. Of particular interest is that this novel system can generate two-wing hyperchaotic attractor under appropriate parameters and initial conditions. Moreover, the FPGA realization of the novel 5D HFWMS is reported, which proves that the system has complex dynamic behavior. Finally, synchronization of the 5D hyperchaotic system with different structures by active control and a secure signal masking application of the HFWMS are implemented based on numerical simulations and FPGA. This research demonstrates that the hardware-based design of the 5D HFWMS can be applied to various chaos-based embedded system applications including random number generation, cryptography, and secure communication.

1. Introduction

Nonlinear science is a new interdisciplinary subject to study the universality of nonlinear phenomena, which runs through almost every subject of meteorology [1, 2], mathematics [3–6], fluid mechanics [7, 8], complex network [9–12], electronics [13–15], and social science [16, 17]. Chaos is one of the most important achievements of nonlinear science. Its random-like and sensitive initial values make chaos have good potential applications in the fields of random number generation [18–20], cryptosystem [21, 22], image encryption [23–25] and secure communication [26–29]. In recent years, many new multiwing (or multi-scroll) chaotic systems have been discovered and proposed [30–35]. The continuous introduction of various complex chaotic attractor models not only provides research basis for

the development of chaotic system theory, but also provides rich subjects for the practical application of chaotic theory.

Since Rossler proposed the first hyperchaotic system with two positive Lyapunov exponents [36], a large number of researchers have begun to devote themselves to the study of hyperchaotic systems [37–42]. Hyperchaotic systems are more sensitive, pseudorandom, and have larger key space, which makes them more suitable for applications such as secure communication and image encryption than chaotic systems. In order to construct more complex chaotic attractors, a large number of literatures have recently reported the multiwing hyperchaotic systems [43–46]. In [43], in order to overcome the inherent difficulties of iteratively adjusting multiparameters in traditional multiparameter control, a unified step function for single-parameter control is proposed to construct a nonequilibrium multiwing

hyperchaotic system. In [45], by introducing mirror symmetric transformation into the hyperchaotic system, various hyperchaotic attractors with mirror symmetric grids are obtained. In [46], a five-dimensional (5D) autonomous hyperchaotic attractor with four wing is introduced, which has only eight parameters to be controlled and only one equilibrium point.

Memristor is an electronic device that describes the relationship between charge and magnetic flux, which was proposed in 1971 by Chua [47] and for the first time realized by HP Labs in 2008 [48]. Because of its strong nonlinear characteristics, memristors have potential applications in many engineering fields, and their research has attracted more and more attention [49, 50]. Recently, many nonlinear memristive oscillators have been proposed [51–53], creating a memristive hyperchaotic system with a multiwing attractor having a practical significance, which has become a research hotspot [54–57]. In [55], by introducing a flux-controlled memristor into a multiwing system, a multiwing hyperchaotic attractor is observed in a no-equilibrium memristive system. In [56], a hyperchaotic system is constructed by adding only a smooth flux-controlled memristor to the 3D pseudo four-wing chaotic system, which can generate a real four-wing hyperchaotic attractor with a line of equilibrium. In [57], flux-controlled memristors are used to replace the resistors in the circuit of the modified Lü system, and this new memristive system can exhibit the hyperchaotic multiwing attractor with two relatively large positive Lyapunov exponents. However, a review of literature revealed there are no research studies that examined the four-wing behavior and three-positive Lyapunov exponents in memristive hyperchaotic systems with dimensions greater than four. This kind of high-dimensional hyperchaotic systems cannot be ignored. Because of their complexity, signal generation is usually used for random number generation and secure communication just to name a few.

In recent years, the main methods to realize chaotic or hyperchaotic attractors are analog circuits, such as breadboards based on discrete components [55–57] and integrated circuits (ICs) based on CMOS technology [14, 33, 34, 37]. With the change of time and temperature in analog circuit, the device will have temperature drift and poor control accuracy. Therefore, it is difficult to realize the chaotic system with high precision by analog circuit, and the breadboard is not easy to carry and digitally store. The design of high-dimensional chaotic systems using CMOS technology generally requires multipliers, which are difficult to design. At the same time, ICs have the shortcomings of long development cycle and high cost [58–60]. Therefore, researchers began to focus on digital circuits with low cost, short design cycle, fast speed, low power consumption, and high accuracy, such as digital signal processor (DSP) [61, 62] and field programmable gate array (FPGA) [63–66]. It takes a long time for DSPs to generate chaotic signals at high frequencies and DSP chips to perform operations in order to calculate the value of output signals. On the other hand, FPGA chips have a relatively flexible architecture to achieve parallel operation, and the design and test cycles of the chips is particularly low [67]. In order to increase and expand

engineering applications based on chaos, chaotic systems are diversified and need flexible architecture support. With the digitalization and reconfigurability of the FPGA, chaotic systems and their applications can be more flexible. Thus, different forms of signals can be easily generated with the change of parameters of chaotic systems. In addition, the related memristive chaotic system can also be realized alternately by various memristor functions. At present, there are several studies related to designs of chaotic systems based on FPGA. Tuna et al. [63] implemented the Liu-Chen chaotic system on the Xilinx virtex-6 FPGA chip using the 32-bit IQ-Math fixed-point number Heun algorithm. Ahmadi et al. [64] designed a 5D chaotic system on the Xilinx Kintex-7 KC-705 kit FPGA chip using the IEEE 754 32-bit fixed-point number Euler's method. Xu et al. [65] designed a 3D memristive chaotic system on the Xilinx Spartan-6 FPGA chip using the Euler's method of IEEE 754 32-bit floating-point number standard. As far as we know, few literatures have reported the realization of the 5D memristive hyperchaotic system based on FPGA.

Synchronization of chaotic systems has attracted much attention in recent years due to their applications in chemical reactors, secure communication, and the development of secure cryptosystems [68, 69]. Aiming at chaotic synchronization, several methods such as linear feedback control [70], sliding mode control [71], adaptive control [72–74], backstepping nonlinear control [75], shape control [76, 77], and active control [78–80] have been proposed for synchronization of chaotic systems. Compared with other synchronization methods, the active control method is simple, efficient, and flexible which has been successfully applied to the synchronization of chaotic systems. In [79], the synchronization and antisynchronization of the fractional-order chaotic financial system with market confidence are studied by using the active control method. The results show that the speed of synchronization (antisynchronization) increases with the increase of the order. In [80], the synchronization of chaotic systems with different orders under the influence of unknown model uncertainties and external disturbances is studied by using robust generalized active control approach. With the rapid development of computer technology, more and more attention has been paid to information security [81–91]. Secure communication based on chaotic synchronization is an important branch of information security research, which has been widely studied by many scholars [92–96]. Because of the pseudorandomness, unpredictability, and initial sensitivity of memristive chaotic systems, the encrypted information can be hidden in chaotic signals which are highly similar to the noise. In [97], based on the synchronization of the memristive chaotic system, the encrypting and decrypting of information signals are carried out to realize the secure communication with the help of LabVIEW. However, whether chaotic synchronization is achieved by the active control method [78–80] or secure communication based on chaotic synchronization [92–96], numerical simulations is used to achieve these designed methods. In some chaotic information systems, such as chaotic-based CDMA communications and many other chaotic digital information systems, digital implementation may be required [98–100].

Motivated by the above discussions, based on a flux-controlled memristor model and the 4D hyperchaotic system introduced in [39], a 5D hyperchaotic system is proposed. Most importantly, the new system generates four-wing and two-wing hyperchaotic attractor phenomenon with three and two positive Lyapunov exponents, respectively and exhibits hyperchaos with multiline equilibrium. Complete dynamic properties of this new system are studied. Also, with the help of FPGA implementation, this 5D hyperchaotic four-wing memristive system (HFWMS) is realized. Finally, active control synchronization of the 5D hyperchaotic system with different structures and a secure signal masking application of the 5D HFWMS are implemented based on numerical simulations and FPGA.

This paper is organized as follows. In Section 2, the novel 5D HFWMS with multiline equilibrium is introduced and its dynamic properties are discussed. Section 3 is devoted to design, test, and analysis results of FPGA-based HFWMS. In addition, the active control synchronization and chaotic secure communication design of the 5D HFWMS are achieved, and the FPGA experimental results are presented. Section 4 concludes this paper with a summary of the main results.

2. Novel 5D HFWMS and Its Dynamic Properties

2.1. The 5D HFWMS. Recently, Volos et al. [39] have announced a novel 4D four-wing hyperchaotic system, which is described by

$$\begin{cases} \dot{x} = ax + y + yz - cw, \\ \dot{y} = yz - xz, \\ \dot{z} = -z - mxy + b, \\ \dot{w} = x, \end{cases} \quad (1)$$

where a, b, c , and m are all constants and x, y, z , and w are the state variables. System (1) has two positive Lyapunov exponents, showing the four-wing hyperchaotic attractor. Unlike most existing hyperchaotic systems, this hyperchaotic system has a saddle-focus equilibrium and the second equation of the system has no linear term.

In this paper, by introducing a flux-controlled memristor to the first equation of system (1), a novel 5D HFWMS is derived by

$$\begin{cases} \dot{x} = ax + dW(\varphi)y + yz - cw, \\ \dot{y} = yz - xz, \\ \dot{z} = -z - mxy + b, \\ \dot{w} = x, \\ \dot{\varphi} = y, \end{cases} \quad (2)$$

where d is a positive parameter, expressed as memristor strength and $W(\varphi)$ is a memductance function, defined as $W(\varphi) = dq(\varphi)/d\varphi$. Here, the $\varphi - q$ characteristic curve of the memristor is given by a smooth continuous cubic monotone increasing nonlinearity [46–49], and then the memductance is given by

$$W(\varphi) = \frac{dq(\varphi)}{d\varphi} = \frac{d(e\varphi + n\varphi^3)}{d\varphi} = e + 3n\varphi^2, \quad (3)$$

where e and n are two positive constants. This flux-controlled memristor is easier to analyze and implement. At present, many researchers use the special nonlinear dynamic characteristics of this memristor to construct complex chaotic oscillators [54–57].

2.2. Equilibria and Stability. The equilibria of system (2) are obtained by setting its right-hand side to zero, that is,

$$\begin{cases} ax + d(e + 3n\varphi^2)y + yz - cw = 0, \\ yz - xz = 0, \\ -z - mxy + b = 0, \\ x = 0, \\ y = 0. \end{cases} \quad (4)$$

Through equation (4), we can easily observe that the equilibria of system (2) is a multiline equilibrium point $O = \{(x, y, z, w) | x = y = w = 0, z = b, \varphi = \eta\}$, where b is an integer and η is an arbitrary real constant.

The Jacobian matrix of system (2) at the multiline equilibrium point is

$$J_O = \begin{bmatrix} a & d(e + 3n\varphi^2) + z & y & -c & 6n\varphi dy \\ -z & z & y - x & 0 & 0 \\ -my & -mx & -1 & 0 & 0 \\ 1 & 0 & 0 & 0 & 0 \\ 0 & 1 & 0 & 0 & 0 \end{bmatrix}. \quad (5)$$

According to the Jacobian matrix (5), we can obtain the characteristic equation of system (2) as follows:

$$\lambda(\lambda + 1)[\lambda^3 - (a + b)\lambda^2 + (b^2 + dbe + 3dbn\varphi^2 + c + ab)\lambda - bc] = 0. \quad (6)$$

Equation (6) can be rewritten to as follows:

$$\lambda(\lambda + 1)[\lambda^3 + m1\lambda^2 + m2\lambda + m3] = 0, \quad (7)$$

where

$$\begin{cases} m1 = -(a + b), \\ m2 = (b^2 + dbe + 3dbn\varphi^2 + c + ab), \\ m3 = -bc. \end{cases} \quad (8)$$

From the eigenvalue equation (7), it can be seen that Jacobian matrix (5) has one zero eigenvalue, one negative eigenvalue, and three nonzero eigenvalues. To judge whether system (2) is stable, it is necessary to discriminate the three nonzero eigenvalues. According to the Routh–Hurwitz stability criterion, the need equation (8) satisfies

$$\begin{cases} m1 > 0, \\ m3 > 0, \\ m1m2 - m3 > 0. \end{cases} \quad (9)$$

If all three conditions in equation (9) are satisfied, the multiline equilibrium point O is stable, otherwise it is unstable. The unstable equilibrium of the system will lead to chaotic behavior. When $a = 1, b = 1, c = 0.7, m = 1, d = 0.2, e = 0.1, n = 0.01, m_1$, and m_2 are both less than zero, so we can judge that system (2) is unstable.

2.3. Symmetry and Dissipativity. The proposed 5D HFWMS has the same symmetry as system (1), and both of them are invariant with respect to z -axis symmetry under coordinate transformation $(x, y, z, w, \varphi) \rightarrow (-x, -y, z, -w, -\varphi)$.

Furthermore, by calculating

$$\nabla V = \frac{\partial \dot{x}}{\partial x} + \frac{\partial \dot{y}}{\partial y} + \frac{\partial \dot{z}}{\partial z} + \frac{\partial \dot{w}}{\partial w} + \frac{\partial \dot{\varphi}}{\partial \varphi} = a + z - 1, \quad (10)$$

when $a + z < 1$, system (2) is dissipative and converges exponentially.

2.4. Analysis of the 5D HFWMS. Here, the dynamic behavior of the 5D HFWMS is numerically investigated by the use of several tools such as the phase portraits, Poincaré map, Lyapunov exponentials, and bifurcation diagram.

2.4.1. Four-Wing Hyperchaotic Attractor. When the system parameters are selected $a = 1, b = 1, c = 0.7, m = 1, d = 0.2, e = 0.1$, and $n = 0.01$ and the initial condition is set to $[1, -1, 1, 1, 1]$, the phase portraits of system (2) shown in Figure 1 are obtained by Matlab simulation, which is a typical four-wing chaotic attractor, and the time variations of state equations x, y, z , and w are provided in Figure 2.

The Lyapunov exponent is used to measure the perturbation caused by initial conditions. If there are slight differences in the system, two adjacent trajectories in the phase space are separated exponentially with time. The Lyapunov exponent is a useful tool for measuring chaotic systems, in particular, it usually determines whether a chaotic system is chaotic or hyperchaotic according to the number of positive Lyapunov exponents. According to the given system parameters and initial conditions, the Lyapunov exponent of $a \in [-1, 1]$ is simulated by the Jacobi matrix method. The numerical results are shown in Figure 3(a) (the five LE5 is out of plot). From Figure 3(a), we can clearly see that the system has complex dynamic behaviors such as periodic orbit, chaos, and hyperchaos. When $a \in [-1, -0.03]$ and $a \in (0.22, 0.3)$, the system is a periodic orbit, and Figure 4 are the phase portraits of system (2) when $a = -1$ (the LEs are 0, $-0.0424, -0.4394, -0.6696$, and -3.4835). When $a = 0.2$, the LEs are $0.0790, -0.0078, -0.0627, -0.1078$, and -1.9274 , with a positive Lyapunov exponent, so system (2) is in chaotic state ($a \in [0.3, 0.48]$ and $a \in (-0.03, 0.22]$). When $a \in [0.48, 1]$, the system is hyperchaotic, and the typical four-wing hyperchaotic attractor is shown in Figure 1. When $a = 0.78$, the LEs are $LE1 = 0.1712, LE2 = 0.0907, LE3 = 0.0107, LE4 = 0$, and $LE5 = -2.3243$, and it can be judged that system (2) is hyperchaotic and has three positive Lyapunov exponents.

Figure 3(b) describes the bifurcation diagram of system (2) varying with parameter a . With the increase of a , the system changes from period to chaos. The Kaplan–Yorke dimension of system (2) can be calculated by the following formula:

$$D_L = j + \sum_{i=1}^j \frac{L_j}{|L_j + 1|} = 4 + \frac{0.1712 + 0.0907 + 0.0107 - 0}{2.3243} = 4.1172, \quad (11)$$

where j is the largest integer satisfying $\sum_{i=1}^j L_j \geq 0$ and $\sum_{i=1}^{j+1} L_j < 0$. It can be seen from $D_L = 4.1172$ that the Lyapunov dimension of system (2) is fractional. Therefore, the proposed 5D FWMHS is a real hyperchaotic system with strong complexity.

As an important analytical tool, the Poincaré map is used to further study the dynamic characteristics of the 5D HFWMS. Figure 5(a) shows the Poincaré map of the $x - y$ plane at $z = 0$ and four branches can be seen; Figure 5(b) shows the Poincaré map of the $x - z$ plane at $y = 0$ and has many branches; Figure 5(c) shows the Poincaré map of the $y - z$ plane at $w = 0$ and the outline of the four wings can be seen, indicating the existence of the four-wing phenomenon. Figure 5 shows that system (2) has a four-wing chaotic attractor with fractal structure.

2.4.2. Two-Wing Hyperchaotic Attractor. When the system parameters are chosen as $a = 11, c = 0.7, m = 1, d = 0.2, e = 0.1$, and $n = 0.01$ and the initial condition is set to $[0, 1, 0, 0, 0]$, and the numerical results of the Lyapunov exponent varying with the system parameter b is shown in Figure 6(a). Figure 6(b) is a bifurcation diagram corresponding to Figure 6(a). From Figure 6, we can see that system (2) has more complex dynamic behavior in the parameter $b \in [-10, 0]$ interval, such as quasi-periodicity, period, chaos, and hyperchaos. Table 1 classifies these dynamical behaviors and then makes a detailed analysis of LEs and their dynamical behaviors varying with parameter b as follows:

- (i) When $b \in (-4.4, 0]$, the Lyapunov exponents of system (2) at $b = -1$ are $0.5791, 0.1087, -0.0316, -0.2607$, and -4.5443 . The system is in a hyperchaotic state, and the corresponding phase portraits are shown in Figure 7(a).
- (ii) When $b \in [-5.55, -4.4]$, the Lyapunov exponents of system (2) at $b = -5$ are $0, -0.0132, -0.2670, -0.4978$, and -2.1754 . The system is in a period-5 state, and the corresponding phase portraits are shown in Figure 7(b).
- (iii) When $b \in [-7, -6.6]$ and $b \in [-10, -7.2]$, the Lyapunov exponents of system (2) at $b = -8$ are $0.0279, -0.0271, -0.2093, -0.3481$, and -1.9681 . The phase portraits shown in Figure 7(c) show that the system is in a quasi-periodic state.
- (iv) When $b \in (-6.6, -5.55)$ and $b \in (-7.2, -7)$, the Lyapunov exponents of system (2) at $b = -6.15$ are $0.0918, -0.0091, -0.16-0.3278$, and -2.2332 . The

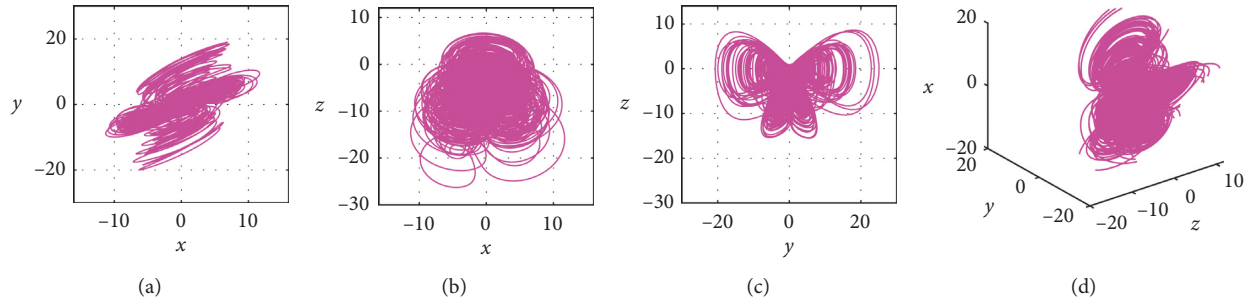


FIGURE 1: The four-wing hyperchaotic attractor of system (2): (a) in the $x - y$ plane, (b) in the $x - z$ plane, (c) in the $y - z$ plane, and (d) in the $x - y - z$ space.

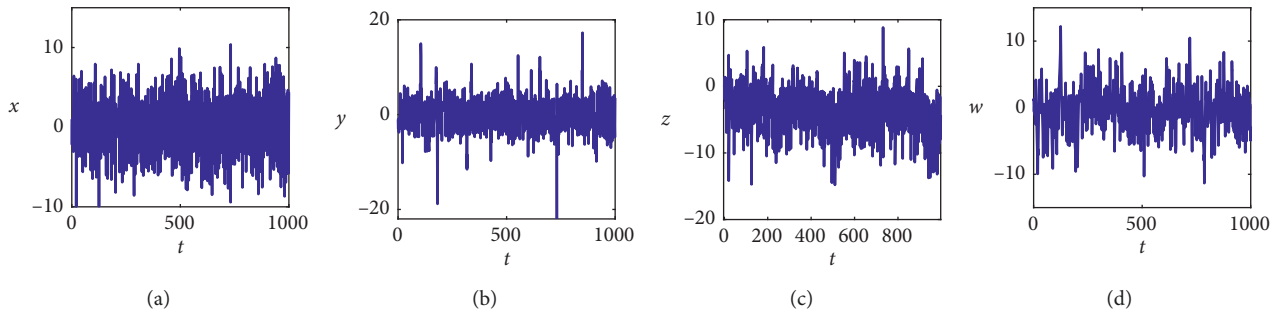


FIGURE 2: The time variation of state equations $x, y, z,$ and w of system (2): (a) $t - x,$ (b) $t - y,$ (c) $t - z,$ and (d) $t - w.$

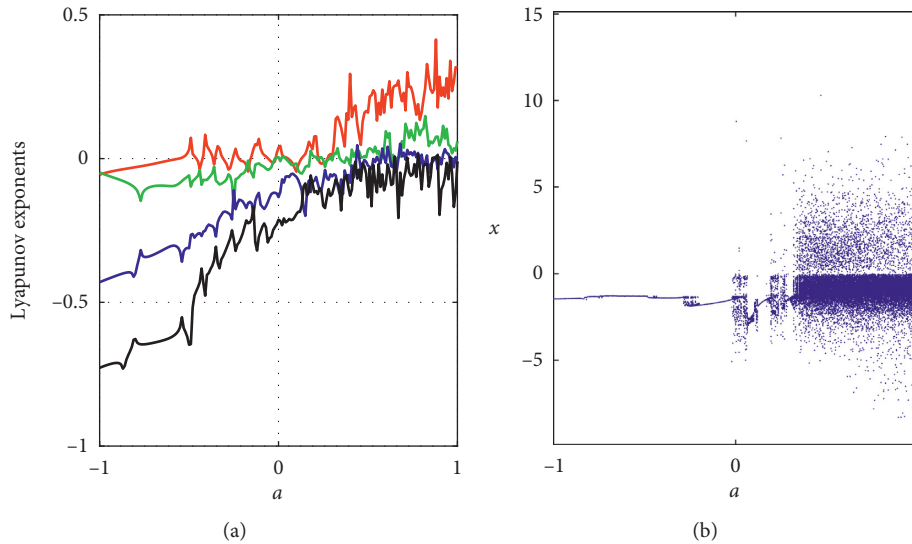


FIGURE 3: Lyapunov exponents and bifurcation diagram for increasing parameter a (the five LE5 is out of plot).

system shows a chaotic state, and the corresponding phase portraits are shown in Figure 7(d).

2.4.3. *Complexity Analysis by Spectral Entropy.* The complexity of spectral entropy (SE) is based on the discrete Fourier transformation. The distribution of energy in Fourier transform domain is calculated, and then the SE value is calculated by Shannon entropy, which reflects the

disorder of time series in frequency domain [61, 101, 102]. The chaotic diagram using the complexity of SE usually reflects the spatial complexity of chaotic system parameters. In this section, the SE algorithm is used to analyze the complexity of system (2). Figure 8 shows the complexity of SE of system (2) under initial condition $[1, -1, 1, 1, 1]$. It can be seen that Figure 8(a) corresponds well to the maximum Lyapunov exponent in Figure 3. The control parameters a and b of the chaotic system are divided into 101×101 parts,

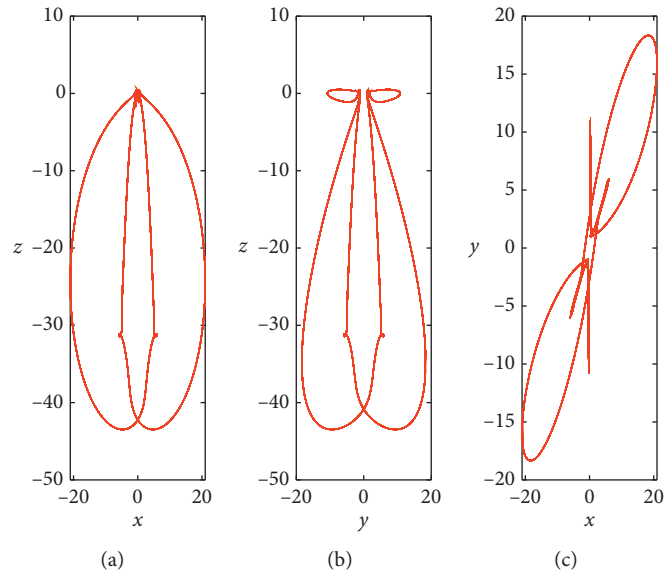


FIGURE 4: Periodic phase portraits of system (2) with $a = -1$: (a) in the $x-z$ plane, (b) in the $y-z$ plane, and (c) in the $x-y$ plane.

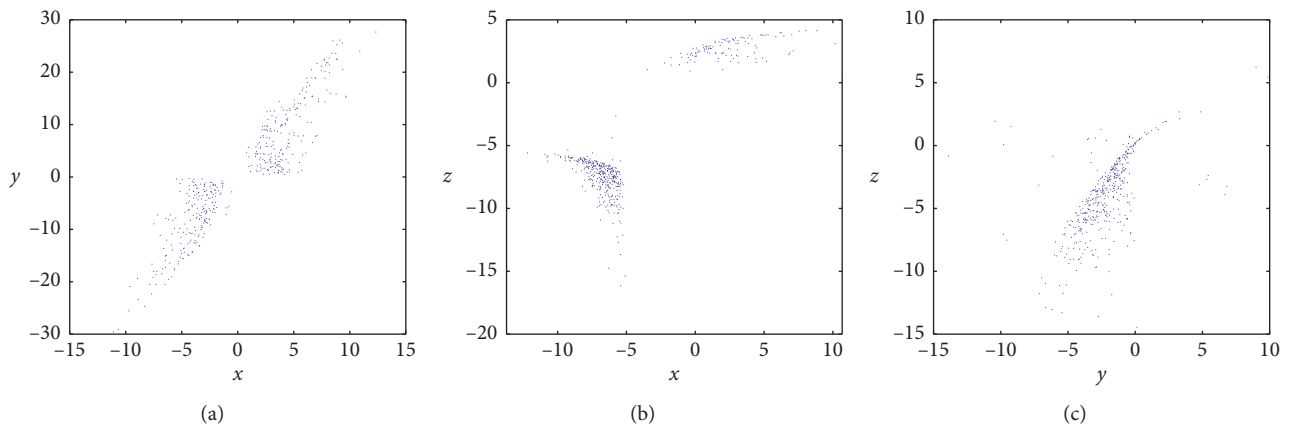


FIGURE 5: Poincaré map of system (2) with parameters $a = 1$: (a) projection on $x-y$ plane with $z = 0$, (b) projection on $x-z$ plane with $y = 0$, and (c) projection on $y-z$ plane with $w = 0$.

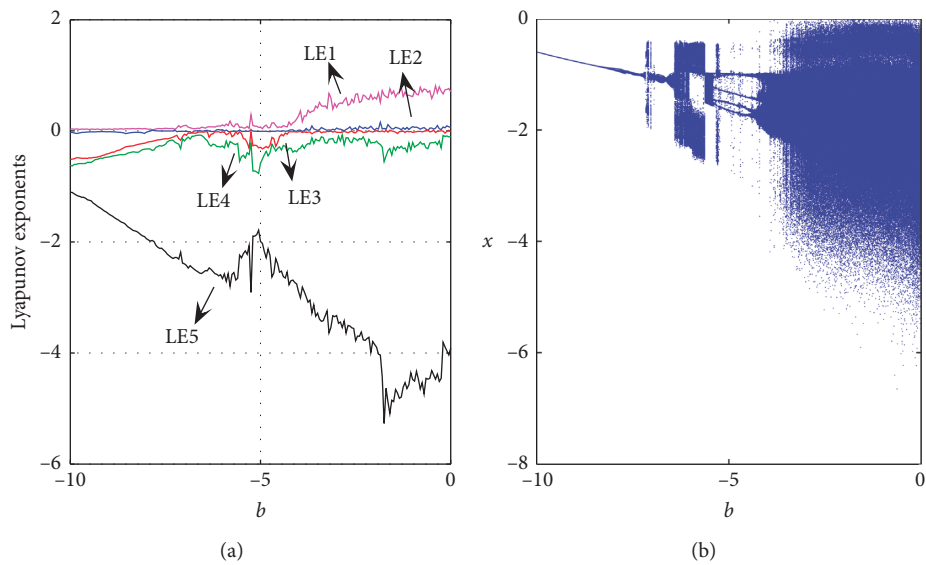
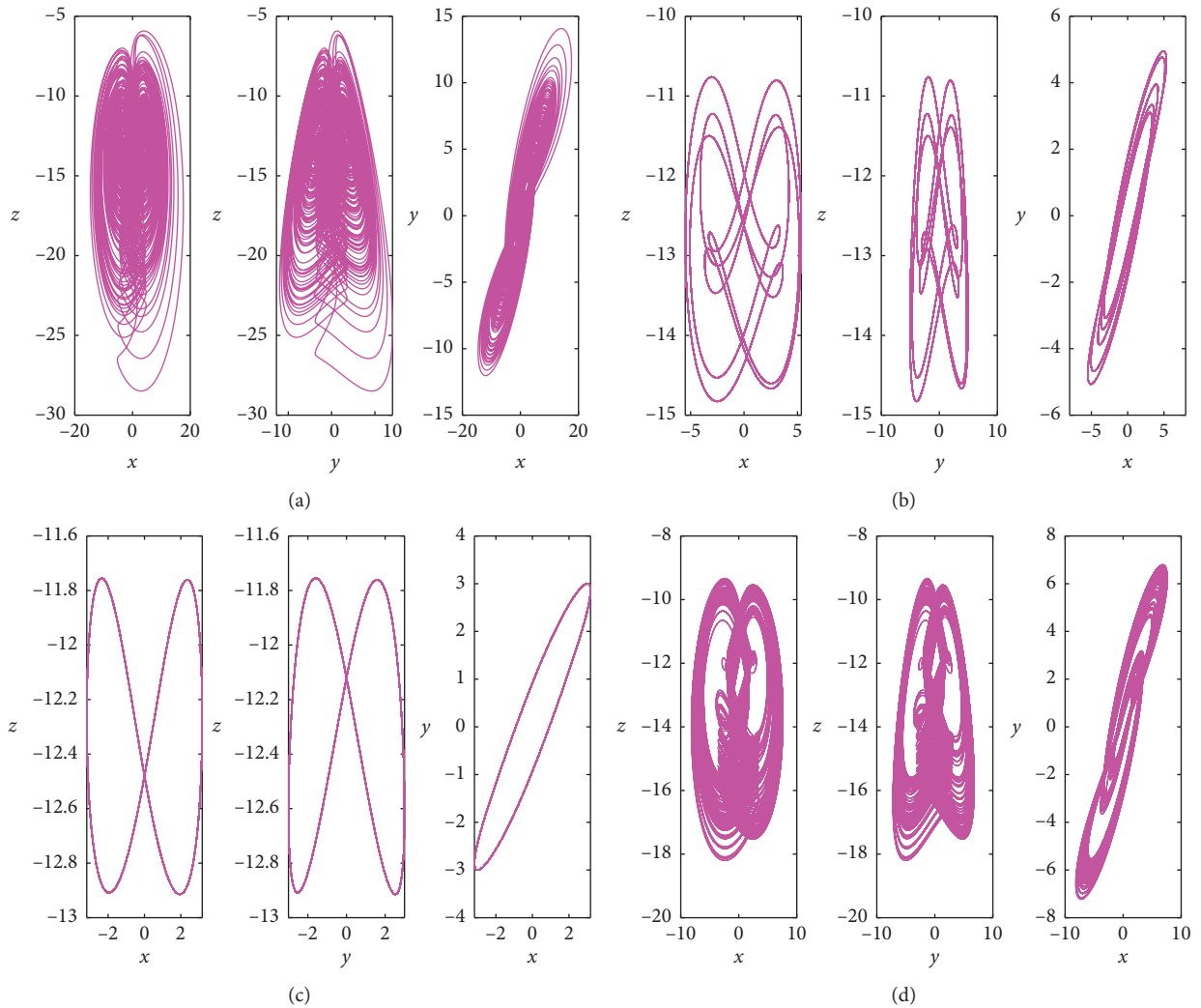


FIGURE 6: Lyapunov exponents and bifurcation diagram for increasing parameter b .

TABLE 1: The LEs and dynamical behavior under different parameter range of b .

b	(LE1, LE2, LE3, LE4, LE5)	Dynamic
$(-4.4, 0]$	$(+, +, 0, -, -)$	Hyperchaotic
$[-5.55, -4.4]$	$(0, -, -, -, -)$	Periodic
$(-6.6, -5.55)$	$(+, 0, -, -, -)$	Chaotic
$[-7, -6.6]$	$(0, 0, -, -, -)$	Torus
$(-7.2, -7)$	$(+, 0, -, -, -)$	Chaotic
$[-10, -7.2]$	$(0, 0, -, -, -)$	Quasi-periodic

FIGURE 7: Simulated phase portraits of system (2) with different b : (a) $b = -1$, (b) $b = -5$, (c) $b = -8$, and (d) $b = -6.15$.

including $a \in [-1, 1]$ and $b \in [0, 5]$. Then, calculate the SE of each point (a, b) in the parameter space, as shown in Figure 8(b). The results show that with the increase of parameter a , the more complex the chaotic system is, and the higher the complexity of the system is mainly concentrated in $a \in [0.5, 1]$. Figure 9 is the SE diagram of system (2) under initial condition $[0, 1, 0, 0, 0]$, where $a \in [10, 20]$ and $b \in [-10, 0]$. Figure 9(a) corresponds well to the maximum Lyapunov exponent in Figure 6. Figure 9(b) shows the complexity of SE in the plane of control parameters a and b . The results show that when $a = 11$, with the increase of

parameter b , the larger the SE value is, and the higher the complexity of the system is mainly concentrated in $b \in [-3.8, 0]$.

3. The FPGA-Based Model of the Novel 5D HFWMS

Devices in analog circuits are easy to aging and inflexible, which makes more and more researchers begin to pay attention to digital devices on the FPGA. With the characteristics of high-speed operation, high integration, and free

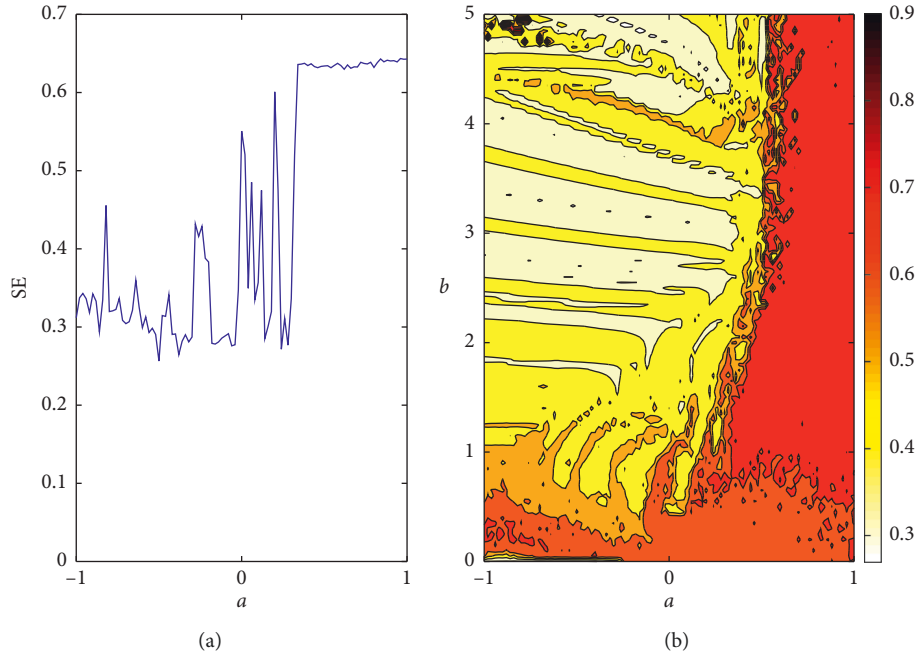


FIGURE 8: The complexity of SE of system (2): (a) SE versus a when $b = 1$ and (b) in the $a - b$ plane.

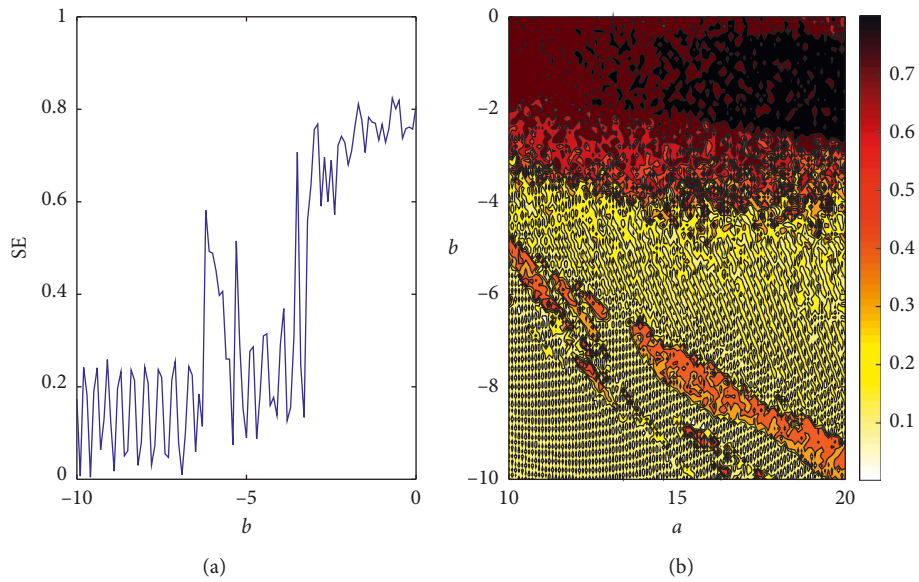


FIGURE 9: The complexity of SE of system (2): (a) SE versus b when $a = 11$ and (b) in the $a - b$ plane.

design, FPGA can easily generate chaotic signals. Nowadays, many numerical algorithms are used to solve the nonlinear differential equations of chaotic systems. The Euler algorithm is the simplest of all algorithms, but its accuracy is not high [64, 65]. The Heun algorithm is more sensitive than the Euler method [63]. The Runge-Kutta algorithm is better than other algorithms in operation effect, with high accuracy, stable calculation process, and easy realization. RK-4 is easier to implement than RK-5, so RK-4 is widely used to solve chaotic systems [103]. Equation (12) gives the formula for calculating K_1, K_2, K_3 , and K_4 , which represents the slope value of $[y_0, y_i]$:

$$\begin{aligned}
 t_{i+1} &= t_i + h, \\
 K_1 &= f(t_i, y_i), \\
 K_2 &= f\left(t_i + \frac{h}{2}, y_i + \frac{h}{2}K_1\right), \\
 K_3 &= f\left(t_i + \frac{h}{2}, y_i + \frac{h}{2}K_2\right), \\
 K_4 &= f(t_i + h, y_i + hK_3).
 \end{aligned} \tag{12}$$

For the designed HFWMS, the initial conditions $x(0) = 1, y(0) = -1, z(0) = 1, w(0) = 1$, and $\varphi(0) = 1$ and the step size $h = 0.01$ are given. Five equations in HFWMS are calculated according to the RK-4 algorithm flow chart and equation (12). By using the RK-4 algorithm of Verilog, the designed HFWMS is implemented on FPGA. The central idea of designing a chaotic signal generator with FPGA is to divide the whole system into several functional modules, including RK-4 solving module, data selector module, y_s module, and numerical conversion module. The function module contains many arithmetic units, including multiplier, adder, and subtractor. These arithmetic units are created in cooperation with the IP core generator and follow the standard of IEEE 754.

The top-level block diagram of the chaotic signal generator based on FPGA using the RK-4 algorithm is shown in Figure 10. As can be seen from Figure 10, the design system has three inputs and six outputs. The output signal consists of five 32-bit output signals ($X_out, Y_out, Z_out, W_out$, and φ_out) and 1 bit flag signal $XYZW\varphi_ready$. When the calculation produces $X_out, Y_out, Z_out, W_out$, and φ_out , the signal $XYZW\varphi_ready$ will be set to a valid bit. Clock signal (Clk) and Reset are both 1 bit signals, which are used to ensure synchronization between the system and other modules; 32 bit Δh represents step size, which is used to determine the sensitivity of the algorithm.

The second block diagram of the chaotic signal generator based on FPGA using the RK-4 algorithm is displayed in Figure 11, which consists of a Multiplier (MUX) and 5D HFWMS oscillator. As can be seen from that the MUX unit is used to obtain the initial condition signal at the first operation. These signals were initially defined by the designer, and then obtained as feedback signals by the output signals ($X_out, Y_out, Z_out, W_out$, and φ_out). Figure 12 is the third block diagram of the chaotic signal generator based on FPGA using the RK-4 algorithm, which consists of three parts: MUX unit, HFWMS oscillator unit, and data processing unit. $K1$ unit, $K2$ unit, $K3$ unit, $K4$ unit, and y_s are important components of the HFWMS oscillator, which are pipelined structures used in the calculation of Runge-Kutta algorithm. y_s unit can make the chaotic oscillator produce output signal in a definite clock period. I.C. (initial conditions) are initially defined by the designer. When HFWMS generates a set of output values, the value of $XYZW\varphi_ready$ is set to a valid bit and the values of $x(k+1), y(k+1), z(k+1), w(k+1)$, and $\varphi(k+1)$ generated by the oscillator are fed back to MUX as the initial values of the next operation. The data processing unit has two functions: (1) converting 32-bit floating-point signals ($X_out, Y_out, Z_out, W_out$, and φ_out) generated by the oscillator into 14-bit fixed-point signals and (2) converting signed fixed-point signals into unsigned fixed-point signals. The digital-to-analog converter AN9767 (DAC) converts 14-digit digital signals into analog signals for easy display on the oscilloscope.

The digital hardware implementation of the 5D hyperchaotic oscillator based on RK-4 has been synthesized on the Xilinx ZYNQ-XC7Z020 FPGA chip. This design is implemented, synthesized, and downloaded using Vivado 2018.3.

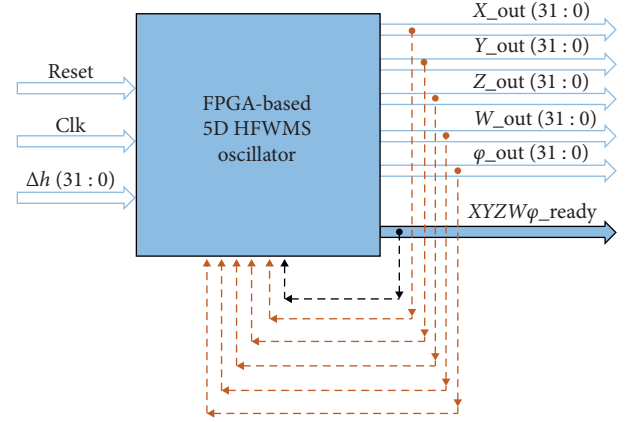


FIGURE 10: The top-level block diagram of the FPGA-based 5D HFWMS.

The parameter statistics of the related resource utilization of the FPGA and the clock speed of each module are calculated. In order to better analyze the experimental results, we convert the experimental data into hexadecimal. Figure 13 shows a discrete time series ($X_out, Y_out, Z_out, W_out$, and φ_out) obtained for the HFWMS oscillator based on FPGA, which corresponds to the x, y, z, w , and φ signals of the continuous chaotic system. Figure 14 are the phase portraits of Y_out and Z_out which are displayed by the 5D HFWMS on the oscilloscope. From Figure 14, it can be seen that several kinds of phase portraits designed based on FPGA are consistent with the Matlab simulation diagrams, which means that the designed HFWMS based on FPGA can be implemented well. Table 2 provides statistical data on resource utilization, chip speed, and performance of the Xilinx ZYNQ-XC7Z020 FPGA chip. The minimum clock period and maximum operating frequency of HFWMS based on FPGA are 6.763 ns and 147.863 MHz.

3.1. Active Control Synchronization and Secure Communication of the Novel 5D HFWMS

3.1.1. Synchronization of the Novel 5D HFWMS by the Active Control Method. Synchronization design is the key to secure communication. Therefore, it is necessary to synchronize the designed chaotic system before realizing secure communication. A synchronization system consists of two parts, one is the master system and the other is the slave system. In this section, the active control method is used to synchronize system (2), and system (2) is set as the master system and rewritten as

$$\begin{cases} \dot{x}_1 = ax_1 + dW(\varphi_1)y_1 + y_1z_1 - cw_1, \\ \dot{y}_1 = y_1z_1 - x_1z_1, \\ \dot{z}_1 = -z_1 - mx_1y_1 + b, \\ \dot{w}_1 = x_1, \\ \dot{\varphi}_1 = y_1. \end{cases} \quad (13)$$

Here, the slave system uses a 5D hyperchaotic system proposed by Yang and Bai [104], which is described as

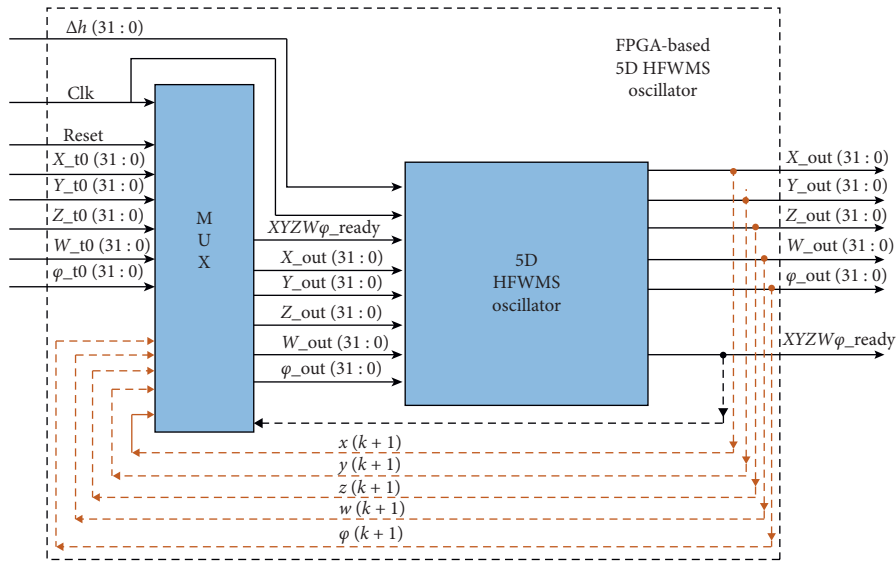


FIGURE 11: The second-level block diagram of the FPGA-based 5D HFWMS.

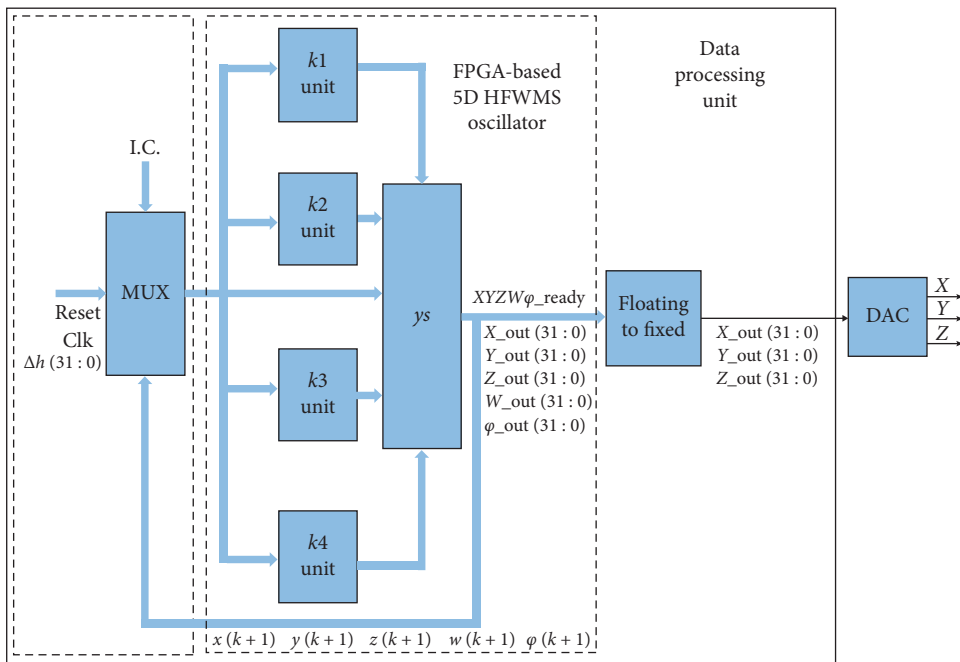


FIGURE 12: The third-level block diagram of the FPGA-based 5D HFWMS.

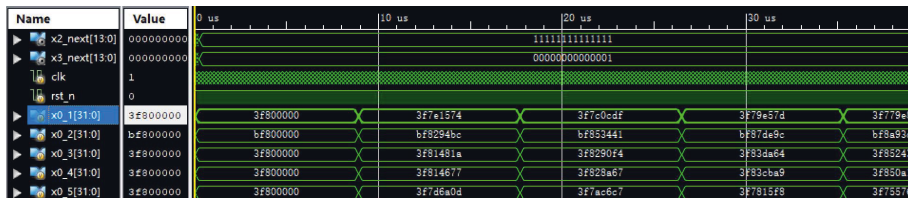


FIGURE 13: Simulation results of the FPGA-based HFWMS signal generator with the RK-4 algorithm.

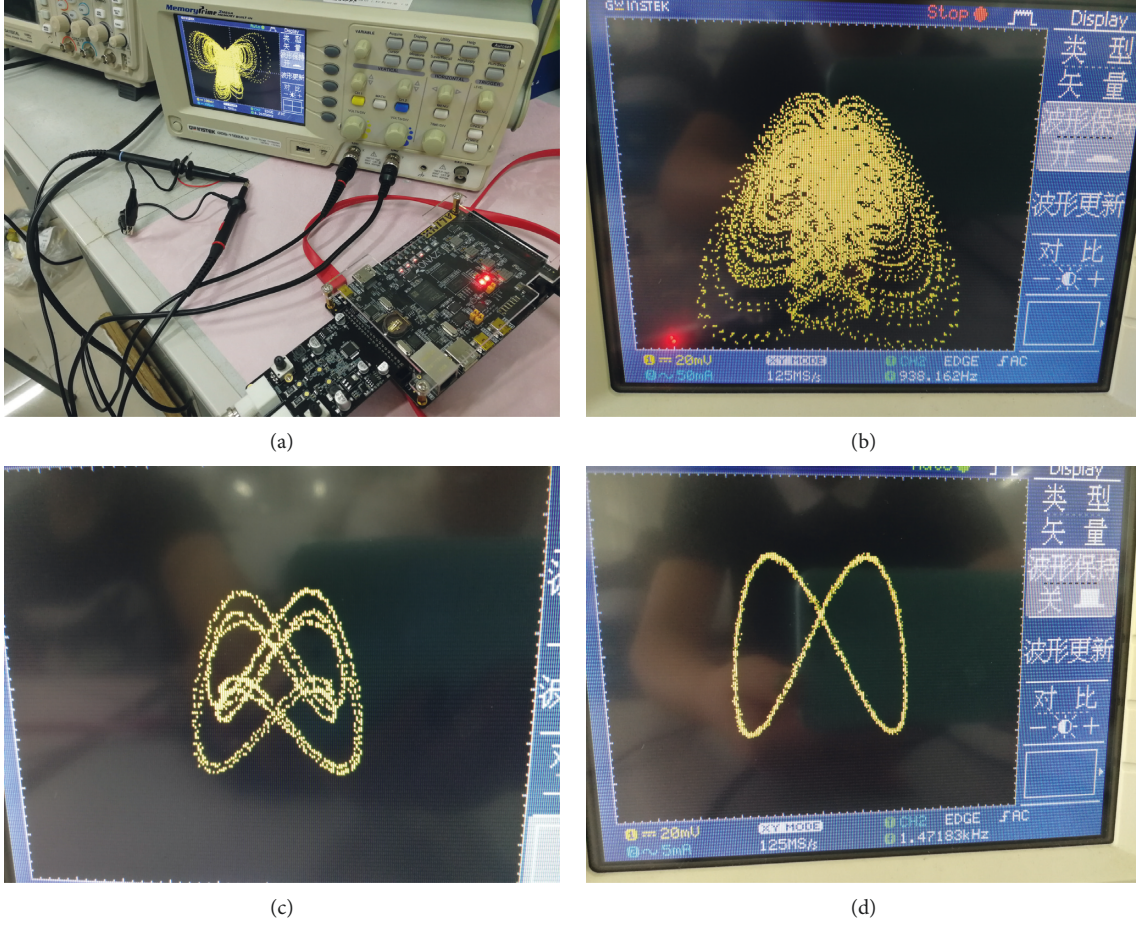


FIGURE 14: Implementation platform and exemplificative phase portraits generated by the FPGA implementation of the proposed HFWS: (a) four-wing hyperchaotic attractor, (b) two-wing hyperchaotic attractor, (c) period-5 state, and (d) quasi-periodic state.

TABLE 2: Xilinx ZYNQ-XC7Z020 FPGA chip hardware usage statistics of the 5D HFWS.

Resource	Used	Available	Utilization (%)
Slice register	26893	106400	25
Number of slice LUTs	23173	53200	43
Number of bonded IOBs	30	125	24
Number of BUFG	1	32	3
Max. clock frequency	147.863 MHz	—	—
Latency	13.53 ns	—	—
Throughput	59.15 Mbit/s	—	—
Power	0.275 W	—	—

$$\begin{cases} \dot{x}_2 = a_1(y_2 - x_2) + u_1, \\ \dot{y}_2 = c_1x_2 + d_1y_2 - x_2z_2 + \varphi_2 + u_2, \\ \dot{z}_2 = -b_1z_2 - x_2^2 + u_3, \\ \dot{w}_2 = g_1y_2 + f_1w_2 + u_4, \\ \dot{\varphi}_2 = -r_1x_2 - k_1\varphi_2 + u_5, \end{cases} \quad (14)$$

where $a_1, b_1, c_1, d_1, g_1, f_1, r_1$, and k_1 are the system parameters and $u = [u_1, u_2, u_3, u_4, u_5]^T$ is the active controller of synchronous systems, which can make the master and slave

systems gradually synchronize under different initial conditions. Define the errors as

$$\begin{cases} e_1 = x_2 - x_1, \\ e_2 = y_2 - y_1, \\ e_3 = z_2 - z_1, \\ e_4 = w_2 - w_1, \\ e_5 = \varphi_2 - \varphi_1. \end{cases} \quad (15)$$

Then, the error dynamic system can be obtained as

$$\begin{cases} \dot{e}_1 = (a - a_1)e_1 + (a_1 + dg)e_2 - ce_4 + cw_2 - ax_2 - dgy_2 + a_1(y_1 - x_1) - y_1z_1 - 3dn\varphi_1^2y_1 + u_1, \\ \dot{e}_2 = c_1e_1 + d_1e_2 + e_5 + \varphi_1 - x_2z_2 + x_1z_1 - y_1z_1 + c_1x_1 + d_1y_1 + u_2, \\ \dot{e}_3 = -b_1e_3 - e_3 + x_2^2 + mx_1y_1 - b + z_2 - b_1z_1 + u_3, \\ \dot{e}_4 = g_1e_1 + g_1y_1 + f_1e_4 + f_1w_1 + e_1 - x_2 + u_4, \\ \dot{e}_5 = -r_1e_1 - k_1e_5 - r_1x_1 - k_1\varphi_1 - y_2 + e_2 + u_5. \end{cases} \quad (16)$$

By simplifying the linear term of equation (16), the active controller can be obtained as

$$\begin{cases} u_1 = -cw_2 + ax_2 + dgy_2 - a_1(y_1 - x_1) + y_1z_1 + 3dn\varphi_1^2y_1 + v_1, \\ u_2 = -\varphi_1 + x_2z_2 - x_1z_1 + y_1z_1 - c_1x_1 - d_1y_1 + v_2, \\ u_3 = -x_2^2 - mx_1y_1 + b - z_2 + b_1z_1 + v_3, \\ u_4 = -g_1y_1 - f_1w_1 + x_2 + v_4, \\ u_5 = r_1x_1 + k_1\varphi_1 + y_2 + v_5, \end{cases} \quad (17)$$

where $v = [v_1, v_2, v_3, v_4, v_5]^T$ is the control input. The substitution of (17) in (16) leads to a linear error dynamics equation without the active controller:

$$\begin{cases} \dot{e}_1 = (a - a_1)e_1 + (a_1 + dg)e_2 - ce_4 + v_1, \\ \dot{e}_2 = c_1e_1 + d_1e_2 + e_5 + v_2, \\ \dot{e}_3 = -b_1e_3 - e_3 + v_3, \\ \dot{e}_4 = g_1e_1 + f_1e_4 + e_1 + v_4, \\ \dot{e}_5 = -r_1e_1 - k_1e_5 + e_2 + v_5. \end{cases} \quad (18)$$

In order to achieve synchronization of different structures, it is necessary to

$$\lim_{x \rightarrow \infty} e_i = 0, \quad i = 1, 2, 3, 4, 5. \quad (19)$$

Equation (17) shows that if system (18) tends to be stable over time and under the control of input $v = [v_1, v_2, v_3, v_4, v_5]^T$, the error variable $e = [e_1, e_2, e_3, e_4, e_5]^T$ tends to zero, and then the master system (12) and the slave system (13) realize the synchronization with different structures. To achieve this goal, we define a matrix A to represent the relationship between the error system and the control input, which can be expressed as

$$v = A \cdot e. \quad (20)$$

According to the stability criterion, if equation (20) is stable, all eigenvalues of matrix A are negative. Thus, equation (20) can be expressed as

$$\begin{bmatrix} v_1 \\ v_2 \\ v_3 \\ v_4 \\ v_5 \end{bmatrix} = \begin{bmatrix} a_1 - a - 1 & -a_1 - dg & 0 & c & 0 \\ -c_1 & -d_1 - 1 & 0 & 0 & -1 \\ 0 & 0 & b_1 & 0 & 0 \\ -1 & -e_1 & 0 & -f_1 - 1 & 0 \\ r_1 & -1 & 0 & 0 & k_1 - 1 \end{bmatrix} \begin{bmatrix} e_1 \\ e_2 \\ e_3 \\ e_4 \\ e_5 \end{bmatrix}, \quad (21)$$

where matrix A is

$$\begin{bmatrix} a_1 - a - 1 & -a_1 - dg & 0 & c & 0 \\ -c_1 & -d_1 - 1 & 0 & 0 & -1 \\ 0 & 0 & b_1 & 0 & 0 \\ -1 & -e_1 & 0 & -f_1 - 1 & 0 \\ r_1 & -1 & 0 & 0 & k_1 - 1 \end{bmatrix}. \quad (22)$$

Therefore, equation (21) can be transformed into

$$\begin{cases} v_1 = (a_1 - a - 1)(x_2 - x_1) + c(w_2 - w_1) - (a_1 + dg)(y_2 - y_1), \\ v_2 = -c_1(x_2 - x_1) - (d_1 + 1)(y_2 - y_1) - (u_2 - u_1), \\ v_3 = b_1(z_2 - z_1), \\ v_4 = -(x_2 - x_1) - g_1(y_2 - y_1) - (f_1 + 1)(w_2 - w_1), \\ v_5 = -(y_2 - y_1) - k_1(\varphi_2 - \varphi_1) + r_1(x_2 - x_1). \end{cases} \quad (23)$$

By substituting equations (23) and (17) into equation (14), the expression of slave system is obtained as follows:

$$\begin{cases} \dot{x}_2 = -x_2 + 2x_1 + d(g + 3n\varphi_1^2)y_1 + y_1z_1 - cw_1, \\ \dot{y}_2 = y_1z_1 - x_1z_1 - y_2 + y_1, \\ \dot{z}_2 = -z_2 - mx_1y_1 + b, \\ \dot{w}_2 = x_1 - w_2 + w_1, \\ \dot{\varphi}_2 = y_1 - \varphi_2 + \varphi_1. \end{cases} \quad (24)$$

(1) *Numerical Simulation Results Based on Matlab.* The effectiveness of synchronization results of active control for different structures is verified by numerical simulation. Choose the parameters of system (13) as $a = 1, b = 1, c = 0.7, m = 1, d = 0.2, g = 0.1$, and $n = 0.01$ and initial states as $[1, -1, 1, 1, 1]$; the parameters of system (14) as $a_1 = 35, b_1 = 7, c_1 = 35, d_1 = -5, g_1 = 10.6, f_1 = 1, r_1 = 5$, and $k_1 = 0.05$ and initial states as $[0.01, -0.01, 0.01, 0.01, 0.01]$. Figure 15 shows the

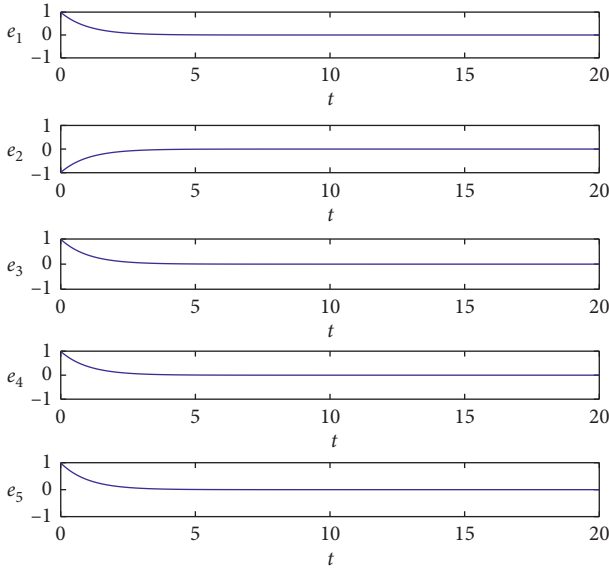


FIGURE 15: The trajectories of the synchronization errors $e_1, e_2, e_3, e_4,$ and e_5 based on Matlab.

time behaviors of the error states. As we can see, the error states converge to 0 in 3 seconds, which means that the two hyperchaotic systems with different structures can achieve synchronization.

(2) *Implementation Results Based on FPGA.* Because of the aging and temperature change of analog devices, the device values are easy to change. Synchronization requires that the parameters of the transmitter and the receiver be highly matched. This indicates that there are a series of problems in synchronization using analog devices. It is an ideal choice to synchronize the chaotic system with FPGA, which has high reliability because it does not have the problem of temperature drift of components. In this section, according to the principle of active control synchronization, two different 5D hyperchaotic systems with different structures are synchronized on ModelSim. The Verilog design is simulated by Vivado's built-in simulator. The simulation results of synchronization errors in FPGA are shown in Figure 16. From the graph, it can be seen that all synchronization errors tend to zero. This is the same as the Matlab simulation in Figure 15 of synchronization errors. Therefore, the synchronization of 5D hyperchaotic systems with different structures designed by FPGA can work normally on hardware.

3.1.2. *Chaotic Masking Communication of the Novel 5D HFWMS.* The main idea of chaotic masking secure communication design is to superimpose the signal generated by the chaotic system on the useful signal to form a modulation signal, and then use the channel for transmission. The receiver demodulates the modulated signal by the output signal of the chaotic system

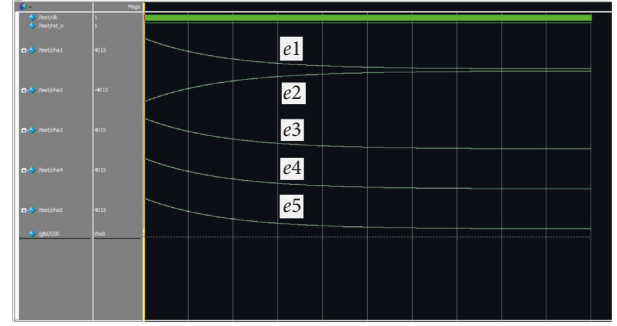


FIGURE 16: The trajectories of the synchronization errors $e_1, e_2, e_3, e_4,$ and e_5 based on FPGA.

synchronized with the transmitter and recovers the original useful signal. The application of secure communication studied in this paper is based on active control synchronization between two 5D hyperchaotic systems with different structures. The schematic diagram of the designed secure communication scheme is shown in Figure 17, where $s(t)$ is the information signal, $m(t)$ is the chaotic signal generated by the master system, $p(t)$ is the mixed signal encrypted by $m(t)$ to $s(t)$, $n(t)$ is the chaotic signal generated by the slave system, and $d(t)$ is the decrypted signal. The signal transmitted in the channel is a kind of chaotic signal similar to noise, from which it is difficult to obtain useful signals. The controller unit can synchronize the master system and slave system, which is the key of chaotic secure communication. The original useful signal can be recovered effectively by using the signal generated by the synchronized chaotic system of the controller to decrypt the encrypted signal. Set the information signal to be encrypted at the transmitter as

$$s(t) = 0.125 \sin(0.1\pi t). \quad (25)$$

The encryption function and decryption function of the chaotic masking communication are, respectively, adopted as

$$p(t) = s(t) \cdot [1 + km(t)],$$

$$d(t) = \frac{p(t)}{[1 + kn(t)]}. \quad (26)$$

The error signal between the information signal and the decrypted signal is

$$e(t) = s(t) - d(t). \quad (27)$$

(1) *Numerical Simulation Results Based on Matlab.* Through the encryption function, decryption function, and synchronization-related parameters, the numerical simulation results are shown in Figure 18 with $k = 10$. As can be seen that the signal $p(t)$ is really difficult to be decrypted; the signal $d(t)$ generated by the decryption function corresponds well with the information signal, which

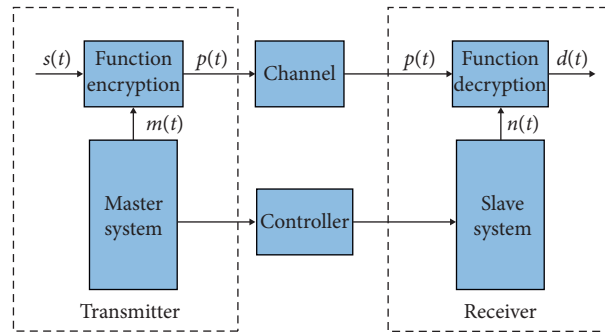


FIGURE 17: The schematic diagram of chaotic masking communication.

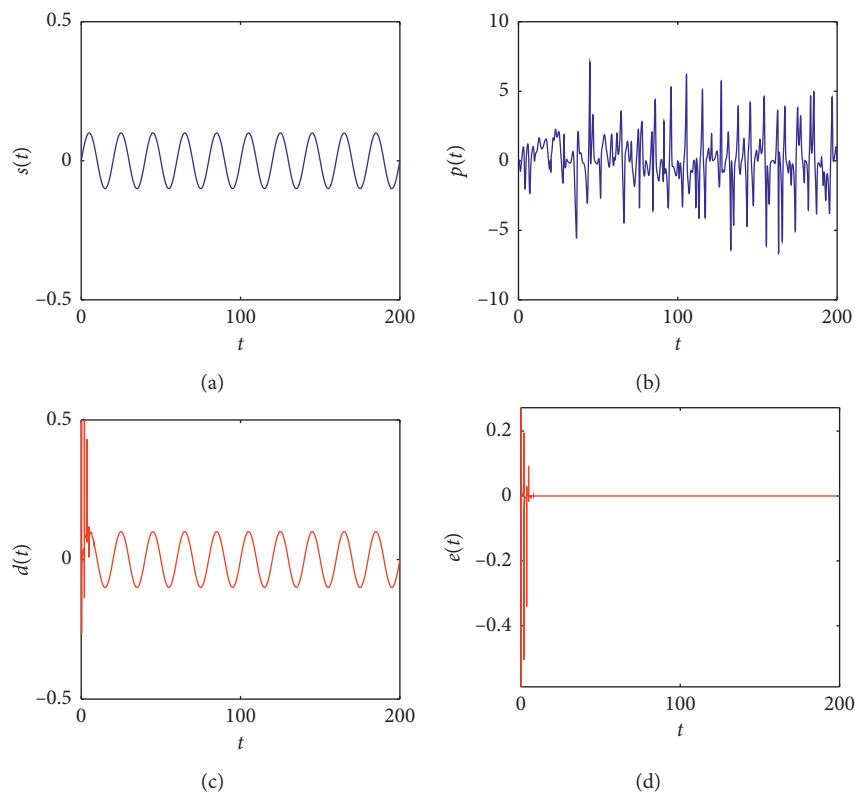


FIGURE 18: (a) Original signal $s(t)$, (b) transmitted signal $p(t)$, (c) recovered signal $d(t)$, and (d) error $e(t) = s(t) - d(t)$.

means that the receiver can recover the information signal very well.

(2) *Implementation Results Based on FPGA.* In order to verify the correctness of the proposed chaotic masking secure communication scheme, ModelSim is selected as the experimental platform of FPGA. According to the scheme shown in Figure 17, the hardware experiment results of the FPGA are shown in Figure 19. From Figure 19, we can see that the effective information signal $s(t)$ can be completely hidden in the chaotic sequence, the encrypted signal has strong concealment, and the received decrypted signal has good restoration quality, which is the same as the pre-encrypted signal.

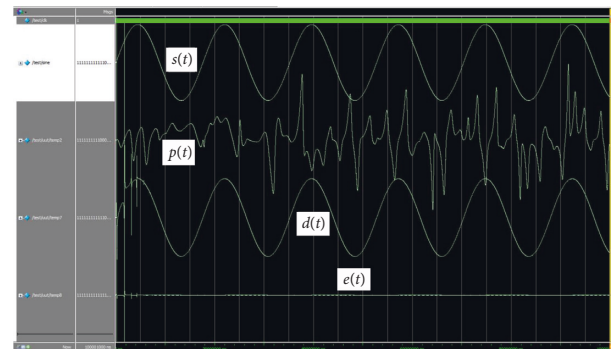


FIGURE 19: Experimental results of chaotic masking secure communication based on FPGA.

4. Conclusion

In this study, a novel 5D continuous time HFWMS with multiline equilibrium and three positive Lyapunov exponents are first introduced. Dynamical analysis is performed in terms of equilibrium points, phase portraits, Poincare map, Lyapunov exponential spectrum, bifurcation diagram, and spectral entropy. Then, the four-wing, two-wing, period-5, and quasi-periodic phase portraits of the novel 5D hyperchaotic memristive system are carried out on FPGA, and a discrete time FPGA-based design of the 5D HFWMS is implemented on ModelSim using the RK-4 algorithm. The maximum operating frequency of the designed chaos-based system reaches 147.863 MHz. Finally, an active control synchronization of the 5D hyperchaotic system with different structures and a secure chaotic masking communication application are implemented on the platform of Matlab and FPGA, respectively. All these results justify the successful applications of the novel 5D HFWMS in active control synchronization and various chaos-based embedded secure chaotic masking communication systems. Our future work is to study whether the system has multistability, and to apply the system to image encryption and random number generator.

Data Availability

All data used to support the findings of this study are available from the corresponding author upon request.

Conflicts of Interest

The authors declare that they have no conflicts of interest.

Acknowledgments

This work was supported by the National Natural Science Foundation of China under Grants 61504013, 61702052, 61772087, 61674054, and 61901169, Natural Science Foundation of Hunan Province under Grants 2019JJ50648, 2016jj2005, 2017JJ2049, and 2019JJ40190, Scientific Research Fund of Hunan Provincial Education Department under Grant 18A137, and the National Key Research and Development Project under Grant 2018YFE0111200.

References

- [1] S. R. Fulton, "Multigrid solution of non-linear balance equations in meteorology," *Communications in Applied Numerical Methods*, vol. 8, no. 10, pp. 695–706, 1992.
- [2] J. Wu, X. Chen, H. Yao, L. Gao, Y. Chen, and M. Liu, "Non-linear relationship of hydrological drought responding to meteorological drought and impact of a large reservoir," *Journal of Hydrology*, vol. 551, pp. 495–507, 2017.
- [3] M. Long, F. Peng, and Y. Zhu, "Identifying natural images and computer generated graphics based on binary similarity measures of PRNU," *Multimedia Tools and Applications*, vol. 78, no. 1, pp. 489–506, 2019.
- [4] Y.-S. Huang and Z.-Y. Wang, "Decentralized adaptive fuzzy control for a class of large-scale MIMO nonlinear systems with strong interconnection and its application to automated highway systems," *Information Sciences*, vol. 274, pp. 210–224, 2014.
- [5] Q. Xie, X. Wang, Z. Han, Y. Zuo, and M. Tang, "Immersion and invariance control of a class of nonlinear cascaded discrete systems," *Neurocomputing*, vol. 171, pp. 1661–1665, 2016.
- [6] Y.-S. Huang and M. Wu, "Robust decentralized direct adaptive output feedback fuzzy control for a class of large-scale nonaffine nonlinear systems," *Information Sciences*, vol. 181, no. 11, pp. 2392–2404, 2011.
- [7] A. M. A. Nasar, B. D. Rogers, A. Revell, and P. K. Stansby, "Flexible slender body fluid interaction: vector-based discrete element method with Eulerian smoothed particle hydrodynamics," *Computers & Fluids*, vol. 179, pp. 563–578, 2019.
- [8] N. Nguyen, A. Wineman, and A. Waas, "Contact problem of a non-linear viscoelastic spherical membrane enclosing incompressible fluid between two rigid parallel plates," *International Journal of Non-Linear Mechanics*, vol. 50, pp. 97–108, 2013.
- [9] V.-T. Pham, A. Buscarino, L. Fortuna, and M. Frasca, "Autowaves in memristive cellular neural networks," *International Journal of Bifurcation and Chaos*, vol. 22, no. 8, p. 1230027, 2012.
- [10] F. Yu, L. Liu, L. Xiao, K. Li, and S. Cai, "A robust and fixed-time zeroing neural dynamics for computing time-variant nonlinear equation using a novel nonlinear activation function," *Neurocomputing*, vol. 350, pp. 108–116, 2019.
- [11] L. Zhou, F. Tan, F. Yu, and W. Liu, "Cluster synchronization of two-layer nonlinearly coupled multiplex networks with multi-links and time-delays," *Neurocomputing*, vol. 359, pp. 264–275, 2019.
- [12] W. Yao, C. Wang, J. Cao, Y. Sun, and C. Zhou, "Hybrid multisynchronization of coupled multistable memristive neural networks with time delays," *Neurocomputing*, vol. 363, pp. 281–294, 2019.
- [13] V.-T. Pham, S. Vaidyanathan, E. Tlelo-Cuautle, and T. Kapitaniak, "Memory circuit elements: complexity, complex systems, and applications," *Complexity*, vol. 2019, Article ID 4936123, 4 pages, 2019.
- [14] X. Zhang and C. Wang, "A novel multi-attractor period multi-scroll chaotic integrated circuit based on CMOS wide adjustable CCCII," *IEEE Access*, vol. 7, no. 1, pp. 16336–16350, 2019.
- [15] R. P. Wu and C. H. Wang, "A new simple chaotic circuit based on memristor," *International Journal of Bifurcation and Chaos*, vol. 26, no. 9, pp. 1–11, 2016.
- [16] R. Condorelli, "Applied nonlinear dynamical system in social science. A nonlinear model for social control system: an application to Italian coercion system," *Quality & Quantity*, vol. 47, no. 2, pp. 1173–1198, 2013.
- [17] C. Liu and Z.-K. Zhang, "Information spreading on dynamic social networks," *Communications in Nonlinear Science and Numerical Simulation*, vol. 19, no. 4, pp. 896–904, 2014.
- [18] F. Yu, L. Li, Q. Tang, S. Cai, Y. Song, and Q. Xu, "A survey on true random number generators based on chaos," *Discrete Dynamics in Nature and Society*, vol. 2019, Article ID 2545123, 2019.
- [19] O. Reyad and Z. Kotulski, "Statistical analysis of the chaos-driven elliptic curve pseudo-random number generators," *Communications in Computer and Information Science*, vol. 448, pp. 38–48, 2014.
- [20] H. Xu, X. Tong, and X. Meng, "An efficient chaos pseudo-random number generator applied to video encryption," *Optik*, vol. 127, no. 20, pp. 9305–9319, 2016.

- [21] X. Wang and C. Yu, "Cryptanalysis and improvement on a cryptosystem based on a chaotic map," *Computers & Mathematics with Applications*, vol. 57, no. 3, pp. 476–482, 2009.
- [22] R. Rhouma and S. Belghith, "Cryptanalysis of a chaos-based cryptosystem on DSP," *Communications in Nonlinear Science and Numerical Simulation*, vol. 16, no. 2, pp. 876–884, 2011.
- [23] Q. Yin and C. Wang, "A new chaotic image encryption scheme using breadth-first search and dynamic diffusion," *International Journal of Bifurcation and Chaos*, vol. 28, no. 4, p. 1850047, 2018.
- [24] Y. Li, C. Wang, and H. Chen, "A hyper-chaos-based image encryption algorithm using pixel-level permutation and bit-level permutation," *Optics and Lasers in Engineering*, vol. 90, pp. 238–246, 2017.
- [25] G. Cheng, C. Wang, and H. Chen, "A novel color image encryption algorithm based on hyperchaotic system and permutation-diffusion architecture," *International Journal of Bifurcation and Chaos*, vol. 29, no. 9, Article ID 1950115, 2019.
- [26] F. Yu and C. Wang, "Secure communication based on a four-wing chaotic system subject to disturbance inputs," *Optik*, vol. 125, no. 20, pp. 5920–5925, 2014.
- [27] N. Vafamand, S. Khorshidi, and A. Khayatian, "Secure communication for non-ideal channel via robust TS fuzzy observer-based hyperchaotic synchronization," *Chaos, Solitons & Fractals*, vol. 112, pp. 116–124, 2018.
- [28] L. Zhou, C. Wang, and H. He, "Time-controllable combinatorial inner synchronization and outer synchronization of anti-star networks and its application in secure communication," *Communications in Nonlinear Science and Numerical Simulation*, vol. 22, no. 1–3, pp. 623–640, 2015.
- [29] L. Zhou, F. Tan, and F. Yu, "A robust synchronization-based chaotic secure communication scheme with double-layered and multiple hybrid networks," *IEEE Systems Journal*, 2019.
- [30] F. Yu, L. Gao, K. Gu, B. Yin, Q. Wan, and Z. Zhou, "A fully qualified four-wing four-dimensional autonomous chaotic system and its synchronization," *Optik*, vol. 131, pp. 79–88, 2017.
- [31] F. Yu, P. Li, K. Gu, and B. Yin, "Research progress of multi-scroll chaotic oscillators based on current-mode devices," *Optik*, vol. 127, no. 13, pp. 5486–5490, 2016.
- [32] C. H. Wang, H. Xu, and F. Yu, "A novel approach for constructing high-order Chua's circuit with multi-directional multi-scroll chaotic attractors," *International Journal of Bifurcation and Chaos*, vol. 23, no. 2, Article ID 1350022, 2013.
- [33] J. Jin, "Programmable multi-direction fully integrated chaotic oscillator," *Microelectronics Journal*, vol. 75, pp. 27–34, 2018.
- [34] J. Jin and L. Zhao, "Low voltage low power fully integrated chaos generator," *Journal of Circuits, Systems and Computers*, vol. 27, no. 10, p. 1850155, 2018.
- [35] X. Zhang, C. Wang, W. Yao, and H. Lin, "Chaotic system with bondorbital attractors," *Nonlinear Dynamics*, vol. 97, no. 4, pp. 2159–2174, 2019.
- [36] O. E. Rossler, "An equation for hyperchaos," *Physics Letters A*, vol. 71, no. 2–3, pp. 155–157, 1979.
- [37] J. Jin and L. Cui, "Fully integrated memristor and its application on the scroll-controllable hyperchaotic system," *Complexity*, vol. 2019, Article ID 4106398, 8 pages, 2019.
- [38] F. Yu, C. Wang, and H. He, "Grid multiscroll hyperchaotic attractors based on colpitts oscillator mode with controllable grid gradient and scroll numbers," *Journal of Applied Research and Technology*, vol. 11, no. 3, pp. 371–380, 2013.
- [39] C. Volos, J.-O. Maaita, S. Vaidyanathan, V.-T. Pham, I. Stouboulos, and I. Kyprianidis, "A novel four-dimensional hyperchaotic four-wing system with a saddle-focus equilibrium," *IEEE Transactions on Circuits and Systems II: Express Briefs*, vol. 64, no. 3, pp. 339–343, 2017.
- [40] V.-T. Pham, S. Vaidyanathan, C. Volos, S. Jafari, and S. T. Kingni, "A no-equilibrium hyperchaotic system with a cubic nonlinear term," *Optik*, vol. 127, no. 6, pp. 3259–3265, 2016.
- [41] K. Rajagopal, A. J. M. Khalaf, Z. Wei, V.-T. Pham, A. Alsaedi, and T. Hayat, "Hyperchaos and coexisting attractors in a modified van der Pol-duffing oscillator," *International Journal of Bifurcation and Chaos*, vol. 29, no. 5, Article ID 1950067, 2019.
- [42] X. Zhang and C. Wang, "Multiscroll hyperchaotic system with hidden attractors and its circuit implementation," *International Journal of Bifurcation and Chaos*, vol. 29, no. 9, Article ID 1950117, 2019.
- [43] C. X. Zhang and S. M. Yu, "A novel methodology for constructing a multi-wing chaotic and hyperchaotic system with a unified step function switching control," *Chinese Physics B*, vol. 25, no. 5, Article ID 050503, 2016.
- [44] C. Zhang, "Theoretical design approach of four-dimensional piecewise-linear multi-wing hyperchaotic differential dynamic system," *Optik*, vol. 127, no. 11, pp. 4575–4580, 2016.
- [45] C. Zhang, "Mirror symmetry multi-wing attractors generated from a novel four-dimensional hyperchaotic system," *Optik*, vol. 127, no. 5, pp. 2924–2930, 2016.
- [46] A. Zarei, "Complex dynamics in a 5-D hyper-chaotic attractor with four-wing, one equilibrium and multiple chaotic attractors," *Nonlinear Dynamics*, vol. 81, no. 1–2, pp. 585–605, 2015.
- [47] L. Chua, "Memristor—the missing circuit element," *IEEE Transactions on Circuit Theory*, vol. 18, no. 5, pp. 507–519, 1971.
- [48] D. B. Strukov, G. S. Snider, D. R. Stewart, and R. S. Williams, "The missing memristor found," *Nature*, vol. 453, no. 7191, pp. 80–83, 2008.
- [49] S. P. Wang, C. L. He, J. Tang et al., "Electronic synapses based on ultrathin quasi-two-dimensional gallium oxide memristor," *Chinese Physics B*, vol. 28, no. 1, pp. 183–188, 2019.
- [50] P. Prakash, J. P. Singh, and B. K. Roy, "Fractional-order memristor-based chaotic system with a stable equilibrium point, its fractional-order PI-based sliding mode control and switching synchronisation," *Pramana*, vol. 92, no. 2, 2019.
- [51] V.-T. Pham, A. Buscarino, L. Fortuna, and M. Frasca, "Simple memristive time-delay chaotic systems," *International Journal of Bifurcation and Chaos*, vol. 23, no. 4, Article ID 1350073, 2013.
- [52] C. K. Volos, A. Akgul, V. T. Pham et al., "Antimonotonicity, crisis and multiple attractors in a simple memristive circuit," *Journal of Circuits, Systems and Computers*, vol. 27, no. 2, pp. 80–83, 2018.
- [53] C. Wang, X. Liu, and H. Xia, "Multi-piecewise quadratic nonlinearity memristor and its 2N-scroll and 2N+1-scroll chaotic attractors system," *Chaos*, vol. 27, no. 3, Article ID 033114, 2017.
- [54] J. Ma, Z. Chen, Z. Wang, and Q. Zhang, "A four-wing hyperchaotic attractor generated from a 4-D memristive system with a line equilibrium," *Nonlinear Dynamics*, vol. 81, no. 3, pp. 1275–1288, 2015.

- [55] L. Zhou, C. Wang, and L. Zhou, "A novel no-equilibrium hyperchaotic multi-wing system via introducing memristor," *International Journal of Circuit Theory and Applications*, vol. 46, no. 1, pp. 84–98, 2018.
- [56] L. Zhou, C. Wang, and L. Zhou, "Generating four-wing hyperchaotic attractor and two-wing, three-wing, and four-wing chaotic attractors in 4D memristive system," *International Journal of Bifurcation and Chaos*, vol. 27, no. 2, p. 1750027, 2017.
- [57] L. Zhou, C. Wang, and L. Zhou, "Generating hyperchaotic multi-wing attractor in a 4D memristive circuit," *Nonlinear Dynamics*, vol. 85, no. 4, pp. 2653–2663, 2016.
- [58] F. Yu, Q. Tang, W. Wang, and H. Wu, "A 2.7 GHz low-phase-noise LC-QVCO using the gate-modulated coupling technique," *Wireless Personal Communications*, vol. 86, no. 2, pp. 671–681, 2016.
- [59] F. Yu, L. Gao, L. Liu, S. Qian, S. Cai, and Y. Song, "A 1 V, 0.53 ns, 59 μ W current comparator using standard 0.18 μ m CMOS technology," *Wireless Personal Communications*, 2019.
- [60] F. Yu, "A low-voltage and low-power 3-GHz CMOS LC VCO for S-band wireless applications," *Wireless Personal Communications*, vol. 78, no. 2, pp. 905–914, 2014.
- [61] S. He, K. Sun, and H. Wang, "Complexity analysis and DSP implementation of the fractional-order Lorenz hyperchaotic system," *Entropy*, vol. 17, no. 12, pp. 8299–8311, 2015.
- [62] Z. Xiao-Hong and Z. Zhi-Guang, "Digital circuit design and simulation of a new time-delay hyperchaotic system," *Communications in Computer and Information Science*, vol. 234, pp. 411–417, 2011.
- [63] M. Tuna, M. Alçın, İ. Koyuncu, C. B. Fidan, and İ. Pehlivan, "High speed FPGA-based chaotic oscillator design," *Microprocessors and Microsystems*, vol. 66, pp. 72–80, 2019.
- [64] A. Ahmadi, K. Rajagopal, F. E. Alsaadi, V.-T. Pham, F. E. Alsaadi, and S. Jafari, "A novel 5D chaotic system with extreme multi-stability and a line of equilibrium and its engineering applications: circuit design and FPGA implementation," *Iranian Journal of Science and Technology, Transactions of Electrical Engineering*, 2019.
- [65] Y. M. Xu, L. D. Wang, and S. K. Duan, "A memristor-based chaotic system and its field programmable gate array implementation," *Acta Physica Sinica*, vol. 65, no. 12, p. 120503, 2016.
- [66] E. Tlelo-Cuautle, A. D. Pano-Azucena, J. J. Rangel-Magdaleno, V. H. Carbajal-Gomez, and G. Rodriguez-Gomez, "Generating a 50-scroll chaotic attractor at 66 MHz by using FPGAs," *Nonlinear Dynamics*, vol. 85, no. 4, pp. 2143–2157, 2016.
- [67] J.-L. Zhang, W.-Z. Wang, X.-W. Wang, and Z.-H. Xia, "Enhancing security of FPGA-based embedded systems with combinational logic binding," *Journal of Computer Science and Technology*, vol. 32, no. 2, pp. 329–339, 2017.
- [68] L. Yong, "Lag synchronization of autocatalytic chemical reaction in continuous stirred tank reactors," *Acta Physica Sinica*, vol. 57, no. 10, pp. 6099–6102, 2008.
- [69] X. Wu, C. Bai, and H. Kan, "A new color image cryptosystem via hyperchaos synchronization," *Communications in Nonlinear Science and Numerical Simulation*, vol. 19, no. 6, pp. 1884–1897, 2014.
- [70] M. Rafikov and J. M. Balthazar, "On control and synchronization in chaotic and hyperchaotic systems via linear feedback control," *Communications in Nonlinear Science and Numerical Simulation*, vol. 13, no. 7, pp. 1246–1255, 2008.
- [71] C.-L. Li and L. Wu, "Sliding mode control for synchronization of fractional permanent magnet synchronous motors with finite time," *Optik*, vol. 127, no. 6, pp. 3329–3332, 2016.
- [72] F. Yu and Y. Song, "Complete switched generalized function projective synchronization of a class of hyperchaotic systems with unknown parameters and disturbance inputs," *Journal of Dynamic Systems, Measurement, and Control*, vol. 136, no. 1, Article ID 014505, 2013.
- [73] F. Yu, C. Wang, Q. Wan, and Y. Hu, "Complete switched modified function projective synchronization of a five-term chaotic system with uncertain parameters and disturbances," *Pramana*, vol. 80, no. 2, pp. 223–235, 2013.
- [74] F. Yu, C. H. Wang, Y. Hu, and J. W. Yin, "Anti-synchronization of a novel hyperchaotic system with parameter mismatch and external disturbances," *Pramana*, vol. 79, no. 1, pp. 81–93, 2012.
- [75] J. Yu, J. Lei, and L. Wang, "Backstepping synchronization of chaotic system based on equivalent transfer function method," *Optik*, vol. 130, pp. 900–913, 2017.
- [76] Y.-Y. Huang, Y.-H. Wang, and Y. Zhang, "Shape synchronization of drive-response for a class of two-dimensional chaotic systems via continuous controllers," *Nonlinear Dynamics*, vol. 78, no. 4, pp. 2331–2340, 2014.
- [77] Y. Huang, Y. Wang, H. Chen, and S. Zhang, "Shape synchronization control for three-dimensional chaotic systems," *Chaos, Solitons & Fractals*, vol. 87, pp. 136–145, 2016.
- [78] S. Çiçek, A. Ferikoğlu, and İ. Pehlivan, "A new 3D chaotic system: dynamical analysis, electronic circuit design, active control synchronization and chaotic masking communication application," *Optik*, vol. 127, no. 8, pp. 4024–4030, 2016.
- [79] C. Huang and J. Cao, "Active control strategy for synchronization and anti-synchronization of a fractional chaotic financial system," *Physica A: Statistical Mechanics and its Applications*, vol. 473, pp. 262–275, 2017.
- [80] I. Ahmad, A. B. I. Saaban, A. B. Saaban, A. B. Ibrahim, M. Shahzad, and N. Naveed, "The synchronization of chaotic systems with different dimensions by a robust generalized active control," *Optik*, vol. 127, no. 11, pp. 4859–4871, 2016.
- [81] K. Xie, X. Ning, X. Wang et al., "An efficient privacy-preserving compressive data gathering scheme in WSNs," *Information Sciences*, vol. 390, no. 2, pp. 702–715, 2016.
- [82] M. Long, F. Peng, and H.-Y. Li, "Separable reversible data hiding and encryption for HEVC video," *Journal of Real-Time Image Processing*, vol. 14, no. 1, pp. 171–182, 2018.
- [83] K. Gu, K. Wang, and L. Yang, "Traceable attribute-based signature," *Journal of Information Security and Applications*, vol. 49, pp. 1–16, 2019.
- [84] K. Gu, N. Wu, B. Yin, and W. Jia, "Secure data sequence query framework based on multiple fogs," *IEEE Transactions on Emerging Topics in Computing*, 2019.
- [85] K. Gu, N. Wu, B. Yin, and W. Jia, "Secure data query framework for cloud and fog computing," *IEEE Transactions on Network and Service Management*, 2019.
- [86] K. Gu, W. Jia, G. Wang et al., "Efficient and secure attribute-based signature for monotone predicates," *Acta Informatica*, vol. 54, pp. 521–541, 2017.
- [87] Z. Xia, Z. Fang, F. Zou, J. Wang, and A. K. Sangaiah, "Research on defensive strategy of real-time price attack based on multiperson zero-determinant," *Security and Communication Networks*, vol. 2019, pp. 1–13, 2019.
- [88] S. He, W. Zeng, K. Xie et al., "PPNC: privacy preserving scheme for random linear network coding in smart grid," *KSI Transactions on Internet and Information Systems*, vol. 11, pp. 1510–1533, 2017.

- [89] L. Xiang, X. Shen, J. Qin, and W. Hao, "Discrete multi-graph hashing for large-scale visual search," *Neural Processing Letters*, vol. 49, no. 3, pp. 1055–1069, 2019.
- [90] L. Xiang, Y. Li, W. Hao et al., "Reversible natural Language watermarking using synonym substitution and arithmetic coding," *CMC: Computers, Materials and Continua*, vol. 55, no. 3, pp. 541–559, 2018.
- [91] K. Gu, L. Yang, Y. Wang, and S. Wen, "Traceable identity-based group signature," *RAIRO-Theoretical Informatics and Applications*, vol. 50, no. 3, pp. 193–226, 2016.
- [92] Z. Sun, L. Si, Z. Shang, and J. Lei, "Finite-time synchronization of chaotic PMSM systems for secure communication and parameters identification," *Optik*, vol. 157, pp. 43–55, 2018.
- [93] W. Wang, X. Jia, X. Luo, J. Kurths, and M. Yuan, "Fixed-time synchronization control of memristive MAM neural networks with mixed delays and application in chaotic secure communication," *Chaos, Solitons & Fractals*, vol. 126, pp. 85–96, 2019.
- [94] S. Khorashadizadeh and M.-H. Majidi, "Chaos synchronization using the Fourier series expansion with application to secure communications," *AEU-International Journal of Electronics and Communications*, vol. 82, pp. 37–44, 2017.
- [95] M. F. Hassan and M. Hammuda, "A new approach for constrained chaos synchronization with application to secure data communication," *Journal of the Franklin Institute*, vol. 356, no. 12, pp. 6697–6723, 2019.
- [96] M. Xu, W. Pan, and L. Zhang, "Secure remote synchronization and secure key distribution in electro-optic networks revealed by symmetries," *Optics Communications*, vol. 418, pp. 41–45, 2018.
- [97] M. E. Sahin, Z. G. Cam Taskiran, H. Guler, and S. E. Hamamci, "Simulation and implementation of memristive chaotic system and its application for communication systems," *Sensors and Actuators A: Physical*, vol. 290, pp. 107–118, 2019.
- [98] R. Ramesh Babu and R. Karthikeyan, "Adaptive synchronization of novel chaotic system and its FPGA implementation," in *Proceedings of the 2015 International Conference on Smart Technologies and Management for Computing, Communication, Controls, Energy and Materials (ICSTM)*, pp. 449–454, Chennai, India, May 2015.
- [99] T. Tami, T. Messaoudene, A. Ferdjouni et al., "Chaos secure communication' implementation in FPGA," in *Proceedings of the 2018 International Conference on Applied Smart Systems (ICASS)*, Medea, Algeria, November 2018.
- [100] K. Rajagopal, A. Durdu, S. Jafari, Y. Uyaroglu, A. Karthikeyan, and A. Akgul, "Multiscroll chaotic system with sigmoid nonlinearity and its fractional order form with synchronization application," *International Journal of Non-Linear Mechanics*, vol. 116, pp. 262–272, 2019.
- [101] S. He, K. Sun, and S. Banerjee, "Dynamical properties and complexity in fractional-order diffusionless Lorenz system," *European Physical Journal Plus*, vol. 131, p. 254, 2016.
- [102] S. He, K. Sun, X. Mei et al., "Numerical analysis of fractional-order chaotic system based on conformable fractional-order derivative," *European Physical Journal Plus*, vol. 132, p. 36, 2017.
- [103] M. Tuna and C. B. Fidan, "Electronic circuit design, implementation and FPGA-based realization of a new 3D chaotic system with single equilibrium point," *Optik*, vol. 127, no. 24, pp. 11786–11799, 2016.
- [104] Q. Yang and M. Bai, "A new 5D hyperchaotic system based on modified generalized Lorenz system," *Nonlinear Dynamics*, vol. 88, no. 1, pp. 189–221, 2017.

Research Article

Research on Grid Scroll Chaotic Extended Sequence Algorithm and Its Circuit Implementation for F-OFDM System

Yingjie Ma,¹ Ya Li ,² Geng Zhao,¹ Ping Zeng,¹ and Yatao Yang¹

¹Beijing Electronic Science and Technology Institute, Beijing, CO 100070, China

²Guangdong Polytechnic Normal University, Guangdong, CO 510665, China

Correspondence should be addressed to Ya Li; liya2829@gmail.com

Received 6 September 2019; Revised 15 October 2019; Accepted 1 November 2019; Published 28 November 2019

Guest Editor: Serdar Çiçek

Copyright © 2019 Yingjie Ma et al. This is an open access article distributed under the Creative Commons Attribution License, which permits unrestricted use, distribution, and reproduction in any medium, provided the original work is properly cited.

High peak-to-average power ratio (PAPR), a main problem of 5G Filtered-Orthogonal Frequency Division Multiplexing (F-OFDM) system, seriously affects the system's transmission efficiency. Aiming at the shortcomings of the traditional selective mapping (SLM) algorithm, the grid scroll chaotic extended sequence (GSCES) algorithm is proposed to solve the high PAPR problem. The proposed grid multiscroll chaotic maps are used as random phase sequence vectors instead of the traditional pseudo random sequence, which provide a large number of random sequences with good correlation characteristics, random characteristics, and high security. The proposed random phase sequence vectors can meet the needs of 5G mass connections. The original input signals are divided into real part and imaginary part, which are, respectively, dot produced with the proposed grid multiscroll chaotic maps. The numerical simulation results show that the proposed GSCES algorithm effectively increases the number of candidate sequences, reduces the PAPR values, and improves the transmission efficiency and security. Moreover, the hardware experimental results produce a $2 \times 2 \times 2$ -grid multiscroll chaotic attractor, which further proves the physical realization of the proposed system. The proposed schemes have a broad application prospect in 5G multicarrier modulation technology.

1. Introduction

In 2015, Filtered-OFDM (F-OFDM) technology was first put forward publicly at the World Mobile Communication Congress. It is an adaptive airport waveform modulation technology whose subcarrier bandwidth can be adjusted according to specific application scenarios. F-OFDM technology has many advantages, such as no need for strict synchronization, reduced out-of-band energy leakage, the different waveform modulation, multiple access technology and frame structure based on the mobile communication application scene and business requirements, the dynamic soft interface parameter configuration according to the 5G business needs, and packet traffic transmission suitable for Internet of things [1–5]. In the F-OFDM system, when subcarriers of sub-band are superimposed after IFFT operation, multiple subcarriers will reach the peak value at the same time, resulting in higher peak-to-average power ratio

(PAPR) of synthetic signal, which seriously affects the system performance and limits its application in 5G.

The characteristics of selective mapping (SLM) scrambling technology are simple structure and obvious effect, but there are a large side band information and high computational complexity. Many researchers have improved the traditional SLM algorithm. The cyclic-SLM scheme is proposed to omit the side information (SI) and apply only one IFFT. In the time domain, the original signal and its periodic shift signal are added and the minimum PAPR is selected as the candidate signal [6]. The time-frequency domain encryption technique is proposed based on the multichaos and SLM PAPR suppression algorithm. The Lozi and Logistic maps are used to interfere the carrier in the time-frequency domain. In a 100 kilometer single-mode fiber, 8.9 Gb/s encrypted OFDM signal is transmitted safely [7]. A method is proposed to decrease the PAPR of the 16-QAM OFDM system, which combines the chaotic map and SLM algorithm

so that the phase rotation factors are controlled by chaotic sequence [8]. The improved SLM algorithm based on the Lehmer random phase sequence vector is proposed to embed side band information into the 16-PSK transmit signal [9]. The improved SLM algorithm is proposed to reduce PAPR, combining interlaced IDCT transform with pulse forming technology [10]. The low complexity improved SLM algorithm and μ -law compression scheme are proposed to reduce the PAPR and computational complexity of the OFDMA system [11]. The low-complexity SLM improvement algorithm without SI is proposed to reduce the PAPR of the coherent light OFDM system [12]. The blind differential improved SLM algorithm is proposed to reduce the PAPR of Alamouti DSFBC-OFDM system [13].

In this paper, a model of the new system is constructed to produce grid multiscroll chaotic attractors, using different sign functions acted as nonlinear function. Moreover, the design of the hardware circuit produces at $2 \times 2 \times 2$ -grid multiscroll hardware experimental results. The produced grid multiscroll chaotic maps are used as random phase sequence vectors instead of the traditional pseudo random sequence. The grid scroll chaotic extended sequence (GSCES) algorithm is proposed to solve the high PAPR problem. The numerical simulation results show that the proposed GSCES algorithm effectively increases the numbers of candidate sequences, reduces the PAPR values, and improves the transmission efficiency and security.

2. Methods

2.1. F-OFDM System Modes. F-OFDM system dynamically configures suitable waveform parameters such as bandwidth, cycle prefix (CP) length, subcarrier spacing, and FFT points for each sub-band according to service requirements, which improves the flexibility and scalability of 5G communication system. The downlink of the F-OFDM system is shown in Figure 1.

As shown in Figure 1, the frequency bands of the system are divided into M sub-bands, which are subcarrier mapping, IFFT transformation, and plus CP operation, respectively, and each sub-band is filtered through the sub-band filter for coupling transmission. The biggest difference between the F-OFDM system and traditional OFDM system is the sub-band filter added at the transmitter and receiver. For each sub-band, at the transmitter, the input signal of the sub-band filter is the traditional OFDM signal. The function of the sub-band filter is to complete the baseband shaping of each sub-band, and its output signal is the F-OFDM signal. At the receiving end, the function of sub-band filter is to filter each sub-band signal and complete sub-band decoupling.

The data symbol of the i th sub-band of the F-OFDM system is given by

$$x_i(n) = g_i(n) * f_i(n), \quad i = 1, 2, \dots, M, \quad (1)$$

where $g_i(n)$ is the i th sub-band symbol before filtering, $f_i(n)$ is the impulse response of the i th sub-band filter at the beginning, and M is the number of sub-band.

The transmit signal of the F-OFDM system is as follows:

$$x(n) = \sum_{i=0}^{M-1} x_i(n). \quad (2)$$

The channel output signal is given by

$$\begin{aligned} r(n) &= x(n) * h(n) + z(n) \\ &= \sum_{i=0}^{M-1} x_i(n) * h(n) + z(n) \\ &= \sum_{i=0}^{M-1} [g_i(n) * f_i(n) * h(n)] + z(n). \end{aligned} \quad (3)$$

2.2. Construction of Grid Multiscroll Chaotic System. In this paper, the new grid multiscroll chaotic system is constructed with the combination of sign functions, which act as nonlinear functions. So, the dimensionless equation of the state is constructed by the following equation:

$$\begin{cases} \frac{dx}{dt} = y - a \cdot \text{sgn}(y), \\ \frac{dy}{dt} = z - b \cdot \text{sgn}(z), \\ \frac{dz}{dt} = -cx - cy - dz + e \cdot \text{sgn}(x + y). \end{cases} \quad (4)$$

When control parameters $a = 1.4$, $b = 1.4$, $c = 1.5$, $d = 0.8$, and $e = 3.9$, the grid multiscroll chaotic system is in a state of chaos.

2.3. Grid Scroll Chaotic Extended Sequence Algorithm. The traditional SLM algorithm is a kind of PAPR suppression algorithm without signal distortion. However, the receiver needs to know the selected random phase sequence to demodulate, so it also needs to transmit the corresponding random phase sequence information in addition to the data information. It is restricted in practical application. In this paper, the pseudo random sequences are generated by the proposed grid multiscroll chaotic maps. The pseudo random sequences are generated by the initial value iterations. It only needs to transmit its initial value, which reduces the complexity of the operation and the side band information transmission. Aiming at the shortcomings of the traditional SLM algorithm, the grid scroll chaotic extended sequence (GSCES) algorithm is proposed in this paper. The original signals are divided into real part and imaginary part, the proposed grid multiscroll chaotic maps are used as random phase sequence vectors, the IFFT transforms are performed, respectively, the PAPR is calculated by linear superposition, and the minimum PAPR is selected for transmission as shown in Figure 2.

As shown in Figure 2, the 5G F-OFDM data block is $x(t)$, the serial input signal $x(t)$ is symbol mapped, which is divided into $2M$ subchannels with serial-to-parallel conversion, the signal $x(t)$ is divided into the real part and the imaginary part, and the transmission is carried out on the M

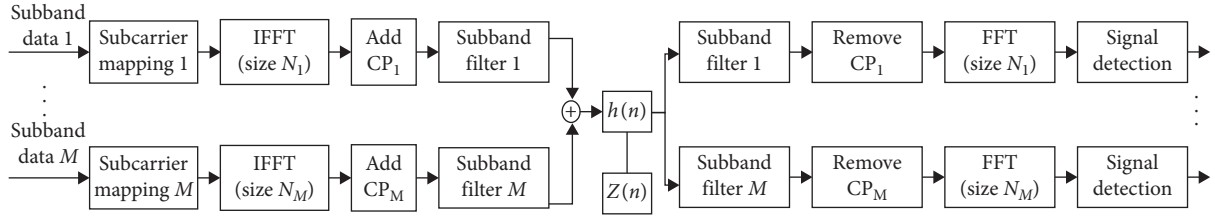


FIGURE 1: The downlink of F-OFDM system.

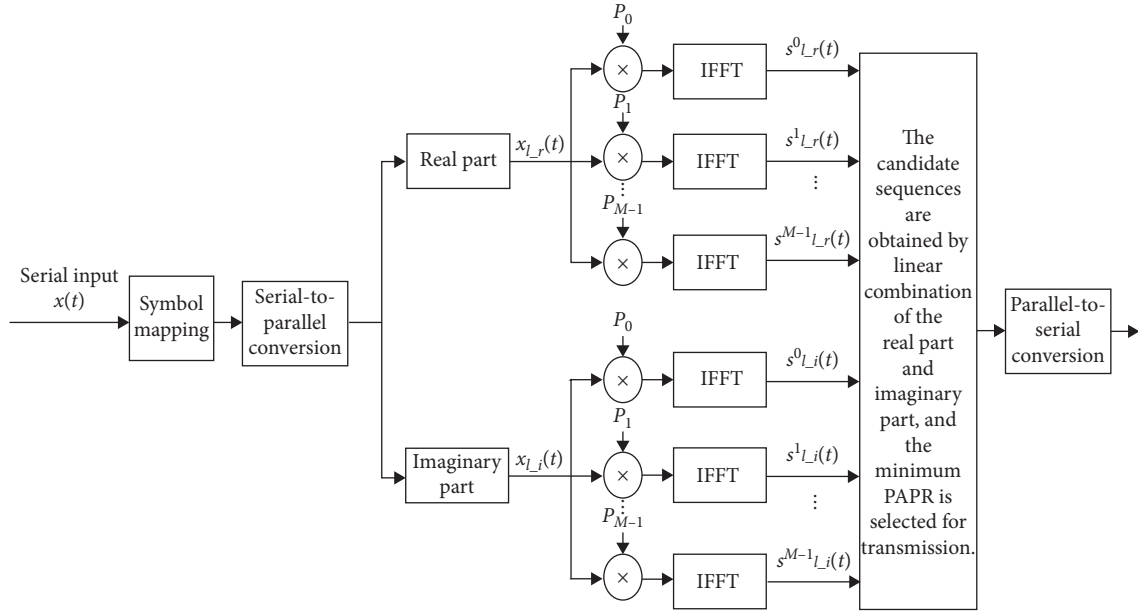


FIGURE 2: Schematic diagram of the grid scroll chaotic extended sequence algorithm.

subchannel, respectively. The proposed grid multiscroll chaotic maps are used to generate random phase sequence vector P with different N lengths, and then the m th random phase sequence vector is $P_m = (P_{m,0}, P_{m,1}, \dots, P_{m,N-1})$, $0 \leq m \leq M-1$. The l th data block $x_l(t)$ is divided into the real part $x_{l,r}(t)$ and the imaginary part $x_{l,i}(t)$, which are, respectively, dot produced with the m th random phase sequence vector P_m , then IFFT transforms are performed, and the candidate transmission sequences $s_{l,r}^m(t)$ and $s_{l,i}^m(t)$ are produced:

$$\begin{aligned} s_{l,r}^m(t) &= \text{IFFT}(x_{l,r}(t) \otimes P_m) \\ &= \text{IFFT}(x_{l,r,0}(t)P_{m,0}, x_{l,r,1}(t)P_{m,1}, \dots, x_{l,r,N-1}(t)P_{m,N-1}), \\ &\quad 0 \leq m \leq M-1, \\ s_{l,i}^m(t) &= \text{IFFT}(x_{l,i}(t) \otimes P_m) \\ &= \text{IFFT}(x_{l,i,0}(t)P_{m,0}, x_{l,i,1}(t)P_{m,1}, \dots, x_{l,i,N-1}(t)P_{m,N-1}), \\ &\quad 0 \leq m \leq M-1, \end{aligned} \quad (5)$$

where \otimes is dot product operation between two vectors, IFFT is discrete Fourier inverse transformation, $s_{l,r}^m(t)$ is the real part of the candidate sequence, and $s_{l,i}^m(t)$ is the imaginary part of the candidate sequence.

The candidate sequence $s_l^{k,q}(t)$ are obtained by linear combination of the real part $s_{l,r}^k(t)$ and imaginary part $s_{l,i}^q(t)$:

$$\begin{aligned} s_l^{k,q}(t) &= \alpha_k s_{l,r}^k(t) \pm j\beta_g s_{l,i}^q(t) \\ &= \alpha_k \text{IFFT}(x_{l,r}(t) \otimes P_k) \pm j\beta_g \text{IFFT}(x_{l,i}(t) \otimes P_q). \end{aligned} \quad (6)$$

If $\alpha_k P_k \pm j\beta_g P_q$ is the unit phase sequence vector, that is $|\alpha_k| = |\beta_g| = 1/\sqrt{2}$, and the positive and negative polarity have the same PAPR, then

$$\begin{aligned} s_l^{k,q}(t) &= \frac{1}{\sqrt{2}} \text{IFFT}(x_{l,r}(t) \otimes P_k \pm jx_{l,i}(t) \otimes P_q) \\ &= \frac{1}{\sqrt{2}} (s_{l,r}^k(t) \pm js_{l,i}^q(t)). \end{aligned} \quad (7)$$

According to equation (7), the number of expanded candidate transmission sequences $s_{el}(t)$ increases from original M to M^2 , and it is expressed as

$$\begin{aligned} s_{el}(t) &= \{s_l^0(t), s_l^1(t), \dots, s_l^n(t), \dots, s_l^{M^2-1}(t)\}, \\ &\quad 0 \leq n \leq M^2 - 1. \end{aligned} \quad (8)$$

In the candidate transmission sequence of l th data block, the minimum PAPR is selected as D_b , namely,

$$D_l = \arg \min_{0 \leq n \leq M^2-1} \{\text{PAPR}(s_l^n(t))\}, \quad 0 \leq l \leq M-1. \quad (9)$$

So, the output sequence is as follows:

$$D = \sum_{l=0}^{M-1} D_l. \quad (10)$$

3. Experiment

According to the modular circuit design method, equation (4) has been carried out by the differential-integral transforms; we have the following equation:

$$\begin{cases} x = \int [y - a \cdot \text{sgn}(y)] d\tau, \\ y = \int [z - b \cdot \text{sgn}(z)] d\tau, \\ z = \int [-cx - cy - dz + e \cdot \text{sgn}(x + y)] d\tau. \end{cases} \quad (11)$$

According to equation (11), the design of the circuit is shown in Figure 3. The model of the operational amplifier is TL082. The power supply voltage of all active devices is ± 15 V. All resistors are precision adjustable resistors or precision adjustable potentiometers.

4. Results and Discussion

4.1. Dynamics of Lyapunov Exponents. For the system corresponding equation (4), the Runge–Kutta integration method is used with the length of time $t = (0, 200)$, initial values $(x, y, z) = (0.02, 0.01, 0.03)$, and the numerical simulation result of the Lyapunov exponents is shown in Figure 4.

The Lyapunov exponents of the proposed system are given as $LE_1 = 0.055545$, $LE_2 = 0.025606$, and $LE_3 = -0.881151$, also $LE_1 + LE_2 + LE_3 = -0.8$. Moreover, the fractal dimension is given by

$$\begin{aligned} LD &= j + \frac{1}{|LE_{j+1}|} \sum_{i=1}^j LE_i = 2 + \frac{0.055545 + 0.025606}{0.881151} \\ &= 2.0921. \end{aligned} \quad (12)$$

The proposed system has positive Lyapunov exponent and the dimension of Lyapunov is fractional, which further confirms that the system is in the state of chaos and the calculated Lyapunov exponent is reasonable. Moreover, this system produces strange attractor dimension $LD = 2.0921$, in line with the geometric characteristics of the chaotic attractor.

4.2. Poincare Map of Grid Multiscroll Chaotic System. For the system corresponding equation (4), the Runge–Kutta integration method is used with the length of time $t = (0, 2600)$ and initial values $(x, y, z) = (0.02, 0.01, 0.03)$. The

Poincare map of the grid multiscroll chaotic system is shown in Figure 5.

A Poincare section is selected in the phase space, which is used to cut off all the motion trajectories for observing section cut point. From Figure 5, we can see that the Poincare map of the grid multiscroll chaotic system is a piece of dense point set and has a hierarchical structure, which verifies the system's chaotic motion state.

4.3. Hardware Results. The hardware circuits shown in Figure 3 can be obtained, and experimental results are shown in Figure 6.

From Figure 6, it can be seen that the hardware circuit experiment results of the analog oscilloscope generate $2 \times 2 \times 2$ -grid multiscroll chaotic attractors, which verifies the physical feasibility of the proposed system. The phase rails of the proposed grid multiscroll chaotic attractor are separated in more directions and have more complex characteristics. Therefore, the grid multiscroll chaotic map is used as random phase sequence vectors. Compared with the traditional pseudo random sequences, the proposed grid multiscroll chaotic sequence can provide a large number of random sequences with good correlation characteristics, random characteristics, and high security, which meet the requirement of 5G mass connection.

4.4. PAPR Performance Simulation Results. In this paper, the QPSK modulation is adopted, the subcarrier number equals to 128, and the complementary cumulative distribution function (CCDF) is used to describe the PAPR distribution of the proposed system. In paper [6], the selected data utilization (SDU) algorithm is proposed to rotate the phase factor with specific selection conditions, which improves the PAPR performance of the traditional SLM algorithm. The PAPR performance comparison between the proposed GSCES algorithm and the traditional SLM algorithm and the SDU algorithm is shown in Figure 7.

In Figure 7, the variable original is the PAPR value calculated by 1×128 original signal.

In the traditional SLM algorithm, the 1×128 original signal is input data, L groups input data are copied and are dot product of random phase vectors, IFFT transforms are calculated, and the PAPR values are obtained, and the variable SLM is the minimum PAPR value of the L candidate sequences. The traditional SLM algorithm using random phase vectors requires the transmission of phase information of subchannel, so the side band information is very huge, which not only increases the complexity but also reduces the efficiency of the system.

In the proposed GSCES algorithm, the 1×128 original signal is the input data, L groups input data are copied, the real part and the imaginary part of input data are separated, L random phase vectors are generated by the proposed grid multiscroll chaotic maps, the real part and the imaginary part are separately dot product with the random phase vectors, IFFT transforms are calculated, and real and imaginary data are linearly added. The proposed GSCES algorithm extends the candidate sequence to L^2 groups, and

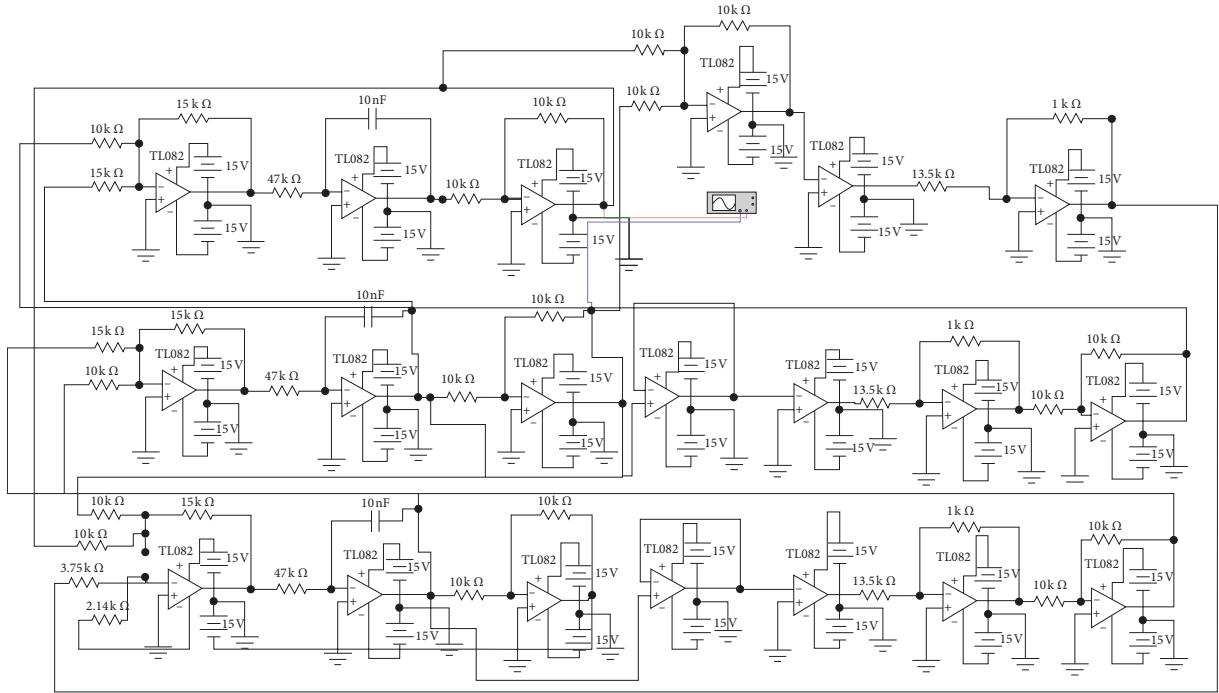


FIGURE 3: Hardware circuit diagram.

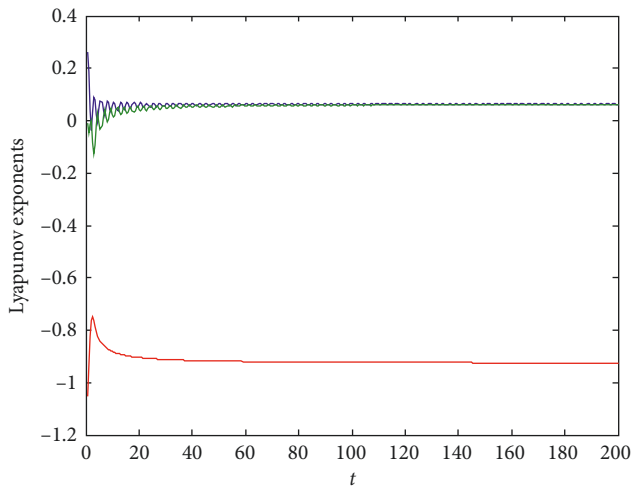


FIGURE 4: Lyapunov exponents of the proposed system.

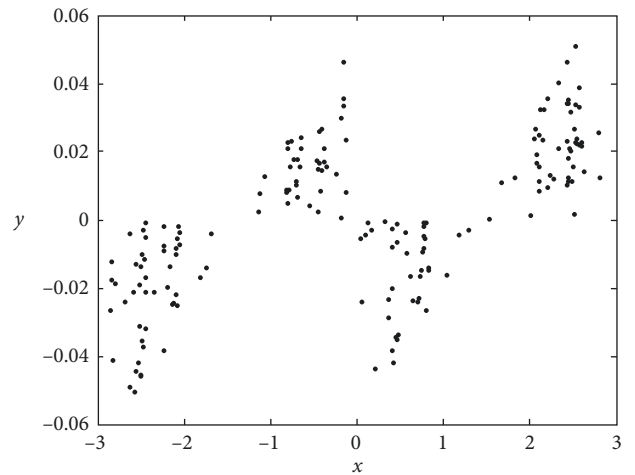


FIGURE 5: Poincaré map of the grid multiscroll chaotic system.

variable LSLM is the minimum PAPR value of L^2 candidate sequences.

In Figure 7, compared with the traditional SLM algorithm and SDU algorithm, the proposed GSCES algorithm effectively reduces the PAPR of the 5G F-OFDM system, increases the candidate sequences, reduces calculation, and transmits data more efficiently.

4.5. BER Performance Simulation Results. The F-OFDM signal divides the frequency band of the system into several different sub-bands, which can be configured with different link parameters according to the actual service requirements, such as different subcarrier spacing, IFFT/FFT size, and CP

length. In this section, we evaluate the bit error rate (BER) performance of the proposed GSCES algorithm in the F-OFDM system. In the additive white Gaussian noise (AWGN) channel, the system performance test is carried out, and the specific simulation parameter configuration of the F-OFDM system is shown in Table 1.

The configuration of link parameters in this paper is shown in Table 1. In the F-OFDM system, the BER performance of the proposed GSCES algorithm is shown in Figure 8.

From Figure 8, it can be seen that the BER performance of the proposed GSCES algorithm has a certain degree of degradation compared with the original signal, but the degree of degradation is not large. Combining with Figure 7,

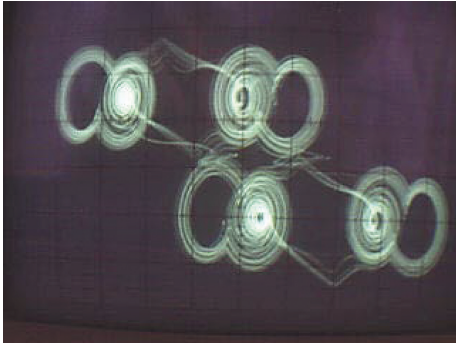


FIGURE 6: Hardware circuit experimental results.

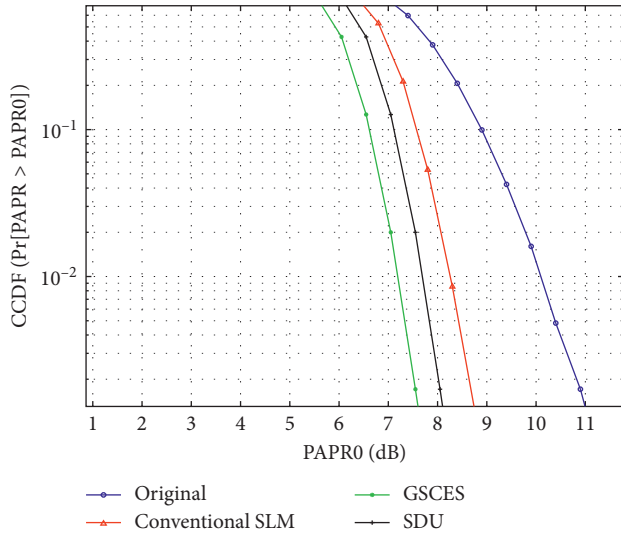


FIGURE 7: The PAPR performance comparison results.

TABLE 1: Simulation setup.

Parameter	Value/description
Subcarrier size	64
IFFT/FFT size	1024
Baseband modulation mode	QPSK
Subcarrier spacing	15 KHz
CP length	16
Symbol duration	66.7 μ s
Channel model	AWGN
Type of filters	Square root raised cosine

it can be seen that the proposed GSCES algorithm can effectively improve the PAPR performance of the system, and when the transmission signal meets certain signal-to-noise ratio (SNR) conditions, it will not affect the BER performance of the system.

4.6. Computational Complexity Analysis. Assuming that both the SLM algorithm and the proposed GSCES algorithm generate L^2 candidate sequences, the number of subcarriers is R , the oversampling rate is Q , and the IFFT transformation of RQ points requires $(RQ/2)\log_2 RQ$ complex

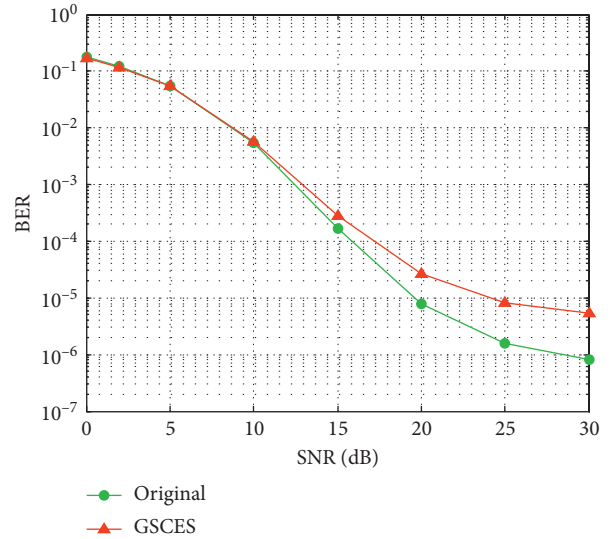


FIGURE 8: The BER performance results.

TABLE 2: Computational complexity comparison of different algorithms.

Algorithm	Number of complex multiplications	Number of complex additions
SLM	$(L^2 RQ/2)\log_2 RQ$	$L^2 RQ \log_2 RQ$
GSCES	$(LRQ/2)\log_2 RQ$	$LRQ \log_2 RQ + L^2 RQ$
GSCES/SLM	$1/L$	$(1/L) + (1/\log_2 RQ)$

multiplications and $RQ \log_2 RQ$ complex additions. The SLM algorithm needs L^2 IFFT transforms to generate L^2 phase sequences, i.e., a total of $(L^2 RQ/2)\log_2 RQ$ complex multiplications and $L^2 RQ \log_2 RQ$ complex additions. For the proposed GSCES algorithm, the L th IFFT transform generates the real and imaginary parts of L candidate sequences.

That is to say, $(LRQ/2)\log_2 RQ$ complex multiplications and $LRQ \log_2 RQ$ complex additions are needed. Then, the linear combination of the real and imaginary parts of L candidate sequences is used to generate L^2 candidate sequences, which requires $L^2 RQ$ complex additions.

When the number of the candidate sequence equals to L^2 , the computational complexity of the proposed GSCES algorithm is compared with that of the SLM algorithm as shown in Table 2.

Table 2 shows that when the numbers of candidate sequences are all L^2 , the number of complex multiplication needed by the proposed GSCES algorithm is $1/L$ of that of the SLM algorithm and the number of complex addition is $((1/L) + (1/\log_2 RQ))$ of the SLM algorithm. With the increase of the number of candidate sequences, the ratio decreases continuously. So, the proposed GSCES algorithm expands the number of candidate sequences by using the segmentation method and linear combination transformation. Compared with the SLM algorithm, the computational complexity is greatly reduced and the data can be transmitted more efficiently.

5. Conclusions

Aiming at the shortcomings of the traditional SLM algorithm, the GSCES algorithm is proposed to solve the high PAPR problem of 5G F-OFDM systems. The proposed grid multiscroll chaotic maps instead of the traditional pseudo random sequence are used as random phase sequence vectors, which provide a large number of random sequences with good correlation characteristics, random characteristics, and high security. The proposed random phase sequence vectors can meet the needs of 5G mass connections. The original input signals are divided into real part and imaginary part, which are, respectively, multiplied by the proposed grid multiscroll chaotic sequences. The IFFT transforms are performed, respectively, the PAPR values are calculated by linear superposition, and the minimum PAPR value is selected for transmission. The numerical simulation results show that the proposed GSCES algorithm effectively increases the numbers of candidate sequences, reduces the PAPR values, the redundant information transmission, and the side band information transmission, and improves the transmission efficiency and security of the 5G F-OFDM system. Moreover, the hardware experimental results produce at $2 \times 2 \times 2$ -grid multiscroll chaotic attractor, which further proves the physical realization of the proposed system. The proposed schemes have a broad application prospect in 5G multicarrier modulation technology.

Abbreviations

PAPR:	Peak-to-average power ratio
F-OFDM:	Filtered-orthogonal frequency division multiplexing
SLM:	Selective mapping
GSCES:	Grid scroll chaotic extended sequence
SI:	Side information
CP:	Cycle prefix
CCDF:	Cumulative distribution function
BER:	Bit error rate
AWGN:	Additive white Gaussian noise
SNR:	Signal-to-noise ratio
SDU:	Selected data utilization.

Data Availability

The data used to support the findings of this study are included within the article.

Conflicts of Interest

The authors declare that they have no conflicts of interest.

Authors' Contributions

Yingjie Ma wrote the majority of the text and performed the design and implementation of the algorithm. Ya Li performed the design and implementation of the hardware circuit. Geng Zhao performed the numerical simulation experiment. Ping Zeng and Yatao Yang contributed text to earlier versions of the manuscript and commented on and

approved the manuscript. All authors read and approved the final manuscript.

Acknowledgments

This work is supported by the National Natural Science Foundation of China (no. 61772047), Science and Technology Program of Guangzhou, China (201904010302), and Doctoral Scientific Research Startup Fund of Guangdong Polytechnic Normal University (991512204).

References

- [1] C. Jayawickrama, S. Kumar, and H. Song, "Novel wideband chaotic approach LNA with microcontroller compatibility for 5G wireless secure communication," *Microwave and Optical Technology Letters*, vol. 60, no. 2, pp. 488–494, 2018.
- [2] G. U. Maheswari, A. Govindasamy, and S. J. Thiruvengadam, "Performance analysis of filter bank multicarrier system with non-linear high power amplifiers for 5G wireless networks," *IET Signal Processing*, vol. 11, no. 1, pp. 66–72, 2017.
- [3] N.-T. Le, D. Jayalath, and J. Coetsee, "Spectral-efficient resource allocation for mixed services in OFDMA-based 5G heterogeneous networks," *Transactions on Emerging Telecommunications Technologies*, vol. 29, no. 1, p. e3267, 2018.
- [4] A. Kheli, L. Talbi, D. Slimani, and J. LeBel, "MRC SC-FDMA scheme performance evaluation based on measurements at 30 GHz for 5G communications," *Physical Communication*, vol. 25, pp. 462–468, 2017.
- [5] S. Wang, J. S. Thompson, and P. M. Grant, "Closed-form expressions for ICI/ISI in filtered OFDM systems for asynchronous 5G uplink," *IEEE Transactions on Communications*, vol. 65, no. 11, pp. 4886–4898, 2017.
- [6] P. D. Pamungkasari and Y. Sanada, "Shift estimation with delayed correlation cyclic-selective mapping (Cyclic-SLM) PAPR reduction in OFDM system," *Wireless Personal Communications*, vol. 91, no. 2, pp. 739–753, 2016.
- [7] Y. Xiao, Z. Wang, J. Cao et al., "Time-frequency domain encryption with SLM scheme for physical-layer security in an OFDM-PON system," *Journal of Optical Communications and Networking*, vol. 10, no. 1, pp. 46–51, 2018.
- [8] W.-W. Hu, "SLM-based ACO-OFDM VLC system with low-complexity minimum amplitude difference decoder," *Electronics Letters*, vol. 54, no. 3, pp. 144–146, 2018.
- [9] S. Vaiyamalai, S. Mahesula, and S. K. S. Dhamodharan, "PAPR reduction in SLM-OFDM system using lehmer sequence without explicit side information," *Wireless Personal Communications*, vol. 97, no. 4, pp. 5527–5542, 2017.
- [10] S. A. Adegbite, S. McMeeke, and B. G. Stewart, "Computational efficient SLM-OFDM receiver for time-invariant indoor fading channel," *Wireless Personal Communications*, vol. 97, no. 1, pp. 661–674, 2017.
- [11] V. Sudha, M. Syamkumar, and D. S. Kumar, "A low complexity modified SLM and companding based PAPR reduction in localized OFDMA," *Wireless Personal Communications*, vol. 96, no. 2, pp. 3207–3226, 2017.
- [12] J.-g. Yuan, Q. Shen, J.-x. Wang, Y. Wang, J.-z. Lin, and Y. Pang, "A novel improved SLM scheme of the PAPR reduction technology in CO-OFDM systems," *Optoelectronics Letters*, vol. 13, no. 2, pp. 138–142, 2017.
- [13] M. Fallahzadeh and M. Ferdosizadeh, "Blind SLM for PAPR reduction of Alamouti DSFBC systems," *IET Communications*, vol. 11, no. 3, pp. 451–457, 2017.

Research Article

Dimensionality Reduction Reconstitution for Extreme Multistability in Memristor-Based Colpitts System

Yunzhen Zhang,¹ Zhong Liu ,¹ Mo Chen ,² Huagan Wu ,²
Shengyao Chen,¹ and Bocheng Bao ²

¹Department of Electronic Engineering, Nanjing University of Science and Technology, Nanjing 210094, China

²School of Information Science and Engineering, Changzhou University, Changzhou 213164, China

Correspondence should be addressed to Bocheng Bao; baobc@cczu.edu.cn

Received 28 May 2019; Revised 30 June 2019; Accepted 17 July 2019; Published 26 November 2019

Guest Editor: Lazaros Moysis

Copyright © 2019 Yunzhen Zhang et al. This is an open access article distributed under the Creative Commons Attribution License, which permits unrestricted use, distribution, and reproduction in any medium, provided the original work is properly cited.

In this paper, a four-dimensional (4-D) memristor-based Colpitts system is reaped by employing an ideal memristor to substitute the exponential nonlinear term of original three-dimensional (3-D) Colpitts oscillator model, from which the initials-dependent extreme multistability is exhibited by phase portraits and local basins of attraction. To explore dynamical mechanism, an equivalent 3-D dimensionality reduction model is built using the state variable mapping (SVM) method, which allows the implicit initials of the 4-D memristor-based Colpitts system to be changed into the corresponding explicitly initials-related system parameters of the 3-D dimensionality reduction model. The initials-related equilibria of the 3-D dimensionality reduction model are derived and their initials-related stabilities are discussed, upon which the dynamical mechanism is quantitatively explored. Furthermore, the initials-dependent extreme multistability is depicted by two-parameter plots and the coexistence of infinitely many attractors is demonstrated by phase portraits, which is confirmed by PSIM circuit simulations based on a physical circuit.

1. Introduction

Chua's circuit [1] and Colpitts oscillator [2] are two important physical circuits used for generating chaos. In the Chua's circuit, the unique nonlinear negative resistor is generally realized based on operational amplifier [3], which makes the oscillating frequency limited. By contrast, in the Colpitts oscillator, the nonlinear circuit element is implemented by a bipolar junction transistor [2], which allows the oscillating frequency to be adjusted from a few hertz up to the microwave region (gigahertz), depending on the technology. Due to the natural nonlinearities [4], memristors can be introduced into some existing circuits or systems to easily achieve chaotic oscillations. In the past few years, various memristor-based nonlinear oscillating circuits and systems were proposed, such as memristive Hindmarsh-Rose neuron model [5], memristive cellular nonlinear/neural network [6], memristive band-pass filter circuit [7], memristive spiking and bursting neuron circuit [8], memristive jerk circuit [9], memristive hypogenetic jerk system [10], memristive hyper-jerk system [11], memristive Twin-T oscillator [12],

memristive Chua's circuit [13], memristive canonical Chua's circuit [14], memristive multi-scroll Chua's circuit [15], and memristive Chua's hyperchaotic circuit [16]. However, relatively little attention has been received on the memristor-based Colpitts oscillator [17–19]. In addition, the memristive Colpitts oscillator implemented by replacing the bipolar junction transistor with memristor has not yet been reported. Because of the nanosized property, memristor is characterized by small size and low power consumption, leading to the fact that memristor-based Colpitts oscillator could have a good application prospect under some certain conditions.

The careful dynamical analyses of these constructed memristive systems show that the memristor initials do play a crucial role in dynamical characteristics of these systems [20, 21]. Particularly, memristive systems based on ideal memristors can produce the extreme multistability phenomenon of coexisting infinitely many attractors [22, 23]. Such a special phenomenon is commonly triggered in the systems with no equilibrium [24] or infinitely many equilibria [16, 25–28], entirely different from those generated from the offset-boostable flow by introducing an extra periodic

signal [29–31]. In [17], a memristor-based Colpitts chaotic oscillator was proposed by introducing a nonideal extended memristor into original Colpitts oscillator [2]. This memristive system only had unique equilibrium and exhibited the rich parameters-dependent dynamics. Like the reported ideal memristor-based systems, when an ideal memristor is introduced into original Colpitts oscillator, a natural question to ask is whether it will produce extreme multistability. Therefore, it is necessary to seek this special phenomenon in the ideal memristor-based Colpitts system.

The initials-dependent multistability [32, 33], or extreme multistability [34–36], pushes forward an immense influence on the study of dynamical characteristics in many nonlinear systems. Under the fixed system parameters, the solution trajectories of the systems can be represented by diverse stable states with the varied initials. Such a special phenomenon not only renders a nonlinear dynamical circuit or system to supply great flexibility for its potential uses in chaos-based information engineering applications [37], but also leads to new challenges for its control of the existing multiple stable states [32]. One might argue that this special phenomenon can hardly be achieved in practical engineering applications, as it is highly dependent on the initials. Moreover, due to the existence of zero eigenvalue at the equilibrium, it also presents new impediments for the traditional theoretical analysis of dynamical mechanisms. Interestingly enough, these problems can be solved by simplifying the mathematical models using proper state variables or applying reasonable approximation and simplification [38, 39].

Latterly, to solve the abovementioned problem, flux-charge analysis method [13, 14, 22, 23] for the memristor-based dynamical circuits and state variable mapping (SVM) method [11, 40] for the memristor-based dynamical systems were proposed to achieve an equivalent dimensionality reduction model, leading to the fact that the circuit goes from high-order to low-order or the system goes from high-dimensional to low-dimensional. With these methods, the implicit initials in the original circuit or system can be changed into explicitly initials-related circuit/system parameters appearing in the dimensionality reduction model, and multiple stable states can be controlled by changing the initials-related circuit/system parameters [14], upon which the mechanism explanation for initials-dependent dynamics can be realized. Moreover, dimensionality reduction modeling can reduce the complexity of quantitative analyses and numerical simulations, which is of theoretical significance and engineering application value.

The aforementioned analytic strategies have been preliminarily verified in several memristor-based Chua's circuits [13, 14, 22] and memristor-based hyperjerk system [11]. However, for memristor-based Colpitts system, applicability and effectivity of the state variable mapping method still need comprehensive investigations and the concept of dimensionality reduction reconstitution is insistent to be clarified. Enlightened by the above ideas, a novel four-dimensional (4-D) memristor-based Colpitts system is reaped by employing an ideal memristor [24] to substitute the exponential nonlinear term of the original three-dimensional (3-D) Colpitts oscillator model [2, 41]. The proposed memristive Colpitts

system exhibits the initials-dependent extreme multistability. To focus on the revelation and reconstitution of this special phenomenon, an equivalent 3-D dimensionality reduction model is obtained using the SVM method reported in [11] and several determined isolated equilibria are thereby yielded. Consequently, the implicit initials of the 4-D memristor-based Colpitts system are transformed into the explicitly initials-related system parameters of the 3-D dimensionality reduction model. Meanwhile, the initials-dependent extreme multistability in the 4-D memristor-based Colpitts system is reconstituted by the initials-related parameters-dependent dynamics in the dimensionality reduction model through traditional quantitative analyses.

The rest of this paper is organized as follows. In Section 2, a 4-D memristor-based Colpitts system is presented and the initials-dependent extreme multistability is revealed by phase portraits and two-dimensional (2-D) local basins of attraction. Thereafter, the equivalent 3-D dimensionality reduction model for the proposed memristive Colpitts system is built by the SVM method. In Section 3, to explore the dynamical mechanism, the initials-related equilibria of the 3-D dimensionality reduction model are derived and the initials-related stabilities are evaluated quantitatively. Furthermore, the initials-dependent extreme multistability is depicted by two-parameter bifurcation plots and the coexistence of infinitely many attractors is demonstrated by phase portraits. In Section 4, with the circuit implementation of the dimensionality reduction model, PSIM circuit simulations are used to validate the numerical simulations. The conclusion is drawn in Section 5.

2. Memristor-Based Colpitts System and Dimensionality Reduction Modeling

2.1. 4-D Memristor-Based Colpitts System and Initials-Dependent Extreme Multistability. The constructing scheme is adopted through imitating the method narrated in [10]. For the input x and output y , an incoming ideal memristor with an inner state variable φ can be modeled as

$$\begin{aligned} y &= W(\varphi)x \\ \dot{\varphi} &= x \end{aligned} \quad (1a)$$

Inspired by [24], the memductance $W(\varphi)$ chosen here is quadratic in φ , which is characterized by

$$W(\varphi) = \alpha - \beta\varphi^2 \quad (1b)$$

where the parameters α and β are two positive constants. Note that the circuit module of $W(\varphi)$ can be synthesized by referring to [24].

TABLE 1: Attractor types with different initials of system (3).

Initials	Attractor types	Phase portraits
$(10^{-9}, 0, 0, \pm 3.6)$	Asymmetric chaotic double-scroll attractors	Figure 1(a)
$(10^{-9}, 0, 0, \pm 3.3)$	Period-2 limit cycles	Figure 1(b)
$(-1, 2, 0, 2.55)$	Spiral chaotic attractor	Figure 1(c) (red)
$(10^{-9}, 0, 0, 0)$	Symmetric chaotic double-scroll attractor	Figure 1(c) (blue)
$(10^{-9}, -1.5, 0, -2)$	Period-2 limit cycle	Figure 1(d) (red)
$(10^{-9}, 0, 0, -0.8)$	Period-3 limit cycle	Figure 1(d) (blue)
$(-1, 0, 0, -3.4)$	Period-1 limit cycle	Figure 1(e) (red)
$(-1, 0, 0, -3.2)$	Point attractor	Figure 1(e) (blue)
$(-1, 2, 0, 2.2)$	Unbounded orbit	Figure 1(f)

A classic 3-D Colpitts oscillator model with an exponential nonlinear term was reported in [2, 41], which was described as

$$\begin{aligned}\dot{x}_1 &= \frac{g}{Q(1-k)} [x_3 - n(x_2)] \\ \dot{x}_2 &= \frac{g}{Qk} x_3 \\ \dot{x}_3 &= -\frac{Qk(1-k)}{g} (x_1 + x_2) - \frac{1}{Q} x_3\end{aligned}\quad (2a)$$

where Q and g are positive real constants, $k = 0.5$, and the exponential nonlinear term

$$n(x_2) = e^{-x_2} - 1 \quad (2b)$$

is used to characterize the voltage-current relation of the bipolar junction transistor in the Colpitts oscillator. When the parameters appearing in (2a) are set as $Q = 1.415$ and $g = 3.1623$ [2], the 3-D Colpitts oscillator model (2a) and (2b) is chaotic and displays a spiral attractor.

Based on the 3-D Colpitts oscillator model presented in (2a), a novel 4-D memristor-based Colpitts system is reaped by employing the proposed memristor given in (1a) and (1b) to substitute the exponential nonlinear term described in (2b), whose mathematical model is formulated as

$$\begin{aligned}\dot{x}_1 &= ax_3 - aW(x_4)x_2 \\ \dot{x}_2 &= ax_3 \\ \dot{x}_3 &= \frac{-0.5(x_1 + x_2)}{a} - bx_3 \\ \dot{x}_4 &= x_2\end{aligned}\quad (3)$$

where $W(x_4) = \alpha - \beta x_4^2$ and two positive parameters $a = 2g/Q$, $b = 1/Q$ are introduced for simplicity [41]. To focus on the revelation and reconstitution of extreme multistability, the parameters are determined as $a = 5.2$, $b = 0.9$, $\alpha = 0.5$, and $\beta = 0.1$.

The ideal memristor (1a) and (1b) causes system (3) to possess line equilibrium therein, leading to the emergence of complex and sensitive initials-dependent extreme multistability with coexisting infinitely many attractors [22, 23]. To show the intriguing phenomenon, some intuitions about the extreme multistability of system (3) are exhibited by phase portraits, as shown in Table 1 and Figure 1, where the point attractor in Figure 1(e) is marked as five-pointed star. Apparently, a variety of disconnected attractors with different topologies, periodicities, and locations are coined in system (3) under different initials. Particularly, asymmetric chaotic double-scroll attractors (Figure 1(a)), symmetric chaotic double-scroll attractor, and chaotic spiral attractor (Figure 1(c)) can be observed in Figure 1, which are completely different from the chaotic spiral attractor reported in the original 3-D Colpitts oscillator model (2a) and (2b) [2]. It is demonstrated that system (3) has more complex attractor structure.

The phase portraits of coexisting infinitely many attractors in Figure 1 demonstrate that dynamical behaviors of system (3) are extremely depended on their initials. To inspect the dynamical behaviors distributed in the initial planes, 2-D local basins of attraction in different initial planes are drawn, as shown in Figure 2, where only the periodicities of the state variable x_1 are considered and the topologies and locations of the attractors are ignored here. The red regions marked by CH represent chaotic behaviors. The black and blue regions labeled by DE and P0 denote unbounded divergent and stable point behaviors respectively. Whereas the other color regions labeled by P1 ~ P4 stand for periodic behaviors with different periodicities. Therefore, the emergence of extreme multistability is disclosed, indicating the coexistence of infinitely many attractors in the 4-D memristor-based Colpitts system.

In addition, lots of unbounded divergent behaviors can be observed in Figure 2, which is rarely reported in a general memristive chaotic system [14], indicating that the proposed 4-D memristor-based Colpitts system (3) is less robust to the initials.

2.2. Dimensionality Reduction Modeling. To explore dynamical mechanism of the initials-dependent extreme multistability emerged in system (3), an equivalent dimensionality reduction model for system (3) needs to be built [11, 13, 14, 22,

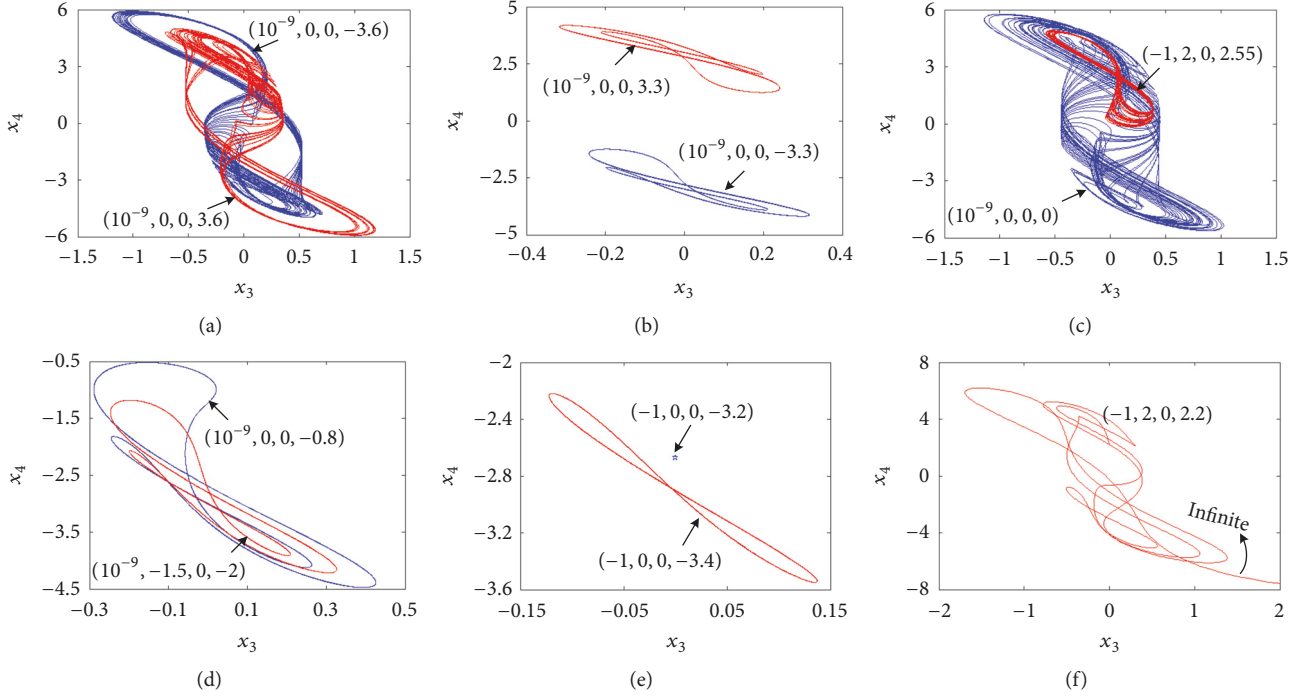


FIGURE 1: Phase portraits of coexisting infinitely many attractors in the x_3 – x_4 plane for different initials $(x_1(0), x_2(0), x_3(0), x_4(0))$. (a) Asymmetric chaotic double-scroll attractors for $(10^{-9}, 0, 0, \pm 3.6)$. (b) Period-2 limit cycles for $(10^{-9}, 0, 0, \pm 3.3)$. (c) Chaotic attractors with different topologies for $(10^{-9}, 0, 0, 0)$ and $(-1, 2, 0, 2.55)$. (d) Period-2 and period-3 limit cycles for $(10^{-9}, -1.5, 0, -2)$ and $(10^{-9}, 0, 0, -0.8)$. (e) Period-1 limit cycle and point attractor for $(-1, 0, 0, -3.2)$ and $(-1, 0, 0, -3.4)$. (f) Unbounded orbit for $(-1, 2, 0, 2.2)$.

23]. Pursuant to the SVM method [11], integrating the four equations of (3) from 0 to τ , one gets

$$\begin{aligned} x_1(\tau) - \delta_1 &= -a\alpha X_2 + aX_3 + a\beta \int_0^\tau x_4^2(\xi) x_2(\xi) d\xi \\ x_2(\tau) - \delta_2 &= aX_3 \\ x_3(\tau) - \delta_3 &= \frac{-0.5(X_1 + X_2)}{a} - bX_3 \\ x_4(\tau) - \delta_4 &= X_2 \end{aligned} \quad (4)$$

where

$$\begin{aligned} X_i(\tau) &= \int_0^\tau x_i(\xi) d\xi, \\ \delta_i &= x_i(0) \\ (i &= 1, \dots, 4) \end{aligned} \quad (5)$$

Recalling the fourth equation of (3), there exists $dx_4(\xi) = x_2(\xi)d\xi$. Thus the integral term in (4) is signified as

$$\begin{aligned} \int_0^\tau x_4^2(\xi) x_2(\xi) d\xi &= \int_0^\tau x_4^2(\xi) dx_4(\xi) = \frac{x_4^3(\tau)}{3} - \frac{\delta_4^3}{3} \\ &= \frac{(X_2 + \delta_4)^3}{3} - \frac{\delta_4^3}{3} \\ &= \frac{X_2^3}{3} + \delta_4 X_2^2 + \delta_4^2 X_2 \end{aligned} \quad (6)$$

Then system (4) can be rewritten as

$$\begin{aligned} \dot{X}_1 &= -a\alpha X_2 + aX_3 + a\beta \left(\frac{X_2^3}{3} + \delta_4 X_2^2 + \delta_4^2 X_2 \right) + \delta_1 \\ \dot{X}_2 &= aX_3 + \delta_2 \\ \dot{X}_3 &= \frac{-0.5(X_1 + X_2)}{a} - bX_3 + \delta_3 \\ \dot{X}_4 &= X_2 + \delta_4 \end{aligned} \quad (7)$$

From (7), it is not difficult to find that the right-hand sides of the first three equations do not depend on X_4 , i.e., the fourth equation of (7) is independent of the other three equations. Therefore, an equivalent 3-D dimensionality reduction model can be described as

$$\begin{aligned} \dot{X}_1 &= (a\beta\delta_4^2 - a\alpha) X_2 + aX_3 + \frac{a\beta X_2^3}{3} + a\beta\delta_4 X_2^2 + \delta_1 \\ \dot{X}_2 &= aX_3 + \delta_2 \\ \dot{X}_3 &= \frac{-0.5(X_1 + X_2)}{a} - bX_3 + \delta_3 \end{aligned} \quad (8)$$

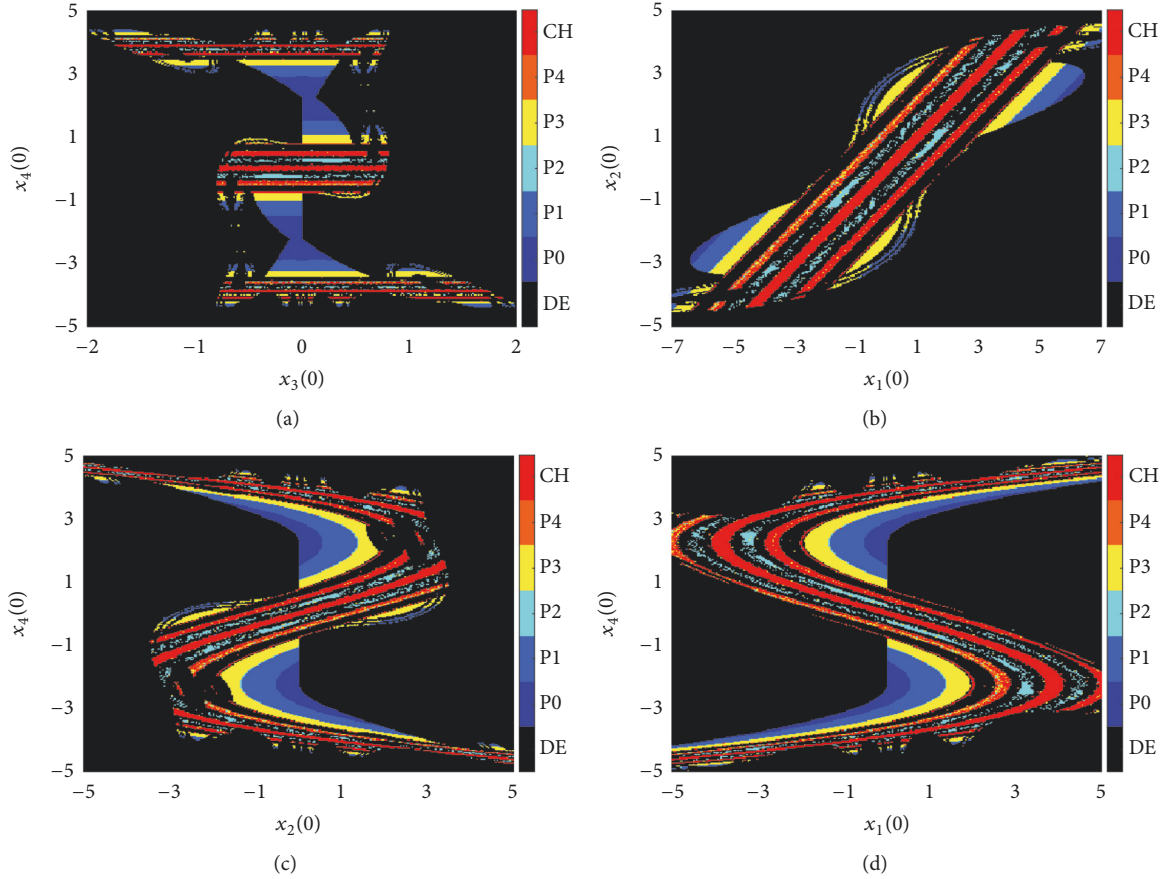


FIGURE 2: Two-dimensional local basins of attraction of system (3) in different initial planes for four sets of the initials $(x_1(0), x_2(0), x_3(0), x_4(0))$. (a) The $x_3(0) - x_4(0)$ initial plane with $x_1(0) = x_2(0) = 0$. (b) The $x_1(0) - x_2(0)$ initial plane with $x_3(0) = x_4(0) = 0$. (c) The $x_2(0) - x_4(0)$ initial plane with $x_2(0) = x_3(0) = 0$. (d) The $x_1(0) - x_4(0)$ initial plane with $x_2(0) = x_3(0) = 0$.

Similar to [11], there are correspondences between the state variables of systems (3) and (8) such that

$$\begin{aligned}
 x_1 &= \dot{X}_1, \\
 x_2 &= aX_3 + \delta_2, \\
 x_3 &= \dot{X}_3, \\
 x_4 &= X_2 + \delta_4
 \end{aligned}
 \tag{9}$$

Based on the relations in (9), the dynamical behaviors in (8) can be transformed back into those in (3).

Noteworthy, the implicit initials $x_i(0)$ of the 4-D memristor-based Colpitts system are mapped as explicitly initials-related system parameters δ_i appearing in the 3-D dimensionality reduction model. What needs illustration is that, under the situation $X_1(0) = X_2(0) = X_3(0) = 0$, system (8) exhibits the completely same dynamical behaviors as the proposed system (3) [11]. To easily distinguish the different system parameters in system (8), we call a, b, α, β as the intrinsic system parameters and $\delta_1, \delta_2, \delta_3, \delta_4$ as the extrinsic initials-related system parameters. It follows that the aforementioned 3-D dimensionality reduction model can be utilized for quantitatively investigating the initials-dependent

dynamics of the 4-D memristor-based Colpitts system by changing the initials-related system parameters δ_i .

System (8) is a 3-D nonlinear system, whose initials can also influence the dynamical behaviors. Similar to [11, 42], under the fixed initials-related system parameters, system (8) only exhibits two kinds of oscillating states. Taking $\delta_1 = 10^{-9}$ and $\delta_2 = \delta_3 = \delta_4 = 0$ as an illustration, a bounded chaotic behavior under the initials $(0, 5, 0)$ and an unbounded behavior under $(-9, 0, 0)$ are coexisted in the $X_1 - X_3$ plane, as shown in Figure 3(a). Furthermore, the local basin of attraction in the $X_1(0) - X_2(0)$ initial plane with $X_3(0) = 0$ is depicted, as shown in Figure 3(b); it can be easily observed that there are only two oscillating states, namely, the bounded chaotic behavior (red) and unbounded divergent behavior (yellow), respectively. Consequently, the 3-D dimensionality reduction model is less sensitive than the 4-D memristor-based Colpitts system to the initials.

3. Dynamical Mechanism Illustrations for Extreme Multistability

3.1. Equilibria and Stabilities Depending on the Initials-Related System Parameters. By setting $\dot{X}_1 = \dot{X}_2 = \dot{X}_3 = 0$ and solving

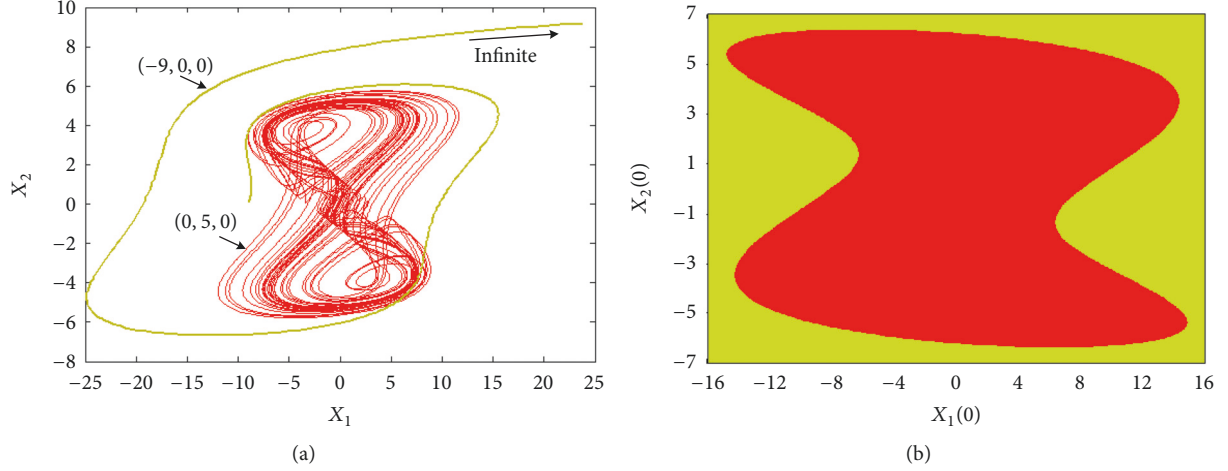


FIGURE 3: Illustrations for the bounded chaotic behavior (red) and unbounded divergent behavior (yellow). (a) Phase portraits under the initials $(0, 5, 0)$ and $(-9, 0, 0)$. (b) Local basin of attraction in the $X_1(0) - X_2(0)$ initial plane with $X_3(0) = 0$.

TABLE 2: The equilibrium of the dimensionality reduction model (8).

Δ	\bar{X}_2	\bar{X}_1	Equilibrium
$\Delta > 0$	$\bar{X}_{2,1}$	$-\bar{X}_{2,1} + 2b\delta_2 + 2a\delta_3$	$S_1 = (-\bar{X}_{2,1} + 2b\delta_2 + 2a\delta_3, \bar{X}_{2,1}, -\delta_2/a)$
$\Delta = 0$	$\bar{X}_{2,1}, -\sqrt[3]{-0.5Q}$	$-\bar{X}_{2,1} + 2b\delta_2 + 2a\delta_3$	$S_{2,1} = (-\bar{X}_{2,1} + 2b\delta_2 + 2a\delta_3, \bar{X}_{2,1}, -\delta_2/a)$
		$\sqrt[3]{-0.5Q} + 2b\delta_2 + 2a\delta_3$	$S_{2,2} = (\sqrt[3]{-0.5Q} + 2b\delta_2 + 2a\delta_3, -\sqrt[3]{-0.5Q}, -\delta_2/a)$
$\Delta < 0$	$\bar{X}_{2,1}, \bar{X}_{2,2}, \bar{X}_{2,3}$	$-\bar{X}_{2,1} + 2b\delta_2 + 2a\delta_3$	$S_{3,1} = (-\bar{X}_{2,1} + 2b\delta_2 + 2a\delta_3, \bar{X}_{2,1}, -\delta_2/a)$
		$-\bar{X}_{2,2} + 2b\delta_2 + 2a\delta_3$	$S_{3,2} = (-\bar{X}_{2,2} + 2b\delta_2 + 2a\delta_3, \bar{X}_{2,2}, -\delta_2/a)$
		$-\bar{X}_{2,3} + 2b\delta_2 + 2a\delta_3$	$S_{3,3} = (-\bar{X}_{2,3} + 2b\delta_2 + 2a\delta_3, \bar{X}_{2,3}, -\delta_2/a)$

for the equilibrium of system (8), one gets

$$S = \left(-\bar{X}_2 + 2b\delta_2 + 2a\delta_3, \bar{X}_2, \frac{-\delta_2}{a} \right) \quad (10)$$

in which \bar{X}_2 is solved by

$$\bar{X}_2^3 + 3\delta_4\bar{X}_2^2 + 3\left(\delta_4^2 - \frac{\alpha}{\beta}\right)\bar{X}_2 + \frac{3(\delta_1 - \delta_2)}{a\beta} = 0 \quad (11)$$

Define P and Q as

$$P = -\frac{3\alpha}{\beta} \quad (12a)$$

$$Q = \frac{3(\delta_1 - \delta_2)}{a\beta} - 3\delta_4\left(\delta_4^2 - \frac{\alpha}{\beta}\right) + 2\delta_4^3 \quad (12b)$$

In pursuance of the classical Cardan discriminant $\Delta = (Q/2)^2 + (P/3)^3$ [14, 43], the roots of (11) are derived as

$$\bar{X}_{2,1} = \sqrt[3]{-0.5Q + \sqrt{\Delta}} + \sqrt[3]{-0.5Q - \sqrt{\Delta}} - \delta_4 \quad (13a)$$

$$\begin{aligned} \bar{X}_{2,2} = 0.5(-1 + j\sqrt{3})\sqrt[3]{-0.5Q + \sqrt{\Delta}} \\ + 0.5(-1 - j\sqrt{3})\sqrt[3]{-0.5Q - \sqrt{\Delta}} - \delta_4 \end{aligned} \quad (13b)$$

$$\begin{aligned} \bar{X}_{2,3} = 0.5(-1 - j\sqrt{3})\sqrt[3]{-0.5Q + \sqrt{\Delta}} \\ + 0.5(-1 + j\sqrt{3})\sqrt[3]{-0.5Q - \sqrt{\Delta}} - \delta_4 \end{aligned} \quad (13c)$$

The detailed breakdowns of the equilibrium S are given in Table 2. With reference to these results, it can be found that system (8) has only one determined equilibrium when $\Delta > 0$ and only two determined equilibria when $\Delta = 0$. In contrast, system (8) has three determined equilibria when $\Delta < 0$. Based on the characteristic polynomial at the determined equilibrium S of system (8), the stability analysis of system (8) can be effectively performed. By the Routh-Hurwitz criterion, if and only if

$$\sqrt{\frac{\alpha}{\beta}} < |\bar{X}_2 + \delta_4| < \sqrt{\frac{(\alpha\beta + 2b)}{a\beta}} \quad (14)$$

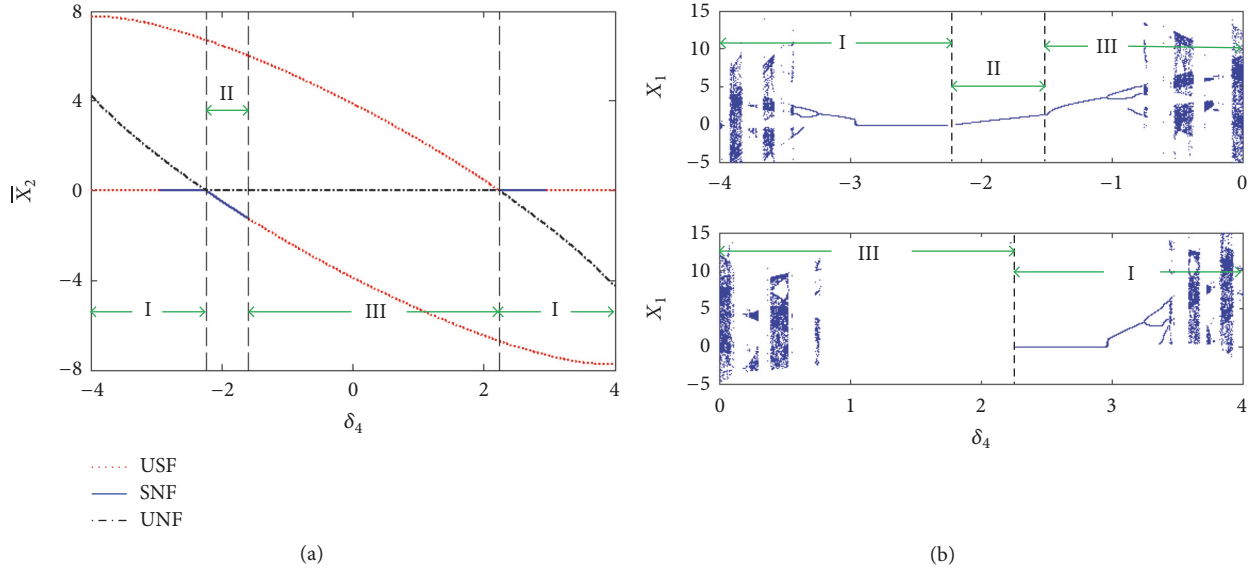


FIGURE 4: Dynamics with the variation of δ_4 at $\delta_1 = 10^{-9}$, $\delta_2 = \delta_3 = 0$. (a) The \bar{X}_2 coordinates and stabilities of the three equilibria. (b) Bifurcation diagram of X_1 , the upper: $\delta_4 \in [-4, 0]$; the lower: $\delta_4 \in [0, 4]$.

is satisfied, the determined equilibrium S is stable and a point attractor will be prevailed in its neighborhood. The intuition of Table 2 and (14) is that, under the fixed intrinsic system parameters, the equilibrium locations and stabilities are decided by the initials-related system parameters δ_i ($i = 1, 2, 3, 4$). Thus, the initials-dependent extreme multistability presented in 4-D memristor-based Colpitts system can be deduced from the evolutions of the determined equilibrium in the 3-D dimensionality reduction model [40, 42].

Take $\delta_1 = 10^{-9}$ and $\delta_2 = \delta_3 = 0$ as an example. When the initials-related system parameter δ_4 varies within $[-4, 4]$, system (8) invariably has three equilibria $S_{3,1}$, $S_{3,2}$, and $S_{3,3}$; the \bar{X}_2 coordinates of the determined equilibria are depicted in Figure 4(a). Stabilities of these three determined equilibria are evaluated by their eigenvalues and denoted with different colored lines, where the red dash, blue solid, and black dash-dot lines denote the unstable saddle-focus (USF), stable node-focus (SNF), and unstable node-focus (UNF), respectively. More specifically, the USF denotes the equilibrium S has one negative real root and a pair of conjugated complex roots with positive real parts; the SNF indicates the equilibrium S is of one negative real root and a pair of conjugated complex roots with negative real parts; the UNF represents the equilibrium S has one positive real root and a pair of conjugated complex roots with negative real parts. The corresponding bifurcation diagram of the state variable X_1 is presented in Figure 4(b), in which $[X_1(0), X_2(0), X_3(0)] = [0, 0, 0]$ are determined; the upper is the bifurcation diagram such that δ_4 varies from -4 to 0 , and the lower is bifurcation diagram such that δ_4 varies from 0 to 4 . It can be seen that the representing dynamics in Figure 4(b) matches with the stabilities of three determined equilibria stated in Figure 4(a).

Since the trajectory of system (8) starts from the original point, its evolution route is mainly elicited by the stability of the equilibrium neighboring to the original point and

somewhat affected by the other equilibria. The bifurcation behaviors are symmetric for the negative and positive δ_4 in the region I, but are asymmetric in the regions II and III. More narrowly, in the region I, when δ_4 varies within $[-4, -2.9488]$, the three equilibria $S_{3,1}$, $S_{3,2}$, and $S_{3,3}$ are all unstable, such that the system orbit may be randomly pushed toward one of these three unstable equilibria. And system (8) starts from the chaotic state and goes into the periodic state via reverse period-doubling bifurcation route. In the region $[-2.9488, -2.2592]$ of I and region II, $S_{3,2}$ becomes a stable equilibrium, $S_{3,1}$ and $S_{3,3}$ are still unstable equilibria. The dynamical behaviors of system (8) are mainly determined by the stable equilibrium $S_{3,2}$, leading to the occurrence of point attractors. In the region III, the three equilibria are all unstable and the system orbit will randomly push toward one of these unstable equilibria, resulting in the generation of limit cycle, chaotic attractor, or unbounded orbit. In the region $[2.2592, 4]$, system (8) displays the almost symmetric dynamical behaviors as those in $[-4, -2.2592]$. Accordingly, the stability distributions of these three determined equilibria related to the initials-related system parameter δ_4 lead to the emergence of complex dynamical behaviors in system (8).

3.2. Extreme Multistability Reconstitution. Observed from Figure 4(b), we know that system (8) can display rich dynamical behaviors hinging on the initials-related system parameters δ_1 , δ_2 , δ_3 , and δ_4 . For intuitively manifesting the coexistence of infinitely many attractors, two-parameter bifurcation plots in different initials-related parameter planes are plotted, as shown in Figure 5. Here the two-parameter bifurcation plots are depicted by examining the periodicities of the state variable X_1 , which are different from the parameter-space plots given in [44]. Similar to the color regions shown in Figure 2, the red region labeled by CH represents chaos, the black region by DE indicates

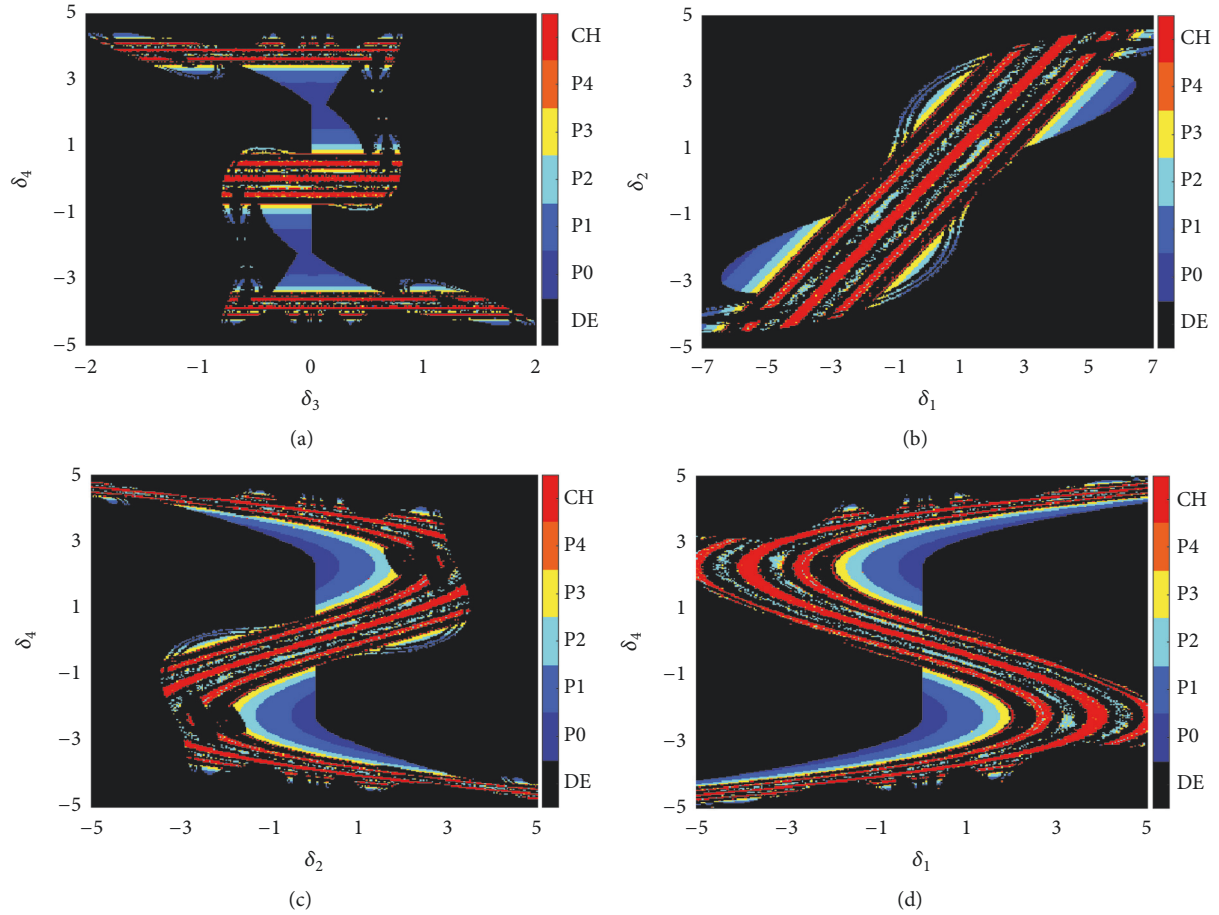


FIGURE 5: Two-parameter bifurcation plots depicted by the periodicities of the state variable X_1 in different initials-related parameter planes for four sets of the initials-related system parameters $(\delta_1, \delta_2, \delta_3, \delta_4)$. (a) Bifurcation plot in the $\delta_3 - \delta_4$ plane with $\delta_1 = \delta_2 = 0$. (b) Bifurcation plot in the $\delta_1 - \delta_2$ plane with $\delta_3 = \delta_4 = 0$. (c) Bifurcation plot in the $\delta_2 - \delta_4$ plane with $\delta_1 = \delta_3 = 0$. (d) Bifurcation plot in the $\delta_1 - \delta_4$ plane with $\delta_2 = \delta_3 = 0$.

divergence, the blue region by P0 denotes stable point, and the other color regions by P1 ~ P4 stand for periodic limit cycles with different periodicities. Comparing the numerical results in Figure 5 with those in Figure 2, the similarity of dynamical behaviors can be observed and the fact that the 3-D dimensionality reduction model can be utilized for quantitatively investigating the initials-dependent dynamics of the 4-D memristor-based Colpitts system by changing the initials-related system parameters is further validated. As the original state variables in the system (3) are the derivatives of the new state variables in system (8) and the computational errors always exist in numerical simulations [45], there are some slight differences between the numerical results in Figures 2 and 5. Therefore, it can be concluded that the 3-D dimensionality reduction model is the equivalent representation of the 4-D memristor-based Colpitts system.

When the initials-related system parameters $\delta_1 = \delta_2 = 0$, the coexistence of infinitely many attractors in the $\delta_3 - \delta_4$ parameter plane can be observed in Figure 5(a). In the regions $[-5, -3]$ and $[3, 5]$ of δ_4 , the system can generate asymmetric chaotic double-scroll attractors. In contrast, the intuition of the region $[-1, 1]$ of δ_4 is that the system can

generate symmetric chaotic double-scroll attractors. Furthermore, when $\delta_3 = \delta_4 = 0$, $\delta_1 = \delta_3 = 0$, and $\delta_2 = \delta_3 = 0$, Figures 5(b), 5(c), and 5(d) reveal the coexistence of infinitely many attractors in different initials-related system parameter planes, respectively, and the emerged dynamical distributions are completely different from those shown in Figure 5(a).

Corresponding to the part of different color areas in Figure 5, different types of coexisting attractors are listed in Table 3. Automatically, referring to Figure 1, for eleven sets of different initials-related system parameters $(\delta_1, \delta_2, \delta_3, \delta_4)$ in different color areas of Figure 5, the phase portraits of coexisting attractors in the $X_1 - X_2$ plane are numerically simulated, as displayed in Figure 6, where the point attractor in Figure 6(e) is marked as five-pointed star homogeneously. Obviously, Figure 6 shows exactly the same dynamical characteristics as Figure 1. It can be seen that many different kinds of disconnected attractors, such as chaotic attractors with different topologies, limit cycles with different topologies and periodicities, stable point, and unbounded orbit, can be observed in system (8). As a result, the initials-related parameters-dependent dynamics featured by Figure 6 intuitively verify the initials-dependent extreme

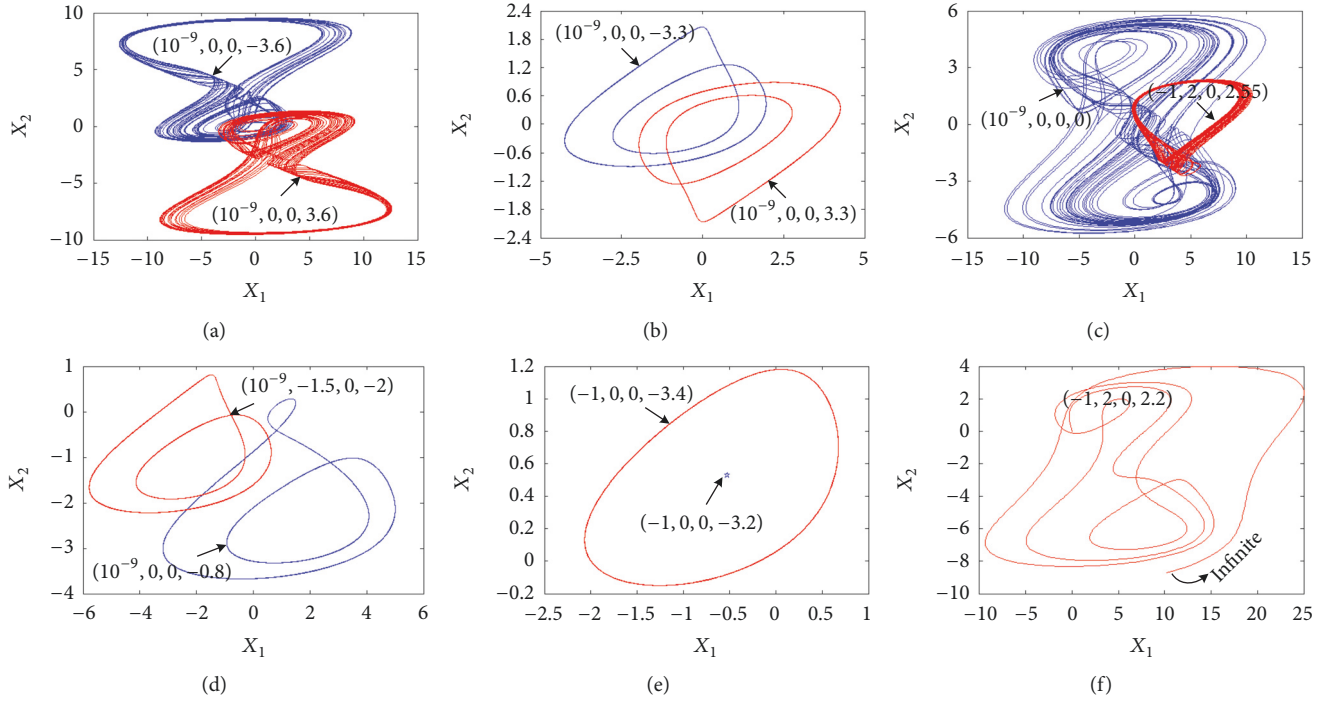


FIGURE 6: MATLAB simulated phase portraits of coexisting infinitely many attractors in the X_1 - X_2 plane for different initial-related system parameters $(\delta_1, \delta_2, \delta_3, \delta_4)$. (a) Upper- and lower-asymmetric chaotic double-scroll attractors. (b) Upper- and lower-period-2 limit cycles. (c) Chaotic attractor with different topologies. (d) Period-2 and period-3 limit cycles. (e) Period-1 limit cycle and point attractor. (f) Unbounded orbit.

multistability in the proposed 4-D memristor-based Colpitts system.

4. PSIM Circuit Simulations

The 3-D dimensionality reduction model described by (8) is equivalently implemented in an analog circuit form, as manifested in Figure 7, where the gains of two multipliers M_1 and M_2 are set as 1. According to basic circuit theory, the circuit state equations are formulated in a general form as

$$\begin{aligned} RC\dot{v}_1 &= (\alpha\beta\delta_4^2 - \alpha\alpha)v_2 + av_3 + \frac{a\beta v_2^3}{3} + \alpha\beta\delta_4 v_2^2 + \delta_1 \\ RC\dot{v}_2 &= av_3 + \delta_2 \\ RC\dot{v}_3 &= \frac{-0.5(v_1 + v_2)}{a} - bv_3 + \delta_3 \end{aligned} \quad (15)$$

where v_1 , v_2 , and v_3 represent the state variables and RC is the integrating time constant. The initial-related system parameters δ_1 , δ_2 , δ_3 , and δ_4 are implemented by additional DC voltage sources or directly linking to the ground. Note that the R_6 in Figure 7 is only a negative feedback resistor to ensure the dissipativity of the physical circuit without self-excited oscillation, which is used to implement the self-feedback term in Equation (15). More details about the circuit design principle can refer to the operational amplifier stability in [46, 47].

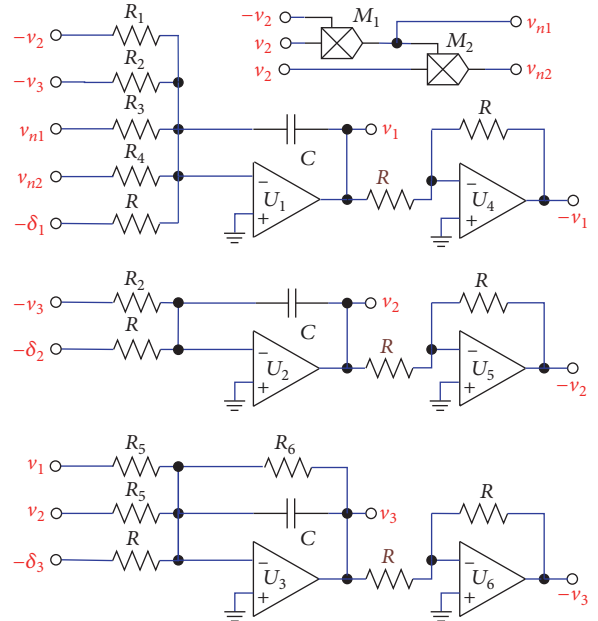


FIGURE 7: Physical circuit implementing the 3-D dimensionality reduction model (8).

To better confirm the extreme multistability generated from the equivalent circuit in Figure 7, PSIM circuit simulations are considered to confirm the phase portraits of coexisting attractors given in Figure 6. The circuit parameters

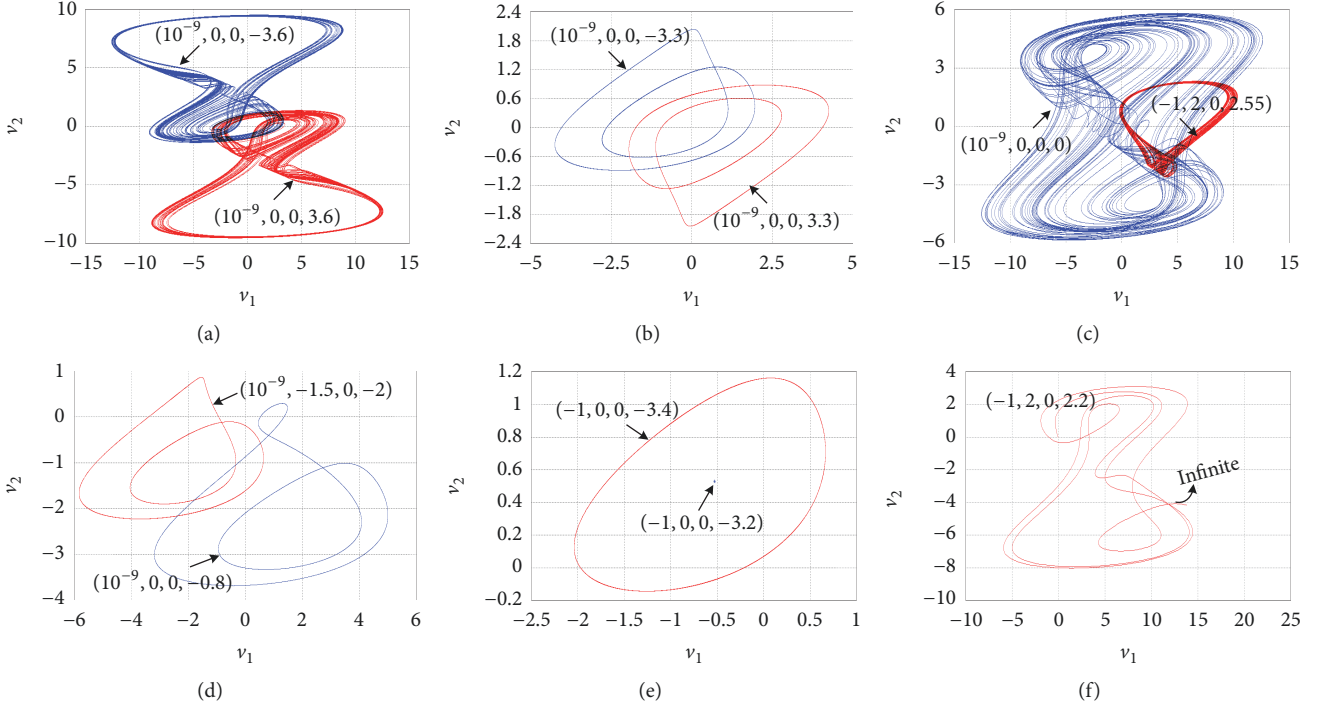


FIGURE 8: PSIM simulated phase portraits of coexisting infinitely many attractors in the $v_1 - v_2$ plane for different initial-related system parameters $(\delta_1, \delta_2, \delta_3, \delta_4)$. (a) Upper- and lower-asymmetric chaotic double-scroll attractors. (b) Upper- and lower-period-2 limit cycles. (c) Chaotic attractor with different topologies. (d) Period-2 and period-3 limit cycles. (e) Period-1 limit cycle and point attractor. (f) Unbounded orbit.

TABLE 3: Different color regions and the coexisting attractor types.

Colors in Figure 5	Coexisting attractor types	Examples in Figure 6
Red	Upper- and lower-asymmetric chaotic double-scroll attractors	Figure 6(a)
Cyan	Upper- and lower-period-2 limit cycles	Figure 6(b)
Red	Symmetric chaotic double-scroll attractor and chaotic spiral attractor	Figure 6(c)
Cyan and yellow	Period-2 and period-3 limit cycles	Figure 6(d)
Cadet blue and blue	Period-1 limit cycle and point attractor	Figure 6(e)
Black	Unbounded orbit	Figure 6(f)

shown in Figure 7 are taken as $R = 10 \text{ k}\Omega$, $R_1 = R/(a\beta\delta_4^2 - a\alpha)$, $R_2 = R/a = 1.9231 \text{ k}\Omega$, $R_3 = R/a\beta\delta_4$, $R_4 = 3R/a\beta = 57.6923 \text{ k}\Omega$, $R_5 = 2aR = 104 \text{ k}\Omega$, $R_6 = R/b = 11.1111 \text{ k}\Omega$, and $C = 100 \text{ nF}$. The initials $[v_1(0), v_2(0), v_3(0)]$ are assigned as $(0 \text{ V}, 0 \text{ V}, 0 \text{ V})$ and the initial-related system parameters $(\delta_1, \delta_2, \delta_3, \delta_4)$ are assigned as the same values by referring to those in Figure 6. PSIM intercepted phase plane plots in the $v_1 - v_2$ plane are shown in Figure 8. Ignoring the computational errors in PSIM simulations, PSIM simulated results in Figure 8 verify the complex phenomenon revealed in Figure 6 and illustrate that extreme multistability does exist in the proposed 4-D memristor-based Colpitts system. What needs to be specified is that the initials of the 4-D memristor-based Colpitts system are in the explicit form in the physical circuit of the 3-D dimensionality reduction model described by (8), which can be used to easily achieve the controllable strategy for extreme

multistability in the 4-D memristor-based Colpitts system [14, 23].

5. Conclusion

In this paper, a dimensionality reduction reconstitution scheme for extreme multistability in memristor-based Colpitts system was introduced. By employing an ideal memristor to substitute the exponential nonlinear term of original 3-D Colpitts oscillator model, a novel 4-D memristor-based Colpitts system was obtained. The initials-dependent extreme multistability of the proposed system was exhibited via phase portraits and local basins of attraction. To explore dynamical mechanism, an equivalent 3-D dimensionality reduction model was constructed using SVM method. As a consequence, the implicit initials of the 4-D memristor-based

Colpitts system were transformed into the explicitly initial-related system parameters of the 3-D dimensionality reduction model. Meanwhile, the dynamical mechanism was quantitatively explored by deriving the initial-related equilibria and discussing the equilibrium stabilities in the 3-D dimensionality reduction model. Furthermore, the initial-dependent extreme multistability was verified by two-parameter bifurcation plots and the coexistence of infinitely many attractors was demonstrated by phase portraits and confirmed by PSIM circuit simulations based on a physical circuit. To sum up, this work has multiple advantages: (1) the proposed 4-D memristor-based Colpitts system has great practical importance, as it has much smaller size, lower power consumption, and more complex attractor structure; (2) the dimensionality reduction model greatly reduces the computational overhead, as the system goes from the 4-D to 3-D; (3) the traditional quantitative analyses can be used for exploring the extreme multistability phenomenon, because the implicit initials of the 4-D memristor-based Colpitts system are transformed into the explicitly initial-related system parameters of the 3-D dimensionality reduction model; (4) the physical control and mechanism explanation for extreme multistability are realized through dimensionality reduction reconstitution.

Data Availability

The data used to support the findings of this study are available from the corresponding author upon request.

Conflicts of Interest

The authors declare that they have no conflicts of interest.

Acknowledgments

This research issue was supported by the grants from the National Natural Science Foundations of China under Grant Nos. 61671245, 51777016, 51607013, and 61601062.

References

- [1] E. Bilotta, P. Pantano, and F. Stranges, "A gallery of chua attractors: part i," *International Journal of Bifurcation and Chaos*, vol. 17, no. 01, pp. 1–60, 2011.
- [2] G. M. Maggio, O. De Feo, and M. P. Kennedy, "Nonlinear analysis of the Colpitts oscillator and applications to design," *IEEE Transactions on Circuits and Systems I: Fundamental Theory and Applications*, vol. 46, no. 9, pp. 1118–1130, 1999.
- [3] B. C. Bao, Q. D. Li, N. Wang, and Q. Xu, "Multistability in Chua's circuit with two stable node-foci," *Chaos: An Interdisciplinary Journal of Nonlinear Science*, vol. 26, no. 4, Article ID 043111, 2016.
- [4] L. O. Chua, "The fourth element," *Proceedings of the IEEE*, vol. 100, no. 6, pp. 1920–1927, 2012.
- [5] H. Bao, A. H. Hu, W. B. Liu, and B. C. Bao, "Hidden bursting firings and bifurcation mechanisms in memristive neuron model with threshold electromagnetic induction," *IEEE Transactions on Neural Networks and Learning Systems*, 2019.
- [6] S. Duan, X. Hu, Z. Dong, L. Wang, and P. Mazumder, "Memristor-based cellular nonlinear/neural network: design, analysis, and applications," *IEEE Transactions on Neural Networks and Learning Systems*, vol. 26, no. 6, pp. 1202–1213, 2015.
- [7] B. Bao, T. Jiang, Q. Xu, M. Chen, H. Wu, and Y. Hu, "Coexisting infinitely many attractors in active band-pass filter-based memristive circuit," *Nonlinear Dynamics*, vol. 86, no. 3, pp. 1711–1723, 2016.
- [8] Y. Babacan, F. Kaçar, and K. Gürkan, "A spiking and bursting neuron circuit based on memristor," *Neurocomputing*, vol. 203, pp. 86–91, 2016.
- [9] J. Kengne, A. N. Negou, and D. Tchiotso, "Antimonotonicity, chaos and multiple attractors in a novel autonomous memristor-based jerk circuit," *Nonlinear Dynamics*, vol. 88, no. 4, pp. 2589–2608, 2017.
- [10] H. Bao, N. Wang, B. Bao, M. Chen, P. Jin, and G. Wang, "Initial condition-dependent dynamics and transient period in memristor-based hypogenetic jerk system with four line equilibria," *Communications in Nonlinear Science and Numerical Simulation*, vol. 57, pp. 264–275, 2018.
- [11] M. Chen, Y. Feng, B. C. Bao, Y. J. Yu, H. G. Wu, and Q. Xu, "State variable mapping method for studying initial-dependent dynamics in memristive hyper-jerk system with line equilibrium," *Chaos, Solitons & Fractals*, vol. 115, pp. 313–324, 2018.
- [12] L. Zhou, C. Wang, X. Zhang, and W. Yao, "Various attractors, coexisting attractors and antimonotonicity in a simple fourth-order memristive Twin-T Oscillator," *International Journal of Bifurcation and Chaos*, vol. 28, no. 4, Article ID 1850050, 18 pages, 2018.
- [13] M. Chen, M. Sun, H. Bao, Y. Hu, and B. Bao, "Flux-charge analysis of two-memristor-based chua's circuit: dimensionality decreasing model for detecting extreme multistability," *IEEE Transactions on Industrial Electronics*, pp. 1–1, 2019.
- [14] H. Bao, T. Jiang, K. Chu, M. Chen, Q. Xu, and B. Bao, "Memristor-based canonical chua's circuit: extreme multistability in voltage-current domain and its controllability in flux-charge domain," *Complexity*, vol. 2018, Article ID 5935637, 13 pages, 2018.
- [15] C. Wang, X. Liu, and H. Xia, "Multi-piecewise quadratic nonlinearity memristor and its 2N-scroll and 2N + 1-scroll chaotic attractors system," *Chaos: An Interdisciplinary Journal of Nonlinear Science*, vol. 27, no. 3, Article ID 033114, 2017.
- [16] B. Bao, T. Jiang, G. Wang, P. Jin, H. Bao, and M. Chen, "Two-memristor-based Chua's hyperchaotic circuit with plane equilibrium and its extreme multistability," *Nonlinear Dynamics*, vol. 89, no. 2, pp. 1157–1171, 2017.
- [17] L. Lu, C. D. Li, Z. C. Zhao, B. C. Bao, and Q. Xu, "Colpitts chaotic oscillator coupling with a generalized memristor," *Mathematical Problems in Engineering*, vol. 2015, Article ID 249102, 9 pages, 2015.
- [18] H. M. Deng and D. P. Wang, "A memristor-based Colpitts like oscillator," in *Proceedings of the International Conference on Information Engineering and Communications Technology*, pp. 252–257, Shanghai, China, 2016.
- [19] H. Deng and D. Wang, "Circuit simulation and physical implementation for a memristor-based colpitts oscillator," *AIP Advances*, vol. 7, no. 3, Article ID 035118, 2017.
- [20] H. G. Wu, Y. Ye, B. C. Bao, M. Chen, and Q. Xu, "Memristor initial boosting behaviors in a two-memristor-based hyperchaotic system," *Chaos, Solitons & Fractals*, vol. 121, pp. 178–185, 2019.

- [21] B.-C. Bao, Q. Xu, H. Bao, and M. Chen, "Extreme multistability in a memristive circuit," *IEEE Electronics Letters*, vol. 52, no. 12, pp. 1008–1010, 2016.
- [22] M. Chen, B. Bao, T. Jiang et al., "Flux-charge analysis of initial state-dependent dynamical behaviors of a memristor emulator-based Chua's circuit," *International Journal of Bifurcation and Chaos*, vol. 28, no. 10, Article ID 1850120, 17 pages, 2018.
- [23] M. Chen, M. Sun, B. Bao, H. Wu, Q. Xu, and J. Wang, "Controlling extreme multistability of memristor emulator-based dynamical circuit in flux—charge domain," *Nonlinear Dynamics*, vol. 91, no. 2, pp. 1395–1412, 2018.
- [24] B. C. Bao, H. Bao, N. Wang, M. Chen, and Q. Xu, "Hidden extreme multistability in memristive hyperchaotic system," *Chaos, Solitons & Fractals*, vol. 94, pp. 102–111, 2017.
- [25] F. Yuan, G. Wang, and X. Wang, "Extreme multistability in a memristor-based multi-scroll hyper-chaotic system," *Chaos: An Interdisciplinary Journal of Nonlinear Science*, vol. 26, no. 7, Article ID 073107, 2016.
- [26] L. Zhou, C. Wang, and L. Zhou, "Generating four-wing hyperchaotic attractor and two-wing, three-wing, and four-wing chaotic attractors in 4d memristive system," *International Journal of Bifurcation and Chaos*, vol. 27, no. 2, Article ID 1750027, 2017.
- [27] C. Li, F. Min, Q. Jin, and H. Ma, "Extreme multistability analysis of memristor-based chaotic system and its application in image decryption," *AIP Advances*, vol. 7, no. 12, Article ID 125204, 2017.
- [28] Z. T. Njitacke, J. Kengne, R. Wafo Tapche, and F. B. Pelap, "Uncertain destination dynamics of a novel memristive 4D autonomous system," *Chaos, Solitons & Fractals*, vol. 107, pp. 177–185, 2018.
- [29] C. Li, W. Joo-Chen Thio, J. C. Sprott, H. H. Iu, and Y. Xu, "Constructing infinitely many attractors in a programmable chaotic circuit," *IEEE Access*, vol. 6, pp. 29003–29012, 2018.
- [30] C. Li, J. C. Sprott, and Y. Mei, "An infinite 2-D lattice of strange attractors," *Nonlinear Dynamics*, vol. 89, no. 4, pp. 2629–2639, 2017.
- [31] C. Li and J. C. Sprott, "An infinite 3-D quasiperiodic lattice of chaotic attractors," *Physics Letters A*, vol. 382, no. 8, pp. 581–587, 2018.
- [32] A. N. Pisarchik and U. Feudel, "Control of multistability," *Physics Reports*, vol. 540, no. 4, pp. 167–218, 2014.
- [33] A. T. Azar, N. M. Adele, T. Alain, R. Kengne, and F. H. Bertrand, "Multistability analysis and function projective synchronization in relay coupled oscillators," *Complexity*, vol. 2018, Article ID 3286070, 12 pages, 2018.
- [34] S. Jafari, A. Ahmadi, S. Panahi, and K. Rajagopal, "Extreme multi-stability: When imperfection changes quality," *Chaos, Solitons & Fractals*, vol. 108, pp. 182–186, 2018.
- [35] M. S. Patel, U. Patel, A. Sen et al., "Experimental observation of extreme multistability in an electronic system of two coupled Rössler oscillators," *Physical Review E: Statistical, Nonlinear, and Soft Matter Physics*, vol. 89, no. 2, Article ID 022918, 2014.
- [36] S. Jafari, A. Ahmadi, A. J. M. Khalaf, H. R. Abdolmohammadi, V.-T. Pham, and F. E. Alsaadi, "A new hidden chaotic attractor with extreme multi-stability," *AEÜ - International Journal of Electronics and Communications*, vol. 89, pp. 131–135, 2018.
- [37] A. Ngo Mouelas, T. Fozin Fozin, R. Kengne, J. Kengne, H. B. Fotsin, and B. Z. Essimbi, "Extremely rich dynamical behaviors in a simple nonautonomous Jerk system with generalized nonlinearity: hyperchaos, intermittency, offset-boosting and multistability," *International Journal of Dynamics and Control*, 2019.
- [38] B. Bao, H. Leung, and Z. Liu, "Is memristor a dynamic element?" *IEEE Electronics Letters*, vol. 49, no. 24, pp. 1523–1525, 2013.
- [39] B. Bao, F. Hu, Z. Liu, and J. Xu, "Mapping equivalent approach to analysis and realization of memristor-based dynamical circuit," *Chinese Physics B*, vol. 23, no. 7, Article ID 070503, 2014.
- [40] M. Chen, Y. Feng, H. Bao, B. Bao, H. Wu, and Q. Xu, "Hybrid state variable incremental integral for reconstructing extreme multistability in memristive jerk system with cubic nonlinearity," *Complexity*, vol. 2019, Article ID 8549472, 16 pages, 2019.
- [41] B. C. Bao, G. H. Zhou, J. P. Xu, and Z. Liu, "Multiscroll chaotic attractors from a modified colpitts oscillator model," *International Journal of Bifurcation and Chaos*, vol. 20, no. 07, pp. 2203–2211, 2010.
- [42] H. Bao, W. Liu, and M. Chen, "Hidden extreme multistability and dimensionality reduction analysis for an improved non-autonomous memristive FitzHugh–Nagumo circuit," *Nonlinear Dynamics*, vol. 96, no. 3, pp. 1879–1894, 2019.
- [43] C. Y. Han, S. M. Yu, and G. Y. Wang, "A sinusoidally driven lorenz system and circuit implementation," *Mathematical Problems in Engineering*, vol. 2015, Article ID 706902, 11 pages, 2015.
- [44] P. C. Rech, "Period-adding and spiral organization of the periodicity in a Hopfield neural network," *International Journal of Machine Learning and Cybernetics*, vol. 6, no. 1, pp. 1–6, 2015.
- [45] N. V. Kuznetsov, G. A. Leonov, M. V. Yuldashev, and R. V. Yuldashev, "Hidden attractors in dynamical models of phase-locked loop circuits: limitations of simulation in MATLAB and SPICE," *Communications in Nonlinear Science and Numerical Simulation*, vol. 51, pp. 39–49, 2017.
- [46] T. Green, *Operational Amplifier Stability Part 6 of 15: Capacitance-Load Stability: RISO, High Gain and CF, Noise Gain*, Texas Instruments, Dallas, TX, USA, 2005.
- [47] J. Steele and T. Green, "Tame those versatile current-source circuits," *Electronic Design*, vol. 61, 1992.

Research Article

Complex Dynamical Behaviors of a Fractional-Order System Based on a Locally Active Memristor

Yajuan Yu,¹ Han Bao ,² Min Shi ,³ Bocheng Bao ,⁴ Yangquan Chen ,⁵ and Mo Chen ⁴

¹Aliyun School of Big Data, Changzhou University, Changzhou 213164, China

²College of Automation Engineering, Nanjing University of Aeronautics and Astronautics, Nanjing 210016, China

³Institute of Advanced Technology, Nanjing University of Posts and Telecommunications, Nanjing 210042, China

⁴School of Information Science and Engineering, Changzhou University, Changzhou 213164, China

⁵Mechatronics, Embedded Systems and Automation Lab, School of Engineering, University of California, Merced, Merced, CA 95343, USA

Correspondence should be addressed to Bocheng Bao; baobc@cczu.edu.cn

Received 10 May 2019; Revised 30 August 2019; Accepted 8 October 2019; Published 20 November 2019

Guest Editor: Lazaros Moysis

Copyright © 2019 Yajuan Yu et al. This is an open access article distributed under the Creative Commons Attribution License, which permits unrestricted use, distribution, and reproduction in any medium, provided the original work is properly cited.

A fractional-order locally active memristor is proposed in this paper. When driven by a bipolar periodic signal, the generated hysteresis loop with two intersections is pinched at the origin. The area of the hysteresis loop changes with the fractional order. Based on the fractional-order locally active memristor, a fractional-order memristive system is constructed. The stability analysis is carried out and the stability conditions for three equilibria are listed. The expression of the fractional order related to Hopf bifurcation is given. The complex dynamical behaviors of Hopf bifurcation, period-doubling bifurcation, bistability and chaos are shown numerically. Furthermore, the bistability behaviors of the different fractional order are validated by the attraction basins in the initial value plane. As an alternative to validating our results, the fractional-order memristive system is implemented by utilizing Simulink of MATLAB. The research results clarify that the complex dynamical behaviors are attributed to two facts: one is the fractional order that affects the stability of the equilibria, and the other is the local activeness of the fractional-order memristor.

1. Introduction

Nonlinear electronic circuits provide powerful and analytical platforms for people to realize and understand the complex dynamical behaviors in physics [1]. Chaotic circuits especially have become effective tools for studying chaos theory. The memristor, originally defined as the fourth element of the circuit by Chua in 1971 [2], is a nonlinear circuit device besides the nonlinear resistor, capacitor, and inductor. As a result, many novel memristive circuits have been constructed by integrating the memristors with versatile nonlinearities into some existing linear or nonlinear circuits [3–11]. In these memristive circuits, rich dynamical behaviors have been reported and tested by numerical simulations and hardware experiments, such as chaos and hyperchaos [12, 13], hyperchaotic multiwing attractors [14, 15], coexisting multiple attractors [16, 17], hidden

attractors [18, 19], and complex transient chaos and hyperchaos [20]. It should be noted that the simplest chaotic circuit has been proposed based on a locally active nonlinear memristive element [4]. Compared to the chaotic circuit shown in [21], the simplest chaotic circuit has following characteristics: (1) the circuit components are connected in a single way, i.e., in series; (2) the number of the circuit components is decreased from four to three; (3) the memristor is locally active.

At a given moment, the resistance of an ideal memristor is represented by the integration of all states before the current moment. This means that the ideal memristor has no memory loss. But the work [22] shows that the width of the doped layer of the HP TiO₂ linear model cannot be equal to zero or the whole width of the model. The HP TiO₂ linear memristor has memory loss. From the definition, the fractional-order derivative depends on the previous history

of the variable and is not a strictly local operator [23]. The order of the fractional-order derivative is related to the memory loss or the “proximity effect” of some characteristics [12]. Then the nonideal memristor with memory loss mentioned in [22] can be modeled by a fractional-order derivative with the order between 0 and 1 [24]. According to this, there are many memristors modeled with the fractional-order derivative [25–27]. As shown in [24], the fractional-order memristor in the series circuits has capacitive properties or inductive properties by choosing a suitable fractional order; i.e., the fractional order can be regarded as a parameter which is used to control the memory strength and dynamics of the circuit. In [25], the fractional order can be used to control the time period in which the resistance of the memristor increases from the initial value to its maximum. In addition, a noncommensurate fractional-order autonomous memristor-based circuit is proposed in [27], where the chaotic behavior can be suppressed by applying periodic impulses. In addition, the dynamical system with the locally active equipment can exhibit complexity and emergent behaviors [28, 29]. Then, it is significant to model the memristor or locally active memristor with the fractional-order derivative and display the dynamics induced by these fractional-order memristors.

The main purpose of this paper is to study the complex dynamical behaviors of a fractional-order system based on a locally active voltage-controlled memristor. By theoretical analyses, the stability conditions of the fractional-order memristive system are listed. The complex dynamical behaviors, such as Hopf bifurcation, period-doubling bifurcation, bistability, and chaos, are displayed numerically. The rest of the paper is organized as follows. In Section 2, the mathematical model of the fractional-order memristor is presented. The fractional-order memristor’s fingerprints and local activeness are addressed. In Section 3, an integer-order locally active memristive system is generalized into a fractional-order locally active memristive system. The stability conditions are listed. The complex dynamical behaviors are stated, and numerical simulations are displayed. As an alternative to validating the numerical results, the fractional-order memristive system is implemented by utilizing Simulink of MATLAB. In Section 4, the effect of the local activeness on complex dynamical behaviors is stated. Section 5 ends with some concluding remarks.

2. Fractional-Order Locally Active Nonlinear Memristor

2.1. The Model of the Fractional-Order Memristor. Generally, the memristor can be seen as a sliding resistor whose resistance changes with the charge crossing it. Driven by a bipolar periodic signal, the memristor exhibits a hysteresis loop pinched at the origin in the current-voltage plane. An integer-order nonlinear voltage-controlled memristor is stated as follows [30]:

$$\begin{cases} i = W(x_m)v = (x_m^2 - x_m - 1)v, \\ \dot{x}_m = p_1x_m - p_2x_m^3 + p_4v - p_4x_mv, \end{cases} \quad (1)$$

where v and i are the voltage and current of the memristor, respectively, x_m is the internal state of the memristor and $W(x_m) = x_m^2 - x_m - 1$ is the memductance, and $p_1, p_2, p_3,$ and p_4 are the system parameters. By using the trial and error method [30], the parameters are decided as $p_1 = 1.8, p_2 = 3.9,$ $p_3 = 1.4,$ and $p_4 = 1.5$. Considering the memory effect from the memristor, a fractional-order voltage-controlled memristor M_α corresponding to (1) is modeled as follows:

$$\begin{cases} i = W_\alpha(x_m)v = (x_m^2 - x_m - 1)v, \\ {}^C_0D_t^\alpha x_m = 1.8x_m - 3.9x_m^3 + 1.4v - 1.5x_mv, \end{cases} \quad (2)$$

where

$${}^C_0D_t^\alpha x_m(t) = \frac{1}{\Gamma(1-\alpha)} \int_0^t \frac{\dot{x}_m(\tau)}{(t-\tau)^\alpha} d\tau, \quad 0 < \alpha \leq 1, \quad (3)$$

is α -order derivative of $x_m(t)$ in the sense of Caputo’s definition given in [23], $\dot{x}_m(\tau)$ denotes the first-order derivative of $x_m(\tau)$ with respect to τ , and $W_\alpha(x_m) = x_m^2 - x_m - 1$ is the memductance of α -order memristor M_α . The integral process in (3) is the memory process of the memristor. In the circuits, the proposed fractional-order memristor is marked as Figure 1(a).

2.2. The Characteristics of the Fractional-Order Memristor. Driven by a sinusoidal voltage source $v(t) = \sin(\omega t)$, hysteresis loops generated in the current-voltage plane are plotted numerically in Figure 2, where ω is the stimulus frequency. One has the following:

- (1) Under different stimulus frequencies or different fractional orders, the hysteresis loops of the fractional-order memristor are pinched at the origin.
- (2) The larger the area of the hysteresis loop, the stronger the memory [31]. Let the order $\alpha = 0.98$. Figure 2(a) shows that the smaller the stimulus frequency ω , the stronger the memory. As $\omega = 1$ rad/s, there is another intersection in the hysteresis loop besides the origin and another area S^* is displayed. Currently, there are few reports on the new intersection which reflects the nonlinearity of the memristor.
- (3) As fixing $\omega = 1$ rad/s and decreasing α from 1 to 0, the area of the hysteresis loop increases; i.e., the strength of the memory increases, referring to Figure 2(b). Simultaneously, the quadrants which the hysteresis loops lie in change from II and IV to II, III, and IV.

2.3. Local Activeness of the Fractional-Order Memristor. A component being capable of providing a power gain is called an active component. If the component provides the power gain within the local range of its variables, the component is locally active.

Based on (2), as $(1 - \sqrt{5})/2 < x_m < (1 + \sqrt{5})/2$, one has $W_\alpha(x_m) = x_m^2 - x_m - 1 < 0$, the power $p = v \cdot i = W_\alpha(x_m) \cdot v^2 < 0$, and the memristor can provide the power gain; as $x_m < (1 - \sqrt{5})/2$ or $x_m > (1 + \sqrt{5})/2$, one has $W_\alpha(x_m) = x_m^2 - x_m - 1 > 0$, the power $p = v \cdot i = W_\alpha(x_m) \cdot v^2 > 0$, and

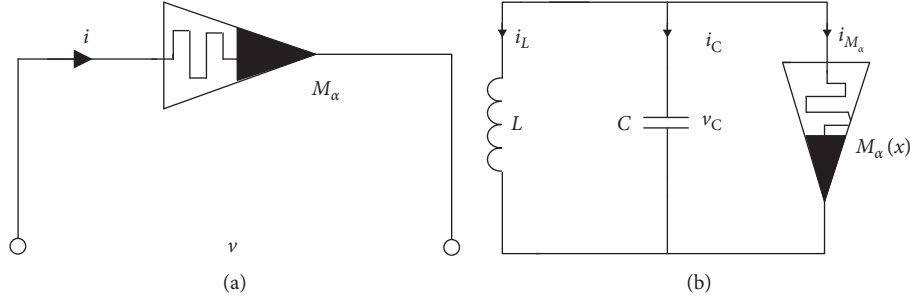


FIGURE 1: (a) The fractional-order memristor M_α ; (b) the fractional-order memristive circuit.

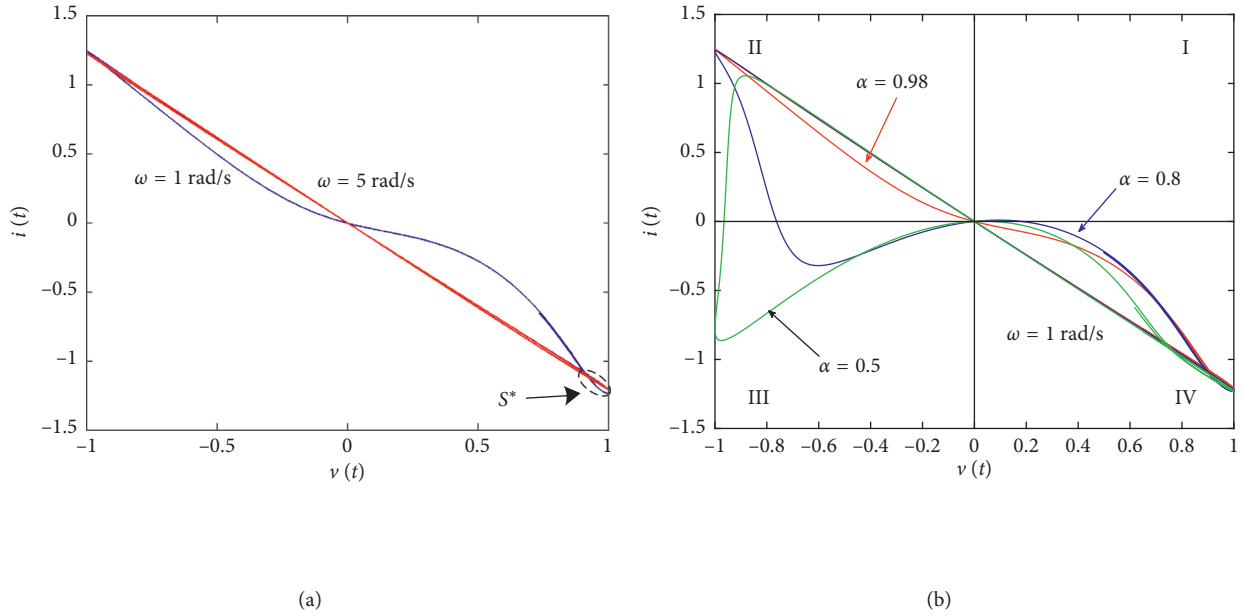


FIGURE 2: $v(t)$ versus $i(t)$ of the fractional-order memristor. (a) The order $\alpha=0.98$ with two different frequencies; (b) the frequency $\omega=1$ rad/s with three different fractional orders.

the memristor cannot provide the power gain. So the memristor is locally active.

The above statement implies that the local activeness of the memristor can be decided by the sign of the memductance $W_\alpha(x_m)$. Referring to Figure 2, the slope of the hysteresis loop is the memductance. Obviously, the changing of the quadrants of the hysteresis loops changes the sign of the slope or the sign of the memductance $W_\alpha(x_m)$. Remembering the characteristics shown in Figure 2(b), it is easy to know that the fractional order has influences on the activeness of the memristor.

3. Fractional-Order Memristor-Based System

Besides the memristor can be modeled by the fractional-order derivative, the capacitor and the inductor can also be modeled by the fractional-order derivative due to the memory effect [12, 32]. With the fractional-order locally active memristor, a fractional-order memristive circuit is generalized from an integer-order memristive circuit [30], as shown in Figure 1(b), which is modeled by Caputo's fractional-order derivative

$$\begin{cases} {}^C_0D_t^\alpha v_C = -a[(x_m^2 - x_m - 1)v_C + i_L], \\ {}^C_0D_t^\alpha i_L = bv_C, \\ {}^C_0D_t^\alpha x_m = 1.8x_m - 3.9x_m^3 + 1.4v_C - 1.5x_mv_C, \end{cases} \quad (4)$$

where $0 < \alpha \leq 1$, $a = 1/C > 0$, $b = 1/L > 0$, and C , L , v_C , and i_L are the capacitance, inductance, capacitor voltage, and inductor current, respectively. Letting $\alpha=1$, model (4) is changed into the integer-order model stated in [30].

Denoting $x = v_C$, $y = i_L$, and $z = x_m$, (4) is converted into the dimensionless form

$$\begin{cases} {}^C_0D_t^\alpha x = -a[(z^2 - z - 1)x + y], \\ {}^C_0D_t^\alpha y = bx, \\ {}^C_0D_t^\alpha z = 1.8z - 3.9z^3 + 1.4x - 1.5zx. \end{cases} \quad (5)$$

For any values of the parameters a and b , system (5) has three equilibria: $E_1 = (0, 0, -0.6794)$, $E_2 = (0, 0, 0)$, and $E_3 = (0, 0, 0.6794)$. For simplicity, the three equilibria are denoted uniformly by E_{z_0} , where $E_{z_0} = (0, 0, z_0)$. Thus, $E_{z_0} = E_1$ as $z_0 = -0.6794$, $E_{z_0} = E_2$ as $z_0 = 0$, and $E_{z_0} = E_3$ as $z_0 = 0.6794$.

3.1. *The Stability of the Equilibria.* The Jacobian matrix of system (5) at E_{z_0} is

$$J_E = \begin{pmatrix} -a(z_0^2 - z_0 - 1) & -a & 0 \\ b & 0 & 0 \\ 1.4 - 1.5z_0 & 0 & 1.8 - 11.7z_0^2 \end{pmatrix}. \quad (6)$$

The characteristic polynomial equation of system (5) at E_{z_0} is yielded as

$$(\lambda - 1.8 + 11.7z_0^2)[\lambda^2 + a(z_0^2 - z_0 - 1)\lambda + ab] = 0, \quad (7)$$

which indicates that roots of (7) depend on the three equilibria. The roots of (7) are called the eigenvalues of Jacobian matrix J_E . The following lemma is needed.

Lemma 1 [33]. *The fractional-order nonlinear system*

$${}_0^C D_t^\alpha \mathbf{X} = \mathbf{f}(\mathbf{X}), \quad 0 < \alpha \leq 1, \quad (8)$$

is asymptotically stable at the equilibrium $E = (x_0, y_0, z_0)$ if all eigenvalues λ of Jacobian matrix J_E satisfy the condition

$$|\arg(\lambda)| > \frac{\alpha\pi}{2}, \quad (9)$$

where $\mathbf{X} = (x, y, z)^T$, $\mathbf{f}(\mathbf{X}) = [f_1(\mathbf{X}), f_2(\mathbf{X}), f_3(\mathbf{X})]^T$, $f_i(\mathbf{X}) = f_i(x, y, z)$ ($i = 1, 2, 3$), and $\arg(\lambda)$ is the principal argument of the eigenvalue λ .

Obviously, equation (7) has a real root $\lambda_1 = 1.8 - 11.7z_0^2$. Considering the sign of λ_1 , two cases are discussed hereinafter.

Case 1. λ_1 is positive

If $\lambda_1 > 0$, one has $|z_0| < 0.3922$ and the equilibrium E_{z_0} is unstable. Besides the positive root λ_1 , equation (7) has another two roots:

$$-a(z_0^2 - z_0 - 1) \begin{cases} < 0, & z_0 < -0.618 \text{ or } z_0 > 1.618, \\ > 0, & -0.618 < z_0 < -0.3299 \text{ or } 0.3299 < z_0 < 1.618. \end{cases} \quad (13)$$

where $(1 - \sqrt{5})/2 \approx -0.618$ and $(1 + \sqrt{5})/2 \approx 1.618$. The inequalities $-0.618 < z_0 < -0.3299$ and $z_0 > 1.618$ can be neglected because z_0 of the three equilibria is not in these regions. As $z_0 < -0.618$, one has $\lambda_2 < 0$ and $\lambda_3 < 0$. As $0.3299 < z_0 < 1.618$, one has $\lambda_2 > 0$ and $\lambda_3 > 0$.

- (2) λ_2 and λ_3 are the complex roots. The inequality $(z_0^2 - z_0 - 1)^2 < 4b/a$ holds. As $z_0 < -0.618$, λ_2 and λ_3 are the conjugate complex roots with negative real parts $\text{Re}(\lambda_{2,3}) = -a(z_0^2 - z_0 - 1)/2 < 0$. As $0.3299 < z_0 < 1.618$, λ_2 and λ_3 are the conjugate complex roots

$$\lambda_{2,3} = \frac{-a(z_0^2 - z_0 - 1) \pm \sqrt{a^2(z_0^2 - z_0 - 1)^2 - 4ab}}{2}. \quad (10)$$

It is easy to know that $-0.454 < z_0^2 - z_0 - 1 < -1.2384$ as $|z_0| < 0.3922$. Two cases are listed:

- (1) λ_2 and λ_3 are the real roots and $(z_0^2 - z_0 - 1)^2 \geq 4b/a$ holds. Based on (10), one has $\lambda_1 > 0$, $\lambda_2 > 0$, and $\lambda_3 > 0$.
(2) λ_2 and λ_3 are the complex roots; i.e., $(z_0^2 - z_0 - 1)^2 < 4b/a$ holds. The real parts of the conjugate complex roots are $\text{Re}(\lambda_{2,3}) = -a(z_0^2 - z_0 - 1)/2 > 0$.

Case 2. λ_1 is negative

As $\lambda_1 = 1.8 - 11.7z_0^2 < 0$, one has $|z_0| > 0.3922$. Similar to Case 1, two cases are stated as follows:

- (1) λ_2 and λ_3 are the real roots. Then $(z_0^2 - z_0 - 1)^2 \geq 4b/a$ holds and

$$\text{sgn}(\lambda_2) = \text{sgn}(\lambda_3) = \text{sgn}(-a(z_0^2 - z_0 - 1)), \quad (11)$$

where $\text{sgn}(\cdot)$ is the symbolic function. Due to

$$g(z_0) = z_0^2 - z_0 - 1 = \left[z_0 - \frac{1 - \sqrt{5}}{2} \right] \left[z_0 - \frac{1 + \sqrt{5}}{2} \right], \quad (12)$$

one has

with positive real parts $\text{Re}(\lambda_{2,3}) = -a(z_0^2 - z_0 - 1)/2 > 0$.

The above discussion can be concluded in Tables 1 and 2. Tables 1 and 2 show that $E_1 = (0, 0, -0.6794)$ is stable and $E_2 = (0, 0, 0)$ is unstable for any $a > 0$, $b > 0$, and any order $\alpha \in (0, 1]$. But for $E_3 = (0, 0, 0.6794)$, two cases are stated:

- (1) if $1.4831 \geq 4b/a$, E_3 is unstable for any order α because $\lambda_2 > 0$ and $\lambda_3 > 0$;
(2) if $1.4831 < 4b/a$, there are two conjugated complex roots at E_3 as

$$\lambda_{2,3} = \text{Re}(\lambda_{2,3}) \pm j\text{Im}(\lambda_{2,3}) = \frac{-a(z_0^2 - z_0 - 1) \pm j\sqrt{4ab - a^2(z_0^2 - z_0 - 1)^2}}{2}, \quad (14)$$

TABLE 1: The eigenvalues as $(z_0^2 - z_0 - 1)^2 \geq 4b/a$.

z_0	$(-\infty, -0.618)$	$(-0.3299, 0.3299)$	$(0.3299, 1.618)$
λ_1	$\lambda_1 < 0$	$\lambda_1 > 0$	$\lambda_1 < 0$
λ_2	$\lambda_2 < 0$	$\lambda_2 > 0$	$\lambda_2 > 0$
λ_3	$\lambda_3 < 0$	$\lambda_3 > 0$	$\lambda_3 > 0$
Equilibrium	E_1	E_2	E_3

TABLE 2: The eigenvalues as $(z_0^2 - z_0 - 1)^2 < 4b/a$.

z_0	$(-\infty, -0.618)$	$(-0.3299, 0.3299)$	$(0.3299, 1.618)$
λ_1	$\lambda_1 < 0$	$\lambda_1 > 0$	$\lambda_1 < 0$
λ_2	$\text{Re}(\lambda_2) < 0$	$\text{Re}(\lambda_2) > 0$	$\text{Re}(\lambda_2) > 0$
λ_3	$\text{Re}(\lambda_3) < 0$	$\text{Re}(\lambda_3) > 0$	$\text{Re}(\lambda_3) > 0$
Equilibrium	E_1	E_2	E_3

where $j^2 = -1$. If $|\arg(\lambda_{2,3})| > (\alpha\pi)/2$ holds, one has

$$\frac{\sqrt{4ab - 1.4831a^2}}{1.2178a} > \tan \frac{\alpha\pi}{2}. \quad (15)$$

By Lemma 1, $E_3 = (0, 0, 0.6794)$ is stable as $\sqrt{4ab - 1.4831a^2}/(1.2178a) > \tan(\alpha\pi/2)$ holds; E_3 is unstable as $\sqrt{4ab - 1.4831a^2}/(1.2178a) < \tan(\alpha\pi/2)$ does not hold.

Based on the above discussion, the following theorem is established.

Theorem 1. For system (5) ($\alpha \in (0, 1]$), the stabilities of three equilibria E_1 , E_2 , and E_3 are as follows:

- (1) Equilibrium $E_1 = (0, 0, -0.6794)$ is stable for any $a > 0$, $b > 0$ and any order $\alpha \in (0, 1]$;
- (2) Equilibrium $E_2 = (0, 0, 0)$ is unstable for any $a > 0$, $b > 0$ and any order $\alpha \in (0, 1]$;
- (3) As $1.4831 \geq 4b/a$, E_3 is unstable for any order $\alpha \in (0, 1]$; as $1.4831 < 4b/a$, E_3 is stable if $\sqrt{4ab - 1.4831a^2}/(1.2178a) > \tan(\alpha\pi/2)$, and E_3 is unstable if $\sqrt{4ab - 1.4831a^2}/(1.2178a) < \tan(\alpha\pi/2)$.

Remark 1. For a fractional-order system, at a parameter $\varepsilon = \varepsilon_0$, a pair of conjugated complex eigenvalues $\lambda_{1,2}$ satisfy $|\arg(\lambda_{1,2})| = (\alpha\pi)/2$ and other eigenvalues are in stable zones. While the parameter $\varepsilon > \varepsilon_0$, $|\arg(\lambda_{1,2})| < (\alpha\pi)/2$, Hopf bifurcation is generated at $\varepsilon = \varepsilon_0$ [34].

For system (5), based on Table 2, at $E_3 = (0, 0, 0.6794)$, as $1.4831 < 4b/a$ holds, one has

- (1) $\lambda_1 < 0$;
- (2) $|\arg(\lambda_{2,3})| > (\alpha\pi)/2$ as $\alpha < (2/\pi)\arctan(\sqrt{4ab - 1.4831a^2}/1.2178a)$;
- (3) $|\arg(\lambda_{2,3})| < (\alpha\pi)/2$ as $\alpha > (2/\pi)\arctan(\sqrt{4ab - 1.4831a^2}/1.2178a)$. This means that Hopf bifurcation is generated as the order $\alpha = (2/\pi)\arctan(\sqrt{4ab - 1.4831a^2}/1.2178a)$ at the equilibrium E_3 .

Remark 2. For simplicity, the eigenvalues $(\lambda_1, \lambda_2, \lambda_3)$ are denoted as $(\gamma, \sigma + j\omega, \sigma - j\omega)$, where γ, σ , and ω are all real

numbers. A saddle-focus point is called a saddle-focus point of index 1 if $\gamma > 0$ and $\sigma < 0$, and a saddle-focus point is called a saddle-focus point of index 2 if $\gamma < 0$ and $\sigma > 0$ [35]. As pointed out in [35], the saddle-focus points of index 2 are crucial to the generation of chaotic attractors. Usually, in chaotic systems, scrolls are generated around the saddle-focus points of index 2, and the saddle-focus points of index 1 are responsible only for connecting the scrolls.

3.2. Numerical Illustrations. For better comparisons with the integer-order memristive circuit systems, in this section, the parameter is chosen as $a = 10/3$ [30].

Case 1. $a = 10/3$, and $b = 10$.

In this case, $a = 10/3$ ($C = 300$ mF) and $b = 10$ ($L = 100$ mH) satisfy $4b/a = 12 > 1.4831$. To make E_3 stable, by Theorem 1, the order α is satisfied as

$$\begin{aligned} \alpha &< \left(\frac{2}{\pi}\right)\arctan\left(\frac{\sqrt{4ab - 1.4831a^2}}{1.2178a}\right) \\ &= \left(\frac{2}{\pi}\right)\arctan\left(\frac{\sqrt{4 \cdot (10/3) \cdot 10 - 1.4831 \cdot (10/3)^2}}{1.2178 \cdot (10/3)}\right) \\ &= 0.7713. \end{aligned} \quad (16)$$

Then equilibrium $E_3 = (0, 0, 0.6794)$ is stable as the order $\alpha < 0.7713$, and E_3 is unstable as the order $\alpha > 0.7713$. By Remark 1, at equilibrium E_3 , Hopf bifurcation is generated as $\alpha = 0.7713$.

At the equilibrium E_2 , the two complex eigenvalues are

$$\begin{aligned} \lambda_{2,3} &= \frac{-a(z_0^2 - z_0 - 1) \pm j\sqrt{4ab - a^2(z_0^2 - z_0 - 1)^2}}{2} \\ &= \frac{5 \pm 5\sqrt{11}j}{2}, \quad (j^2 = -1). \end{aligned} \quad (17)$$

If $\tan(\arg(\lambda_{2,3})) = \sqrt{11} > \tan(\alpha\pi/2)$, one has $\alpha < 0.8136$. This means that the two complex eigenvalues $\lambda_{2,3}$ of the equilibrium E_2 lie in the stable zone. Due to $\lambda_1 > 0$ and Remark 2, E_2 is an unstable saddle-focus with index 1 and E_3 is an unstable saddle-focus with index 2. While $\alpha > 0.8136$, the two complex eigenvalues $\lambda_{2,3}$ of the equilibrium E_2 lie in the unstable zone, E_2 is an unstable node-focus, and E_3 is an unstable saddle-focus with index 2. The types of three equilibria are listed in Table 3. One has the following:

- (1) As $0 < \alpha < 0.7713$, there are two steady states of E_1 and E_3 .
- (2) As $0.7713 < \alpha < 0.8136$, there are two steady states of E_1 and the limit cycle bifurcated from unstable saddle-focus E_3 .
- (3) As $0.8136 < \alpha < 1$, the stability of E_1 is unchanged. E_2 is changed from unstable saddle-focus into unstable node-focus because the two complex roots $\lambda_{2,3}$ of E_2 enter into the unstable zone.

TABLE 3: The types of the equilibria.

α	E_1	E_2	E_3
(0, 0.7713)	Stable	Unstable saddle-focus	Stable
0.7713	Stable	Unstable saddle-focus	Hopf bifurcation point
(0.7713, 0.8136)	Stable	Unstable saddle-focus	Unstable saddle-focus
0.8136	Stable	Unstable point	Unstable saddle-focus
(0.8136, 1)	Stable	Unstable node-focus	Unstable saddle-focus

Remark 3. It is found that E_3 is an unstable saddle-focus with index 2 as the order $\alpha > 0.7713$. Due to Remark 2, for system (5), chaotic attractors may be generated as the order $\alpha > 0.7713$.

Fix the initial values (0.1, 0.1, 0.2). Figure 3(a) is the bifurcation diagram of the local maxima of the variable z about the order α , which shows that Hopf bifurcation is generated at $\alpha = 0.7713$. As $0.7713 < \alpha < 0.8136$, system (5) displays a limit cycle bifurcated from the equilibrium E_3 . As $0.8136 < \alpha < 0.84$, the limit cycle induced by Hopf bifurcation disappears and the phase portrait limits to the stable point E_1 . Increasing α from 0.84 to 1, the period-doubling bifurcation occurs in system (5). Figure 3(b) is the first two Lyapunov exponents of system (5) according to the MATLAB code of [36]. As $\alpha > 0.97$, the first Lyapunov exponent $LE_1 > 0$ and system (5) enters into the chaos.

Case 2. $\alpha = 0.99$, and $a = 10/3$.

In this case, if the inequality $4b/a > 1.4831$ holds, one has $b > 1.2359$. Same as the integer-order case [30], the parameter L is set in [70 mH; 100 mH]; i.e., the parameter b is in [10, 100/7]. If E_3 is stable, by Theorem 1, the parameter b should be satisfied as

$$\begin{aligned}
 b &> \frac{[1.2178^2 \cdot a \cdot \tan^2(\alpha\pi/2) + 1.4831a]}{4} \\
 &= \frac{[1.2178^2 \cdot (10/3) \cdot \tan^2(0.99\pi/2) + 1.4831(10/3)]}{4} \\
 &= 5009.2.
 \end{aligned} \tag{18}$$

This means that E_3 is a saddle-focus with index 2 for any $b \in [10, 100/7]$ or any $L \in [70 \text{ mH}, 100 \text{ mH}]$. Thus, chaotic attractors may be generated at E_3 as L increases from 70 mH to 100 mH.

At the equilibrium E_2 , two complex eigenvalues are

$$\begin{aligned}
 \lambda_{2,3} &= \frac{-a(z_0^2 - z_0 - 1) \pm j\sqrt{4ab - a^2(z_0^2 - z_0 - 1)^2}}{2} \\
 &= \frac{(10/3) \pm j\sqrt{4(10/3)b - (10/3)^2}}{2}.
 \end{aligned} \tag{19}$$

If $\tan(\arg(\lambda_{2,3})) = \sqrt{120b - 100}/10 > \tan(0.99\pi/2)$, one has $b > 3377.65$ or $L < 0.2961 \text{ mH}$. This means that two

complex eigenvalues $\lambda_{2,3}$ of the equilibrium E_2 lie in the unstable zone as $L \in [70 \text{ mH}, 100 \text{ mH}]$. Due to $\lambda_1 > 0$, E_2 is an unstable node-focus which is that same as the former case of $0.8136 < \alpha < 1$.

The bifurcation diagram of the variable z about the parameter L is plotted numerically in Figure 3(c). The first two Lyapunov exponents are shown in Figure 3(d). It is found that system (5) goes into chaos by the period-doubling bifurcation. After system (5) enters into chaos, there suddenly appears several periodic windows (PWs) as $L > 86 \text{ mH}$. Compared to the integer-order model in [30], the fractional-order memristive system described by system (5) has more periodic windows. The minimum of the parameter L for system (5) entering into chaos is larger than the minimum of the parameter L shown in [30].

Therefore, the generated complicated dynamical behaviors of system (5) are related to the coexistence of the stable point E_1 , the unstable node-focus E_2 , and the saddle-focus E_3 .

3.3. Bistability Behaviors. Fixing the parameter values and choosing different initial values, a nonlinear system shows two steady states. This behavior is called the bistability behavior. The bistability behavior reflects the sensitivity of the system to its initial values. For different order α or different inductance L , different bistability behaviors appear in system (5), which is listed in Tables 4 and 5.

Bistability behaviors for different fractional orders are plotted numerically in Figure 4. Figure 4(a) is two steady states of the stable points E_1 and E_3 , Figure 4(b) is two steady states of the stable point E_1 and period-2 cycle, Figure 4(c) is two steady states of the stable point E_1 and period-4 cycle, and Figure 4(d) is two steady states of the stable point E_1 and chaotic attractor. Compared to the bistability of stable point and chaotic attractor in the integer-order model, a conclusion that the fractional-order derivative can enrich the bistability behaviors is drawn.

Furthermore, the attraction basins in the $x(0) - z(0)$ plane are used to validate the bistability behaviors of system (5) for four different orders α , as shown in Figure 5, where $y(0) = 0.1$. The light blue, green, yellow, and magenta regions represent the initial value regions for generating period-2, period-4, chaotic, and stable point behaviors, respectively.

3.4. Block Designs of System (5) in Simulink of MATLAB. By utilizing Simulink of MATLAB, the fractional-order system (5) can be implemented to confirm the above numerical plots.

Figure 6 is the block diagrams in Simulink of MATLAB. Figure 6(a) is the α -order differentiator block design. The top in Figure 6(a) is the masked block of the α -order derivative and the bottom in Figure 6(a) is the filter in fractional-order differentiator (here the Oustaloup recursive filter is used). The masking technique of `fo_diff.mdl` is provided in [37]. Double clicking the block of Fractional Der s^α , the order α can be changed by the parameter dialog box. Furthermore, if

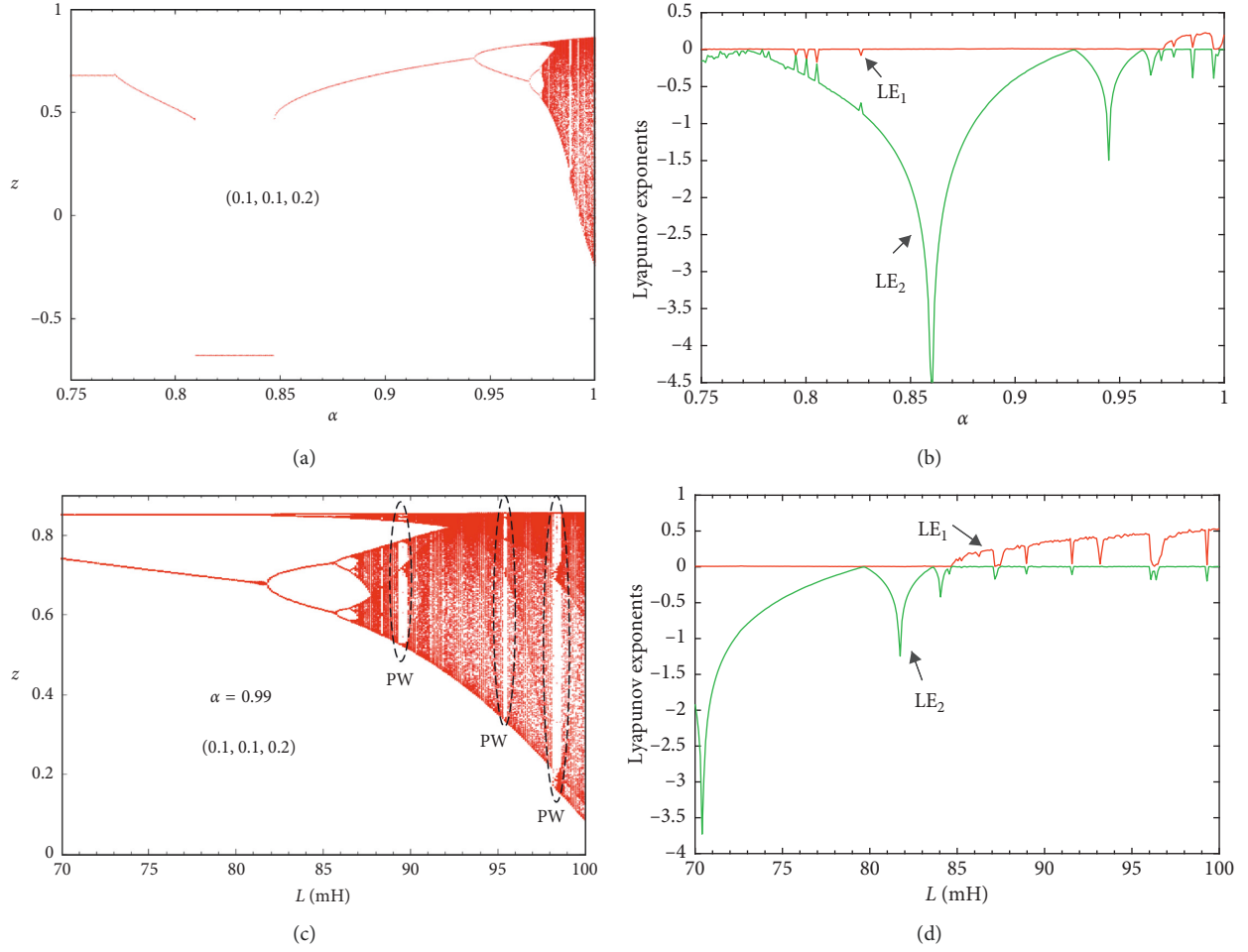


FIGURE 3: Numerical simulations of system (5), $a = 10/3$, $b = 10$, and the initial values $(0.1, 0.1, 0.2)$. (a) Bifurcation diagram of the local maxima of the variable z about the order α ; (b) first two Lyapunov exponents of Case 1; (c) bifurcation diagram of the local maxima of the variable z about the parameter L ; (d) first two Lyapunov exponents of Case 2.

TABLE 4: Bistability in the case of $a = 10/3$ and $b = 10$.

α	Two steady states
$(0, 0.7713)$	Two stable points of E_1 and E_2
$(0.7713, 0.84)$	Stable point E_1 and limit cycle
$(0.84, 0.97)$	Stable point E_1 and limit cycle
$(0.97, 1)$	Stable point E_1 and chaotic attractor

$${}_0^C D_t^\alpha x(t) = f(t), \quad 0 < \alpha < 1, \quad (20)$$

one has [38]

$${}_0^C D_t^{1-\alpha} ({}_0^C D_t^\alpha x(t)) = \frac{dx(t)}{dt}, \quad (21)$$

or

$$\frac{dx(t)}{dt} = {}_0^C D_t^{1-\alpha} f(t). \quad (22)$$

Then in the block diagram of the fractional-order memristor or in Figure 6(b), the α -order fractional-order derivative of the state is obtained by an integrator.mdl and the **fo_diff**.mdl of Fractional Der $s^{(1-\alpha)}$.

TABLE 5: Bistability in the case of $\alpha = 0.99$ and $a = 10/3$.

L mH	Two steady states
$(70, 86)$	Stable point E_1 and limit cycle
$(86, 100)$	Stable point E_1 and chaotic attractor

The input voltage in Figure 6(b) is $v(t) = \sin(\omega t)$. Fixing the order $\alpha = 0.98$, the hysteresis loops of different input frequency ω obtained in the scope (XY graph) are shown in Figure 7(a). Fixing the input frequency $\omega = 1$ rad/s, the hysteresis loops of different order α obtained in the scope (XY graph) are shown in Figure 7(b). Figure 7 plotted in Simulink of MATABL is consistent with Figure 2.

The block diagram of system (5) in Simulink of MATABL is designed in Figure 8. By using (22), the α -order fractional-order derivative of the state is obtained by an integrator.mdl and the **fo_diff**.mdl of Fractional Der $s^{(1-\alpha)}$. The initial values of the states are set in three integrators. Setting $1 - \alpha = 0.25$ in Figure 8, bistability behaviors of $\alpha = 0.75$ obtained in the scope (XZ graph) are shown in Figure 9(a). Setting $1 - \alpha = 0.01$ in Figure 8, bistability behaviors of $\alpha = 0.99$ obtained in the scope (XZ graph) are shown in Figure 9(b).

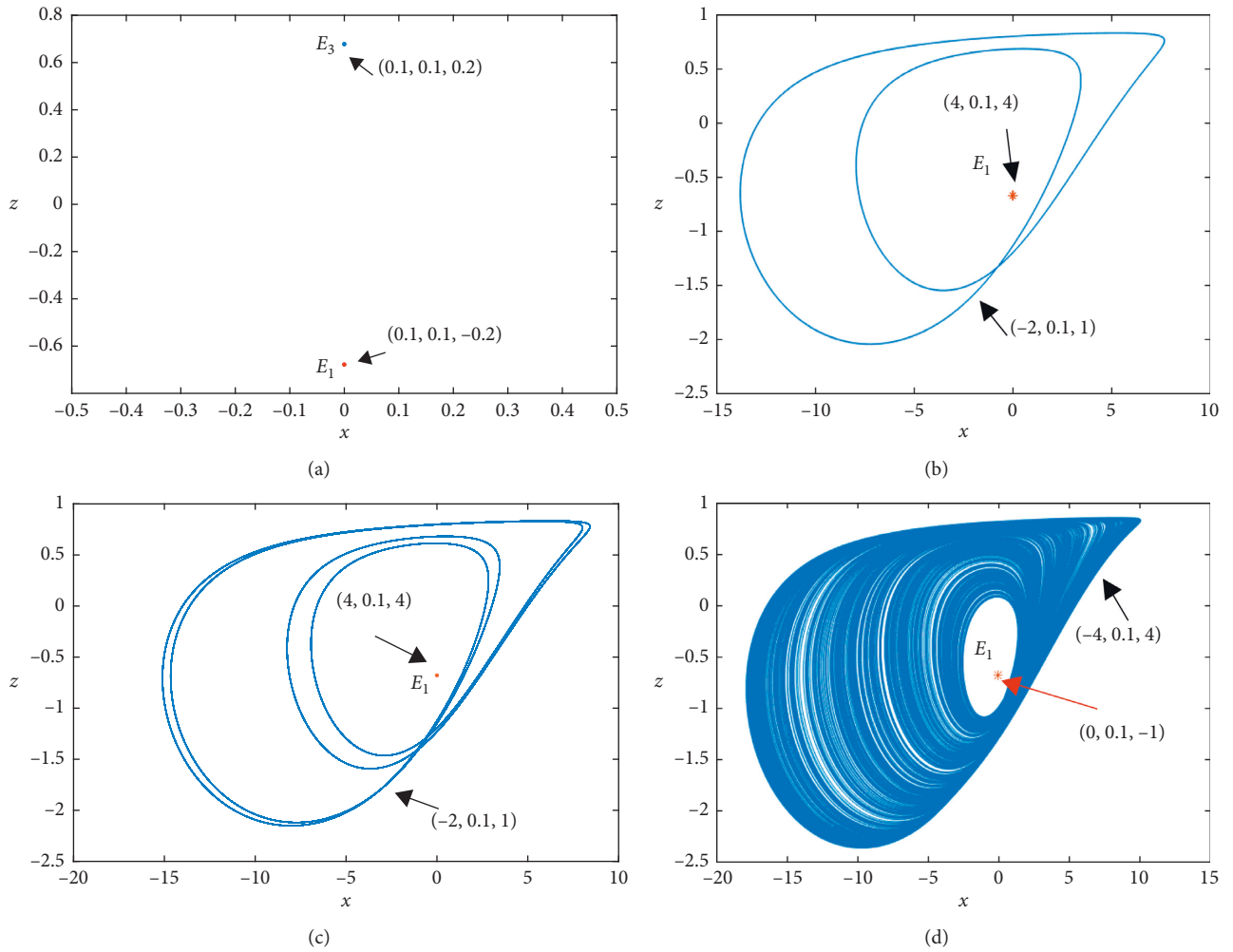


FIGURE 4: Bistability behaviors with different fractional orders. (a) $\alpha = 0.75$, two sets of the initial values $(0.1, 0.1, 0.2)$ and $(0.1, 0.1, -0.2)$; (b) $\alpha = 0.96$ and two sets of the initial values $(4, 0.1, 4)$ and $(-2, 0.1, 1)$; (c) $\alpha = 0.97$ and two sets of the initial values $(4, 0.1, 4)$ and $(-2, 0.1, 1)$; (d) $\alpha = 0.99$ and two sets of the initial values $(-4, 0.1, 4)$ and $(0, 0.1, -1)$.

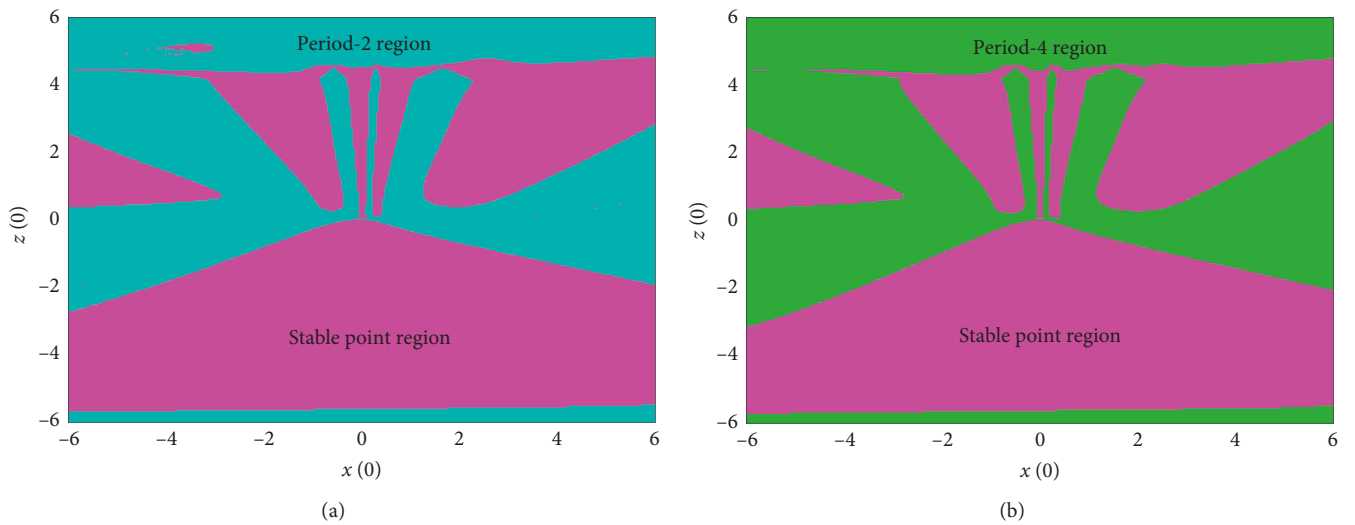


FIGURE 5: Continued.

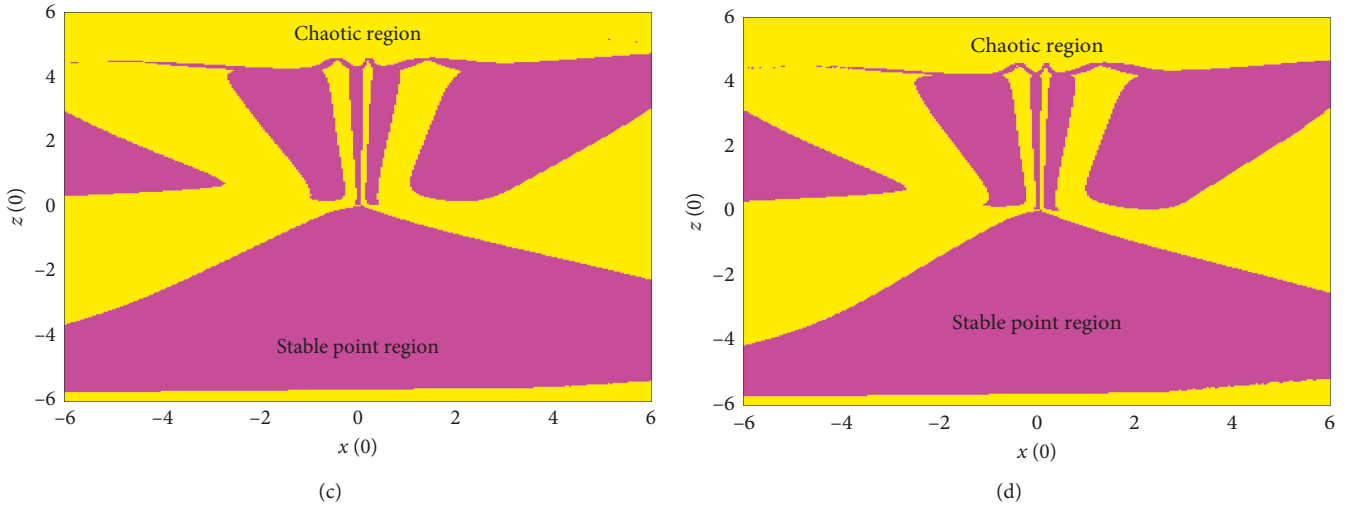


FIGURE 5: Bistability behaviors demonstrated by the attraction basins in the $x(0) - y(0)$ plane for four different fractional orders with $y(0) = 0.1$. (a) Attraction basin for $\alpha = 0.96$; (b) attraction basin for $\alpha = 0.97$; (c) attraction basin for $\alpha = 0.98$; (d) attraction basin for $\alpha = 0.99$.

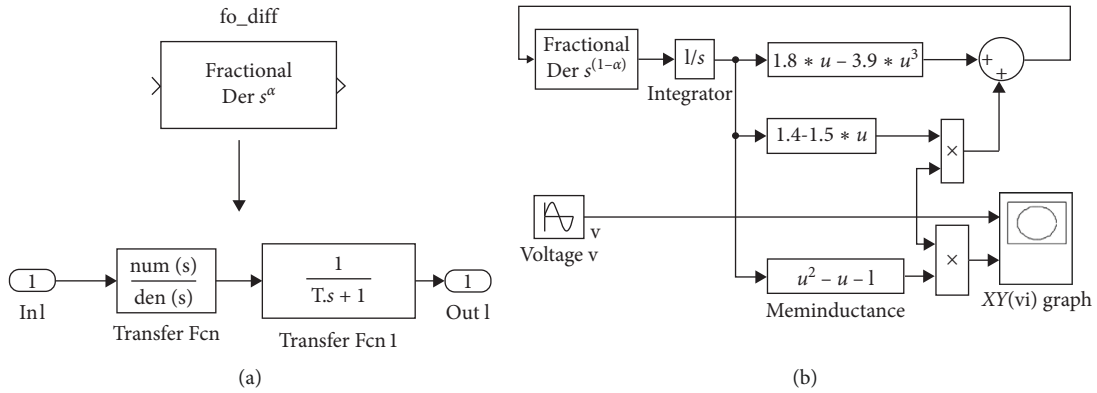


FIGURE 6: Block diagrams in Simulink of MATLAB. (a) Differentiator block design4 of the order α ; (b) block diagram of the fractional-order memristor.

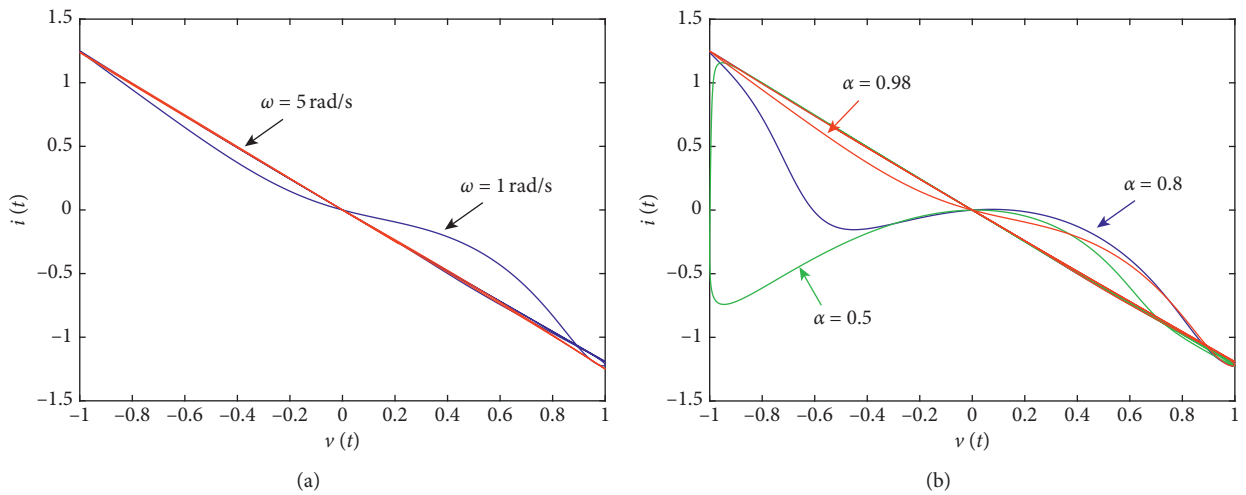


FIGURE 7: $v(t)$ versus $i(t)$ of the fractional-order memristor from the scope (XY Graph) in Figure 6(b). (a) The order $\alpha = 0.98$ with two different frequencies; (b) the frequency $\omega = 1$ rad/s with three different fractional orders.

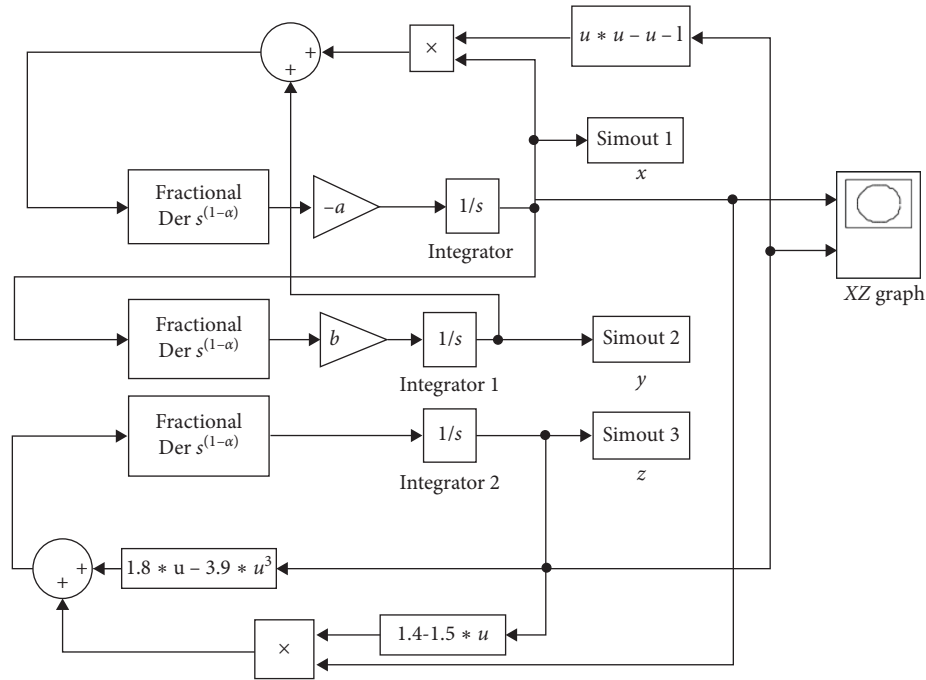


FIGURE 8: The block diagram of system (5) in Simulink of MATLAB.

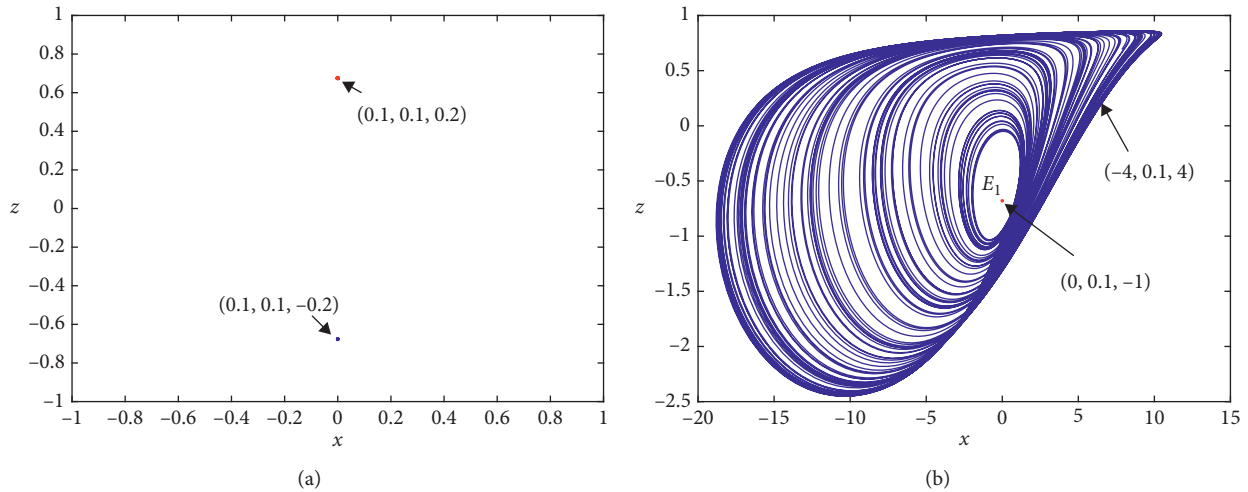


FIGURE 9: Bistability behaviors obtained in Simulink of MATLAB, the running time $t = 100$ s. (a) $\alpha = 0.75$, two sets of the initial values $(0.1, 0.1, 0.2)$ and $(0.1, 0.1, -0.2)$; (b) $\alpha = 0.99$, two sets of the initial values $(-4, 0.1, 4)$ and $(0, 0.1, -1)$.

To obtain the bistability behaviors of $\alpha = 0.96$ and $\alpha = 0.97$ in Simulink of MATLAB, the values of $(1 - \alpha)$ in Figure 8 are set at $1 - \alpha = 0.04$ and $1 - \alpha = 0.03$, which are omitted here.

4. Local Activeness and Stability

A locally active kinetic equation can exhibit complex dynamics such as limit cycles or chaos. The passive (not locally active) kinetic equation must converge to a unique steady state [39]. Furthermore, the time t can be set to be large when the steady states of the system are concerned.

As parameters $a = 10/3$ and $b = 10$, for the fractional-order memristor in system (5) with the large time t , one has the following.

Fix the initial values $(0.1, 0.1, 0.2)$. As $\alpha = 0.75$, the memristor is active because the power $p = W_{0.75}(x_m) \cdot v^2$ keeps negative, which is shown in Figure 10(a); as $\alpha = 0.82$, the memristor is passive because the power $p = W_{0.82}(x_m) \cdot v^2$ keeps positive for time $t > t_0$ (such as $t_0 = 50$), which is shown in Figure 10(b). As mentioned before, system (5) with $\alpha = 0.75$ or $\alpha = 0.82$ converges to stable points. As $\alpha = 0.9$ or $\alpha = 0.99$, the memristor is locally active because the power $p = W_{\alpha}(x_m) \cdot v^2$ changes between the positive and the

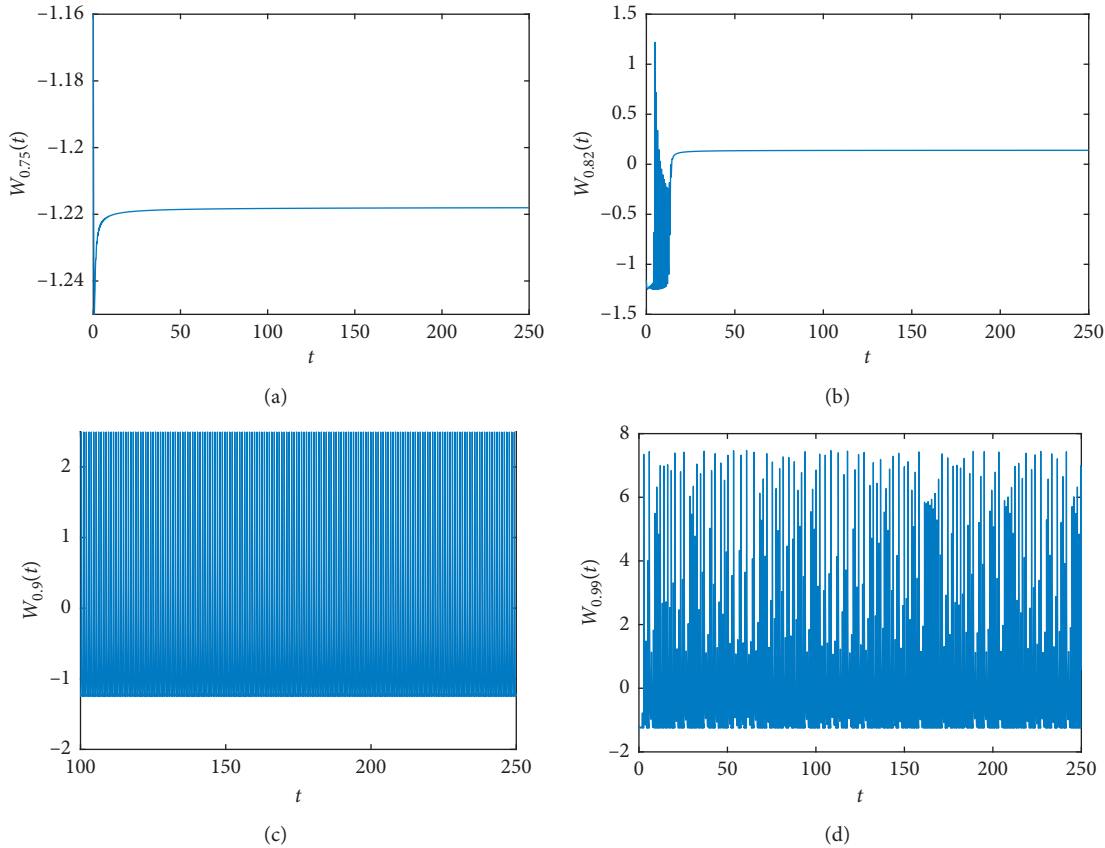


FIGURE 10: The memductance $W_\alpha(t)$ with initial values (0.1, 0.1, 0.2). (a) Memductance $W_{0.75}(t)$; (b) memductance $W_{0.82}(t)$; (c) memductance $W_{0.9}(t)$; (d) memductance $W_{0.99}(t)$.

negative, as shown in Figures 10(c) and 10(d). When the locally active memristor is included in system (5), the limit circle is generated as $\alpha = 0.9$ and chaos is generated as $\alpha = 0.99$.

It is found that the complex dynamics of the limit cycle and chaos are not displayed in system (5) when the memristor is active ($\alpha = 0.75$) or the memristor is passive ($\alpha = 0.82$), while the complex dynamics of the limit cycle and the chaos are generated when the memristor is locally active ($\alpha = 0.9$ and $\alpha = 0.99$). As stated at the beginning of this section, complex dynamics of limit cycle and chaos in system (5) are related to the local activeness of the memristor.

5. Conclusions

In this paper, a chaotic system with a fractional-order locally active memristor is discussed. The fractional order in the memristive system makes the equilibrium vary from unstable to stable, leading to the occurrence of Hopf bifurcation. Moreover, the fractional-order memristive system enters into chaos via period-doubling bifurcation route and triggers more periodic windows than the corresponding integer-order system. Given the suitable parameters, say, a and b , the fractional-order memristive system shows bistability behaviors. For different fractional order and different inductance, the fractional-order memristive system displays different bistability behaviors. The fractional order of the system and the local activeness of the memristor are the

main reasons for the complicated dynamical behaviors. Besides, the fractional-order memristive system is implemented using the block diagram of Simulink of MATLAB and its hardware implementation and corresponding experiments will be our future works.

Data Availability

The data used to support the findings of this study are available from the corresponding author upon request.

Conflicts of Interest

The authors declare that they have no conflicts of interest.

Acknowledgments

This work was supported by the National Natural Science Foundations of China under Grant nos. 11602035, 11402125, 61601062, and 61801054 and the Natural Science Foundation of Jiangsu Province under Grant no. BK20191451.

References

- [1] A. P. Kuznetsov, S. P. Kuznetsov, E. Mosekilde, and N. V. Stankevich, "Co-existing hidden attractors in a radio-physical system," *Journal of Physics A: Mathematical and Theoretical*, vol. 48, no. 12, Article ID 125101, 2015.

- [2] L. Chua, "Memristor-the missing circuit element," *IEEE Transactions on Circuit Theory*, vol. 18, no. 5, pp. 507–519, 1971.
- [3] B. Bao, T. Jiang, Q. Xu, M. Chen, H. Wu, and Y. Hu, "Coexisting infinitely many attractors in active band-pass filter-based memristive circuit," *Nonlinear Dynamics*, vol. 86, no. 3, pp. 1711–1723, 2016.
- [4] B. Muthuswamy and L. O. Chua, "Simplest chaotic circuit," *International Journal of Bifurcation and Chaos*, vol. 20, no. 5, pp. 1567–1580, 2010.
- [5] H. Wu, B. Bao, Z. Liu, Q. Xu, and P. Jiang, "Chaotic and periodic bursting phenomena in a memristive Wien-bridge oscillator," *Nonlinear Dynamics*, vol. 83, no. 1-2, pp. 893–903, 2016.
- [6] B.-C. Bao, M. Chen, H. Bao, and Q. Xu, "Extreme multi-stability in a memristive circuit," *Electronics Letters*, vol. 52, no. 12, pp. 1008–1010, 2016.
- [7] Q. Li, H. Zeng, and J. Li, "Hyperchaos in a 4D memristive circuit with infinitely many stable equilibria," *Nonlinear Dynamics*, vol. 79, no. 4, pp. 2295–2308, 2015.
- [8] N. H. Alombah, H. Fotsin, E. B. M. Ngouonkadi, and T. Nguazon, "Dynamics, analysis and implementation of a multi-scroll memristor-based chaotic circuit," *International Journal of Bifurcation and Chaos*, vol. 26, no. 8, Article ID 1650128, 2016.
- [9] M. Kountchou, P. Louodop, S. Bowong, H. Fotsin, and J. Kurths, "Optimal synchronization of a memristive chaotic circuit," *International Journal of Bifurcation and Chaos*, vol. 26, no. 6, Article ID 1650093, 2016.
- [10] Q. Xu, Y. Lin, B. Bao, and M. Chen, "Multiple attractors in a non-ideal active voltage-controlled memristor based Chua's circuit," *Chaos, Solitons & Fractals*, vol. 83, pp. 186–200, 2016.
- [11] B. C. Bao, P. Y. Wu, H. Bao, Q. Xu, and M. Chen, "Numerical and experimental confirmations of quasi-periodic behavior and chaotic bursting in third-order autonomous memristive oscillator," *Chaos, Solitons & Fractals*, vol. 106, pp. 161–170, 2018.
- [12] I. Petras, "Fractional-order memristor-based Chua's circuit," *IEEE Transactions on Circuits and Systems II: Express Briefs*, vol. 57, no. 12, pp. 975–979, 2010.
- [13] J. Kengne, G. D. Leutcho, and A. N. Kengnou Telem, "Reversals of period doubling, coexisting multiple attractors, and offset boosting in a novel memristive diode bridge-based hyperjerk circuit," *Analog Integrated Circuits and Signal Processing*, pp. 1–21, 2018.
- [14] J. Ma, Z. Chen, Z. Wang, and Q. Zhang, "A four-wing hyperchaotic attractor generated from a 4-D memristive system with a line equilibrium," *Nonlinear Dynamics*, vol. 81, no. 3, pp. 1275–1288, 2015.
- [15] L. Zhou, C. Wang, and L. Zhou, "Generating hyperchaotic multi-wing attractor in a 4D memristive circuit," *Nonlinear Dynamics*, vol. 85, no. 4, pp. 2653–2663, 2016.
- [16] J. Kengne, Z. Njitacke Tabekoueng, V. Nguomkam Negou, and A. Negou, "Periodicity, chaos, and multiple attractors in a memristor-based Shinriki's circuit," *Chaos: An Interdisciplinary Journal of Nonlinear Science*, vol. 25, no. 10, Article ID 103126, 2015.
- [17] Z. T. Njitacke, J. Kengne, H. B. Fotsin, A. N. Negou, and D. Tchiotso, "Coexistence of multiple attractors and crisis route to chaos in a novel memristive diode bridge-based Jerk circuit," *Chaos Solitons & Fractals*, vol. 91, pp. 180–197, 2016.
- [18] P. Saha, D. C. Saha, A. Ray, and A. R. Chowdhury, "Memristive non-linear system and hidden attractor," *The European Physical Journal Special Topics*, vol. 224, no. 8, pp. 1563–1574, 2015.
- [19] B. C. Bao, A. H. Hu, H. Bao, Q. Xu, M. Chen, and H. G. Wu, "Three-dimensional memristive hindmarsh-rose neuron model with hidden coexisting asymmetric behaviors," *Complexity*, vol. 2018, Article ID 3872573, 11 pages, 2018.
- [20] A. I. Ahamed and M. Lakshmanan, "Non-smooth bifurcations, transient hyper-chaos and hyperchaotic beats in a memristive Murali-Lakshmanan-Chua circuit," *International Journal of Bifurcation and Chaos*, vol. 23, no. 6, Article ID 1350098, 2013.
- [21] R. Barboza and L. O. Chua, "The four-element Chua's circuit," *International Journal of Bifurcation and Chaos*, vol. 18, no. 4, pp. 943–955, 2008.
- [22] D. B. Strukov, G. S. Snider, D. R. Stewart, and R. S. Williams, "The missing memristor found," *Nature*, vol. 453, no. 7191, pp. 80–83, 2008.
- [23] I. Podlubny, *Fractional Differential Equations*, Academic Press, Cambridge, MA, USA, 1999.
- [24] Y. J. Yu and Z. H. Wang, "A fractional-order memristor model and the fingerprint of the simple series circuits including a fractional-order memristor," *Acta. Phys. Sinica*, vol. 64, no. 23, Article ID 238401, 2015.
- [25] M. E. Fouda and A. G. Radwanon, "The fractional-order memristor model," *Journal of Fractional Calculus and Applications*, vol. 4, no. 1, pp. 1–7, 2013.
- [26] D. Cafagna and G. Grassi, "On the simplest fractional-order memristor-based chaotic system," *Nonlinear Dynamics*, vol. 70, no. 2, pp. 1185–1197, 2012.
- [27] M.-F. Danca, W. K. S. Tang, and G. Chen, "Suppressing chaos in a simplest autonomous memristor-based circuit of fractional order by periodic impulses," *Chaos, Solitons & Fractals*, vol. 84, pp. 31–40, 2016.
- [28] R. Dogaru and L. O. Chua, "Edge of chaos and local activity domain of FitzHugh-Nagumo equation," *International Journal of Bifurcation and Chaos*, vol. 8, no. 2, pp. 211–257, 1998.
- [29] R. Dogaru and L. O. Chua, "Edge of chaos and local activity domain of the Brusselator CNN," *International Journal of Bifurcation and Chaos*, vol. 8, no. 6, pp. 1107–1130, 1998.
- [30] P. Jin, G. Wang, H. H.-C. Iu, and T. Fernando, "A locally active memristor and its application in a chaotic circuit," *IEEE Transactions on Circuits and Systems II: Express Briefs*, vol. 65, no. 2, pp. 246–250, 2018.
- [31] D. Bialek, V. Bialek, and Z. Bialek, "Interpreting area of pinched memristor hysteresis loop," *Electronics Letters*, vol. 50, no. 2, pp. 74–75, 2014.
- [32] S. Westerlund and L. Ekstam, "Capacitor theory," *IEEE Transactions on Dielectrics and Electrical Insulation*, vol. 1, no. 5, pp. 826–839, 1994.
- [33] E. Ahmed, A. M. A. El-Sayed, and H. A. A. El-Saka, "Equilibrium points, stability and numerical solutions of fractional-order predator-prey and rabies models," *Journal of Mathematical Analysis and Applications*, vol. 325, no. 1, pp. 542–553, 2007.
- [34] H. A. El-Saka, E. Ahmed, M. I. Shehata, and A. M. A. El-Sayed, "On stability, persistence, and Hopf bifurcation in fractional order dynamical systems," *Nonlinear Dynamics*, vol. 56, no. 1–2, pp. 121–126, 2009.
- [35] L. Chua, M. Komuro, and T. Matsumoto, "The double scroll family," *IEEE Transactions on Circuits and Systems*, vol. 33, no. 11, pp. 1072–1118, 1986.
- [36] M.-F. Danca and N. Kuznetsov, "Matlab code for Lyapunov exponents of fractional-order systems," *International Journal of Bifurcation and Chaos*, vol. 28, no. 5, Article ID 1850067, 2018.

- [37] C. A. Monje, Y. Q. Chen, B. M. Vinagre, D. Y. Xue, and V. Feliu, *Fractional-Order Systems and Controls: Fundamentals and Applications*, Springer-Verlag, London, UK, 2010.
- [38] C. Li and W. Deng, "Remarks on fractional derivatives," *Applied Mathematics and Computation*, vol. 187, no. 2, pp. 777–784, 2007.
- [39] L. O. Chua, "Local activity is the origin of complexity," *International Journal of Bifurcation and Chaos*, vol. 15, no. 11, pp. 3435–3456, 2005.

Research Article

A Fractional-Order Model for Zika Virus Infection with Multiple Delays

R. Rakkiyappan ¹, V. Preethi Latha,¹ and Fathalla A. Rihan ²

¹Department of Mathematics, Bharathiar University, Coimbatore-641 046, Tamil Nadu, India

²Department of Mathematical Sciences, College of Science, UAE University, Al Ain 15551, UAE

Correspondence should be addressed to Fathalla A. Rihan; frihan@uaeu.ac.ae

Received 19 August 2019; Revised 21 October 2019; Accepted 31 October 2019; Published 14 November 2019

Guest Editor: Serdar Çiçek

Copyright © 2019 R. Rakkiyappan et al. This is an open access article distributed under the Creative Commons Attribution License, which permits unrestricted use, distribution, and reproduction in any medium, provided the original work is properly cited.

Time delays and fractional order play a vital role in biological systems with memory. In this paper, we propose an epidemic model for Zika virus infection using delay differential equations with fractional order. Multiple time delays are incorporated in the model to consider the latency of the infection in a vector and the latency of the infection in the infected host. We investigate the necessary and sufficient conditions for stability of the steady states and Hopf bifurcation with respect to three time delays τ_1 , τ_2 , and τ_3 . The model undergoes a Hopf bifurcation at the threshold parameters τ_1^* , τ_2^* , and τ_3^* . Some numerical simulations are given to show the effectiveness of obtained results. The numerical simulations confirm that combination of fractional order and time delays in the epidemic model effectively enriches the dynamics and strengthens the stability condition of the model.

1. Introduction

Zika infection is a mosquito-borne disease, transmitted to humans through the bite of an infected *Aedes* mosquito. It was first discovered in Uganda in 1947 in rhesus monkey. The first human cases were reported in Nigeria in 1954. Zika was thought to cause mild symptoms in humans, including mild fever, skin rashes, conjunctivitis, muscle and joint pain, and headache, which lasts for three to twelve days normally. However, the World Health Organization (WHO) has concluded that Zika virus infection during pregnancy is also a cause of congenital brain abnormalities, including microcephaly [1]. Moreover, Zika virus is a trigger of Guillain-Barre syndrome [2]. There is no doubt that mathematical modeling of Zika infection plays an important role in gaining understanding of transmission of disease and to predict the behaviour of any outbreak [3, 4].

Recently, mathematical modeling of dynamics of infectious diseases, using differential equations with memory (time-delay terms or fractional orders), has attracted much attention of many researchers (see, e.g., [5] and references therein). Time delay in models of population dynamics and

in particular in macroscopic models of the immune response are natural and common [6]. Naturally, time delay or memory is an unavoidable factor in dynamics of most real-life phenomena. Time delay has influence on dynamical behaviours of biological systems in various aspects. Therefore, considering time delays in the investigation of biological systems is significant in both theoretical and practical point of views. In fact, when immune system works against the non-self-cells, it may take some time (time lag) to interact with the pathogen. Therefore, time delays cannot be ignored in models for immune response. Accordingly, the analysis of dynamical properties of system with time delays is important (see [5, 7–12]). Dengue fever is analyzed in [13], using a system of four nonlinear differential equations with two time delays. In [12], the authors considered the vector-borne epidemic model with time delay. The authors intensively discussed the impact of time delay in the host-to-vector transmission term that can destabilize the system. Periodic solutions can also be raised through Hopf bifurcation.

In the existing literature, most of the biological problems are studied through the integer-order mathematical modeling

by using ordinary, partial, and delay differential equations [9, 10, 14]. In the last few decades, fractional-order models have been incorporated in several areas of science, engineering, applied mathematics, economics, and bioengineering [15–20]. One advantage of the fractional-order differential equation is that they provide a powerful instrument for incorporation of memory and hereditary properties of the systems as opposed to the integer-order models, where such effects are neglected or difficult to incorporate. In addition, when fitting data, the fractional models have one more degree of freedom than the integer-order model (see [21]). Based on these advantages, some authors have developed interesting applications to investigate the dynamics of such fractional-order models with systems of memory [22–26]. In [5, 22], the authors studied fractional-order cancer immune systems. In [25], a fractional-order model for HIV with nonlinear incidence has been considered and stability for various equilibrium points has also been discussed. The authors in [27] investigated the dynamics of Ebola virus with time delay and fractional order and reported that combination of time delay and fractional order can effectively enrich the dynamics and strengthen the stability condition of the infection model. Analysis and dynamics of Zika transmission have been examined by many researchers (see, e.g., [3, 28, 29]). In [3], a mathematical model for transmission of Zika virus has been proposed with control measures of Zika virus. Stability properties of the Zika infection model have been investigated in [30]. The authors in [31] have compared the Zika infection model with dengue to show effect of the virus on population. The dynamical analysis of the SIS model is studied by considering bifurcation parameters in [32]. The authors [33] have discussed absence and presence of diffusion in the Zika virus disease model. The stability analysis and Hopf bifurcation point for various generalized epidemic models have been discussed in the literature [33–35]. However, the dynamics of fractional order with multiple time-delay models for Zika virus infection has not been yet studied in mathematical epidemiology.

Herein, we demonstrate that a nonlinear fractional-order differential equations model, with multiple time delays, can simulate the dynamics of Zika virus infection much more than the classical epidemic models. The application of fractional derivatives is in several cases justified because they provide a better model than integer-order derivative models do [36, 37]. One important feature of fractional derivatives is that they are nonlocal opposed to the local behaviour of integer derivatives. In this way, the next state of a fractional system depends not only upon its current state but also upon all of its historical states [38–40].

Motivated by the above discussion, in this paper, we investigate the dynamics of Zika virus infection with fractional order and time delays. In Section 2, we formulate the model and study the nonnegativity of the solutions. In Section 3, we investigate the asymptotic stability analysis and Hopf bifurcation properties by taking time-delay parameters as bifurcation parameters. Sufficient conditions are derived to ensure the asymptotic stability and Hopf bifurcation behaviours of the addressed model. Finally, some numerical simulations are provided with various

fractional orders and time delays to demonstrate the effectiveness of our theoretical findings in Section 4. We then conclude in Section 5.

Before we start analysis, we provide some useful preliminaries.

1.1. Preliminaries. Herein, we provide some basic definitions and properties of integration and differentiation with fractional-order (free order) α (see [41]).

Definition 1. Let $\alpha \in (0, \infty)$, the operator I_a^α on $L_1[a, b]$ is defined by

$$I_a^\alpha f(t) = \frac{1}{\Gamma(\alpha)} \int_a^t (t-s)^{\alpha-1} f(s) ds, \quad f \in L_1[a, b], t \in [a, b], \quad (1)$$

which is called the fractional integral (or Riemann–Liouville integral) of order α , where $I_a^0 = \text{Id}$ is the identity operator.

Definition 2. Let $\alpha \in [0, \infty)$ and $n = [\alpha]$, where $[x] = \min\{k \in \mathbb{Z} : k \geq x\}$, and the operator ${}_{\text{RL}}D_a^\alpha$ is defined for $f \in L_1[a, b]$ by

$${}_{\text{RL}}D_a^\alpha f(t) = \frac{1}{\Gamma(n-\alpha)} \left(\frac{d}{dt}\right)^n \int_a^t (t-s)^{n-\alpha-1} f(s) ds, \quad (2)$$

which is called the Riemann–Liouville fractional derivative of order α .

Definition 3. Let $\alpha \in [0, \infty)$ and f is such that $I_a^{n-\alpha} f^{(n)}$ exists, where $n = [\alpha]$, $f \in A^n[a, b]$ (the set of all function $f : [a, b] \rightarrow \mathbb{R}$ provided that $f^{(n-1)}$ be absolutely continuous), then we define the operator ${}_CD_a^\alpha$ by

$${}_CD_a^\alpha f(t) = \frac{1}{\Gamma(n-\alpha)} \int_a^t (t-s)^{n-\alpha-1} f^{(n)}(s) ds, \quad (3)$$

which exists for almost everywhere $x \in [a, b]$. The operator ${}_CD_a^\alpha f(t)$ is called the Caputo fractional derivative of order α . In particular, when $0 < \alpha \leq 1$, we have

$${}_CD_a^\alpha f(t) = \frac{1}{\Gamma(1-\alpha)} \int_a^t \frac{f'(s)}{(t-s)^\alpha} ds. \quad (4)$$

Remark 1. Let $\beta, \gamma \in \mathbb{R}_+$ and $\alpha \in (0, 1)$. Then,

- (i) If $I_a^\beta : L_1 \rightarrow L_1$ and if $f(t) \in L_1$, then $I_a^\beta I_a^\gamma f(t) = I_a^{\beta+\gamma} f(t)$
- (ii) $\lim_{\beta \rightarrow n} I_a^\beta f(x) = I_a^n f(t)$ uniformly on $[a, b]$, $n = 1, 2, 3, \dots$, where $I_a^1 f(t) = \int_a^t f(s) ds$
- (iii) $\lim_{\beta \rightarrow 0} I_a^\beta f(t) = f(t)$ weakly
- (iv) If $f(t)$ is absolutely continuous on $[a, b]$, then $\lim_{\alpha \rightarrow 1} D_a^\alpha f(t) = df(t)/dt$
- (v) Thus, $D_a^\alpha f(t) = (d/dt)I_a^{1-\alpha} f(t)$ (Riemann–Liouville sense) and $D_a^\alpha f(t) = I_a^{1-\alpha}(d/dt)f(t)$ (Caputo sense)

Remark 2. We notice that the fractional derivatives involve an integration and are nonlocal operators, which can be used for modeling systems with memory.

We should mention here that Caputo's definition of fractional derivative is a modification of the Riemann–Liouville definition and has the advantage of dealing with initial value problems in a proper way.

2. Model Formulation

The literature reveals that most mathematical modeling of biological systems with memory is based either on delay differential equations (DDEs) with integer-order or fractional-order differential equations without a delay. However, fractional-order calculus is more suitable, than integer-order ones, in modeling biological systems with intrinsic memory and long-range interactions such as epidemic evolution systems [42]. Modeling of such systems by fractional-order differential equations has more advantages than classical integer-order mathematical modeling, in which the effects of memory or long-range interactions are neglected. Indeed, memory effects play an essential role in the spreading of diseases. Including memory effects in the susceptible-infected-recovered (SIR) epidemic models seems very appropriate for such an investigation (see Remark 2). Herein, we investigate the impact of combining both time delays and fractional order in an epidemic model for Zika virus infection.

The underlying model is governed by a system of fractional-order differential equations with multiple time delays for Zika virus infection. The model includes the dynamics of susceptible individuals, $H_S(t)$, with Zika symptoms and infected portion, $H_I(t)$, and recovered portion, $H_R(t)$, individuals recovered from Zika, the susceptible mosquitoes, $M_S(t)$, in infected mosquitoes, $M_I(t)$. Thus, the total human population $N_H(t) = H_S(t) + H_I(t) + H_R(t)$. The overall vector (mosquito) population, at time t , is $N_m(t) = M_S(t) + M_I(t)$. Assume that β_h is the transmission rate from humans to mosquitoes. β_m is the transmission rate of Zika from the vector (mosquitoes) to humans. Natural death rate of host is denoted by d_h . The recruitment rate into susceptible population is denoted by λ_h . Natural death rate of vector is denoted by d_m . η is the recovery rate from treatment. λ_m is the recruitment rate into susceptible mosquito population. Also, γ is the average infectious period for humans. We use time delays in the model to consider the latency of the infection in a vector and the latency of the infection in an infected host. In our model, we consider time-delay τ_1 to represent the transferring of the infection from infected mosquitoes into suspected humans. The incubation period (time delay) τ_2 is incorporated to represent the time required for an individual/susceptible to become infectious, after becoming infected. τ_3 is the incubation period of susceptible mosquitoes to become infectious (see Figure 1). The memory of the earlier times, which are represented by time lags, could have less effect on the present situation, as compared to more recent times. However, it is expected that long-range memory,

represented by fractional order, effects decay in time more slowly than an exponential decay but can typically behave like a power-law damping function. The model then takes the following form:

$$\begin{aligned} D^\alpha H_S(t) &= \lambda_h - \beta_h H_S(t - \tau_1) M_I(t - \tau_1) \\ &\quad - \beta_h H_S(t - \tau_2) H_I(t - \tau_2) - d_h H_S, \\ D^\alpha H_I(t) &= \beta_h H_S(t - \tau_1) M_I(t - \tau_1) \\ &\quad + \beta_h H_S(t - \tau_2) H_I(t - \tau_2) - d_h H_I - \gamma H_I, \\ D^\alpha H_R(t) &= \gamma H_I - d_h H_R + \eta H_I, \\ D^\alpha M_S(t) &= \lambda_m - \beta_m M_S(t - \tau_3) H_I(t - \tau_3) - d_m M_S, \\ D^\alpha M_I(t) &= \beta_m M_S(t - \tau_3) H_I(t - \tau_3) - d_m M_I. \end{aligned} \quad (5)$$

The initial conditions for system (5) should be provided so that $H_R(0) = H_{R_0}$, $H_S(t) = \phi_1(t)$, $H_I(t) = \phi_2(t)$, $M_S(t) = \phi_3(t)$, and $M_I(t) = \phi_4(t)$, when $t \in [\max\{-\tau_i\}, 0]$ for $i = 1, 2, 3$, time lag, $\tau_i \geq 0$.

Remark 3. The fractional derivative $\alpha \in (0, 1]$ is defined by Caputo sense (4), so that introducing a convolution integral with a power-law memory kernel is useful to describe memory effects in dynamical systems. The decaying rate of the memory kernel (a time correlation function) depends on α . A lower value of α corresponds to more slowly decaying time-correlation functions (long memory). Therefore, as $\alpha \rightarrow 1$, the influence of memory decreases.

2.1. Nonnegative Solution. Since model (5) monitors the dynamics of human populations, therefore, all the parameters are assumed to be nonnegative. Furthermore, it can be shown that all state variables of the model are nonnegative and bounded for all time $t \geq 0$ (see [42]).

Lemma 1. *The closed set $\Omega = \{(H_S, H_I, H_R, M_S, M_I) \in \mathbb{R}_+^5 : H_S + H_I + H_R \leq (\lambda_h/d_h), M_S + M_I \leq (\lambda_m/d_m)\}$ is positively invariant with respect to model (5).*

Proof. In order to prove the nonnegativity of system (5), it is assumed that there exists a $t_* > t_0$ such that $H_S(t_*) = 0$ and $H_S(t) < 0$ for $t \in (t_*, t_1]$ where t_1 is sufficiently close to t_* . If $H_S(t) = 0$,

$$D^\alpha H_S(t_*) = \lambda_h. \quad (6)$$

Thus, one obtains $D^\alpha H_S(t) > 0$ for all $t \in [t_*, t_1]$ and $D^\alpha H_S > \epsilon H_S$, where $\epsilon > 0$. Hence, one derives

$$H_S(t) > H_S(t_*) E_\alpha(\epsilon(t - t_*)^\alpha), \quad t \in [t_*, t_1]. \quad (7)$$

Since $H_S(t_*) = 0$, one gets $H_S(t) > 0$, $t \in [t_*, t_1]$, which contradicts the assumption. Hence, $H_S(t) > 0$ for any $t > t_0$. In the same manner, we have $H_I(t), H_R(t), M_S(t)$, and $M_I(t)$ are nonnegative.

To show that the system is bounded, we add the first three equations of System (5), and we get

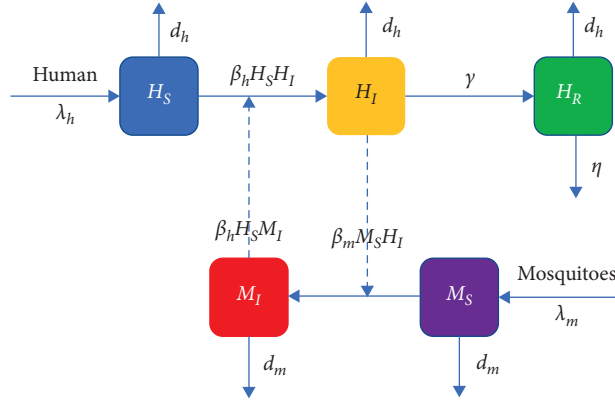


FIGURE 1: Transmission and dynamics of Zika virus infection between the host (human) and the vector (mosquitoes).

$$D^\alpha (H_S + H_I + H_R) = \lambda_h - d_h H_S - d_h H_I - d_h H_R + \eta H_I. \quad (8)$$

We know that all parameters value is positive, and one can obtain

$$D^\alpha (H_S + H_I + H_R) \leq \lambda_h - d_h (H_S + H_I + H_R), \quad (9)$$

$$D^\alpha N_H \leq \lambda_h - d_h N_H,$$

where $N_H = H_S(t) + H_I(t) + H_R(t)$, and solving this equation, we have

$$N_H(t) \leq \left(\frac{\lambda_h}{d_h} + N_H(0) \right) E_\alpha(-d_h t^\alpha) + \frac{\lambda_h}{d_h}. \quad (10)$$

The solution is given by $N_H(t) = N_H(0)E_{\alpha,1}(-d_h t^\alpha) + \lambda_h t^\alpha E_{\alpha,\alpha+1}(-d_h t^\alpha)$, where $E_{\alpha,\beta}$ is the Mittag-Leffler function. Considering the fact that Mittag-Leffler function has an asymptotic behaviour,

$$E_{\alpha,\beta}(z) \sim -\sum_{K=1}^{\omega} \frac{z^{-K}}{\Gamma(\beta - \alpha K)} + \mathcal{O}(|z|^{-1-\omega}), \quad (11)$$

$$|z| \longrightarrow \infty, \quad \frac{\alpha\pi}{2} < |\arg(z)| \leq \pi.$$

One can observe that $N_H(t) \longrightarrow \lambda_h/d_h$ as $t \longrightarrow \infty$. The proof of the mosquitoes (vector) population is similar to human (host) population, and we obtain $N_M(t) \longrightarrow \lambda_m/d_m$. Therefore, all solutions of the model with initial conditions in Ω remain bounded in the positively invariant region Ω for all $t \in [0, \infty)$. The region Ω is positively invariant with respect to model (5). \square

The equilibrium points (steady states) are obtained by setting $D^\alpha H_S = D^\alpha H_I = D^\alpha H_R = D^\alpha M_S = D^\alpha M_I = 0$, in model (5). The model has two equilibrium points: (i) disease-free equilibrium point $E^0 = (H_S^0, H_I^0, H_R^0, M_I^0, M_S^0) = ((\lambda_h/d_h), 0, 0, (\lambda_m/d_m), 0)$ and (ii) endemic steady state E^* , which is

$$E^* \left(\frac{\lambda_h}{\beta_h (\beta_m \lambda_m H_I^*/d_m (\beta_m H_I^* + d_m)) + \beta_h H_I^* + d_h}, \right. \quad (12)$$

$$H_I^*, \frac{H_I^* (\eta + \gamma)}{d_h}, \frac{\lambda_m}{\beta_m H_I^* + d_m}, \frac{\beta_m \lambda_m H_I^*}{d_m (\beta_m H_I^* + d_m)} \left. \right).$$

Here, H_I^* is the positive root of the following equation:

$$\beta_h \left(\frac{\lambda_h}{\beta_h (\beta_m \lambda_m H_I^*/d_m (\beta_m H_I^* + d_m)) + \beta_h H_I^* + d_h} \frac{\beta_m \lambda_m H_I^*}{d_m (\beta_m H_I^* + d_m)} \right) + \quad (13)$$

$$\beta_h \left(\frac{\lambda_h}{\beta_h (\beta_m \lambda_m H_I^*/d_m (\beta_m H_I^* + d_m)) + \beta_h H_I^* + d_h} H_I^* \right) - d_h H_I^* - \gamma H_I^* = 0.$$

3. Stability and Bifurcation Analysis

To study the stability of model (5), suppose $E^* (H_S^*, H_I^*, H_R^*, M_S^*, M_I^*)$ is the steady state of the linearized system:

$$\begin{aligned}
D^\alpha H_S(t) &= -\beta_h H_S^* M_I(t - \tau_1) - \beta_h M_I^* H_S(t - \tau_1) - \beta_h H_S^* H_I(t - \tau_2) - \beta_h H_I^* H_S(t - \tau_2) - d_h H_S, \\
D^\alpha H_I(t) &= \beta_h H_S^* M_I(t - \tau_1) + \beta_h M_I^* H_S(t - \tau_1) + \beta_h H_S^* H_I(t - \tau_2) + \beta_h H_I^* H_S(t - \tau_2) - d_h H_I - \gamma H_I, \\
D^\alpha H_R(t) &= \gamma H_I + \eta H_I - d_h H_R, \\
D^\alpha M_S(t) &= -\beta_m M_S^* H_I(t - \tau_3) - \beta_m H_I^* M_S(t - \tau_3) - d_m M_S, \\
D^\alpha M_I(t) &= \beta_m M_S^* H_I(t - \tau_3) + \beta_m H_I^* M_S(t - \tau_3) - d_m M_I.
\end{aligned} \tag{14}$$

Taking Laplace transform [43] on both sides of the linearized system (14), we obtain

$$\begin{aligned}
s^\alpha X_1(s) &= s^{\alpha-1} \varphi_1(0) + \beta_h H_S^* e^{-s\tau_1} \left[-X_5(s) - \int_{-\tau_1}^0 e^{-st} \varphi_5(t) dt \right] \\
&\quad + \beta_h M_I^* e^{-s\tau_1} \left[-X_1(s) - \int_{-\tau_1}^0 e^{-st} \varphi_1(t) dt \right] + \beta_h H_S^* e^{-s\tau_2} \left[-X_2(s) - \int_{-\tau_2}^0 e^{-st} \varphi_2(t) dt \right] \\
&\quad + \beta_h H_I^* e^{-s\tau_2} \left[-X_1(s) - \int_{-\tau_2}^0 e^{-st} \varphi_1(t) dt \right] - d_h X_1(s), \\
s^\alpha X_2(s) &= s^{\alpha-1} \varphi_2(0) + \beta_h H_S^* e^{-s\tau_1} \left[X_5(s) + \int_{-\tau_1}^0 e^{-st} \varphi_5(t) dt \right] \\
&\quad + \beta_h M_I^* e^{-s\tau_1} \left[X_1(s) + \int_{-\tau_1}^0 e^{-st} \varphi_1(t) dt \right] + \beta_h H_S^* e^{-s\tau_2} \left[X_2(s) + \int_{-\tau_2}^0 e^{-st} \varphi_2(t) dt \right] \\
&\quad + \beta_h H_I^* e^{-s\tau_2} \left[X_1(s) + \int_{-\tau_2}^0 e^{-st} \varphi_1(t) dt \right] - d_h X_2(s) - \gamma X_2(s), \\
s^\alpha X_3(s) &= s^{\alpha-1} \varphi_3(0) + \gamma X_2(s) + \eta X_2(s) - d_h X_3(s), \\
s^\alpha X_4(s) &= s^{\alpha-1} \varphi_4(0) + \beta_m M_S^* e^{-s\tau_3} \left[-X_2(s) - \int_{-\tau_3}^0 e^{-st} \varphi_2(t) dt \right] \\
&\quad + \beta_m H_I^* e^{-s\tau_3} \left[-X_4(s) - \int_{-\tau_3}^0 e^{-st} \varphi_4(t) dt \right] - d_m X_4(s), \\
s^\alpha X_5(s) &= s^{\alpha-1} \varphi_5(0) + \beta_m M_S^* e^{-s\tau_3} \left[X_2(s) + \int_{-\tau_3}^0 e^{-st} \varphi_2(t) dt \right] \\
&\quad + \beta_m H_I^* e^{-s\tau_3} \left[X_4(s) + \int_{-\tau_3}^0 e^{-st} \varphi_4(t) dt \right] - d_m X_5(s),
\end{aligned} \tag{15}$$

where $X_1(s)$, $X_2(s)$, $X_3(s)$, $X_4(s)$, and $X_5(s)$ are Laplace transforms of H_S , H_I , H_R , M_S , and M_I , respectively, with $X_1(s) = \mathcal{L}\{H_S(t)\}$, $X_2(s) = \mathcal{L}\{H_I(t)\}$, $X_3(s) = \mathcal{L}\{H_R(t)\}$, $X_4(s) = \mathcal{L}\{M_S(t)\}$, and $X_5(s) = \mathcal{L}\{M_I(t)\}$. Then, (15) can be written in the following matrix form as

$$\Delta(s) \begin{pmatrix} X_1(s) \\ X_2(s) \\ X_3(s) \\ X_4(s) \\ X_5(s) \end{pmatrix} = \begin{pmatrix} k_1(s) \\ k_2(s) \\ k_3(s) \\ k_4(s) \\ k_5(s) \end{pmatrix}, \tag{16}$$

in which

$$\Delta(s) = \begin{pmatrix} s^\alpha + a_1 e^{-s\tau_1} + a_2 e^{-s\tau_2} + a_3 & a_4 e^{-s\tau_2} & 0 & 0 & a_4 e^{-s\tau_1} \\ -a_1 e^{-s\tau_1} - a_2 e^{-s\tau_2} & s^\alpha - a_4 e^{-s\tau_2} + a_5 & 0 & 0 & -a_4 e^{-s\tau_1} \\ 0 & a_6 & s^\alpha + a_3 & 0 & 0 \\ 0 & a_7 e^{-s\tau_3} & 0 & s^\alpha + a_8 e^{-s\tau_3} + a_9 & 0 \\ 0 & -a_7 e^{-s\tau_3} & 0 & -a_8 e^{-s\tau_3} & s^\alpha + a_9 \end{pmatrix},$$

$$k_1(s) = s^{\alpha-1} \varphi_1(0) - \beta_h e^{-s\tau_1} H_S^* \int_{-\tau_1}^0 e^{-st} \varphi_5(t) dt - \beta_h e^{-s\tau_1} M_I^* \int_{-\tau_1}^0 e^{-st} \varphi_1(t) dt$$

$$- \beta_h e^{-s\tau_2} H_S^* \int_{-\tau_2}^0 e^{-st} \varphi_2(t) dt - \beta_h e^{-s\tau_2} H_I^* \int_{-\tau_2}^0 e^{-st} \varphi_1(t) dt,$$

$$k_2(s) = s^{\alpha-1} \varphi_2(0) + \beta_h e^{-s\tau_1} H_S^* \int_{-\tau_1}^0 e^{-st} \varphi_5(t) dt + \beta_h e^{-s\tau_1} M_I^* \int_{-\tau_1}^0 e^{-st} \varphi_1(t) dt$$

$$+ \beta_h e^{-s\tau_2} H_S^* \int_{-\tau_2}^0 e^{-st} \varphi_2(t) dt + \beta_h e^{-s\tau_2} H_I^* \int_{-\tau_2}^0 e^{-st} \varphi_1(t) dt,$$

$$k_3(s) = s^{\alpha-1} \varphi_3(0),$$

$$k_4(s) = s^{\alpha-1} \varphi_4(0) - \beta_m M_S^* e^{-s\tau_3} \int_{-\tau_3}^0 e^{-st} \varphi_2(t) dt - \beta_m e^{-s\tau_3} H_I^* \int_{-\tau_3}^0 e^{-st} \varphi_4(t) dt,$$

$$k_5(s) = s^{\alpha-1} \varphi_5(0) + \beta_m M_S^* e^{-s\tau_3} \int_{-\tau_3}^0 e^{-st} \varphi_2(t) dt + \beta_m e^{-s\tau_3} H_I^* \int_{-\tau_3}^0 e^{-st} \varphi_4(t) dt,$$

where $a_1 = \beta_h M_I^*$, $a_2 = \beta_h H_I^*$, $a_3 = d_h$, $a_4 = \beta_h H_S^*$, $a_5 = d_h + \gamma$, $a_6 = -\eta - \gamma$, $a_7 = \beta_m M_S^*$, $a_8 = \beta_m H_I^*$, and $a_9 = d_m$ and $\Delta(s)$ is considered as the characteristic matrix of system (5). The characteristic polynomial is then

$$\begin{aligned} \mathcal{P}(s) &= \mathbb{P}_1(s) + \mathbb{P}_2(s)e^{-s\tau_1} + \mathbb{P}_3(s)e^{-s\tau_2} + \mathbb{P}_4(s)e^{-s\tau_3} \\ &+ \mathbb{P}_5(s)e^{-2s\tau_1} + \mathbb{P}_6(s)e^{-2s\tau_2} \\ &+ \mathbb{P}_7(s)e^{-s(\tau_1+\tau_2)} + \mathbb{P}_8(s)e^{-s(\tau_2+\tau_3)} \\ &+ \mathbb{P}_9(s)e^{-s(\tau_1+\tau_3)} + \mathbb{P}_{10}(s)e^{-2s\tau_1-s\tau_3} \\ &+ \mathbb{P}_{11}(s)e^{-2s\tau_2-s\tau_3} + \mathbb{P}_{12}(s)e^{-s(\tau_1+\tau_2+\tau_3)}. \end{aligned} \quad (18)$$

The coefficients $\mathbb{P}_i(s)$, $i = 1, \dots, 12$, are estimated by Mathematica and given in Appendix.

Case 1. $\tau_1 > 0$, $\tau_2 = 0$, and $\tau_3 = 0$.

When $\tau_1 > 0$, $\tau_2 = 0$, and $\tau_3 = 0$, the characteristic equation (18) becomes

$$\mathcal{P}_1(s) + \mathcal{P}_2(s)e^{-s\tau_1} + \mathcal{P}_3(s)e^{-2s\tau_1} = 0, \quad (19)$$

where

$$\begin{aligned} \mathcal{P}_1(s) &= \mathbb{P}_1(s) + \mathbb{P}_3(s) + \mathbb{P}_4(s) + \mathbb{P}_6(s) + \mathbb{P}_8(s) + \mathbb{P}_{11}(s) \\ &= s^{5\alpha} + D_1 s^{4\alpha} + D_2 s^{3\alpha} + D_3 s^{2\alpha} + D_4 s^\alpha + D_5, \\ \mathcal{P}_2(s) &= \mathbb{P}_2(s) + \mathbb{P}_7(s) + \mathbb{P}_9(s) + \mathbb{P}_{12}(s) \\ &= G_1 s^{4\alpha} + G_2 s^{3\alpha} + G_3 s^{2\alpha} + G_4 s^\alpha + G_5, \\ \mathcal{P}_3(s) &= \mathbb{P}_5(s) + \mathbb{P}_{10}(s) = H_1 s^{3\alpha} + H_2 s^{2\alpha} + H_3 s^\alpha + H_4. \end{aligned} \quad (20)$$

Now, we prove that the characteristic equation (19) has no pure imaginary roots for any $\tau_1 > 0$. Assume that characteristic equation (19) has pure imaginary root, and let it be $s = i\xi = \xi(\cos(\pi/2) + i\sin(\pi/2))$, $\xi > 0$. If we multiply $e^{s\tau_1}$ on both sides of equation (19), we get

$$\mathcal{P}_1(s)e^{s\tau_1} + \mathcal{P}_2(s) + \mathcal{P}_3(s)e^{-s\tau_1} = 0. \quad (21)$$

Now, we substitute the expression of s into (21) to have

$$(\mathcal{A}_1 + i\mathcal{B}_1)e^{s\tau_1} + \mathcal{A}_2 + i\mathcal{B}_2 + (\mathcal{A}_3 + i\mathcal{B}_3)e^{-s\tau_1} = 0. \quad (22)$$

The coefficients $\mathcal{A}_1, \mathcal{A}_2$, and \mathcal{A}_3 and $\mathcal{B}_1, \mathcal{B}_2$, and \mathcal{B}_3 are real and imaginary parts of $\mathcal{P}_1(s)$, $\mathcal{P}_2(s)$, and $\mathcal{P}_3(s)$, respectively, so that

$$\begin{aligned}
\mathcal{A}_1 &= \xi^{5\alpha} \cos \frac{5\alpha\pi}{2} + D_1 \xi^{4\alpha} \cos \frac{4\alpha\pi}{2} + D_2 \xi^{3\alpha} \cos \frac{3\alpha\pi}{2} \\
&\quad + D_3 \xi^{2\alpha} \cos \frac{2\alpha\pi}{2} + D_4 \xi^\alpha \cos \frac{\alpha\pi}{2} + D_5, \\
\mathcal{B}_1 &= \xi^{5\alpha} \sin \frac{5\alpha\pi}{2} + D_1 \xi^{4\alpha} \sin \frac{4\alpha\pi}{2} + D_2 \xi^{3\alpha} \sin \frac{3\alpha\pi}{2} \\
&\quad + D_3 \xi^{2\alpha} \sin \frac{2\alpha\pi}{2} + D_4 \xi^\alpha \sin \frac{\alpha\pi}{2}, \\
\mathcal{A}_2 &= G_1 \xi^{4\alpha} \cos \frac{4\alpha\pi}{2} + G_2 \xi^{3\alpha} \cos \frac{3\alpha\pi}{2} + G_3 \xi^{2\alpha} \cos \frac{2\alpha\pi}{2} \\
&\quad + G_4 \xi^\alpha \cos \frac{\alpha\pi}{2} + G_5, \\
\mathcal{B}_2 &= G_1 \xi^{4\alpha} \sin \frac{4\alpha\pi}{2} + G_2 \xi^{3\alpha} \sin \frac{3\alpha\pi}{2} + G_3 \xi^{2\alpha} \sin \frac{2\alpha\pi}{2} \\
&\quad + G_4 \xi^\alpha \sin \frac{\alpha\pi}{2}, \\
\mathcal{A}_3 &= H_1 \xi^{3\alpha} \cos \frac{3\alpha\pi}{2} + H_2 \xi^{2\alpha} \cos \frac{2\alpha\pi}{2} + H_3 \xi^\alpha \cos \frac{\alpha\pi}{2} + H_4, \\
\mathcal{B}_3 &= H_1 \xi^{3\alpha} \sin \frac{3\alpha\pi}{2} + H_2 \xi^{2\alpha} \sin \frac{2\alpha\pi}{2} + H_3 \xi^\alpha \sin \frac{\alpha\pi}{2}.
\end{aligned} \tag{23}$$

Separating real and imaginary parts yields

$$\begin{aligned}
\mathcal{A}_1 \cos \xi\tau_1 - \mathcal{B}_1 \sin \xi\tau_1 &= -(\mathcal{A}_3 \cos \xi\tau_1 + \mathcal{B}_3 \sin \xi\tau_1 + \mathcal{A}_2), \\
\mathcal{A}_1 \sin \xi\tau_1 - \mathcal{B}_1 \cos \xi\tau_1 &= -(\mathcal{B}_3 \cos \xi\tau_1 - \mathcal{A}_3 \sin \xi\tau_1 + \mathcal{B}_2).
\end{aligned} \tag{24}$$

It follows from (14) that

$$\begin{aligned}
\mathcal{A}_1^2 + \mathcal{B}_1^2 - \mathcal{A}_2^2 - \mathcal{B}_2^2 - \mathcal{A}_3^2 - \mathcal{B}_3^2 &= 2[\mathcal{B}_3(\mathcal{A}_2 \sin \xi\tau_1 \\
&\quad + \mathcal{B}_2 \cos \xi\tau_1) + \mathcal{A}_3(\mathcal{A}_2 \cos \xi\tau_1 - \mathcal{B}_2 \sin \xi\tau_1)].
\end{aligned} \tag{25}$$

Using the fact that $\cos^2 \theta + \sin^2 \theta = 1$, we have $\sin \xi\tau_1 = \sqrt{1 - \cos^2 \xi\tau_1}$, and then (25) can be written in the following form:

$$\frac{ds}{d\tau_1} = \frac{-s\mathcal{P}_1(s)e^{s\tau_1} + s\mathcal{P}_3(s)e^{-s\tau_1}}{\mathcal{P}'_1(s)e^{s\tau_1} + \tau_1\mathcal{P}_1(s)e^{s\tau_1} + \mathcal{P}'_2(s) + \mathcal{P}'_3(s)e^{-s\tau_1} - \tau_1\mathcal{P}_3(s)e^{-s\tau_1}} = \frac{M(s)}{N(s)}. \tag{32}$$

From (32), by some computation, we deduce that

$$\operatorname{Re} \left(\frac{ds}{d\tau_1} \right) \Big|_{\tau_1=\tau_1^*, \xi=\xi_0} = \frac{M_1 N_1 + M_2 N_2}{N_1^2 + N_2^2}, \tag{33}$$

$$\begin{aligned}
&[\mathcal{A}_1^2 + \mathcal{B}_1^2 - \mathcal{A}_2^2 - \mathcal{B}_2^2 - \mathcal{A}_3^2 - \mathcal{B}_3^2 - 2(\mathcal{B}_2\mathcal{B}_3 + \mathcal{A}_2\mathcal{A}_3)\cos \xi\tau_1]^2 \\
&= \left[2\sqrt{1 - \cos^2 \xi\tau_1} (\mathcal{B}_3\mathcal{A}_2 - \mathcal{A}_3\mathcal{B}_2) \right]^2.
\end{aligned} \tag{26}$$

It can be concluded from (26) that

$$\mathcal{Q}_1 \cos^2 \xi\tau + \mathcal{Q}_2 \cos \xi\tau + \mathcal{Q}_3 = 0, \tag{27}$$

where

$$\begin{aligned}
\mathcal{Q}_1 &= 4\mathcal{A}_2^2\mathcal{A}_3^2 + 4\mathcal{A}_3^2\mathcal{B}_2^2 + 4\mathcal{A}_2^2\mathcal{B}_3^2 + 4\mathcal{B}_2^2\mathcal{B}_3^2, \\
\mathcal{Q}_2 &= 4(\mathcal{B}_2\mathcal{B}_3 + \mathcal{A}_2\mathcal{A}_3)(-\mathcal{A}_1^2 - \mathcal{B}_1^2 + \mathcal{A}_2^2 + \mathcal{B}_2^2 + \mathcal{A}_3^2 + \mathcal{B}_3^2), \\
\mathcal{Q}_3 &= [\mathcal{A}_1^2 - (\mathcal{A}_2 - \mathcal{B}_3)^2 - (\mathcal{A}_3 - \mathcal{B}_1 + \mathcal{B}_2)(\mathcal{A}_3 + \mathcal{B}_2 + \mathcal{B}_1)] \\
&\quad \cdot [\mathcal{A}_1^2 - (\mathcal{A}_2 + \mathcal{B}_3)^2 - (\mathcal{A}_3 - \mathcal{B}_1 - \mathcal{B}_2)(\mathcal{A}_3 + \mathcal{B}_1) - \mathcal{B}_2].
\end{aligned} \tag{28}$$

The quadratic equation (27) has roots, so we can obtain the expression of $\cos \xi\tau_1$ and denote $\cos \xi\tau_1 = f_1(\xi)$, where $f_1(\xi)$ is a function of ξ .

Substituting the expression of $\cos \xi\tau_1 = \sqrt{1 - \sin^2 \xi\tau_1}$ into (27), we can get expression of $\sin \xi\tau_1$. Assume that $\sin \xi\tau_2 = f_2(\xi)$. Moreover, we have $f_1^2(\xi) + f_2^2(\xi) = 1$. Thus, it follows from $\cos \xi\tau_1 = f_1(\xi)$ that

$$\tau_1 = \frac{1}{\xi} [\arccos(f_1(\xi)) + 2k\pi], \quad k = 0, 1, 2, \dots \tag{29}$$

We suppose that $f_1^2(\xi) + f_2^2(\xi) = 1$ has at least one positive root, and thus, the bifurcation point is defined as

$$\tau_1^* = \min\{\tau_1^{(k)}\}, \quad k = 0, 1, 2, \dots \tag{30}$$

Now, differentiating equation (21) with respect to τ_1 , we obtain

$$\begin{aligned}
&\mathcal{P}'_1(s)e^{s\tau_1} \frac{ds}{d\tau_1} + \mathcal{P}_1 e^{s\tau_1} \left(\tau_1 \frac{ds}{d\tau_1} + s \right) + \mathcal{P}'_2(s) \frac{ds}{d\tau_1} \\
&\quad + \mathcal{P}'_3(s)e^{-s\tau_1} \frac{ds}{d\tau_1} + \mathcal{P}_3 e^{-s\tau_1} \left(-\tau_1 \frac{ds}{d\tau_1} - s \right) = 0,
\end{aligned} \tag{31}$$

where $\mathcal{P}'_1(s)$, $\mathcal{P}'_2(s)$, and $\mathcal{P}'_3(s)$ are derivatives of $\mathcal{P}_1(s)$, $\mathcal{P}_2(s)$, and $\mathcal{P}_3(s)$, respectively. It follows that

where M_1, N_1 and M_2, N_2 are the real and imaginary parts of $M(s), N(s)$. Also, ξ_0 stands for the critical value and τ_1^* denotes the bifurcation point. Here,

$$\begin{aligned}
M_1 &= \mathcal{A}_1 \xi_0 \sin \xi_0 \tau_1^* + \mathcal{B}_1 \xi_0 \cos \xi_0 \tau_1^* + \mathcal{A}_3 \xi_0 \sin \xi_0 \tau_1^* - \mathcal{B}_3 \xi_0 \sin \xi_0 \tau_1^*, \\
M_2 &= -\mathcal{A}_1 \xi_0 \cos \xi_0 \tau_1^* + \mathcal{B}_1 \xi_0 \sin \xi_0 \tau_1^* + \xi_0 \mathcal{A}_3 \cos \xi_0 \tau_1^* - \mathcal{B}_3 \xi_0 \cos \xi_0 \tau_1^*, \\
N_1 &= \mathcal{A}_1^* \cos \xi_0 \tau_1^* - \mathcal{B}_1^* \sin \xi_0 \tau_1^* + \tau_1^* \mathcal{A}_1 \cos \xi_0 \tau_1^* - \tau_1^* \mathcal{B}_1 \sin \xi_0 \tau_1^* + \mathcal{A}_2^* + \mathcal{A}_3^* \cos \xi_0 \tau_1^* + \mathcal{B}_3^* \sin \xi_0 \tau_1^* \\
&\quad - \tau_1^* \mathcal{A}_3 \cos \xi_0 \tau_1^* - \tau_1^* \mathcal{B}_3 \sin \xi_0 \tau_1^*, \\
N_2 &= \mathcal{A}_1^* \sin \xi_0 \tau_1^* + \mathcal{B}_1^* \cos \xi_0 \tau_1^* + \tau_1^* \mathcal{A}_1 \sin \xi_0 \tau_1^* + \tau_1^* \mathcal{B}_1 \cos \xi_0 \tau_1^* + \mathcal{B}_2^* - \mathcal{A}_3^* \sin \xi_0 \tau_1^* + \mathcal{B}_3^* \cos \xi_0 \tau_1^* \\
&\quad + \tau_1^* \mathcal{A}_3 \sin \xi_0 \tau_1^* - \tau_1^* \mathcal{B}_3 \cos \xi_0 \tau_1^*, \\
\mathcal{A}_1^* &= 5\alpha \xi_0^{5\alpha-1} \frac{\cos(5\alpha-1)\pi}{2} + 4\alpha D_1 \xi_0^{4\alpha-1} \frac{\cos(4\alpha-1)\pi}{2} + 3\alpha D_2 \xi_0^{3\alpha-1} \frac{\cos(3\alpha-1)\pi}{2} \\
&\quad + 2\alpha D_3 \xi_0^{2\alpha-1} \frac{\cos(2\alpha-1)\pi}{2} + \alpha D_4 \xi_0^{\alpha-1} \frac{\cos(\alpha-1)\pi}{2}, \\
\mathcal{B}_1^* &= 5\alpha \xi_0^{5\alpha-1} \frac{\sin(5\alpha-1)\pi}{2} + 4\alpha D_1 \xi_0^{4\alpha-1} \frac{\sin(4\alpha-1)\pi}{2} + 3\alpha D_2 \xi_0^{3\alpha-1} \frac{\sin(3\alpha-1)\pi}{2} \\
&\quad + 2\alpha D_3 \xi_0^{2\alpha-1} \frac{\sin(2\alpha-1)\pi}{2} + \alpha D_4 \xi_0^{\alpha-1} \frac{\sin(\alpha-1)\pi}{2}, \\
\mathcal{A}_2^* &= 4\alpha G_1 \xi_0^{4\alpha-1} \frac{\cos(4\alpha-1)\pi}{2} + 3\alpha G_2 \xi_0^{3\alpha-1} \frac{\cos(3\alpha-1)\pi}{2} + 2\alpha G_3 \xi_0^{2\alpha-1} \frac{\cos(2\alpha-1)\pi}{2} + \alpha G_4 \xi_0^{\alpha-1} \frac{\cos(\alpha-1)\pi}{2}, \\
\mathcal{B}_2^* &= 4\alpha G_1 \xi_0^{4\alpha-1} \frac{\sin(4\alpha-1)\pi}{2} + 3\alpha G_2 \xi_0^{3\alpha-1} \frac{\sin(3\alpha-1)\pi}{2} + 2\alpha G_3 \xi_0^{2\alpha-1} \frac{\sin(2\alpha-1)\pi}{2} + \alpha G_4 \xi_0^{\alpha-1} \frac{\sin(\alpha-1)\pi}{2}, \\
\mathcal{A}_3^* &= 3\alpha H_1 \xi_0^{3\alpha-1} \frac{\cos(3\alpha-1)\pi}{2} + 2\alpha H_2 \xi_0^{2\alpha-1} \frac{\cos(2\alpha-1)\pi}{2} + \alpha H_3 \xi_0^{\alpha-1} \frac{\cos(\alpha-1)\pi}{2}, \\
\mathcal{B}_3^* &= 3\alpha H_1 \xi_0^{3\alpha-1} \frac{\sin(3\alpha-1)\pi}{2} + 2\alpha H_2 \xi_0^{2\alpha-1} \frac{\sin(2\alpha-1)\pi}{2} + \alpha H_3 \xi_0^{\alpha-1} \frac{\sin(\alpha-1)\pi}{2}.
\end{aligned} \tag{34}$$

Case 2. $\tau_1 = 0, \tau_2 > 0$, and $\tau_3 = 0$.

When $\tau_1 = 0, \tau_2 > 0, \tau_3 = 0$, the characteristic equation (18) becomes

$$\mathcal{P}_4(s) + \mathcal{P}_5(s)e^{-s\tau_2} + \mathcal{P}_6(s)e^{-2s\tau_2} = 0, \tag{35}$$

where

$$\begin{aligned}
\mathcal{P}_4(s) &= \mathbb{P}_1(s) + \mathbb{P}_2(s) + \mathbb{P}_4(s) + \mathbb{P}_5(s) + \mathbb{P}_9(s) \\
&\quad + \mathbb{P}_{10}(s) = s^{5\alpha} + J_1 s^{4\alpha} + J_2 s^{3\alpha} + J_3 s^{2\alpha} + J_4 s^\alpha + J_5, \\
\mathcal{P}_5(s) &= \mathbb{P}_3(s) + \mathbb{P}_7(s) + \mathbb{P}_8(s) + \mathbb{P}_{12}(s) = L_1 s^{4\alpha} + L_2 s^{3\alpha} \\
&\quad + L_3 s^{2\alpha} + L_4 s^\alpha + L_5, \\
\mathcal{P}_6(s) &= \mathbb{P}_6(s) + \mathbb{P}_{11}(s) = R_1 s^{3\alpha} + R_2 s^{2\alpha} + R_3 s^\alpha + R_4.
\end{aligned} \tag{36}$$

Now, we prove that the characteristic equation (35) has no pure imaginary roots for any $\tau_2 > 0$. Assume that characteristic equation (35) has pure imaginary root, and let it be $s = i\xi = \xi(\cos(\pi/2) + i\sin(\pi/2))$, $\xi > 0$. Now, multiplying $e^{s\tau_2}$ on both sides of equation (35), we get

$$\mathcal{P}_4(s)e^{s\tau_2} + \mathcal{P}_5(s) + \mathcal{P}_6(s)e^{-s\tau_2} = 0. \tag{37}$$

Substitute the expression of s into (37) to have

$$(\mathcal{A}_4 + i\mathcal{B}_4)e^{s\tau_2} + \mathcal{A}_5 + i\mathcal{B}_5 + (\mathcal{A}_6 + i\mathcal{B}_6)e^{-s\tau_2} = 0, \tag{38}$$

where $\mathcal{A}_4, \mathcal{A}_5, \mathcal{A}_6$ and $\mathcal{B}_4, \mathcal{B}_5, \mathcal{B}_6$ are real and imaginary parts of $\mathcal{P}_4(s), \mathcal{P}_5(s)$, and $\mathcal{P}_6(s)$, respectively. Here,

$$\begin{aligned}
\mathcal{A}_4 &= \xi^{5\alpha} \cos \frac{5\alpha\pi}{2} + J_1 \xi^{4\alpha} \cos \frac{4\alpha\pi}{2} + J_2 \xi^{3\alpha} \cos \frac{3\alpha\pi}{2} \\
&\quad + J_3 \xi^{2\alpha} \cos \frac{2\alpha\pi}{2} + J_4 \xi^\alpha \cos \frac{\alpha\pi}{2} + J_5, \\
\mathcal{B}_4 &= \xi^{5\alpha} \sin \frac{5\alpha\pi}{2} + J_1 \xi^{4\alpha} \sin \frac{4\alpha\pi}{2} + J_2 \xi^{3\alpha} \sin \frac{3\alpha\pi}{2} \\
&\quad + J_3 \xi^{2\alpha} \sin \frac{2\alpha\pi}{2} + J_4 \xi^\alpha \sin \frac{\alpha\pi}{2}, \\
\mathcal{A}_5 &= L_1 \xi^{4\alpha} \cos \frac{4\alpha\pi}{2} + L_2 \xi^{3\alpha} \cos \frac{3\alpha\pi}{2} + L_3 \xi^{2\alpha} \cos \frac{2\alpha\pi}{2} \\
&\quad + L_4 \xi^\alpha \cos \frac{\alpha\pi}{2} + L_5, \\
\mathcal{B}_5 &= L_1 \xi^{4\alpha} \sin \frac{4\alpha\pi}{2} + L_2 \xi^{3\alpha} \sin \frac{3\alpha\pi}{2} + L_3 \xi^{2\alpha} \sin \frac{2\alpha\pi}{2} \\
&\quad + L_4 \xi^\alpha \sin \frac{\alpha\pi}{2}, \\
\mathcal{A}_6 &= R_1 \xi^{3\alpha} \cos \frac{3\alpha\pi}{2} + R_2 \xi^{2\alpha} \cos \frac{2\alpha\pi}{2} + R_3 \xi^\alpha \cos \frac{\alpha\pi}{2} + R_4, \\
\mathcal{B}_6 &= R_1 \xi^{3\alpha} \sin \frac{3\alpha\pi}{2} + R_2 \xi^{2\alpha} \sin \frac{2\alpha\pi}{2} + R_3 \xi^\alpha \sin \frac{\alpha\pi}{2}.
\end{aligned} \tag{39}$$

Separating real and imaginary parts yields

$$\begin{aligned}
\mathcal{A}_4 \cos \xi\tau_2 - \mathcal{B}_4 \sin \xi\tau_2 &= -(\mathcal{A}_6 \cos \xi\tau_2 + \mathcal{B}_6 \sin \xi\tau_2 + \mathcal{A}_5), \\
\mathcal{A}_4 \sin \xi\tau_2 - \mathcal{B}_4 \cos \xi\tau_2 &= -(\mathcal{B}_6 \cos \xi\tau_2 - \mathcal{A}_6 \sin \xi\tau_2 + \mathcal{B}_5).
\end{aligned} \tag{40}$$

It follows from (40) that

$$\begin{aligned}
\mathcal{A}_4^2 + \mathcal{B}_4^2 - \mathcal{A}_5^2 - \mathcal{B}_5^2 - \mathcal{A}_6^2 - \mathcal{B}_6^2 &= 2[\mathcal{B}_6(\mathcal{A}_5 \sin \xi\tau_2 \\
&\quad + \mathcal{B}_5 \cos \xi\tau_2) + \mathcal{A}_6(\mathcal{A}_5 \cos \xi\tau_2 - \mathcal{B}_5 \sin \xi\tau_2)].
\end{aligned} \tag{41}$$

We know that $\cos^2 \theta + \sin^2 \theta = 1$; by using it, we have $\sin \xi\tau_2 = \sqrt{1 - \cos^2 \xi\tau_2}$, and then (41) can be written in the following form:

$$\begin{aligned}
&[\mathcal{A}_4^2 + \mathcal{B}_4^2 - \mathcal{A}_5^2 - \mathcal{B}_5^2 - \mathcal{A}_6^2 - \mathcal{B}_6^2 \\
&\quad - 2(\mathcal{B}_5 \mathcal{B}_6 + \mathcal{A}_5 \mathcal{A}_6) \cos \xi\tau_2]^2 \\
&= [2\sqrt{1 - \cos^2 \xi\tau_2} (\mathcal{B}_6 \mathcal{A}_5 - \mathcal{A}_6 \mathcal{B}_5)]^2.
\end{aligned} \tag{42}$$

It can be concluded from (42) that

$$\mathcal{Q}_4 \cos^2 \xi\tau + \mathcal{Q}_5 \cos \xi\tau + \mathcal{Q}_6 = 0, \tag{43}$$

where

$$\begin{aligned}
\mathcal{Q}_4 &= 4\mathcal{A}_5^2 \mathcal{A}_6^2 + 4\mathcal{A}_6^2 \mathcal{B}_5^2 + 4\mathcal{A}_5^2 \mathcal{B}_6^2 + 4\mathcal{B}_5^2 \mathcal{B}_6^2, \\
\mathcal{Q}_5 &= 4(\mathcal{B}_5 \mathcal{B}_6 + \mathcal{A}_5 \mathcal{A}_6)(-\mathcal{A}_4^2 - \mathcal{B}_4^2 + \mathcal{A}_5^2 + \mathcal{B}_5^2 + \mathcal{A}_6^2 + \mathcal{B}_6^2), \\
\mathcal{Q}_6 &= [\mathcal{A}_4^2 - (\mathcal{A}_5 - \mathcal{B}_6)^2 - (\mathcal{A}_6 - \mathcal{B}_4 + \mathcal{B}_5)(\mathcal{A}_6 + \mathcal{B}_5 + \mathcal{B}_4)] \\
&\quad \cdot [\mathcal{A}_4^2 - (\mathcal{A}_5 + \mathcal{B}_6)^2 - (\mathcal{A}_6 - \mathcal{B}_4 - \mathcal{B}_5)(\mathcal{A}_6 + \mathcal{B}_4) - \mathcal{B}_5].
\end{aligned} \tag{44}$$

As we know, the quadratic equation (43) has roots, we can obtain the expression of $\cos \xi\tau_2$ and denote $\cos \xi\tau_2 = f_1(\xi)$, where $f_1(\xi)$ is a function of ξ .

Substituting the expression of $\cos \xi\tau_2 = \sqrt{1 - \sin^2 \xi\tau_2}$ into (43), we can get expression of $\sin \xi\tau_2$. Let us denote $\sin \xi\tau_2 = f_2(\xi)$, where $f_2(\xi)$ is a function with respect to ξ . Moreover, $f_1^2(\xi) + f_2^2(\xi) = 1$. Thus, it follows from $\cos \xi\tau_2 = f_1(\xi)$ that

$$\tau_2 = \frac{1}{\xi} [\arccos(f_1(\xi)) + 2k\pi], \quad k = 0, 1, 2, \dots \tag{45}$$

Clearly, $f_1^2(\xi) + f_2^2(\xi) = 1$ has at least one positive root. The bifurcation point is defined as

$$\tau_2^* = \min\{\tau_2^{(k)}\}, \quad k = 0, 1, 2, \dots \tag{46}$$

We obtain the transversality condition of the occurrence for Hopf bifurcation at $\tau_2 = \tau_2^*$.

Differentiating equation (37) with respect to τ_2 yields

$$\begin{aligned}
\mathcal{P}'_4(s) e^{s\tau_2} \frac{ds}{d\tau_2} + \mathcal{P}_4(s) e^{s\tau_2} \left(\tau_2 \frac{ds}{d\tau_2} + s \right) + \mathcal{P}'_5(s) \frac{ds}{d\tau_2} \\
+ \mathcal{P}'_6(s) e^{-s\tau_2} \frac{ds}{d\tau_2} + \mathcal{P}_6(s) e^{-s\tau_2} \left(-\tau_2 \frac{ds}{d\tau_2} - s \right) = 0,
\end{aligned} \tag{47}$$

where $\mathcal{P}'_4(s)$, $\mathcal{P}'_5(s)$, and $\mathcal{P}'_6(s)$ are derivatives of $\mathcal{P}_4(s)$, $\mathcal{P}_5(s)$, and $\mathcal{P}_6(s)$, respectively. It follows that

$$\frac{ds}{d\tau_2} = \frac{-s\mathcal{P}_4(s)e^{s\tau_2} + s\mathcal{P}_6(s)e^{-s\tau_2}}{\mathcal{P}'_4(s)e^{s\tau_2} + \tau_2\mathcal{P}_4(s)e^{s\tau_2} + \mathcal{P}'_5(s) + \mathcal{P}'_6(s)e^{-s\tau_2} - \tau_2\mathcal{P}_6(s)e^{-s\tau_2}} = \frac{\mathcal{M}(s)}{\mathcal{N}(s)}. \tag{48}$$

From (48), by some computation, we deduce that

$$\operatorname{Re} \left(\frac{ds}{d\tau_2} \right) \Big|_{\tau_2=\tau_2^*, \xi=\xi_0} = \frac{\mathcal{M}_1 \mathcal{N}_1 + \mathcal{M}_2 \mathcal{N}_2}{\mathcal{N}_1^2 + \mathcal{N}_2^2}, \tag{49}$$

where $\mathcal{M}_1, \mathcal{N}_1$ and $\mathcal{M}_2, \mathcal{N}_2$ are the real and imaginary parts of $\mathcal{M}(s), \mathcal{N}(s)$. Also ξ_0 stands for the critical value and τ_2^* denotes bifurcation point. Here,

$$\begin{aligned}
\mathcal{M}_1 &= \mathcal{A}_4 \xi_0 \sin \xi_0 \tau_2^* + \mathcal{B}_4 \xi_0 \cos \xi_0 \tau_2^* + \mathcal{A}_6 \xi_0 \sin \xi_0 \tau_2^* - \mathcal{A}_6 \xi_0 \sin \xi_0 \tau_2^*, \\
\mathcal{M}_2 &= -\mathcal{A}_4 \xi_0 \cos \xi_0 \tau_2^* + \mathcal{B}_4 \xi_0 \sin \xi_0 \tau_2^* + \xi_0 \mathcal{A}_6 \cos \xi_0 \tau_2^* - \mathcal{B}_6 \xi_0 \cos \xi_0 \tau_2^*, \\
\mathcal{N}_1 &= \mathcal{A}_4^* \cos \xi_0 \tau_2^* - \mathcal{B}_2^* \sin \xi_0 \tau_2^* + \tau_2^* \mathcal{A}_4 \cos \xi_0 \tau_2^* - \tau_2^* \mathcal{B}_4 \sin \xi_0 \tau_2^* + \mathcal{A}_5^* + \mathcal{A}_6^* \cos \xi_0 \tau_1^* + \mathcal{B}_6^* \sin \xi_0 \tau_2^* \\
&\quad - \tau_2^* \mathcal{A}_6 \cos \xi_0 \tau_2^* - \tau_2^* \mathcal{B}_6 \sin \xi_0 \tau_2^*, \\
\mathcal{N}_2 &= \mathcal{A}_4^* \sin \xi_0 \tau_2^* + \mathcal{B}_4^* \cos \xi_0 \tau_2^* + \tau_2^* \mathcal{A}_4 \sin \xi_0 \tau_2^* + \tau_2^* \mathcal{B}_4 \cos \xi_0 \tau_2^* + \mathcal{B}_5^* - \mathcal{A}_6^* \sin \xi_0 \tau_2^* + \mathcal{B}_6^* \cos \xi_0 \tau_2^* \\
&\quad + \tau_2^* \mathcal{A}_6 \sin \xi_0 \tau_2^* - \tau_2^* \mathcal{B}_6 \cos \xi_0 \tau_2^*, \\
\mathcal{A}_4^* &= 5\alpha \xi_0^{5\alpha-1} \frac{\cos(5\alpha-1)\pi}{2} + 4\alpha J_1 \xi_0^{4\alpha-1} \frac{\cos(4\alpha-1)\pi}{2} + 3\alpha J_2 \xi_0^{3\alpha-1} \frac{\cos(3\alpha-1)\pi}{2} \\
&\quad + 2\alpha J_3 \xi_0^{2\alpha-1} \frac{\cos(2\alpha-1)\pi}{2} + \alpha J_4 \xi_0^{\alpha-1} \frac{\cos(\alpha-1)\pi}{2}, \\
\mathcal{B}_4^* &= 5\alpha \xi_0^{5\alpha-1} \frac{\sin(5\alpha-1)\pi}{2} + 4\alpha J_1 \xi_0^{4\alpha-1} \frac{\sin(4\alpha-1)\pi}{2} + 3\alpha J_2 \xi_0^{3\alpha-1} \frac{\sin(3\alpha-1)\pi}{2} \\
&\quad + 2\alpha J_3 \xi_0^{2\alpha-1} \frac{\sin(2\alpha-1)\pi}{2} + \alpha J_4 \xi_0^{\alpha-1} \frac{\sin(\alpha-1)\pi}{2}, \\
\mathcal{A}_5^* &= 4\alpha L_1 \xi_0^{4\alpha-1} \frac{\cos(4\alpha-1)\pi}{2} + 3\alpha L_2 \xi_0^{3\alpha-1} \frac{\cos(3\alpha-1)\pi}{2} + 2\alpha L_3 \xi_0^{2\alpha-1} \frac{\cos(2\alpha-1)\pi}{2} \\
&\quad + \alpha L_4 \xi_0^{\alpha-1} \frac{\cos(\alpha-1)\pi}{2}, \\
\mathcal{B}_5^* &= 4\alpha L_1 \xi_0^{4\alpha-1} \frac{\sin(4\alpha-1)\pi}{2} + 3\alpha L_2 \xi_0^{3\alpha-1} \frac{\sin(3\alpha-1)\pi}{2} + 2\alpha L_3 \xi_0^{2\alpha-1} \frac{\sin(2\alpha-1)\pi}{2} \\
&\quad + \alpha L_4 \xi_0^{\alpha-1} \frac{\sin(\alpha-1)\pi}{2}, \\
\mathcal{A}_6^* &= 3\alpha R_1 \xi_0^{3\alpha-1} \frac{\cos(3\alpha-1)\pi}{2} + 2\alpha R_2 \xi_0^{2\alpha-1} \frac{\cos(2\alpha-1)\pi}{2} + \alpha R_3 \xi_0^{\alpha-1} \frac{\cos(\alpha-1)\pi}{2}, \\
\mathcal{B}_6^* &= 3\alpha R_1 \xi_0^{3\alpha-1} \frac{\sin(3\alpha-1)\pi}{2} + 2\alpha R_2 \xi_0^{2\alpha-1} \frac{\sin(2\alpha-1)\pi}{2} + \alpha R_3 \xi_0^{\alpha-1} \frac{\sin(\alpha-1)\pi}{2}.
\end{aligned} \tag{50}$$

Case 3. $\tau_1 = 0, \tau_2 = 0$, and $\tau_3 > 0$.

When $\tau_1 = 0, \tau_2 = 0$, and $\tau_3 > 0$, the characteristic equation (18) becomes

$$\mathcal{P}_7(s) + \mathcal{P}_8(s)e^{-s\tau_3} = 0, \tag{51}$$

where

$$\begin{aligned}
\mathcal{P}_7(s) &= \mathbb{P}_1(s) + \mathbb{P}_2(s) + \mathbb{P}_3(s) + \mathbb{P}_5(s) + \mathbb{P}_6(s) + \mathbb{P}_7(s) \\
&= s^{5\alpha} + U_1 s^{4\alpha} + U_2 s^{3\alpha} + U_3 s^{2\alpha} + U_4 s^\alpha + U_5, \\
\mathcal{P}_8(s) &= \mathbb{P}_4(s) + \mathbb{P}_8(s) + \mathbb{P}_9(s) + \mathbb{P}_{10}(s) + \mathbb{P}_{11}(s) + \mathbb{P}_{12}(s) \\
&= V_1 s^{4\alpha} + V_2 s^{3\alpha} + V_3 s^{2\alpha} + V_4 s^\alpha + V_5.
\end{aligned} \tag{52}$$

Again, we prove that the characteristic equation (51) has no pure imaginary roots for any $\tau_2 > 0$. Here, we assume that characteristic equation (51) has pure imaginary root, let it be $s = i\xi = \xi(\cos(\pi/2) + i\sin(\pi/2))$, $\xi > 0$. Now, we substitute the expression of s into (51), and we have

$$\mathcal{A}_7 + i\mathcal{B}_7 + (\mathcal{A}_8 + i\mathcal{B}_8)e^{-s\tau_3} = 0, \tag{53}$$

where $\mathcal{A}_7, \mathcal{A}_8$ and $\mathcal{B}_7, \mathcal{B}_8$ are real and imaginary parts of $\mathcal{P}_7(s)$ and $\mathcal{P}_8(s)$, respectively. Here,

$$\begin{aligned}
\mathcal{A}_7 &= \xi^{5\alpha} \cos \frac{5\alpha\pi}{2} + U_1 \xi^{4\alpha} \cos \frac{4\alpha\pi}{2} + U_2 \xi^{3\alpha} \cos \frac{3\alpha\pi}{2} \\
&\quad + U_3 \xi^{2\alpha} \cos \frac{2\alpha\pi}{2} + U_4 \xi^\alpha \cos \frac{\alpha\pi}{2} + U_5, \\
\mathcal{B}_7 &= \xi^{5\alpha} \sin \frac{5\alpha\pi}{2} + U_1 \xi^{4\alpha} \sin \frac{4\alpha\pi}{2} + U_2 \xi^{3\alpha} \sin \frac{3\alpha\pi}{2} \\
&\quad + U_3 \xi^{2\alpha} \sin \frac{2\alpha\pi}{2} + U_4 \xi^\alpha \sin \frac{\alpha\pi}{2}, \\
\mathcal{A}_5 &= V_1 \xi^{4\alpha} \cos \frac{4\alpha\pi}{2} + V_2 \xi^{3\alpha} \cos \frac{3\alpha\pi}{2} + V_3 \xi^{2\alpha} \cos \frac{2\alpha\pi}{2} \\
&\quad + V_4 \xi^\alpha \cos \frac{\alpha\pi}{2} + V_5, \\
\mathcal{B}_5 &= V_1 \xi^{4\alpha} \sin \frac{4\alpha\pi}{2} + V_2 \xi^{3\alpha} \sin \frac{3\alpha\pi}{2} + V_3 \xi^{2\alpha} \sin \frac{2\alpha\pi}{2} \\
&\quad + V_4 \xi^\alpha \sin \frac{\alpha\pi}{2}.
\end{aligned} \tag{54}$$

Separation of real and imaginary parts yields

$$\begin{aligned}
\mathcal{A}_8 \cos \xi\tau_3 + \mathcal{B}_8 \sin \xi\tau_3 &= -\mathcal{A}_7, \\
-\mathcal{A}_8 \sin \xi\tau_3 + \mathcal{B}_8 \cos \xi\tau_3 &= -\mathcal{B}_7.
\end{aligned} \tag{55}$$

From (14), we have

$$\begin{aligned}
\cos \xi\tau_3 &= \frac{-\mathcal{A}_7 \mathcal{A}_8 - \mathcal{B}_7 \mathcal{B}_8}{\mathcal{A}_8^2 + \mathcal{B}_8^2} = \bar{f}_1(\xi), \\
\sin \xi\tau_3 &= \frac{\mathcal{B}_7 \mathcal{A}_8 - \mathcal{A}_7 \mathcal{B}_8}{\mathcal{A}_8^2 + \mathcal{B}_8^2} = \bar{f}_2(\xi).
\end{aligned} \tag{56}$$

It is clear that $\cos^2 \theta + \sin^2 \theta = 1$; from (56),

$$(\bar{f}_1(\xi))^2 + (\bar{f}_2(\xi))^2 = 1. \tag{57}$$

Hence, it follows from $\cos \xi\tau_3 = \bar{f}_1(\xi)$ that

$$\tau_3 = \frac{1}{\xi} [\arccos(\bar{f}_1(\xi)) + 2k\pi], \quad k = 0, 1, 2, \dots \tag{58}$$

We suppose that (57) have at least one positive root. The bifurcation point is defined as

$$\tau_3^* = \min\{\tau_3^{(k)}\}, \quad k = 0, 1, 2, \dots \tag{59}$$

We obtain the transversality condition of the occurrence for Hopf bifurcation at $\tau_3 = \tau_3^*$.

Now, differentiating equation (51) with respect to τ_3 , we obtain

$$\mathcal{P}_7'(s) \frac{ds}{d\tau_3} + \mathcal{P}_8'(s) e^{-s\tau_3} \frac{ds}{d\tau_3} + \mathcal{P}_8(s) e^{-s\tau_3} \left(-\tau_3 \frac{ds}{d\tau_3} - s \right) = 0, \tag{60}$$

where $\mathcal{P}_7'(s)$ and $\mathcal{P}_8'(s)$ are derivatives of $\mathcal{P}_7(s)$ and $\mathcal{P}_8(s)$, respectively. It follows that

$$\frac{ds}{d\tau_3} = \frac{-s\mathcal{P}_8(s)e^{s\tau_3}}{\mathcal{P}_7'(s) + \mathcal{P}_8'(s)e^{-s\tau_3} - \tau_3\mathcal{P}_8(s)e^{-s\tau_3}} = \frac{\mathcal{M}(s)}{\mathcal{N}(s)}. \tag{61}$$

From (61), by some computation, we deduce that

$$\operatorname{Re} \left(\frac{ds}{d\tau_3} \right) \Big|_{\tau_3=\tau_3^*, \xi=\xi_0} = \frac{\mathcal{M}_1 \mathcal{N}_1 + \mathcal{M}_2 \mathcal{N}_2}{\mathcal{N}_1^2 + \mathcal{N}_2^2}, \tag{62}$$

where $\mathcal{M}_1, \mathcal{N}_1$ and $\mathcal{M}_2, \mathcal{N}_2$ are the real and imaginary parts of $\mathcal{M}(s), \mathcal{N}(s)$. Also ξ_0 stands for the critical value and τ_3^* denotes bifurcation point. Here,

$$\begin{aligned}
\mathcal{M}_1 &= \mathcal{A}_8 \xi_0 \sin \xi_0 \tau_3^* - \mathcal{B}_8 \xi_0 \cos \xi_0 \tau_3^*, \\
\mathcal{M}_2 &= \mathcal{A}_8 \xi_0 \cos \xi_0 \tau_3^* + \mathcal{B}_8 \xi_0 \sin \xi_0 \tau_3^*, \\
\mathcal{N}_1 &= \mathcal{A}_7^* + \mathcal{A}_8^* \cos \xi_0 \tau_3^* + \mathcal{B}_8^* \sin \xi_0 \tau_3^* - \tau_3^* [\mathcal{A}_8 \cos \xi_0 \tau_3^* + \mathcal{B}_8 \sin \xi_0 \tau_3^*], \\
\mathcal{N}_2 &= \mathcal{B}_7^* + \mathcal{B}_8^* \cos \xi_0 \tau_3^* - \mathcal{A}_8^* \sin \xi_0 \tau_3^* - \tau_3^* [\mathcal{B}_8 \cos \xi_0 \tau_3^* - \mathcal{A}_8 \sin \xi_0 \tau_3^*], \\
\mathcal{A}_7^* &= 5\alpha \xi_0^{5\alpha-1} \frac{\cos(5\alpha-1)\pi}{2} + 4\alpha U_1 \xi_0^{4\alpha-1} \frac{\cos(4\alpha-1)\pi}{2} + 3\alpha U_2 \xi_0^{3\alpha-1} \frac{\cos(3\alpha-1)\pi}{2} \\
&\quad + 2\alpha U_3 \xi_0^{2\alpha-1} \frac{\cos(2\alpha-1)\pi}{2} + \alpha U_4 \xi_0^{\alpha-1} \frac{\cos(\alpha-1)\pi}{2}, \\
\mathcal{B}_7^* &= 5\alpha \xi_0^{5\alpha-1} \frac{\sin(5\alpha-1)\pi}{2} + 4\alpha U_1 \xi_0^{4\alpha-1} \frac{\sin(4\alpha-1)\pi}{2} + 3\alpha U_2 \xi_0^{3\alpha-1} \frac{\sin(3\alpha-1)\pi}{2} \\
&\quad + 2\alpha U_3 \xi_0^{2\alpha-1} \frac{\sin(2\alpha-1)\pi}{2} + \alpha U_4 \xi_0^{\alpha-1} \frac{\sin(\alpha-1)\pi}{2}, \\
\mathcal{A}_8^* &= 4\alpha V_1 \xi_0^{4\alpha-1} \frac{\cos(4\alpha-1)\pi}{2} + 3\alpha V_2 \xi_0^{3\alpha-1} \frac{\cos(3\alpha-1)\pi}{2} + 2\alpha V_3 \xi_0^{2\alpha-1} \frac{\cos(2\alpha-1)\pi}{2} + \alpha V_4 \xi_0^{\alpha-1} \frac{\cos(\alpha-1)\pi}{2}, \\
\mathcal{B}_5^* &= 4\alpha V_1 \xi_0^{4\alpha-1} \frac{\sin(4\alpha-1)\pi}{2} + 3\alpha V_2 \xi_0^{3\alpha-1} \frac{\sin(3\alpha-1)\pi}{2} + 2\alpha V_3 \xi_0^{2\alpha-1} \frac{\sin(2\alpha-1)\pi}{2} + \alpha V_4 \xi_0^{\alpha-1} \frac{\sin(\alpha-1)\pi}{2}.
\end{aligned} \tag{63}$$

TABLE 1: ξ_0 values and τ_1^* values for different fractional-order α .

Fractional order (α)	Critical frequency (ξ_0)	Bifurcation point (τ_1^*)
1	0.30125	1.2104
0.9	0.17811	4.5874
0.8	0.09392	11.8356
0.7	0.04573	23.2562
0.6	0.00152	744.420

Case 4. $\tau_1 = \tau_2 = \tau_3 = 0$.

When $\tau_1 = \tau_2 = \tau_3 = 0$, the characteristic equation (18) becomes

$$\omega^{5\alpha} + Z_1\omega^{4\alpha} + Z_2\omega^{3\alpha} + Z_3\omega^{2\alpha} + Z_4\omega^\alpha + Z_5 = 0. \quad (64)$$

Here,

$$Z_1 = 2a_3 + a_5 + 2a_9 + a_1 - a_4 + a_2 + a_8,$$

$$Z_2 = a_3^2 + 4a_3a_9 + 2a_3a_5 + 2a_5a_9 + a_9^2 + a_1a_3 - 2a_3a_4 + a_1a_5 + 2a_1a_9 - 2a_4a_9 + a_2a_3 + a_2a_5 + 2a_2a_9 + 2a_3a_8 \\ + a_5a_8 + a_8a_9 - a_1a_4 + a_2a_4 + a_1a_4 - a_2a_4 + a_2a_8 - a_4a_7 + a_1a_8 - a_4a_8,$$

$$Z_3 = 2a_3a_9^2 + a_5a_9^2 + 2a_3^2a_9 + a_5^2a_9 + 4a_3a_5a_9 - a_3^2a_4 + a_1a_3a_5 + 2a_1a_3a_9 - 4a_3a_4a_9 + 2a_1a_5a_9 + a_1a_9^2 - a_4a_9^2 \\ + a_2a_3a_5 + 2a_2a_3a_9 + 2a_2a_5a_9 + a_2a_9^2 + a_3^2a_8 + 2a_3a_5a_8 + 2a_3a_8a_9 + a_5a_8a_9 - a_1a_3a_4 - 2a_1a_4a_9 + a_2a_3a_4 \\ + 2a_2a_4a_9 + a_1a_3a_4 - a_2a_3a_4 + 2a_1a_4a_9 - 2a_2a_4a_9 + a_2a_3a_8 + a_2a_5a_8 + a_2a_8a_9 - 2a_3a_4a_7 + a_1a_3a_8 - 2a_3a_4a_8 \\ + a_1a_5a_8 - a_4a_7a_9 + a_1a_8a_9 - a_4a_8a_9,$$

$$Z_4 = a_3^2a_9^2 + 2a_3a_5a_9^2 + 2a_3^2a_5a_9 - 2a_3^2a_4a_9 + 2a_1a_3a_5a_9 + a_1a_3a_9^2 - 2a_3a_4a_9^2 + a_1a_5a_9^2 + a_2a_3a_9^2 + a_2a_5a_9^2 \\ + 2a_2a_3a_5a_9 + a_3^2a_5a_8 + a_3^2a_8a_9 + 2a_3a_5a_8a_9 - a_1a_4a_9^2 - 2a_1a_3a_4a_9 + 2a_2a_3a_4a_9 + a_1a_4a_9^2 - a_2a_4a_9^2 + a_2a_3a_5a_8 \\ + a_2a_3a_8a_9 + a_2a_5a_8a_9 - a_3^2a_4a_7 + a_1a_3a_5a_8 - a_3^2a_4a_8 - 2a_3a_4a_7a_9 + a_1a_3a_8a_9 - 2a_3a_4a_8a_9 + a_1a_5a_8a_9 - a_1a_3a_4a_8 \\ - a_1a_4a_8a_9 + a_2a_3a_4a_8 + a_2a_4a_8a_9 + a_1a_3a_4a_8 - a_2a_3a_4a_8 + a_1a_4a_8a_9 - a_2a_4a_8a_9,$$

$$Z_5 = a_3^2a_5a_9^2 - a_3^2a_4a_9^2 + a_1a_3a_5a_9^2 + a_2a_3a_5a_9^2 + a_3^2a_5a_8a_9 - a_1a_3a_4a_9^2 + a_2a_3a_4a_9^2 - a_2a_3a_4a_8a_9 + a_2a_3a_5a_8a_9 - a_3^2a_4a_7a_9 \\ + a_1a_3a_5a_8a_9.$$

(65)

From the Routh–Hurwitz criteria, if we choose $Z_i > 0$, $i = 1, 2, 3, 4, 5$, $Z_1Z_2Z_3 > Z_3^2 + Z_1^2Z_4$ and $(Z_1Z_4 - Z_5)(Z_1Z_2Z_3 - Z_3^2 - Z_1^2Z_4) > Z_5(Z_1Z_2 - Z_3)^2 + Z_1Z_5^2$, then the five eigenvalues of the characteristic equation (64) have negative real parts. Hence, the steady state fractional-order system (5) is asymptotically stable when $\tau_1 = \tau_2 = \tau_3 = 0$ (without time delays).

We arrive at the following theorem.

Theorem 1. *If $\alpha \in (0, 1]$ and an endemic equilibrium point E^* exists for system (5), then the following results hold:*

- (i) *When $\tau_1 > 0$, $\tau_2 = 0$, and $\tau_3 = 0$, the endemic steady state E^* is asymptotically stable for $\tau_1 \in [0, \tau_1^*)$ and the system undergoes a Hopf bifurcation at the origin at $\tau_1 = \tau_1^*$ and the transversality condition holds, $\text{Re}(ds/d\tau_1)|_{\tau_1=\tau_1^*, \xi=\xi_0} \neq 0$*
- (ii) *When $\tau_1 = 0$, $\tau_2 > 0$, and $\tau_3 = 0$, the endemic steady state E^* is asymptotically stable for $\tau_2 \in [0, \tau_2^*)$ and*

system undergoes a Hopf bifurcation at the origin when $\tau_2 = \tau_2^$ and the transversality condition holds, $\text{Re}(ds/d\tau_2)|_{\tau_2=\tau_2^*, \xi=\xi_0} \neq 0$*

- (iii) *When $\tau_1 = 0$, $\tau_2 = 0$, and $\tau_3 > 0$, E^* of is asymptotically stable for $\tau_3 \in [0, \tau_3^*)$ and system (5) undergoes a Hopf bifurcation at the origin at $\tau_3 = \tau_3^*$ and transversality condition holds, $\text{Re}(ds/d\tau_3)|_{\tau_3=\tau_3^*, \xi=\xi_0} \neq 0$*

- (iv) *When $Z_1Z_2Z_3 > Z_3^2 + Z_1^2Z_4$ and $(Z_1Z_4 - Z_5)(Z_1Z_2Z_3 - Z_3^2 - Z_1^2Z_4) > Z_5(Z_1Z_2 - Z_3)^2 + Z_1Z_5^2$ holds, the endemic steady state E^* is asymptotically stable for $\tau_1 = \tau_2 = \tau_3 = 0$*

Remark 4. Theorem 1 reports the asymptotic stability of the endemic equilibrium point E^* . The analysis can be extended to investigate the stability of infection-free equilibrium points E^0 for the fractional-order model.

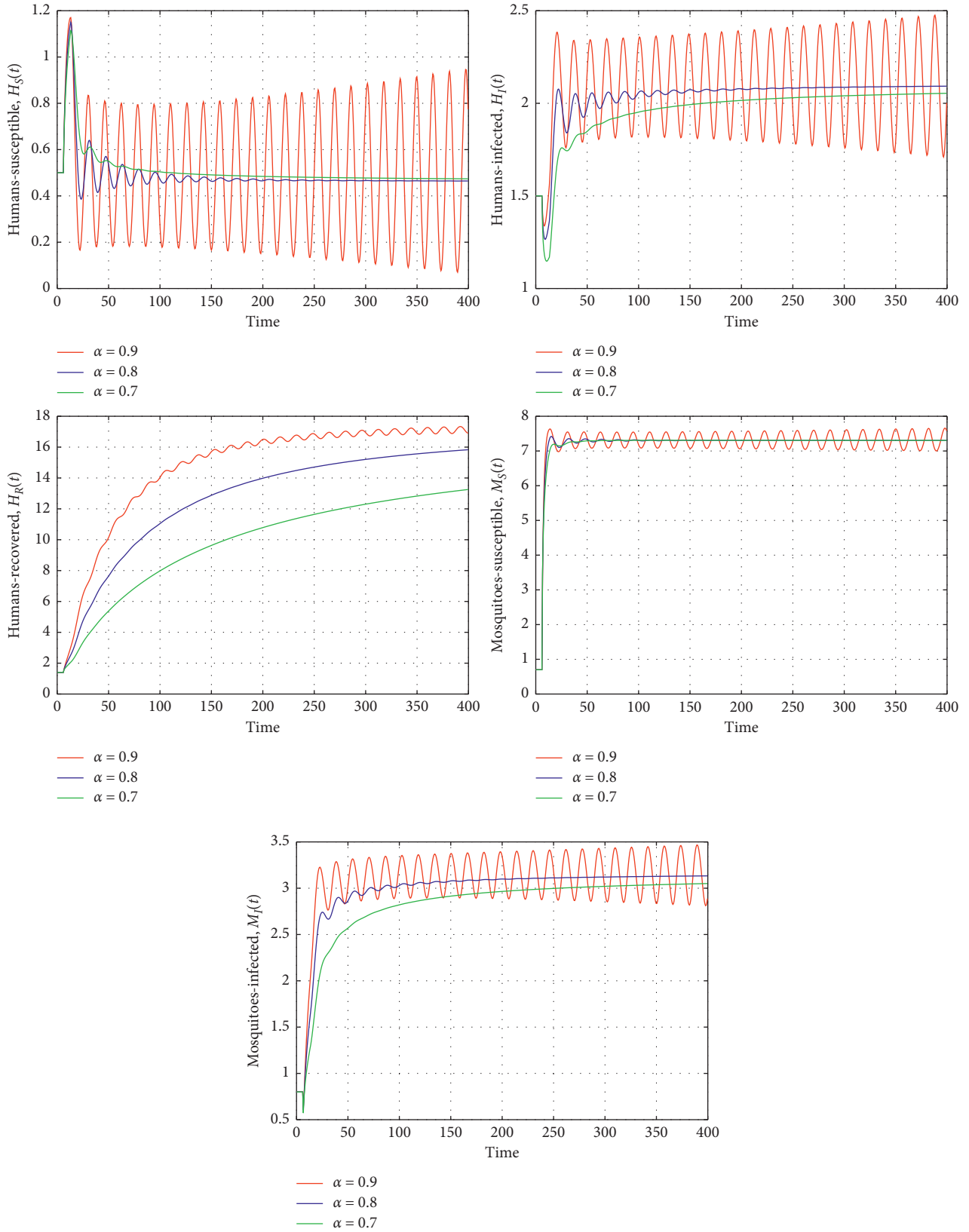


FIGURE 2: State trajectories for model (5) with $\alpha = 0.9, 0.8,$ and 0.7 and $\tau_1 = 10, \tau_2 = 0.0,$ and $\tau_3 = 0.0$. For $\alpha = 0.9$ and $\tau_1 = 10 > \tau_1^*$, the equilibrium point is unstable (red trajectory) for (5); however, for $\tau_1 < \tau_1^*$ and $\alpha = 0.8, 0.7,$ it is asymptotically stable (blue and green trajectories).

4. Numerical Simulations and Observations

In this section, we provide some numerical simulations for system (5) to demonstrate the effectiveness of our main results. The simulations have been done by using stable implicit Euler approximation scheme, discussed in [44]. Of course, many other methods have been used for fractional-order delay differential equations such as the Adams–Bashforth–Moulton scheme [45]. The parameter values of system (5) are taken as follows:

$$\begin{aligned}
 \lambda_h &= 0.5, \\
 \lambda_m &= 4.58, \\
 \beta_h &= 0.05, \\
 \beta_m &= 0.09, \\
 \eta &= 0.01, \\
 \gamma &= 0.2, \\
 d_h &= 0.714, \\
 d_m &= 0.437.
 \end{aligned} \tag{66}$$

Case 1. $\tau_1 > 0$, $\tau_2 = 0$, and $\tau_3 = 0$. In this case, time-delay τ_1 is chosen as the bifurcation parameter. We then discuss the dynamic effect of system (5) with the above parameter values. We calculate the critical frequency ξ_0 and bifurcation point τ_1^* of various fractional-order α . Figure 2 shows the numerical simulations of model (5) when $\tau_1 = 10$, $\tau_2 = 0.0$, and $\tau_3 = 0.0$, with different fractional orders $\alpha = 0.9, 0.8$, and 0.7 and estimated bifurcation point $\tau_1^* = 4.587, 11.835$, and 23.256 (see Table 1). Here, $\tau_1 = 10 \notin [0, \tau_1^*]$ for the fractional-order $\alpha = 0.9$ and whereas $\tau_1 = 10 \in [0, \tau_1^*]$ which satisfies the condition (i) in Theorem 1. The equilibrium E^* of the model (5) is asymptotically stable for $\alpha = 0.8, 0.7$. When $\tau_1 = 10 \notin [0, \tau_1^*]$, which does not satisfies the condition (i) of Theorem 1, the system undergoes a Hopf bifurcation for the functional-order $\alpha = 0.9$.

Case 2. $\tau_1 = 0$, $\tau_2 > 0$, and $\tau_3 = 0$. We choose time-delay τ_2 as a bifurcation parameter of system (5) with parameter values:

$$\begin{aligned}
 \lambda_h &= 0.5, \\
 \lambda_m &= 4.58, \\
 \beta_h &= 0.05, \\
 \beta_m &= 0.08, \\
 \eta &= 0.05, \\
 \gamma &= 0.2, \\
 d_h &= 0.3, \\
 d_m &= 0.78.
 \end{aligned} \tag{67}$$

We then calculate the critical frequency ξ_0 and bifurcation point τ_2^* of various fractional-order α (see Table 2). Figure 3 shows the dynamics of system (5) for $\tau_1 = 0.0$, $\tau_2 = 14$, and $\tau_3 = 0.0$, with values of $\alpha = 1, 0.9$, and 0.8 .

TABLE 2: ξ_0 values and τ_2^* values for different fractional-order α .

Fractional order (α)	Critical frequency (ξ_0)	Bifurcation point (τ_2^*)
1	0.12290	11.1762
0.9	0.09602	14.2931
0.8	0.05174	35.797
0.7	0.0363	47.963
0.6	0.0158	131.001

TABLE 3: ξ_0 values and τ_3^* values for different fractional-order α .

Fractional order (α)	Critical frequency (ξ_0)	Bifurcation point (τ_3^*)
1	0.3777	2.255
0.9	0.2943	3.281
0.8	0.2172	4.912
0.7	0.01490	7.755
0.6	0.0920	13.404

The corresponding bifurcation point is $\tau_2^* = 11.176, 14.293$, and 35.797 . $\tau_2 = 14 \in [0, \tau_2^*]$ satisfies the condition (ii) of Theorem 1. Therefore, the equilibrium E^* of the model (5) is asymptotically stable for $\alpha = 0.9$ and 0.8 , which is shown in Figure 3. However, for $\tau_2 = 14 \notin [0, \tau_2^*]$, a Hopf bifurcation occurs for the functional-order $\alpha = 1$.

Case 3. $\tau_1 = 0$, $\tau_2 = 0$, and $\tau_3 > 0$. We consider time-delay τ_3 as a bifurcation parameter of system (5) with parameter values:

$$\begin{aligned}
 \lambda_h &= 0.5, \\
 \lambda_m &= 10, \\
 \beta_h &= 0.05, \\
 \beta_m &= 0.4, \\
 \eta &= 0.05, \\
 \gamma &= 0.2, \\
 d_h &= 0.714, \\
 d_m &= 0.437.
 \end{aligned} \tag{68}$$

We calculate the critical frequency ξ_0 and bifurcation point τ_3^* of various fractional-order α . When $\tau_1 = 0.0$, $\tau_2 = 0.0$, and $\tau_3 = 8.0$, the dynamics of system (5) is shown in Figure 4 with different fractional-order $\alpha = 1, 0.9$, and 0.8 , its corresponding bifurcation points $\tau_3^* = 2.255, 3.281$, and 4.912 (see Table 1). Here, $\tau_3 = 8 \notin [0, \tau_3^*]$ and a Hopf bifurcation occurs for the fractional-order $\alpha = 1, 0.9$, and 0.8 which not satisfies the condition (iii) in Theorem 1. Therefore, the equilibrium point E^* of model (5) is unstable, which is shown in Figure 4.

Case 4. $\tau_1 = 0$, $\tau_2 = 0$, and $\tau_3 = 0$, without time delays. Assume the parameter values:

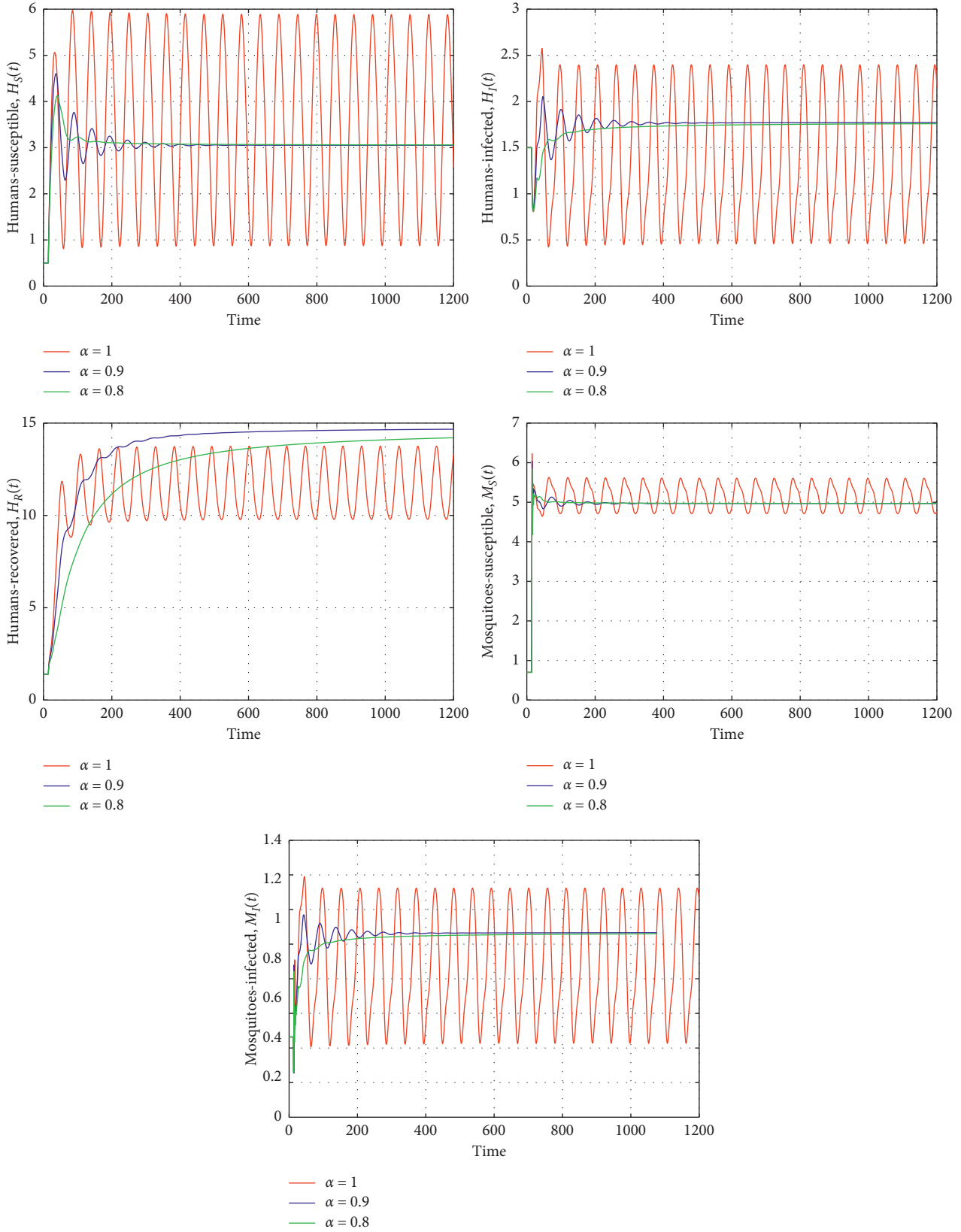


FIGURE 3: State trajectories for model (5) for $\alpha = 1, 0.9$, and 0.8 and $\tau_1 = 0.0$, $\tau_2 = 14$, and $\tau_3 = 0.0$, when $\alpha = 1$ and $\tau_2 = 14 > \tau_2^*$; the equilibrium point is unstable (red trajectory) for (5). However, for $\tau_2 < \tau_2^*$ with $\alpha = 0.9$ and 0.8 , it is asymptotically stable (blue and green trajectories).

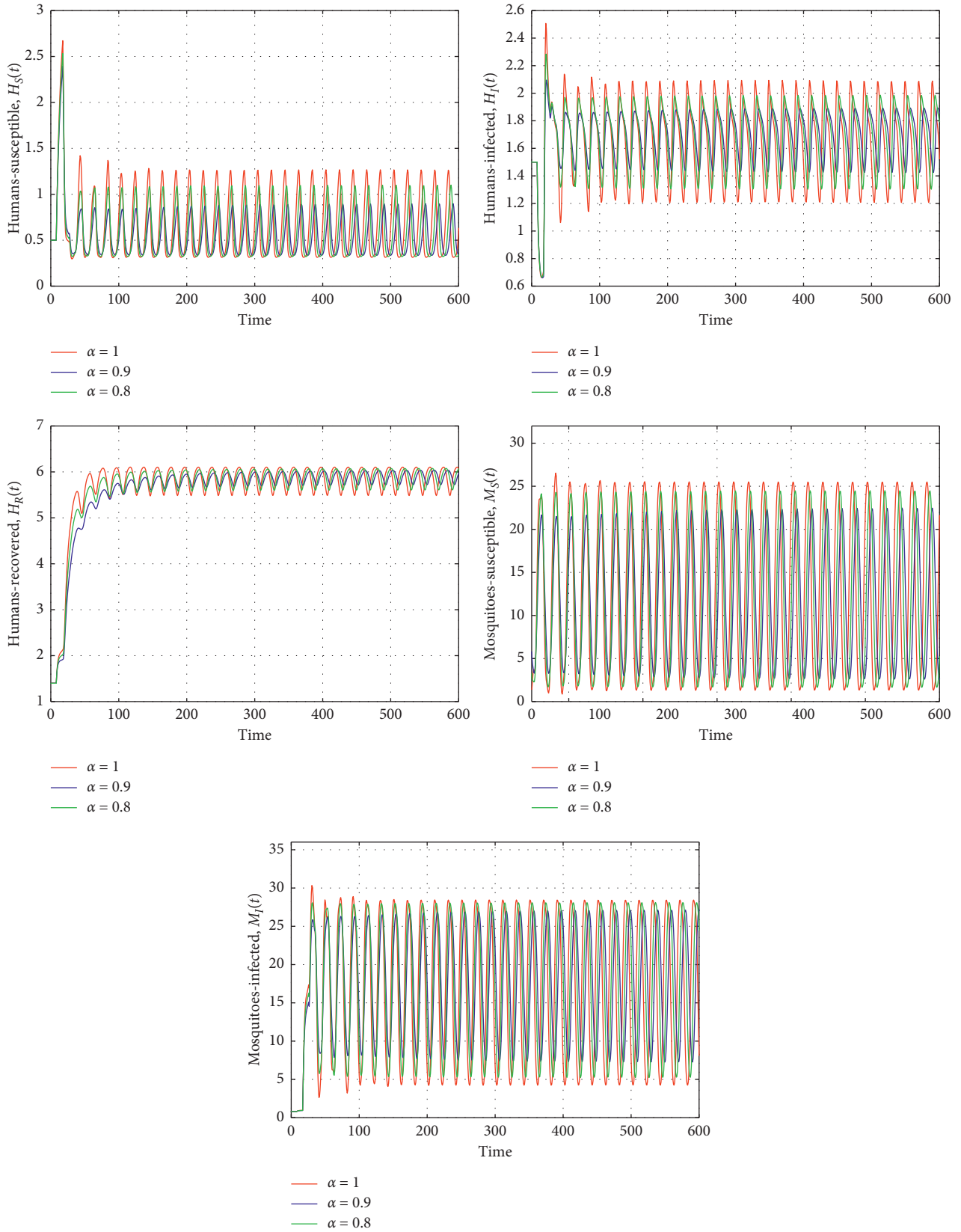


FIGURE 4: State trajectories for the model (5) for various values of $\alpha = 1, 0.9,$ and 0.8 and $\tau_1 = 0.0, \tau_2 = 0.0,$ and $\tau_3 = 8$. The equilibrium point E^* is unstable when $\tau_3 \notin [0, \tau_3^*]$.

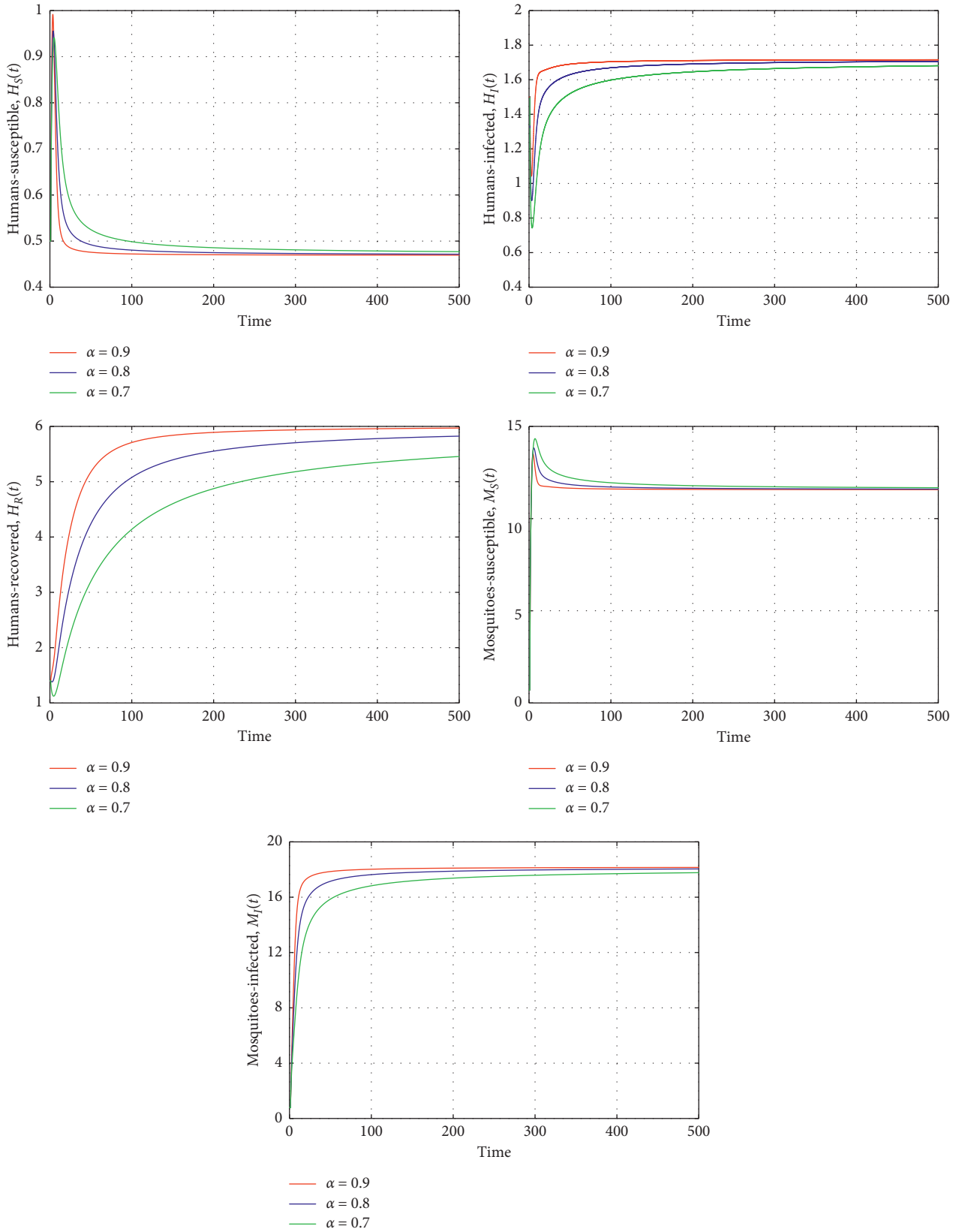


FIGURE 5: State trajectories of model (5) for various values of $\alpha = 0.9, 0.8,$ and $0.7,$ when $\tau_1 = \tau_2 = \tau_3 = 0.$ The steady state of the system is asymptotically stable.

$$\begin{aligned}
\lambda_h &= 0.5, \\
\lambda_m &= 10, \\
\beta_h &= 0.05, \\
\beta_m &= 0.4, \\
\eta &= 0.05, \\
\gamma &= 0.2, \\
d_h &= 0.714, \\
d_m &= 0.437.
\end{aligned} \tag{69}$$

Hence, system (5) is asymptotically stable, which is shown in Figure 5.

5. Conclusion

Fractional derivatives have the unique property of capturing the history of the variable; that is, they have short and long memory. This cannot be easily done by means of the integer-order derivatives. In this paper, we proposed a fractional-order model for Zika virus infection with multiple time delays τ_1 , τ_2 , and τ_3 . We studied the asymptotic stability and Hopf bifurcation properties for the model. Time delays and

fractional order play a vital role in the stability and complexity of the model. By evaluating the characteristics, some sufficient conditions have derived to ensure the asymptotic stability in terms of the fractional order and time delays. Moreover, we estimated the thresholds bifurcation parameters: τ_1^* , τ_2^* , and τ_3^* . The transversality conditions have been obtained to confirm the existence of Hopf bifurcations for different values at the threshold parameters and particular values of fractional orders. Our findings illustrate that using the time delays as bifurcation points, one can conclude that when time delay increases, the equilibrium loses its stability and Hopf bifurcation occurs. These models can be used to understand key aspects of the viral life cycle and to predict antiviral efficacy. Finally, numerical simulations show that a combination of fractional order and time delays in the model effectively enriches the dynamics and strengthens the stability condition of the model.

Including control variables in the model is desirable to determine the best strategy of treatment and control and eliminate the infection, which will be considered in future work.

Appendix

The coefficients of equation (18) are as follows:

$$\begin{aligned}
\mathbb{P}_1(s) &= s^{5\alpha} + s^{4\alpha}(a_3 + 2a_9) + s^{3\alpha}(a_3^2 + 2a_3a_5 + 2a_5a_9 + a_9^2) + s^{2\alpha}(a_3^2a_5 + 4a_3a_5a_9 + 2a_3a_9^2 + a_5a_9^2) \\
&\quad + s^\alpha(2a_3^2a_5a_9 + 2a_3a_5a_9^2) + a_3^2a_9^2, \\
\mathbb{P}_2(s) &= s^{4\alpha}a_1 + s^{3\alpha}(a_1a_3 + a_1a_5 + 2a_1a_9) + s^{2\alpha}(a_1a_3a_5 + 2a_1a_3a_9 + 2a_1a_5a_9 + a_1a_9^2) + s^\alpha(2a_1a_3a_5a_9 + a_1a_3a_9^2 + a_1a_5a_9^2) \\
&\quad + a_1a_3a_5a_9^2, \\
\mathbb{P}_3(s) &= s^{4\alpha}(a_2 - a_4) + s^{3\alpha}(a_2a_3 - 2a_3a_4 + a_2a_5 + 2a_2a_9 - 2a_4a_9) + s^{2\alpha}(-a_2^2a_4 + a_2a_3a_5 + 2a_2a_3a_9 - 4a_3a_4a_9 + a_2a_5a_9 \\
&\quad + a_2a_9^2 - a_4a_9^2) + s^\alpha(-2a_2^2a_4a_9 + 2a_2a_3a_5a_9 + a_2a_3a_9^2 - 2a_3a_4a_9^2 + a_2a_5a_9^2) + a_2a_3a_5a_9^2 - a_2^2a_4a_9^2, \\
\mathbb{P}_4(s) &= s^{4\alpha}a_8 + s^{3\alpha}(2a_3a_8 + a_5a_8 + a_8a_9) + s^{2\alpha}(a_3^2a_8 + 2a_3a_5a_8 + 2a_3a_8a_9 + a_5a_8a_9) + s^\alpha(a_3^2a_5a_8 + a_3^2a_8a_9 + a_3a_5a_8a_9) \\
&\quad + a_3^2a_5a_8a_9, \\
\mathbb{P}_5(s) &= s^{3\alpha}(a_1a_4) + s^{2\alpha}(a_1a_3a_4 - 2a_1a_4a_9 - a_1a_3a_5a_9) + s^\alpha(a_1a_3a_4a_7 + a_1a_4a_9^2), \\
\mathbb{P}_6(s) &= s^{3\alpha}(a_2a_4) + s^{2\alpha}(a_2a_3a_4 + 2a_2a_4a_9) + s^\alpha(a_2a_4a_9^2 + a_2a_3a_4a_9) + a_2a_3a_4a_9^2, \\
\mathbb{P}_7(s) &= s^{4\alpha}(-a_4) + s^{3\alpha}(-a_2a_4 + a_1a_8 - a_4a_7) + s^{2\alpha}(a_2a_3a_5 + 2a_1a_5a_9 + a_4a_9^2) + s^\alpha(a_2a_9^2 + a_1a_4a_9^2) + a_1a_3a_4a_9^2 - a_2a_3a_4a_9^2, \\
\mathbb{P}_8(s) &= s^{3\alpha}(-a_4a_7 + a_2a_8 - a_4a_8) + s^{2\alpha}(-2a_3a_4a_7 + a_2a_3a_8 + a_3a_4a_8 + a_2a_5a_8 - a_4a_7a_9 + a_2a_8a_9 + a_4a_8a_9) \\
&\quad + s^\alpha(-a_3^2a_4a_7 - a_3^2a_4a_8 - 2a_3a_4a_7a_9 - a_2a_3a_8a_9 - 2a_3a_4a_8a_9 + a_2a_5a_8a_9) - a_3^2a_4a_7a_9 + a_2a_3a_5a_8a_9, \\
\mathbb{P}_9(s) &= s^{3\alpha}a_1a_8 + s^{2\alpha}(a_1a_4a_7 + a_1a_3a_8 + a_1a_5a_8 + a_1a_8a_9) + s^\alpha(a_1a_3a_5a_8 + a_1a_3a_8a_9 + a_1a_5a_8a_9) + a_1a_3a_5a_7a_9, \\
\mathbb{P}_{10}(s) &= s^\alpha(a_1a_3a_4a_7 + a_1a_4a_7a_9) + a_1a_3a_4a_7a_9, \\
\mathbb{P}_{11}(s) &= s^\alpha(-a_2a_4a_7 - a_2a_3a_4a_7 - a_2a_4a_7a_9) - a_2a_3a_4a_7a_9, \\
\mathbb{P}_{12}(s) &= s^{2\alpha}(-a_1a_4a_7 + a_2a_4a_7) + s^\alpha(-a_1a_3a_4a_7 + a_2a_3a_4a_7 - a_1a_4a_7a_9 + a_2a_4a_7a_9) - a_1a_3a_7a_9 + a_2a_3a_4a_8a_9.
\end{aligned} \tag{A.1}$$

Data Availability

Data sharing is not applicable to this article as no new data were created or analyzed in this study.

Conflicts of Interest

The authors declare that they have no conflicts of interest.

Acknowledgments

This manuscript was funded from the project no. 31S265 (UAE University) and DST-SERB Project # SB/FTP/MS-045/2013 (Bharathiar University).

References

- [1] G. Calvet, R. S. Aguiar, A. S. O. Melo et al., "Detection and sequencing of zika virus from amniotic fluid of fetuses with microcephaly in Brazil: a case study," *The Lancet Infectious Diseases*, vol. 16, no. 6, pp. 653–660, 2016.
- [2] F. Krauer, M. Riesen, L. Reveiz et al., "Zika virus infection as a cause of congenital brain abnormalities and Guillain-Barré syndrome: systematic review," *PLoS Medicine*, vol. 14, no. 1, Article ID e1002203, 2017.
- [3] E. Bonyah and K. O. Okosun, "Mathematical modeling of zika virus," *Asian Pacific Journal of Tropical Disease*, vol. 6, no. 9, pp. 673–679, 2016.
- [4] D. Gao, Y. Lou, D. He et al., "Prevention and control of zika as a mosquito-borne and sexually transmitted disease: a mathematical modeling analysis," *Scientific Reports*, vol. 6, no. 1, Article ID 28070, 2016.
- [5] F. A. Rihan, S. Lakshmanan, and H. Maurer, "Optimal control of tumour-immune model with time-delay and immunotherapy," *Applied Mathematics and Computation*, vol. 353, no. 7, pp. 147–165, 2019.
- [6] N. MacDonald, *Biological Delay Systems*, Cambridge University Press, Cambridge, UK, 1989.
- [7] N. Burić and D. Todorović, "Dynamics of delay-differential equations modelling immunology of tumor growth," *Chaos, Solitons & Fractals*, vol. 13, no. 4, pp. 645–655, 2002.
- [8] S. Gao, L. Chen, and Z. Teng, "Pulse vaccination of an SEIR epidemic model with time delay," *Nonlinear Analysis: Real World Applications*, vol. 9, no. 2, pp. 599–607, 2008.
- [9] M. Y. Li and H. Shu, "Global dynamics of an in-host viral model with intracellular delay," *Bulletin of Mathematical Biology*, vol. 72, no. 6, pp. 1492–1505, 2010.
- [10] F. A. Rihan and D. H. Abdel Rahman, "Delay differential model for tumour-immune dynamics with HIV infection of CD4⁺ T-cells," *International Journal of Computer Mathematics*, vol. 90, no. 3, pp. 594–614, 2013.
- [11] K. Wang, W. Wang, H. Pang, and X. Liu, "Complex dynamic behavior in a viral model with delayed immune response," *Physica D: Nonlinear Phenomena*, vol. 226, no. 2, pp. 197–208, 2007.
- [12] H.-M. Wei, X.-Z. Li, and M. Martcheva, "An epidemic model of a vector-borne disease with direct transmission and time delay," *Journal of Mathematical Analysis and Applications*, vol. 342, no. 2, pp. 895–908, 2008.
- [13] W. Sakdanupaph, E. J. Moore, G. Maroulis, and T. E. Simos, "A delay differential equation model for dengue fever transmission in selected countries of south-east asia," *AIP Conference Proceedings*, vol. 1148, pp. 816–819, 2009.
- [14] C. Chiyaka, J. M. Tchuente, W. Garira, and S. Dube, "A mathematical analysis of the effects of control strategies on the transmission dynamics of malaria," *Applied Mathematics and Computation*, vol. 195, no. 2, pp. 641–662, 2008.
- [15] W.-C. Chen, "Nonlinear dynamics and chaos in a fractional-order financial system," *Chaos, Solitons & Fractals*, vol. 36, no. 5, pp. 1305–1314, 2008.
- [16] K. S. Cole, "Electric conductance of biological systems," *Cold Spring Harbor Symposia on Quantitative Biology*, vol. 1, pp. 107–116, 1933.
- [17] R. Hilfer, *Applications of Fractional Calculus in Physics*, World Scientific, Singapore, 2000.
- [18] H. Sheng, Y. Chen, and T. Qiu, *Fractional Processes and Fractional-Order Signal Processing: Techniques and Applications*, Springer, New York, NY, USA, 2012.
- [19] C. A. Pinto and A. M. Carvalho, "Fractional dynamics of an infection model with time-varying drug exposure," *Journal of Computational and Nonlinear Dynamics*, vol. 13, no. 9, p. 16, 2018.
- [20] G. Zaslavsky, "Chaos, fractional kinetics, and anomalous transport," *Physics Reports*, vol. 371, no. 6, pp. 461–580, 2002.
- [21] F. A. Rihan, M. Sheek-Hussein, A. Tridane, and R. Yafia, "Dynamics of hepatitis C virus infection: mathematical modeling and parameter estimation," *Mathematical Modelling of Natural Phenomena*, vol. 12, no. 5, pp. 33–47, 2017.
- [22] E. Ahmed, A. Hashish, and F. A. Rihan, "On fractional order cancer model," *Journal of Fractional Calculus and Applied Analysis*, vol. 3, no. 2, pp. 1–6, 2012.
- [23] C. L. Althaus, V. V. Ganusov, and R. J. De Boer, "Dynamics of CD8⁺ T cell responses during acute and chronic lymphocytic choriomeningitis virus infection," *The Journal of Immunology*, vol. 179, no. 5, pp. 2944–2951, 2007.
- [24] F. A. Rihan, D. Baleanu, S. Lakshmanan, and R. Rakkiyappan, "On fractional SIRC model with salmonella bacterial infection," *Abstract and Applied Analysis*, vol. 2014, Article ID 136263, 9 pages, 2014.
- [25] L. Zhang, G. Huang, A. Liu, and R. Fan, "Stability analysis for a fractional HIV infection model with nonlinear incidence," *Discrete Dynamics in Nature and Society*, vol. 2015, Article ID 563127, 11 pages, 2015.
- [26] V. P. Latha, F. A. Rihan, R. Rakkiyappan, and G. Velmurugan, "A fractional-order model for ebola virus infection with delayed immune response on heterogeneous complex networks," *Journal of Computational and Applied Mathematics*, vol. 339, pp. 134–146, 2018.
- [27] V. P. Latha, F. A. Rihan, R. Rakkiyappan, and G. Velmurugan, "A fractional-order delay differential model for ebola infection and CD8⁺ T-cells response: stability analysis and hopf bifurcation," *International Journal of Biomathematics*, vol. 10, no. 8, Article ID 1750111, 2017.
- [28] A. J. Kucharski, S. Funk, R. M. Eggo et al., "Transmission dynamics of zika virus in island populations: a modelling analysis of the 2013–14 French polynesia outbreak," *PLoS Neglected Tropical Diseases*, vol. 10, no. 5, Article ID e0004726, 2016.
- [29] V. M. Moreno, B. Espinoza, D. Bichara, S. A. Holechek, and C. Castillo-Chavez, "Role of short-term dispersal on the dynamics of zika virus in an extreme idealized environment," *Infectious Disease Modelling*, vol. 2, no. 1, pp. 21–34, 2017.
- [30] S. Usman, I. I. Adamu, and U. Dahiru, "Stability analysis of a mathematical model for the transmission dynamics of zika virus infection," *Journal of the Nigerian Association of Mathematical Physics*, vol. 40, 2017.

- [31] F. Brauer, C. Castillo-Chavez, and Z. Feng, "Dengue fever and the zika virus," in *Texts in Applied Mathematics*, pp. 409–425, Springer, Berlin, Germany, 2019.
- [32] X. Wang, Z. Wang, and H. Shen, "Dynamical analysis of a discrete-time sis epidemic model on complex networks," *Applied Mathematics Letters*, vol. 94, pp. 292–299, 2019.
- [33] Z. Wang, Y. Xie, J. Lu, and Y. Li, "Stability and bifurcation of a delayed generalized fractional-order prey-predator model with interspecific competition," *Applied Mathematics and Computation*, vol. 347, pp. 360–369, 2019.
- [34] X. Wang, Z. Wang, X. Huang, and Y. Li, "Dynamic analysis of a delayed fractional-order sir model with saturated incidence and treatment functions," *International Journal of Bifurcation and Chaos*, vol. 28, no. 14, Article ID 1850180, 2018.
- [35] X. Wang, Z. Wang, and J. Xia, "Stability and bifurcation control of a delayed fractional-order eco-epidemiological model with incommensurate orders," *Journal of the Franklin Institute*, vol. 356, no. 15, pp. 8278–8295, 2019.
- [36] F. A. Rihan, S. Lakshmanan, A. H. Hashish, R. Rakkiyappan, and E. Ahmed, "Fractional-order delayed predator-prey systems with Holling type-II functional response," *Nonlinear Dynamics*, vol. 80, no. 1-2, pp. 777–789, 2015.
- [37] A. A. Tateishi, H. V. Ribeiro, and E. K. Lenzi, "The role of fractional time-derivative operators on anomalous diffusion," *Frontiers in Physics*, vol. 5, no. 1–9, 2017.
- [38] A. Atangana, "Blind in a commutative world: simple illustrations with functions and chaotic attractors," *Chaos, Solitons & Fractals*, vol. 114, pp. 347–363, 2018.
- [39] A. Atangana, "Non validity of index law in fractional calculus: a fractional differential operator with Markovian and non-Markovian properties," *Physica A: Statistical Mechanics and Its Applications*, vol. 505, pp. 688–706, 2018.
- [40] A. Atangana and J. F. Gómez-Aguilar, "Decolonisation of fractional calculus rules: breaking commutativity and associativity to capture more natural phenomena," *European Physical Journal Plus*, vol. 133, no. 4, p. 166, 2018.
- [41] I. Podlubny, *Fractional Differential Equations*, Academic Press, Cambridge, MA, USA, 1999.
- [42] R. M. Anderson and R. M. May, *Infectious Diseases of Humans: Dynamics and Control*, Oxford University Press, Oxford, UK, 1992.
- [43] E. J. Muth, *Transform Methods: with Applications to Engineering and Operations Research*, Prentice-Hall, Upper Saddle River, NJ, USA, 1977.
- [44] F. A. Rihan, "Numerical modeling of fractional-order biological systems," *Abstract and Applied Analysis*, vol. 2013, Article ID 816803, 11 pages, 2013.
- [45] B. P. Moghaddam, S. Yaghoobi, and J. A. Tenreiro Machado, "An extended predictor-corrector algorithm for variable-order fractional delay differential equations," *Journal of Computational and Nonlinear Dynamics*, vol. 11, no. 6, Article ID 061001, 7 pages, 2016.

Research Article

Combination Synchronization of Three Different Fractional-Order Delayed Chaotic Systems

Bo Li,¹ Xiaobing Zhou ,² and Yun Wang¹

¹School of Computer Science and Engineering, Southeast University, Nanjing 211189, China

²School of Information Science and Engineering, Yunnan University, Kunming 650091, China

Correspondence should be addressed to Xiaobing Zhou; zhoubx.cn@gmail.com

Received 3 July 2019; Accepted 15 October 2019; Published 7 November 2019

Guest Editor: Mahendra K. Gupta

Copyright © 2019 Bo Li et al. This is an open access article distributed under the Creative Commons Attribution License, which permits unrestricted use, distribution, and reproduction in any medium, provided the original work is properly cited.

Time delay is a frequently encountered phenomenon in some practical engineering systems and introducing time delay into a system can enrich its dynamic characteristics. There has been a plenty of interesting results on fractional-order chaotic systems or integer-order delayed chaotic systems, but the problem of synchronization of fractional-order chaotic systems with time delays is in the primary stage. Combination synchronization of three different fractional-order delayed chaotic systems is investigated in this paper. It is an extension of combination synchronization of delayed chaotic systems or combination synchronization of fractional-order chaotic systems. With the help of stability theory of linear fractional-order systems with multiple time delays, we design controllers to achieve combination synchronization of three different fractional-order delayed chaotic systems. In addition, numerical simulations have been performed to demonstrate and verify the theoretical analysis.

1. Introduction

Since it was reported that nature and engineering fields existed in many fractional dimensions in 1983 [1], fractional calculus has attracted researchers from academia and industry. More and more researches have shown that fractional-order differential equations are useful tools to investigate complex dynamical behaviors and describe various physical and engineering systems. Time delays are found to exist widely in real world systems, such as electronic circuits, chemical, and economical systems [2–7]. It is very necessary to include time delays into a system to model a real-world application. Therefore, scientists from various fields begin to focus on the study of fractional-order delayed differential equations (FDDEs), due to their wide potential applications. Many chaotic systems of FDDEs were proposed and their synchronizations were studied. The fractional-order delayed Liu system was presented and the existence of chaos was investigated in [8], and the impulsive synchronization and robust predictive synchronization were investigated in [9, 10], respectively. The nonlinear dynamics and chaos were studied for the fractional-order delayed financial system in [11], and the sliding-mode

synchronization was investigated in [12]. In [13], hybrid projective synchronization between the two aforementioned systems was done. The fractional-order delayed Chen system was considered in [14], and its adaptive synchronization was investigated in [15].

All the synchronization schemes mentioned above are based on the usual drive-response method, which only has one drive system and one response system. In [16], Luo et al. generalized the usual drive-response synchronization scheme to combination synchronization, which has two drive systems and one response system. Combination synchronization has stronger antidecode and antiattack ability than that of the drive-response synchronization in secure communication, because the origin message can be divided into two segments and each segment can be separated into two distinct drive systems. The authors [17] applied robust adaptive sliding-mode control method to investigate combination synchronization of Lorenz system with time delay. In [18], phase and antiphase combination synchronization of three delayed systems were studied using active control. The adaptive function projective combination synchronization of three fractional-order chaotic systems was investigated in [19]. Jiang et al. [20] analyzed complex

combination synchronization of three fractional-order chaotic complex-variable systems. Delavari and Mohadeszadeh [21] proposed adaptive sliding-mode control method for synchronization of nonidentical fractional-order chaotic and hyperchaotic systems. In [22], combination synchronization of a new fractional-order Lorenz-like system with two stable node-foci was analyzed with the help of nonlinear feedback control method. Although fractional-order delayed chaotic systems were considered in the literature [23], the method used for synchronization was not combination synchronization. The generalization of combination-combination synchronization of chaotic n -dimensional fractional-order dynamical systems is studied in [24]. There exist many works focusing on the combination synchronization of integer-order delayed chaotic systems; however, the conclusions on those works cannot be used on fractional-order delayed chaotic system directly. The problem of combination synchronization of fractional-order delay chaotic system is still an open challenging problem.

Motivated by the above analysis, we consider combination synchronization of three fractional-order delayed chaotic systems, which is an extension of combination synchronization of delayed chaotic systems or combination synchronization of fractional-order chaotic systems. The

Adams-Bashforth-Mounton method is used for numerical solutions of fractional-order delay chaotic system.

2. Preliminaries

Fractional calculus is an old mathematical topic and is an extension of integration and differentiation to noninteger-order fundamental operator ${}_a D_t^r$, which is described by

$${}_a D_t^r = \begin{cases} \frac{d^r}{dt^r}, & r > 0, \\ 1, & r = 0, \\ \int_a^t (d\tau)^{-r}, & r < 0. \end{cases} \quad (1)$$

One of the commonly used definitions for the fractional-order differential operator is the Caputo definition [25, 26], which is defined as

$${}_a D_t^r f(t) = \frac{1}{\Gamma(n-r)} \int_a^t \left(\frac{f(\tau)}{t-\tau} \right)^{r-n+1} d\tau, \quad (2)$$

where $1 < r < n$.

The following is the n -dimensional linear fractional-order differential system with multiple time delays:

$$\begin{cases} D^{\alpha_1} x_1(t) = a_{11}x_1(t - \tau_{11}) + a_{12}x_2(t - \tau_{12}) + \dots + a_{1n}x_n(t - \tau_{1n}), \\ D^{\alpha_2} x_2(t) = a_{21}x_1(t - \tau_{21}) + a_{22}x_2(t - \tau_{22}) + \dots + a_{2n}x_n(t - \tau_{2n}), \\ \vdots \\ D^{\alpha_n} x_n(t) = a_{n1}x_1(t - \tau_{n1}) + a_{n2}x_2(t - \tau_{n2}) + \dots + a_{nm}x_n(t - \tau_{nm}), \end{cases} \quad (3)$$

where α_i is the order of the fractional derivative, which is real and lies in $(0, 1)$, $x_i(t)$ is the state variable, $\tau_{ij} > 0$ is the time delay, the initial value $x_i(t) = \phi_i(t)$ is given by $-\max \tau_{ij} = -\tau_{\max} \leq t \leq 0$, $A = [a_{ij}] \in R_{n \times n}$ is the coefficient matrix.

In order to study the stability of system (3), we first take Laplace transform on system (3) and have

$$\Delta(s) \cdot X(s) = b(s), \quad (4)$$

where $X(s) = (X_1(s), X_2(s), \dots, X_n(s))^T$ is the Laplace transform of $x(t) = (x_1(t), x_2(t), \dots, x_n(t))^T$, $b(s) = (b_1(s), b_2(s), \dots, b_n(s))^T$ is the remaining nonlinear part, and the characteristic matrix of system (3) is

$$\Delta(s) = \begin{pmatrix} s^{\alpha_1} - a_{11}e^{-s\tau_{11}} & -a_{12}e^{-s\tau_{12}} & \dots & -a_{1n}e^{-s\tau_{1n}} \\ -a_{21}e^{-s\tau_{21}} & s^{\alpha_2} - a_{22}e^{-s\tau_{22}} & \dots & -a_{2n}e^{-s\tau_{2n}} \\ \vdots & \vdots & \ddots & \vdots \\ -a_{n1}e^{-s\tau_{n1}} & -a_{n2}e^{-s\tau_{n2}} & \dots & s^{\alpha_n} - a_{nm}e^{-s\tau_{nm}} \end{pmatrix}. \quad (5)$$

Here are some results for system (3).

Theorem 1 (see [27]). *If all the roots of the characteristic equation $\det(\Delta(s)) = 0$ have negative real parts, then the zero*

solution of system (3) is Lyapunov globally asymptotically stable.

Corollary 1 (see [27]). *If $\alpha_1 = \alpha_2 = \dots = \alpha_n = \beta \in (0, 1)$, all the eigenvalues λ of the coefficient matrix A satisfy $|\arg(\lambda)| > \beta\pi/2$, and the characteristic equation $\det(\Delta(s)) = 0$ has no purely imaginary roots for any $\tau_{ij} > 0, i, j = 1, 2, \dots, n$, then the zero solution of system (3) is Lyapunov globally asymptotically stable.*

3. Combination Synchronization of Three Fractional-Order Delayed Systems

In this section, we investigate combination synchronization of three different fractional-order delayed systems.

The following system is considered as the first drive system:

$$\begin{aligned} D^\alpha x(t) &= x(t) + x(t - \tau) + A(x(t), x(t - \tau)), \\ x(t) &= x(0), \quad t \in [-\tau, 0]. \end{aligned} \quad (6)$$

The following system is taken as the second drive system:

$$\begin{aligned} D^\alpha y(t) &= y(t) + y(t - \tau) + B(y(t), y(t - \tau)), \\ y(t) &= y(0), \quad t \in [-\tau, 0]. \end{aligned} \quad (7)$$

And the following system is used as the response system:

$$\begin{aligned} D^\alpha z(t) &= z(t) + z(t - \tau) + C(z(t), z(t - \tau)) + U, \\ z(t) &= z(0), \quad t \in [-\tau, 0], \end{aligned} \quad (8)$$

in which $\alpha \in (0, 1)$ is the order of the fractional differential equations, $\tau > 0$ is the time delay, $U = (U_1, U_2, U_3)$ is the controller vector to be designed later, $x = (x_1, x_2, \dots, x_n)^T \in R^n$, $y = (y_1, y_2, \dots, y_n)^T \in R^n$, and $z = (z_1, z_2, \dots, z_n)^T \in R^n$ are state vectors, and $A: R^{2n} \rightarrow R^n$, $B: R^{2n} \rightarrow R^n$, and $C: R^{2n} \rightarrow R^n$ are continuous vector functions.

The error state vector is defined as

$$e(t) = Fz(t) - Gx(t) - Hy(t), \quad (9)$$

where $e(t) = (e_1, e_2, \dots, e_n)^T \in R^n$, $F = \text{diag}\{f_1, f_2, \dots, f_n\} \in R^{n \times n}$, $G = \text{diag}\{g_1, g_2, \dots, g_n\} \in R^{n \times n}$, and $H = \text{diag}\{h_1, h_2, \dots, h_n\} \in R^{n \times n}$ are real scaling matrix.

Definition 1 (see [21]). The drive systems (6) and (7) and the response system (11) are defined to be combination synchronization if there are three constant matrixes, $F, G, H \in R^n$ and $F \neq 0$ such that

$$\lim_{t \rightarrow +\infty} \|Fz(t) - Gx(t) - Hy(t)\| = 0, \quad (10)$$

where $\|\cdot\|$ stands for the matrix norm.

Remark 1. If the scaling matrix $G = 0$ or $H = 0$, the combination synchronization mentioned above is correspondingly simplified to hybrid synchronization.

Remark 2. When $\tau = 0$, the combination synchronization scheme of fractional-order delayed systems is simplified to the combination synchronization scheme of fractional-order systems.

To achieve combination synchronization of the above systems, a nonlinear controller is constructed:

$$\begin{aligned} U &= \tilde{K}e(t) + GA(x(t), x(t - \tau)) + HB(y(t), y(t - \tau)) \\ &\quad - FC(z(t), z(t - \tau)), \end{aligned} \quad (11)$$

where $\tilde{K} = K - I$, I is an n -dimensional identity matrix, and $K = \text{diag}\{k_1, k_2, \dots, k_n\}$ is a feedback gain matrix.

From equations (6)–(8) and (11), we can get the following error system:

$$D^\alpha e(t) = (\tilde{k} + I)e(t) + e(t - \tau) = Ke(t) + e(t - \tau). \quad (12)$$

When we use the controller U to control fractional-order delay-delayed response system, the combination synchronization problem of the two fractional-order delayed drive systems (6) and (7) and fractional-order delayed response system (8) is changed into the analysis of the asymptotical stability of system (15).

According to Corollary 1, we can have the following sufficient condition to achieve combination synchronization between systems (6) and (7) and system (8).

Theorem 2. *Combination synchronization between the drive systems (6) and (7) and the response system (8) can be achieved if there exists a matrix $K = \text{diag}\{k_1, k_2, \dots, k_n\}$ in equation (15) such that $k_i < (-1/\sin(\alpha\pi/2))$ ($i = 1, 2, \dots, n$).*

Proof. $A = K + I$ is the coefficient matrix for the fractional-order delayed error system (12). Because $k_i < (-1/\sin(\alpha\pi/2))$, $\alpha \in (0, 1)$, the eigenvalues of A are $\lambda_i = k_i + 1 < 0$ ($i = 1, 2, \dots, n$). Therefore, $|\arg(\lambda)| > \pi/2 > \alpha\pi/2$ holds.

Taking Laplace transform on equation (15) gives

$$\Delta(s) \cdot E(s) = s^{\alpha-1}e(0) + e(0)e^{-s\tau} \int_{-\tau}^0 e^{-s\tau} d\tau, \quad (13)$$

where $E(s)$ is the Laplace transform of $e(t)$, $e(0) = Fz(0) - Gx(0) - Hy(0)$, and $\Delta(s) = s^\alpha I - K - e^{-s\tau}I$ is the characteristic matrix. Consequently

$$\begin{aligned} \det(\Delta(s)) &= |s^\alpha I - K - e^{-s\tau}I| = (s^\alpha - k_1 - e^{-s\tau}) \\ &\quad \cdot (s^\alpha - k_2 - e^{-s\tau}) \dots (s^\alpha - k_n - e^{-s\tau}) = 0. \end{aligned} \quad (14)$$

Suppose

$$(s^\alpha - k_i - e^{-s\tau}) = 0, \quad i = 1, 2, \dots, n, \quad (15)$$

has a root $s = wi = |w|(\cos(\pi/2) + i \sin(\pm\pi/2))$. Then

$$|w|^\alpha \left(\cos\left(\frac{\alpha\pi}{2}\right) + i \sin\left(\frac{\pm\alpha\pi}{2}\right) \right) - k_i - \cos(\omega\tau) + i \sin(\omega\tau) = 0. \quad (16)$$

Separating the real and imaginary parts in system (16) yields

$$|w|^\alpha \cos\left(\frac{\alpha\pi}{2}\right) - k_i = \cos(\omega\tau), \quad (17)$$

$$|w|^\alpha \sin\left(\frac{\pm\alpha\pi}{2}\right) = -\sin(\omega\tau).$$

From system (17), we have

$$|w|^{2\alpha} - 2k_i \cos\left(\frac{\alpha\pi}{2}\right) |w|^\alpha + k_i^2 - 1 = 0. \quad (18)$$

Because $k_i < (-1/\sin(\alpha\pi/2))$, $\alpha \in (0, 1)$, then the discriminant of the roots satisfies

$$\begin{aligned} \Delta &= \left(-2k_i \cos\left(\frac{\alpha\pi}{2}\right)\right)^2 - 4(k_i^2 - 1) \\ &= 4\left(1 - k_i^2 \sin^2\left(\frac{\alpha\pi}{2}\right)\right) \\ &< 0, \end{aligned} \quad (19)$$

which means that equation (18) has no real solutions. Consequently, equation (14) has no purely imaginary roots.

According to Corollary 1, the zero solution of the fractional-order delayed error system (12) is globally asymptotically stable; i.e., combination synchronization is obtained between the drive systems (6) and (7) and the response system (8).

The completes the proof. \square

4. Numerical Simulations

In what follows, numerical simulations are performed to illustrate the above-proposed combination synchronization of three different fractional-order delayed systems.

The fractional-order delayed financial system [14] is considered as the first drive system:

$$\begin{cases} D^\alpha x_1 = x_3 - a_1 x_1 + x_1 x_2(t - \tau), \\ D^\alpha x_2 = 1 - b_1 x_2 - x_1^2(t - \tau), \\ D^\alpha x_3 = -x_1(t - \tau) - c_1 x_3. \end{cases} \quad (20)$$

System (20) exhibits a chaotic attractor, as shown in Figure 1.

System (20) can be rewritten as

$$\begin{aligned} D^\alpha x(t) &= x(t) + x(t - \tau) + A(x(t), x(t - \tau)), \\ x(t) &= x(0), \quad t \in [-\tau, 0], \end{aligned} \quad (21)$$

where

$$A(x(t), x(t - \tau)) = \begin{pmatrix} x_3 - (a_1 + 1)x_1 + x_1 x_2(t - \tau) - x_1(t - \tau) \\ 1 - (b_1 + 1)x_2 - x_1^2(t - \tau) - x_2(t - \tau) \\ -x_1(t - \tau) - (c_1 + 1)x_3 - x_3(t - \tau) \end{pmatrix}. \quad (22)$$

The fractional-order delayed Liu system [11] is considered as the second drive system:

$$\begin{cases} D^\alpha y_1 = a_2(y_2 - y_1), \\ D^\alpha y_2 = b_2 y_1(t - \tau) - y_1 y_3, \\ D^\alpha y_3 = -c_2 y_3(t - \tau) + 4y_1^2. \end{cases} \quad (23)$$

System (23) displays a chaotic attractor, as shown in Figure 2.

System (23) can be rewritten as

$$\begin{aligned} D^\alpha y(t) &= y(t) + y(t - \tau) + B(y(t), y(t - \tau)), \\ y(t) &= y(0), \quad t \in [-\tau, 0], \end{aligned} \quad (24)$$

where

$$B(y(t), y(t - \tau)) = \begin{pmatrix} a_2(y_2 - y_1) - y_1 - y_1(t - \tau) \\ b_2 y_1(t - \tau) - y_1 y_3 - y_2 - y_2(t - \tau) \\ -(c_2 + 1)y_3(t - \tau) + 4y_1^2 - y_3 \end{pmatrix}. \quad (25)$$

The fractional-order delayed Lorenz system [15] is the response system given by

$$\begin{cases} D^\alpha z_1 = a_3(z_2 - z_1) + U_1, \\ D^\alpha z_2 = c_3 z_1 - z_2 - z_1 z_3 + U_2, \\ D^\alpha z_3 = z_1 z_2 - b_3 z_3(t - \tau) + U_3, \end{cases} \quad (26)$$

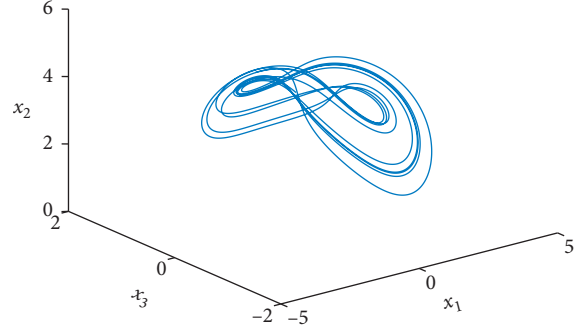


FIGURE 1: Chaotic attractor of financial system: $\alpha = 0.92$, $\tau = 0.01$.

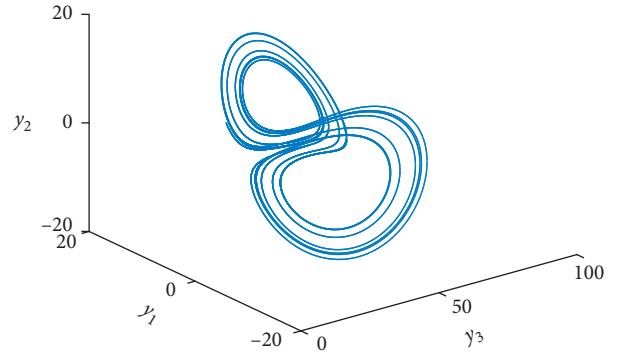


FIGURE 2: Chaotic attractor of Liu system: $\alpha = 0.92$, $\tau = 0.01$.

where U_1 , U_2 , and U_3 are controllers to be determined later. Without the controllers, system (26) displays a chaotic attractor, as shown in Figure 3.

System (26) can be rewritten as

$$\begin{aligned} D^\alpha z(t) &= z(t) + z(t - \tau) + C(z(t), z(t - \tau)) + U, \\ z(t) &= z(0), \quad t \in [-\tau, 0], \end{aligned} \quad (27)$$

where

$$C(z(t), z(t - \tau)) = \begin{pmatrix} a_3(z_2 - z_1) - z_1 - z_1(t - \tau) \\ c_3 z_1 - 2z_2 - z_1 z_3 - z_2(t - \tau) \\ z_1 z_2 - (b_3 + 1)z_3(t - \tau) - z_3 \end{pmatrix}. \quad (28)$$

In the following analysis, we suppose that $F = \text{diag}(f_1, f_2, f_3)$, $G = \text{diag}(g_1, g_2, g_3)$, and $H = \text{diag}(h_1, h_2, h_3)$.

The error states are defined by

$$\begin{cases} e_1 = f_1 z_1 - g_1 x_1 - h_1 y_1, \\ e_2 = f_2 z_2 - g_2 x_2 - h_2 y_2, \\ e_3 = f_3 z_3 - g_3 x_3 - h_3 y_3, \end{cases} \quad (29)$$

such that

$$\begin{cases} \lim_{t \rightarrow \infty} \|f_1 z_1 - g_1 x_1 - h_1 y_1\| = 0, \\ \lim_{t \rightarrow \infty} \|f_2 z_2 - g_2 x_2 - h_2 y_2\| = 0, \\ \lim_{t \rightarrow \infty} \|f_3 z_3 - g_3 x_3 - h_3 y_3\| = 0. \end{cases} \quad (30)$$

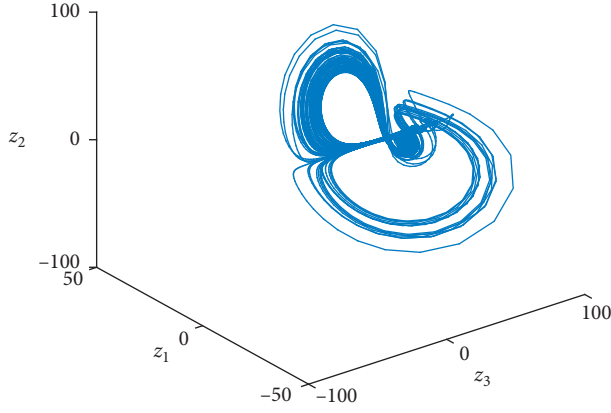


FIGURE 3: Chaotic attractor of Lorenz system: $\alpha = 0.92$, $\tau = 0.1$.

Subtracting (20) and (23) from (26), the error dynamical systems are obtained as follows:

$$\begin{cases} D^\alpha e_1 = f_1 D^\alpha z_1 - g_1 D^\alpha x_1 - h_1 D^\alpha y_1, \\ D^\alpha e_2 = f_2 D^\alpha z_2 - g_2 D^\alpha x_2 - h_2 D^\alpha y_2, \\ D^\alpha e_3 = f_3 D^\alpha z_3 - g_3 D^\alpha x_3 - h_3 D^\alpha y_3. \end{cases} \quad (31)$$

Substituting equations (20), (23), and (26) into equation (31) gives

$$\begin{cases} D^\alpha e_1 = f_1 [a_3 (z_2 - z_1)] - g_1 [x_3 - a_1 x_1 + x_1 x_2 (t - \tau)] \\ \quad - h_1 [a_2 (y_2 - y_1)] + f_1 U_1, \\ D^\alpha e_2 = f_2 (c_3 z_1 - z_2 - z_1 z_3) - g_2 (1 - b_1 x_2 - x_1^2 (t - \tau)) \\ \quad - h_2 (b_2 y_1 (t - \tau) - y_1 y_3) + f_2 U_2, \\ D^\alpha e_3 = f_3 (z_1 z_2 - b_3 z_3 (t - \tau)) - g_3 (-x_1 (t - \tau) - c_1 x_3) \\ \quad - h_3 (-c_2 y_3 (t - \tau) + 4y_1^2) + f_3 U_3. \end{cases} \quad (32)$$

Here are our results.

Theorem 3. *Combination synchronization between the driven systems (20) and (23) and the response system (26) can be obtained by presenting controllers as follows:*

$$\begin{cases} U_1 = \frac{1}{f_1} \{ (k_1 - 1) (f_1 z_1 - g_1 x_1 - h_1 y_1) + g_1 (x_3 - (a_1 + 1)x_1 + x_1 x_2 (t - \tau) - x_1 (t - \tau)) \\ \quad + h_1 (a_2 (y_2 - y_1) - y_1 - y_1 (t - \tau)) - f_1 (a_3 z_2 - (a_3 + 1)z_1 - z_1 (t - \tau)) \}, \\ U_2 = \frac{1}{f_2} \{ (k_2 - 1) (f_2 z_2 - g_2 x_2 - h_2 y_2) + g_2 (1 - (b_1 + 1)x_2 - x_1^2 (t - \tau) - x_2 (t - \tau)) \\ \quad + h_2 (b_2 y_1 (t - \tau) - y_1 y_3 - y_2 - y_2 (t - \tau)) - f_2 (c_3 z_1 - 2z_2 - z_1 z_3 - z_2 (t - \tau)) \}, \\ U_3 = \frac{1}{f_3} \{ (k_3 - 1) (f_3 z_3 - g_3 x_3 - h_3 y_3) + g_3 (-x_1 (t - \tau) - (c_1 + 1)x_3 - x_3 (t - \tau)) \\ \quad + h_3 (-c_2 y_3 (t - \tau) + 4y_1^2 - y_3) - f_3 (z_1 z_2 - (b_3 + 1)z_3 (t - \tau) - z_3) \}. \end{cases} \quad (33)$$

Corollary 2

(i) Suppose that $g_1 = g_2 = g_3 = 0$, and f_1 , f_2 , and f_3 are nonzero, projective synchronization between the

drive system (23) and the response system (26) can be obtained by presenting controllers as follows:

$$\begin{cases} U_1 = \frac{1}{f_1} \{ (k_1 - 1) (f_1 z_1 - h_1 y_1) + h_1 (a_2 (y_2 - y_1) - y_1 - y_1 (t - \tau)) - f_1 (a_3 z_2 - (a_3 + 1)z_1 - z_1 (t - \tau)) \}, \\ U_2 = \frac{1}{f_2} \{ (k_2 - 1) (f_2 z_2 - h_2 y_2) + h_2 (b_2 y_1 (t - \tau) - y_1 y_3 - y_2 - y_2 (t - \tau)) - f_2 (c_3 z_1 - 2z_2 - z_1 z_3 - z_2 (t - \tau)) \}, \\ U_3 = \frac{1}{f_3} \{ (k_3 - 1) (f_3 z_3 - h_3 y_3) + h_3 (-c_2 y_3 (t - \tau) + 4y_1^2 - y_3) - f_3 (z_1 z_2 - (b_3 + 1)z_3 (t - \tau) - z_3) \}. \end{cases} \quad (34)$$

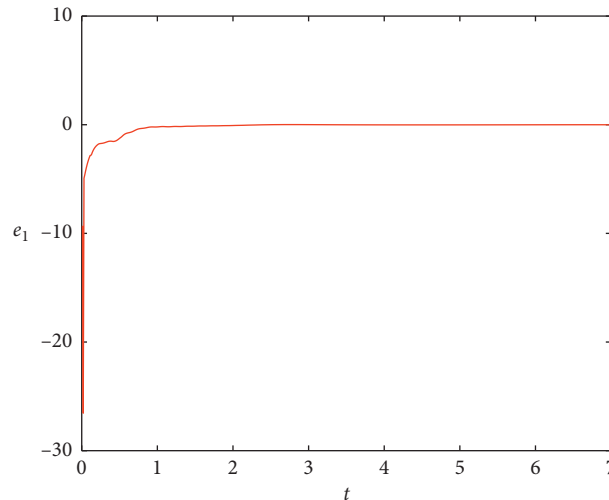


FIGURE 4: Combination synchronization errors e_1 between drive systems (20) and (23) and response system (26).

(ii) Accordingly, suppose that $h_1 = h_2 = h_3 = 0$, and f_1, f_2 , and f_3 are nonzero, projective synchronization between the drive system (20) and the

response system (26) can be obtained by presenting controllers as follows:

$$\begin{cases} U_1 = \frac{1}{f_1} \{ (k_1 - 1)(f_1 z_1 - g_1 x_1) + g_1(x_3 - (a_1 + 1)x_1 + x_1 x_2(t - \tau) - x_1(t - \tau)) - f_1(a_3 z_2 - (a_3 + 1)z_1 - z_1(t - \tau)) \}, \\ U_2 = \frac{1}{f_2} \{ (k_2 - 1)(f_2 z_2 - g_2 x_2) + g_2(1 - (b_1 + 1)x_2 - x_1^2(t - \tau) - x_2(t - \tau)) - f_2(c_3 z_1 - 2z_2 - z_1 z_3 - z_2(t - \tau)) \}, \\ U_3 = \frac{1}{f_3} \{ (k_3 - 1)(f_3 z_3 - g_3 x_3) + g_3(-x_1(t - \tau) - (c_1 + 1)x_3 - x_3(t - \tau)) - f_3(z_1 z_2 - (b_3 + 1)z_3(t - \tau) - z_3) \}. \end{cases} \quad (35)$$

Corollary 3. Suppose that $g_1 = g_2 = g_3 = 0, h_1 = h_2 = h_3 = 0$, and f_1, f_2 , and f_3 are nonzero, system (26) can be

stabilized to its equilibrium $O(0, 0, 0)$ with the following controllers:

$$\begin{cases} U_1 = \frac{1}{f_1} \{ (k_1 - 1)(f_1 z_1) - f_1(a_3 z_2 - (a_3 + 1)z_1 - z_1(t - \tau)) \}, \\ U_2 = \frac{1}{f_2} \{ (k_2 - 1)(f_2 z_2) - f_2(c_3 z_1 - 2z_2 - z_1 z_3 - z_2(t - \tau)) \}, \\ U_3 = \frac{1}{f_3} \{ (k_3 - 1)(f_3 z_3) - f_3(z_1 z_2 - (b_3 + 1)z_3(t - \tau) - z_3) \}. \end{cases} \quad (36)$$

In the numerical simulations, the system parameters are set as $a_1 = 3, b_1 = 0.1, c_1 = 1, a_2 = 10, b_2 = 40, c_2 = 2.5, a_3 = 10, b_3 = 8/3$, and $c_3 = 28$, respectively. For simplicity, suppose $f_1 = f_2 = f_3 = 1, g_1 = g_2 = g_3 = 1$, and $h_1 = h_2 = h_3 = 1$. The initial values for all of the systems are set as

$(x_1(0), x_2(0), x_3(0)) = (0.1, 4, 0.5), (y_1(0), y_2(0), y_3(0)) = (1.2, 2.4, 11)$, and $(z_1(0), z_2(0), z_3(0)) = (-8, 2, 3)$, respectively. Figures 4–6 display time responses of the combination synchronization errors e_1, e_2 , and e_3 . From Figures 4–6, we can observe that error states converge to zero;

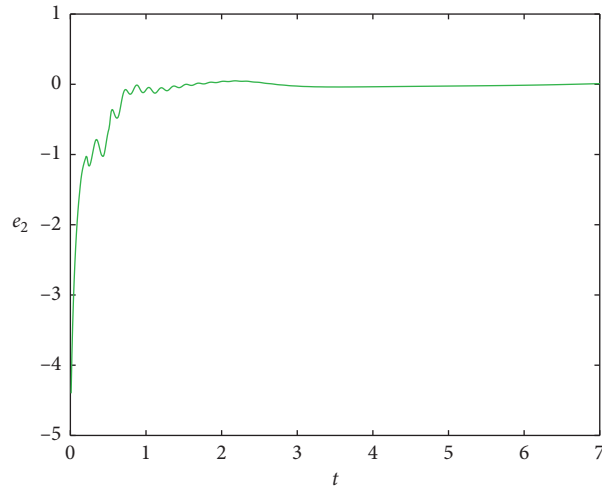


FIGURE 5: Combination synchronization errors e_2 between drive systems (20) and (23) and response system (26).

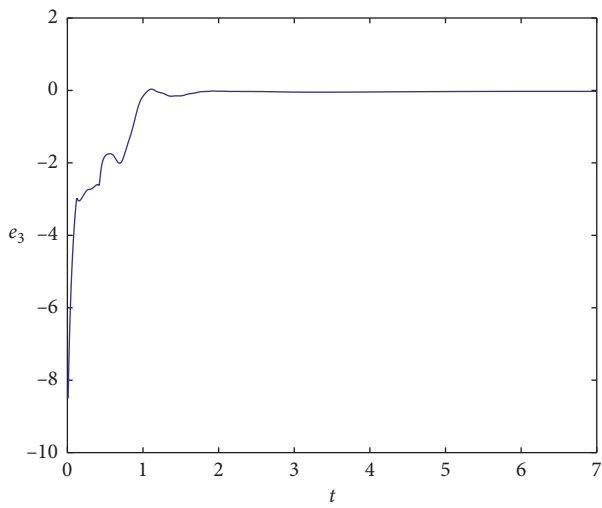
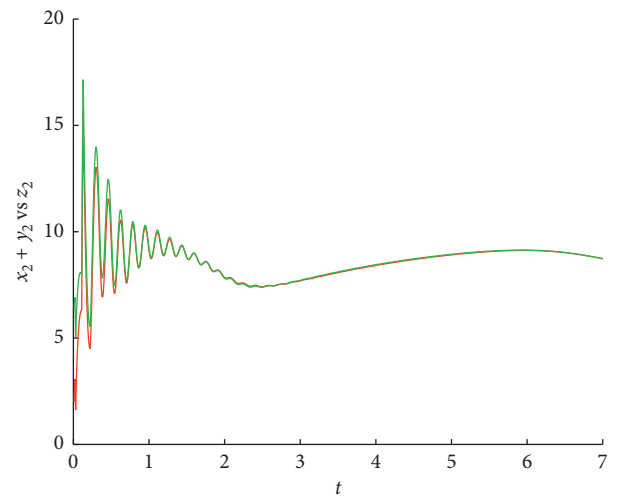
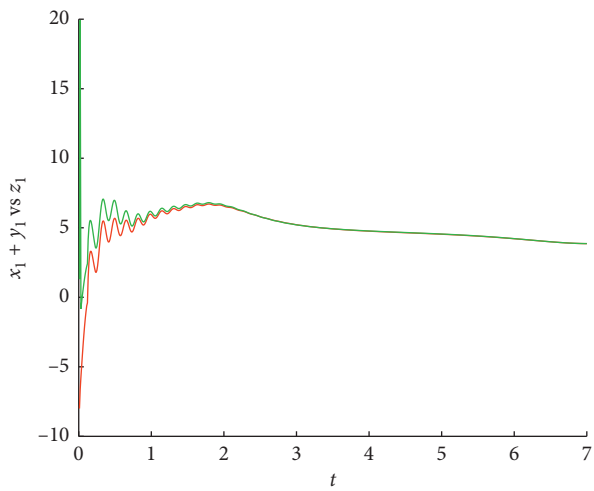


FIGURE 6: Combination synchronization errors e_3 between drive systems (20) and (23) and response system (26).



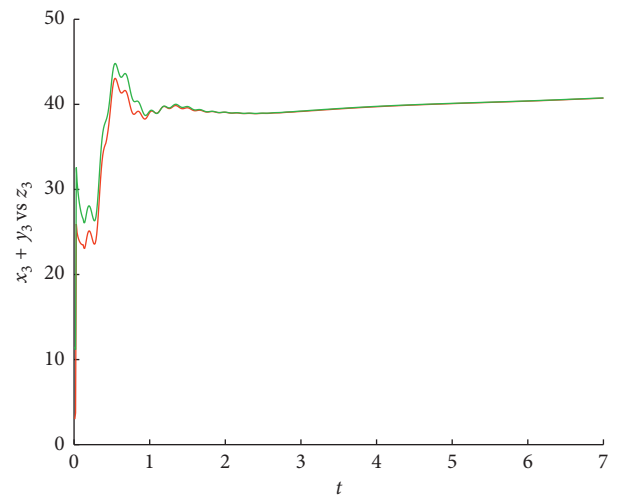
— z_2
— $x_2 + y_2$

FIGURE 8: Time responses for state $x_2 + y_2$ versus z_2 .



— z_1
— $x_1 + y_1$

FIGURE 7: Time responses for state $x_1 + y_1$ versus z_1 .



— z_3
— $x_3 + y_3$

FIGURE 9: Time responses for state $x_3 + y_3$ versus z_3 .

i.e., combination synchronization is achieved. Figures 7–9 illustrate the time responses of the states $x_1 + y_1$ versus z_1 , $x_2 + y_2$ versus z_2 , $x_3 + y_3$ versus z_3 , respectively.

5. Conclusions

In this paper, we investigate combination synchronization of three different fractional-order delayed chaotic systems by generalizing combination synchronization of delayed chaotic systems or combination synchronization of fractional-order chaotic systems. With the help of the stability theory for linear fractional-order systems with multiple time delays, controllers are proposed to achieve combination synchronization of three different fractional-order delayed chaotic systems. In addition, projective synchronization [28] of three different fractional-order delayed chaotic systems is a special case of our work. Numerical simulations are presented to demonstrate and verify the applicability and feasibility of our theoretical analysis.

Data Availability

The data used to support the findings of this study are available from the corresponding author upon request.

Conflicts of Interest

The authors declare that they have no conflicts of interest.

Acknowledgments

This work was supported by the Natural Science Foundations of China under Grant 61463050 and the NSF of Yunnan Province under Grant 2015FB113.

References

- [1] B. B. Mandelbrot, *The Fractal Geometry of Nature*, WH freeman, New York, USA, 1983.
- [2] J.-P. Richard, "Time-delay systems: an overview of some recent advances and open problems," *Automatica*, vol. 39, no. 10, pp. 1667–1694, 2003.
- [3] G. M. Mahmoud, E. E. Mahmoud, and A. A. Arafa, "On modified time delay hyperchaotic complex Lü system," *Nonlinear Dynamics*, vol. 80, no. 1-2, pp. 855–869, 2015.
- [4] Y. Fan, X. Huang, Y. Li, J. Xia, and G. Chen, "Aperiodically intermittent control for quasi-synchronization of delayed memristive neural networks: an interval matrix and matrix measure combined method," *IEEE Transactions on Systems, Man, and Cybernetics: Systems*, vol. 49, no. 11, pp. 2254–2265, 2019.
- [5] Y. Fan, X. Huang, H. Shen, and J. Cao, "Switching event-triggered control for global stabilization of delayed memristive neural networks: an exponential attenuation scheme," *Neural Networks*, vol. 117, pp. 216–224, 2019.
- [6] L. Xiong, J. Cheng, J. Cao, and Z. Liu, "Novel inequality with application to improve the stability criterion for dynamical systems with two additive time-varying delays," *Applied Mathematics and Computation*, vol. 321, pp. 672–688, 2018.
- [7] J. Jia, X. Huang, Y. Li, J. Cao, and A. Alsaedi, "Global stabilization of fractional-order memristor-based neural networks with time delay," *IEEE Transactions on Neural Networks and Learning Systems*, pp. 1–13, 2019.
- [8] S. Bhalekar and V. Daftardar-Gejji, "Fractional ordered Liu system with time-delay," *Communications in Nonlinear Science and Numerical Simulation*, vol. 15, no. 8, pp. 2178–2191, 2010.
- [9] D. Li and X. Zhang, "Impulsive synchronization of fractional order chaotic systems with time-delay," *Neurocomputing*, vol. 216, pp. 39–44, 2016.
- [10] A. Mohammadzadeh, S. Ghaemi, O. Kaynak, and S. K. Mohammadi, "Robust predictive synchronization of uncertain fractional-order time-delayed chaotic systems," *Soft Computing*, vol. 23, no. 16, pp. 6883–6898, 2019.
- [11] Z. Wang, X. Huang, and G. Shi, "Analysis of nonlinear dynamics and chaos in a fractional order financial system with time delay," *Computers & Mathematics with Applications*, vol. 62, no. 3, pp. 1531–1539, 2011.
- [12] H. Liu and J. Yang, "Sliding-mode synchronization control for uncertain fractional-order chaotic systems with time delay," *Entropy*, vol. 17, no. 6, pp. 4202–4214, 2015.
- [13] S. Wang, Y. Yu, and G. Wen, "Hybrid projective synchronization of time-delayed fractional order chaotic systems," *Nonlinear Analysis: Hybrid Systems*, vol. 11, pp. 129–138, 2014.
- [14] V. Daftardar-Gejji, S. Bhalekar, and P. Gade, "Dynamics of fractional-ordered Chen system with delay," *Pramana*, vol. 79, no. 1, pp. 61–69, 2012.
- [15] X. Song, S. Song, and B. Li, "Adaptive synchronization of two time-delayed fractional-order chaotic systems with different structure and different order," *Optik*, vol. 127, no. 24, pp. 11860–11870, 2016.
- [16] R. Luo, Y. Wang, and S. Deng, "Combination synchronization of three classic chaotic systems using active backstepping design," *Chaos: An Interdisciplinary Journal of Nonlinear Science*, vol. 21, no. 4, Article ID 043114, 2011.
- [17] A. Khan, "Combination synchronization of time-delay chaotic system via robust adaptive sliding mode control," *Pramana*, vol. 88, no. 6, p. 91, 2017.
- [18] G. M. Mahmoud, A. A. Arafa, and E. E. Mahmoud, "On phase and anti-phase combination synchronization of time delay nonlinear systems," *Journal of Computational and Nonlinear Dynamics*, vol. 13, no. 11, p. 111001, 2018.
- [19] H. Xi, Y. Li, and X. Huang, "Adaptive function projective combination synchronization of three different fractional-order chaotic systems," *Optik*, vol. 126, no. 24, pp. 5346–5349, 2015.
- [20] C. Jiang, S. Liu, and D. Wang, "Generalized combination complex synchronization for fractional-order chaotic complex systems," *Entropy*, vol. 17, no. 8, pp. 5199–5217, 2015.
- [21] H. Delavari and M. Mohadeszadeh, "Robust finite-time synchronization of non-identical fractional-order hyperchaotic systems and its application in secure communication," *IEEE/CAA Journal of Automatica Sinica*, vol. 6, no. 1, pp. 228–235, 2019.
- [22] Z. Alam, L. Yuan, and Q. Yang, "Chaos and combination synchronization of a new fractional-order system with two stable node-foci," *IEEE/CAA Journal of Automatica Sinica*, vol. 3, no. 2, pp. 157–164, 2016.
- [23] S. He, K. Sun, and H. Wang, "Synchronisation of fractional-order time delayed chaotic systems with ring connection," *The European Physical Journal Special Topics*, vol. 225, no. 1, pp. 97–106, 2016.
- [24] G. M. Mahmoud, T. M. Abed-Elhameed, and M. E. Ahmed, "Generalization of combination-combination synchronization of chaotic n -dimensional fractional-order dynamical

- systems,” *Nonlinear Dynamics*, vol. 83, no. 4, pp. 1885–1893, 2016.
- [25] I. Podlubny, *Fractional Differential Equations: An Introduction to Fractional Derivatives, Fractional Differential Equations, to Methods of Their Solution and Some of Their Applications*, Academic Press, New York, USA, 1999.
- [26] S. G. Samko, A. A. Kilbas, and O. I. Marichev, *Fractional Integrals and Derivatives: Theory and Applications*, Taylor & Francis, New York, USA, 1993.
- [27] W. Deng, C. Li, and J. Lü, “Stability analysis of linear fractional differential system with multiple time delays,” *Nonlinear Dynamics*, vol. 48, no. 4, pp. 409–416, 2007.
- [28] G. M. Mahmoud, E. E. Mahmoud, and A. A. Arafa, “Projective synchronization for coupled partially linear complex-variable systems with known parameters,” *Mathematical Methods in the Applied Sciences*, vol. 40, no. 4, pp. 1214–1222, 2017.

Research Article

Robust Control of Disturbed Fractional-Order Economical Chaotic Systems with Uncertain Parameters

Song Xu ^{1,2}, Hui Lv ³, Heng Liu ⁴ and Aijing Liu⁵

¹School of Economics and Management, Anhui Jianzhu University, Hefei 230009, China

²School of Economics and Management, Huainan Normal University, Huainan 232038, China

³Department of Applied Mathematics, Huainan Normal University, Huainan 232038, China

⁴School of Science, Guangxi University for Nationalities, Nanning 530006, China

⁵School of Mathematical Sciences, Qufu Normal University, Qufu 273165, China

Correspondence should be addressed to Heng Liu; liuheng122@gmail.com

Received 16 May 2019; Revised 22 August 2019; Accepted 5 September 2019; Published 31 October 2019

Guest Editor: Lazaros Moysis

Copyright © 2019 Song Xu et al. This is an open access article distributed under the Creative Commons Attribution License, which permits unrestricted use, distribution, and reproduction in any medium, provided the original work is properly cited.

This paper focuses on the robust control of fractional-order economical chaotic system (FOECS) with parametric uncertainties and external disturbances. The dynamical behavior of FOECS is studied by numerical simulation, and circuit implementations of FOECS are also given. Based on fractional-order Lyapunov stability theorems, a robust adaptive controller, which can guarantee that all signals remain bounded and the tracking error tends to a small region, is designed. The proposed method can be used to control a large range of fractional-order systems with system uncertainties. Fractional-order adaptation laws are constructed to update the estimation of adaptive parameters. Finally, the robustness and effectiveness of our control method are indicated by simulation results.

1. Introduction

It has been shown that fractional-order nonlinear systems (FONSs) have been investigated by a lot of engineers and physicists because FONSs have wide potential applications in many domains [1–3]. In fact, the fractional calculus brings some advantages in modeling nonlinear systems. The fractional calculus can model real-world models in the whole-time domain, and it has memory. It should be mentioned that the integer-order one does not have these abilities. Thus, the fractional calculus will play a great role in modeling many actual systems, for example, stochastic diffusion, molecular spectroscopy, control theory, viscoelastic dynamics, quantum mechanics, and many research results can be seen in [4–8] and the references therein. On the contrary, it is well known that chaotic system is a supremely intricate nonlinear system that has been widely investigated due to its successful applications in signal processing, combinatorial optimization, secure communication, and many others. Especially, a chaotic system has the property that it is sensitive to the changing of

initial conditions and the variations of the system parameters. Consequently, a large number of meritorious results on control and synchronization of fractional-order chaotic dynamics of nonlinear systems have become a hot research topic and a lot of interesting results have been reported, for example, in [9–13].

In the last two decades, the study of economical system has become more and more popular [14–24]. A lot of works have been done to describe properties of economical date and the dynamic behavior of economical systems. Recently, many researchers have made a lot of efforts to investigate main features of economic theory, e.g., overlapping waves of structural changes or commercial demand and irregular and erratic economic fluctuations. In fact, economists usually consider a model that has a simple behavior and composed of only endogenous variables. Thus, they can consider exogenous shock variables based on weather variables, political events, and other human factors. To describe the complicated economical behavior, some mathematical models were also introduced, for example, the van der Pol model [25] and

the IS-LM model [26]. Actually, there are many kinds of nonlinear systems that show chaotic behavior [27]. Thus, if economical systems show chaotic phenomenon, it is hard for people to provide feasible economic decision making. That is to say, it is advisable to study and control economical chaotic systems.

The remainder of our work is organized as follows: Section 2 presents the development of research in this field, the existing research gaps, and the contributions of this study. Section 3 gives some preliminaries about the fractional calculus and the description and dynamical behavior of fractional-order economical chaotic systems (FOECSs). Section 4 presents the controller design procedure and the stability analysis. Simulation results are shown in Section 5. Finally, Section 6 gives a brief conclusion of this paper.

2. Literature Review

The chaotic dynamics in economical systems were first founded in 1985, and after that, many control and synchronization methods for economical chaotic systems have been reported [16, 28–30]. In [16], a robust adaptive controller was given to control chaos in FOECSs, where the matched system uncertainties were considered, whereas in [16], the $\text{sign}(\cdot)$ function was used in the controller design which will lead to chattering phenomenon. In order to control a representative chaotic fractional finance system, an adaptive fuzzy control approach was given in [31] where fuzzy systems were used to approximate nonlinear functions. A new aspect of robust synchronization of a FOECS has been addressed in [32]. The fixed points and chaotic and periodic motions are given in [33], and dynamical behavior of a FOECS with time delay was studied in [34]. Dadras and Momeni [28] provided an adaptive control method to study the synchronization problem of FOECSs based on a sliding surface. The system studied in [28] was known, but it is impossible to accurately model an actual system in real life. And in the controller design, in order to make the sliding mode exist at every point of the sliding mode surface, the control law was constructed by using the sign function so that the chattering was unavoidable. In the final stability analysis, the integer-order Lyapunov stability theory was applied. Therefore, compared with [16], Dadras and Momeni [28] did not completely study the fractional-order economic chaotic system with the fractional-order stability theory. It should be mentioned that in the above literature considering the control or synchronization of FOECSs, the system model should be known in advance. However, it is well known that most systems suffer from system uncertainties and disturbances in nature. In actual life, we know that economical systems may suffer from weather changes, the limited size of transport, political influence, monetary policy, and many other human factors. Consequently, we should take system uncertainties and external disturbances into consideration when we investigate the control of FOECSs.

Due to limitations of available theoretical tools for analyzing the stability of nonlinear fractional systems, the number of research studies in this field is still low in comparison to that of integer-order systems. Based on the above discussion, in this paper, we investigate the control of FOECSs with unmatched system uncertainties and external disturbances. The fractional Lyapunov stability method is utilized to design the robust controller and analyze the system's stability. Compared with some related works, the main contribution of our work can be concluded as follows. (1) A robust adaptive controller is designed for FOECSs with unmatched system uncertainties. The system uncertainties model we considered is representative, and many models used in the literature, for example, in [16], can be seen as a special case of our model. (2) The stability analysis is proven strictly. The stability analysis method we used is very similar to that of the integer-order systems. It should be pointed out that our main result (see, Theorem 1) of our method provides a framework which can be easily referenced to analyze stability of fractional-order systems.

3. Preliminaries

3.1. Fractional Calculus. The α -th fractional-order integral is

$$\mathbb{D}_t^{-\alpha} f(t) = \frac{1}{\Gamma(\alpha)} \int_0^t (t-\tau)^{\alpha-1} f(\tau) d\tau, \quad (1)$$

where $\Gamma(\cdot)$ represents Euler's function.

Caputo's α -th derivative is given as

$$\mathbb{D}_t^\alpha f(t) = \frac{1}{\Gamma(n-\alpha)} \int_0^t (t-\tau)^{n-\alpha-1} f^{(n)}(\tau) d\tau, \quad (2)$$

where $n-1 \leq \alpha < n$.

For fractional calculus, we give the following results to facilitate the controller design as well as the stability analysis.

Definition 1 (see [1]). The Mittag-Leffler function is given as

$$E_{\alpha,\beta}(z) = \sum_{k=0}^{\infty} \frac{z^k}{\Gamma(\alpha k + \beta)}, \quad (3)$$

with $\alpha, \beta > 0$ and $z \in \mathbb{C}$.

The Laplace transform of (3) can be given as

$$\mathcal{L}\{t^{\beta-1} E_{\alpha,\beta}(-at^\alpha)\} = \frac{s^{\alpha-\beta}}{s^\alpha + a}, \quad (4)$$

where $a \in \mathbb{R}^+$ is a constant.

Lemma 1 (see [1]). Let $\beta \in \mathbb{C}$, $0 < \alpha < 2$, $\mu \in \mathbb{R}$, and

$$\frac{\pi\alpha}{2} < \mu < \min\{\pi, \pi\alpha\}, \quad (5)$$

and then it holds

$$E_{\alpha,\beta}(z) = -\sum_{j=1}^n \frac{1}{\Gamma(\beta - \alpha j)z^j} + o\left(\frac{1}{|z|^{n+1}}\right), \quad |z| \rightarrow \infty, \quad (6)$$

where $n \in \mathbb{N}$ and $\mu \leq |\arg(z)| \leq \pi$.

Lemma 2 (see [1]). Suppose that $0 < \alpha < 2$ and $\beta \in \mathbb{R}$. For $\mu > 0$ and $(\pi\alpha/2) < \mu \leq \min\{\pi, \pi\alpha\}$, it holds

$$|E_{\alpha,\beta}(z)| \leq \frac{a}{1+|z|}, \quad (7)$$

with $a > 0$ and $\mu \leq |\arg(z)| \leq \pi$ and $|z| \geq 0$.

Lemma 3 (see [35]). Let $x(t)$ be a smooth function. Suppose that $x(t) = 0$ is an equilibrium of

$$\mathbb{D}_t^\alpha x(t) = f(x), \quad (8)$$

where $f(x)$ is a continuous nonlinear function. If

$$\begin{aligned} g_1(\|x\|) &\leq V(t, x(t)) \leq g_2(\|x\|), \\ \mathbb{D}_t^\beta V(t, x(t)) &\leq -g_3(\|x\|), \end{aligned} \quad (9)$$

with $0 < \beta < 1$ and $g_1(\cdot), g_2(\cdot)$, and $g_3(\cdot)$ being class- k functions, then system (8) is asymptotically stable.

Lemma 4 (see [7, 36]). Suppose that $x(t) \in \mathbb{R}^n$ is a smooth function. For $0 < \alpha < 1$, it holds

$$\frac{1}{2} \mathbb{D}_t^\alpha x^T(t)x(t) \leq x^T(t) \mathbb{D}_t^\alpha x(t). \quad (10)$$

Lemma 5 (see [1]). Let $x(t) \in \mathbb{C}^1[0, T]$ with $T > 0$ and $0 < \alpha \leq 1$, then it holds

$$\begin{aligned} \mathbb{D}_t^{-\alpha} \mathbb{D}_t^\alpha x(t) &= x(t) - x(0), \\ \mathbb{D}_t^\alpha \mathbb{D}_t^{-\alpha} x(t) &= x(t). \end{aligned} \quad (11)$$

In the following parts, we will use an algorithm to solve fractional-order differential equations. A brief explanation of this algorithm is given below.

Consider

$$\begin{cases} \mathbb{D}_t^\alpha y(t) = f(t, y(t)), \\ y(0) = y_0. \end{cases} \quad (12)$$

Based on Lemma 5, (12) can be rewritten as

$$y(t) = y_0 + \frac{1}{\Gamma(\alpha)} \int_0^t (t-\tau)^{\alpha-1} f(\tau, y(\tau)) d\tau. \quad (13)$$

Define $h = (T/N)$, $N \in \mathbb{Z}$, $t_n = nh$, $n = 0, 1, \dots, N$. Thus, (13) is estimated as [1]

$$\begin{aligned} y_h(t_{n+1}) &= y_0 + \frac{h^\alpha}{\Gamma(\alpha+2)} f(t_n+1, y_h^p(t_{n+1})) \\ &\quad + \frac{h^\alpha}{\Gamma(\alpha+2)} \sum_{j=0}^n a_{j,n+1} f(t_j, y_h(t_j)), \end{aligned} \quad (14)$$

with $a_{j,n+1} = n^{\alpha+1} - (n-\alpha)(n+1)^\alpha$ for $j=0$ and $a_{j,n+1} = (n-j+2)^{\alpha+1} + (n-j)^{\alpha+1} - 2(n-j+1)^{\alpha+1}$ for $1 \leq j \leq n$, $y_h^p(t_{n+1}) = y_0 + (1/\Gamma(\alpha)) \sum_{j=0}^n b_{j,n+1} f(t_j, y_h(t_j))$, $p = \alpha + 1$, and $b_{j,n+1} = (h^\alpha/\alpha)((n+1-j)^\alpha - (n-j)^\alpha)$.

The approximation error can be obtained as $\max|y(t_j) - y_h(t_j)| = o(h^p)$ [1].

3.2. The FOECS. The FOECS can be described by

$$\begin{cases} \mathbb{D}_t^\alpha \zeta_1(t) = \zeta_3(t) + (\zeta_2(t) - a)\zeta_1(t) + a_1\zeta_4(t), \\ \mathbb{D}_t^\alpha \zeta_2(t) = 1 - b\zeta_2(t) - \zeta_1^2(t) + a_2\zeta_4(t), \\ \mathbb{D}_t^\alpha \zeta_3(t) = -\zeta_1(t) - c\zeta_3(t) + a_3\zeta_4(t), \\ \mathbb{D}_t^\alpha \zeta_4(t) = -\zeta_1(t)\zeta_2(t)\zeta_3(t), \end{cases} \quad (15)$$

where $0 < \alpha \leq 1$ is the fractional order, $\zeta_1(t)$ represents the interest rate of the market, $\zeta_2(t)$ is the investment demand, $\zeta_3(t)$ corresponds to the price index, $\zeta_4(t)$ is the confidence of the market, a stands for the saving amount, b is the cost in each investment, c represents the demand elasticity, and a_1, a_2 , and a_3 are impact parameters. Let $\zeta(t) = [\zeta_1(t), \zeta_2(t), \zeta_3(t), \zeta_4(t)]^T$ be the state vector.

Let $a = 2.10$, $b = 0.01$, $c = 2.61$, $a_1 = 8.41$, $a_2 = 6.40$, $a_3 = 2.21$, and the initial condition be $\zeta(0) = [1.0, 5.0, 4.1, 3.0]^T$.

It has been shown in [37] that, under above parameters, when $\alpha > 0.88$, the system (15) exhibits chaotic behavior. Figure 1 shows the chaotic behavior of system (15) for $\alpha = 0.90$.

Now, let us consider the circuit implementation of the FOECS. Just as the results in [38], the approximation of $(1/s^{0.9})$ can be given by

$$\frac{1}{s^{0.9}} \approx \frac{2.2675(s + 1.292)(s + 215.4)}{(s + 0.01292)(s + 2.154)(s + 359.4)}. \quad (16)$$

Thus, a unit circuit is designed to implement the function $(1/s^{0.9})$ which is shown in Figure 2. Here, the chain fractance consists of three resistors R_a, R_b , and R_d and three capacitors C_a, C_b , and C_d . The transfer function FC(s) of this chain can be given by

$$FC(s) = \frac{(C_0/C_a)}{s + (1/R_a C_a)} + \frac{(C_0/C_b)}{s + (1/R_b C_b)} + \frac{(C_0/C_d)}{s + (1/R_d C_d)}. \quad (17)$$

Let $C_0 = 1\mu\text{F}$; from (16) and (17), we can gain $R_a = 62.84\text{M}\Omega$, $R_b = 250\text{k}\Omega$, $R_d = 205\text{k}\Omega$, $C_a = 1.23\mu\text{F}$, $C_b = 1.835\mu\text{F}$, $C_d = 1.1\mu\text{F}$, and $FC(t) \approx (1/t^{0.9})$.

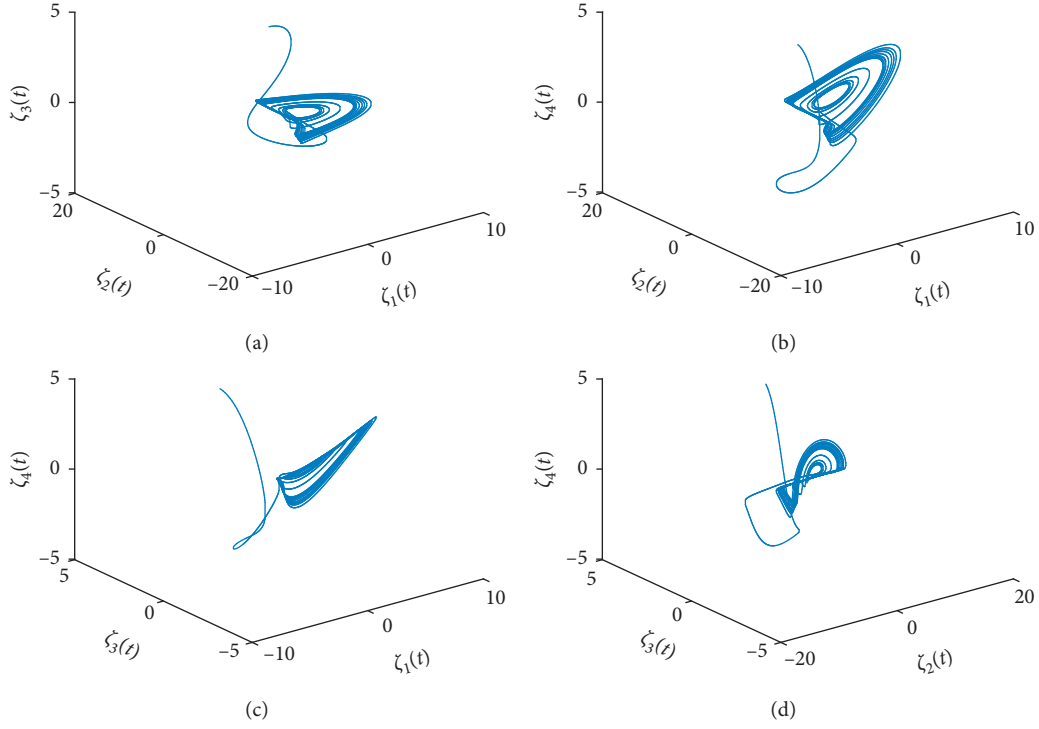


FIGURE 1: Chaotic phenomenon of (15) with $\alpha = 0.92$.

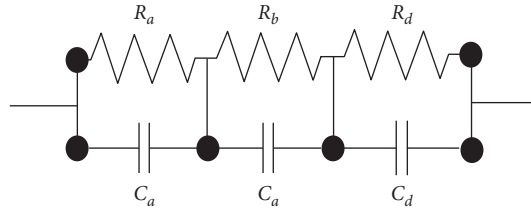


FIGURE 2: Unit circuit for realizing $(1/s^{0.9})$.

To implement the FOECS, an electronic circuit is constructed by using R-C components, analog multipliers, and

operational amplifiers. The circuit diagram is depicted in Figure 3, whose mathematical equations are given as follows:

$$\left\{ \begin{array}{l} \mathbb{D}_t^\alpha \zeta_1(t) = \frac{1}{R_6 C_1} \zeta_3(t) + \frac{1}{R_1 R_2 C_1} \zeta_1(t) \zeta_2(t) + \frac{1}{R_5 R_{12} C_1} \zeta_4(t) - \frac{1}{R_3 R_4 C_1} \zeta_1(t), \\ \mathbb{D}_t^\alpha \zeta_2(t) = 1 - \frac{1}{R_7 C_2} \zeta_2(t) - \frac{1}{R_8 C_2} \zeta_1^2(t) + \frac{1}{R_9 R_{13} C_2} \zeta_4(t), \\ \mathbb{D}_t^\alpha \zeta_3(t) = -\frac{1}{R_{10} C_3} \zeta_1(t) - \frac{1}{R_{11} R_{14} C_3} \zeta_3(t) + \frac{1}{R_{15} R_{16} C_3} \zeta_4(t), \\ \mathbb{D}_t^\alpha \zeta_4(t) = -\frac{1}{R_{17} C_4} \zeta_1(t) \zeta_2(t) \zeta_3(t), \end{array} \right. \quad (18)$$

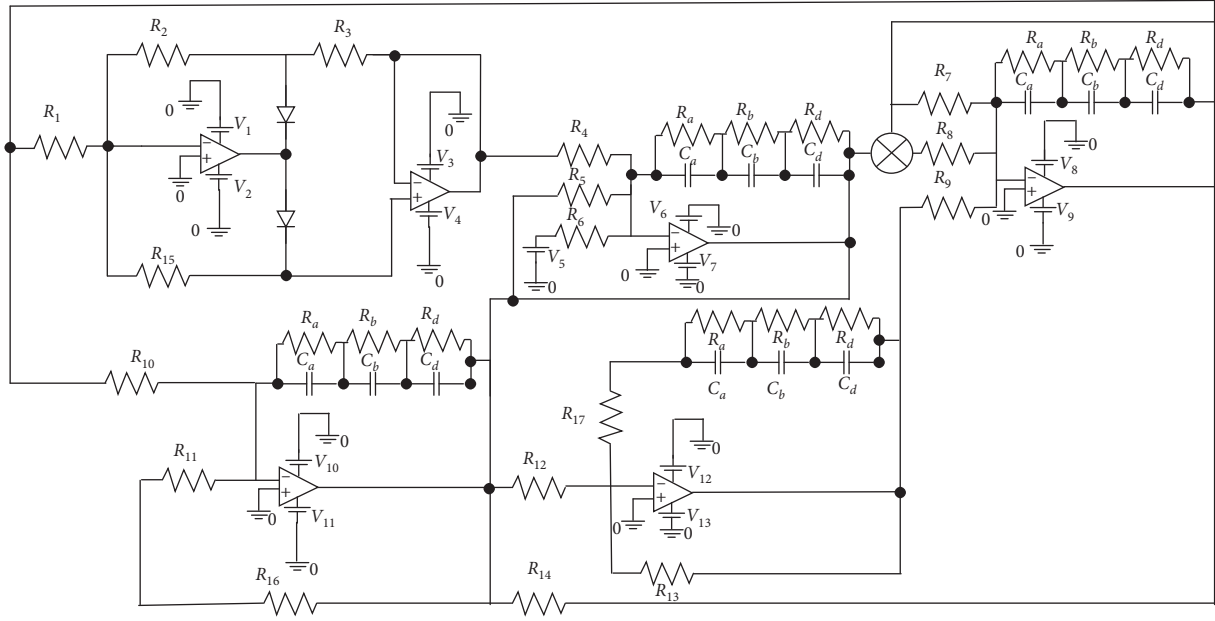


FIGURE 3: Simulation circuit of the FOECS.

where C_1, C_2 , and C_3 are three fractional capacitors, and they are implemented by R_a, R_b, R_d, C_a, C_b , and C_d . In order to satisfy the FOECS, we choose the values of resistors and capacitors as $R_1 = R_2 = 1 \text{ k}\Omega$, $R_3 = R_5 = 4 \text{ k}\Omega$, $R_4 = 120 \Omega$, $R_6 = R_8 = R_{10} = R_{17} = 1 \text{ M}\Omega$, $R_7 = 100 \text{ M}\Omega$, $R_{16} = 90 \Omega$, $R_9 = R_{11} = R_{12} = 30 \Omega$, $R_{13} = R_{15} = 5 \text{ k}\Omega$, $R_{14} = 12 \text{ k}\Omega$, and $C_1 = C_2 = C_3 = C_4 = 1 \mu\text{F}$.

Remark 1. In the circuit implementation of the FOECS, the order of the system is set as $\alpha = 0.9$. Noting that the system parameters in (15) are very hard to be approximated by the circuit, the parameters in (18) are different with those in (15) (in fact, we used the approximate quantity of the parameters in (15)).

Remark 2. Based on [18], we know that the financial variables of financial systems could have long memory, such as stock market prices, gross domestic product, interest rates, and foreign exchange rates. Compared with the integer-order calculus, the fractional-order calculus introduced into the system (15) can more accurately describe the long-term memory effect in the financial system.

4. Controller Design and Stability Analysis

Taking uncertain parameters and disturbances into consideration, the controlled FOECS can be described as

$$\begin{cases} \mathbb{D}_t^\alpha \zeta_1(t) = \zeta_3(t) + (\zeta_2(t) - a)\zeta_1(t) + a_1\zeta_4(t) + u_1(t) + d_1(t) + \varphi_1^T(\zeta(t))\theta_1, \\ \mathbb{D}_t^\alpha \zeta_2(t) = 1 - b\zeta_2(t) - \zeta_1^2(t) + a_2\zeta_4(t) + u_2(t) + d_2(t) + \varphi_2^T(\zeta(t))\theta_2, \\ \mathbb{D}_t^\alpha \zeta_3(t) = -\zeta_1(t) - c\zeta_3(t) + a_3\zeta_4(t) + u_3(t) + d_3(t) + \varphi_3^T(\zeta(t))\theta_3, \\ \mathbb{D}_t^\alpha \zeta_4(t) = -\zeta_1(t)\zeta_2(t)\zeta_3(t) + u_4(t) + d_4(t) + \varphi_4^T(\zeta(t))\theta_4, \end{cases} \quad (19)$$

where $u_i(t) \in \mathbb{R}$ represents the controller, $d_i(t) \in \mathbb{R}$ denotes the external disturbance, $\varphi_i(\zeta(t)): \mathbb{R}^4 \mapsto \mathbb{R}^{m_i}$ is a known bounded nonlinear function, and $\theta_i \in \mathbb{R}^{m_i}$ is an unknown constant vector with $i = 1, 2, 3, 4$ and $m_i \in \mathbb{N}$.

Remark 3. In fact, the economical systems usually suffer from system uncertainties and unknown disturbances, for example, unknown price and cost fluctuation, market's human intervention, and system model uncertainties. Note that we assume that $\varphi_1(\cdot), \varphi_2(\cdot), \varphi_3(\cdot)$, and $\varphi_4(\cdot)$ can have different dimensions, and it is easy to know that the uncertain terms considered in system (19)

stand for a large range of system uncertainties. Thus, the economical model considered in some recent literature, for example, [10, 16, 18, 37–39], is a special case of our model (19).

Our objective here is to design a proper controller $u_i(t)$ such that the state vector $\zeta(t)$ could track the desired signal $\zeta_d(t) = [\zeta_{d1}(t), \zeta_{d2}(t), \zeta_{d3}(t), \zeta_{d4}(t)]^T \in \mathbb{R}^4$. The tracking error is defined as $e(t) = [e_1(t), e_2(t), e_3(t), e_4(t)]^T = \zeta(t) - \zeta_d(t)$. To proceed, we need the following assumption.

Assumption 1. The nonlinear function $d_i(t)$ is bounded, i.e., there exists a constant $d_i^* > 0$ such that

$$|d_i(t)| \leq d_i^*. \quad (20)$$

Assumption 2. The referenced signal $\zeta_d(t)$ is a known continuous bounded function and has bounded known continuous first-order derivative.

Lemma 6 (see [40]). *If a is a positive constant, it holds $|x| - x \tanh(x/a) \leq 0.2785a = a'$.*

According to the definition of $e(t)$, it follows from (15) that

$$\begin{cases} \mathbb{D}_t^\alpha e_1(t) = \zeta_3(t) + (\zeta_2(t) - a)\zeta_1(t) + a_1\zeta_4(t) + u_1(t) + \varphi_1^T(\zeta(t))\theta_1 - D_t^\alpha \zeta_{d1}(t) + d_1(t), \\ \mathbb{D}_t^\alpha e_2(t) = 1 - b\zeta_2(t) - \zeta_1^2(t) + a_2\zeta_4(t) + u_2(t) + d_2(t) - D_t^\alpha \zeta_{d2}(t) + \varphi_2^T(\zeta(t))\theta_2, \\ \mathbb{D}_t^\alpha e_3(t) = -\zeta_1(t) - c\zeta_3(t) + a_3\zeta_4(t) + u_3(t) + d_3(t) + \varphi_3^T(\zeta(t))\theta_3 - D_t^\alpha \zeta_{d3}(t), \\ \mathbb{D}_t^\alpha e_4(t) = -\zeta_1(t)\zeta_2(t)\zeta_3(t) + u_4(t) + d_4(t) + \varphi_4^T(\zeta(t))\theta_4 - D_t^\alpha \zeta_{d4}(t). \end{cases} \quad (21)$$

Thus, the controller can be designed as

$$\begin{cases} u_1(t) = -k_1 e_1(t) - \zeta_3(t) - (\zeta_2(t) - a)\zeta_1(t) - a_1\zeta_4(t) - \varphi_1^T(\zeta(t))\widehat{\theta}_1(t) + D_t^\alpha \zeta_{d1}(t) - \tanh\left(\frac{e_1(t)}{a_1}\right), \\ u_2(t) = -k_2 e_2(t) + \zeta_1^2(t) - a_2\zeta_4(t) - \tanh\left(\frac{e_2(t)}{a_2}\right) - \varphi_2^T(\zeta(t))\widehat{\theta}_2(t) + D_t^\alpha \zeta_{d2}(t) - 1 + b\zeta_2(t), \\ u_3(t) = -k_3 e_3(t) + \zeta_1(t) - \tanh\left(\frac{e_3(t)}{a_3}\right) - \varphi_3^T(\zeta(t))\widehat{\theta}_3(t) + D_t^\alpha \zeta_{d3}(t) + c\zeta_3(t) - a_3\zeta_4(t), \\ u_4(t) = -k_4 e_4(t) + \zeta_1(t)\zeta_2(t)\zeta_3(t) - \tanh\left(\frac{e_4(t)}{a_4}\right) - \varphi_4^T(\zeta(t))\widehat{\theta}_4(t) + D_t^\alpha \zeta_{d4}(t), \end{cases} \quad (22)$$

where $k_i > 0$ is a design parameter, $a_i > 0$ is a constant, and $\widehat{d}_i^*(t)$ and $\widehat{\theta}_i(t)$ are the estimation of d_i^* and θ_i , respectively.

Remark 4. In this work, an adaptive controller (22) which seems complicated is designed. In this controller, all inputs, i.e., $u_i(t)$, $i = 1, 2, 3, 4$, have the same structure. Take $u_1(t)$ as an example; it contains four parts, i.e., a nonlinear function $-\zeta_3(t) - (\zeta_2(t) - a)\zeta_1(t) - a_1\zeta_4(t)$ consisting of system variables, a feedback term of the tracking error $-k_1 e_1(t) - \tanh(e_1(t)/a_1)$, an adaptive term $-\varphi_1^T(\zeta(t))\widehat{\theta}_1(t)$, and a smooth function of the referenced signal $D_t^\alpha \zeta_{d1}(t)$. It can be observed that all inputs are easy to be implemented.

Substituting (22) into (21) gives

$$\mathbb{D}_t^\alpha e_i(t) = -k_i e_i(t) + d_i(t) - \tanh\left(\frac{e_i(t)}{a_i}\right) - \varphi_i^T(\zeta(t))\widetilde{\theta}_i(t), \quad (23)$$

with $i = 1, 2, 3, 4$, and

$$\widetilde{\theta}_i(t) = \widehat{\theta}_i(t) - \theta_i, \quad (24)$$

is the estimation error of the unknown constant vector θ_i .

Multiplying $e_i(t)$ to both sides of (23), and according to Assumption 1 and Lemma 6, we have

$$\begin{aligned} e_i(t)\mathbb{D}_t^\alpha e_i(t) &= -k_i e_i^2(t) + e_i(t)d_i(t) - e_i(t)\tanh\left(\frac{e_i(t)}{a_i}\right) \\ &\quad - e_i(t)\varphi_i^T(\zeta(t))\widetilde{\theta}_i(t) \\ &\leq -k_i e_i^2(t) + |e_i(t)|d_i^* - e_i(t)\tanh\left(\frac{e_i(t)}{a_i}\right) \\ &\quad - e_i(t)\varphi_i^T(\zeta(t))\widetilde{\theta}_i(t) \\ &\leq -k_i e_i^2(t) + |e_i(t)| - e_i(t)\tanh\left(\frac{e_i(t)}{a_i}\right) \\ &\quad - e_i(t)\varphi_i^T(\zeta(t))\widetilde{\theta}_i(t) \\ &= -k_i e_i^2(t) - a'_i - e_i(t)\varphi_i^T(\zeta(t))\widetilde{\theta}_i(t), \end{aligned} \quad (25)$$

where $a'_i > 0$.

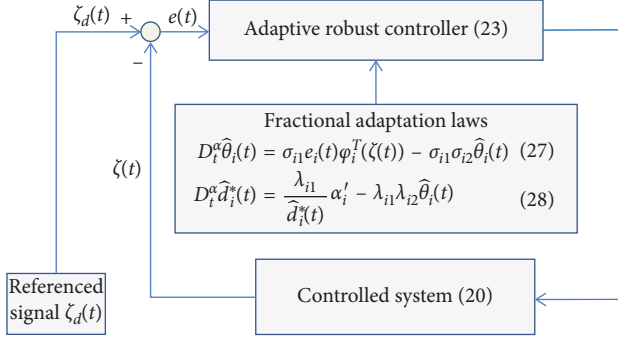


FIGURE 4: The structure of the proposed method.

Let the fractional-order adaptation laws be

$$\mathbb{D}_t^\alpha \hat{\theta}_i(t) = \sigma_{i1} e_i(t) \varphi_i^T(\zeta(t)) - \sigma_{i1} \sigma_{i2} \hat{\theta}_i(t), \quad (26)$$

$$\mathbb{D}_t^\alpha \tilde{d}_i^*(t) = \frac{\lambda_{i1}}{\tilde{d}_i^*(t)} \alpha'_i - \lambda_{i1} \lambda_{i2} \tilde{d}_i^*(t), \quad (27)$$

with $i = 1, 2, 3, 4$, $\lambda_{i1}, \lambda_{i2}, \sigma_{i1}, \sigma_{i2} > 0$, and $\tilde{d}_i^*(t) = \hat{d}_i^*(t) - d_i^*$ is the estimation error of the unknown constant d_i^* . The structure of the proposed method is shown in Figure 4.

Based on above discussion, we can give the following theorem.

Theorem 1. *Based on Assumptions 1 and 2, the controller (22) of the system (19) together with the fractional-order adaptation laws (26) and (27) can guarantee that all variables remain bounded and the tracking error $e(t)$ converges to a small neighborhood of the origin.*

Proof. Let the Lyapunov function be

$$V(t) = \frac{1}{2} \sum_{i=1}^4 e_i^2(t) + \frac{1}{2} \sum_{i=1}^4 \frac{1}{\sigma_{i1}} \tilde{\theta}_i^T(t) \tilde{\theta}_i(t) + \frac{1}{2} \sum_{i=1}^4 \frac{1}{\lambda_{i1}} \tilde{d}_i^{*2}(t). \quad (28)$$

From (25)–(27) and Lemma 4, one has

$$\begin{aligned} \mathbb{D}_t^\alpha V(t) &= \frac{1}{2} \sum_{i=1}^4 \mathbb{D}_t^\alpha e_i^2(t) + \frac{1}{2} \sum_{i=1}^4 \frac{1}{\sigma_{i1}} \mathbb{D}_t^\alpha \tilde{\theta}_i^T(t) \tilde{\theta}_i(t) \\ &\quad + \frac{1}{2} \sum_{i=1}^4 \frac{1}{\lambda_{i1}} \mathbb{D}_t^\alpha \tilde{d}_i^{*2}(t) \\ &\leq \sum_{i=1}^4 e_i(t) \mathbb{D}_t^\alpha e_i(t) + \sum_{i=1}^4 \frac{1}{\sigma_{i1}} \tilde{\theta}_i^T(t) \mathbb{D}_t^\alpha \tilde{\theta}_i(t) \\ &\quad + \sum_{i=1}^4 \frac{1}{\lambda_{i1}} \tilde{d}_i^*(t) \mathbb{D}_t^\alpha \tilde{d}_i^*(t) \\ &= - \sum_{i=1}^4 k_i e_i^2(t) - \sum_{i=1}^4 e_i(t) \varphi_i^T(\zeta(t)) \tilde{\theta}_i(t) \\ &\quad + \sum_{i=1}^4 \frac{1}{\sigma_{i1}} \tilde{\theta}_i^T(t) \mathbb{D}_t^\alpha \tilde{\theta}_i(t) + \sum_{i=1}^4 \frac{1}{\lambda_{i1}} \tilde{d}_i^*(t) \mathbb{D}_t^\alpha \tilde{d}_i^*(t) - \sum_{i=1}^4 \alpha'_i. \end{aligned} \quad (29)$$

It follows from (29) that

$$\begin{aligned} \mathbb{D}_t^\alpha V(t) &\leq - \sum_{i=1}^4 \alpha'_i - \sum_{i=1}^4 e_i(t) \varphi_i^T(\zeta(t)) \tilde{\theta}_i(t) + \sum_{i=1}^4 \tilde{\theta}_i^T(t) \\ &\quad \cdot [e_i(t) \varphi_i^T(\zeta(t)) - \sigma_{i2} \tilde{\theta}_i(t)] - \sum_{i=1}^4 k_i e_i^2(t) \\ &\quad + \sum_{i=1}^4 \tilde{d}_i^*(t) \left[\frac{\alpha'_i}{\tilde{d}_i^*(t)} - \lambda_{i2} \tilde{d}_i^*(t) \right] \\ &= - \sum_{i=1}^4 k_i e_i^2(t) - \sum_{i=1}^4 \lambda_{i2} \tilde{d}_i^*(t) \tilde{d}_i^*(t) - \sum_{i=1}^4 \sigma_{i2} \tilde{\theta}_i^T(t) \tilde{\theta}_i(t) \\ &= - \sum_{i=1}^4 k_i e_i^2(t) - \sum_{i=1}^4 \lambda_{i2} \tilde{d}_i^*(t) (\tilde{d}_i^*(t) + d_i^*) \\ &\quad - \sum_{i=1}^4 \sigma_{i2} \tilde{\theta}_i^T(t) (\tilde{\theta}_i(t) + \theta_i) \\ &= - \sum_{i=1}^4 k_i e_i^2(t) - \sum_{i=1}^4 \lambda_{i2} \tilde{d}_i^{*2}(t) - \sum_{i=1}^4 \lambda_{i2} \tilde{d}_i^*(t) d_i^* \\ &\quad - \sum_{i=1}^4 \sigma_{i2} \tilde{\theta}_i^T(t) \theta_i - \sum_{i=1}^4 \sigma_{i2} \tilde{\theta}_i^T(t) \tilde{\theta}_i(t) \\ &\leq - \sum_{i=1}^4 k_i e_i^2(t) - \sum_{i=1}^4 \frac{\lambda_{i2}}{2} \tilde{d}_i^{*2}(t) + \sum_{i=1}^4 \frac{\lambda_{i2}}{2} d_i^{*2} \\ &\quad + \sum_{i=1}^4 \frac{\sigma_{i2}}{2} \theta_i^T \theta_i - \sum_{i=1}^4 \frac{\sigma_{i2}}{2} \tilde{\theta}_i^T(t) \tilde{\theta}_i(t) \\ &\leq - \underline{k} \sum_{i=1}^4 e_i^2(t) - \frac{\underline{\lambda}_2}{2} \sum_{i=1}^4 \tilde{d}_i^{*2}(t) \\ &\quad - \frac{\underline{\sigma}_2}{2} \sum_{i=1}^4 \tilde{\theta}_i^T(t) \tilde{\theta}_i(t) + A \\ &\leq -BV(t) + A, \end{aligned} \quad (30)$$

where $\underline{k} = \min_{1 \leq i \leq 4} \{k_i\}$, $\underline{\sigma}_2 = \min_{1 \leq i \leq 4} \{\lambda_{i2}\}$, $\underline{\sigma}_2 = \min_{1 \leq i \leq 4} \{\sigma_{i2}\}$, $B = \min\{2\underline{k}, \underline{\lambda}_2 \underline{\lambda}_1, \underline{\sigma}_2 \underline{\sigma}_1\}$, $\underline{\lambda}_1 = \max_{1 \leq i \leq 4} \{\lambda_{i1}\}$, $\underline{\sigma}_1 = \max_{1 \leq i \leq 4} \{\sigma_{i1}\}$, and $A = \sum_{i=1}^4 (\lambda_{i2}/2) d_i^{*2} + \sum_{i=1}^4 (\sigma_{i2}/2) \theta_i^T \theta_i$. According to (30), we have

$$\mathbb{D}_t^\alpha V(t) + y(t) = -BV(t) + A, \quad (31)$$

where $y(t) > 0$.

The Laplace transform of (31) is given as

$$\begin{aligned} V(s) &= \frac{s^{\alpha-1}}{s^\alpha + B} V(0) + \frac{A}{s(s^\alpha + B)} - \frac{Y(s)}{s^\alpha + B} \\ &= \frac{s^{\alpha-1}}{s^\alpha + B} V(0) + \frac{s^{\alpha-(1+\alpha)} A}{(s^\alpha + B)} - \frac{Y(s)}{s^\alpha + B}. \end{aligned} \quad (32)$$

According to (4), we can solve (32) as

$$\begin{aligned} V(t) &= V(0)E_{\alpha,1}(-Bt^\alpha) + At^\alpha E_{\alpha,1+\alpha}(-Bt^\alpha) \\ &\quad - y(t) * t^{-1}E_{\alpha,0}(-Bt^\alpha), \end{aligned} \quad (33)$$

where $*$ represents the convolution operator. Noting $t^{-1}E_{\alpha,0}(-Bt^\alpha) \geq 0$ and $y(t) \geq 0$, we have $y(t) * t^{-1}E_{\alpha,0}(-Bt^\alpha) \geq 0$.

Then, we obtain

$$V(t) \leq V(0)E_{\alpha,1}(-Bt^\alpha) + At^\alpha E_{\alpha,1+\alpha}(-Bt^\alpha). \quad (34)$$

Because $\arg(-Bt^\alpha) = -\pi$, $|-Bt^\alpha| \geq 0$, and $0 < \alpha \leq 1$, based on Lemma 2, it holds

$$|E_{\alpha,1}(-Bt^\alpha)| \leq \frac{C}{1 + Bt^\alpha}, \quad (35)$$

where $C > 0$. Then, we have

$$\lim_{t \rightarrow \infty} V(0)E_{\alpha,1}(-Bt^\alpha) = 0. \quad (36)$$

That is to say, with respect to any $\mu > 0$, one can find $t_1 > 0$ so that

$$V(0)E_{\alpha,1}(-Bt^\alpha) < \mu. \quad (37)$$

It follows from Lemma 1 that

$$t^\alpha E_{\alpha,\alpha+1}(-Bt^\alpha) \leq \frac{A}{B} + \mu. \quad (38)$$

Noting that we can find proper design parameters such that $(A/B) \leq \mu$, according to (34), (37), and (38), we know

$$V(t) < 3\mu. \quad (39)$$

Based on the definition of $V(t)$, it is easy to know that the boundedness of all signals can be guaranteed. On the contrary, the tracking error can be arbitrarily small. \square

Remark 5. In this paper, we design adaptation laws (26) and (27) to update $\hat{\theta}_i(t)$ and $\hat{d}_i^*(t)$, respectively. These laws update the parameters by using fractional differential equations. In fact, this kind of laws can also be seen in some literature, e.g., in [41–44]. However, in the abovementioned literature, the fractional adaptation laws only have one term, i.e., the positive term. Noting that the fractional derivatives of the updated parameters are greater than zero, and thus, according to the properties of the fractional derivative, the updated parameters are monotonically increasing. That is to say, the boundedness of the updated parameters cannot be guaranteed. However, in this work, by introducing the second term $-\sigma_{i1}\sigma_{i2}\hat{\theta}_i$ in (26), we can guarantee the boundedness of the updated parameter.

Remark 7. In the proof of Theorem 1, we can see that $\|e(t)\| \leq \sqrt{6\mu}$. To drive the tracking error $e(t)$ as small as possible, we can set (A/B) as small as possible. To obtain this objective, according to the form of A and B , we can choose large k_i , λ_{i1} , and σ_{i1} and small σ_{i2} and λ_{i2} .

Remark 8. To analyze the fractional-order system's stability, a commonly used Lyapunov function is $V(t) = e^T(t)e(t)$. It should be emphasized that its fractional derivative is [45]

$$\begin{aligned} \mathbb{D}_t^\alpha V(t) &= \sum_{i=1}^{\infty} \frac{\Gamma(1+\alpha)}{\Gamma(1+i)\Gamma(1-i+\alpha)} \mathbb{D}_t^i e(t) \mathbb{D}_t^{\alpha-i} e(t) \\ &\quad + 2e^T(t) \mathbb{D}_t^\alpha e(t). \end{aligned} \quad (40)$$

In fact, this complicated form is very hard to be used. However, in this paper, by using our method, it is not necessary to use (40) in the stability analysis.

5. Simulation Studies

In the simulation, the parameters are $a = 2.10$, $b = 0.01$, $c = 2.61$, $a_1 = 8.41$, $a_2 = 6.40$, and $a_3 = 2.21$ and the disturbances are chosen as $d_1(t) = \cos(\zeta_1(t))$, $d_2(t) = \cos(\zeta_2(t))$, $d_3(t) = \cos(\zeta_3(t))$, and $d_4(t) = \cos(\zeta_4(t))$ which are activated when $t = 5$. Let the initial condition be $\zeta(0) = [1.5, -2, 3, -3]^T$. The fractional order is $\alpha = 0.95$.

The parametric uncertain vectors are chosen as $\theta_1(t) = [1.1, -0.5, 2, 1.5]^T$, $\theta_3(t) = [2, 1, -0.5]^T$, and $\theta_2(t) \equiv \theta_4(t) \equiv 0$, and the basis functions are chosen as $\varphi_1(\zeta(t)) = [\zeta_1(t), \zeta_2(t), \zeta_3(t), \zeta_4(t)]^T$ and $\varphi_3(\zeta(t)) = [\zeta_1(t)\sin\zeta_2(t), \cos\zeta_3(t), \sin\zeta_4(t)]^T$.

The controller design parameters are given as $k_i = 0.2$, $\lambda_{i1} = \sigma_{i1} = 5$, and $\lambda_{i2} = \sigma_{i2} = 0.005$ with $i = 1, 2, 3, 4$.

First, let the desired signal be $\zeta_d(t) \equiv [0, 0, 0, 0]^T$. The simulation results are given in Figures 5–9. Figure 5 shows the time response of the state variables $\zeta_1(t)$, $\zeta_2(t)$, $\zeta_3(t)$, and $\zeta_4(t)$. We can see these variables tend to zero in about 2 s and stay in a very small neighborhood of zero thereafter. The control inputs are depicted in Figure 6. The estimations for $\theta_1(t)$ as well $\theta_3(t)$ are given in Figures 8 and 9, respectively. According to Figures 7–9, we can see that the boundedness of the updated parameters can be guaranteed, just like the results in Theorem 1 and the statements in Remark 5. These simulation results indicate that our control method has satisfactory control performance and good robustness.

Let the desired signal be $\zeta_d(t) = [\cos t, \sin t, \cos t, \sin t]^T$. The other parameters and values are chosen as the same as above. The simulation results can be seen in Figures 10–12.

Remark 9. The simulation results of [16] are that the designed controllers were activated at $t = 30$ s, whereas in our paper, the proposed controllers are activated at about $t = 2$ s. Compared with the simulation results in [16], it is not difficult to see that the controller we designed does not use the symbolic function cited in [16]. Therefore, there is no

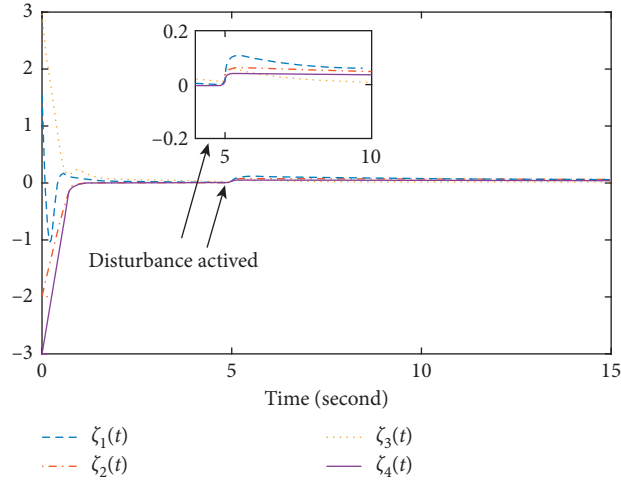


FIGURE 5: Time response of state variables.

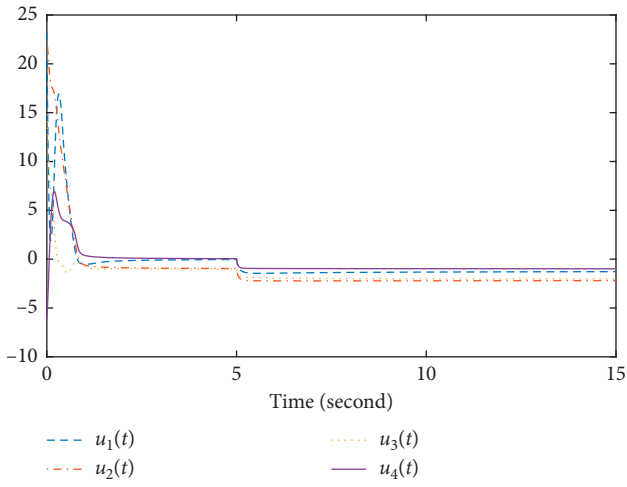


FIGURE 6: Time response of control inputs.

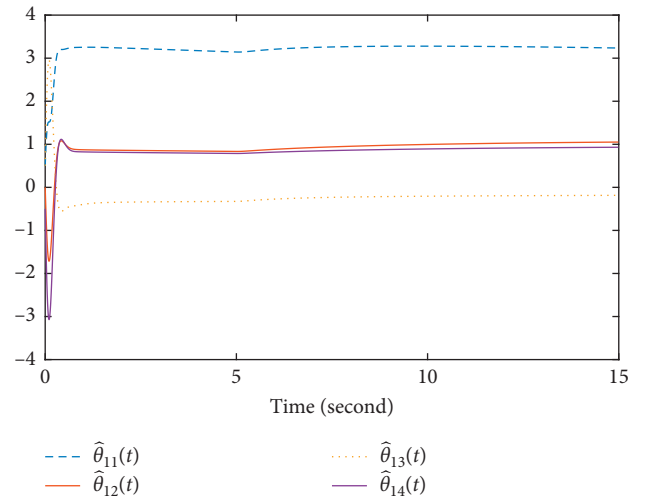


FIGURE 8: The estimation of $\theta_1(t)$.

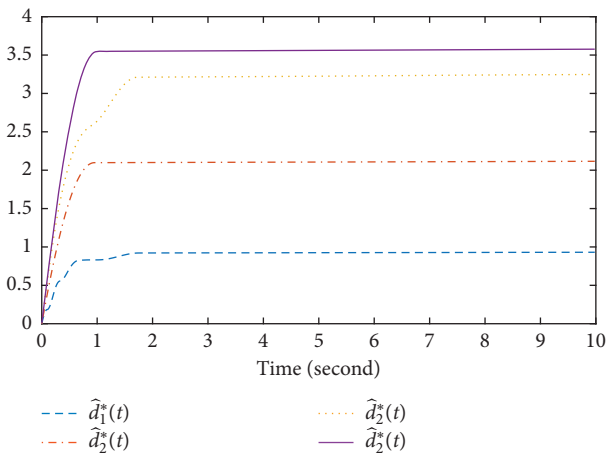


FIGURE 7: The estimations of d_1^* , d_2^* , d_3^* , and d_4^* .

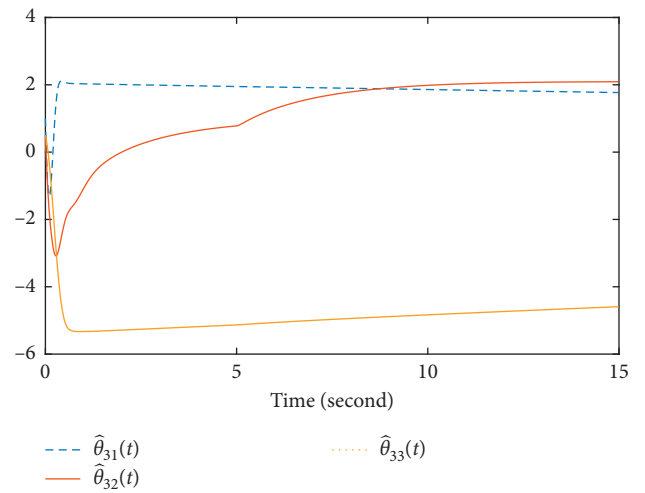


FIGURE 9: The estimation of $\theta_3(t)$.

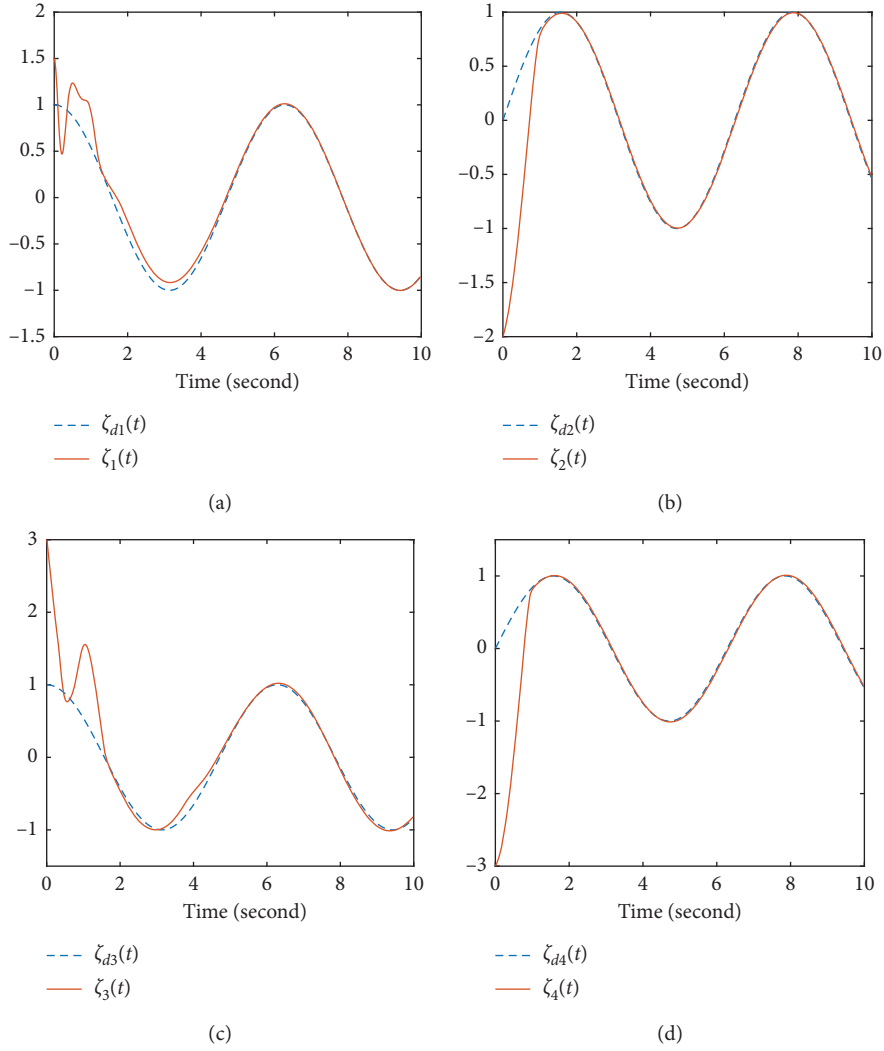


FIGURE 10: Tracking performance of state variables.

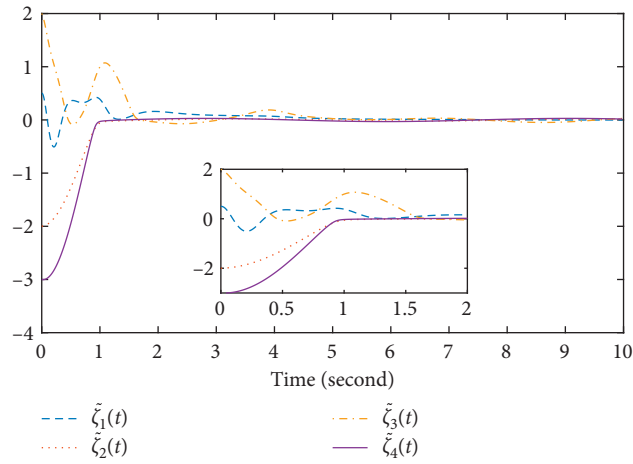


FIGURE 11: Tracking errors.

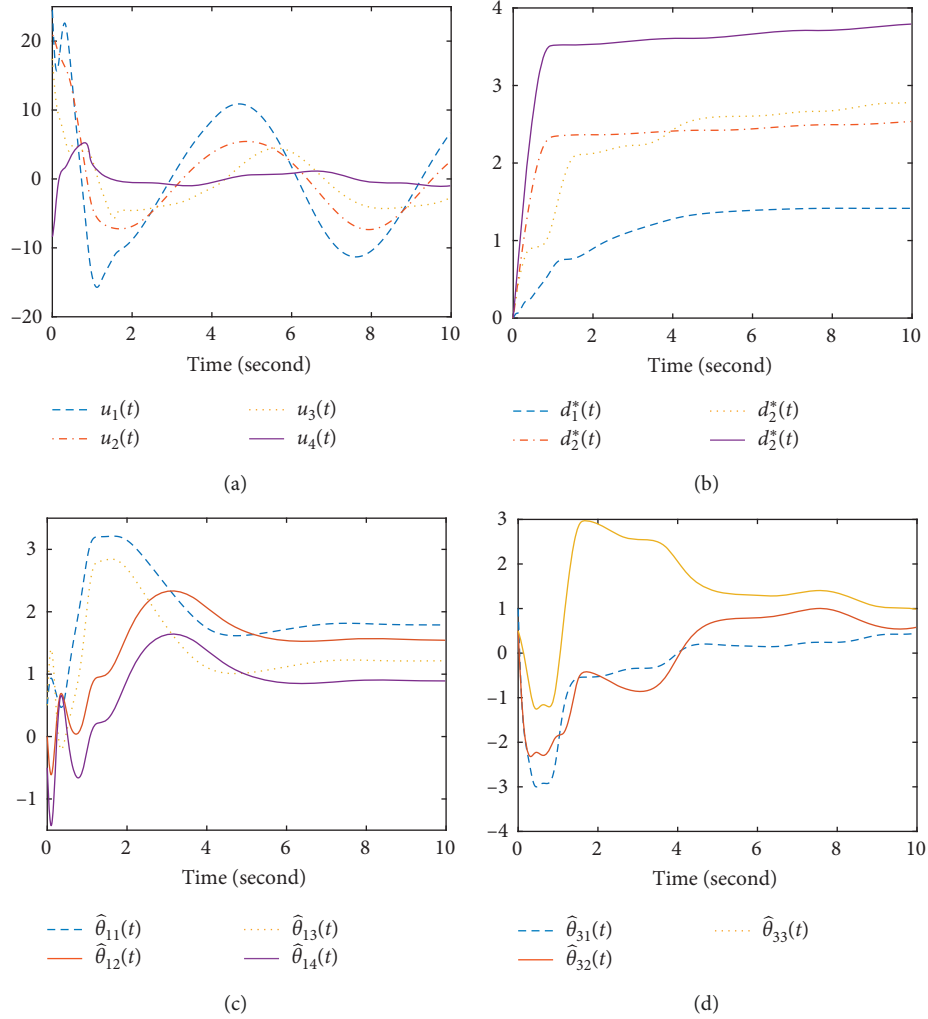


FIGURE 12: Control inputs and the updated parameters.

chattering phenomenon in our simulation results. Although $\arctan(10\cdot)$ was used to approximate $\text{sign}(\cdot)$ in the simulation of [16], the controller designed by us can work more effectively in terms of comparing the convergence rate of simulation results. Since we directly use the proposed controller to obtain simulation results, our simulation results can more effectively prove the theory of this paper.

6. Conclusions

In this paper, an adaptive robust control method of FOECSs subject to unmatched system uncertainties as well as external disturbances is investigated. It has been shown by our work that (1) the quadratic Lyapunov function can be used in the stability analysis of FOECSs based on the fractional stability criterion and (2) the parameters can be updated by fractional-order differential equations. The proposed method gives an easy way to analyze the stability of fractional-order systems. Simulation results have verified the feasibility of our control method. On the contrary, it is assumed that the unknown parameter is a constant vector, i.e., when the

uncertain term is time-varying, the method presented in this paper is powerless. In addition, four control inputs are used, which reduce the real-world applications of our approach. How to solve aforementioned problems is one of our future research directions.

Data Availability

The data used to support the findings of this study are available from the corresponding author upon request.

Conflicts of Interest

The authors declare that there are no conflicts of interest.

Acknowledgments

This study was supported in part by the Excellent Top-Notch Talent Cultivation Project of Colleges and Universities of Anhui Province of China under grant no. gxyqZD2017075 and in part by the Key Natural Science Projects of Colleges and Universities of Anhui Education Department under grant no. KJ2019A0695.

References

- [1] I. Podlubny, *Fractional Differential Equations*, Academic Press, Cambridge, MA, USA, 1999.
- [2] V. Ervin, N. Heuer, and J. Roop, "Regularity of the solution to 1-d fractional order diffusion equations," *Mathematics of Computation*, vol. 87, no. 313, pp. 2273–2294, 2018.
- [3] H. Liu, Y. Pan, and J. Cao, "Composite learning adaptive dynamic surface control of fractional-order nonlinear systems," *IEEE Transactions on Cybernetics*, 2019.
- [4] K. Rajagopal, A. Karthikeyan, and A. K. Srinivasan, "Fpga implementation of novel fractional-order chaotic systems with two equilibriums and no equilibrium and its adaptive sliding mode synchronization," *Nonlinear Dynamics*, vol. 87, no. 4, pp. 2281–2304, 2017.
- [5] I. Petráš, *Fractional-order Nonlinear Systems: Modeling, Analysis and Simulation*, Springer Science & Business Media, Berlin, Germany, 2011.
- [6] A. Atangana and I. Koca, "Chaos in a simple nonlinear system with atangana–baleanu derivatives with fractional order," *Chaos, Solitons and Fractals*, vol. 89, pp. 447–454, 2016.
- [7] M. A. Duarte-Mermoud, N. Aguila-Camacho, J. A. Gallegos, and R. Castro-Linares, "Using general quadratic lyapunov functions to prove lyapunov uniform stability for fractional order systems," *Communications in Nonlinear Science and Numerical Simulation*, vol. 22, no. 1, pp. 650–659, 2015.
- [8] Y. Wei, W. T. Peter, Z. Yao, and Y. Wang, "Adaptive backstepping output feedback control for a class of nonlinear fractional order systems," *Nonlinear Dynamics*, vol. 86, no. 2, pp. 1047–1056, 2016.
- [9] H. Liu, Y. Pan, S. Li, and Y. Chen, "Synchronization for fractional-order neural networks with full/under-actuation using fractional-order sliding mode control," *International Journal of Machine Learning and Cybernetics*, vol. 9, no. 7, pp. 1219–1232, 2018.
- [10] A. Boulkroune, A. Bouzeriba, and T. Bouden, "Fuzzy generalized projective synchronization of incommensurate fractional-order chaotic systems," *Neurocomputing*, vol. 173, pp. 606–614, 2016.
- [11] S. Ha, H. Liu, S. Li, and A. Liu, "Backstepping-based adaptive fuzzy synchronization control for a class of fractional-order chaotic systems with input saturation," *International Journal of Fuzzy Systems*, vol. 21, no. 5, pp. 1571–1584, 2019.
- [12] O. Mofid, S. Mobayen, and M.-H. Khooban, "Sliding mode disturbance observer control based on adaptive synchronization in a class of fractional-order chaotic systems," *International Journal of Adaptive Control and Signal Processing*, vol. 33, no. 3, pp. 462–474, 2019.
- [13] W. Zhang, J. Cao, R. Wu, F. E. Alsaadi, and A. Alsaedi, "Lag projective synchronization of fractional-order delayed chaotic systems," *Journal of the Franklin Institute*, vol. 356, no. 3, pp. 1522–1534, 2019.
- [14] E. Neave, *The Economic Organisation of a Financial System*, Routledge, Abingdon, UK, 2017.
- [15] A. Zattoni, M. A. Witt, W. Q. Judge et al., "Does board independence influence financial performance in IPO firms? The moderating role of the national business system," *Journal of World Business*, vol. 52, no. 5, pp. 628–639, 2017.
- [16] H. Liu, S. Li, G. Li, and H. Wang, "Robust adaptive control for fractional-order financial chaotic systems with system uncertainties and external disturbances," *Information Technology And Control*, vol. 46, no. 4, pp. 246–259, 2017.
- [17] A. Hajipour and H. Tavakoli, "Analysis and circuit simulation of a novel nonlinear fractional incommensurate order financial system," *Optik*, vol. 127, no. 22, pp. 10643–10652, 2016.
- [18] B. Xin and J. Zhang, "Finite-time stabilizing a fractional-order chaotic financial system with market confidence," *Nonlinear Dynamics*, vol. 79, no. 2, pp. 1399–1409, 2015.
- [19] I. Pan, S. Das, and S. Das, "Multi-objective active control policy design for commensurate and incommensurate fractional order chaotic financial systems," *Applied Mathematical Modelling*, vol. 39, no. 2, pp. 500–514, 2015.
- [20] B. Chen-Charpentier, G. González-Parra, and A. J. Arenas, "Fractional order financial models for awareness and trial advertising decisions," *Computational Economics*, vol. 48, no. 4, pp. 555–568, 2016.
- [21] W. Gu, Y. Yu, and W. Hu, "Artificial bee colony algorithm based parameter estimation of fractional-order chaotic system with time delay," *IEEE/CAA Journal of Automatica Sinica*, vol. 4, no. 1, pp. 107–113, 2017.
- [22] Z. Ke, W. Zhi-Hui, G. Li-Ke, S. Yue, and M. Tie-Dong, "Robust sliding mode control for fractional-order chaotic economical system with parameter uncertainty and external disturbance," *Chinese Physics B*, vol. 24, no. 3, p. 30504, 2015.
- [23] A. Hajipour, M. Hajipour, and D. Baleanu, "On the adaptive sliding mode controller for a hyperchaotic fractional-order financial system," *Physica A: Statistical Mechanics and Its Applications*, vol. 497, pp. 139–153, 2018.
- [24] J. Chen, J. Mi, and Y. Lin, "A graph approach for fuzzy-rough feature selection," *Fuzzy Sets and Systems*, 2019.
- [25] K. Sasakura, "On the dynamic behavior of schinasi's business cycle model," *Journal of Macroeconomics*, vol. 16, no. 3, pp. 423–444, 1994.
- [26] L. De Cesare and M. Sportelli, "A dynamic is-lm model with delayed taxation revenues," *Chaos, Solitons and Fractals*, vol. 25, no. 1, pp. 233–244, 2005.
- [27] M. S. Tavazoei and M. Haeri, "Chaotic attractors in incommensurate fractional order systems," *Physica D: Nonlinear Phenomena*, vol. 237, no. 20, pp. 2628–2637, 2008.
- [28] S. Dadras and H. R. Momeni, "Control of a fractional-order economical system via sliding mode," *Physica A: Statistical Mechanics and Its Applications*, vol. 389, no. 12, pp. 2434–2442, 2010.
- [29] N. Wang, M. J. Er, J.-C. Sun, and Y.-C. Liu, "Adaptive robust online constructive fuzzy control of a complex surface vehicle system," *IEEE Transactions on Cybernetics*, vol. 46, no. 7, pp. 1511–1523, 2016.
- [30] R. Babaghasabha, M. A. Khosravi, and H. D. Taghirad, "Adaptive robust control of fully-constrained cable driven parallel robots," *Mechatronics*, vol. 25, pp. 27–36, 2015.
- [31] I. Pan, A. Korre, S. Das, and S. Durucan, "Chaos suppression in a fractional order financial system using intelligent regrouping pso based fractional fuzzy control policy in the presence of fractional Gaussian noise," *Nonlinear Dynamics*, vol. 70, no. 4, pp. 2445–2461, 2012.
- [32] A. Jajarmi, M. Hajipour, and D. Baleanu, "New aspects of the adaptive synchronization and hyperchaos suppression of a financial model," *Chaos, Solitons and Fractals*, vol. 99, pp. 285–296, 2017.
- [33] W.-C. Chen, "Nonlinear dynamics and chaos in a fractional-order financial system," *Chaos, Solitons and Fractals*, vol. 36, no. 5, pp. 1305–1314, 2008.
- [34] Z. Wang, X. Huang, and G. Shi, "Analysis of nonlinear dynamics and chaos in a fractional order financial system with time delay," *Computers and Mathematics with Applications*, vol. 62, no. 3, pp. 1531–1539, 2011.

- [35] Y. Li, Y. Chen, and I. Podlubny, "Mittag-leffler stability of fractional order nonlinear dynamic systems," *Automatica*, vol. 45, no. 8, pp. 1965–1969, 2009.
- [36] N. Aguila-Camacho, M. A. Duarte-Mermoud, and J. A. Gallegos, "Lyapunov functions for fractional order systems," *Communications in Nonlinear Science and Numerical Simulation*, vol. 19, no. 9, pp. 2951–2957, 2014.
- [37] C. Huang and J. Cao, "Active control strategy for synchronization and anti-synchronization of a fractional chaotic financial system," *Physica A: Statistical Mechanics and Its Applications*, vol. 473, pp. 262–275, 2017.
- [38] V.-T. Pham, S. T. Kingni, C. Volos, S. Jafari, and T. Kapitaniak, "A simple three-dimensional fractional-order chaotic system without equilibrium: dynamics, circuitry implementation, chaos control and synchronization," *AEU-international Journal of Electronics and Communications*, vol. 78, pp. 220–227, 2017.
- [39] P. Balasubramaniam, P. Muthukumar, and K. Ratnavelu, "Theoretical and practical applications of fuzzy fractional integral sliding mode control for fractional-order dynamical system," *Nonlinear Dynamics*, vol. 80, no. 1-2, pp. 249–267, 2015.
- [40] Y. Wang, L. Cao, S. Zhang, X. Hu, and F. Yu, "Command filtered adaptive fuzzy backstepping control method of uncertain non-linear systems," *IET Control Theory and Applications*, vol. 10, no. 10, pp. 1134–1141, 2016.
- [41] H. Liu, S. Li, J. Cao, G. Li, A. Alsaedi, and F. E. Alsaadi, "Adaptive fuzzy prescribed performance controller design for a class of uncertain fractional-order nonlinear systems with external disturbances," *Neurocomputing*, vol. 219, pp. 422–430, 2017.
- [42] N. Bigdeli and H. A. Ziazi, "Finite-time fractional-order adaptive intelligent backstepping sliding mode control of uncertain fractional-order chaotic systems," *Journal of the Franklin Institute*, vol. 354, no. 1, pp. 160–183, 2017.
- [43] K. M. Owolabi, "Robust and adaptive techniques for numerical simulation of nonlinear partial differential equations of fractional order," *Communications in Nonlinear Science and Numerical Simulation*, vol. 44, pp. 304–317, 2017.
- [44] H. Liu, Y. Pan, S. Li, and Y. Chen, "Adaptive fuzzy backstepping control of fractional-order nonlinear systems," *IEEE Transactions on Systems, Man, and Cybernetics: Systems*, vol. 47, no. 8, pp. 2209–2217, 2017.
- [45] G. Li, J. Cao, A. Alsaedi, and B. Ahmad, "Limit cycle oscillation in aeroelastic systems and its adaptive fractional-order fuzzy control," *International Journal of Machine Learning and Cybernetics*, vol. 9, no. 8, pp. 1297–1305, 2018.

Research Article

Master-Slave Synchronization of Chaotic Φ^6 Duffing Oscillators by Linear State Error Feedback Control

Ke Ding ^{1,2}

¹School of Information Management, Jiangxi University of Finance and Economics, Nanchang 330013, China

²Jiangxi E-Commerce High Level Engineering Technology Research Centre, Nanchang 330013, China

Correspondence should be addressed to Ke Ding; keding@jxufe.edu.cn

Received 18 July 2019; Accepted 10 September 2019; Published 30 October 2019

Guest Editor: Viet-Thanh Pham

Copyright © 2019 Ke Ding. This is an open access article distributed under the Creative Commons Attribution License, which permits unrestricted use, distribution, and reproduction in any medium, provided the original work is properly cited.

This paper is concerned with master-slave synchronization of chaotic Φ^6 Duffing oscillators by using linear state error feedback control. Compared with some existing methods and results, this paper estimates the bound of the first trajectory (variable) of the controlled slave system and uses this bound to derive synchronization criteria for two chaotic Φ^6 Duffing oscillators. The effectiveness of synchronization criteria is illustrated by three simulation examples.

1. Introduction

Synchronization of chaotic systems has received considerable attention due to its theoretical importance and practical applications in secure communication and signal processing (see for example, [1–31] and references therein).

As is well known, some models for damped and driven oscillators, such as stiffening springs, beam bulking, and superconducting Josephson parametric amplifiers, can be described as Φ^6 Duffing oscillators which have been widely used in mechanical and electrical systems [1, 9–11, 32–36]. With proper parameters, Duffing oscillators have exhibited chaotic behaviors. For chaotic Φ^6 Duffing oscillators, Njah [10, 11] used the active control to achieve master-slave synchronization, in which the active control removed all nonlinear terms of the error system. For chaotic Φ^4 Duffing oscillators which is the special case of Φ^6 Duffing oscillators, synchronization criteria were derived by the active control in [32–34, 37] and [35] in which the linear error system and synchronization criteria were derived. It should be pointed out that chaotic Φ^6 Duffing oscillators are nonlinear systems in which the nonlinear terms play a key role in the generation of chaotic attractors. Thus, how to use the nonlinear properties of the error system and how to use linear state error feedback control to derive synchronization criteria for

chaotic Φ^6 Duffing oscillators is one motivation of this paper.

The bounds of trajectories of the master system and slave system have been widely used to derive the synchronization criteria for chaotic systems (see for example, [36, 38–40]). But it was difficult to estimate the bounds of slave systems. Therefore, how to derive the bound of some (not all) trajectories of the controlled slave system before the master system and the slave system achieve synchronization and how to use the derived bound to achieve synchronization criteria for the chaotic Φ^6 Duffing oscillators is another motivation of this paper.

In this paper, we will construct a master-slave synchronization scheme for chaotic Φ^6 Duffing oscillators by using linear state error feedback control. We will use the linear state error feedback control to derive the bound of the first trajectory of the slave system before the master system and the slave system achieve synchronization and use this bound to obtain synchronization criteria. Moreover, we will use three examples to illustrate the effectiveness of our synchronization criteria.

The rest of this paper is as follows. In Section 2, the related problems and concepts will be introduced. In Section 3, the synchronization results for chaotic Φ^6 Duffing oscillators will be given. As applications, the synchronization

results for classic Φ^4 Duffing oscillators and parametrically excited Φ^4 Duffing oscillators will be provided in Section 4. In Section 5, three simulation results will be given. Conclusions and future works will be presented in Section 6.

2. Problem Statement

The mathematical model of Φ^6 Duffing oscillator is

$$\ddot{x}(t) = -c\dot{x}(t) - dx(t) - lx^3(t) - ax^5(t) + q \cos \omega t, \quad (1)$$

where $x(t)$ is the displacement of rotation angle; $\dot{x}(t) = dx(t)/dt$; $\ddot{x}(t) = d^2(x(t))/dt^2$; a, c, d, l, q , and ω are constants; $q \cos \omega t$ is the excitation; $c\dot{x}(t)$ is the linear damping term; $dx(t) + lx^3(t)$ is a nonlinear force; and the initial condition is $x(0) = x_0$ and $\dot{x}(0) = x'_0$. The potential of (1) is $W_6(x) = (1/2)dx^2(t) + (1/4)lx^4(t) + (1/6)ax^6(t)$, which is the reason why system (1) is called Φ^6 Duffing oscillator.

Remark 1. If $a = 0$, system (1) reduces to the following Φ^4 Duffing oscillator:

$$\ddot{x}(t) = -c\dot{x}(t) - dx(t) - lx^3(t) + q \cos \omega t, \quad (2)$$

with the potential $W_4(x) = (1/2)dx^2(t) + (1/4)lx^4(t)$.

Let $y_1(t) = x(t)$ and $y_2(t) = \dot{y}_1(t)$. The non-autonomous system (1) can be written as the following dimensionless system:

$$\begin{cases} \dot{y}_1(t) = y_2(t), \\ \dot{y}_2(t) = -dy_1(t) - cy_2(t) + g(y_1(t)) + p(t), \end{cases} \quad (3)$$

where

$$\begin{aligned} p(t) &= q \cos \omega t, \\ g(y_1(t)) &= -ly_1^3(t) - ay_1^5(t). \end{aligned} \quad (4)$$

The initial condition of system (3) is given by $y_1(0) = y_{1_0}, y_2(0) = y_{2_0}$.

Let $y(t) = \begin{pmatrix} y_1(t) \\ y_2(t) \end{pmatrix} \in \mathbb{R}^2$. Write the system described by (3) as

$$\dot{y}(t) = Ay(t) + \varphi(y(t)) + r(t), \quad (5)$$

where

$$\begin{aligned} A &= \begin{pmatrix} 0 & 1 \\ -d & -c \end{pmatrix}, \\ r(t) &= \begin{pmatrix} 0 \\ p(t) \end{pmatrix}, \\ \varphi(y(t)) &= \begin{pmatrix} 0 \\ g(y_1(t)) \end{pmatrix}. \end{aligned} \quad (6)$$

Let $z(t) = \begin{pmatrix} z_1(t) \\ z_2(t) \end{pmatrix} \in \mathbb{R}^2$. We can construct the following synchronization scheme for the system described by (5):

$$\mathcal{M} : \dot{y}(t) = Ay(t) + \varphi(y(t)) + r(t), \quad (7)$$

$$\mathcal{S} : \dot{z}(t) = Az(t) + \varphi(z(t)) + r(t) + u(t), \quad (8)$$

$$\mathcal{C} : u(t) = K(y(t) - z(t)), \quad (9)$$

with the master system described by \mathcal{M} and the slave system described by \mathcal{S} , where $u(t) = \begin{pmatrix} u_1(t) \\ u_2(t) \end{pmatrix} \in \mathbb{R}^2$ is the controller and $K = \begin{pmatrix} k_1 & 1 \\ k_2 & k_3 \end{pmatrix}$ in which $k_1 > 0$, k_2 , and k_3 are gains which can be determined later. The initial condition of system (8) is given by $z_1(0) = z_{1_0}$ and $z_2(0) = z_{2_0}$.

Defining a signal $e(t) = y(t) - z(t) = \begin{pmatrix} e_1(t) \\ e_2(t) \end{pmatrix} \in \mathbb{R}^2$, one can obtain the error system

$$\begin{cases} \dot{e}_1(t) = -k_1 e_1(t), \\ \dot{e}_2(t) = -(k_2 + d)e_1(t) - (k_3 + c)e_2(t) + g(y_1(t)) - g(z_1(t)). \end{cases} \quad (10)$$

In view of differential mean theorem, one can have

$$g(y_1(t)) - g(z_1(t)) = g'(\xi(t))(y_1(t) - z_1(t)), \quad (11)$$

where

$$g'(\xi(t)) = \left. \frac{dg(\rho)}{d\rho} \right|_{\rho=\xi(t)} = -(3l\xi^2(t) + 5a\xi^4(t)), \quad (12)$$

for $\xi(t) \in (\min\{y_1(t), z_1(t)\}, \max\{y_1(t), z_1(t)\})$, which results in

$$\dot{e}(t) = \widehat{K}(t)e(t), \quad (13)$$

where

$$\widehat{K}(t) = \begin{pmatrix} -k_1 & 0 \\ -(k_2 + d) + g'(\xi(t)) & -(k_3 + c) \end{pmatrix}. \quad (14)$$

The initial condition of system (10) is $e_1(0) = y_{1_0} - z_{1_0}, e_2(0) = y_{2_0} - z_{2_0}$.

Notice that the master system described by (7) is chaotic. Thus, there exist two scales $m_1 > 0$ and $m_2 > 0$ for any y_{1_0} and y_{2_0} in the attracting area such that

$$|y_i(t)| \leq m_i, \quad i = 1, 2, \forall t > 0. \quad (15)$$

From the first equation of system described by (10), we have

$$e_1(t) = (y_{1_0} - z_{1_0}) \exp(-k_1 t), \quad (16)$$

which indicates that

$$z_1(t) = y_1(t) - (y_{1_0} - z_{1_0}) \exp(-k_1 t). \quad (17)$$

From the equation described by (17), we have

$$\begin{aligned} |z_1(t)| &\leq |y_1(t)| + |y_{1_0} - z_{1_0}| \\ &\leq m_1 + |y_{1_0} - z_{1_0}|, \quad \forall t > 0, k_1 > 0. \end{aligned} \quad (18)$$

From inequalities (15) and (18) and equation (11), there exists a scale $\lambda > 0$ such that

$$|g'(\xi(t))| \leq \lambda, \quad (19)$$

where

$$\begin{aligned} \lambda &= (3|l| + 5|a|\sigma)\sigma, \\ \sigma &= \max\{\zeta^2(t)\}, \end{aligned} \quad (20)$$

$$\forall \zeta(t) \in (\min\{y_1(t), z_1(t)\}, \max\{y_1(t), z_1(t)\}).$$

Remark 2. Since the bounds of $y_1(t)$ and $z_1(t)$ for any $t > 0$ are given by (15) and (18), respectively, and $g(\cdot)$ and $g'(\cdot)$ are defined and differentiable, the bound of $|g'(\xi(t))|$ for $\xi(t) \in (\min\{y_1(t), z_1(t)\}, \max\{y_1(t), z_1(t)\})$ can be estimated by (19).

Remark 3. For the cascaded system described by

$$\dot{\zeta}_1(t) = \phi_1(t, \zeta_1(t)) + \chi(t, \zeta_1(t), \zeta_2(t)), \quad (21)$$

$$\dot{\zeta}_2(t) = \phi_2(t, \zeta_2(t)), \quad (22)$$

where ϕ_1, ϕ_2 , and χ are smooth, the origin $(0, 0)$ is uniformly globally asymptotically stable if $\dot{\zeta}_1(t) = \phi_1(t, \zeta_1(t))$ and $\dot{\zeta}_2(t) = \phi_2(t, \zeta_2(t))$ are uniformly globally asymptotically stable and the solutions of (21) and (22) are uniformly globally bounded (Lemma 2, [41]). The system described by (10) can be regarded as a cascaded system. Although, it is easy to obtain the conditions to ensure that $\dot{\zeta}_1(t) = -k_1 e_1(t)$ and $\dot{\zeta}_2(t) = -(k_3 + c)e_2(t)$ are uniformly globally asymptotically stable, we cannot directly claim that the solutions of (10) are uniformly globally bounded. Thus, we cannot directly use Lemma 2 of [41] to study the stability of the error system (10).

The purpose of this paper is to investigate the master-slave synchronization for the system described by (1) and to find the controller gain K , such that the system described by (10) is globally asymptotically stable, which indicates that the system described by (7)–(9) synchronizes.

3. Main Results: Master-Slave Synchronization Criteria

In this section, we give some stability criteria for the error system described by (10), which ensures that the system described by (7)–(9) synchronizes.

Choosing the following Lyapunov function:

$$V(t) = e^T(t)Pe(t), \quad (23)$$

where $P = \begin{pmatrix} p_{11} & p_{12} \\ p_{12} & p_{22} \end{pmatrix} \in \mathbb{R}^{2 \times 2}$ is a real positive matrix, we state and establish the following result.

Proposition 1. *The error system described by (10), (15), and (19) is globally asymptotically stable, i.e., the master system described by (7) and the slave system described by (8) achieve synchronization if*

$$\begin{cases} \Theta_1 = -(k_2 + d)p_{12} - p_{11}k_1 + \lambda|p_{12}| < 0, \\ \Theta_2 = -p_{22}(k_3 + c) < 0, \\ (|-(k_1 + k_3 + c)p_{12} - (k_2 + d)p_{22}| + \lambda p_{22})^2 \leq 4\Theta_1\Theta_2. \end{cases} \quad (24)$$

Proof. Taking the derivative of $V(t)$ with respect to t along the trajectory of (10) yields

$$\dot{V}(t) = e^T(t)L(t)e(t), \quad (25)$$

where

$$L(t) = \widehat{K}^T(t)P + P\widehat{K}(t) = \begin{pmatrix} l_{11}(t) & l_{12}(t) \\ l_{12}(t) & l_{22}(t) \end{pmatrix}, \quad (26)$$

with

$$\begin{aligned} l_{11}(t) &= 2((g'(\xi(t)) - k_2 - d)p_{12} - p_{11}k_1), \\ l_{12}(t) &= -(k_1 + k_3 + c)p_{12} + (g'(\xi(t)) - k_2 - d)p_{22}, \\ l_{22}(t) &= -2p_{22}(k_3 + c). \end{aligned} \quad (27)$$

Conditions

$$\begin{aligned} l_{11}(t) &< 0, \\ l_{22}(t) &< 0, \\ l_{12}^2(t) &< l_{11}(t)l_{22}(t), \end{aligned} \quad (28)$$

can ensure

$$\dot{V}(t) < 0, \quad \forall e_1(t), e_2(t) \neq 0. \quad (29)$$

It follows from (19) and (27) that

$$\begin{aligned} \frac{l_{11}(t)}{2} &= g'(\xi(t))p_{12} - (k_2 + d)p_{12} - p_{11}k_1 \\ &\leq -(k_2 + d)p_{12} - p_{11}k_1 + |g'(\xi(t))||p_{12}| \\ &\leq -(k_2 + d)p_{12} - p_{11}k_1 + \lambda|p_{12}| \\ &= \Theta_1, \end{aligned}$$

$$\frac{l_{22}(t)}{2} = -p_{22}(k_3 + c) = \Theta_2,$$

$$\begin{aligned} l_{12}^2(t) &= (-(k_1 + k_3 + c)p_{12} + (g'(\xi(t)) - k_2 - d)p_{22})^2 \\ &\leq (|-(k_1 + k_3 + c)p_{12} - (k_2 + d)p_{22}| + |g'(\xi(t))|p_{22})^2 \\ &\leq (|-(k_1 + k_3 + c)p_{12} - (k_2 + d)p_{22}| + \lambda p_{22})^2. \end{aligned} \quad (30)$$

From (30), one can see that inequalities (24) can guarantee inequalities (28). Thus, it follows from inequalities (19), (24), and (29) that the error system described by (10) is globally asymptotically stable. This completes the proof. Q.E.D.

Let $P = \begin{pmatrix} 1 & 0 \\ 0 & 1 \end{pmatrix}$. One can derive the following synchronization result by Proposition 1.

Proposition 2. *The error system described by (10), (15), and (19) is globally asymptotically stable, i.e., the master system described by (7) and the slave system described by (8) achieve synchronization if*

$$\begin{cases} k_1 > 0, c + k_3 > 0, \\ 2\sqrt{k_1(c + k_3)} - |d + k_2| > \lambda. \end{cases} \quad (31)$$

If $k_1 = k_3 = k$, we have the following corollary.

Corollary 1. *The error system described by (10), (15), and (19) is globally asymptotically stable, i.e., the master system described by (7) and the slave system described by (8) achieve synchronization if*

$$\begin{cases} k > 0, c + k > 0, \\ 2\sqrt{k(c + k)} - |d + k_2| > \lambda. \end{cases} \quad (32)$$

If $k_1 = k_3 = k$ and $k_2 = 0$, the following result is obtained.

Corollary 2. *The error system described by (10), (15), and (19) is globally asymptotically stable, i.e., the master system described by (7) and the slave system described by (8) achieve synchronization if*

$$\begin{cases} k > 0, c + k > 0, \\ 2\sqrt{k(c + k)} - |d| > \lambda. \end{cases} \quad (33)$$

In some applications, one can only measure the position variables for a chaotic system, which means that we only use $y_1(t) - z_1(t)$ in the feedback control. In this situation, one can obtain $k_3 = 0$. The corresponding result is given as follows.

Corollary 3. *The error system described by (10), (15), and (19) is globally asymptotically stable, i.e., the master system described by (7) and the slave system described by (8) achieve synchronization if*

$$\begin{cases} k_1 > 0, c > 0, \\ 2\sqrt{k_1 c} - |d + k_2| > \lambda. \end{cases} \quad (34)$$

Furthermore, in the case of $k_2 = k_3 = 0$, one can have the following result.

Corollary 4. *The error system described by (10), (15), and (19) is globally asymptotically stable, i.e., the master system described by (7) and the slave system described by (8) achieve synchronization if*

$$\begin{cases} k_1 > 0, c > 0, \\ 2\sqrt{k_1 c} - |d| > \lambda. \end{cases} \quad (35)$$

Remark 4. Njah [10, 11] constructed the master-slave synchronization scheme for the Φ^6 Duffing equation and studied master-slave synchronization by the active control,

in which the active controller $u(t) = \begin{pmatrix} u_1(t) \\ u_2(t) \end{pmatrix} \in \mathbb{R}^2$ was

$$\begin{cases} u_1(t) = -\widehat{a}e_1(t) - \widehat{b}e_2(t), \\ u_2(t) = -a(y_1^5(t) - z_1^5(t)) - l(y_1^3(t) - z_1^3(t)) \\ \quad -\eta_1 e_1(t) - \eta_2 e_2(t), \end{cases} \quad (36)$$

where $\widehat{a}, \widehat{b}, \eta_1$, and η_2 are parameters for control inputs. Then, one can have the error system

$$\begin{cases} \dot{e}_1(t) = \widehat{a}e_1(t) + (1 + \widehat{b})e_2(t), \\ \dot{e}_2(t) = -(d - \eta_1)e_1(t) - (c - \eta_2)e_2(t). \end{cases} \quad (37)$$

Obviously, a linear error system described by (37) can be perfectly derived by the control (36) in [10, 11] which removed all nonlinear terms of the error system, and the stability criterion for the linear error system described by (37) can be easily obtained. However, the original Duffing oscillator (1) was completely canceled. Compared with control (36) in [10, 11], control (9) in this paper has two advantages. The first advantage is that the nonlinear term $y_1^3(t) - z_1^3(t)$ of the error system described by (10) is kept which means that the error system described by (10) is a nonlinear system, rather than a linear error system (37) in [10, 11]. The second advantage is that it is easy to estimate the bounds for $z_1(t)$ and $g'(\xi(t))$ by using (18) and (19), respectively, which are necessary for deriving the stability criterion for the error system described by (10).

Remark 5. In this paper, we only use the bound of $z_1(t)$ because it can be estimated by (18).

4. Applications to Master-Slave Synchronization of Chaotic Φ^4 Duffing Oscillators

4.1. Master-Slave Synchronization of Classic Φ^4 Duffing Oscillators. Now, we can study the synchronization of classic Φ^4 Duffing oscillator (2). Let $y_1(t) = x(t)$ and $y_2(t) = \dot{y}_1(t)$. One can derive the dimensionless system (3), in which $g(y_1(t))$ is replaced by $-ly_1^3(t)$. From (19), the bound of $g'(\cdot)$ can be estimated as

$$|g'(\xi(t))| \leq \widetilde{\lambda}, \quad (38)$$

where $\widetilde{\lambda} = 3|l|\sigma$ in which $\sigma = \max\{\zeta^2(t)\}$, $\forall \zeta(t) \in (\min\{y_1(t), z_1(t)\}, \max\{y_1(t), z_1(t)\})$. One can construct the synchronization scheme described by (7)–(9) for the system described by (2) and derive the error system described by (13), where $g(y_1(t))$ is replaced by $-ly_1^3(t)$. Employing the Lyapunov function described by (23), one can have the following synchronization criterion for the Φ^4 Duffing oscillator described by (2).

Proposition 3. *The error system described by (13), (15), and (38) is globally asymptotically stable, i.e., the master system*

described by (7) and the slave system described by (8) achieve synchronization if

$$\begin{cases} \Theta_1 = -(k_2 + d)p_{12} - p_{11}k_1 + \tilde{\lambda}|p_{12}| < 0, \\ \Theta_2 = -p_{22}(k_3 + c) < 0, \\ (|-(k_1 + k_3 + c)p_{12} - (k_2 + d)p_{22}| + \tilde{\lambda}p_{22})^2 \leq 4\Theta_1\Theta_2. \end{cases} \quad (39)$$

If $P = \begin{pmatrix} 1 & 0 \\ 0 & 1 \end{pmatrix}$ in (23), one can obtain the following synchronization criterion for Φ^4 Duffing oscillator (2).

Proposition 4. *The error system described by (13), (15), and (38) is globally asymptotically stable, i.e., the master system described by (7) and the slave system described by (8) achieve synchronization if*

$$\begin{cases} k_1 > 0, c + k_3 > 0, \\ 2\sqrt{k_1(c + k_3)} - |d + k_2| > \tilde{\lambda}. \end{cases} \quad (40)$$

Remark 6. Jiang [3] and Nijmeijer and Berghuis [9] studied the tracking control for Duffing oscillators which can be equivalent to master-slave synchronization for Duffing oscillators. The stability criteria for the error system were derived by using the control $u(t) = \tilde{K}e(t) - \zeta(t)$ [3], where $\tilde{K} = \begin{pmatrix} 0 & 0 \\ k_4 & k_5 \end{pmatrix}$ and $\zeta(t) = \begin{pmatrix} 0 \\ 3k_6z_1^2(t)e_1(t) \end{pmatrix}$ in which k_4, k_5 , and k_6 are gains, and the control $u(t) = \tilde{K}e(t) - v(t)$ [9], where $\tilde{K} = \begin{pmatrix} 0 & 0 \\ k_7 & k_8 \end{pmatrix}$ and $v(t) = \begin{pmatrix} 0 \\ 3y_1(t)z_1(t)e_1(t) \end{pmatrix}$ in which k_7 and k_8 are gains. It should be pointed out that those controls in [3, 9] were nonlinear feedback controls. Our control (9) $u(t) = K(y(t) - z(t))$ is a linear feedback control.

Remark 7. Han et al. [32] and Njah and Vincent [37] used the active control to derive synchronization criteria for chaotic Φ^4 Duffing oscillators, in which the active controller

$$u(t) = \begin{pmatrix} u_1(t) \\ u_2(t) \end{pmatrix} \in \mathbb{R}^2 \text{ was}$$

$$\begin{cases} u_1(t) = -z_1(t) + y_1(t) + \check{k}_1e_1(t), \\ u_2(t) = dz_1(t) + cz_2(t) + lz_1^3(t) - dy_1(t) - cy_2(t) \\ \quad -ly_1^3(t) + \check{k}_2e_2(t), \end{cases} \quad (41)$$

where \check{k}_1 and \check{k}_2 are feedback gains. Thus, the error system was

$$\begin{cases} \dot{e}_1(t) = -\check{k}_1e_1(t), \\ \dot{e}_2(t) = -\check{k}_2e_2(t). \end{cases} \quad (42)$$

As discussed in Remark 4, the error system described by (42) was a linear system. Compared with the control method in [32, 37], we keep the linear and nonlinear terms and fully

use the term $-dy_1(t) - cy_2(t) - ly_1^3(t)$ to derive the synchronization criterion Proposition 3.

4.2. Master-Slave Synchronization of Parametrically Excited Φ^4 Duffing Oscillators. Wu et al. [36] studied the following parametrically excited Φ^4 Duffing oscillator:

$$\begin{cases} \dot{y}_1(t) = y_2(t), \\ \dot{y}_2(t) = (1 + \mu \sin \omega t)y_1(t) - y_1^3(t) - cy_2(t), \end{cases} \quad (43)$$

where μ and ω are constants, which can be rewritten as

$$\dot{y}(t) = \check{A}(t)y(t) + \check{\varphi}(y(t)), \quad (44)$$

where

$$\begin{aligned} y(t) &= \begin{pmatrix} y_1(t) \\ y_2(t) \end{pmatrix} \in \mathbb{R}^2, \\ \check{A}(t) &= \begin{pmatrix} 0 & 1 \\ 1 + \mu \sin \omega t & -c \end{pmatrix}, \\ \check{\varphi}(y(t)) &= \begin{pmatrix} 0 \\ -y_1^3(t) \end{pmatrix}. \end{aligned} \quad (45)$$

In [36], the master-slave scheme was constructed as follows:

$$\mathcal{M} : \dot{y}(t) = \check{A}(t)y(t) + \check{\varphi}(y(t)), \quad (46)$$

$$\mathcal{S} : \dot{z}(t) = \check{A}(t)z(t) + \check{\varphi}(z(t)) + u(t), \quad (47)$$

$$\mathcal{E} : u(t) = \check{K}(y(t) - z(t)), \quad (48)$$

where $z(t) = \begin{pmatrix} z_1(t) \\ z_2(t) \end{pmatrix} \in \mathbb{R}^2$ and $\check{K} = \begin{pmatrix} \check{k}_{11} & \check{k}_{12} \\ \check{k}_{21} & \check{k}_{22} \end{pmatrix}$ is a gain matrix which can be determined. The initial conditions of the master and slave system were $y_1(0) = y_{1_0}, y_2(0) = y_{2_0}$, and $z_1(0) = z_{1_0}, z_2(0) = z_{2_0}$, respectively. The error system was

$$\dot{e}(t) = (\check{A}(t) + M(t) - \check{K})e(t), \quad (49)$$

where

$$\begin{aligned} e(t) &= y(t) - z(t) = \begin{pmatrix} e_1(t) \\ e_2(t) \end{pmatrix} = \begin{pmatrix} y_1(t) - y_2(t) \\ z_1(t) - z_2(t) \end{pmatrix}, \\ M(t)e(t) &= \check{\varphi}(y(t)) - \check{\varphi}(z(t)) \text{ with } M(t) = \begin{pmatrix} 0 & 0 \\ -F(t) & 0 \end{pmatrix}, \\ F(t) &= (y_1^2(t) + z_1^2(t) + y_1(t)z_1(t)). \end{aligned} \quad (50)$$

The initial conditions of the error system were $e_1(0) = e_{1_0} = y_1(0) - z_1(0), e_2(0) = e_{2_0} = y_2(0) - z_2(0)$.

Choosing our method, one can use the control as follows:

$$\mathcal{E} : u(t) = \bar{K}(y(t) - z(t)), \quad (51)$$

where $\bar{K} = \begin{pmatrix} \bar{k}_1 & 1 \\ \bar{k}_2 & \bar{k}_3 \end{pmatrix}$ in which $\bar{k}_1 > 0, \bar{k}_2$, and \bar{k}_3 can be determined later. From master-slave schemes (46), (47), and (51), one can have the following error system:

$$\begin{cases} \dot{e}_1(t) = -\bar{k}_1 e_1(t), \\ \dot{e}_2(t) = (1 + \mu \sin \omega t - \bar{k}_2) e_1(t) + (\bar{g}(y_1(t)) - \bar{g}(z_1(t))) \\ \quad - (c + \bar{k}_3) e_2(t), \end{cases} \quad (52)$$

where

$$\bar{g}(y_1(t)) = -y_1^3(t), \quad (53)$$

and the initial condition is $e_1(0) = e_{1_0}$ and $e_2(0) = e_{2_0}$. From (19), one can obtain

$$\begin{aligned} \bar{g}(y_1(t)) - \bar{g}(z_1(t)) &= -y_1^3(t) + z_1^3(t) = \bar{g}'(\xi(t)) \\ &\quad \cdot (y_1(t) - z_1(t)), \\ \bar{g}'(\xi(t)) &= -3\xi^2(t), \xi(t) \in (\min\{y_1(t), z_1(t)\}, \\ &\quad \max\{y_1(t), z_1(t)\}). \end{aligned} \quad (54)$$

Then, the error system described by (52) can be rewritten as

$$\dot{e}(t) = \dot{K}(t)e(t), \quad (55)$$

where

$$\dot{K}(t) = \begin{pmatrix} -\bar{k}_1 & 0 \\ 1 + \mu \sin \omega t - \bar{k}_2 + \bar{g}'(\xi(t)) - c - \bar{k}_3 \end{pmatrix}. \quad (56)$$

It follows from (19) that there exists a scale $\bar{\lambda} > 0$ such that

$$|\bar{g}'(\xi(t))| \leq \bar{\lambda}, \quad (57)$$

where

$$\begin{aligned} \bar{\lambda} &= 3\sigma, \\ \sigma &= \max\{\zeta^2(t)\}, \end{aligned} \quad (58)$$

$\forall \zeta(t) \in (\min\{y_1(t), z_1(t)\}, \max\{y_1(t), z_1(t)\})$. By using the similar proof of Proposition 1, one can have the synchronization result for (43).

Proposition 5. *The error system described by (52) is globally asymptotically stable, i.e., the master system described by (46) and the slave system described by (47) achieve synchronization if*

$$\begin{cases} \bar{k}_1 > 0, c + \bar{k}_3 > 0, \\ 2\sqrt{\bar{k}_1(c + \bar{k}_3)} - |1 + |\mu| + \bar{k}_2| > \bar{\lambda}. \end{cases} \quad (59)$$

5. Simulation Study

5.1. Simulation for Chaotic Φ^6 Duffing Oscillators. Consider the chaotic Φ^6 Duffing oscillator (1) with $a = 0.1$, $c = 0.4$, $d = 1.1$, $l = 0.4$, $q = 1.8$, and $\omega = 2.1$. If we choose the initial condition of (1) as $y_{1_0} = 0$ and $z_{1_0} = -1$, there is an attractor which is demonstrated in Figure 1. From Figure 1, one can obtain that the bound of $|y_1(t)|$ is 1.4, i.e., $m_1 = 1.4$.

For the master-slave scheme (7)–(9) with (1), one can choose the initial condition of the slave system as $z_{1_0} = 0.1$ and $z_{2_0} = -1.5$. By virtue of (18), one can obtain $|z_1(t)| \leq 1.4 + 0.1 = 1.5$. It follows from (19) that $|\bar{g}'(\xi(t))| \leq 5.2313 = \lambda$. Let $k_2 = 0$ and $k_1 = k_3$. From Corollary 2, we have $\sqrt{k_1(c + k_1)} > ((\lambda + d)/2)$, which implies that $k_1 \geq 2.97$. We choose $k_1 = 2.98$.

Figures 2–4 give the simulation results for the master system, the slave system, and the error system with $k_1 = 2.98$, $k_2 = 0$, and $k_3 = 2.98$, respectively, from which one can see that the error system (10) is globally asymptotically stable; i.e., the master-slave synchronization scheme described by (7)–(9) indeed achieves synchronization.

5.2. Simulation for Classic Φ^4 Duffing Oscillators. For the classic Φ^4 Duffing oscillator (2), parameters c, d, l, q , and ω are the same as those defined in the abovementioned Φ^6 Duffing oscillators. If we choose the initial condition of (1) as $y_{1_0} = 0$ and $z_{1_0} = -1$, there is an attractor which is demonstrated in Figure 5. From Figure 5, we have that the bound of $|y_1(t)|$ is 1.4, i.e., $m_1 = 1.4$.

Consider the master-slave scheme (7)–(9) with (2), where the initial condition of the slave system is $z_{1_0} = 0.1$ and $z_{2_0} = 1.5$. From (18), we have $|z_1(t)| \leq 1.4 + 0.1 = 1.5$. It follows from (38) that $|\bar{g}'(\xi(t))| \leq 2.7 = \bar{\lambda}$. Let $k_2 = 0$ and $k_1 = k_3$. From Proposition 4, we have $\sqrt{k_1(c + k_1)} > ((\lambda + d)/2)$, which implies that $k_1 \geq 1.71$. We choose $k_1 = 1.72$.

Figures 6–8 give the simulation results for the master system, the slave system, and the error system with $k_1 = 1.72$, $k_2 = 0$, and $k_3 = 1.72$, respectively. It follows from Figures 6–8 that the error system (10) is globally asymptotically stable; i.e., the master-slave synchronization scheme described by (7)–(9) indeed achieves synchronization.

5.3. Simulation for Parametrically Excited Φ^4 Duffing Oscillators. Now, we study the synchronization of parametrically excited Φ^4 Duffing oscillators (43) where $c = 0.2$, $\mu = 0.5$, and $\omega = 1$. The initial conditions of master system (46) and slave system (47) are $y_1(0) = 1.6$, $y_2(0) = 0.2$ and $z_1(0) = 2$, $z_2(0) = 1.4$, respectively. It follows from Figure 9 that the up bound of $|y_1(t)|$ is 1.66. However, we can see that the up bound of $|z_1(t)|$ is larger than 2 because $z_1(0) = 2$.

It follows from (57) that $|z_1(t)| \leq 1.66 + 0.4 = 2.06$ and $|\bar{g}'(\xi(t))| \leq 3 \times 2.06^2 = 12.7308 = \bar{\lambda}$. Let $\bar{k}_1 = \bar{k}_3$ and $\bar{k}_2 = 0$. Using Proposition 5, one can have $\bar{k}_1 = \bar{k}_3 > 7.01$. Let $\bar{k}_1 = \bar{k}_3 = 7.1$. Figure 10 illustrates that the error system is globally asymptotically stable; i.e., the master-slave

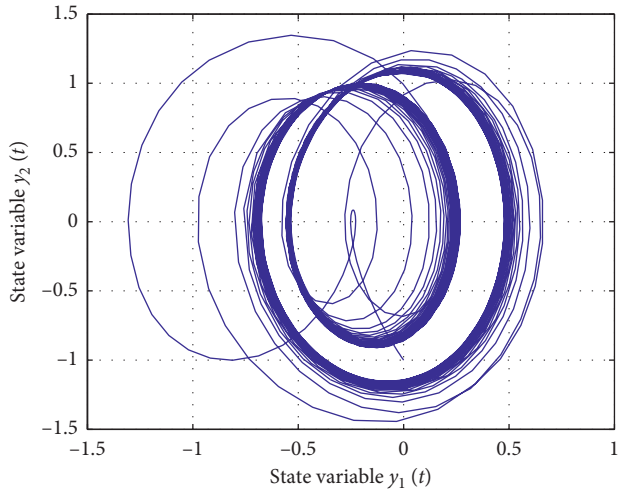


FIGURE 1: The phase diagram of the chaotic Φ^6 Duffing oscillator.

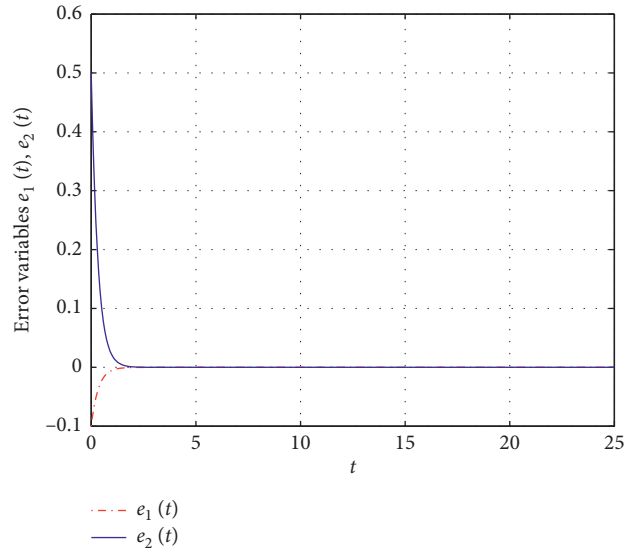


FIGURE 4: The simulation result for the error system with $k_1 = 2.98, k_2 = 0$, and $k_3 = 2.98$.

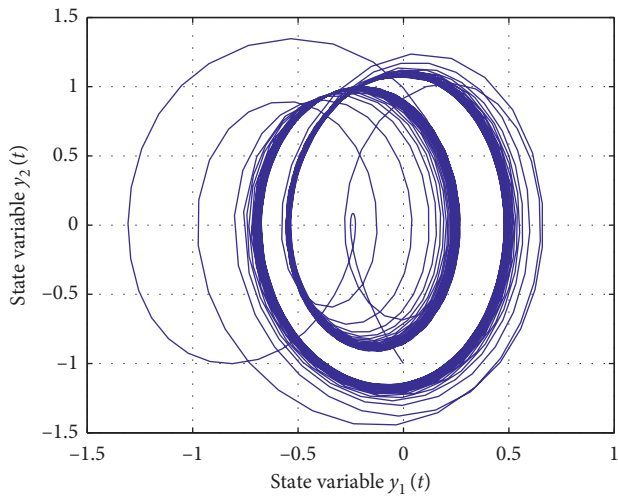


FIGURE 2: The simulation result for the master system.

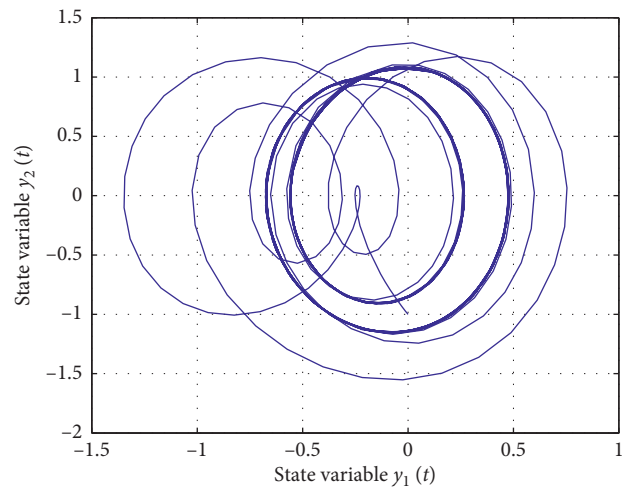


FIGURE 5: The phase diagram of the chaotic Φ^4 Duffing oscillator.

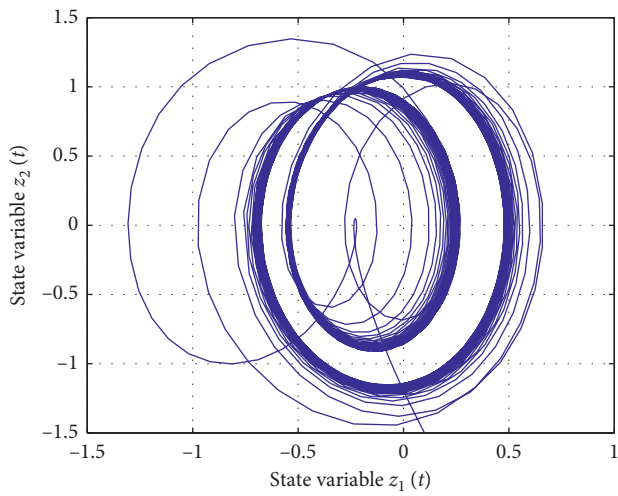


FIGURE 3: The simulation result for the slave system with $k_1 = 2.98, k_2 = 0$, and $k_3 = 2.98$.

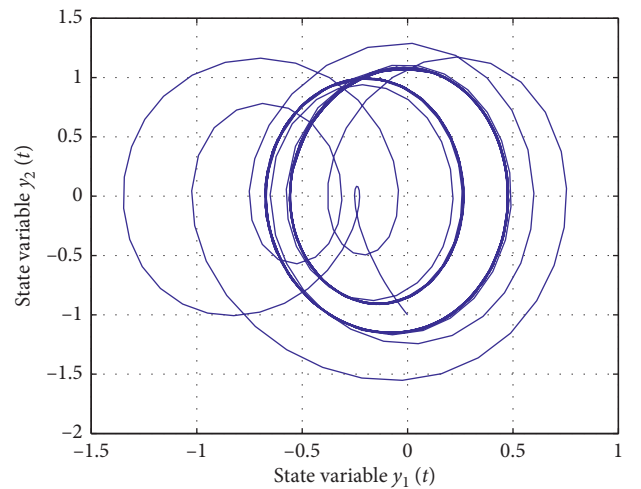


FIGURE 6: The simulation result for the master system.

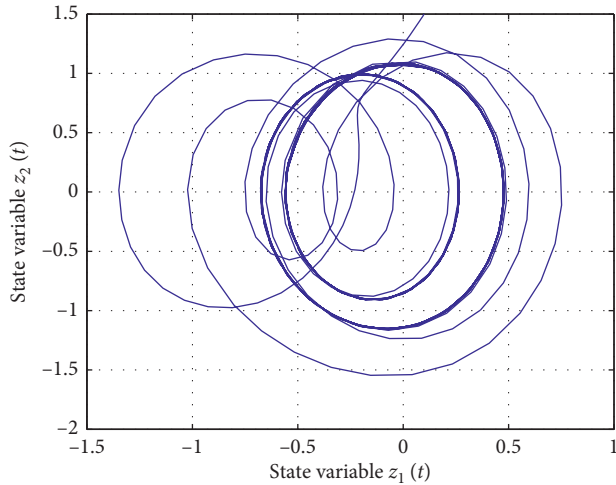


FIGURE 7: The simulation result for the slave system with $k_1 = 1.72, k_2 = 0$, and $k_3 = 1.72$.

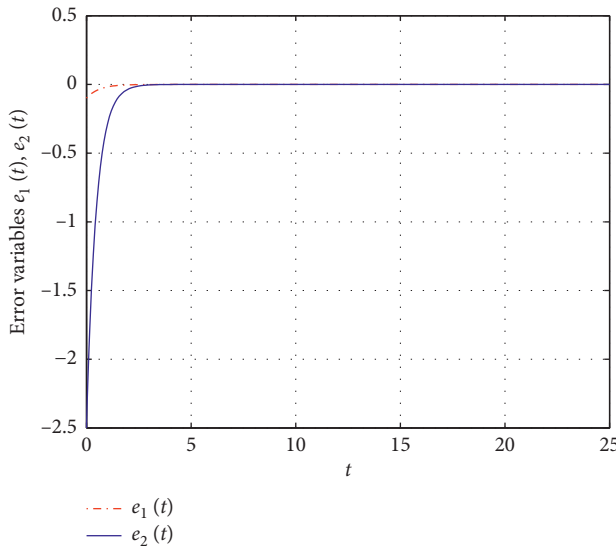


FIGURE 8: The simulation result for error system with $k_1 = 1.72, k_2 = 0$, and $k_3 = 1.72$.

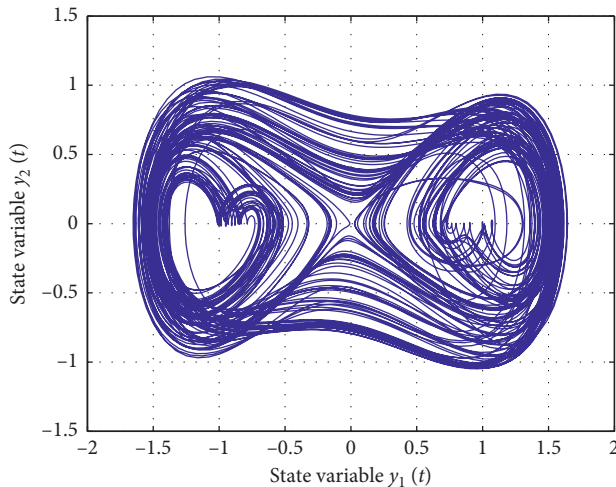


FIGURE 9: The simulation result for the master system.

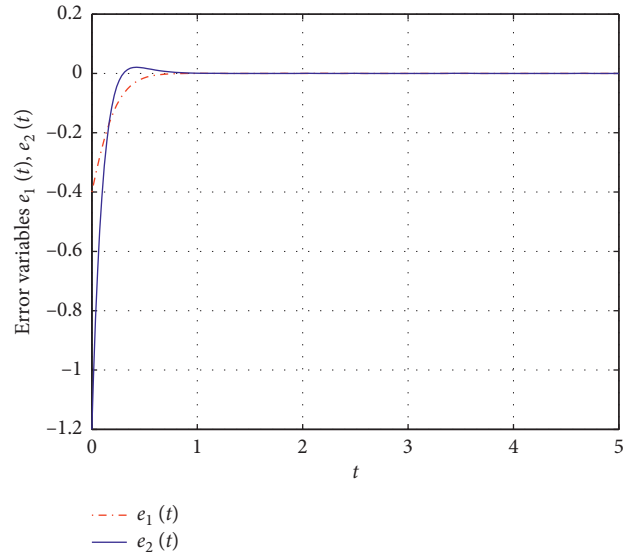


FIGURE 10: The simulation result for the error system with $k_1 = 7.1, k_2 = 0$, and $k_3 = 7.1$.

synchronization scheme described by (46), (47), and (51) indeed achieves synchronization.

6. Conclusion

We have constructed a master-slave synchronization scheme for chaotic Φ^6 Duffing oscillators by using linear feedback control. By estimating the first trajectory of the controlled slave system and keeping the nonlinear property of the error system, we have derived some synchronization criteria. Then, we have used three examples to illustrate the effectiveness of synchronization criteria for Duffing oscillators. In this paper, master and slave systems are all Φ^6 Duffing oscillators. The synchronization between Φ^6 and Φ^4 Duffing oscillators and the synchronization between Φ^6 Duffing oscillators with different parameters are our future research interests. Moreover, how to design the time delayed feedback control to achieve synchronization between Φ^6 Duffing oscillators with different parameters can be our future research interest as well.

Data Availability

The data used to support the findings of this study are included within the article.

Conflicts of Interest

The author declares that there are no conflicts of interest regarding the publication of this paper.

Acknowledgments

This study was partially supported by the National Natural Science Foundation of China under grant 61561023, the key project of Young Scholars of Jiangxi Province China, under grant 20133ACB21009, the Research Project of Humanities

and Social Sciences of Universities of Jiangxi Province under grant GL18123, the Education Research Project of Jiangxi University of Finance and Economics under grant JG2019031, and the Project of Jiangxi e-Commerce High Level Engineering Technology Research Centre.

References

- [1] A. K. Agrawal, J. N. Yang, and J. C. Wu, "Non-linear control strategies for duffing systems," *International Journal of Non-Linear Mechanics*, vol. 33, no. 5, pp. 829–841, 1998.
- [2] M.-C. Ho and Y.-C. Hung, "Synchronization of two different systems by using generalized active control," *Physics Letters A*, vol. 301, no. 5-6, pp. 424–428, 2002.
- [3] Z. P. Jiang, "Advanced feedback control of the chaotic Duffing equation," *IEEE Transactions on Circuits and Systems I: Fundamental Theory and Applications*, vol. 49, no. 2, pp. 244–249, 2002.
- [4] S. M. Lee, S. J. Choi, D. H. Ji, J. H. Park, and S. C. Won, "Synchronization for chaotic Lur'e systems with sector-restricted nonlinearities via delayed feedback control," *Non-linear Dynamics*, vol. 59, no. 1-2, pp. 277–288, 2010.
- [5] S.-Y. Li, C.-H. Yang, S.-A. Chen, L.-W. Ko, and C.-T. Lin, "Fuzzy adaptive synchronization of time-reversed chaotic systems via a new adaptive control strategy," *Information Sciences*, vol. 222, pp. 486–500, 2013.
- [6] S.-Y. Li, H.-K. Chen, L.-M. Tam, S.-C. Huang, and Z.-M. Ge, "Pragmatical adaptive synchronization—new fuzzy model of two different and complex chaotic systems by new adaptive control," *Information Sciences*, vol. 277, pp. 458–480, 2014.
- [7] X. Liao, G. Chen, B. Xu, and Y. Shen, "On global exponential synchronization of Chua circuits," *International Journal of Bifurcation and Chaos*, vol. 15, no. 7, pp. 2227–2234, 2005.
- [8] Y. Lei, W. Xu, and H. Zheng, "Synchronization of two chaotic nonlinear gyros using active control," *Physics Letter A*, vol. 343, no. 1–3, pp. 153–158, 2005.
- [9] H. Nijmeijer and H. Berghuis, "On lyapunov control of the duffing equation," *IEEE Transactions on Circuits and Systems I: Fundamental Theory and Applications*, vol. 42, no. 8, pp. 473–477, 1995.
- [10] A. N. Njah, "Synchronization via active control of identical and non-identical Φ^6 chaotic oscillators with external excitation," *Journal of Sound and Vibrations*, vol. 327, no. 3–5, pp. 322–332, 2009.
- [11] A. N. Njah, "Synchronization via active control of parametrically and externally excited Φ^6 Van der Pol and Duffing oscillators and application to secure communications," *Journal of Vibration and Control*, vol. 17, no. 4, pp. 493–504, 2010.
- [12] T. Song, L. Pan, and G. Páun, "Asynchronous spiking neural P systems with local synchronization," *Information Sciences*, vol. 219, pp. 197–207, 2013.
- [13] Y. Tang, Z. Wang, and J.-A. Fang, "Controller design for synchronization of an array of delayed neural networks using a controllable probabilistic PSO," *Information Sciences*, vol. 181, no. 20, pp. 4715–4732, 2011.
- [14] Z. L. Wan, T. L. Liao, Y. Y. Hou, and J. J. Yan, " H_∞ synchronization of switched chaotic systems and its applications to secure communications," *International Journal of Bifurcation and Chaos*, vol. 22, no. 3, Article ID 1250058, 2012.
- [15] Q. Wang, Q. Lu, and G. Chen, "Synchronization transition induced by synaptic delay in coupled fast-spiking neurons," *International Journal of Bifurcation and Chaos*, vol. 18, no. 4, pp. 1189–1198, 2008.
- [16] Z. Wang, J. Cao, Z. Duan, and X. Liu, "Synchronization of coupled Duffing-type oscillator dynamical networks," *Neurocomputing*, vol. 136, pp. 162–169, 2014.
- [17] C. Peng, J. Zhang, and Q.-L. Han, "Consensus of multiagent systems with nonlinear dynamics using an integrated sampled-data-based event-triggered communication scheme," *IEEE Transactions on Systems, Man, and Cybernetics: Systems*, vol. 49, no. 3, pp. 589–599, 2019.
- [18] C. Peng, M. Wu, X. Xie, and Y.-L. Wang, "Event-triggered predictive control for networked nonlinear systems with imperfect premise matching," *IEEE Transactions on Fuzzy Systems*, vol. 26, no. 5, pp. 2797–2806, 2018.
- [19] C. Peng and Q.-L. Han, "A novel event-triggered transmission scheme and L_2 control co-design for sampled-data control systems," *IEEE Transactions on Automatic Control*, vol. 58, no. 10, pp. 2620–2626, 2013.
- [20] M. Zhao, C. Peng, W. He, and Y. Song, "Event-triggered communication for leader-following consensus of second-order multiagent systems," *IEEE Transactions on Cybernetics*, vol. 48, no. 6, pp. 1888–1897, 2018.
- [21] C. Peng, J. C. Li, and M. R. Fei, "Resilient event-triggering H_∞ load frequency control for multi-area power systems with energy-limited DoS attacks," *IEEE Transactions on Power Systems*, vol. 32, no. 5, pp. 4110–4118, 2017.
- [22] F. W. Yang, Q.-L. Han, and Y. Liu, "Distributed H_∞ state estimation over a filtering network with time-varying and switching topology and partial information exchange," *IEEE Transactions on Cybernetics*, vol. 49, no. 3, pp. 8702–8882, 2019.
- [23] F. W. Yang, N. Xia, and Q. Han, "Event-based networked islanding detection for distributed solar PV generation systems," *IEEE Transactions on Industrial Informatics*, vol. 13, no. 1, pp. 322–329, 2017.
- [24] J. Chen, F. W. Yang, and Q. Han, "Model-free predictive H_∞ control for grid-connected solar power generation systems," *IEEE Transactions on Control Systems Technology*, vol. 22, no. 5, pp. 2039–2047, 2014.
- [25] F. W. Yang, Z. Wang, D. Ho, and M. Gani, "Robust H_∞ control with missing measurements and time delays," *IEEE Transactions on Automatic Control*, vol. 52, no. 9, pp. 1666–1672, 2007.
- [26] C. Volos, I. Kyprianidis, I. Stouboulos, and S. Vaidyanathan, "Design of a chaotic random bit generator using a Duffing-van der Pol system," *International Journal of System Dynamics Applications*, vol. 5, no. 3, pp. 94–111, 2016.
- [27] V. T. Pham, S. Jafari, X. Wang, and J. Ma, "A chaotic system with different shapes of equilibria," *International Journal of Bifurcation and Chaos*, vol. 26, no. 4, Article ID 1650069, 2016.
- [28] V. T. Pham, S. Jafari, and T. Kapitaniak, "Constructing a chaotic system with an infinite number of equilibrium points," *International Journal of Bifurcation and Chaos*, vol. 26, no. 13, article 1650225, 2016.
- [29] Y. F. Zeng, G. Shen, B. Chen, and J. Tang, "Team composition in PES2018 using submodular function optimization," *IEEE Access*, vol. 7, pp. 76194–76202, 2019.
- [30] Y. F. Zeng, B. Ma, B. Chen, J. Tang, and M. He, "Group sparse optimization for learning predictive state representations," *Information Sciences*, vol. 412–413, pp. 1–13, 2017.
- [31] Y. F. Zeng, X. Chen, Y. Ong, J. Tang, and Y. Xiang, "Structured memetic automation for online Human-like social behavior learning," *IEEE Transactions on Evolutionary Computation*, vol. 21, no. 1, pp. 102–115, 2017.
- [32] Q. K. Han, X. Y. Sun, X. Yang, and B. Wen, "External synchronization of a hysteretic system with a duffing system by

- feedback control strategy," *International Journal of Structural Stability and Dynamics*, vol. 9, no. 3, pp. 461–471, 2009.
- [33] B. A. Idowu, U. E. Vincent, and A. N. Njah, "Control and synchronization of chaos in nonlinear gyros via backstepping design," *International Journal of Nonlinear Sciences*, vol. 5, no. 1, pp. 11–19, 2008.
- [34] B. A. Idowu, U. E. Vincent, and A. N. Njah, "Generalized adaptive backstepping synchronization for non-identical parametrically excited systems," *Nonlinear Analysis: Modeling and Control*, vol. 14, no. 2, pp. 165–176, 2009.
- [35] U. E. Vincent, R. K. Odunaike, J. A. Laoye, and A. A. Gbindinnuola, "Adaptive backstepping control and synchronization of a modified and chaotic Van der Pol-Duffing oscillator," *Journal of Control Theory and Applications*, vol. 9, no. 2, pp. 273–277, 2011.
- [36] X. Wu, J. Cai, and M. Wang, "Global chaos synchronization of the parametrically excited Duffing oscillators by linear state error feedback control," *Chaos, Solitons & Fractals*, vol. 36, no. 1, pp. 121–128, 2008.
- [37] A. N. Njah and U. E. Vincent, "Chaos synchronization between single and double wells Duffing–Van der Pol oscillators using active control," *Chaos, Solitons & Fractals*, vol. 37, no. 5, pp. 1356–1361, 2008.
- [38] Y. Lei, K.-L. Yung, and Y. Xu, "Chaos synchronization and parameter estimation of single-degree-of-freedom oscillators via adaptive control," *Journal of Sound and Vibration*, vol. 329, no. 8, pp. 973–979, 2010.
- [39] X. R. Shi and Z. L. Wang, "Complete synchronization of delay hyperchaotic Lü system via a single linear input," *Nonlinear Dynamics*, vol. 69, no. 4, pp. 2245–2253, 2012.
- [40] Z.-L. Wang and X.-R. Shi, "Chaotic bursting lag synchronization of Hindmarsh–Rose system via a single controller," *Applied Mathematics and Computation*, vol. 215, no. 3, pp. 1091–1097, 2009.
- [41] E. Panteley and A. Loria, "Growth rate conditions for uniform asymptotic stability of cascaded time-varying systems," *Automatica*, vol. 37, no. 3, pp. 453–460, 2001.

Research Article

Chaotic Dynamics of an Airfoil with Higher-Order Plunge and Pitch Stiffnesses in Incompressible Flow

Karthikeyan Rajagopal , **Yesgat Admassu**, **Riessom Weldegiorgis**, **Prakash Duraisamy**, and **Anitha Karthikeyan**

Center for Nonlinear Dynamics, Institute of Research and Development, Defence University, Bishoftu, Ethiopia

Correspondence should be addressed to Karthikeyan Rajagopal; rkarthikeyan@gmail.com

Received 15 June 2019; Revised 14 September 2019; Accepted 1 October 2019; Published 30 October 2019

Guest Editor: Lazaros Moysis

Copyright © 2019 Karthikeyan Rajagopal et al. This is an open access article distributed under the Creative Commons Attribution License, which permits unrestricted use, distribution, and reproduction in any medium, provided the original work is properly cited.

Dynamical properties of a two-dimensional airfoil model with higher-order strong nonlinearities are investigated. Firstly, a state-space model is derived considering the plunge and pitch stiffnesses as generalized functions. Then, a stiffness function having square, cubic, and fifth-power nonlinearities is considered for both plunging and pitching stiffnesses, and the dimensionless state equations are derived. Various dynamical properties of the proposed model are investigated using equilibrium points, eigenvalues, and Lyapunov exponents. To further analyze the dynamical behavior of the system, bifurcation plots are derived. It is interesting to note that the new airfoil model with higher-order nonlinearities shows multistability with changing airspeed, and there are infinitely countable number of coexisting attractors generally called as megastability. Both multistability and megastability features of the airfoil model were not captured earlier in the literatures. To be clear, it is the first time a megastable feature is exposed in a physical system. Finally, to analyze the multifrequency effects of the airfoil model, we have presented the bicoherence plots.

1. Introduction

Many literatures have shown that the airfoil (aeroelastic) systems show more complex dynamical behaviors such as limit cycles and chaotic oscillations [1–4]. A persistent flutter in an aeroelastic structure such as an aircraft wing may create dangerous effects to the structure and may cause structural instability [1, 2]. Hence, controlling such unwanted and persistent oscillations has attracted importance among researchers [2–4]. A dynamical model of an airfoil system with cubic nonlinearity considered for the pitching stiffness was proposed in [5, 6], and it is shown that the system exhibits chaotic oscillations when the airspeed crosses a critical limit. A rigid wing supported by a nonlinear spring shows limit cycles as discussed in [7]. The authors investigated piecewise nonlinearities in aeroelastic systems, and the authors address continuous nonlinearities such as those

found in structural systems that exhibit spring hardening or softening effects.

A nonlinear active control method is adopted to control the limit cycle oscillations of an aeroelastic system with quasi-steady aerodynamic models [8, 9]. However, the results are limited to the elevation condition, and the real case should also be considered the actual vibration state and hence, the dynamic state must be set within an internal dynamic state when the nonlinear controller is designed [10]. In [11], a two-dimensional airfoil system with pitch and plunge stiffnesses using subsonic aerodynamics theory and classical nonlinearities, namely, cubic, freeplay, and hysteresis is investigated. Several cases of aerodynamic nonlinearities arising from transonic flow and dynamic stall are discussed, and numerical simulations are conducted. Poincaré mapping method and Floquet theory are adopted to analyze the limit cycle oscillation flutter and

chaotic motion of a two-dimensional airfoil system with combined freeplay and cubic pitch stiffnesses in supersonic and hypersonic flows [12]. It is shown that the Floquet theory can effectively predict the occurrence of limit cycles in the system.

In [13, 14], the aeroelastic airfoil system with freeplay is investigated and the transonic flow characteristics are discussed. The effect of hardening and nonlinearities on aeroelastic system is analyzed in [15]. The chaotic behavior and prediction of it with various methods and its robustness are presented in [16]. The comparative study reveals the effectiveness of Runge–Kutta method over other methods. A two-degree-of-freedom model of airfoil system is derived, and analysis is carried out to study the consequences of cubic nonlinearities [17]. Drastic changes are observed while the system entered to supersonic flow. Using precise integration method the nonlinear effect on airfoil system is simulated in [18]. The results show the presence of intricate behaviors of the system. The investigation on limit cycle oscillation and other aeroelastic responses is described in [19, 20] for system with freeplay in pitch. Challenges and complications during control and design of vibration absorber are discussed elaborately for the aeroelastic model with nonlinearities in [21, 22].

An airfoil model with multiple strong nonlinearities for both pitch and plunge stiffnesses was studied, and incremental harmonic balance method was used to analyze the periodic state of the airfoil flutter [26]. Similarly, to analyze such periodic oscillations in an airfoil system, Monte Carlo method was adopted in [27]. A nonlinear adaptive control technique is used to suppress the flutter and limit cycle oscillations assuming that one state is known and the other states are compensated [28]. A terminal sliding-mode control technique is used to suppress the limit cycle oscillations with an exclusive choice between the plunge displacement and the pitch angle [29]. Differential transformation method (DTM) to examine the nonlinear dynamic response of a typical aeroelastic system with cubic nonlinearities for pitch stiffness under realistic operating parameters was proposed in [30], and the dynamical properties are investigated with bifurcation plots and Lyapunov spectrum. A nonlinear sliding-mode controller was designed to suppress the chaotic oscillations of an airfoil system proposed in [10], and the stability of the controllers was derived using the Lyapunov stability theorem [31]. A nonlinear energy sink (NES) is used to suppress the aeroelasticity of an airfoil with a control surface considering the freeplay and cubic stiffnesses in pitch. The harmonic balance method is used to determine the limit cycle oscillations occurring in the airfoil-NES system [32].

In [29], the authors mentioned that a constant deterioration of wing structure influences on stiffness behavior, which demands higher-order nonlinearity in the dynamic model. In [33], influence of higher-order stiffness on aeroelastic model was discussed but no special properties are analyzed. Motivated by the above

discussions, we are interested in exploring the airfoil system considering both plunge and pitch stiffnesses to be higher-order nonlinearities. This paper reports some new complex behaviors of the airfoil system like multistability and megastability which have not been reported earlier in the literatures. The proposed investigation falls under category 1 and 2 as described in [34].

2. Two-Dimensional Airfoil System with Higher-Order Nonlinear Spring (ASHS)

2.1. Mathematical Model. The dynamical model of an airfoil with cubic pitching stiffness and viscous damping as shown in Figure 1 was proposed in [5, 6]. ρ is the air density, m is the mass, b is the semichord length, ab is the distance of the elastic axis E from the midchord point, $(0.5 + a)b$ is the distance of E from the aerodynamic focus F , $x_a b$ is the distance of the center of gravity from E , $r_a b$ is the radius of gyration of the airfoil with respect to E , and ω_h and ω_α are the eigenfrequencies of the constrained one-degree-of-freedom system associated with the linear plunging and the pitching springs, respectively. The parameter values are considered as follows: $a = -0.1$, $b = 1$ m, $x_a = 0.25$, $r_a^2 = 0.5$, $\omega_h = 28.1$ Hz, and $\omega_\alpha = 62.8$ Hz.

The bifurcation analysis of the proposed model [5, 6] was investigated using harmonic balance method. It is to be noted that the literatures have investigated the dynamical behavior of the airfoil system using cubic nonlinearity stiffness. Such approximations of the nonlinear stiffness have not been useful in identifying the more complex behavior of the system. Hence, we propose a modified dynamical equation of the airfoil system as

$$\begin{aligned} \ddot{h} + 0.25\ddot{\alpha} + 0.1\dot{h} + 0.2h + 0.1\beta\alpha + f(h) &= 0, \\ 0.25\ddot{h} + 0.5\ddot{\alpha} + 0.1\dot{\alpha} + 0.5\alpha - 0.04\beta\alpha + f(\alpha) &= 0, \end{aligned} \quad (1)$$

where $f(\alpha)$ is the pitching stiffness and $f(h)$ is the plunging stiffness. The state h represents the plunging displacement, and α represents the pitching angle. The parameter $\beta = (V/b\omega_\alpha)^2$, where V is the airspeed and ω_α is the eigenfrequency.

With higher-order nonlinear stiffness in an aeroelastic system, limit cycle oscillations occur, which leads to a fatigue in the wing structure as the consequence of a long-term vibration with constant amplitude at an invariant frequency [29]. In [35], the 5th order nonlinearity is introduced and its effects are analyzed; the authors observed that the resonant frequency is shifted toward higher frequency and the bandwidth of higher-order stiffness is wider for frequency up-sweeps. It is very clear that the 5th order nonlinearity increases the complexity, and its effects need to be studied.

In this paper, we consider higher-order pitching and plunging stiffnesses in order to investigate the complex behaviors which have not been reported earlier.

Using $x = \alpha$, $\dot{x} = y$, $z = h$, and $\dot{z} = w$, we derive the dimensionless model as

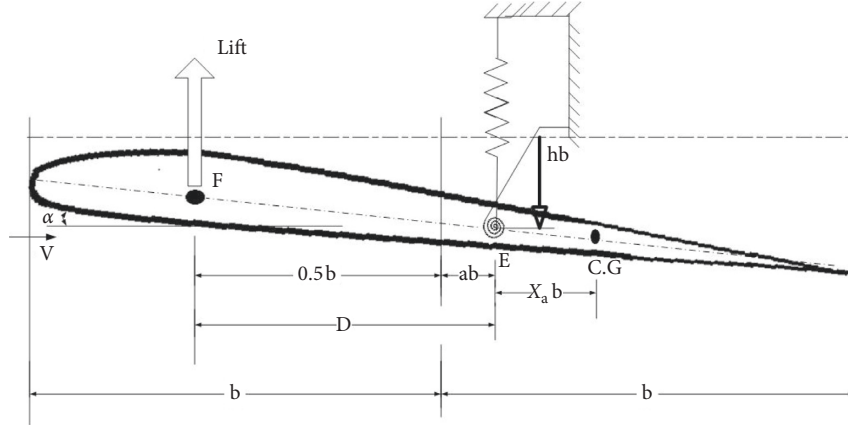


FIGURE 1: Two-degree-of-freedom airfoil model.

$$\begin{aligned} \frac{dx}{dt} &= y, \\ \frac{dy}{dt} &= \frac{1}{1.75} (4x(0.065\beta - 0.5) + 0.1w + 0.2z + f(z) \\ &\quad - 4f(x) - 0.4y), \\ \frac{dz}{dt} &= w, \\ \frac{dw}{dt} &= -\frac{1}{1.75} (x(0.24\beta - 0.5) + 0.2w + 0.4z + 2f(z) \\ &\quad - f(x) - 0.1y), \end{aligned} \quad (2)$$

where $f(z) = 5z^2 + 10z^3 + 40z^5$ and $f(x) = 5x^2 + 20x^3 + 40x^5$ are the higher-order stiffnesses. The parameter β is considered as the bifurcation parameter, and for a fixed value of the airspeed, $\beta = 7.5$, and for the initial conditions $[0.1, 0, 0.1, 0]$, the phase portraits of the system are shown in Figure 2.

2.2. Existence of Attractor. It has been proved in the literatures that nonlinear dissipative systems can produce chaotic attractors. Hence, to show that the ASHS is dissipative, we have computed the corresponding volume contraction rate V_c , using summation of Lyapunov exponents (i.e., $V_c = L.E_1 + L.E_2 + L.E_3 + L.E_4$), and thus, if $V_c < 0$, the system is dissipative, thus experiences or presents attractors. For $V_c = 0$, phase space volume is conserved and the dynamical system is conservative. If $V_c > 0$, the volume in phase space expands, and hence there exist only unstable cycles or possibly chaotic repellers.

For ASHS, $L.E_1 = 0.2014$, $L.E_2 = 0$, $L.E_3 = 0.1852$, and $L.E_4 = 0.1852$. It can be observed that $V_c = -0.169 < 0$ for all state vectors; thus, the introduced system is dissipative.

2.3. Stability of Equilibrium Points. In order to obtain the equilibrium of our model, let $\dot{x} = \dot{y} = \dot{z} = \dot{w} = 0$; then, the only real equilibrium point of ASHS is at the origin.

The Jacobian matrix of the ASHS system evaluated at any equilibrium is given by

$$J(X) = \begin{bmatrix} 0 & 1 & 0 & 0 \\ a_1 & a_2 & a_3 & a_4 \\ 0 & 0 & 0 & 1 \\ a_5 & a_6 & a_7 & a_8 \end{bmatrix}, \quad (3)$$

$$\begin{aligned} a_1 &= \frac{26\beta}{175} - \frac{160x}{7} - \frac{960x^2}{7} - \frac{3200x^4}{7} - \frac{8}{7}, \\ a_2 &= \frac{-8}{35}, \\ a_3 &= \frac{800z^4 + 120z^2 + 40z}{7} + \frac{4}{35}, \\ a_4 &= \frac{2}{35}, \\ a_5 &= \frac{800x^4 + 240x^2 + 40x}{7} - \frac{24\beta}{175} + \frac{2}{7}, \\ a_6 &= \frac{2}{35}, \\ a_7 &= -\frac{80z - 240z + (1600z^4)}{7} - \frac{8}{35}, \\ a_8 &= \frac{-4}{35}. \end{aligned}$$

The eigenvalues associated with the above Jacobian matrix are obtained by solving the following characteristic equation ($\det(M_J - \lambda I_d) = 0$), where I_d is the identity matrix:

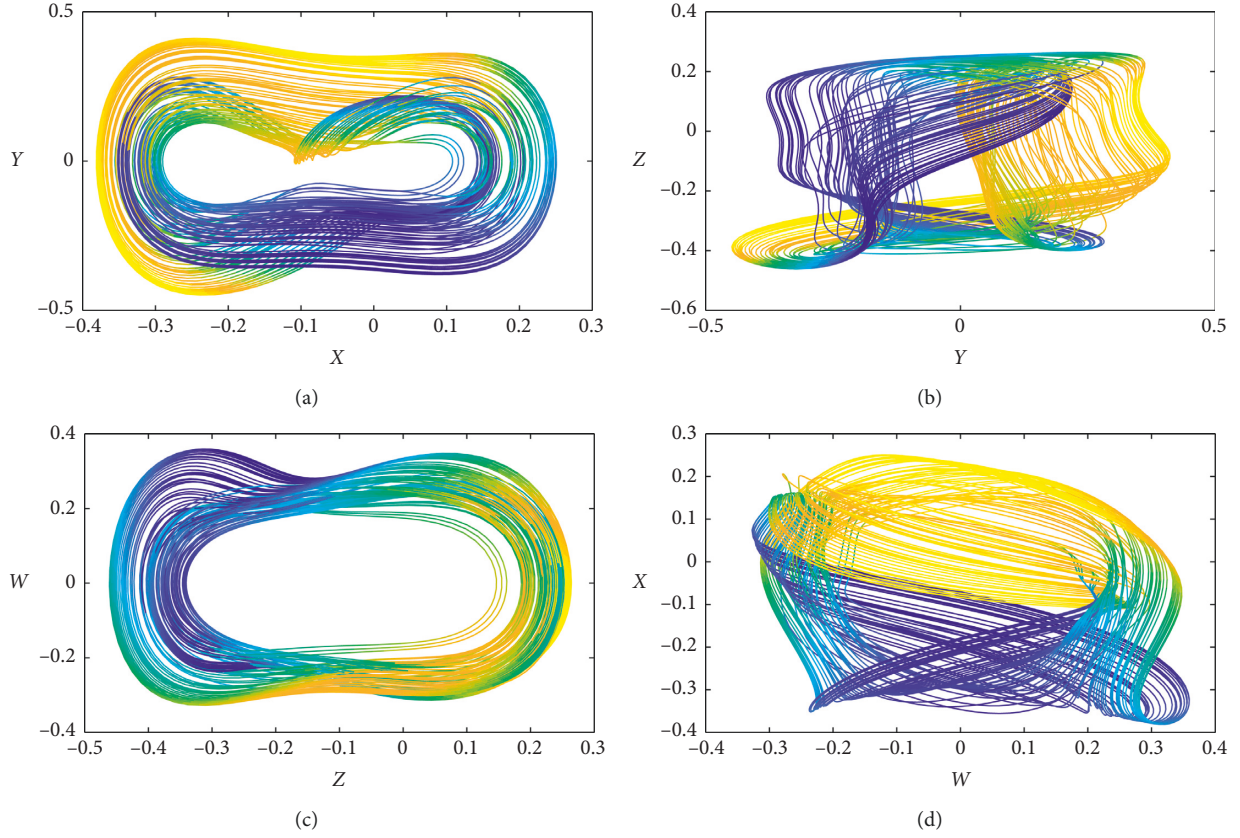


FIGURE 2: 2D phase portraits of the ASHS.

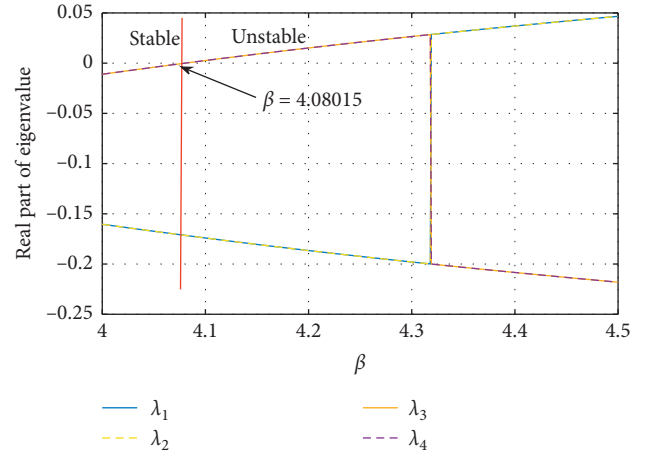
$$\lambda^4 + 0.342\lambda^3 + (1.39 - 0.148\beta)\lambda^2 + (0.16 - (9.14e - 3)\beta)\lambda - 0.0182\beta + 0.229 = 0. \quad (4)$$

Figure 3 shows the stability of the equilibrium point for various values of β . It is to be noted that the system shows unstable oscillations when the airspeed exceeds the critical divergent speed $\beta \geq 4.08015$ which agrees with the results described in [5].

From the Routh–Hurwitz stability criterion, the stability conditions of all the principal minors need to be positive for the ASHS system to be stable. The principal minors are as follows:

$$\begin{aligned} \Delta_1 &= \delta_1 > 0, \\ \Delta_2 &= \begin{vmatrix} \delta_1 & \delta_0 \\ \delta_3 & \delta_2 \end{vmatrix} > 0, \\ \Delta_3 &= \begin{vmatrix} \delta_1 & \delta_0 & 0 \\ \delta_3 & \delta_2 & \delta_1 \\ 0 & 0 & \delta_3 \end{vmatrix} > 0, \end{aligned} \quad (5)$$

that is, $\delta_1 > 0$, $\delta_1\delta_2 - \delta_3 > 0$, and $\delta_3 > 0$, where $\delta_1 = 0.342$, $\delta_2 = (1.39 - 0.148\beta)$, and $\delta_3 = 0.16 - (9.14e - 3)\beta$, where the conditions are satisfied; then, ASHS is stable, leading to the situation of point attractor; otherwise, the system is

FIGURE 3: Stability of the equilibrium point for various values of β .

unstable, and the model can experience periodic or chaotic oscillations.

3. Numerical Simulation

3.1. Bifurcation and Multistability. The bifurcation plots are derived and investigated to study the impact of the parameters on the system behavior. The parameter β is considered as the bifurcation parameter with the other parameters fixed at their respective chaotic values. The initial

condition for the first iteration is taken as $[0.1, 0, 0.1, 0]$. Multistability in physical systems is already discussed in the literatures [36, 37], and it is shown that such coexisting oscillations are dangerous and can affect the structural stability of a system.

To show the existence of multistability, we use a robust way to plot the bifurcation plots where the initial conditions are changed in every iteration to the end values of the state variables wherein the parameter is increased or decreased in tiny steps. It is to be noted that the airfoil system shows multistability as shown in Figure 4 which was not reported earlier in the literatures.

Figure 4 (blue) shows the forward continuation where the parameter β is increased from minimum to maximum, and Figure 4 (red) shows the backward continuation where the parameter β is decreased from maximum to minimum, and the local maxima of the state variables are plotted. The corresponding Lyapunov exponents (LEs) are calculated using Wolf's algorithm [38] for a finite time of 40,000 s. It should be noted that we used the same forward and backward continuation to generate the Lyapunov spectrum for β . Figures 5(a) and 5(b) show the LEs for forward and backward continuation.

The ASHS system takes a period-doubling route to chaos as shown in Figure 6. Also, we could see the period-doubling route to chaos for $\beta \geq 6$ and an inverse period-doubling exit from chaos for $4.7 \leq \beta \leq 5.3$. Such a phenomenon of period doubling and inverse period doubling occurring in a bifurcation diagram is termed as antimonotonicity [39].

Different two-dimensional projections of the ASHS attractor are presented in Figure 6. We can easily note that there is no linear dependency between the state variables of the ASHS and also such dependencies between state vectors can be nonlinear and can involve several of the variables.

From Figures 4 and 5, it is evident that the ASHS shows coexisting attractors. We have plotted the 2D phase portraits of the coexisting attractors for different values of initial conditions and parameter β . It can be seen that a period-1 limit cycle (red) coexists with a chaotic attractor (blue) (Figure 7).

3.2. Megastability. It was Sprott et al. who introduced the term "megastability" which is defined as the coexistence of a countable infinity of attractors in a system. He proposed a system which is a periodically-forced oscillator with a spatially-periodic damping term [40]. The system looks like a cross-sectioned cabbage with multiple layers of periodic, quasiperiodic, and chaotic attractors. A new oscillator with infinite coexisting asymmetric attractors with the megastability property was proposed in [41], in which the attractors are a combination of self-excited and hidden attractors. A two-dimensional chaotic oscillator producing a whirlpool of attractors was proposed in [42]. Similarly, Tang et al. proposed a chaotic system with coexisting attractors which forms a carpet-like structure [43]. To show the controllability of such megastable oscillators, the authors in [44] have proposed a fuzzy-based control algorithm to suppress chaotic oscillations. Most of these oscillators use a periodic forcing term and it was in [45], the forcing term was modified to a quasiperiodic function and was proved that the

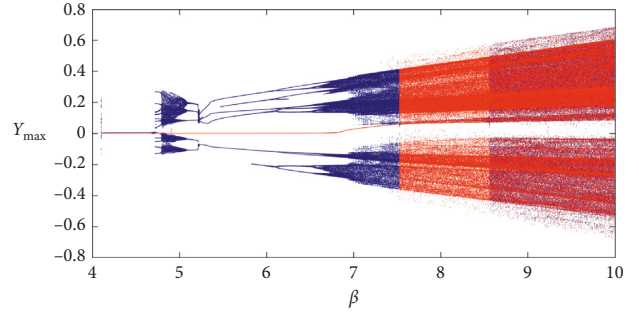


FIGURE 4: Maximum of ASHS with forward (red) and backward (blue) continuation.

quasiperiodic forcing can also produce megastable oscillators. It is to be noted that, in the entire literatures on megastable oscillators, there were no discussions on such megastability in a real physical system. The proposed ASHS model discussed in this paper shows such megastability as shown in Figure 8 for $\beta = 7$ and different initial conditions.

3.3. Bicoherence. Bispectral analysis or bicoherence is a powerful tool in signal processing which offers a way to analyze the nonlinear coupling between frequencies and helps us in areas where linear power spectral analysis provides insufficient information [46]. Bicoherence analysis was used to investigate the nonlinearities in the aeroelastic systems [47]. The nonlinear aspects of the aerodynamic loading are determined from estimates of higher-order spectral moments, namely, the auto- and cross-bispectrum through which the quadratic nonlinear interaction between two frequency components are calculated and are used to detect a quadratic coupling or interaction among different frequency components of a signal [47].

Bicoherence is the squared normalized version of bispectral density. Bicoherence gives a measure of phase coupling between signals at three different frequencies. Bicoherence is mostly used in fault diagnosis because of its ability to trace and analyze multifrequency components. It is most effective in analyzing systems with nonlinear coupling between frequencies and is useful in detecting and quantifying the presence of nonlinearity, thus indicating the severity of the fault in the machine [48, 49]. Bicoherence is also considered as a tool to analyze the coupling effects between states of a dynamical system at different frequencies [50–52].

The power spectrum of a discrete time series $x(n)$ is given by

$$P_{xx}(k) = E[x(k)x_*(k)], \quad (6)$$

where k is the discrete frequency variable. The bispectrum can be defined by

$$B_x(k, l) = E[x(k)x(l)x_*(k+l)]. \quad (7)$$

The bicoherence is the normalized bispectrum given by

$$b^2(k, l) = \frac{[E[x(k)x(l)x_*(k+l)]]^2}{E[x(k)x(l)]^2 E[x(k+l)]^2}. \quad (8)$$

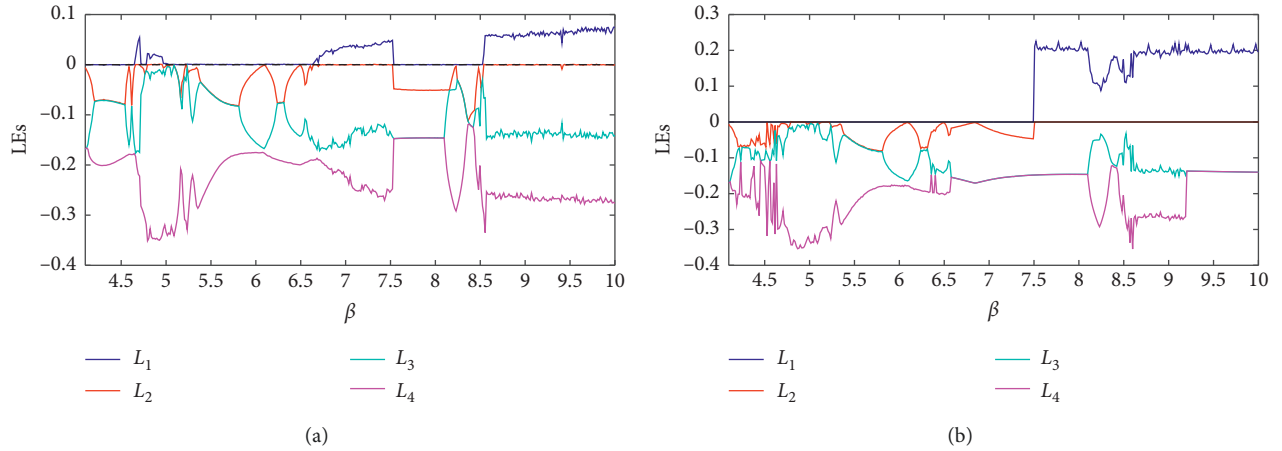


FIGURE 5: Lyapunov exponents for (a) forward continuation and (b) backward continuation.

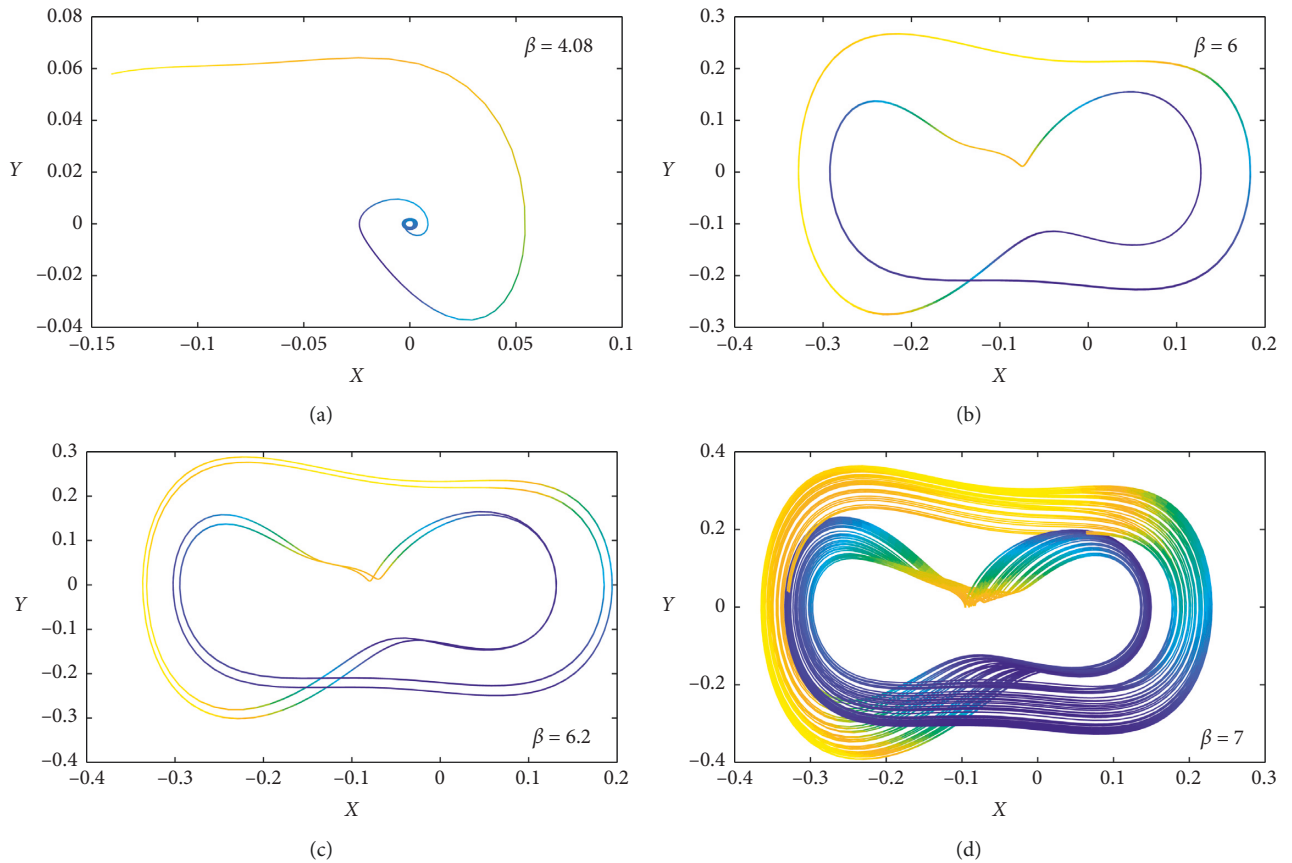


FIGURE 6: Phase portraits in the X - Y plane for various values of β : (a) point attractor; (b) period-1 limit cycle; (c) period-2 limit cycle; (d) chaotic attractor.

The cross bicoherence can be calculated by using the following definition:

$$b_{xy}^2(k, l) = \frac{[E[x(k)x(l)y_*(k+l)]]^2}{E[x(k)x(l)]^2 E[y(k+l)]^2}. \quad (9)$$

The bicoherence at any frequency pair $k+l$ can be interpreted as the fraction of power at frequency $k+l$ which is phase coupled to the component at $k+l$. We have

used the Welch periodogram method to estimate the bispectrum of the airfoil system (ASHS) and then the bicoherence, but the lengths of data required to obtain consistent estimates are longer than those required for power spectrum estimation; hence, we sampled the time series data generated from the ASHS state equations at 1 KHz and have used 30,000 samples for the bicoherence analysis.

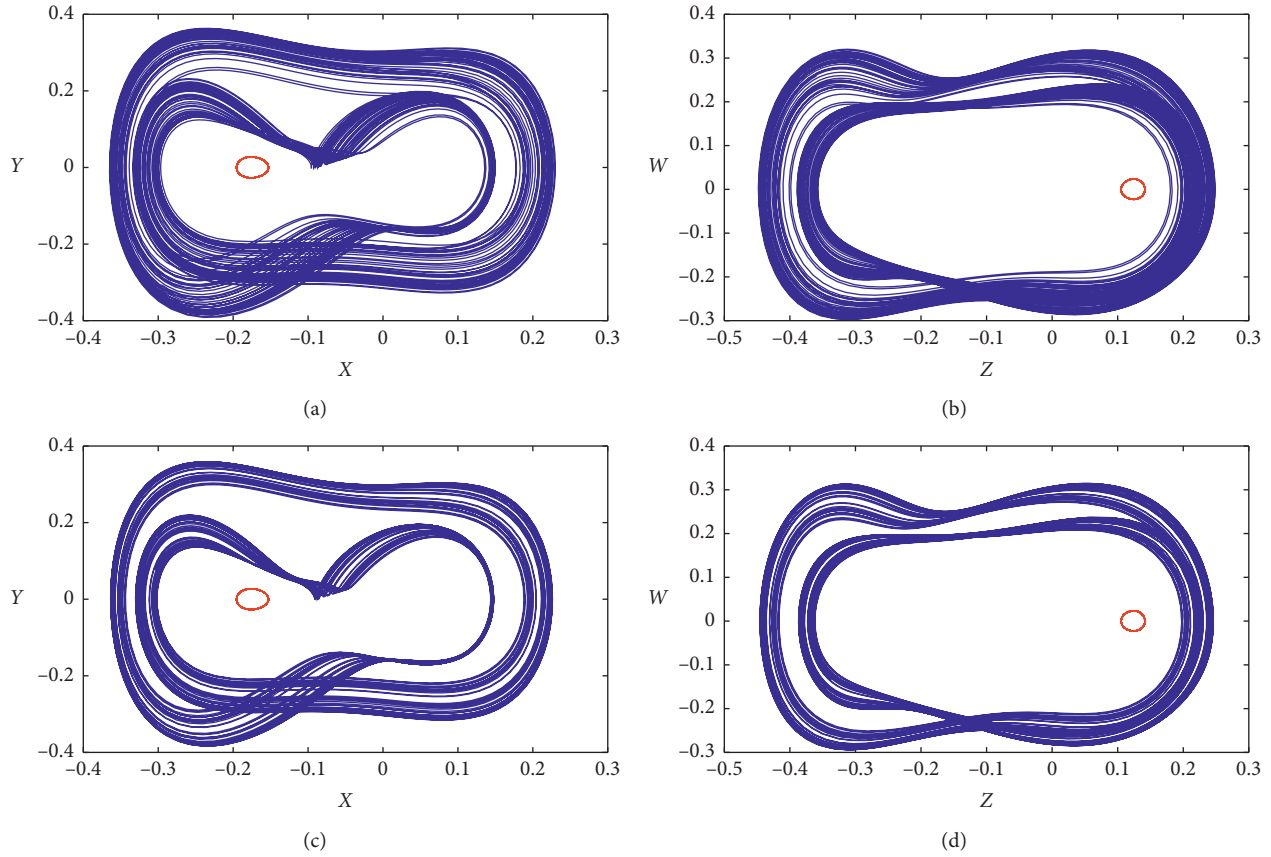


FIGURE 7: Coexisting attractors for different values of β : for $\beta=5$ and initial conditions for (a, b) blue $[-0.012, -0.055, 0.009, -0.125]$; red $[-0.13, 0, 0.09, 0]$; for $\beta=7$ and initial conditions for (c, d) blue $[-0.09, 0.003, 0.13, 0.22]$; red $[-0.17, 0.02, 0.13, -0.02]$.

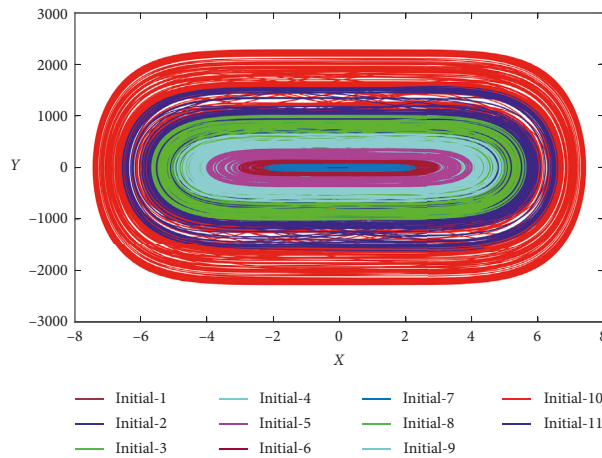


FIGURE 8: Multiple coexisting attractors for $\beta=7$ with different initial conditions $[P, 0, 0.1, 0]$ where P takes the values of $[0.5, 1, 2, 3, 4, 5, 6, 7, 8, 9, 10]$ for initial-1 to initial-11, respectively.

We have presented the bicoherence plots of the ASHS for different values of the parameter β as shown in Figure 9. We could see that the coupling between states are much weaker for $\beta = 4.1$ but becomes stronger (yellow spots) for $\beta = 4.6$ and $\beta = 5$ and forms multiple islands of small bandwidths for $\beta = 7$ indicating the strength of the coupling effects of the frequencies. We have used a fixed initial condition of

$[0.1, 0, 0.1, 0]$. The bicoherence spectrum of surface elevations at the first measured location (Figure 9) far from the focal location indicates that many wave modes were involved in the wave-wave interactions. The bicoherence ($\beta = 5$) at $b^2(0.16, 0.16) = 1.4$ denotes a self wave-wave interactions, while $b^2(0.16, 0.12) = 1.4$ denotes a nonlinear coupling between two different frequencies.

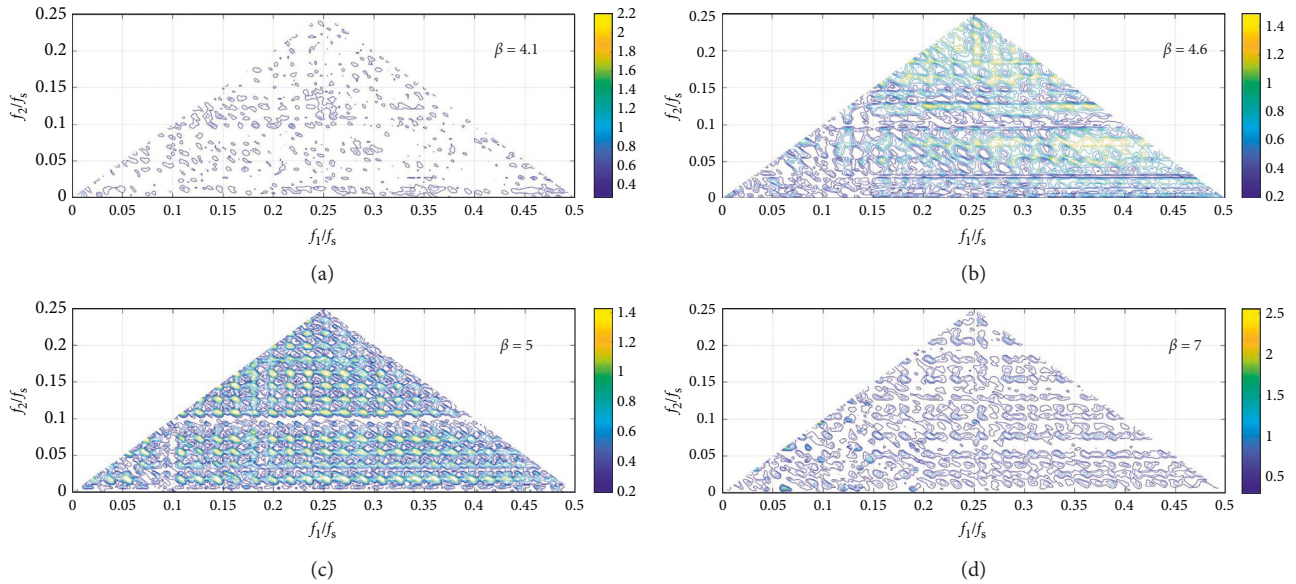


FIGURE 9: Bicoherence plots of the ASHS.

4. Conclusion

We have modified the dynamics of the well-known airfoil system by introducing higher-order nonlinearity in plunging and pitching stiffnesses. Chaotic motions exist in an airfoil system when the airspeed exceeds the critical divergent speed. The dynamical analysis of the proposed model shows unique characters of multistability and infinitely coexisting attractors known as megastability. Such features of an airfoil system were not captured earlier in the literatures. Bicoherence plots are investigated to know the impact of multifrequency terms and coupled nonlinearities on the system.

Data Availability

All the numerical simulation parameters are mentioned in the respective text part, and there are no additional data requirements for the simulation results.

Conflicts of Interest

The authors declare that they have no conflicts of interest.

References

- [1] J. J. Block and T. W. Strganac, "Applied active control for a nonlinear aeroelastic structure," *Journal of Guidance, Control, and Dynamics*, vol. 21, no. 6, pp. 838–845, 1998.
- [2] K. Palaniappan, P. Sahu, J. J. Alonso, and A. Jameson, "Design of adjoint based laws for wing flutter control," in *Proceedings of the 47th AIAA Aerospace Sciences Meeting and Exhibit*, Orlando, Florida, January 2009.
- [3] V. V. Golubev, B. D. Dreyer, T. M. Hollenshade, and M. Visbal, "High-accuracy viscous simulations of gust-airfoil nonlinear aeroelastic interaction," in *Proceedings of the 39th AIAA Fluid Dynamics Conference*, San Antonio, TX, USA, June 2009.
- [4] M. L. Tharayil and A. G. Alleyne, "Modeling and control for smart mesoflap aeroelastic controlflap aeroelastic control," *IEEE/ASME Transactions on Mechatronics*, vol. 9, no. 1, pp. 30–39, 2004.
- [5] L. C. Zhao and Z. C. Yang, "Chaotic motions of an airfoil with non-linear stiffness in incompressible flow," *Journal of Sound and Vibration*, vol. 138, no. 2, pp. 245–254, 1990.
- [6] J.-K. Liu and L.-C. Zhao, "Bifurcation analysis of airfoils in incompressible flow," *Journal of Sound and Vibration*, vol. 154, no. 1, pp. 117–124, 1992.
- [7] T. O'Neill and T. W. Strganac, "Aero elastic response of a rigid wing supported by nonlinear spring," *Journal of Aircraft*, vol. 35, no. 4, pp. 616–622, 1998.
- [8] Y. C. Fung, *An Introduction to the Theory of Aeroelasticity*, Wiley, New York, NY, USA, 1955.
- [9] T. Theodorsen and I. E. Garrick, "Mechanism of flutter: a theoretical and experiment investigation of the flutter problem," Report No. 685, NACA, Boston, MA, USA, 1940.
- [10] T. W. Strganac, J. Ko, and D. E. Thompson, "Identification and control of limit cycle oscillations in aeroelastic systems," *Journal of Guidance, Control, and Dynamics*, vol. 23, no. 6, pp. 1127–1133, 2000.
- [11] B. H. K. Lee, S. J. Price, and Y. S. Wong, "Nonlinear aeroelastic analysis of airfoils: bifurcation and chaos," *Progress in Aerospace Sciences*, vol. 35, no. 3, pp. 205–334, 1999.
- [12] D.-M. Zhao and Qi-C. Zhang, "Bifurcation and chaos analysis for aeroelastic airfoil with freeplay structural nonlinearity in pitch," *Chinese Physics B*, vol. 19, no. 3, Article ID 030518, 2010.
- [13] Z. Yang, S. He, and Y. Gu, "Transonic limit cycle oscillation behavior of an aeroelastic airfoil with free-play," *Journal of Fluids and Structures*, vol. 66, pp. 1–18, 2016.
- [14] S. He, Z. Yang, and Y. Gu, "Nonlinear dynamics of an aeroelastic airfoil with free-play in transonic flow," *Nonlinear Dynamics*, vol. 87, no. 4, pp. 2099–2125, 2017.
- [15] D. A. Pereira, R. M. G. Vasconcelos, M. R. Hajj, and F. D. Marques, "Effects of combined hardening and free-play nonlinearities on the response of a typical aeroelastic section," *Aerospace Science and Technology*, vol. 50, pp. 44–54, 2016.

- [16] H. Dai, X. Yue, J. Yuan, D. Xie, and S. N. Atluri, "A comparison of classical Runge-Kutta and Henon's methods for capturing chaos and chaotic transients in an aeroelastic system with freeplay nonlinearity," *Nonlinear Dynamics*, vol. 81, no. 1-2, pp. 169-188, 2015.
- [17] H.-l. Guo and Y.-s. Chen, "Dynamic analysis of two-degree-of-freedom airfoil with freeplay and cubic nonlinearities in supersonic flow," *Applied Mathematics and Mechanics*, vol. 33, no. 1, pp. 1-14, 2012.
- [18] J. T. Gordon, E. E. Meyer, and R. L. Minogue, "Nonlinear stability analysis of control surface flutter with freeplay effects," *Journal of Aircraft*, vol. 45, no. 6, pp. 1904-1916, 2008.
- [19] D. Zhao, Q. Zhang, and Y. Tan, "Random flutter of a 2-DOF nonlinear airfoil in pitch and plunge with freeplay in pitch," *Nonlinear Dynamics*, vol. 58, no. 4, pp. 643-654, 2009.
- [20] C. C. Cui, J. K. Liu, and Y. M. Chen, "Simulating nonlinear aeroelastic responses of an airfoil with freeplay based on precise integration method," *Communications in Nonlinear Science and Numerical Simulation*, vol. 22, no. 1-3, pp. 933-942, 2015.
- [21] W. J. Al-Mashhadani, E. H. Dowell, H. R. Wasmi, and A. A. Al-Asadi, "Aeroelastic response and limit cycle oscillations for wing-flap-tab section with freeplay in tab," *Journal of Fluids and Structures*, vol. 68, pp. 403-422, 2017.
- [22] E. Verstraelen, G. Dimitriadis, G. D. B. Rossetto, and E. H. Dowell, "Two-domain and three-domain limit cycles in a typical aeroelastic system with freeplay in pitch," *Journal of Fluids and Structures*, vol. 69, pp. 89-107, 2017.
- [23] N. Ebrahimzade, M. Dardel, and R. Shafaghat, "Performance comparison of linear and nonlinear vibration absorbers in aeroelastic characteristics of a wing model," *Nonlinear Dynamics*, vol. 86, no. 2, pp. 1075-1094, 2016.
- [24] Y. Bichiou, M. R. Hajj, and A. H. Nayfeh, "Effectiveness of a nonlinear energy sink in the control of an aeroelastic system," *Nonlinear Dynamics*, vol. 86, no. 4, pp. 2161-2177, 2016.
- [25] F. Chen, L. Zhou, and Y. Chen, "Bifurcation and chaos of an airfoil with cubic nonlinearity in incompressible flow," *Science China Technological Sciences*, vol. 54, no. 8, pp. 1954-1965, 2011.
- [26] M. Cai, J.-k. Liu, and J. Li, "Incremental harmonic balance method for airfoil flutter with multiple strong nonlinearities," *Applied Mathematics and Mechanics*, vol. 27, no. 7, pp. 953-958, 2006.
- [27] D. Poirer and S. J. Price, "Bifurcation characteristics of a two-dimensional structurally non-linear airfoil in turbulent flow," *Nonlinear Dynamics*, vol. 48, no. 4, pp. 423-435, 2007.
- [28] A. Behal, P. Marzocca, V. M. Rao et al., "Nonlinear adaptive control of an aeroelastic two-dimensional lifting surface," *Journal of Guidance, Control, and Dynamics*, vol. 29, no. 2, pp. 382-390, 2006.
- [29] C.-C. Wang, C.-L. Chen, and H.-T. Yau, "Terminal sliding mode control for aeroelastic systems," *Nonlinear Dynamics*, vol. 70, no. 3, pp. 2015-2026, 2012.
- [30] C.-C. Wang, C.-L. Chen, and H.-T. Yau, "Bifurcation and chaotic analysis of aeroelastic systems," *Journal of Computational and Nonlinear Dynamics*, vol. 9, no. 2, Article ID 021004, 2013.
- [31] X.-z. Xu, W.-x. Wu, and W.-g. Zhang, "Sliding mode control for a nonlinear aeroelastic system through backstepping," *Journal of Aerospace Engineering*, vol. 31, no. 1, Article ID 04017080, 2018.
- [32] H. Guo, S. Cao, T. Yang, and Y. Chen, "Aeroelastic suppression of an airfoil with control surface using nonlinear energy sink," *Nonlinear Dynamics*, vol. 94, no. 2, pp. 857-872, 2018.
- [33] P. S. Beran, C. L. Pettit, and D. R. Millman, "Uncertainty quantification of limit-cycle oscillations," *Journal of Computational Physics*, vol. 217, no. 1, pp. 217-247, 2006.
- [34] J. C. Sprott, "A proposed standard for the publication of new chaotic systems," *International Journal of Bifurcation and Chaos*, vol. 21, no. 9, pp. 2391-2394, 2011.
- [35] Y. C. Kim and E. J. Powers, "Digital bispectral analysis and its applications to nonlinear wave interactions," *IEEE Transactions on Plasma Science*, vol. 7, no. 2, pp. 120-131, 1979.
- [36] K. Rajagopal, A. Karthikeyan, P. Duraisamy, and R. Weldegiorgis, "Bifurcation and chaos in integer and fractional order two-degree-of-freedom shape memory alloy oscillators," *Complexity*, vol. 2018, Article ID 8365845, 9 pages, 2018.
- [37] K. Rajagopal, D. Prakash, R. Weldegiorgis, and A. Karthikeyan, "Multistability in horizontal platform system with and without time delays," *Shock and Vibration*, vol. 2018, Article ID 1092812, 8 pages, 2018.
- [38] A. Wolf, J. B. Swift, H. L. Swinney, and J. A. Vastano, "Determining Lyapunov exponents from a time series," *Physica D: Nonlinear Phenomena*, vol. 16, no. 3, pp. 285-317, 1985.
- [39] S. P. Dawson, C. Grebogi, J. A. Yorke, I. Kan, and H. Koçak, "Antimonotonicity: inevitable reversals of period-doubling cascades," *Physics Letters A*, vol. 162, no. 3, pp. 249-254, 1992.
- [40] J. C. Sprott, S. Jafari, A. J. M. Khalaf, and T. Kapitaniak, "Megastability: coexistence of a countable infinity of nested attractors in a periodically-forced oscillator with spatially-periodic damping," *The European Physical Journal Special Topics*, vol. 226, no. 9, pp. 1979-1985, 2017.
- [41] Z. Wang, H. R. Abdolmohammadi, F. E. Alsaadi, T. Hayat, and V.-T. Pham, "A new oscillator with infinite coexisting asymmetric attractors," *Chaos, Solitons & Fractals*, vol. 110, pp. 252-258, 2018.
- [42] Y.-X. Tang, A. J. M. Khalaf, K. Rajagopal, V.-T. Pham, S. Jafari, and Y. Tian, "A new nonlinear oscillator with infinite number of coexisting hidden and self-excited attractors," *Chinese Physics B*, vol. 27, no. 4, Article ID 040502, 2018.
- [43] Y. Tang, H. R. Abdolmohammadi, A. J. M. Khalaf, Y. Tian, and T. Kapitaniak, "Carpet oscillator: a new megastable nonlinear oscillator with infinite islands of self-excited and hidden attractors," *Pramana*, vol. 91, no. 1, p. 11, 2018.
- [44] H. Jahanshahi, K. Rajagopal, A. Akgul, N. N. Sari, H. Namazi, and S. Jafari, "Complete analysis and engineering applications of a megastable nonlinear oscillator," *International Journal of Non-Linear Mechanics*, vol. 107, pp. 126-136, 2018.
- [45] P. Prakash, K. Rajagopal, J. P. Singh, and B. K. Roy, "Megastability in a quasi-periodically forced system exhibiting multistability quasi-periodic behavior, and its analogue circuit simulation," *AEU-International Journal of Electronics and Communications*, vol. 92, pp. 111-115, 2018.
- [46] J. W. A. Fackrell, P. R. White, J. K. Hammond, R. J. Pinnington, and A. T. Parsons, "The interpretation of the bispectra of vibration signals—: I. Theory," *Mechanical Systems and Signal Processing*, vol. 9, no. 3, pp. 257-266, 1995.
- [47] W. Silva, "Identification of nonlinear aeroelastic systems based on the volterra theory: progress and opportunities," *Nonlinear Dynamics*, vol. 39, no. 1-2, pp. 25-62, 2005.
- [48] E. B. Halim, S. L. Shah, M. A. A. S. Choudhury, and R. Kadali, "Application of bicoherence analysis on vibration data for condition based monitoring of rotating machinery," *IFAC Proceedings Volumes*, vol. 41, no. 2, pp. 4517-4522, 2018.

- [49] E. B. Halim, M. A. A. S. Choudhury, S. L. Shah, and M. J. Zuo, "Fault detection of rotating machinery from bicoherence analysis of vibration data," *IFAC Proceedings Volumes*, vol. 39, no. 13, pp. 1348–1353, 2006.
- [50] K. Rajagopal, G. Laarem, A. Karthikeyan, A. Srinivasan, and G. Adam, "Fractional order memristor no equilibrium chaotic system with its adaptive sliding mode synchronization and genetically optimized fractional order PID synchronization," *Complexity*, vol. 2017, Article ID 1892618, 19 pages, 2017.
- [51] K. Rajagopal, A. Karthikeyan, and A. K. Srinivasan, "FPGA implementation of novel fractional order chaotic systems with two equilibriums and no equilibrium and its adaptive sliding mode synchronization," *Nonlinear Dynamics and Chaos in Engineering systems*, Springer, vol. 87, no. 4, pp. 2281–2304, 2017.
- [52] K. Rajagopal, L. Guessas, S. Vaidyanathan, A. Karthikeyan, and A. Srinivasan, "Dynamical analysis and FPGA implementation of a novel hyperchaotic system and its synchronization using adaptive sliding mode control and genetically optimized PID control," *Mathematical Problems in Engineering*, vol. 2017, no. 1, Article ID 7307452, 14 pages, 2017.

Research Article

A New 4D Chaotic System with Two-Wing, Four-Wing, and Coexisting Attractors and Its Circuit Simulation

Lilian Huang , Zefeng Zhang, Jianhong Xiang, and Shiming Wang

College of Information and Communication Engineering, Harbin Engineering University, Harbin 150001, China

Correspondence should be addressed to Lilian Huang; lilian_huang@163.com

Received 16 July 2019; Revised 9 September 2019; Accepted 19 September 2019; Published 29 October 2019

Guest Editor: Serdar Çiçek

Copyright © 2019 Lilian Huang et al. This is an open access article distributed under the Creative Commons Attribution License, which permits unrestricted use, distribution, and reproduction in any medium, provided the original work is properly cited.

In order to further improve the complexity of chaotic system, a new four-dimensional chaotic system is constructed based on Sprott B chaotic system. By analyzing the system's phase diagrams, symmetry, equilibrium points, and Lyapunov exponents, it is found that the system can generate not only both two-wing and four-wing attractors but also the attractors with symmetrical coexistence, and the dynamic characteristics of the new system constructed are more abundant. In addition, the system is simulated by Multisim software, and the simulation results show that the results of circuit simulation and numerical simulation analysis are basically the same.

1. Introduction

Chaos is a complex, apparently random, and often surprising behavior in simple nonlinear dynamical systems [1]. Chaos, as a unique form of motion in nonlinear dynamic systems, is widely used in electronic engineering [2], information engineering [3], and other fields [4–6] because of its initial value sensitivity, boundedness, and inherent randomness [7]. In 1963, American meteorologist Lorenz put forward the first chaotic system model [8], which attracted wide attention of the scientific community, and then, new chaotic systems were constantly discovered. In 1976, Rössler proposed a new system named Rössler chaotic system [9], which had a different topology from Lorenz system. Chua proposed Chua's circuit in 1986 [10, 11], which was one of the simplest chaotic oscillation circuits. In 1994, Sprott constructed several different simple chaotic systems [12]. In 1999, Chen and Ueta . discovered the Chen system while studying the anticontrol of chaos [13]. In 2002, Lü et al. proposed a kind of transition system named Lü system which connected Lorenz and Chen systems [14]. In 2003, Liu and Chen constructed the first four-wing butterfly chaotic attractor [15], which attracted many researchers' attention. To improve the security of chaotic secure communication and chaotic information encryption, more and more

researchers began to find chaotic systems with more complex dynamic behaviors [16–21].

In recent years, coexisting attractors had gradually become a research hotspot [22–24]. Compared with general chaotic attractors, the dynamic behaviors of coexisting attractors are more complex. In order to improve the security of information and reduce the possibility of information being decoded, coexisting attractors are more and more used in the field of encryption [25, 26]. In 2013, Li and Sprott proposed a multistable system with coexisting attractors [27] and found that the dynamic of the equilibrium points of the system depended on its stability and system structure. In 2014, Li and Sprott discovered a coexisting hidden attractor on a simple 4D Lorenz system [28], which had a large parameter region on a quasiperiodic torus. In 2017, Lai et al. proposed a unique 4D autonomous system with a signum function term [29], which can generate various types of coexisting attractors. In 2019, Zhou et al. proposed a chaotic system with multiple asymmetric coexisting attractors [30] and carried out circuit simulation and pulse synchronization research.

In this paper, a new 4D chaotic system based on Sprott B system is proposed. It includes the following elements: (i) It contains eight terms, including three nonlinear terms and one constant term. (ii) It is symmetric about the z -axis.

(iii) It can produce two-wing and four-wing attractors at the same time. (iv) It can also produce symmetric coexisting attractors. (v) The realization of the system circuit in physics is verified by the circuit simulation software, which is favorable for future engineering applications. This paper is organized as follows: In Section 2, a new chaotic system is proposed, and the coexistence of two-wing and four-wing attractors is observed through phase diagrams. In Section 3, we analyze its dynamic behaviors by symmetry, equilibrium points, bifurcation diagrams, Lyapunov exponents, and trajectory diagrams and introduce its symmetric coexisting attractors. An electronic circuit is designed in Section 4, and the correctness of the theoretical analysis is verified by circuit simulation experiment. Finally, the conclusion of this paper is given in Section 5.

2. A New Four-Dimensional Chaotic System

In this section, we mainly design the new chaotic system, and the new system proposed in this paper is described as follows:

$$\begin{cases} \dot{x} = a(y - x), \\ \dot{y} = xz + w, \\ \dot{z} = b - xy, \\ \dot{w} = yz - cw, \end{cases} \quad (1)$$

where positive real numbers a , b , and c are system parameters and x , y , z , and w are state variables. The new system (1) adds a state-feedback controller on the Sprott B chaotic system. Set $a = 6$, $b = 11$, and $c = 5$; the chaotic system can be generated. By calculation, the Lyapunov exponents are $LE_1 = 0.5162$, $LE_2 = -0.0001$, $LE_3 = -4.9208$, and $LE_4 = -6.5954$. The corresponding Lyapunov exponential dimension is as follows:

$$\begin{aligned} D_L &= j + \frac{1}{|LE_{j+1}|} \sum_{i=1}^j LE_i \\ &= 3 + \frac{LE_1 + LE_2 + LE_3}{|LE_4|} \\ &= 3 + \frac{0.5162 - 0.0001 - 4.9208}{|-6.5954|} \\ &= 2.3322. \end{aligned} \quad (2)$$

Therefore, the attractor of the new system is a strange attractor with fractal dimension. Select the initial value $(x, y, z, w) = (10, 10, 0, 0)$. Through numerical simulation, we can get the chaotic attractors of system (1) as shown in Figure 1. As can be seen from Figure 1, system (1) presents two-wing butterfly chaotic attractors in the $x - y$, $x - z$, $y - z$, and $z - w$ phase planes. The four-wing butterfly chaotic attractors appear in the $x - w$ and $y - w$ phase planes. This coexistence can be better observed in Figures 1(g)–1(h). It can be concluded that system (1) can generate chaotic butterfly attractors of two-wing and four-wing at the same time.

3. Some Basic Properties of New System

3.1. Symmetric and Dissipative Properties. The Sprott B system is symmetric about the z -axis, and system (1) is also symmetric about the z -axis. A simple proof is shown in the following equation:

$$\begin{cases} \dot{x} = a(y - x) \\ \dot{y} = xz + w \\ \dot{z} = b - xy \\ \dot{w} = yz - cw \end{cases} \iff \begin{cases} -\dot{x} = a(-y - (-x)) = -a(y - x), \\ -\dot{y} = (-x)z + (-w) = -xz - w, \\ \dot{z} = b - (-x)(-y) = b - xy, \\ -\dot{w} = (-y)z - c(-w) = -yz + cw. \end{cases} \quad (3)$$

The state space of system (1) is four-dimensional, so the vector field of system (1) is defined as follows:

$$f[X] = \begin{bmatrix} f_1(X) \\ f_2(X) \\ f_3(X) \\ f_4(X) \end{bmatrix} = \begin{bmatrix} ay - ax \\ xz + w \\ b - xy \\ yz - cw \end{bmatrix}. \quad (4)$$

The divergence of system (1) is obtained from the vector field as follows:

$$\nabla V = \frac{\partial f_1}{\partial x} + \frac{\partial f_2}{\partial y} + \frac{\partial f_3}{\partial z} + \frac{\partial f_4}{\partial w} = -(a + c). \quad (5)$$

According to equation (5), as long as $(a + c) > 0$, system (1) is dissipative, and the system converges in exponential form $dV/dt = e^{-(a+c)t}$. As $t \rightarrow \infty$, all trajectories of the system will eventually be restricted to a set with a volume of zero, and the extreme motion will converge to an attractor, thus proving the existence of the attractors of the system.

3.2. Equilibria and Stability. In order to obtain the equilibrium points of system (1), let the right side of the equation be equal to zero. The system of equations is as follows:

$$\begin{cases} a(y - x) = 0, \\ xz + w = 0, \\ b - xy = 0, \\ yz - cw = 0. \end{cases} \quad (6)$$

By calculation, we get that the two equilibrium points of system (1) are $S_1 = (\sqrt{b}, \sqrt{b}, 0, 0)$ and $S_2 = (-\sqrt{b}, -\sqrt{b}, 0, 0)$. System (1) has the same characteristic equation at $S_{1,2}$:

$$\lambda^4 + (a + c)\lambda^3 + (b + ac)\lambda^2 + (2ab + bc + b)\lambda + 2abc + 2ab = 0. \quad (7)$$

According to the classical Routh–Hurwitz stability criterion, if $a > 0$, $b > 0$, and $c > 0$, the equilibrium points $S_{1,2}$ is unstable.

Let $a = 6$, $b = 11$, and $c = 5$, we can get the equilibrium points $S_1 = (\sqrt{11}, \sqrt{11}, 0, 0)$ and $S_2 = (-\sqrt{11}, -\sqrt{11}, 0, 0)$. For the first equilibrium point $S_1 = (\sqrt{11}, \sqrt{11}, 0, 0)$, system (1) is linearized to Jacobian matrix as follows:

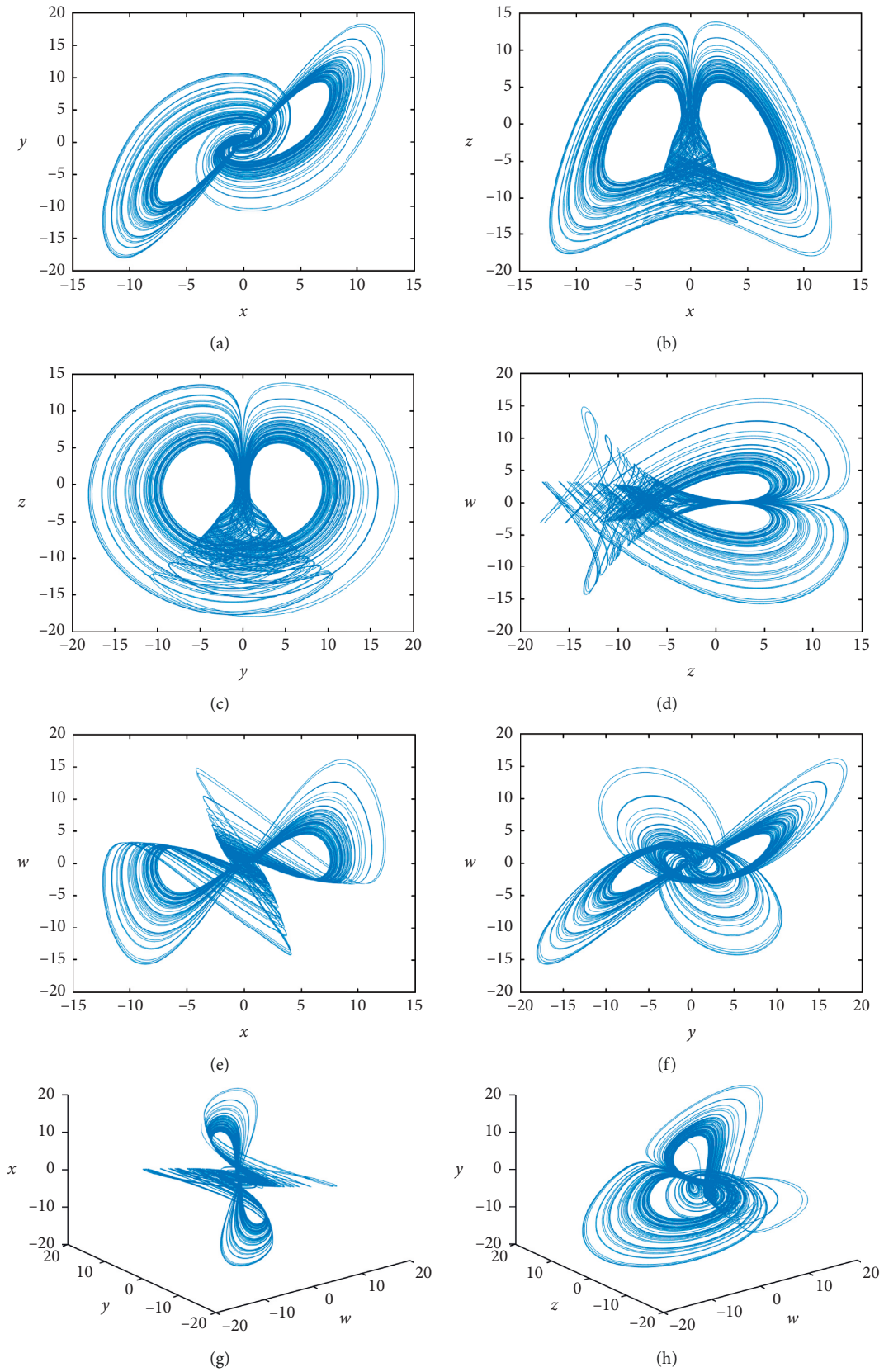


FIGURE 1: The two-wing butterfly chaotic attractors of system (1): (a) $x - y$, (b) $x - z$, (c) $y - z$, and (d) $z - w$. The four-wing butterfly chaotic attractors of system (1): (e) $x - w$ and (f) $y - w$. The coexisting chaotic attractors of system (1): (g) $x - y - w$ and (h) $y - z - w$.

$$J_1 = \begin{bmatrix} -a & a & 0 & 0 \\ z & 0 & x & 1 \\ -y & -x & 0 & 0 \\ 0 & z & y & -c \end{bmatrix} = \begin{bmatrix} -6 & 6 & 0 & 0 \\ 0 & 0 & \sqrt{11} & 1 \\ -\sqrt{11} & -\sqrt{11} & 0 & 0 \\ 0 & 0 & \sqrt{11} & -5 \end{bmatrix}. \quad (8)$$

Let $|\lambda I - J_1| = 0$, the eigenvalues of Jacobian matrix are as follows:

$$\begin{aligned} \lambda_1 &= 0.7301 + 4.4609i, \\ \lambda_2 &= 0.7301 - 4.4609i, \\ \lambda_3 &= -6, \\ \lambda_4 &= -6.4602. \end{aligned} \quad (9)$$

It can be seen that λ_3 and λ_4 are negative real numbers, λ_1 and λ_2 are a pair of conjugate complex numbers, and the real part is positive, so the equilibrium point S_1 is a saddle-focus, and system (1) is unstable at S_1 .

For the second equilibrium point $S_2 = (-\sqrt{11}, -\sqrt{11}, 0, 0)$, system (1) is linearized to Jacobian matrix as follows:

$$J_2 = \begin{bmatrix} -a & a & 0 & 0 \\ z & 0 & x & 1 \\ -y & -x & 0 & 0 \\ 0 & z & y & -c \end{bmatrix} = \begin{bmatrix} -6 & 6 & 0 & 0 \\ 0 & 0 & -\sqrt{11} & 1 \\ \sqrt{11} & \sqrt{11} & 0 & 0 \\ 0 & 0 & -\sqrt{11} & -5 \end{bmatrix}. \quad (10)$$

In the same way, let $|\lambda I - J_2| = 0$, the eigenvalue obtained is shown in equation (9), so the equilibrium point S_2 is also a saddle-focus, and system (1) is unstable at S_2 . Obviously, two saddle-foci are the key to the chaotic motion of system (1).

3.3. Bifurcation Diagrams, Lyapunov Exponents, and Period-Doubling Bifurcation Process. The dynamic behaviors of system (1) can be further analyzed by bifurcation diagrams, Lyapunov exponents, and period-doubling bifurcation process.

Let $a = 6$, $c = 5$, and $b \in [9, 20]$. We draw the bifurcation diagrams of the z peak of system (1) changing with b , as shown in Figure 2(a). In Figure 2(a), the red and blue branches represent the different attractors generated from different initial values $X^+ = (10, 10, 0, 0)$ and $X^- = (-10, -10, 0, 0)$, and the overlapped parts represent the same attractors generated. As b increases in [12, 20], the bifurcation diagrams clearly show the trajectory of system (1) from classical period-doubling bifurcation to chaos. Figures 2(b) and 2(c) show the Lyapunov exponents of system (1) which changes with the increase of parameter b , where $LE_1 > LE_2 > LE_3 > LE_4$. By comparing the three diagrams, it can be seen that the bifurcation diagrams are completely consistent with the dynamic behaviors described by Lyapunov exponents.

Figures 3(a)–3(d) describe in detail the main orbital states through which system (1) operates. When $b = 13.6$, system (1) has a pair of period-1 attractors. When $b = 14.5$, system (1) has a pair of period-2 attractors. When $b = 15$,

system (1) has a pair of strange attractors. When $b = 18.5$, system (1) has a strange attractor.

Table 1 shows the comparison of the Lyapunov exponents of the new system with the literature [12, 28–30]. It can be seen that the maximum LE_1 of the new system is larger. It indicates that the chaotic characteristics of the new system are more obvious, the chaotic degree is higher, and the dynamic characteristics of the system are more difficult to predict.

3.4. Coexisting Attractors. Let $a = 10$, $b = 10$, and $c \in [0, 6]$, and we draw the bifurcation diagrams of the x peak of system (1) changing with parameter c . Similarly, the red and blue branches in Figure 4(a), respectively, represents the different attractors generated from different initial values of $X^+ = (10, 10, 0, 0)$ and $X^- = (-10, -10, 0, 0)$, and the overlaps represent the same attractors generated. Figures 4(b) and 4(c) show the Lyapunov exponents of system (1) changing with the increase of parameter c . It is obvious that $LE_1 > LE_2 > LE_3 > LE_4$. Figure 4 shows that periodic attractors, chaotic attractors, and coexisting attractors exist in system (1).

Figure 4(a) not only shows that system (1) has coexisting attractors but also shows that with the increase of c in [1, 4.18], system (1) shows a trajectory from reverse period-doubling bifurcation to chaos. Figures 5(a)–5(d) describe the major orbital states of ergodic when symmetrically coexisting attractors appear in system (1). When $c = 1.55$, the system gets a pair of strange attractors. When $c = 1.92$, the system has a pair of period-2 attractors. When $c = 2.01$, the system has a pair of period-1 attractors. When $c = 4.3$, the system also has a pair of strange attractors. Figures 4(b)–4(c) Lyapunov exponents verify the above process and determine the property of the attractors.

Figure 6 is a dynamical map, mainly depicting the influence of changing parameters b and c on the dynamical map characteristics of the system. Taking the relationship between the maximum Lyapunov exponent and 0 as the standard, the blue region represents the chaotic state of the system, and the maximum Lyapunov exponent is greater than 0; the yellow region represents the periodic state, and the maximum Lyapunov exponent is equal to 0; and the red region represents the system is stable under this parameter condition, and the maximum Lyapunov exponent is less than 0. It can be seen from the figure that as the parameter c increases, the system state alternates between chaotic state and periodic state and occasionally tends to be stable.

4. Circuit Implementation

In order to verify the dynamic behaviors of chaotic system, an actual circuit is designed to realize the chaotic system according to equation (1). The circuit is mainly realized by linear resistances of different resistance values, linear capacitances, operational amplifier TL082IP, and multiplier AD633. However, it should be noted that in the actual circuit, the allowable voltage range of the analog multiplier is

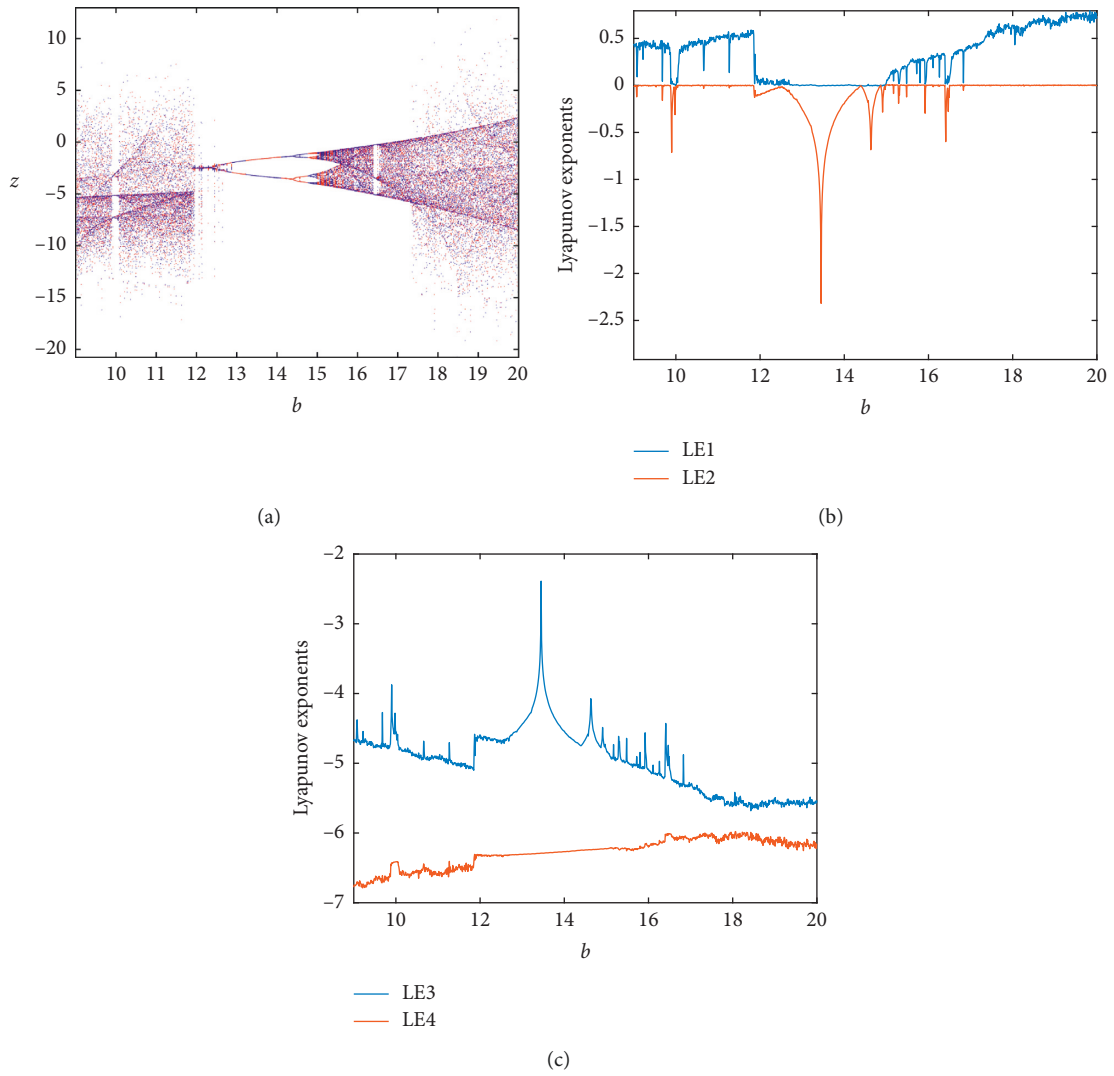


FIGURE 2: Bifurcation diagrams and Lyapunov exponential spectrums of system (1) when $a = 6$, $c = 5$, and $b \in [9, 20]$: (a) bifurcation diagrams of z peak changing with parameter b ; (b) LE_1 and LE_2 ; (c) LE_3 and LE_4 .

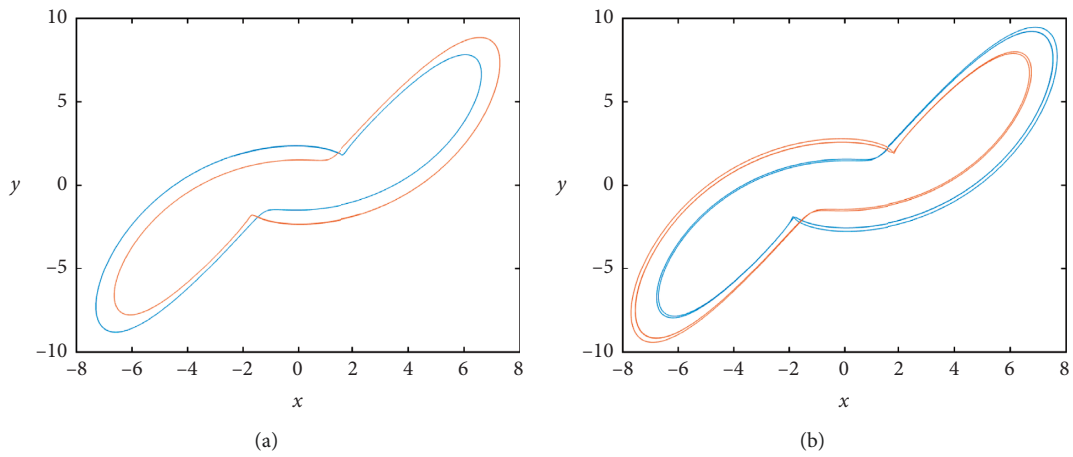


FIGURE 3: Continued.

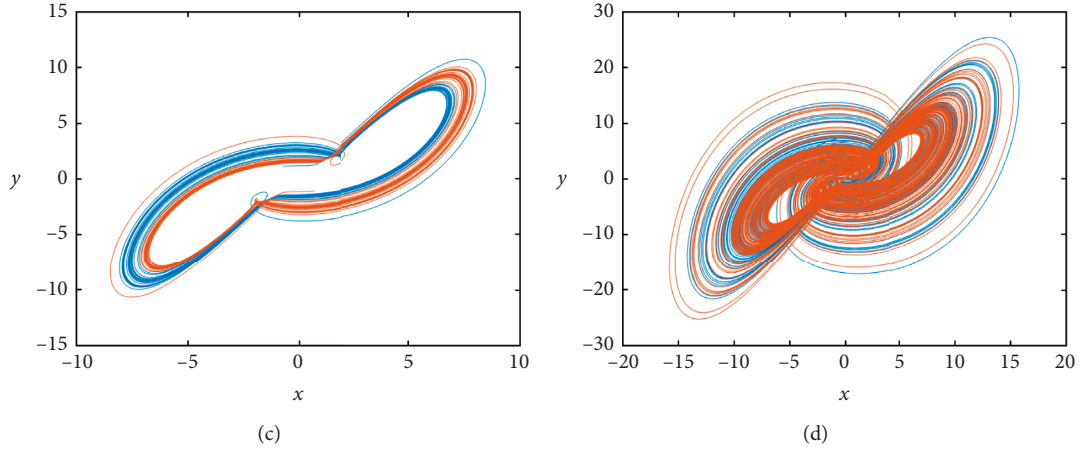


FIGURE 3: Attractors of system (1) with $a = 6$ and $c = 5$: (a) $b = 13.6$, (b) $b = 14.5$, (c) $b = 15$, and (d) $b = 18.5$.

TABLE 1: The Lyapunov exponents of five systems.

Name	System	Parameter values	Lyapunov exponents
Sprott B system	$\dot{x} = yz$ $\dot{y} = x - y$ $\dot{z} = 1 - xy$	None	$LE_1 = 0.210$ $LE_2 = 0$ $LE_3 = -1.210$
Li system	$\dot{x} = y - x$ $\dot{y} = -xz + u$ $\dot{z} = xy - a$ $\dot{u} = -by$	$a = 2.6$ $b = 0.44$	$LE_1 = 0.070$ $LE_2 = 0.013$ $LE_3 = 0$ $LE_4 = -1.083$
Lai system	$\dot{x} = a(y - x)$ $\dot{y} = xz - xw$ $\dot{z} = b - xy$ $\dot{w} = \text{csgn}(z) - kw$	$a = 1$ $b = 1$ $c = 9$ $k = 2$	$LE_1 = 0.211$ $LE_2 = 0$ $LE_3 = -1.210$ $LE_4 = -2$
Zhou system	$\dot{x} = a(w - x)$ $\dot{y} = -by + zw$ $\dot{z} = cx - xw$ $\dot{w} = dy - z + xz$	$a = 2$ $b = 3.9$ $c = 3$ $d = 1$	$LE_1 = 0.092$ $LE_2 = 0$ $LE_3 = -1.988$ $LE_4 = -4.004$
New system	$\dot{x} = a(y - x)$ $\dot{y} = xz + w$ $\dot{z} = b - xy$ $\dot{w} = yz - cw$	$a = 6$ $b = 11$ $c = 5$	$LE_1 = 0.516$ $LE_2 = 0$ $LE_3 = -4.921$ $LE_4 = -6.595$

± 10 V and the allowable voltage range of the operational amplifier is ± 18 V. The dynamic range of variables x , y , z , and w are approximately $[-15, 15]$, $[-20, 20]$, $[-20, 15]$, and $[-20, 20]$, respectively. It is beyond the allowable voltage range of analog multipliers and operational amplifiers, so it is necessary to make appropriate variable proportional compression transformation to the system state variables, so as to facilitate the implementation of the circuit. System (1) is transformed by proportional compression of uniform variables, so that x , y , z , and w are compressed to the original $1/5$, which is $(x, y, z, w) \rightarrow (5x, 5y, 5z, 5w)$. The chaotic system equation after transformation is as follows:

$$\left\{ \begin{array}{l} \frac{dx}{dt} = a(y - x) \\ \frac{dy}{dt} = xz + w \\ \frac{dz}{dt} = b - xy \\ \frac{dw}{dt} = yz - cw \end{array} \right. = \left\{ \begin{array}{l} \frac{d(5x)}{dt} = a(5y - 5x) \\ \frac{d(5y)}{dt} = 5x \cdot 5z + 5w \\ \frac{d(5z)}{dt} = b - 5x \cdot 5y \\ \frac{d(5w)}{dt} = 5y \cdot 5z - 5cw \end{array} \right. = \left\{ \begin{array}{l} \frac{dx}{dt} = ay - ax, \\ \frac{dy}{dt} = 5xz + w, \\ \frac{dz}{dt} = \frac{b}{5} - 5xy, \\ \frac{dw}{dt} = 5yz - cw. \end{array} \right. \quad (11)$$

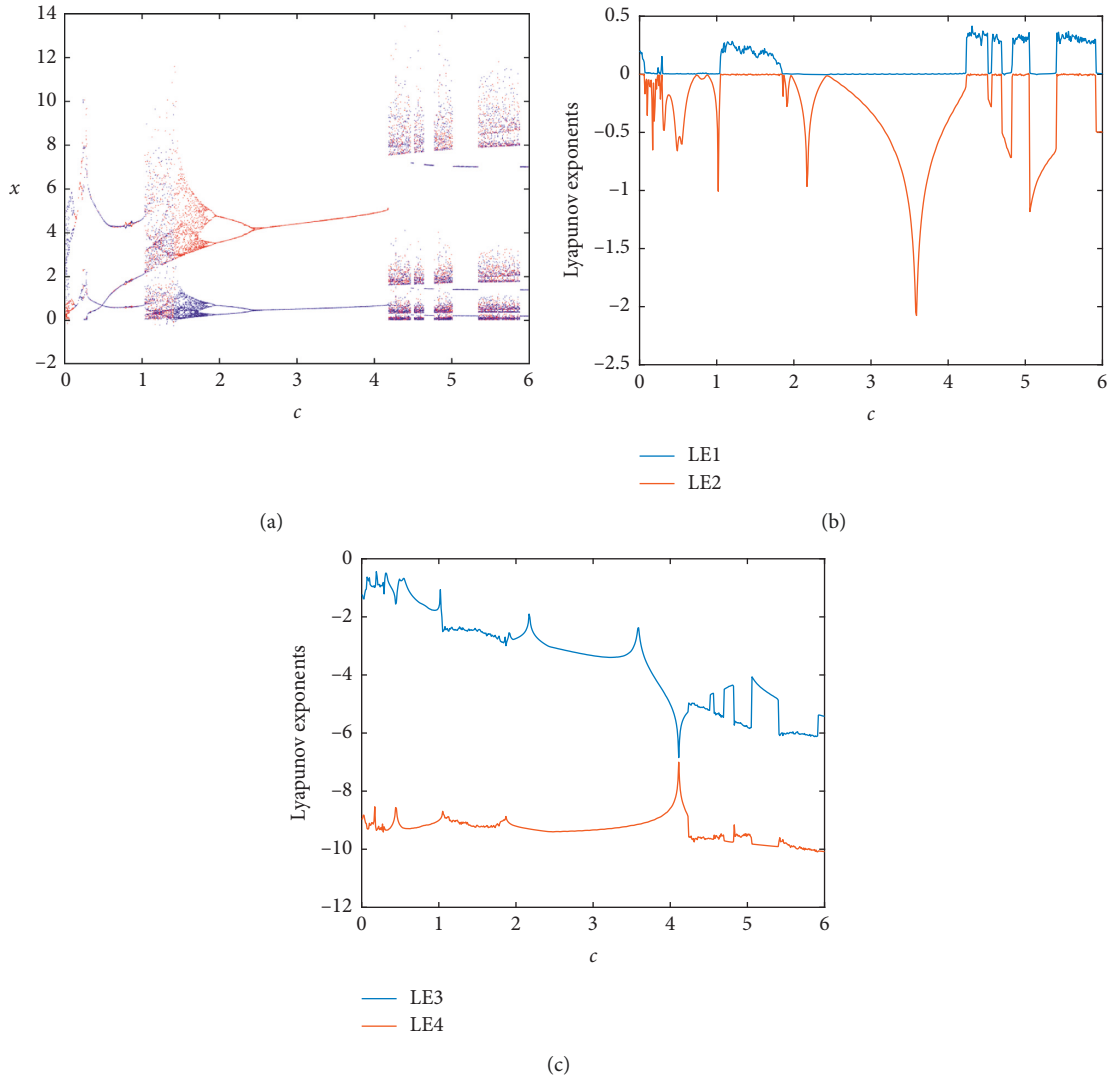


FIGURE 4: Bifurcation diagrams and Lyapunov exponential spectrums of system (1) when $a = 10$, $b = 10$, and $c \in [0, 6]$: (a) bifurcation diagrams of x peak changing with parameter c ; (b) LE_1 and LE_2 ; (c) LE_3 and LE_4 .

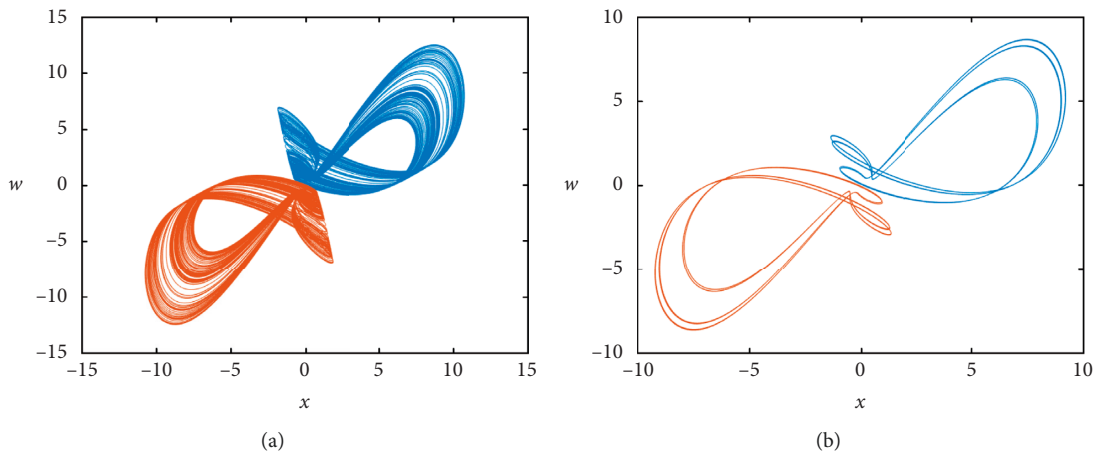


FIGURE 5: Continued.

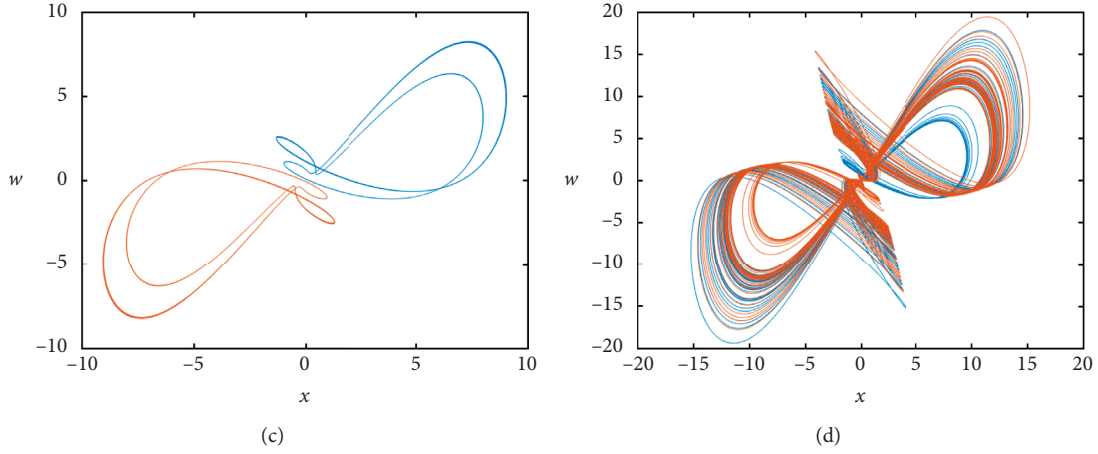


FIGURE 5: Attractors of system (1) with $a = 10$ and $b = 10$: (a) $c = 1.55$, (b) $c = 1.92$, (c) $c = 2.01$, and (d) $c = 4.3$.

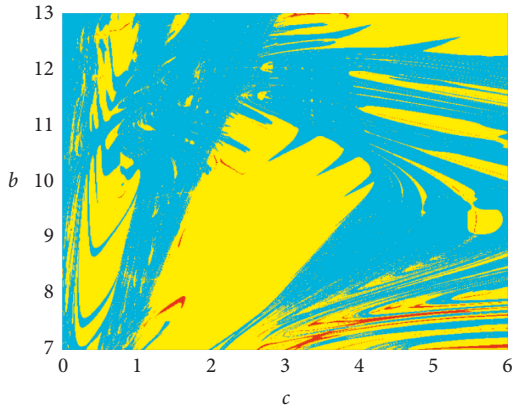


FIGURE 6: Dynamical map with respect to parameters b and c .

In this way, the amplitude of the output chaotic signal can be reduced to 1/5 of the original system.

Make time-scale transformation of equation (11), and transform t into $\tau_0 t$ in the equation, where $\tau_0 = 100$, and the results are as follows:

$$\begin{cases} \frac{dx}{dt} = 100ay - 100ax, \\ \frac{dy}{dt} = 500xz + 100w, \\ \frac{dz}{dt} = 20b - 500xy, \\ \frac{dw}{dt} = 500yz - 100cw. \end{cases} \quad (12)$$

The modular circuit is designed according to the above formula, as shown in Figure 7.

According to the circuit schematic diagrams, the corresponding self-excited oscillation circuit equation is obtained as follows:

$$\begin{cases} \frac{dx}{dt} = -\frac{R_3}{R_2 R_4 C_1} (-y) - \frac{R_3}{R_1 R_4 C_1} x, \\ \frac{dy}{dt} = -\frac{R_9}{R_7 R_{10} C_2} (-w) - \frac{R_9}{10 R_8 R_{10} C_2} (-x)z, \\ \frac{dz}{dt} = -\frac{R_{15}}{R_{13} R_{16} C_3} (-1) - \frac{R_{15}}{10 R_{14} R_{16} C_3} xy, \\ \frac{dw}{dt} = -\frac{R_{21}}{R_{19} R_{22} C_4} w - \frac{R_{21}}{10 R_{20} R_{22} C_4} y(-z). \end{cases} \quad (13)$$

By comparing equation (12) with equation (13), we can get

$$\begin{aligned} a &= \frac{R_3}{100 R_1 R_4 C_1} = \frac{R_3}{100 R_2 R_4 C_1}, \\ 500 &= \frac{R_9}{10 R_8 R_{10} C_2}, \\ 100 &= \frac{R_9}{R_7 R_{10} C_2}, \\ b &= \frac{R_{15}}{20 R_{13} R_{16} C_3}, \\ 500 &= \frac{R_{15}}{10 R_{14} R_{16} C_3}, \\ 500 &= \frac{R_{21}}{10 R_{20} R_{22} C_4}, \\ c &= \frac{R_{21}}{100 R_{19} R_{22} C_4}, \end{aligned} \quad (14)$$

In this paper, Multisim software is used for circuit simulation, in which the output scaling factor of the analog multiplier AD633 is set as 100 mV/1 V and the power supply voltage is ± 12 V. The integral time constant of the four

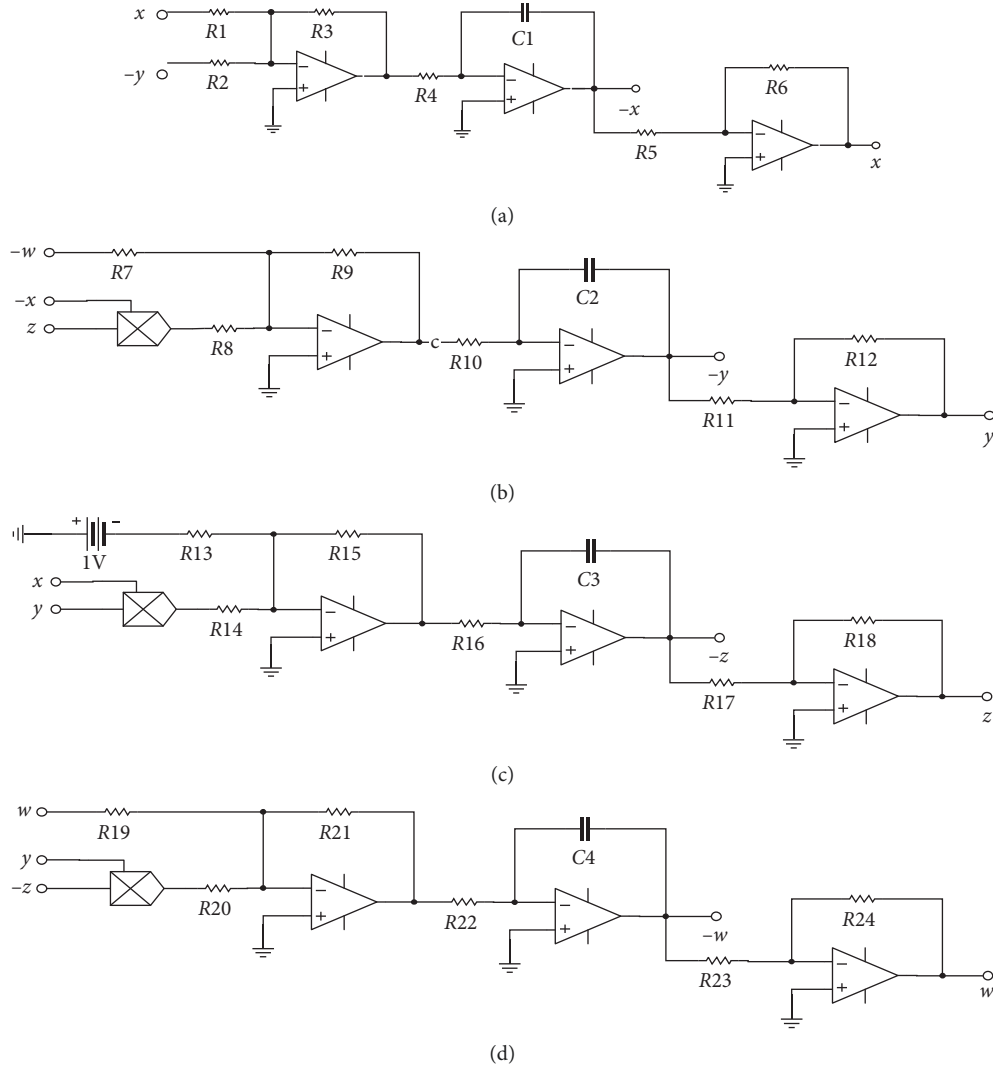


FIGURE 7: Schematic diagrams of chaotic circuit: (a) variable x equivalent circuit, (b) variable y equivalent circuit, (c) variable z equivalent circuit, and (d) variable w equivalent circuit.

circuit channels can be changed by adjusting the capacitance; set $C_1 = C_2 = C_3 = C_4 = 10$ nF, $R_4 = R_{10} = R_{16} = R_{22} = 50$ k Ω , and $R_3 = R_5 = R_6 = R_9 = R_{12} = R_{15} = R_{17} = R_{18} = R_{21} = R_{23} = R_{24} = 100$ k Ω . When $a = 6$, $b = 11$, and $c = 5$, it can be obtained from equation (14) that $R_1 = R_2 = 333$ k Ω , $R_7 = 2000$ k Ω , $R_8 = R_{14} = R_{20} = 40$ k Ω , $R_{13} = 909$ k Ω , and $R_{19} = 400$ k Ω . Circuit simulation results are shown in Figure 8. These trajectories are consistent with numerical simulation results.

Similarly, we can use circuit simulations to observe the orbital states of system (1) as it moves towards chaos. Keep other parameters unchanged, and control the value of parameter b by changing R_{13} . Figures 9(a)–9(d) describe the trajectories starting from the initial value $X^+(10, 10, 0, 0)$, where $R_{13} = 735$ k Ω corresponds to parameter $b = 13.6$, $R_{13} = 690$ k Ω corresponds to parameter $b = 14.5$, $R_{13} = 667$ k Ω corresponds to parameter $b = 15$, and $R_{13} = 540$ k Ω corresponds to $b = 18.5$. By comparing with Figure 3, it can

be seen that the results of circuit simulation and numerical simulation are consistent.

The following circuit simulation is used to verify the symmetric coexisting attractors in system (1), mainly verifying the first three orbital states. Because the parameters have changed, the value of the corresponding resistances in the circuit should also be changed. Equation (14) can be used to calculate the corresponding resistances $R_1 = R_2 = 200$ k Ω and $R_{13} = 1000$ k Ω when $a = 10$ and $b = 10$. The parameter c is controlled by the resistance R_{19} . $c = 1.55 \rightarrow R_{19} = 1290$ k Ω , $c = 1.92 \rightarrow R_{19} = 1042$ k Ω , and $c = 2.01 \rightarrow R_{19} = 995$ k Ω . The left graph of Figure 10 shows the attractors starting from initial value $X^+(10, 10, 0, 0)$, and the right graph of Figure 10 shows the attractors starting from initial value $X^-(-10, -10, 0, 0)$. By comparing the circuit simulation diagrams with the numerical simulation diagrams in the previous section, we can see that the experimental results of the two are in good agreement.

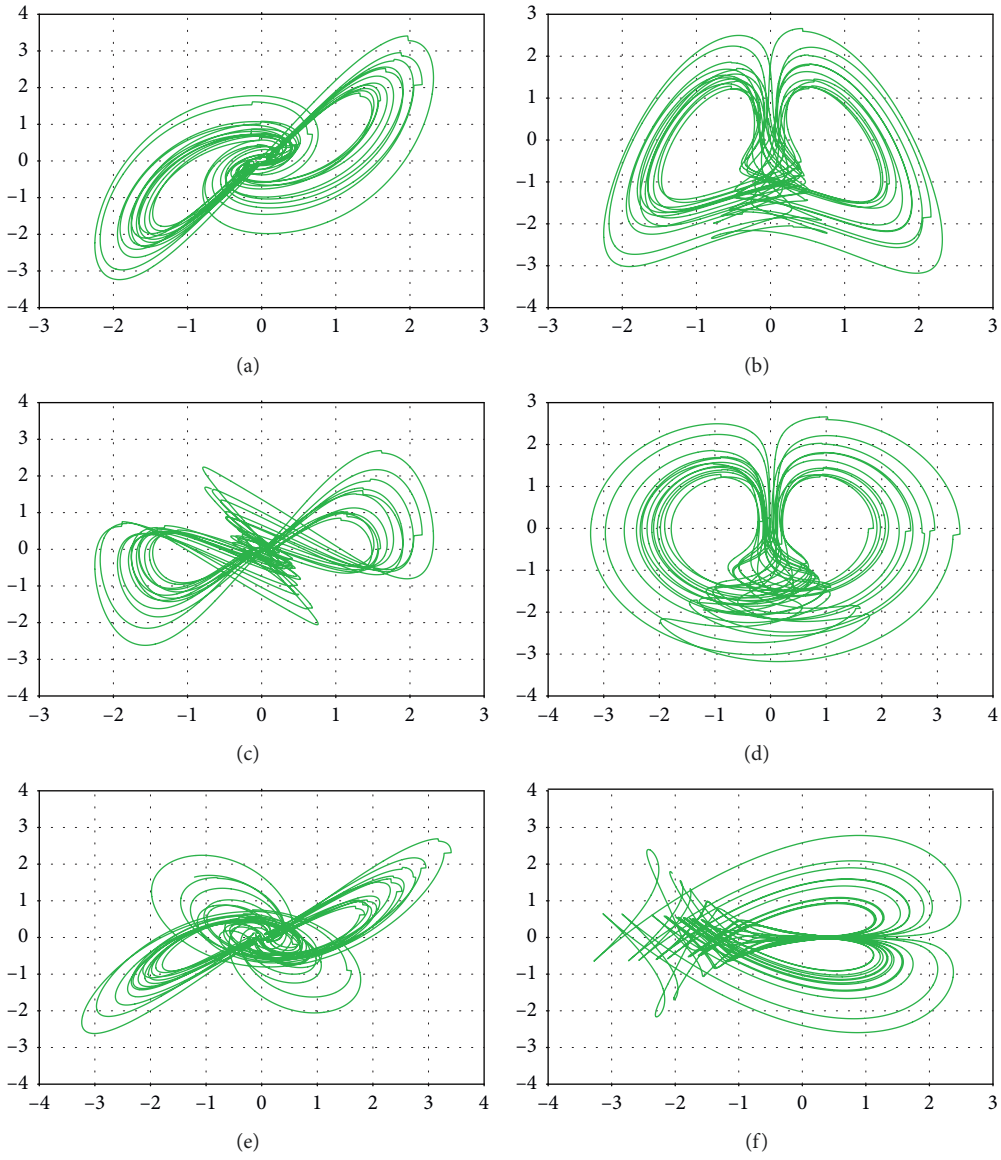


FIGURE 8: The circuit realization of phase diagrams for system (1): (a) $x - y$, (b) $x - z$, (c) $x - w$, (d) $y - z$, (e) $y - w$, and (f) $z - w$.

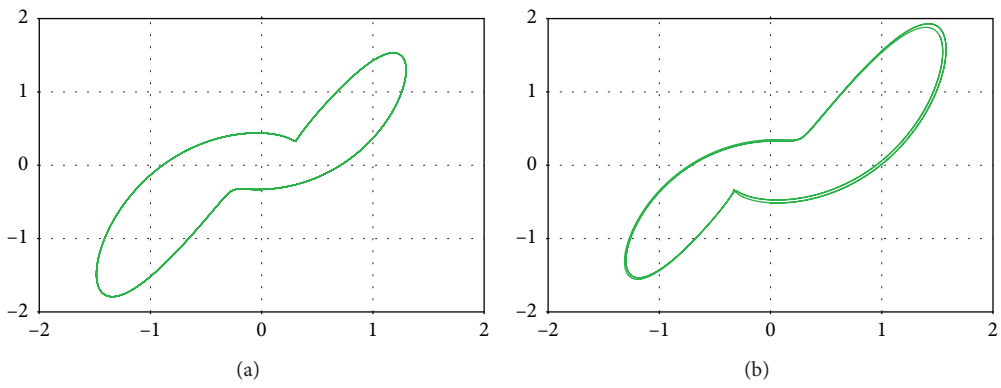


FIGURE 9: Continued.

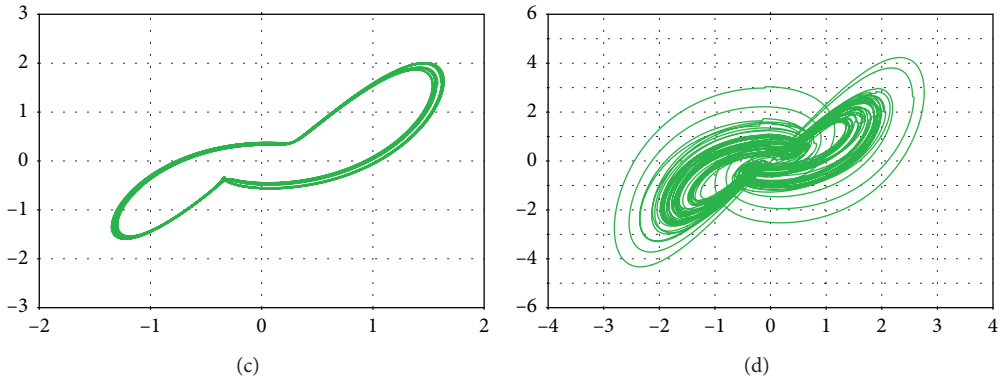


FIGURE 9: The circuit realization of attractors for system (1): (a) $R_{13} = 735 \text{ k}\Omega$, (b) $R_{13} = 690 \text{ k}\Omega$, (c) $R_{13} = 667 \text{ k}\Omega$, and (d) $R_{13} = 540 \text{ k}\Omega$.

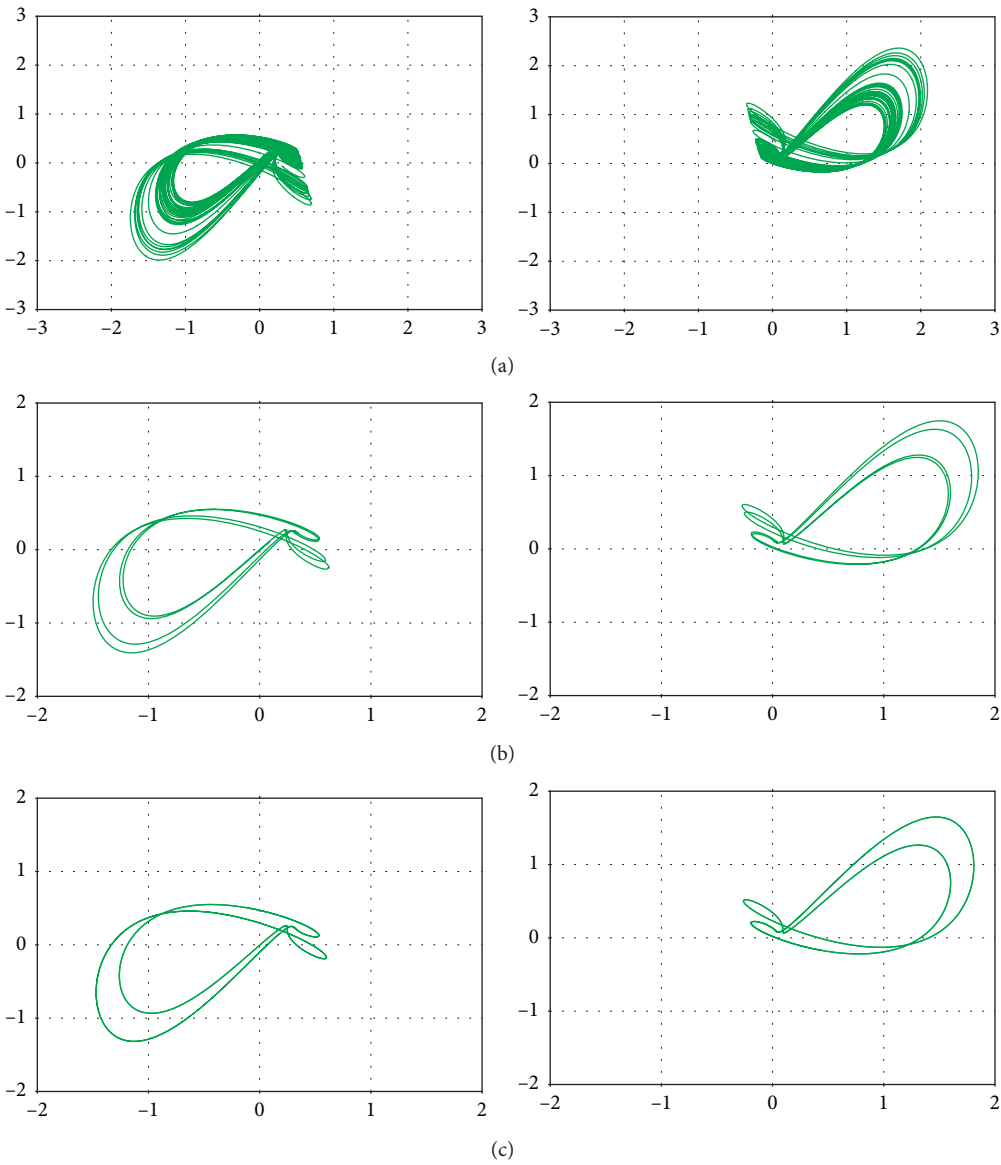


FIGURE 10: The attractors of system (1) from initial value X^+ (10, 10, 0, 0) (left) and attractors from initial value X^- (-10, -10, 0, 0) (right): (a) $R_{19} = 1290 \text{ k}\Omega$, (b) $R_{19} = 1042 \text{ k}\Omega$, and (c) $R_{19} = 995 \text{ k}\Omega$.

5. Conclusion

In this paper, a new four-dimensional chaotic system is designed by adding a state-feedback controller to the Sprott B system. It contains three nonlinear terms and one constant term and is symmetric about z -axis. Through the analysis of system diagrams, bifurcation diagrams, and Lyapunov exponents, it is found that the new system can generate not only two-wing and four-wing attractors but also symmetrical coexisting attractors, and the complexity of the system is further improved. We also design the electronic circuit, and the results of the circuit simulation experiment are consistent with those of the numerical simulation experiment, which proves the correctness of the theoretical analysis and the realizability of the system. The dynamic characteristics of the new system are more abundant, and it has great prospects in the fields of image encryption and secure communication.

Data Availability

The data used to support the findings of this study are included within the article.

Conflicts of Interest

The authors declare no conflicts of interest.

Acknowledgments

This research was funded by the National Natural Science Foundation of China (Nos. 61203004 and 61306142) and Natural Science Foundation of Heilongjiang Province (Grant no. F201220).

References

- [1] J. Gleick and R. C. Hilborn, "Chaos, making a new science," *American Journal of Physics*, vol. 56, no. 11, p. 79, 1998.
- [2] M. Hasler, "Chaotic behaviour in electronic circuits || engineering chaos for encryption and broadband communication," *Philosophical Transactions: Physical Sciences and Engineering*, vol. 353, no. 1701, pp. 115–126, 1995.
- [3] A. V. Oppenheim, G. W. Wornell, S. H. Isabelle, and K. M. Cuomo, "Signal processing in the context of chaotic signals," in *Proceedings of the IEEE International Conference on Acoustics, Speech, and Signal Processing*, pp. 117–120, San Francisco, CA, USA, March 1992.
- [4] T. Elbert, W. J. Ray, Z. J. Skinner, J. E. Skinner, K. E. Graf, and N. Birbaumer, "Chaos and physiology: deterministic chaos in excitable cell assemblies," *Physiological Reviews*, vol. 74, no. 1, pp. 1–47, 1994.
- [5] L. J. Yang and T. L. Chen, "Application of chaos in genetic algorithms," *Communications in Theoretical Physics*, vol. 38, no. 2, pp. 168–172, 2002.
- [6] V. P. Maslov, "Theory of chaos and its application to the crisis of debts and the origin of inflation," *Russian Journal of Mathematical Physics*, vol. 16, no. 1, pp. 103–120, 2009.
- [7] G. CHEN and L. Ü Jinhu, *Dynamics Analysis, Control and Synchronization of Lorenz System Family*, Science Press, Beijing, China, 2003.
- [8] E. N. Lorenz, "Deterministic nonperiodic flow," *Journal of the Atmospheric Sciences*, vol. 20, no. 2, pp. 130–141, 1963.
- [9] O. E. RöSSLER, "An equation for continuous chaos," *Physics Letters A*, vol. 57, no. 5, pp. 397–398, 1976.
- [10] L. Chua, M. Komuro, and T. Matsumoto, "The double scroll family," *IEEE Transactions on Circuits and Systems*, vol. 33, no. 11, pp. 1072–1118, 1986.
- [11] R. N. Madan, *Chua's Circuit: A Paradigm for Chaos*, World Scientific, Singapore, 1993.
- [12] J. C. Sprott, "Some simple chaotic flows," *Physical Review E*, vol. 50, no. 2, pp. 647–650, 1994.
- [13] G. Chen and T. Ueta, "Yet another chaotic attractor," *International Journal of Bifurcation and Chaos*, vol. 9, no. 7, pp. 1465–1466, 1999.
- [14] J. Lü, G. Chen, S. Zhang et al., "Dynamical analysis of a new chaotic attractor," *International Journal of Bifurcation and Chaos*, vol. 12, no. 05, pp. 1001–1015, 2002.
- [15] W. Liu and G. Chen, "A new chaotic system and its generation," *International Journal of Bifurcation and Chaos*, vol. 13, no. 1, pp. 261–267, 2003.
- [16] J. Kengne, Z. T. Njitacke, H. B. Fotsin et al., "Dynamical analysis of a simple autonomous jerk system with multiple attractors," *Nonlinear Dynamics*, vol. 83, no. 1–2, pp. 751–765, 2016.
- [17] X. Wang, S. Vaidyanathan, C. Volos, V.-T. Pham, and T. Kapitaniak, "Dynamics, circuit realization, control and synchronization of a hyperchaotic hyperjerk system with coexisting attractors," *Nonlinear Dynamics*, vol. 89, no. 3, pp. 1673–1687, 2017.
- [18] X. Wang, X. Min, J. Yu, Y. Shen, G. Wang, and H. C. I. Ho, "Realization of a novel logarithmic chaotic system and its characteristic analysis," *International Journal of Bifurcation and Chaos*, vol. 29, no. 2, Article ID 1930004, 2019.
- [19] L. Wang, "3-scroll and 4-scroll chaotic attractors generated from a new 3-D quadratic autonomous system," *Nonlinear Dynamics*, vol. 56, no. 4, pp. 453–462, 2009.
- [20] B. Bao, J. Xu, Z. Liu, and Z. Ma, "Hyperchaos from an augmented Lü system," *International Journal of Bifurcation and Chaos*, vol. 20, no. 11, pp. 3689–3698, 2010.
- [21] P. Li, J. Xu, J. Mou et al., "Fractional-order 4D hyperchaotic memristive system and application in color image encryption," *EURASIP Journal on Image and Video Processing*, vol. 2019, no. 1, pp. 1–11, 2019.
- [22] N. Okafor, B. Zahawi, D. Giaouris, and S. Banerjee, "Chaos, coexisting attractors, and fractal basin boundaries in DC drives with full-bridge converter," in *Proceedings of the 2010 IEEE International Symposium on Circuits and Systems*, pp. 129–132, Paris, France, May–June 2010.
- [23] G. A. Leonov, N. V. Kuznetsov, and V. I. Vagitsev, "Hidden attractor in smooth Chua systems," *Physica D: Nonlinear Phenomena*, vol. 241, no. 18, pp. 1482–1486, 2012.
- [24] J. C. Sprott, X. Wang, and G. Chen, "Coexistence of point, periodic and strange attractors," *International Journal of Bifurcation and Chaos*, vol. 23, no. 5, Article ID 1350093, 2013.
- [25] Z. P. Peng, C. H. Wang, Y. Lin et al., "A novel four-dimensional multi-wing hyper-chaotic attractor and its application in image encryption," *Acta Physica Sinica*, vol. 63, no. 24, pp. 97–106, 2014.
- [26] F. Z. Wang, G. Y. Qi, Z. Q. Chen et al., "On a four-winged chaotic attractor," *Acta Physica Sinica*, vol. 56, no. 6, pp. 3137–3144, 2007.
- [27] C. Li and J. C. Sprott, "Multistability in a butterfly flow," *International Journal of Bifurcation and Chaos*, vol. 23, no. 12, Article ID 1350199, 2013.

- [28] C. Li and J. C. Sprott, "Coexisting hidden attractors in a 4-D simplified Lorenz system," *International Journal of Bifurcation and Chaos*, vol. 24, no. 03, Article ID 1450034, 2014.
- [29] Q. Lai, A. Akgul, X.-W. Zhao, and H. Pei, "Various types of coexisting attractors in a new 4D autonomous chaotic system," *International Journal of Bifurcation and Chaos*, vol. 27, no. 9, Article ID 1750142, 2017.
- [30] C. Zhou, C. Yang, D. Xu, and C. Chen, "Coexisting attractors, circuit realization and impulsive synchronization of a new four-dimensional chaotic system," *Modern Physics Letters B*, vol. 33, no. 3, Article ID 1950026, 2019.

Research Article

Dynamics and Synchronization of a Memristor-Based Chaotic System with No Equilibrium

Hong-Min Li, Yan-Feng Yang, Yang Zhou, Chun-Lai Li , Kun Qian, Zhao-Yu Li, and Jian-Rong Du

College of Physics and Electronics, Hunan Institute of Science and Technology, Yueyang 414006, China

Correspondence should be addressed to Chun-Lai Li; hnistlichl@163.com

Received 26 July 2019; Accepted 17 September 2019; Published 28 October 2019

Guest Editor: Viet-Thanh Pham

Copyright © 2019 Hong-Min Li et al. This is an open access article distributed under the Creative Commons Attribution License, which permits unrestricted use, distribution, and reproduction in any medium, provided the original work is properly cited.

The topics of memristive system and synchronization are two hot fields of research in nonlinear dynamics. In this paper, we introduce a memristor-based chaotic system with no equilibrium. It is found that the memristor-based system under investigation exhibits fruitful dynamic behaviors such as coexisting bifurcation, multistability, transient chaos, and transient quasiperiod. Thus, it is difficult to reproduce the accurate dynamics of the system, which is highly advantageous in encryption and communication. Then, a simple intermittent control scheme with adaptive mechanism is developed to achieve complete synchronization for the introduced system. Because the output signal is transmitted intermittently to the receiver system, more channel capacity can be saved and the security performance can be improved naturally in practical communication.

1. Introduction

As the fourth basic circuitual element along with resistor, inductor, and capacitor, the memristor was postulated by Chua in 1971 [1], and it was then successfully fabricated by the HP laboratories in 2008 [2]. Since then, the memristor was recognized to perfect the symmetry of the four fundamental circuitual variables and has aroused wide interest in academia [3–5]. The memristor is commonly defined as a two-terminal nonlinear component with controllable resistance called memristance that varies according to the amount of charge or flux flowing through it [6]. The fingerprint of a memristor is composed of a current-voltage characteristic curve, which shows a pinched hysteresis loop whose shape varies with frequency and converges to a straight line with the increase of frequency [7].

The memristor is currently used to design flash memory, improve neural networks, and construct chaotic circuits, for the intrinsic characteristics of memory, nanoscale device, and inherent nonlinearity. Itoh and Chua constructed the memristive chaotic oscillator in 2008, by replacing Chua's diodes in Chua's circuit with the piecewise linear memristor

[8]. Afterwards, many memristor-based chaotic oscillators were constructed. For example, by replacing the single diode with a memristor in the original circuit, Pelap postulated an emendatory Tamasevicius oscillator [9]. Bi-Rong designed a simple chaotic circuit consisting of an inductor, a capacitor, and a voltage-controlled memristor [10]. Zhao et al. proposed a memristor-based chaotic system by replacing the nonlinear diode in the Chua circuit with an active flux-controlled memristor [11]. In order to increase the complexity of memristor-based system, Teng et al. used a fourth-degree polynomial memristance to produce a multiscroll chaotic attractor [12]. By replacing Chua's diode with a physical SBT memristor and a negative conductance in the canonical Chua's circuit, a new memristor-based modified Chua's circuit is constructed [13]. There usually emerges special dynamics in this kind of memristive systems, such as initial sensitivity, coexisting bifurcation, coexistence attractors, and transient dynamics. Therefore, the memristive chaotic system will provide more complex dynamics and facilitates the engineering applications of information encryption, secure communication, and signal processing [14–17].

Meanwhile, close attention was paid to chaotic system without equilibrium [18–20]. From the computer-processing perspective, it is challenging to numerically localize the attractor in such system since there is no transient process leading from the vicinity of unstable equilibrium point. In other words, the attracting basin of such system does not intersect with any small neighborhood of its equilibrium point, or the attractor is “hidden” [21–24]. Up to now, little information is known about the dynamical behavior in such system, and what is worse is that the Shilnikov criteria cannot be employed to prove the chaos for the absence of heteroclinic or homoclinic orbit [25, 26].

Because of its application in secure communication, digital signal, neural network, and other fields, the synchronization of chaotic system is a fashionable subject in nonlinear science. Since the first scheme was carried out by Pecora and Carroll for the synchronization of two identical chaotic systems [27], a great diversity of methods have been proposed to synchronize chaotic systems, such as active control, adaptive control, impulsive control, sliding mode control, intermittent control, pinning control, and hybrid control [28–31]. Generally, a chaotic communication system can be constructed based on master-slave synchronization, where the message is modulated by the transmitting system and is then sent to the receiving system. Also, in the receiver, the designed synchronization scheme is used to demodulate the received signal and extract the message [32]. The intermittent synchronization implies that the slave system receives the demodulated information from the master system intermittently. Therefore, the intermittent synchronization scheme will decrease the amount of conveyed information and the communication channel capacity will be reserved for more message transmission. Also, accordingly, the security of the chaotic communication system will be improved since the redundancy of the synchronization information in the channel is reduced. Therefore, the intermittent synchronization scheme is especially fit for the design of practical chaos-based communication system.

In this paper, we introduce a memristor-based chaotic system with no equilibrium. The dynamical evolution of the memristive system is studied by using phase diagram, time-domain trajectory, bifurcation diagram, and Lyapunov exponent. It is found that by changing system parameters or initial condition, the reported system exhibits different topological structures of coexisting bifurcation, multistability, transient dynamics. The coexisting hidden attractors signify that the system has fruitful and complex dynamic behaviors, which is highly advantageous in encryption and communication for the difficulty of reproducing the accurate dynamics of the system. Then, a simple intermittent control scheme with adaptive mechanism is developed to achieve complete synchronization for the introduced memristive system. Since the output signal is transmitted intermittently to the receiver system, more channel capacity can be saved and the security performance of the communication system can be improved naturally in practical communication. Theoretical analysis and illustrative examples are executed to verify the effectiveness of the proposed synchronization scheme.

2. Memristor-Based Chaotic System with No Equilibrium

2.1. Model Description. Based on Sprott A system, the constructed memristive chaotic system can be described by the following differential equations:

$$\begin{cases} \dot{x} = y, \\ \dot{y} = -Wx + yz, \\ \dot{z} = c - y^2, \end{cases} \quad (1)$$

where x, y, z are state variables; the function W represents the model of a flux-controlled memristor, depicted as $W = 3ax^2 + b$; and a, b, c are positive parameters.

The dissipativity is decided by $\nabla V = (\partial \dot{x}/x) + (\partial \dot{y}/y) + (\partial \dot{z}/z) = z$; thus, system (1) is non-Hamiltonian conservative of phase volume [33]. It is palpable that there exists no equilibrium in system (1). Therefore, the strange attractor is “hidden” in the sense of classification method described by Leonov et al. [21], and the Shilnikov method cannot be employed to verify the emergence of chaos since there is no heteroclinic or homoclinic orbit in this system. It is easy to know that the system is symmetric with respect to the y -axis in the sense of coordinate transformation $(x, y, z, t) \rightarrow (-x, y, -z, -t)$.

When choosing the parameters $a = 3$, $b = -1$, and $c = 1$ and initial condition $(0.2, 0.15, 0)$, system (1) appears a chaotic state with the Lyapunov exponents $0.1062, 0, -0.1062$, as illustrated by the phase portrait in Figure 1.

2.2. Coexisting Bifurcation and Multiple Attractors. It is found that the memristive system under consideration can experience rich bifurcation structures when continuously monitoring the bifurcation parameter. Also, the memristive system has completely different bifurcation behaviors when the initial conditions are set to different values.

We assign the parameters b and c of system (1) as $b = -1$ and $c = 1$, and select parameter a serving as the representative bifurcation parameter. The coexisting bifurcation diagrams, produced by the local maxima of the state variable z in terms of control parameter a , are depicted in Figure 2(a) when the system starts with the initial states $(0.1, 0, 0)$ and $(0.2, 0, 0)$. Also, the corresponding maximal Lyapunov exponents are depicted in Figure 2(b). This strategy represents a convenient and intuitive approach to identify the window in which the multiple coexisting attractors arise. We further draw in Figure 3 the enlarged bifurcation diagrams of Figure 2(a) to show the typical regions of multiple coexisting attractors. By taking different initial conditions $(0.1, 0, 0)$ and $(0.2, 0, 0)$, respectively, we plot the coexisting multiple attractors with different parameter a in Figure 4. It is found that there may emerge rich dynamical structures of coexisting chaos, quasi-period or period with different shape for the same parameter a when starting from different initial states.

We also study the dynamics evolution of system (1) by using the initial value $x(0)$ served as the bifurcation parameter. The system parameters are fixed as $a = 3$, $b = -1$, $c = 1$, and the rest initial conditions are assigned to be $y(0) = 0, z(0) = 0$. The bifurcation diagram and spectra of

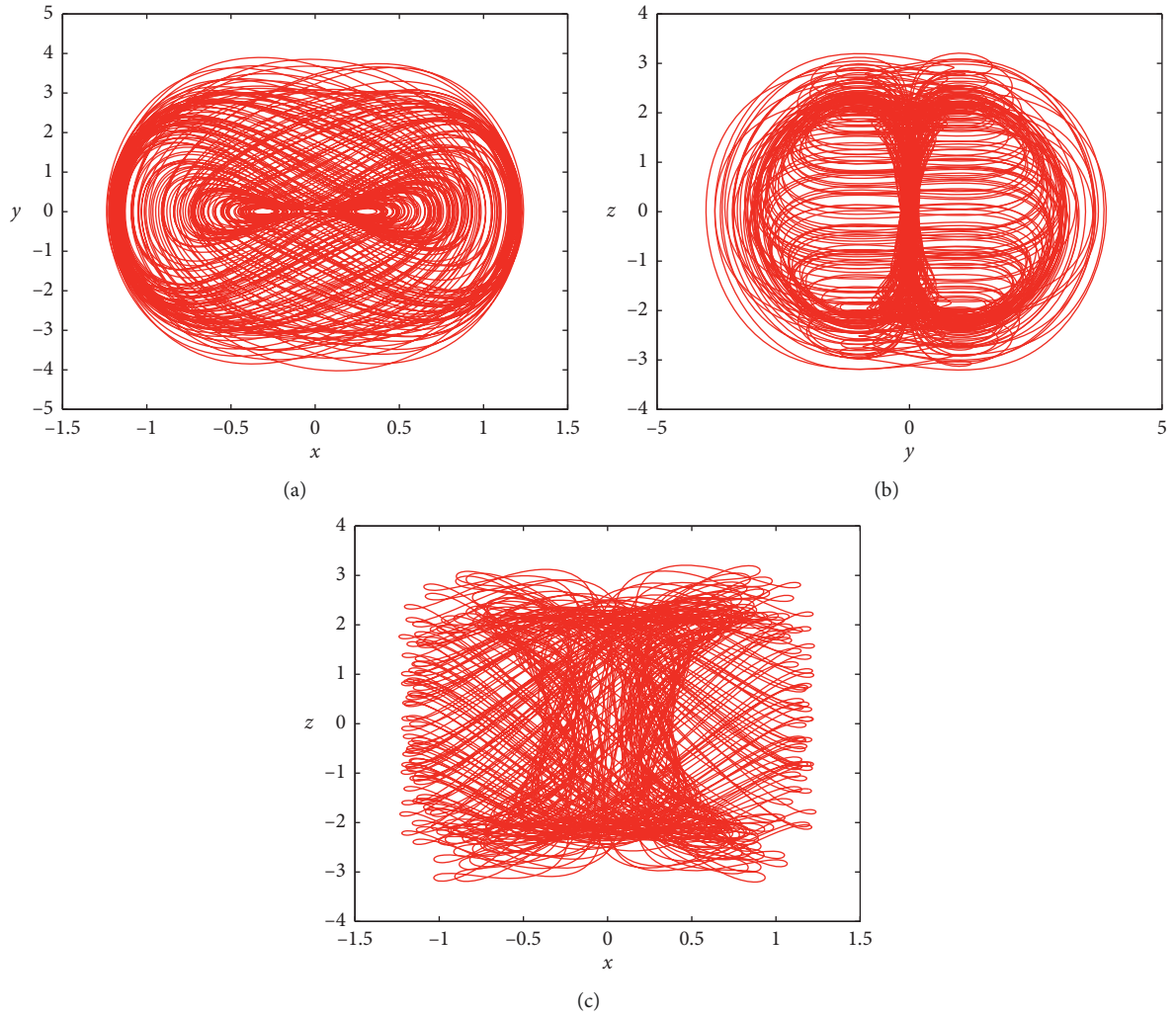


FIGURE 1: Phase portrait projected onto the plane of (a) x - y ; (b) y - z ; (c) x - z .

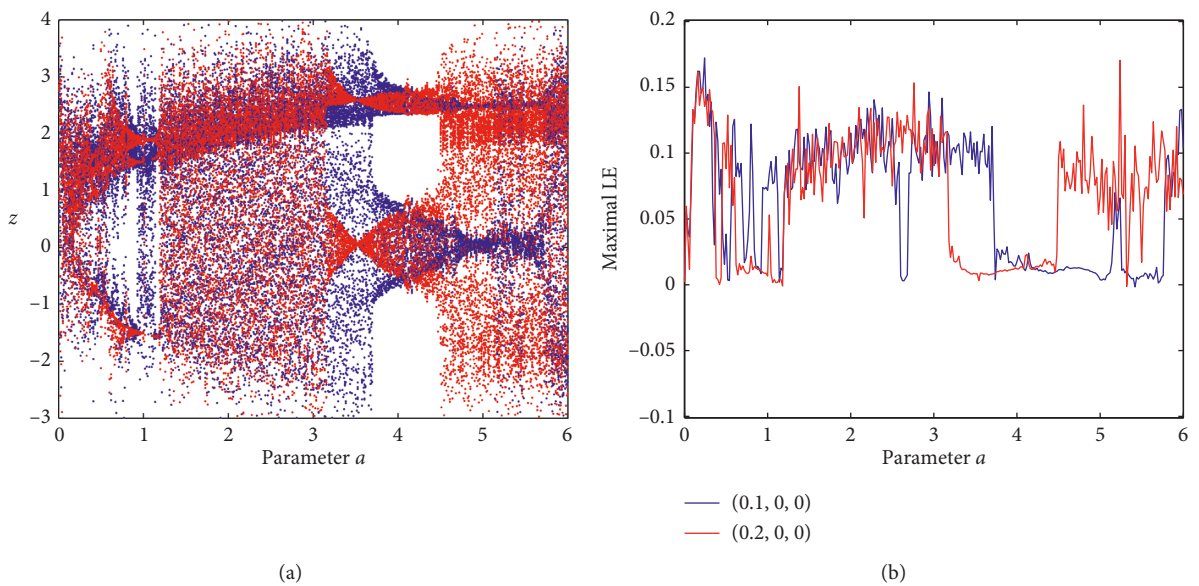


FIGURE 2: (a) Bifurcation diagrams and (b) spectrums of maximal Lyapunov exponent versus parameter a , the initial conditions are $(0.1, 0, 0)$ for blue diagrams and $(0.2, 0, 0)$ for red diagrams.

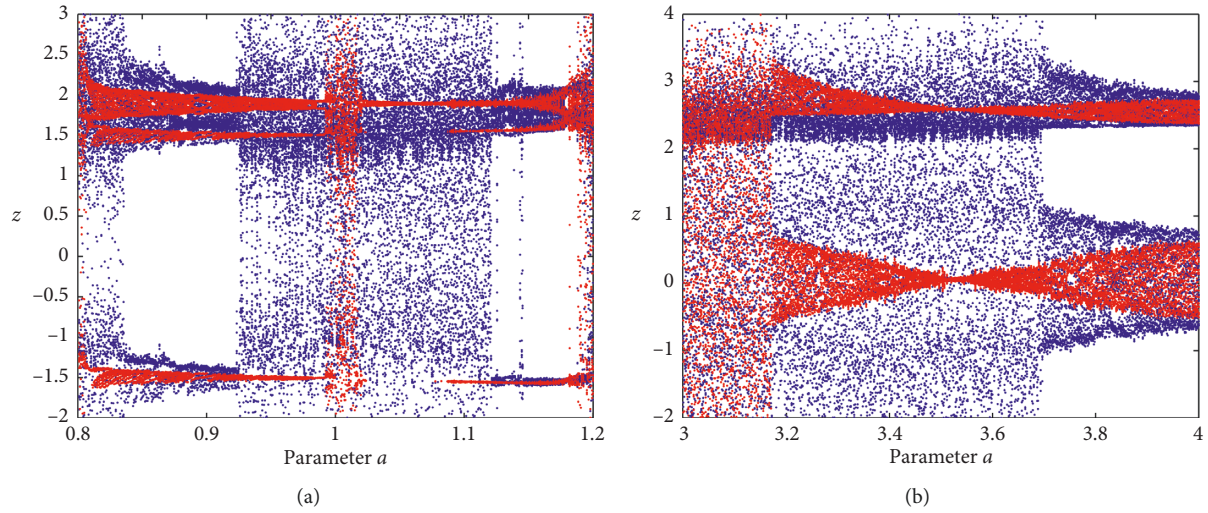


FIGURE 3: Enlargement of the bifurcation diagrams of Figure 2(a) in ranges of (a) $[0.8, 1.2]$ and (b) $[3, 4]$; the initial conditions are $(0.1, 0, 0)$ for blue diagrams and $(0.2, 0, 0)$ for red diagrams.

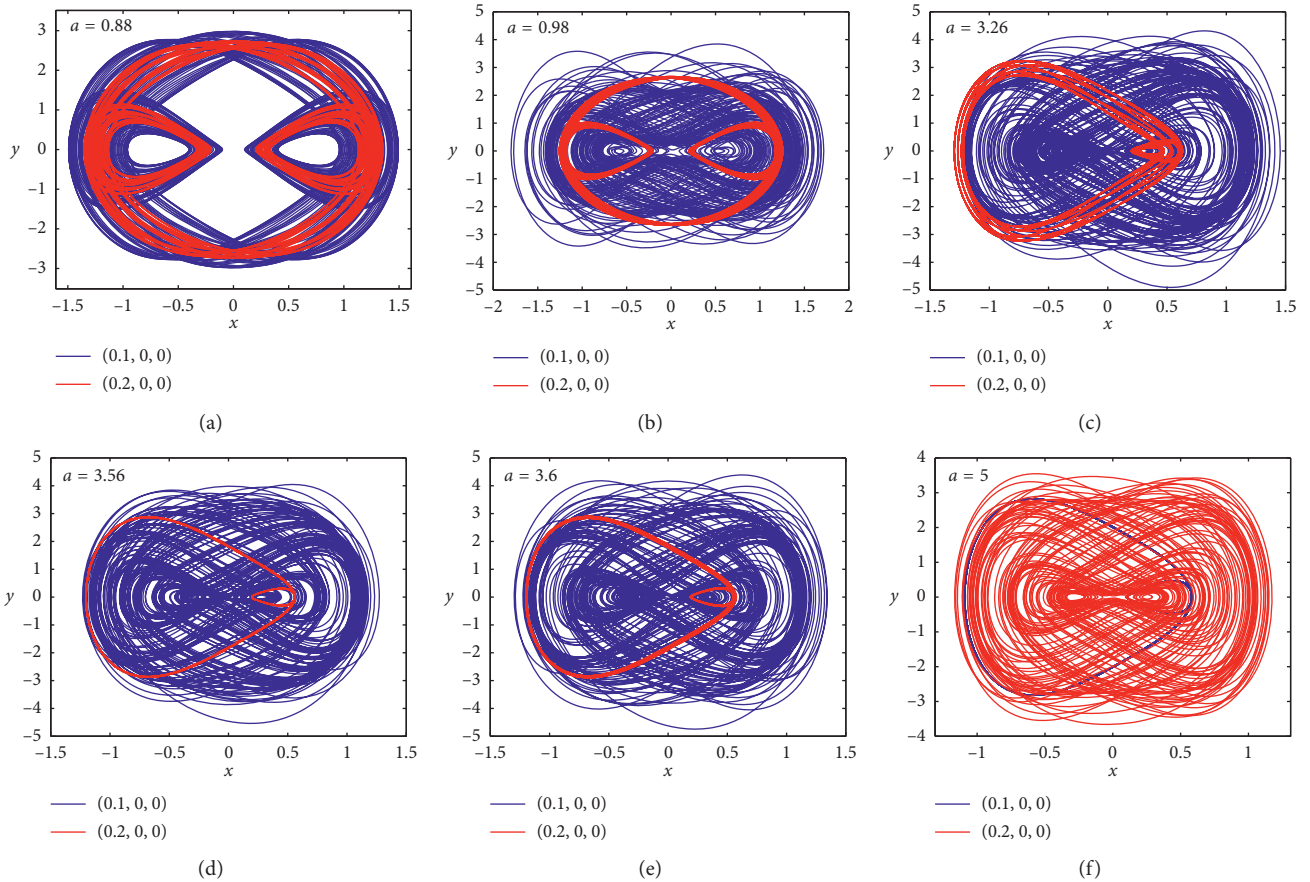


FIGURE 4: Coexistence of different attractors with different parameter a . (a) Quasiperiods with different shape; (b) chaos and quasiperiod; (c) chaos and complicated period; (d) chaos and period-1; (e) chaos and quasiperiod; (f) period and chaos, for the initial conditions $(0.1, 0, 0)$ and $(0.2, 0, 0)$, respectively.

Lyapunov exponent are depicted in Figures 5(a) and 5(b), respectively. It can be found that when increasing initial value $x(0)$ from -2 to 2 , there emerge periodic windows embedded in the chaotic region, and the dynamics is symmetrically

distributed with respect to zero value. In fact, the dynamics is also symmetrically distributed with respect to y -axis and z -axis, as depicted by the dynamical map of $x(0)$ versus $y(0)$ and the dynamical map of $y(0)$ versus $z(0)$ in Figures 6(a)

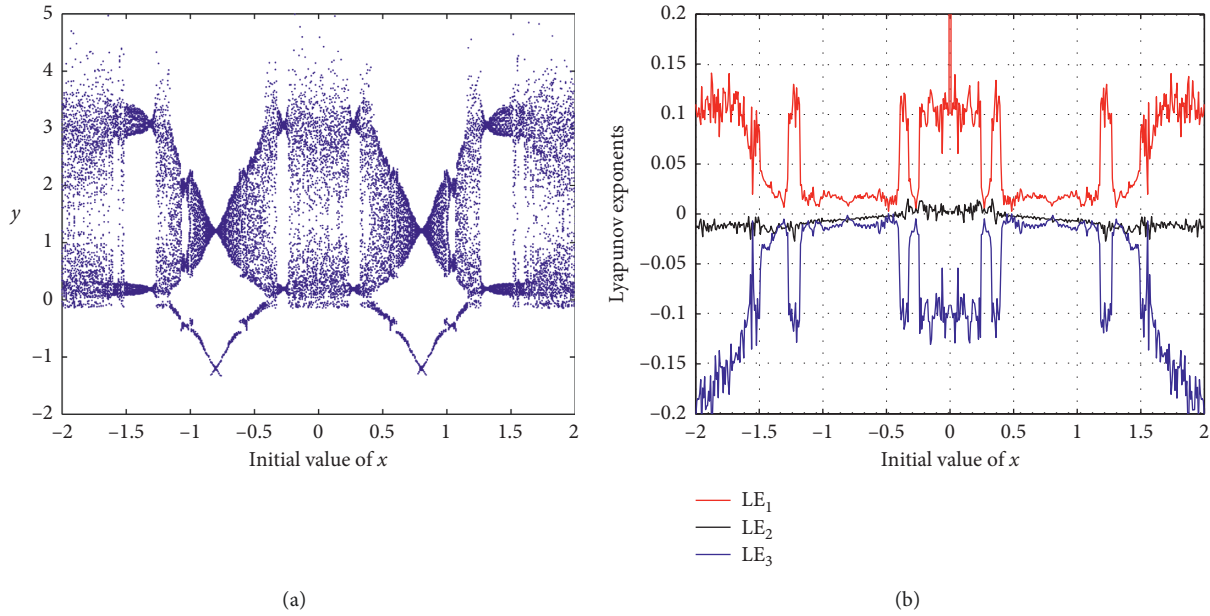


FIGURE 5: (a) Bifurcation diagram; (b) Lyapunov exponent spectrum versus $x(0)$.

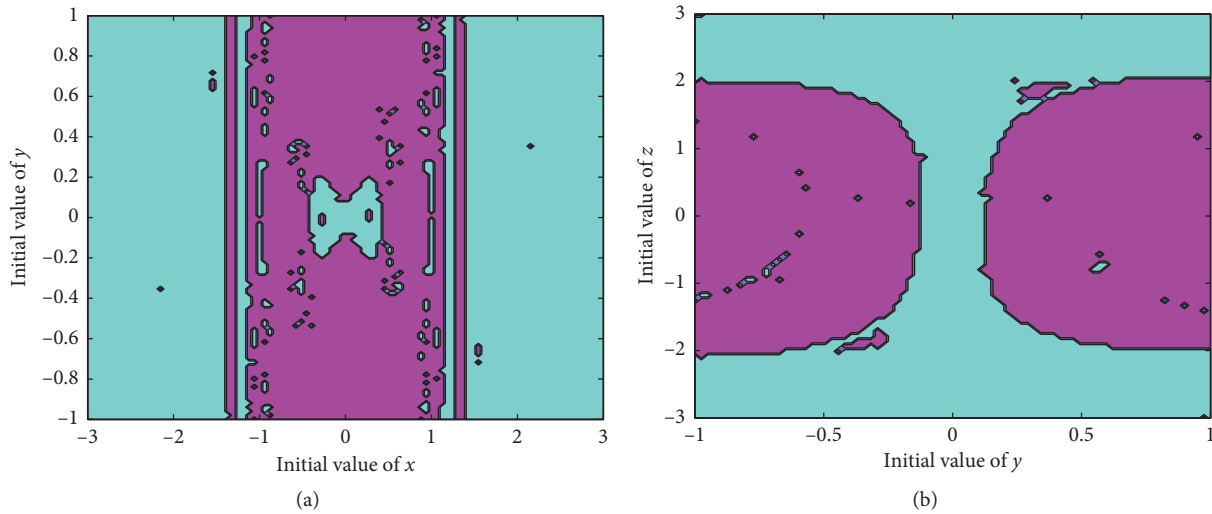


FIGURE 6: Dynamic distributions of system (1) with $a=3$, $b=-1$, $c=1$: (a) $x(0)$ versus $y(0)$ with $z(0)=0$; (b) $y(0)$ versus $z(0)$ with $x(0)=0.1$. The chaotic regions are shown in cyan and the periodic regions are shown in pink.

and 6(b), respectively. In the dynamical map, the system is chaotic in the cyan region and periodic in the pink region. Some representative coexistence attractors of symmetric distribution with respect to $x(0)$ are displayed in Figure 7.

2.3. Transient Dynamics. It is surprising to see in Figure 2(b) that a periodic window appears in the parameter region of $2.586 \leq a \leq 2.688$, but it does show the chaotic behavior in Figure 2(a). The emergence of different dynamical modes is due to the transition from the long term transient period to steady chaos with the time evolutions of system. The transient dynamics can be represented by chaotic orbit before entering the final nonchaotic behavior, and the inverse process is also correct.

Firstly, the case of system parameters $a=3$, $b=-1$, and $c=1$ and initial condition $x(0)=0.1$, $y(0)=0.15$, $z(0)=0.1$ is considered. The time trajectory in the region of $[0 \text{ s}, 800 \text{ s}]$ and the phase diagrams in two different time intervals of $[0 \text{ s}, 400 \text{ s}]$ and $[450 \text{ s}, 800 \text{ s}]$ are depicted in Figure 8, which illustrates the dynamics transformation from transient period to steady chaos.

Then we take the selection of system parameters $a=3$, $b=-1$, and $c=1$ and initial condition $x(0)=0.3$, $y(0)=0.1$, $z(0)=0.6$. The time trajectory in the region of $[0 \text{ s}, 2000 \text{ s}]$ and the phase diagrams in two different time intervals of $[0 \text{ s}, 900 \text{ s}]$ and $[1100 \text{ s}, 2000 \text{ s}]$ are depicted in Figure 9. It is observed in Figure 9 that the trajectory of system (1) starts from a quasiperiodic orbit for a long time and then it transforms into a chaotic state at $t=1050 \text{ s}$. Similarly to transient chaos, we call this dynamic phenomenon as transient quasiperiod.

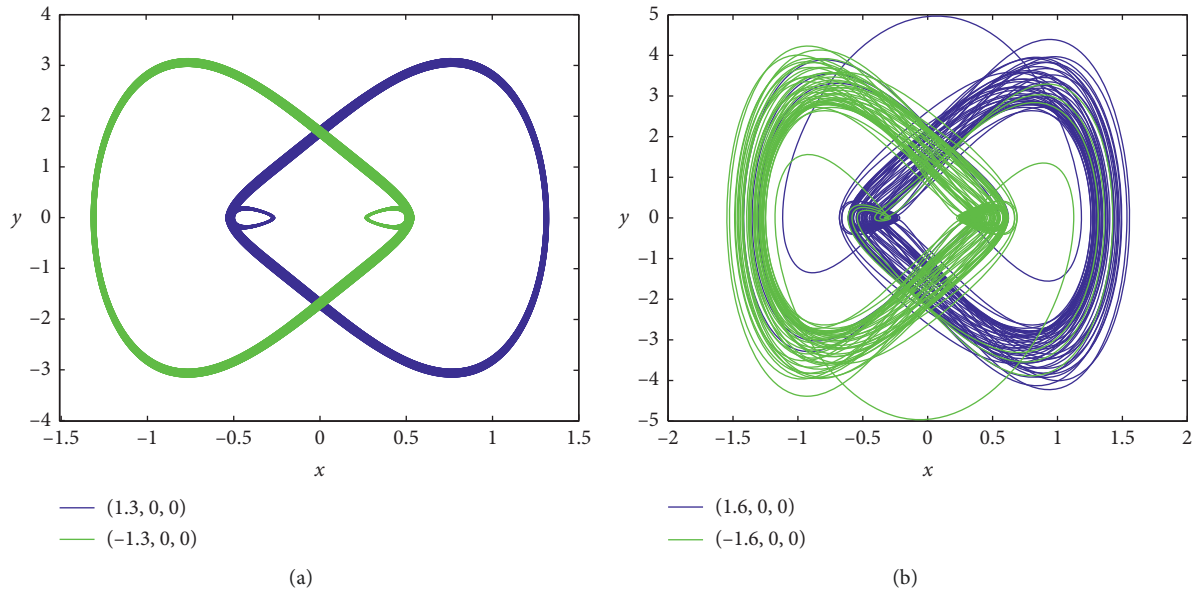


FIGURE 7: Symmetric coexisting attractors with respect to $x(0)$. (a) Period with $x(0) = 1.3$ and -1.3 ; (b) chaos with $x(0) = 1.6$ and -1.6 .

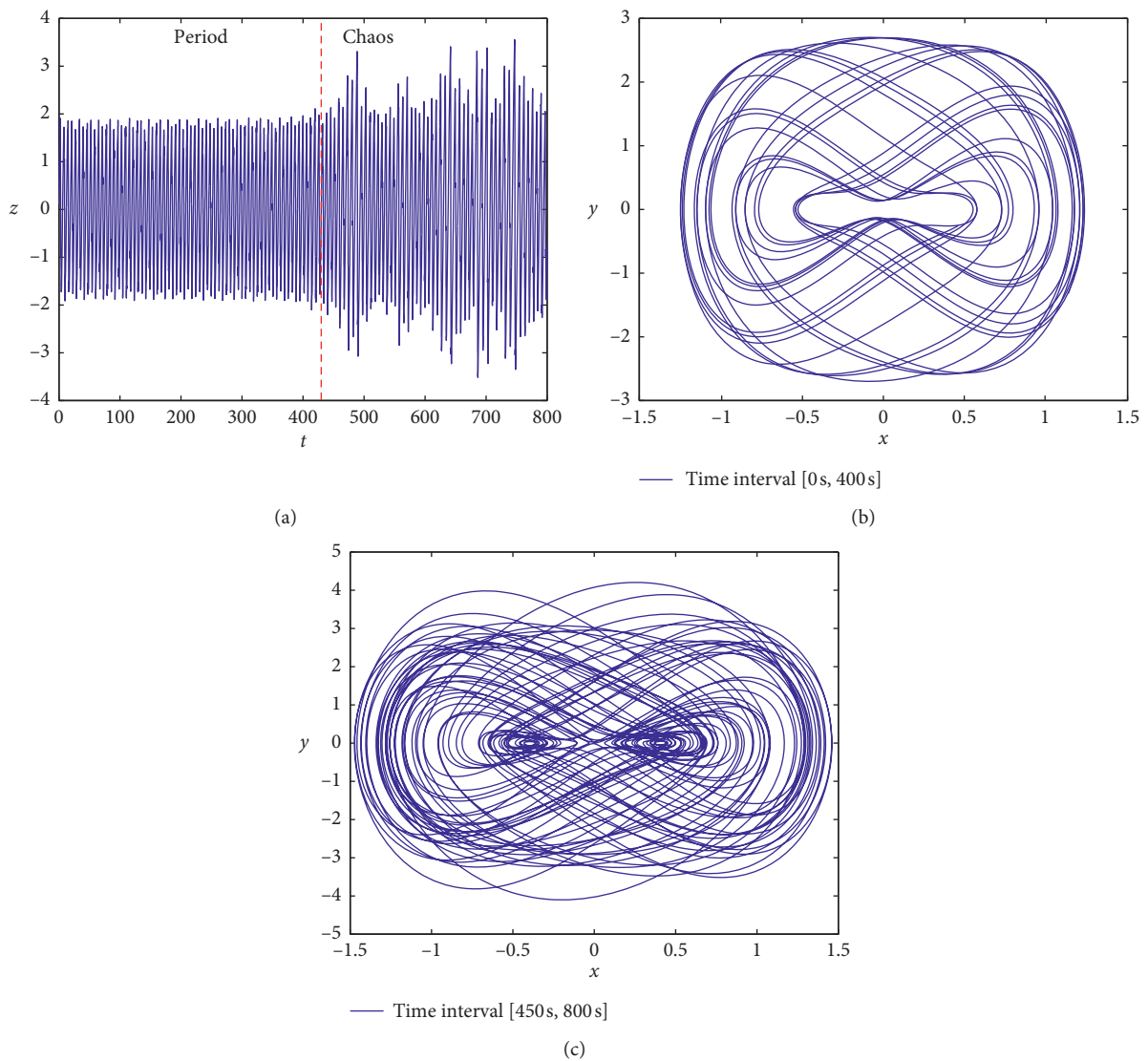


FIGURE 8: (a) Time-domain waveform of z in the region of $[0, 800]$ s; (b) the phase portrait in time interval of $[0, 400]$ s; (c) the phase portrait in time interval of $[450, 800]$ s.

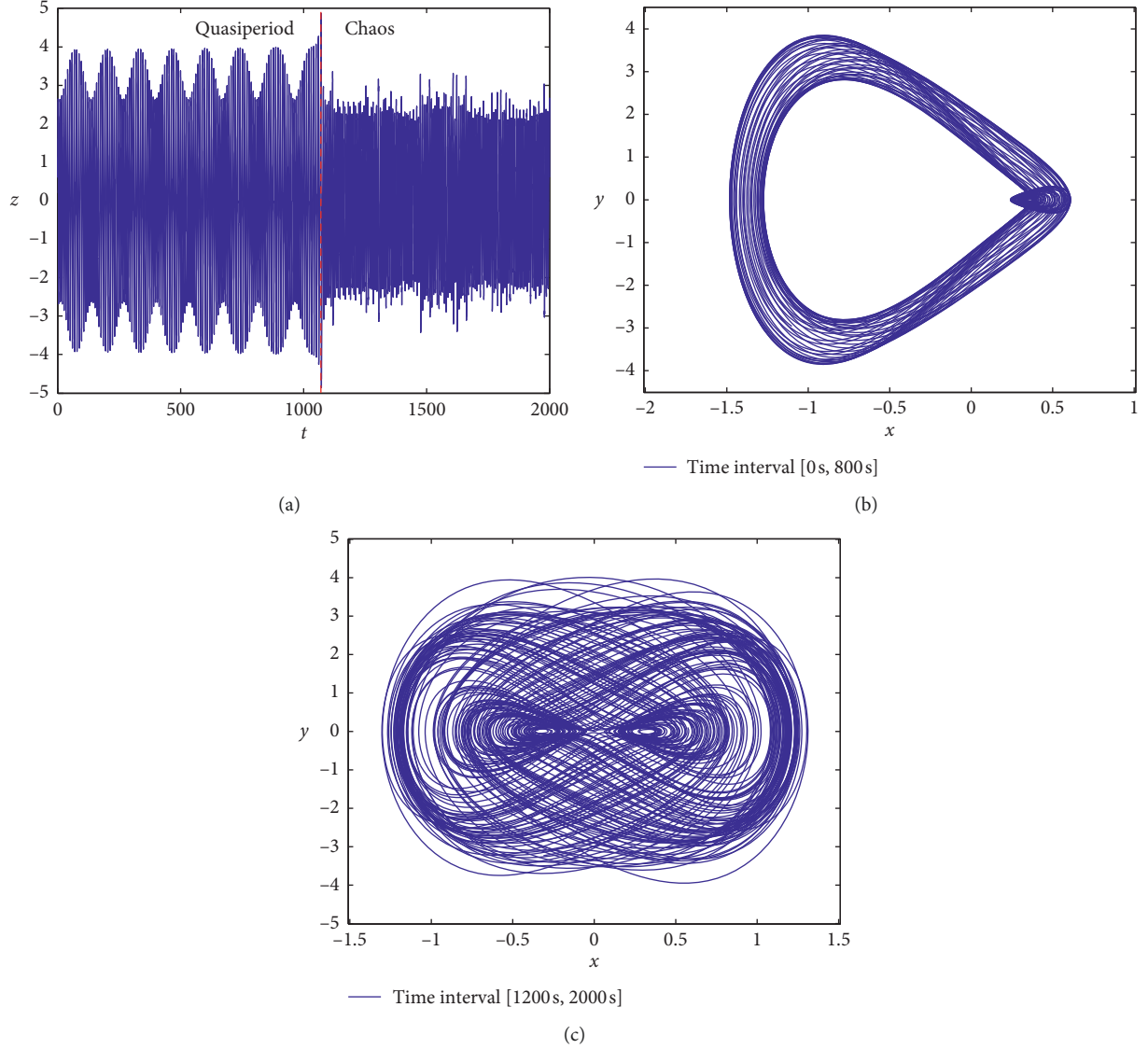


FIGURE 9: (a) Time-domain waveform of z in the region of $[0 \text{ s}, 2000 \text{ s}]$; (b) the phase portrait in time interval of $[0 \text{ s}, 900 \text{ s}]$; (c) the phase portrait in time interval of $[1100 \text{ s}, 2000 \text{ s}]$.

3. Synchronization Control of Memristor-Based Chaotic System

3.1. Synchronization Scheme. We consider the master-slave synchronization scheme for the introduced chaotic system, and the corresponding master-slave systems are described by the compact form:

$$\text{master system } \frac{dx}{dt} = f(x), \quad (2)$$

$$x = (x_1, x_2, x_3) = (x, y, z),$$

$$\text{slave system } \frac{dy}{dt} = f(y), \quad (3)$$

$$y = (y_1, y_2, y_3) = (x', y', z').$$

In which, $f(\cdot) \in R^3$ is the smooth vector field satisfying the Lipschitz condition:

$$\begin{aligned} \|f_i(x) - f_i(y)\| &\leq k \|x_i - y_i\| \leq k \|x - y\|_\infty, \\ \|x - y\|_\infty &= \max_i \|x_i - y_i\|, \\ i &= 1, 2, 3. \end{aligned} \quad (4)$$

To realize the synchronization of systems (2) and (3), we add a single linear controller to the i -th equation of the slave system, as depicted by

$$\begin{aligned} \frac{dy}{dt} &= f(y) + u_i, \\ u_i &= \mu(x_i - y_i). \end{aligned} \quad (5)$$

The synchronization error is defined by $e_i = x_i - y_i$, $i = 1, 2, 3$. Also, we construct the candidate Lyapunov function as $V = (1/2) \sum_{i=1}^3 (x_i - y_i)^2$. The time derivative of V along the synchronization error is deduced by

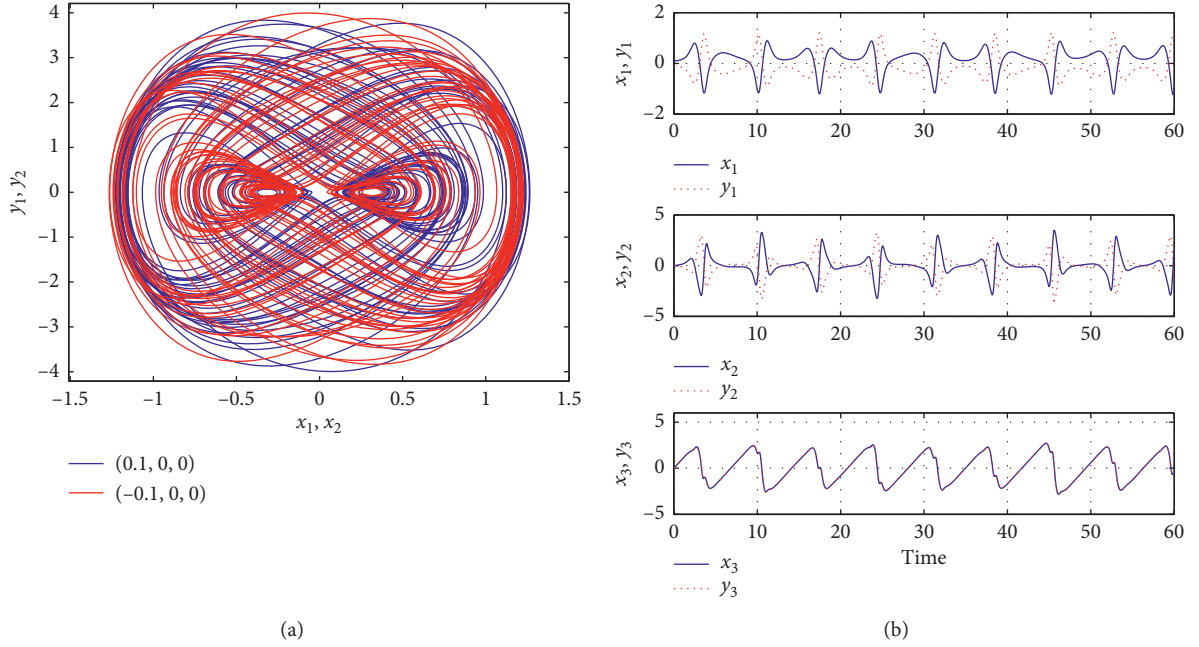


FIGURE 10: (a) Phase diagram and (b) state trajectories with $x(0) = (0.1, 0, 0)$ and $y(0) = (-0.1, 0, 0)$.

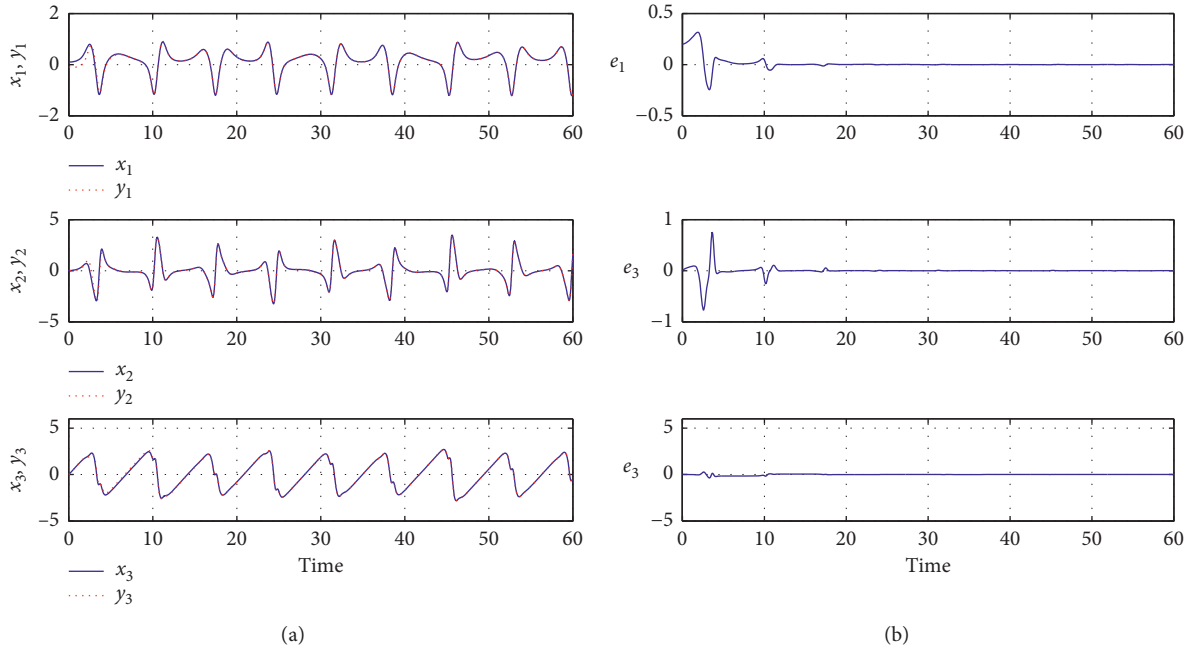


FIGURE 11: (a) Time response of the states and (b) synchronization error with $\mu = 3$, $x(0) = (0.1, 0, 0)$ and $y(0) = (-0.1, 0, 0)$.

$$\begin{aligned}
 \dot{V} &= \sum_{i=1}^3 (x_i - y_i)(\dot{x}_i - \dot{y}_i) \\
 &= \sum_{i=1}^3 (x_i - y_i)(f_i(x) - f_i(y) - u_i) \\
 &= \sum_{i=1}^3 (x_i - y_i)(f_i(x) - f_i(y)) - \mu \sum_{i=1}^3 (x_i - y_i)^2 \\
 &\leq (3k - \mu) \|x - y\|_{\infty}^2.
 \end{aligned} \tag{6}$$

When $\mu \geq 3k$, we have $\dot{V} \leq 0$. Thus, the controlled slave system will asymptotically synchronize with the master system with the simple controller $u_i = \mu(x_i - y_i)$ when $\mu \geq 3k$.

In fact, to reduce the control consumption, we can optimize the controller as

$$u_i = \mu(x_i - y_i) \cdot H(|x_i - y_i| - \varepsilon), \tag{7}$$

where ε is a small positive constant; the function $H(\cdot)$ is described as $H(z) = 1$ when $z \geq 0$ and $H(z) = 0$ when $z < 0$.

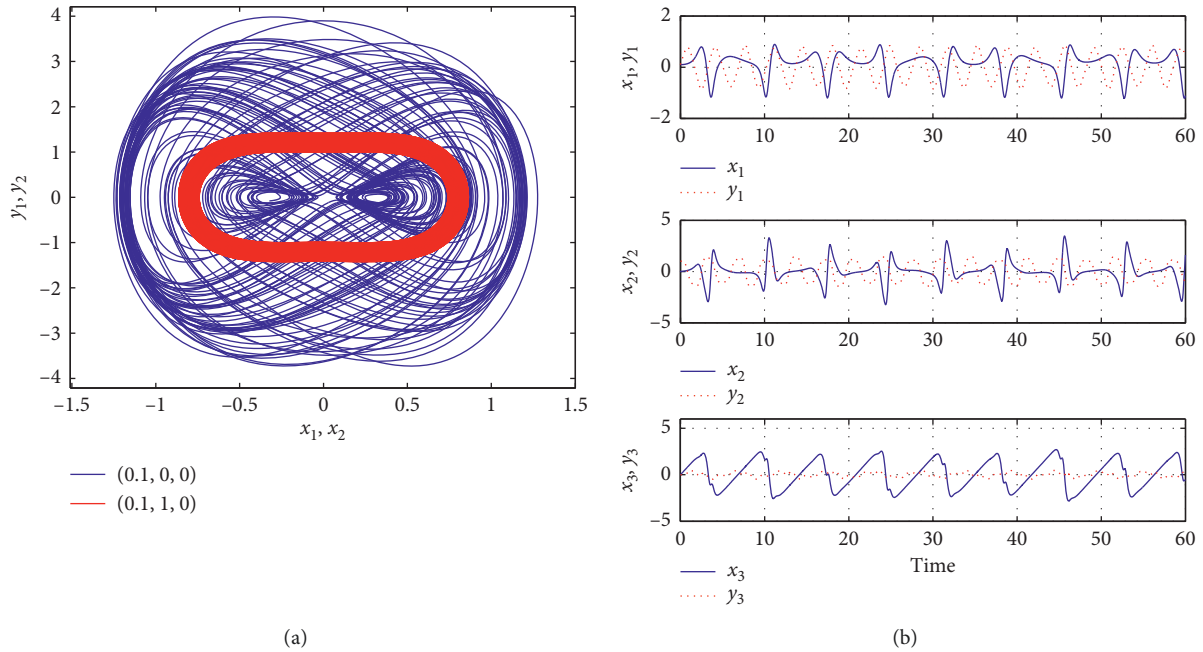


FIGURE 12: (a) Phase diagram and (b) state trajectories with $x(0) = (0.1, 0, 0)$ and $y(0) = (0.1, 1, 0)$.

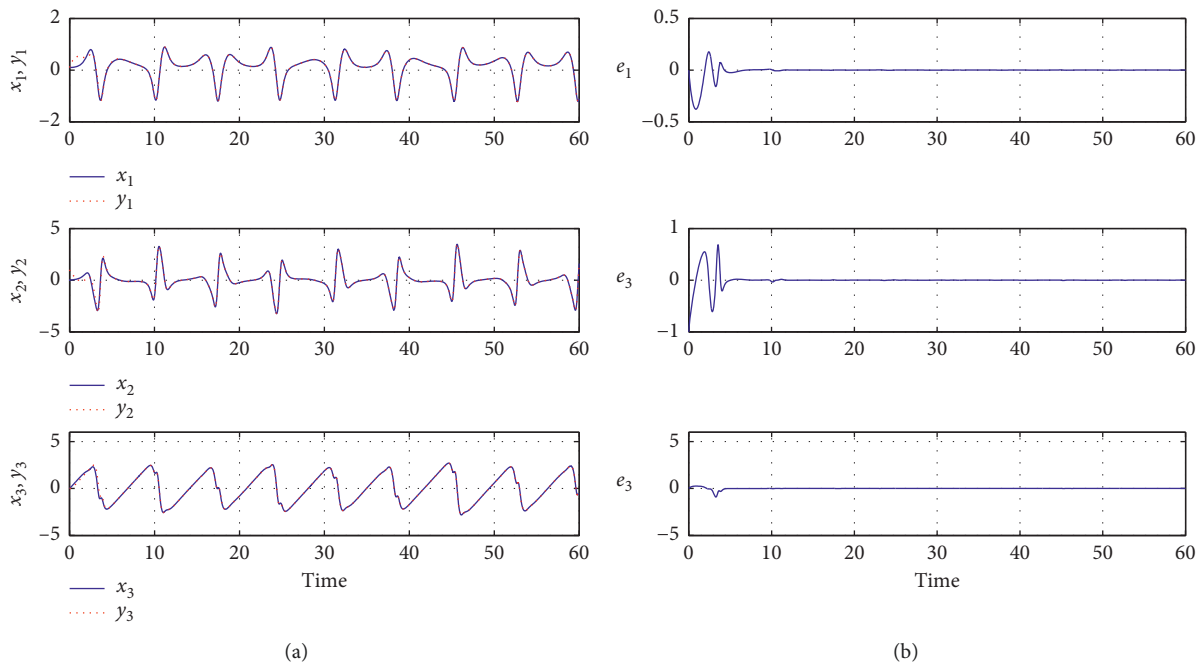


FIGURE 13: (a) Time response of the states and (b) synchronization error with $\mu=2$, $x(0) = (0.1, 0, 0)$ and $y(0) = (0.1, 1, 0)$.

The practical significance of the optimized control scheme is that one imposes the controller $\mu(x_i - y_i)$ to the slave system when $|x_i - y_i| \geq \epsilon$, but the controller does not work when $|x_i - y_i| < \epsilon$. Thus, the controller can realize the system synchronization intermittently with the adaptive mechanism, according to the characteristics of motion trajectories. Therefore, compared with continuous synchronization schemes, intermittent synchronization will reduce the amount of conveyed information, which is of significance in the practical communication since the communication channel

capacity will be reserved for more message transmission. In addition, the security of chaotic communication system will be improved due to the reduction of redundancy of synchronization information in the channel.

3.2. Numerical Simulation. We impose the controller $\mu(x_2 - y_2) \cdot H(|x_2 - y_2| - \epsilon)$ to the second term of the slave system. The system parameters are set as $a = 3$, $b = -1$, and $c = 1$.

We first choose the initial condition of system (2) as $x(0) = (0.1, 0, 0)$ with which system (2) is chaotic, and the initial states of system (4) are taken as $y(0) = (-0.1, 0, 0)$ for also displaying chaotic, as shown in Figure 10. The synchronization result is shown in Figure 11 when the controller gain μ equals 3 and ε is set to be 0.02.

Then, we also set $x(0) = (0.1, 0, 0)$ with which system (2) is chaotic, but the initial states of system (4) are taken as $y(0) = (0.1, 1, 0)$ for displaying quasiperiodic, as shown in Figure 12. The synchronization result is shown in Figure 13 when controller parameters $\mu = 2$ and $\varepsilon = 0.02$.

We know that no matter what the dynamic state of the memristive system is, the synchronization control of the memory system can be easily realized by adopting the designed method.

4. Conclusions

In this paper, we introduce a memristor-based chaotic system with no equilibrium. Various tools including phase diagram, time-domain trajectory, bifurcation diagram, and Lyapunov exponent are exploited to establish the connection between the system parameters and dynamical behaviors. It is found that the reported system exhibits complex dynamics such as coexisting bifurcation, multistability, symmetric coexisting attractors, and transient dynamics, which is helpful for the security improvement of encryption and communication due to the difficulty of reproducing the accurate dynamics. Then, a simple control scheme with single linear couple is developed to achieve complete synchronization for the memristive system. Since the output signal is transmitted intermittently to the receiver system with the adaptive mechanism, the communication channel capacity will be reserved for more message transmission. Also, the security of chaotic communication system will be improved for the reduction of redundancy of synchronization information in the channel.

Data Availability

The data used to support the findings of this study are included within the article.

Conflicts of Interest

The authors declare that there are no conflicts of interest regarding the publication of this paper.

Acknowledgments

This work was supported by the Hunan Provincial Natural Science Foundation of China (no. 2019JJ40109); Research Foundation of Education Bureau of Hunan Province of China (no. 18A314); and Science and Technology Program of Hunan Province (no. 2016TP1021).

References

- [1] L. Chua, "Memristor—the missing circuit element," *IEEE Transactions on Circuit Theory*, vol. 18, no. 5, pp. 507–519, 1971.

- [2] D. B. Strukov, G. S. Snider, D. R. Stewart, and R. S. Williams, "The missing memristor found," *Nature*, vol. 453, no. 7191, pp. 80–83, 2008.
- [3] Q. Zhao, C. Wang, and X. Zhang, "A universal emulator for memristor, memcapacitor, and meminductor and its chaotic circuit," *Chaos: An Interdisciplinary Journal of Nonlinear Science*, vol. 29, no. 1, Article ID 013141, 2019.
- [4] V.-T. Pham, S. Vaidyanathan, C. K. Volos, S. Jafari, N. V. Kuznetsov, and T. M. Hoang, "A novel memristive time-delay chaotic system without equilibrium points," *The European Physical Journal Special Topics*, vol. 225, no. 1, pp. 127–136, 2016.
- [5] D. Ma, G. Wang, C. Han, Y. Shen, and Y. Liang, "A memristive neural network model with associative memory for modeling affections," *IEEE Access*, vol. 6, pp. 61614–61622, 2018.
- [6] H. Bao, N. Wang, H. Wu, Z. Song, and B. Bao, "Bi-stability in an improved memristor-based third-order Wien-bridge oscillator," *IETE Technical Review*, vol. 36, no. 2, pp. 109–116, 2019.
- [7] F. Corinto and M. Forti, "Memristor circuits: bifurcations without parameters," *IEEE Transactions on Circuits and Systems I: Regular Papers*, vol. 64, no. 6, pp. 1540–1551, 2017.
- [8] M. Itoh and L. O. Chua, "Memristor oscillators," *International Journal of Bifurcation and Chaos*, vol. 18, no. 11, pp. 3183–3206, 2008.
- [9] T. F. Fozzin, K. Srinivasan, J. Kengne, and F. B. Pelap, "Coexisting bifurcations in a memristive hyperchaotic oscillator," *AEU-international Journal of Electronics and Communications*, vol. 90, pp. 110–122, 2018.
- [10] X. Bi-Rong, "A simplest parallel chaotic system of memristor," *Acta Physica Sinica*, vol. 62, no. 19, pp. 99–106, 2013.
- [11] Y. Zhao, Y. Jiang, J. Feng, and L. Wu, "Modeling of memristor-based chaotic systems using nonlinear Wiener adaptive filters based on backslash operator," *Chaos, Solitons & Fractals*, vol. 87, pp. 12–16, 2016.
- [12] L. Teng, H. H. C. Iu, X. Wang, and X. Wang, "Chaotic behavior in fractional-order memristor-based simplest chaotic circuit using fourth degree polynomial," *Nonlinear Dynamics*, vol. 77, no. 1-2, pp. 231–241, 2014.
- [13] M. Guo, W. Yang, Y. Xue et al., "Multistability in a physical memristor-based modified Chua's circuit," *Chaos: An Interdisciplinary Journal of Nonlinear Science*, vol. 29, no. 4, Article ID 043114, 2019.
- [14] Y.-B. Zhao, C.-K. Tse, J.-C. Feng, and Y.-C. Guo, "Application of memristor-based controller for loop filter design in charge-pump phase-locked loops," *Circuits, Systems, and Signal Processing*, vol. 32, no. 3, pp. 1013–1023, 2013.
- [15] G. Peng and F. Min, "Multistability analysis, circuit implementations and application in image encryption of a novel memristive chaotic circuit," *Nonlinear Dynamics*, vol. 90, no. 3, pp. 1607–1625, 2017.
- [16] X. Hu, S. Duan, L. Wang, and X. Liao, "Memristive crossbar array with applications in image processing," *Science China Information Sciences*, vol. 55, no. 2, pp. 461–472, 2012.
- [17] W. Wang, X. Yu, X. Luo, and J. Kurths, "Synchronization control of memristive multidirectional associative memory neural networks and applications in network security communication," *IEEE Access*, vol. 6, pp. 36002–36018, 2018.
- [18] V.-T. Pham, A. Akgul, C. Volos, S. Jafari, and T. Kapitaniak, "Dynamics and circuit realization of a no-equilibrium chaotic system with a boostable variable," *AEU—International Journal of Electronics and Communications*, vol. 78, pp. 134–140, 2017.

- [19] S. Jafari, A. Ahmadi, A. J. M. Khalaf, H. R. Abdolmohammadi, V.-T. Pham, and F. E. Alsaadi, "A new hidden chaotic attractor with extreme multi-stability," *AEU—International Journal of Electronics and Communications*, vol. 89, pp. 131–135, 2018.
- [20] D. Cafagna and G. Grassi, "Chaos in a new fractional-order system without equilibrium points," *Communications in Nonlinear Science and Numerical Simulation*, vol. 19, no. 9, pp. 2919–2927, 2014.
- [21] G. A. Leonov, N. V. Kuznetsov, and V. I. Vagitsev, "Hidden attractor in smooth Chua systems," *Physica D: Nonlinear Phenomena*, vol. 241, no. 18, pp. 1482–1486, 2012.
- [22] S. Jafari and J. C. Sprott, "Simple chaotic flows with a line equilibrium," *Chaos, Solitons & Fractals*, vol. 57, pp. 79–84, 2013.
- [23] Z. Wei and Q. Yang, "Dynamical analysis of the generalized Sprott C system with only two stable equilibria," *Nonlinear Dynamics*, vol. 68, no. 4, pp. 543–554, 2012.
- [24] X. Wang and G. Chen, "A chaotic system with only one stable equilibrium," *Communications in Nonlinear Science and Numerical Simulation*, vol. 17, no. 3, pp. 1264–1272, 2012.
- [25] V.-T. Pham, S. Jafari, C. Volos, A. Giakoumis, S. Vaidyanathan, and T. Kapitaniak, "A chaotic system with equilibria located on the rounded square loop and its circuit implementation," *IEEE Transactions on Circuits and Systems II: Express Briefs*, vol. 63, no. 9, pp. 878–882, 2016.
- [26] V.-T. Pham, C. Volos, S. Jafari, S. Vaidyanathan, T. Kapitaniak, and X. Wang, "A chaotic system with different families of hidden attractors," *International Journal of Bifurcation and Chaos*, vol. 26, no. 8, Article ID 1650139, 2016.
- [27] L. M. Pecora and T. L. Carroll, "Synchronization in chaotic systems," *Physical Review Letters*, vol. 64, no. 8, pp. 821–824, 1990.
- [28] C. Li, "Tracking control and generalized projective synchronization of a class of hyperchaotic system with unknown parameter and disturbance," *Communications in Nonlinear Science and Numerical Simulation*, vol. 17, no. 1, pp. 405–413, 2012.
- [29] H. Sang and J. Zhao, "Exponential synchronization and L_2 -gain analysis of delayed chaotic neural networks via intermittent control with actuator saturation," *IEEE Transactions on Neural Networks and Learning Systems*, pp. 1–13, 2019.
- [30] C. Yang, L. Huang, and Z. Cai, "Fixed-time synchronization of coupled memristor-based neural networks with time-varying delays," *Neural Networks*, vol. 116, pp. 101–109, 2019.
- [31] C. Li, Y. Tong, H. Li, and K. Su, "Adaptive impulsive synchronization of a class of chaotic and hyperchaotic systems," *Physica Scripta*, vol. 86, no. 5, Article ID 055003, 2012.
- [32] R. G. Li and H. N. Wu, "Adaptive synchronization control with optimization policy for fractional-order chaotic systems between 0 and 1 and its application in secret communication," *ISA transactions*, vol. 92, pp. 35–48, 2019.
- [33] W. G. Hoover, "Remark on "Some simple chaotic flows"," *Physical Review E*, vol. 51, no. 1, pp. 759–760, 1995.

Research Article

Influence of Piezoelectric Performance on Nonlinear Dynamic Characteristics of MFC Shells

Xiangying Guo ^{1,2}, Pan Jiang,^{1,2} and Dongxing Cao ^{1,2}

¹College of Mechanical Engineering, Beijing University of Technology, Beijing 100124, China

²Beijing Key Laboratory of Nonlinear Vibrations and Strength of Mechanical Structures, Beijing 100124, China

Correspondence should be addressed to Dongxing Cao; caostar@bjut.edu.cn

Received 27 June 2019; Accepted 23 August 2019; Published 9 October 2019

Guest Editor: Viet-Thanh Pham

Copyright © 2019 Xiangying Guo et al. This is an open access article distributed under the Creative Commons Attribution License, which permits unrestricted use, distribution, and reproduction in any medium, provided the original work is properly cited.

Based on the structures of unmanned aerial vehicle (UAV) wings, nonlinear dynamic analysis of macrofiber composite (MFC) laminated shells is presented in this paper. The effects of piezoelectric properties and aerodynamic forces on the dynamic stability of the MFC laminated shell are studied. Firstly, under the flow condition of ideal incompressible fluid, the thin airfoil theory is employed to calculate the effects of the mean camber line to obtain the circulation distribution of the wings in subsonic air flow. The steady aerodynamic lift on UAV wings is derived by using the Kutta–Joukowski lift theory. Then, considering the geometric nonlinearity and piezoelectric properties of the MFC material, the nonlinear dynamic model of the MFC laminated shell is established with Hamilton's principles and the Galerkin method. Next, the effects of electric field, external excitation force, and nonlinear parameters on the stability of the system are studied under 1 : 1 internal resonance and the effects of material parameters on the natural frequency of the structure are also analyzed. Furthermore, the influence of the aerodynamic forces and electric field on the nonlinear dynamic responses of MFC laminated shells is discussed by numerical simulation. The results indicate that the electric field and external excitation have great influence on the structural dynamic responses.

1. Introduction

MFC material, which was invented by NASA in 1996, has great application prospect in many engineering structures, especially in aviation and aerospace field. MFC materials are composed of two main parts: rectangular piezoceramic fibers and interdigitated electrodes. The sheet of aligned rectangular piezoceramic fibers is used to improve flexibility and damage tolerance in comparison with the traditional monolithic piezoceramic. Interdigitated electrode patterns are attached to the top and bottom of a polyamide film to permit in-plane poling and actuation of the piezoelectric fibers. MFCs mainly have two different types, namely, d_{31} and d_{33} modes, based on different laying directions of the piezoelectric fiber material.

Because of the great potential of piezoelectric composite materials, piezoelectric materials become the most commonly used smart materials in active vibration and noise

control, energy harvest, and so on. Tan et al. [1] studied the dynamic characteristics of a beam system with active piezoelectric fiber-reinforced composite layers. Then, more researches are reported on the MFC materials as sensors and actuators in different structures to adjust the deformation or vibration of the system, such as rotating composite thin-walled beams [2], thin beams [3], cylindrical shells [4], and smart composite plates [5].

Recently, the dynamic behaviors of the classical MFC structure are attracting more and more scholars from all over the world. Park and Kim [6] investigated the material properties of MFCs by using classical lamination theory and uniform field model. Bilgen et al. [7] built a linear distributed parameter electromechanical model for frequency-response analysis of MFC actuated clamped-free thin beams and compared their results with experimental results. Cook and Vel [8, 9] considered different stresses of a simply supported laminated plate consisting of an MFC shear actuator

sandwiched between graphite/polymer layers, which were subjected to an electric field perpendicular to the poling direction.

The nonlinear dynamical simulations considering large displacements are taken into account for different MFC structures, such as circular plates [10], functionally graded plates [11], laminated composite plates [12], and thin-walled structures [13]. The effects of different parameters of the structures on the natural frequencies and vibration modes are discussed in these articles. Similarly, actuation properties of MFCs under strong voltages were investigated by Williams et al. [14] through using the theoretical piezoelectric constitutive model with higher-order electric field. Zhang and Shen [15] conducted the three-dimensional analysis for rectangular 1–3 piezoelectric fiber-reinforced composite laminates with the interdigitated electrodes under electromechanical loadings. Belouettar et al. [16] investigated active control of nonlinear vibrations of piezoelectric-elastic-piezoelectric sandwich beams using the method of harmonic balance.

Rafiee et al. [17] investigated the nonlinear vibration and dynamic behavior of simply supported piezoelectric functionally graded shells under electrical, thermal, mechanical, and aerodynamic loadings. Hosseini et al. [18] analyzed the nonlinear free and forced vibrations of cantilever structures resting on a nonlinear elastic foundation with a piecewise piezoelectric actuator layer bonded on the top surface. The effects of various parameters on the free and forced nonlinear responses of the system were discussed. Mareishi et al. [19] considered the geometric nonlinearity of the piezoelectric fiber-reinforced laminated composite beams and analyzed the nonlinear frequencies of the beams with simply supported and clamped boundary conditions. Rafiee et al. [20] provided numerical simulation about the nonlinear dynamics of piezoelectric nanotubes/fibers/polymer multi-scale composite plates, including the effects of different parameters of single-walled carbon nanotubes (SWCNTs) and multiwalled carbon nanotubes (MWCNTs) on the linear and nonlinear natural frequencies. Ninh and Bich [21] studied the electrothermal mechanical vibration of functionally graded carbon nanotube-reinforced composite (FG-CNTRC) cylindrical shells by the numerical analytical method. Lu et al. [22] investigated the nonlinear dynamic characteristics of the time-varying piezoelectric laminated composite plate.

In regard to the analysis methods for laminated composite plates with integrated piezoelectric actuators, several studies have been performed using the classical lamination theory [23], first-order shear deformation theory [24], higher-order theories [25], and the finite element method [26]. Moreover, Prasath and Arockiarajan [27, 28] studied the effect of bonding layer volume fraction on the effective thermo-electro-elastic constants of both d_{33} - and d_{31} -type MFCs by using the finite element method and experiments. Zhang et al. [29] investigated the structural deformation of composite laminated thin-walled structures bonded with orthotropic MFCs by establishing the finite element (FE) model based on linear piezoelectric constitutive equations.

There are many researches on the aerodynamic force of different structures. Kouchakzadeh et al. [30] analyzed the

aerodynamic modeling of structures by applying the classical plate theory along with the von Karman nonlinear strains and linear piston theory. Li et al. [31] used the piezoelectric material to increase the flutter velocities of the supersonic beams and adopted the supersonic piston theory to evaluate the aerodynamic pressure. Kuo [32] investigated the influence of variable fiber spacing on the supersonic flutter of rectangular composite plates and later also [33] discussed the effects of hybrid fiber distribution on the critical buckling temperature, natural frequencies, and flutter boundary of composite laminates by using the finite element method. Zhang et al. [34] considered the aerodynamics of a deploying wing in subsonic air flow and investigated the nonlinear dynamic behaviors of deploying wings in numerical simulations.

Motivated by the above considerations, the nonlinear dynamic analysis of the MFC laminated shell subjected to aerodynamic force is presented here. The effects of piezoelectric properties and aerodynamic force on the dynamic stability of the structure are studied. Nonlinear dynamic equations of the cantilever MFC laminated shell are built based on UAV wings. The effect of different forces on the dynamic behaviors of MFC laminated shells is investigated in numerical simulation. Moderating effects of piezoelectric performance on the stability of the system are also presented here, which would provide guidance in controlling strategy of the nonlinear vibration for UAV wings.

2. Derivation of the Aerodynamic Force on the Deploying Wing

Considering the work situation of UAVs in subsonic air flow, the thin airfoil theory is applied here to calculate aerodynamic forces. Based on the thin airfoil theory, the potential function of the flow field can be divided into two parts: one is the potential function of the original uniform flow and the other is the disturbance potential function generated by the perturbation of the airfoil convection field, which also satisfies Laplace equations. Moreover, the perturbed potential function can be obtained according to the boundary condition of the typical airfoil and the infinite boundary condition of velocity approaching zero, as shown in Figure 1.

Therefore, the boundary condition can be given as follows:

$$\alpha + \frac{V_n}{V_\infty} = \frac{dy}{dx}, \quad (1)$$

where α is the angle of attack, V_n is the normal induced velocity, V_∞ is the uniform flow velocity in direction α , and dy/dx means the slope at any point in the middle arc of the airfoil.

Furthermore, the disturbance potential function equations and boundary conditions can be expressed in terms of the airfoil thickness and velocity potential caused by the camber curvature and attacked angle. When the curvature of the camber line is very small, the vorticity gradient in the y

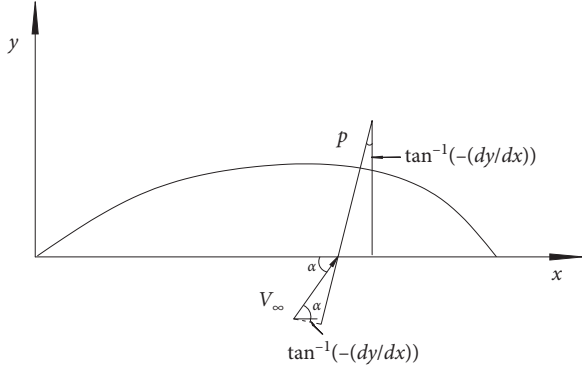


FIGURE 1: Normal velocity of the free stream in the middle curve.

direction is small with respect to a small camber or curvature, as shown in Figure 2.

Therefore, the total circulation of the entire airfoil is expressed as follows:

$$\Gamma = \int_0^c \gamma d\xi, \quad (2)$$

and the boundary condition is transformed into the following form:

$$\alpha + \frac{1}{V_{\infty}} \int_0^c \frac{\gamma(\xi)d\xi}{2\pi(\xi-x)} = \frac{dy}{dx}, \quad (3)$$

where $\gamma(\xi)$ can be expanded to a Fourier series of $\gamma(\theta)$:

$$\gamma(\theta) = 2V_{\infty} \left(A_0 \cot\left(\frac{\theta}{2}\right) + \sum_1^{\infty} A_n \sin(n\theta) \right). \quad (4)$$

Moreover, the boundary conditions are obtained as follows through the transformation $x = (b/2)(1 - \cos \Theta)$:

$$\alpha - A_0 = \frac{1}{\pi} \int_0^{\pi} \frac{dy}{dx} d\Theta, \quad (5a)$$

$$A_n = \frac{2}{\pi} \int_0^{\pi} \left(\frac{dy}{dx} \right) \cos(n\Theta) d\Theta. \quad (5b)$$

Therefore, the total circulation can be rewritten as

$$\begin{aligned} \Gamma = \int_0^c \gamma(x)dx &= V_{\infty} b \int_0^{\pi} \left[A_0 (1 + \cos \Theta) \right. \\ &\left. + \sum_1^{\infty} A_n \sin(n\Theta) \sin \Theta \right] = \pi \alpha b V_{\infty}, \end{aligned} \quad (6)$$

and the lift per unit wingspan is expressed as

$$L = \pi \alpha \rho b V_{\infty}^2. \quad (7)$$

Finally, the total lift on wingspan can be obtained according to the typical airfoil shape modeled in the following sections.

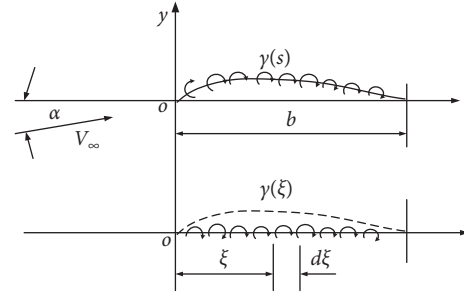


FIGURE 2: Circulation distribution along the airfoil.

3. Mechanical Model

Generally, the induced strain of the $d33$ piezoelectric constant is larger than that of the $d31$ piezoelectric constant for MFC materials. Therefore, a $d33$ MFC laminated hyperbolic shell is considered here to establish the mechanical model of the high-aspect-ratio wings for UAVs. The cylindrical coordinate system is described here with curvatures α and β on the middle surface and perpendicular to the middle surface of the shell, as shown in Figure 3. The Cartesian coordinate system $Oxyz$ is located in the tangent plane of the thin shell. Geometric dimensions of the shell are the lengths a and b and the thickness h , and the principal radii of the curvatures are R_3 and R_4 . The displacements of an arbitrary point within the shell are expressed as u , v , and w , respectively. w is taken as a positive vector going outward from the center of the smallest radius of the curvature. The shell is subjected to the aerodynamic force as $q = f \cos(\Omega_2 t)$. A dynamic electric field is expressed as $E = E \cos(\Omega_1 t)$ and applied in the longitudinal direction of the piezoelectric fibers, as shown in Figure 4.

All piezoelectric fibers are considered to be poled in the α and β directions, which can be assumed that out-of-plane electric fields vanish (that is, $e_{33} = 0$). Therefore, three sets of material coefficients are used to address the constitutive characteristics of the mechanical and electrical fields as well as the coupling between these fields, as follows:

$$\begin{aligned} \sigma_p &= C_{pq} \varepsilon_q - e_{kp} E_k, \\ D_i &= e_{iq} \varepsilon_q + k_{ik} E_k, \end{aligned} \quad (8)$$

where E_k is the electric field intensity, σ_p is the stress, ε_q is the strain, C_{pq} is the coefficient of elasticity, D_i is the electric displacement, and e_{kp} and k_{ik} represent the piezoelectric constants.

Using the nonlinear von Karman's geometric relationship for the thin shell, the strain can be expressed as

$$\begin{aligned} \varepsilon_1 &= \varepsilon_1^0 + \eta \varepsilon_1^1 + \eta^3 \varepsilon_1^2, \\ \varepsilon_2 &= \varepsilon_2^0 + \eta \varepsilon_2^1 + \eta^3 \varepsilon_2^2, \\ \varepsilon_4 &= \varepsilon_4^0 + \eta^2 \varepsilon_4^1, \\ \varepsilon_5 &= \varepsilon_5^0 + \eta^2 \varepsilon_5^1, \\ \varepsilon_6 &= \varepsilon_6^0 + \eta \varepsilon_6^1 + \eta^3 \varepsilon_6^2, \end{aligned} \quad (9)$$

where ε_1^0 , ε_1^1 , and ε_1^2 are described as

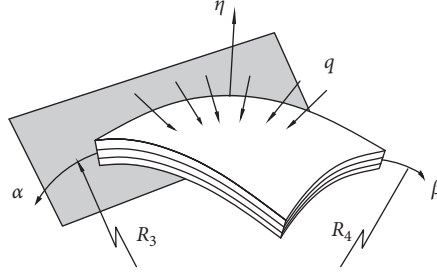


FIGURE 3: Model of the MFC thin shell.

$$\begin{aligned}
 \varepsilon_1^0 &= \frac{\partial u_0}{\partial x} + \frac{w_0}{R_3} + \frac{1}{2} \left(\frac{\partial w_0}{\partial x} \right)^2, \\
 \varepsilon_1^1 &= \frac{\partial \phi_1}{\partial x}, \\
 \varepsilon_1^2 &= -c_1 \left(\frac{\partial \phi_1}{\partial x} + \frac{\partial^2 w_0}{\partial x^2} - \frac{1}{R_3} \frac{\partial u_0}{\partial x} \right), \\
 \varepsilon_2^0 &= \frac{\partial v_0}{\partial y} + \frac{w_0}{R_4} + \frac{1}{2} \left(\frac{\partial w_0}{\partial y} \right)^2, \\
 \varepsilon_2^1 &= \frac{\partial \phi_2}{\partial y}, \\
 \varepsilon_2^2 &= -c_1 \left(\frac{\partial \phi_2}{\partial y} + \frac{\partial^2 w_0}{\partial y^2} - \frac{1}{R_4} \frac{\partial v_0}{\partial y} \right), \\
 \varepsilon_4^0 &= \phi_2 + \frac{\partial w_0}{\partial y} - \frac{v_0}{R_4}, \\
 \varepsilon_4^1 &= -c_2 \left(\phi_2 + \frac{\partial w_0}{\partial y} - \frac{v_0}{R_4} \right), \\
 \varepsilon_5^0 &= \phi_1 + \frac{\partial w_0}{\partial x} - \frac{u_0}{R_4}, \\
 \varepsilon_5^1 &= -c_2 \left(\phi_1 + \frac{\partial w_0}{\partial x} - \frac{u_0}{R_3} \right), \\
 \varepsilon_6^0 &= \frac{\partial u_0}{\partial y} + \frac{\partial v_0}{\partial x} + \frac{\partial w_0}{\partial x} \frac{\partial w_0}{\partial y}, \\
 \varepsilon_6^1 &= \frac{\partial \phi_1}{\partial y} + \frac{\partial \phi_2}{\partial x}, \\
 \varepsilon_6^2 &= -c_1 \left(\frac{\partial \phi_1}{\partial y} + \frac{\partial \phi_2}{\partial x} + 2 \frac{\partial^2 w_0}{\partial x \partial y} - \frac{1}{R_3} \frac{\partial u_0}{\partial y} - \frac{1}{R_4} \frac{\partial v_0}{\partial x} \right).
 \end{aligned} \tag{10}$$

The Lamé coefficients of the shells A_1 and A_2 are expressed as

$$\begin{aligned}
 A_1 &= a_1 \left(1 + \frac{\eta}{R_3} \right) = \sqrt{\Lambda_{11}}, \\
 A_2 &= a_2 \left(1 + \frac{\eta}{R_4} \right) = \sqrt{\Lambda_{22}},
 \end{aligned} \tag{11}$$

where a_i (1, 2) is the surface tensor of the shell.

The displacement of an arbitrary point in the composite shell can be expressed as R and be calculated as follows:

$$dR = \sqrt{\Lambda_{11}} d\alpha + \sqrt{\Lambda_{22}} d\beta + \hat{n} d\eta, \tag{12}$$

where \hat{n} is the unit vector perpendicular to the middle plane of the shell, which is expressed as follows:

$$\hat{n} = \frac{g_1 \times g_2}{a_1 a_2}. \tag{13}$$

Here, g_i (1, 2) is the vector tangent to the cylindrical coordinate axis.

Since the following analysis is carried out in the Cartesian coordinate system, it needs the relations between the cylindrical coordinate system and the Cartesian coordinate system:

$$\begin{Bmatrix} dx \\ dy \\ dz \end{Bmatrix} = \begin{bmatrix} a_1 & 0 & 0 \\ 0 & a_2 & 0 \\ 0 & 0 & 1 \end{bmatrix} \begin{Bmatrix} d\alpha \\ d\beta \\ d\eta \end{Bmatrix}. \tag{14}$$

The displacement field at an arbitrary point in the composite shell is given as follows based on Reddy's third-order theory:

$$u = u_0(x, y, t) + z\phi_1(x, y, t) - \frac{4}{3h^2} z^3 \left(\phi_1 + \frac{\partial w_0}{\partial \alpha} \right), \tag{15a}$$

$$v = v_0(x, y, t) + z\phi_2(x, y, t) - \frac{4}{3h^2} z^3 \left(\phi_2 + \frac{\partial w_0}{\partial \beta} \right), \tag{15b}$$

$$w = w_0(x, y, t), \tag{15c}$$

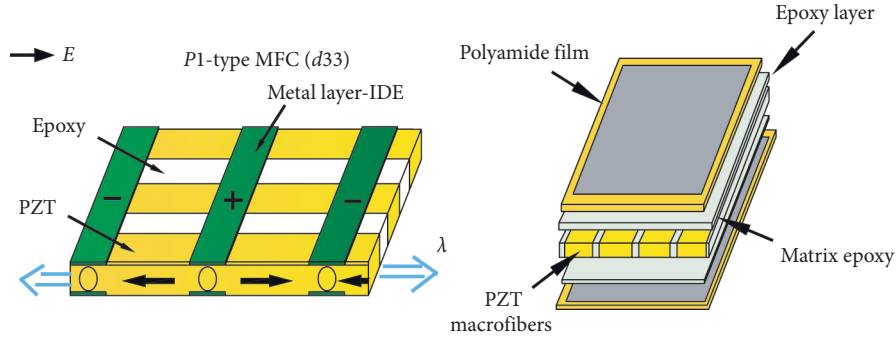


FIGURE 4: MFC-d33 material.

where u_0 , v_0 , and w_0 are the original displacements at the midplane of the MFC shell in the Cartesian coordinate directions and ϕ_1 and ϕ_2 represent the rotations of transverse normal at the midplane about the y and x axes.

The aerodynamic force in the shell structure can be calculated as follows:

$$q = \int_l L ds = \pi \alpha \rho b V_\infty^2 a. \quad (16)$$

Substituting these transformations into equations (15a)–(15c) and applying Hamilton's principle, the non-linear governing equations of motion in terms of generalized displacements for the MFC thin shell can be obtained as follows:

$$\begin{aligned} & -a_{11} \frac{\partial^3 w_0}{\partial x^3} + a_{12} \frac{\partial w_0}{\partial x} \frac{\partial^2 w_0}{\partial x^2} + a_{13} \frac{\partial w_0}{\partial y} \frac{\partial^2 w_0}{\partial x \partial y} + a_{14} \frac{\partial w_0}{\partial x} \frac{\partial^2 w_0}{\partial y^2} \\ & -a_{15} \frac{\partial^3 w_0}{\partial x \partial y^2} + a_{16} \frac{\partial w_0}{\partial x} + a_{17} \frac{\partial^2 u_0}{\partial x^2} + a_{18} \frac{\partial^2 u_0}{\partial y^2} + a_{19} \frac{\partial^2 v_0}{\partial x \partial y} \\ & + a_{20} \frac{\partial^2 \phi_1}{\partial x^2} + a_{21} \frac{\partial^2 \phi_1}{\partial y^2} + a_{22} \frac{\partial^2 \phi_2}{\partial x \partial y} + a_{23} u_0 + a_{24} \phi_1 \\ & -a_{25} E_1 \cos(\Omega_1 t) = I_0 \ddot{u}_0, \end{aligned} \quad (17a)$$

$$\begin{aligned} & -b_{11} \frac{\partial^3 w_0}{\partial y^3} + b_{12} \frac{\partial w_0}{\partial y} \frac{\partial^2 w_0}{\partial y^2} + b_{13} \frac{\partial w_0}{\partial x} \frac{\partial^2 w_0}{\partial x \partial y} + b_{14} \frac{\partial w_0}{\partial y} \frac{\partial^2 w_0}{\partial x^2} \\ & -b_{15} \frac{\partial^3 w_0}{\partial y \partial x^2} + b_{16} \frac{\partial w_0}{\partial y} + b_{17} \frac{\partial^2 v_0}{\partial x^2} + b_{18} \frac{\partial^2 v_0}{\partial y^2} + b_{19} \frac{\partial^2 u_0}{\partial x \partial y} \\ & + b_{20} \frac{\partial^2 \phi_2}{\partial x^2} + b_{21} \frac{\partial^2 \phi_2}{\partial y^2} + b_{22} \frac{\partial^2 \phi_1}{\partial x \partial y} + b_{23} v_0 + b_{24} \phi_2 \\ & -b_{25} E_2 \cos(\Omega_1 t) = I_0 \ddot{v}_0, \end{aligned} \quad (17b)$$

$$\begin{aligned} & -c_{11} \frac{\partial^4 w_0}{\partial x^4} - c_{12} \frac{\partial^4 w_0}{\partial y^4} - c_{13} \frac{\partial^4 w_0}{\partial x^2 \partial y^2} + c_{14} \frac{\partial^2 w_0}{\partial x^2} \\ & + c_{15} \frac{\partial^2 w_0}{\partial y^2} + c_{16} \left(\frac{\partial w_0}{\partial x} \right)^2 + c_{17} \left(\frac{\partial w_0}{\partial y} \right)^2 + c_{18} \frac{\partial^2 w_0}{\partial x^2} \frac{\partial v_0}{\partial x} \\ & + c_{19} \frac{\partial^2 w_0}{\partial y^2} \frac{\partial v_0}{\partial y} + c_{20} \frac{\partial w_0}{\partial x} \frac{\partial^2 u_0}{\partial x^2} + c_{21} \frac{\partial w_0}{\partial y} \frac{\partial^2 v_0}{\partial y^2} \\ & + c_{22} w_0 \frac{\partial^2 w_0}{\partial x^2} + c_{23} w_0 \frac{\partial^2 w_0}{\partial y^2} + c_{24} \left(\frac{\partial w_0}{\partial x} \right)^2 \frac{\partial^2 w_0}{\partial x^2} \\ & + c_{25} \left(\frac{\partial w_0}{\partial y} \right)^2 \frac{\partial^2 w_0}{\partial y^2} + c_{26} \left(\frac{\partial w_0}{\partial y} \right)^2 \frac{\partial^2 w_0}{\partial x^2} + c_{27} \left(\frac{\partial w_0}{\partial x} \right)^2 \frac{\partial^2 w_0}{\partial y^2} \\ & + c_{28} \frac{\partial^2 w_0}{\partial x^2} \frac{\partial v_0}{\partial y} + c_{29} \frac{\partial^2 w_0}{\partial y^2} \frac{\partial u_0}{\partial x} + c_{30} \frac{\partial w_0}{\partial x} \frac{\partial^2 v_0}{\partial x \partial y} \\ & + c_{31} \frac{\partial w_0}{\partial y} \frac{\partial^2 u_0}{\partial x \partial y} + c_{32} \frac{\partial w_0}{\partial x} \frac{\partial w_0}{\partial y} \frac{\partial^2 w_0}{\partial x \partial y} + c_{33} \frac{\partial^2 w_0}{\partial x \partial y} \frac{\partial v_0}{\partial x} \\ & + c_{34} \frac{\partial^2 w_0}{\partial x \partial y} \frac{\partial u_0}{\partial y} + c_{35} \frac{\partial w_0}{\partial y} \frac{\partial^2 v_0}{\partial x^2} + c_{36} \frac{\partial w_0}{\partial x} \frac{\partial^2 u_0}{\partial y^2} \\ & -c_{37} \frac{\partial w_0}{\partial y} \frac{\partial^3 w_0}{\partial x^2 \partial y} - c_{38} \frac{\partial^3 w_0}{\partial x \partial y^2} \frac{\partial w_0}{\partial x} + c_{39} \frac{\partial^3 u_0}{\partial x^3} \\ & + c_{40} \frac{\partial^3 v_0}{\partial y^3} - c_{41} \frac{\partial u_0}{\partial x} - c_{42} \frac{\partial v_0}{\partial y} + c_{43} \frac{\partial^3 u_0}{\partial x \partial y^2} + c_{44} \frac{\partial^3 v_0}{\partial x^2 \partial y} \\ & + c_{45} \frac{\partial^3 \phi_1}{\partial x^3} + c_{46} \frac{\partial^3 \phi_2}{\partial y^3} + c_{47} \frac{\partial^3 \phi_1}{\partial x \partial y^2} + c_{48} \frac{\partial^3 \phi_2}{\partial x^2 \partial y} \\ & + c_{49} \frac{\partial \phi_1}{\partial x} + c_{50} \frac{\partial \phi_2}{\partial y} - c_{51} w_0 + f \cos(\Omega_2 t) - \mu \dot{w}_0 = I_0 \ddot{w}_0 \\ & + (c_1 I_4 - c_1^3 I_6) \left(\frac{\partial \phi_1}{\partial x} + \frac{\partial \phi_2}{\partial y} \right) + c_1^3 I_6 \left(\frac{\partial^2 \dot{w}_0}{\partial x^2} + \frac{\partial^2 \dot{w}_0}{\partial y^2} \right), \end{aligned} \quad (17c)$$

$$\begin{aligned}
& d_{11} \frac{\partial^3 w_0}{\partial x^3} + d_{12} \frac{\partial^3 w_0}{\partial x \partial y^2} + d_{13} \frac{\partial w_0}{\partial x} \frac{\partial^2 w_0}{\partial y^2} \\
& + d_{14} \frac{\partial w_0}{\partial y} \frac{\partial^2 w_0}{\partial x \partial y} + d_{15} \frac{\partial w_0}{\partial x} + d_{16} \frac{\partial^2 u_0}{\partial x^2} + d_{17} \frac{\partial^2 u_0}{\partial y^2} \\
& + d_{18} \frac{\partial^2 v_0}{\partial x \partial y} + d_{19} \frac{\partial^2 \phi_1}{\partial x^2} + d_{20} \frac{\partial^2 \phi_1}{\partial y^2} + d_{21} \frac{\partial^2 \phi_2}{\partial x \partial y} + d_{22} u_0 \\
& + d_{23} \phi_1 + d_{24} E_1 \cos(\Omega_1 t) \\
& = I_2 \ddot{\phi}_1 - c_1 I_4 \ddot{\phi}_1 - c_1 I_4 \frac{\partial \ddot{w}_0}{\partial x} + c_1 \left(-I_4 \ddot{\phi}_1 + c_1 I_6 \ddot{\phi}_1 + c_1 I_6 \frac{\partial \ddot{w}_0}{\partial x} \right),
\end{aligned} \tag{17d}$$

$$\begin{aligned}
& e_{11} \frac{\partial^3 w_0}{\partial y^3} + e_{12} \frac{\partial^3 w_0}{\partial x^2 \partial y} + e_{13} \frac{\partial w_0}{\partial y} \frac{\partial^2 w_0}{\partial x^2} + e_{14} \frac{\partial w_0}{\partial x} \frac{\partial^2 w_0}{\partial x \partial y} \\
& + e_{15} \frac{\partial w_0}{\partial y} + e_{16} \frac{\partial^2 v_0}{\partial x^2} + e_{17} \frac{\partial^2 v_0}{\partial y^2} + e_{18} \frac{\partial^2 u_0}{\partial x \partial y} + e_{19} \frac{\partial^2 \phi_2}{\partial x^2} \\
& + e_{20} \frac{\partial^2 \phi_2}{\partial y^2} + e_{21} \frac{\partial^2 \phi_1}{\partial x \partial y} + e_{22} v_0 + e_{23} \phi_2 + e_{24} E_2 \cos(\Omega_1 t) \\
& = I_2 \ddot{\phi}_2 - c_1 I_4 \ddot{\phi}_2 - c_1 I_4 \frac{\partial \ddot{w}_0}{\partial y} + c_1 \left(-I_4 \ddot{\phi}_2 + c_1 I_6 \ddot{\phi}_2 + c_1 I_6 \frac{\partial \ddot{w}_0}{\partial y} \right),
\end{aligned} \tag{17e}$$

where μ in equation (17c) is the damping coefficient.

The boundary conditions of the cantilever thin shell are expressed as

$$x = 0 : N_{xy} = M_{xx} = M_{xy} - c_1 P_{xy} = \overline{Q}_x = 0, \tag{18a}$$

$$x = a : N_{xy} = M_{xx} = M_{xy} - c_1 P_{xy} = \overline{Q}_x = 0, \tag{18b}$$

$$y = 0 : u_0 = v_0 = w_0 = \phi_1 = \phi_2 = 0, \tag{18c}$$

$$\begin{aligned}
y = b : N_{yy} = N_{xy} = M_{yy} = M_{xy} \\
- c_1 P_{xy} = \overline{Q}_y = 0,
\end{aligned} \tag{18d}$$

$$\begin{aligned}
& x = 0, \\
& a : \int_{-(h/2)}^{(h/2)} N_{xx} dz = \pm \int_{-(h/2)}^{(h/2)} f dz.
\end{aligned} \tag{18e}$$

4. Effects of the Piezoelectric Parameters

Since the polarization of MFC-*d*33 is located in the plane, the vibration amplitudes of the shell in the x direction also need to be analyzed as those in the z direction. Here, the nonlinear coupled vibrations are considered between the in-plane and out-of-plane of the cantilever shell in the following studies. The displacements u_0 , v_0 , w_0 , ϕ_1 , and ϕ_2 , which satisfy the boundary conditions for the shell, are expressed as

$$\begin{aligned}
u_0 &= u_1 \sin \frac{\pi x}{2} \cos \pi y, \\
v_0 &= v_1 \sin \frac{\pi x}{2} \sin \pi y, \\
\phi_1 &= \phi_{11} \sin \frac{\pi x}{2} \cos \pi y,
\end{aligned} \tag{19a}$$

$$\phi_2 = \phi_{21} \left(1 - \cos \frac{\pi x}{2} \right) \sin \pi y,$$

$$w_0 = w_1(t) X(x) Y(y),$$

$$\begin{aligned}
X(x) &= \sin \lambda_1 x - \sinh \lambda_1 x \\
&+ \alpha_1 (\cosh \lambda_1 x - \cos \lambda_1 x),
\end{aligned} \tag{19b}$$

$$Y(y) = \sqrt{3} \left(1 - \frac{2y}{b} \right),$$

$$\cos \lambda_1 a \cosh \lambda_1 a + 1 = 0. \tag{19c}$$

Then, taking all these derived expressions in equations (18a)–(18e) and (19a)–(19c) into equations (17a)–(17e) and applying the Galerkin procedure, two-degree-of-freedom nonlinear ordinary differential equations of the MFC laminated shell with dimensionless variables are obtained as follows:

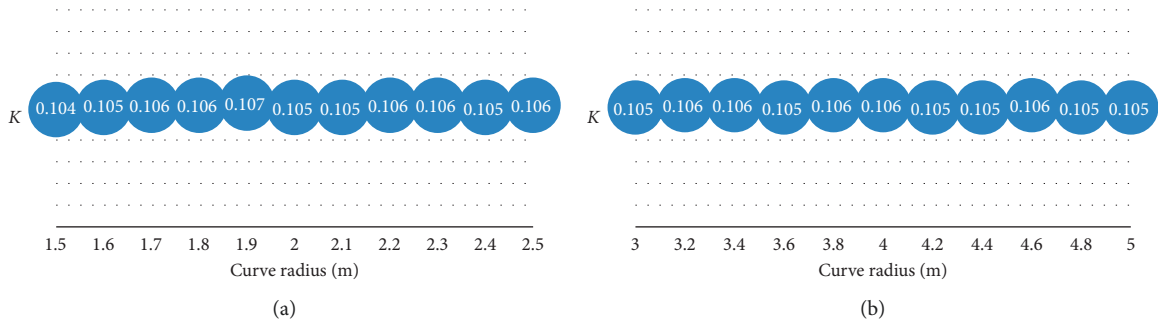
$$\ddot{u}_1 + \omega_1^2 u_1 + \alpha_{11} w_1^2 + \alpha_{12} E_1 \cos(\Omega_1 t) = 0, \tag{20a}$$

$$\begin{aligned}
\ddot{w}_1 + \mu_1 \dot{w}_1 + \omega_2^2 w_1 + \alpha_{21} u_1 + \alpha_{22} u_1 w_1 + \alpha_{23} w_1 E_1 \cos(\Omega_1 t) \\
+ \alpha_{24} w_1^2 + \alpha_{25} w_1^3 + \alpha_{26} E_1 \cos(\Omega_1 t) = \alpha_{27} f \cos(\Omega_2 t).
\end{aligned} \tag{20b}$$

The structural properties are taken as follows: the shell has 7 laminae and the total thickness is $0.002 * 7$ m. The elastic constants of the fiber and matrix are 2.1×10^{11} Pa and 3.5×10^9 Pa, respectively. The density of the shell is 1.96 kg/m^3 , and Poisson's ratio is 0.36. The electric inductivity is 1296, and piezoelectric coefficients are $d_{33} = 509 \text{ pC/N}$ and $d_{31} = -156 \text{ pC/N}$.

Firstly, the effects of the piezoelectric parameters on the deflection ($K = x_1/b$) of the shell are analyzed. Let voltage be 40 kV/cm along the y direction, the volume of the fiber content be 18%, and K be 15° . The radii R_3 and R_4 are divided into two groups: (i) $R_3 = 1.5$ m and $R_4 = 1.5 \sim 2.5$ m and (ii) $R_3 = 3$ m and $R_4 = 3 \sim 5$ m. The relations between the radii of curvature R_3 and R_4 and K are described in Figure 5, which shows that the curves are nearly straight when R_3 and R_4 increase. Therefore, the piezoelectric parameters would not affect the deflection of the thin shell directly.

Then, the voltage is increased from 20 kV/cm to 60 kV/cm and the radii are set as $R_3 = 1.5$ m and $R_4 = 2$ m, as shown in Figure 6. It indicates that the deflection of the thin shell will be amplified with the increasing voltages. The

FIGURE 5: K -curve radius map.

deflection of the thin shell is also affected by the volume of macrofibers, as shown in Figure 7. The deflection K increases from 1.2 to 11.7 when the volume of macrofibers varies from 0 to 20%.

It is summarized from the above results that the voltage and volume of macrofibers play an important role in the deflection of the MFC shell, which could adjust the natural frequency of the shell. It also indicates that voltage and volume of macrofibers are useful controlling parameters for the dynamic responses of the shell.

5. Nonlinear Characteristic Analysis under 1:1 Internal Resonance. Since the resonance of the system has great influence on the structural stability, the primary parameter resonance and 1:1 internal resonance are considered here, and the resonance relationships are expressed as follows:

$$\begin{aligned}\omega_1 &= \Omega_1 - \varepsilon\sigma_1, \\ \omega_2 &= \Omega_2 - \varepsilon\sigma_2, \\ \Omega_1 &= \Omega_2 = 1,\end{aligned}\quad (21)$$

where σ_1 and σ_2 are two detuning parameters, respectively.

The solution of equations (20a) and (20b) can be written as follows according to the method of multiscale:

$$u_1 = u_{10}(T_0, T_1) + \varepsilon u_{11}(T_0, T_1) + \dots, \quad (22a)$$

$$w_1 = w_{10}(T_0, T_1) + \varepsilon w_{11}(T_0, T_1) + \dots. \quad (22b)$$

Equations (21), (22a), and (22b) are introduced into equations (20a) and (20b) to obtain the following conditions. ε^0 order:

$$D_0^2 u_{10} + u_{10} = 0, \quad (23a)$$

$$D_0^2 w_{10} + w_{10} = 0. \quad (23b)$$

ε^1 order:

$$\begin{aligned}D_0^2 u_{11} + u_{11} &= -2D_0 D_1 u_{10} - \alpha_{11} w_{10}^2 \\ &\quad - \alpha_{12} E_1 \cos(\Omega_1 t) + 2\sigma_1 u_{10},\end{aligned}\quad (24a)$$

$$\begin{aligned}D_0^2 w_{11} + w_{11} &= -2D_0 D_1 w_{10} - \mu_1 D_0 w_{10} - \alpha_{21} u_{10} \\ &\quad - \alpha_{22} u_{10} w_{10} - \alpha_{23} w_{10} E_1 \cos(\Omega_1 t) \\ &\quad + 2\sigma_2 w_{10} - \alpha_{24} w_{10}^2 - \alpha_{25} w_{10}^3 \\ &\quad - \alpha_{26} E_1 \cos(\Omega_1 t) + \alpha_{27} F \cos(\Omega_2 t).\end{aligned}\quad (24b)$$

Assume that the solutions of equations (24a) and (24b) are as follows:

$$u_{10} = \prod_1 (T_1) e^{iT_0} + cc, \quad (25a)$$

$$w_{10} = \prod_2 (T_1) e^{iT_0} + cc, \quad (25b)$$

where $\Pi_1 = (1/2)\varsigma_1 e^{i\beta_1}$ and $\Pi_2 = (1/2)\varsigma_2 e^{i\beta_2}$, in which ς_i ($i = 1, 2$) is the amplitude of vibration and β_i ($i = 1, 2$) is the initial phase.

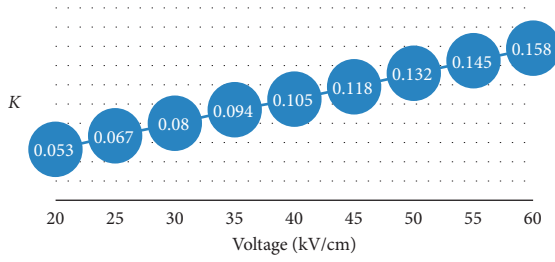
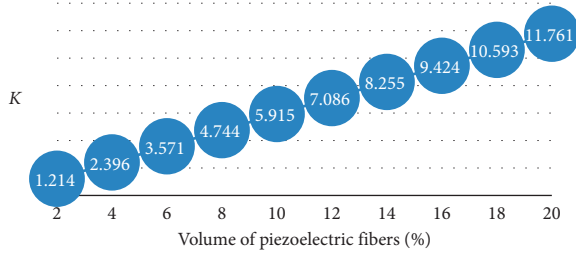
Substituting equations (25a) and (25b) into equations (24a) and (24b) and eliminating the long term, the average equations of the polar form are obtained as follows:

$$\dot{\varsigma}_1 = -\frac{\alpha_{12}}{2} E_1 \sin(\beta_1), \quad (26a)$$

$$\varsigma_1 \dot{\beta}_1 = -\frac{\alpha_{12}}{2} E_1 \cos(\beta_1) - \varsigma_1 \sigma_1, \quad (26b)$$

$$\begin{aligned}\dot{\varsigma}_2 &= -\frac{1}{2} \mu \varsigma_2 - \frac{1}{2} \alpha_{21} \varsigma_1 \sin(\beta_1 - \beta_2) \\ &\quad - \frac{1}{2} (\alpha_{27} f - \alpha_{26} E_1) \sin(\beta_2),\end{aligned}\quad (26c)$$

$$\begin{aligned}\varsigma_2 \dot{\beta}_2 &= \frac{1}{2} \alpha_{21} \varsigma_1 \cos(\beta_1 - \beta_2) - \varsigma_2 \sigma_2 \\ &\quad + \frac{3}{8} \alpha_{25} \varsigma_2^3 + \frac{1}{2} (\alpha_{27} f - \alpha_{26} E_1) \cos(\beta_2).\end{aligned}\quad (26d)$$

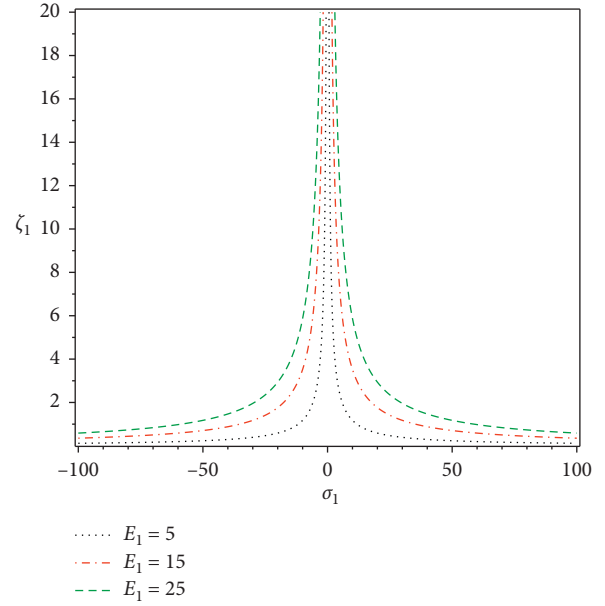
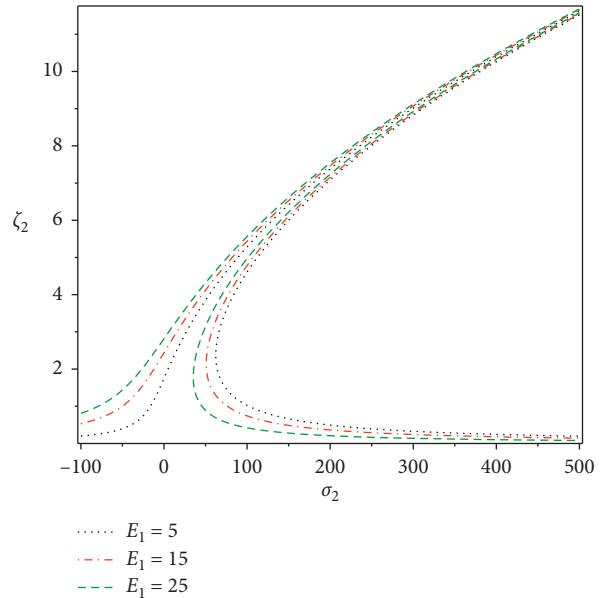
FIGURE 6: K -voltage map.FIGURE 7: K -volume of macrofibers.

When the amplitude achieves a constant nontrivial value, a steady-state vibration exists. Therefore, let the left-hand side of equations (26a)–(26d) equals to zero and eliminate $\beta_1 - \beta_2$ by using the relations between trigonometric functions, and then the frequency-response functions can be obtained:

$$\frac{\alpha_{12}^2 E_1^2}{4} = \zeta_1^2 \sigma_1^2, \quad (27a)$$

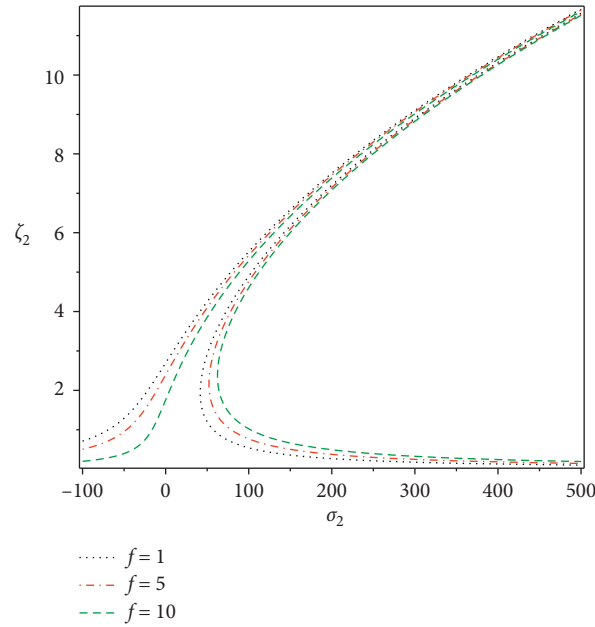
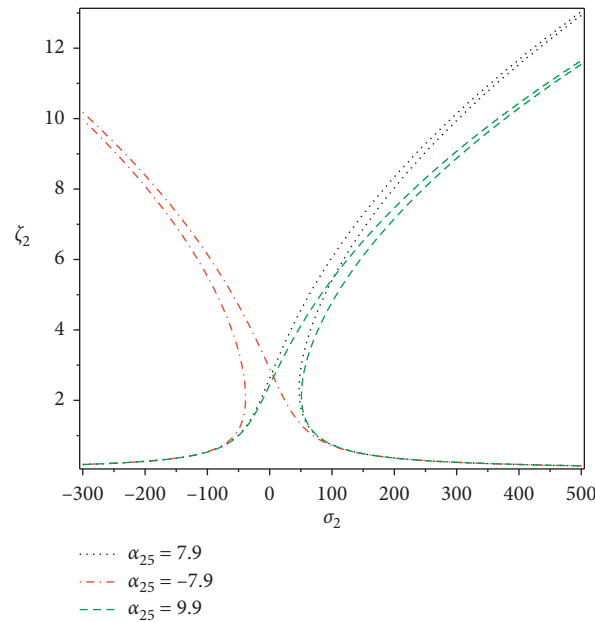
$$\left(-\frac{1}{2} \mu \zeta_2 - \frac{1}{2} (\alpha_{27} f - \alpha_{26} E_1) \sin(\beta_2) \right)^2 + \left(-\zeta_2 \sigma_2 + \frac{3}{8} \alpha_{25} \zeta_2^3 + \frac{1}{2} (\alpha_{27} f - \alpha_{26} E_1) \cos(\beta_2) \right)^2 = \frac{1}{4} \alpha_{21}^2 \zeta_1^2. \quad (27b)$$

Based on equations (27a) and (27b), the effects of electric field, transversal excitation, and nonlinear parameters (α_{25}) on the nonlinear amplitudes are investigated by numerical simulation. Fixing the parameters of the shell as mentioned above, and after the dimensionless calculation, the following parameters are obtained: $\alpha_{12} = 6.7$, $\alpha_{25} = 14.2$, $\alpha_{26} = 9.9$, $\alpha_{27} = 6.9$, $\alpha_{28} = 12.5$, and $E_1 = 20$. Figure 8 illustrates that the resonance regions in the x direction increase with the increasing electric field. The resonance region moves to the left in the z direction and the resonance frequency decreases, as shown in Figure 9. Meanwhile, the system shows the hardening spring characteristic, as shown in Figure 9. Figure 10 expresses the relationship between the resonance region and the transversal excitation, which is similar to that shown in Figure 9. The nonlinear parameters can change the soft and hard spring properties of the system, as shown in Figure 11, and the hard spring characteristic is prominent with the nonlinear parameter increase.

FIGURE 8: Frequency-response curves in the x direction with the electric field.FIGURE 9: Frequency-response curves in the z direction with the electric field.

6. Nonlinear Dynamic Analysis

In this section, the nonlinear dynamic behavior of the MFC laminated thin shell subjected to the aerodynamic force is conducted. A series of numerical experiments are performed through the Runge–Kutta algorithm according to the nonlinear governing equations (20a) and (20b). After the dimensionless calculation of the structural parameters, the following parameters are obtained: $\alpha_{11} = 8.2$, $\alpha_{12} = 6.7$, $\alpha_{13} = 4.7$, $\mu = 0.5$, $\alpha_{21} = 12.7$, $\alpha_{22} = 5.2$, $\alpha_{23} = 8.0$, $\alpha_{24} = 12.0$, $\alpha_{25} = 14.2$, $\alpha_{26} = 9.9$, $\alpha_{27} = 6.9$, $\alpha_{28} = 12.5$, $E_1 = 20$, $x_1 = 0.8$,

FIGURE 10: Frequency-response curves in the z direction with transversal excitation.FIGURE 11: Frequency-response curves in the z direction with the nonlinear parameter.

$x_2 = 1.0$, $x_3 = 0.2$, and $x_4 = 0.9$. With the disturbance force f increased from 0 to 300, the bifurcation diagrams of Poincare sections in the z direction for the displacements of the middle surface of the shell are shown in Figure 12. It is found that the nonlinear responses of the shell are very complex with the increasing disturbance force f . The instability of the structure would last a long time during the process as f increases from 0 to 180, and then after short windows of periodic n motions occurring in 180–230, the motions of the system become chaotic again through the path of periodic doubling bifurcation. Therefore, the motion form of the structure can be changed by controlling

the amplitude of the external excitation in the resonance case.

To reveal the specific forms of different sections in the bifurcation diagram, phase portraits, power spectra, and waveforms of the shell are depicted as shown in the following figures. In Figures 13–15, x_1 and x_2 represent the displacement and velocity in the x direction and x_3 and x_4 represent the displacement and velocity in the z direction. Furthermore, Figures 13(a), 14(a), and 15(a) and Figures 13(b), 14(b), and 15(b) show, respectively, the waveforms in the planes (t, x_1) and (t, x_3) , and Figures 13(c), 14(c), and 15(c) and Figures 13(d), 14(d), and 15(d) show, respectively, the

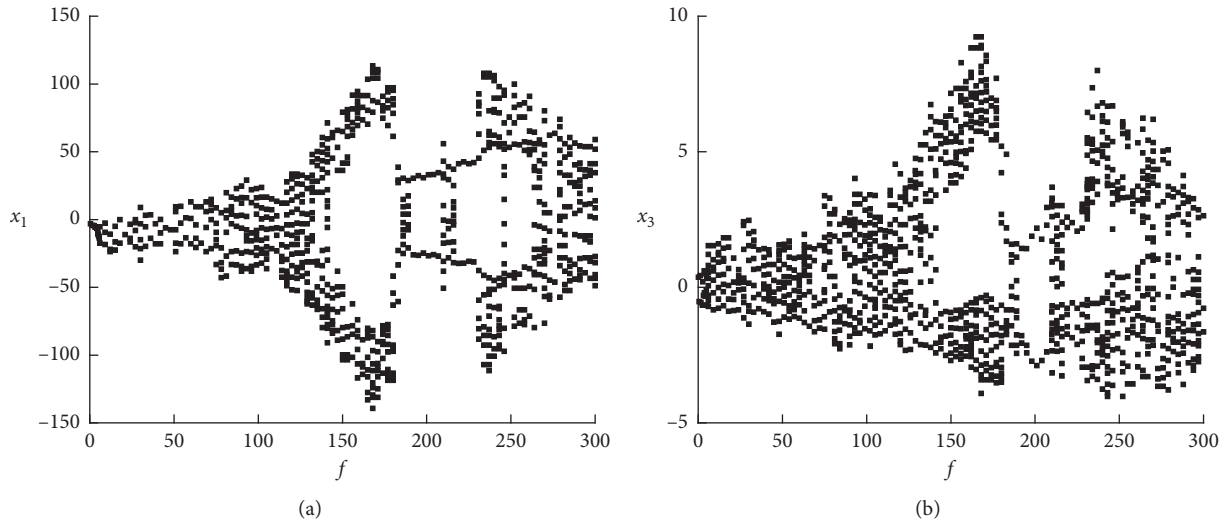


FIGURE 12: Bifurcation diagrams of Poincare sections. (a) $x_1 - f$. (b) $x_3 - f$.

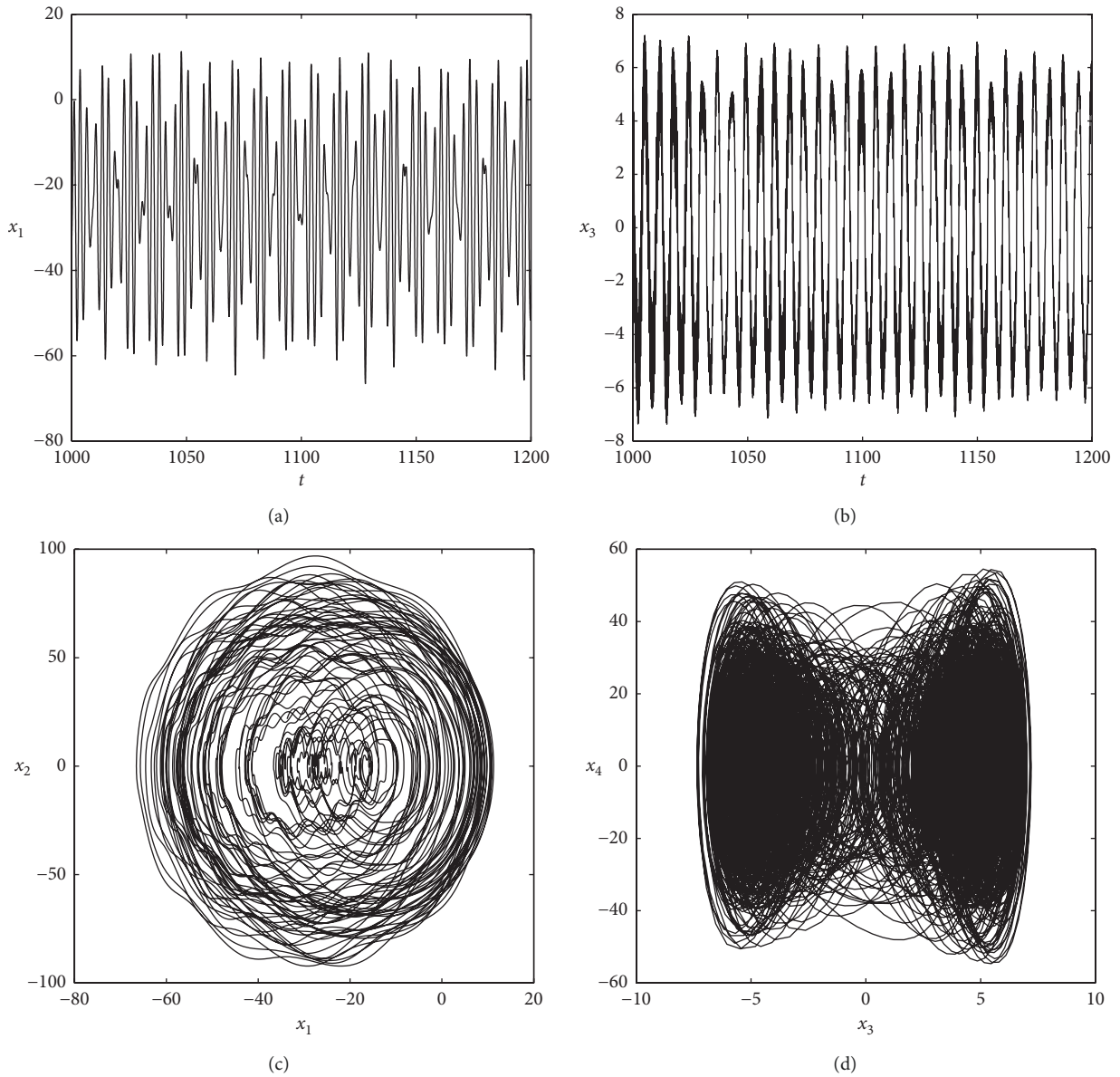


FIGURE 13: Continued.

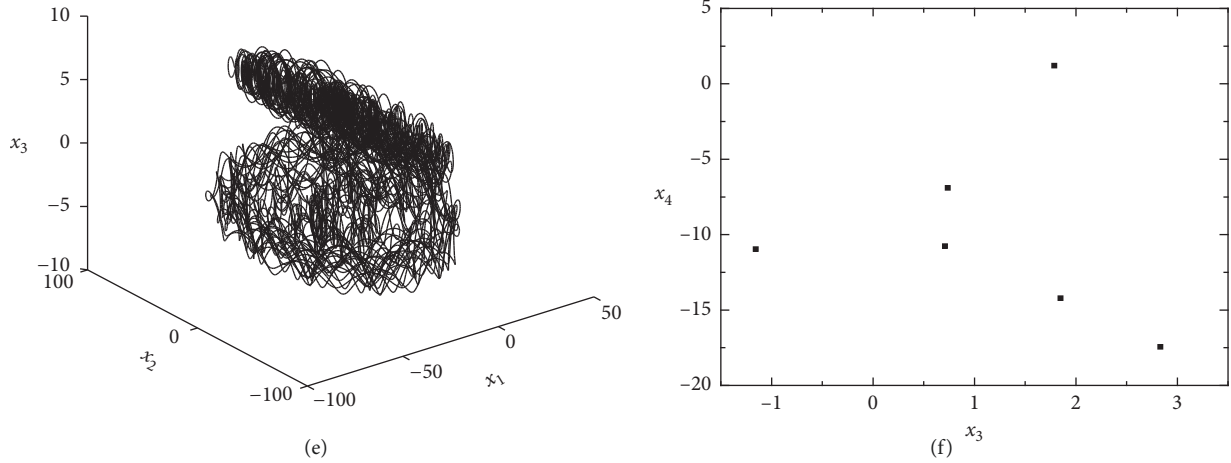


FIGURE 13: Chaotic motion of the composite shell when f equals 100. (a) Waveform in the plane (t, x_1) . (b) Waveform in the plane (t, x_3) . (c) Two-dimensional phase portrait in the plane (x_1, x_2) . (d) Two-dimensional phase portrait in the plane (x_3, x_4) . (e) Three-dimensional phase portrait in the plane (x_1, x_2, x_3) . (f) Poincaré diagram.

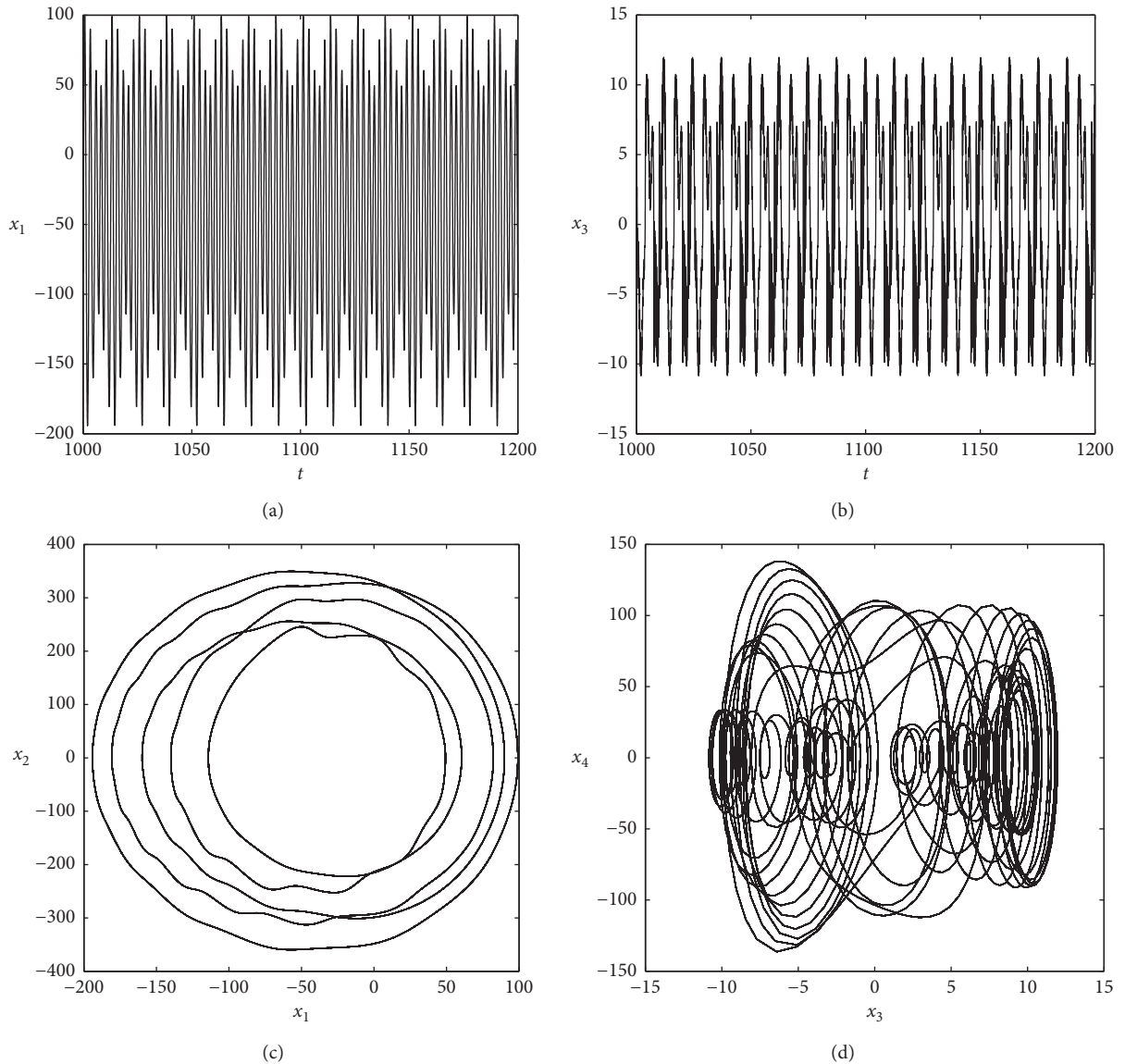


FIGURE 14: Continued.

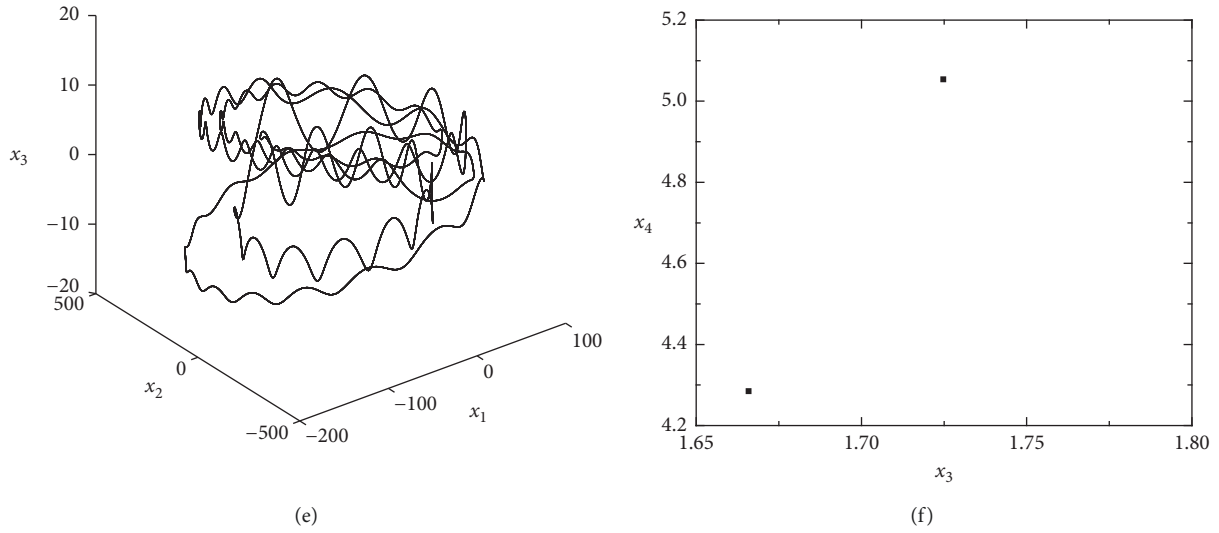


FIGURE 14: Periodic motion of the composite shell. (a) Waveform in the plane (t, x_1) . (b) Waveform in the plane (t, x_3) . (c) Two-dimensional phase portrait in the plane (x_1, x_2) . (d) Two-dimensional phase portrait in the plane (x_3, x_4) . (e) Three-dimensional phase portrait in the plane (x_1, x_2, x_3) . (f) Poincaré diagram.

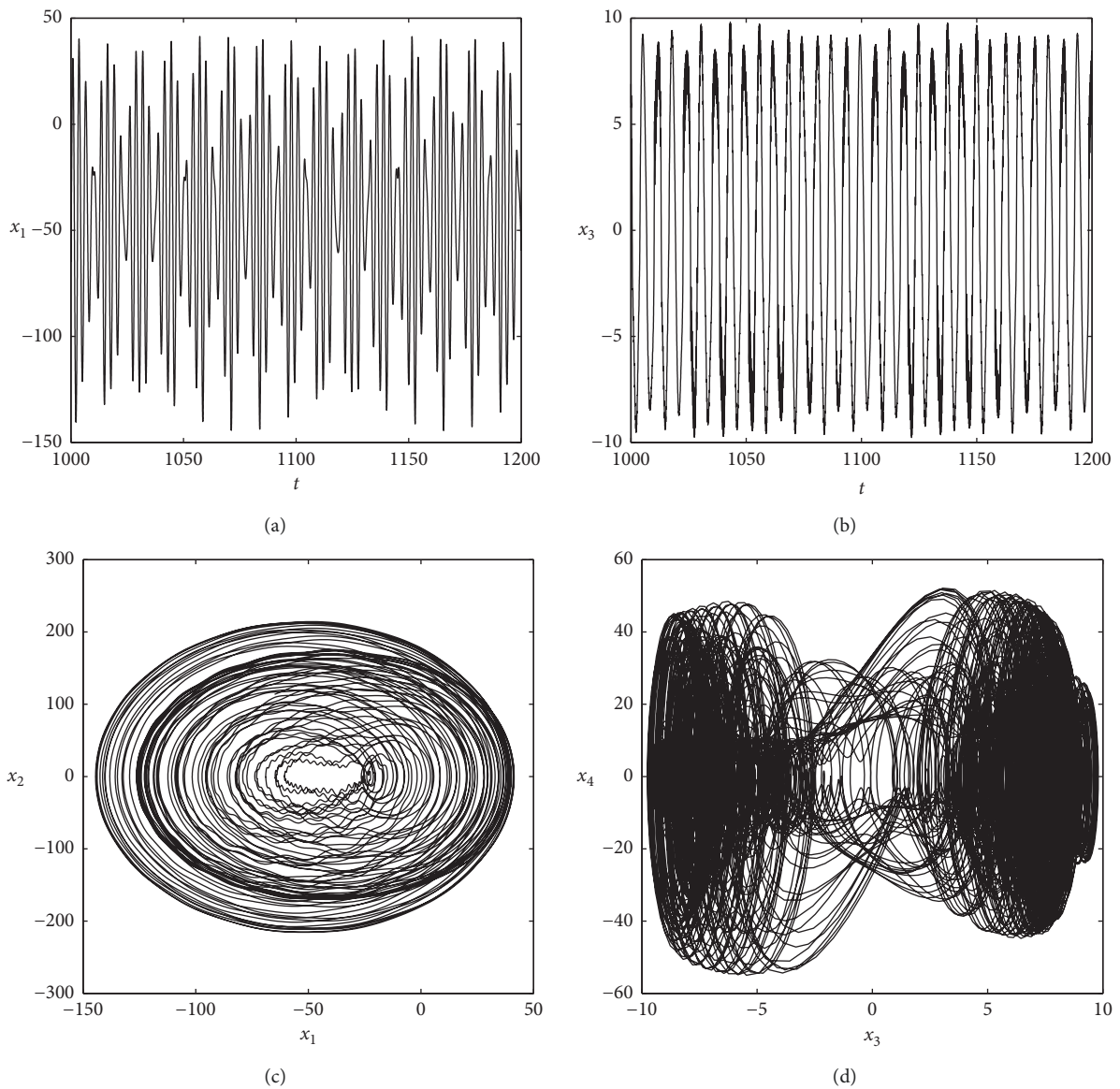


FIGURE 15: Continued.

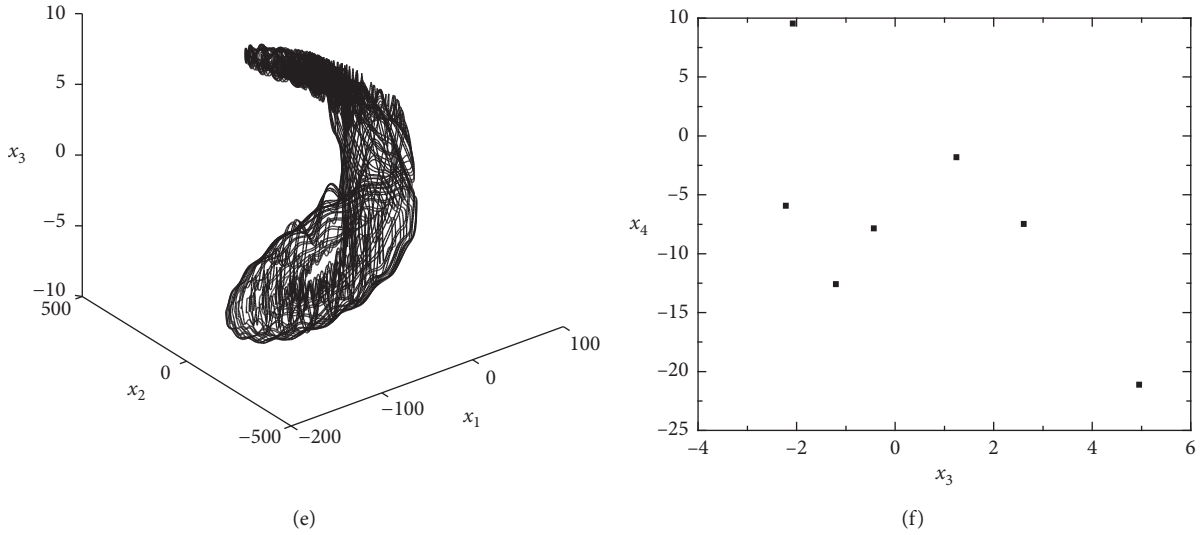


FIGURE 15: Chaotic motion of the composite shell when f increases to 270. (a) Waveform in the plane (t, x_1) . (b) Waveform in the plane (t, x_3) . (c) Two-dimensional phase portrait in the plane (x_1, x_2) . (d) Two-dimensional phase portrait in the plane (x_3, x_4) . (e) Three-dimensional phase portrait in the plane (x_1, x_2, x_3) . (f) Poincaré diagram.

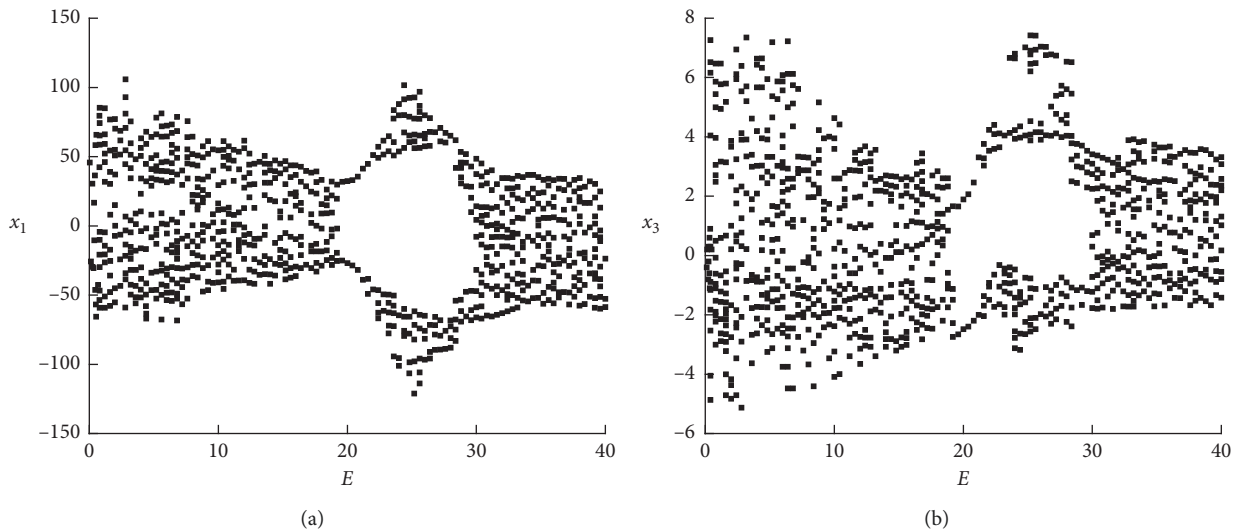


FIGURE 16: Bifurcation diagram of the composite shell with the electric field increase. (a) $x_1 - E$. (b) $x_3 - E$.

two-dimensional phase portraits in the planes (x_1, x_2) and (x_3, x_4) . Figures 13(e), 14(e), and 15(e) show the three-dimensional phase portraits in the space (x_1, x_2, x_3) , while Figures 13(f), 14(f), and 15(f) present the Poincaré diagram. Figure 13 shows a group of characteristics of the chaotic motion for the system when f equals 100. It also indicates that there exists energy transform between the responses of the shell in two different directions in Figure 13(e), which is caused by the nonlinear coupled terms of equations (20a) and (20b).

The periodic n motions of the system are shown in Figure 14 when f increases to 205, and the phenomenon of energy transition between two modes of the shell also exists in Figure 14(e).

Then, when the aerodynamic disturbance force increases to 270, the system enters into chaos, and the specific shape of

the response is shown in Figure 15, which is similar to the chaotic motion in Figure 13.

From the above analysis, it can be seen that the aerodynamic force plays a key role in the dynamic behavior of the structure. Then, the piezoelectric parameters are used to adjust the nonlinear responses of the system. Fixing the above parameters and letting the aerodynamic disturbance force $f = 270$, the bifurcation diagrams of Poincaré sections are obtained in the x and z directions for the displacements of the middle surface of the shell when the electric field E increases from 0 to 40 in Figure 16. It is found that the motion of the system can be adjusted from chaos to the period when E is close to 20, and when the value of E is continuously increased, the system returns back to chaotic motion again.

From the above results of the numerical simulation, it is indicated that the piezoelectric parameters could adjust the

vibration responses of the structure effectively. The electric field can change the piezoelectric performance of the shell through varying the stiffness of the structure, and the resonance of the shell would be restrained.

7. Conclusion

Considering the large geometrical deformation and piezoelectric material properties of the shell, nonlinear dynamic behaviors of a cantilever $d33$ MFC shell are investigated. The aerodynamical force and the electric field are introduced and calculated. Then, the Galerkin method is employed to transform the partial differential equations into two nonlinear ordinary differential equations. Next, the influence of the electric field, external excitation force, and nonlinear parameters on the stability of the system is analyzed under 1:1 internal resonance. Furthermore, the effects of the material parameters on the deflection are discussed, and the complex nonlinear vibration responses of the MFC shell are simulated, including the periodic and chaotic motions.

This paper innovatively analyses the coupled vibration in two directions and points out that the energy transition exists between two coupled vibration directions. It is also revealed that the electric field of the MFC shell could adjust the dynamic stability of the structure from unstable to stable which would be an effective way to control responses for MFC structures. This research work may provide a way to use the MFC material in designing the wings of UAVs in the engineering field. The dynamic behavior of the wing in subsonic air flow conditions can be controlled by adjusting the electric field when the wing is made of the MFC material. Therefore, it could ensure the stability of the wing movement and the flight safety of the UAV.

Data Availability

The data used to support the findings of this study are available from the corresponding author upon request.

Conflicts of Interest

The authors declare that they have no conflicts of interest.

Acknowledgments

The authors gratefully acknowledge the support of the National Natural Science Foundation of China (NNSFC) through grant nos. 11572006, 11772010, and 11672008 and the Funding Project for Academic Human Resources Development in Institutions of Higher Learning under the Jurisdiction of Beijing Municipality (PHRIHLB).

References

- [1] P. Tan, L. Tong, and D. Sun, "Dynamic characteristics of a beam system with active piezoelectric fiber reinforced composite layers," *Composites Part B: Engineering*, vol. 33, no. 7, pp. 545–555, 2002.
- [2] S. C. Choi, J. S. Park, and J. H. Kim, "Vibration control of pre-twisted rotating composite thin-walled beams with piezoelectric fiber composites," *Journal of Sound and Vibration*, vol. 300, no. 1–2, pp. 176–196, 2007.
- [3] R. Schmidt and T. D. Vu, "Nonlinear dynamic FE simulation of smart piezolaminated structures based on first- and third-order transverse shear deformation theory," *Advanced Materials Research*, vol. 79–82, pp. 1313–1316, 2009.
- [4] H. S. Kim, J. W. Sohn, and S.-B. Choi, "Vibration control of a cylindrical shell structure using Macro Fiber Composite actuators," *Mechanics Based Design of Structures and Machines*, vol. 39, no. 4, pp. 491–506, 2011.
- [5] G. Shankar, S. K. Kumar, and P. K. Mahato, "Vibration analysis and control of smart composite plates with delamination and under hygrothermal environment," *Thin-Walled Structures*, vol. 116, pp. 53–68, 2017.
- [6] J.-S. Park and J.-H. Kim, "Analytical development of single crystal Macro Fiber Composite actuators for active twist rotor blades," *Smart Materials and Structures*, vol. 14, no. 4, pp. 745–753, 2005.
- [7] O. Bilgen, A. Erturk, and D. J. Inman, "Analytical and experimental characterization of macro-fiber composite actuated thin clamped-free unimorph benders," *Journal of Vibration and Acoustics*, vol. 132, no. 5, article 051005, 2010.
- [8] A. C. Cook and S. S. Vel, "Multiscale analysis of laminated plates with integrated piezoelectric fiber composite actuators," *Composite Structures*, vol. 94, no. 2, pp. 322–336, 2012.
- [9] A. C. Cook and S. S. Vel, "Multiscale thermopiezoelectric analysis of laminated plates with integrated piezoelectric fiber composites," *European Journal of Mechanics—A/Solids*, vol. 40, no. 1, pp. 11–33, 2013.
- [10] S. Kapuria and P. C. Dumir, "Geometrically nonlinear axisymmetric response of thin circular plate under piezoelectric actuation," *Communications in Nonlinear Science and Numerical Simulation*, vol. 10, no. 4, pp. 411–423, 2005.
- [11] S. Panda and M. C. Ray, "Nonlinear finite element analysis of functionally graded plates integrated with patches of piezoelectric fiber reinforced composite," *Finite Elements in Analysis and Design*, vol. 44, no. 8, pp. 493–504, 2008.
- [12] P. Dash and B. N. Singh, "Nonlinear free vibration of piezoelectric laminated composite plate," *Finite Elements in Analysis and Design*, vol. 45, no. 10, pp. 686–694, 2009.
- [13] M. N. Rao and R. Schmidt, "Static and dynamic finite rotation FE-analysis of thin-walled structures with piezoelectric sensor and actuator patches or layers," *Smart Mater Struct*, vol. 23, no. 9, article 095006, 2014.
- [14] R. B. Williams, D. J. Inman, and W. K. Wilkie, "Nonlinear response of the Macro Fiber Composite actuator to monotonically increasing excitation voltages," in *ASME 2004 International Mechanical Engineering Congress and Exposition*, pp. 49–54, ASME, New York, NY, USA, 2004.
- [15] H. Y. Zhang and Y. P. Shen, "Three-dimensional analysis for rectangular 1–3 piezoelectric fiber-reinforced composite laminates with the interdigitated," *Composites Part B: Engineering*, vol. 37, no. 7–8, pp. 603–611, 2006.
- [16] S. Belouettar, L. Azrar, E. M. Daya, V. Laptev, and M. Potier-Ferry, "Active control of nonlinear vibration of sandwich piezoelectric beams: a simplified approach," *Computers & Structures*, vol. 86, no. 3–5, pp. 386–397, 2008.
- [17] M. Rafiee, M. Mohammadi, B. S. Aragh, and H. Yaghoobi, "Nonlinear free and forced thermo-electro-aero-elastic vibration and dynamic response of piezoelectric functionally graded laminated composite shells," *Composite Structures*, vol. 103, pp. 188–196, 2013.
- [18] S. M. Hosseini, H. Kalhori, A. Shoostari, and S. N. Mahmoodi, "Analytical solution for nonlinear forced response of a

- viscoelastic piezoelectric cantilever beam resting on a nonlinear elastic foundation to an external harmonic excitation,” *Composites Part B: Engineering*, vol. 67, pp. 464–471, 2014.
- [19] S. Mareishi, M. Rafiee, X. Q. He, and K. M. Liew, “Nonlinear free vibration, postbuckling and nonlinear static deflection of piezoelectric fiber-reinforced laminated composite beams,” *Composites Part B: Engineering*, vol. 59, pp. 123–132, 2014.
- [20] M. Rafiee, X. F. Liu, X. Q. He, and S. Kitipornchai, “Geometrically nonlinear free vibration of shear deformable piezoelectric carbon nanotube/fiber/polymer multiscale laminated composite plates,” *Journal of Sound and Vibration*, vol. 333, no. 14, pp. 3236–3251, 2014.
- [21] D. G. Ninh and D. H. Bich, “Characteristics of nonlinear vibration of nanocomposite cylindrical shells with piezoelectric actuators under thermo-mechanical loads,” *Aerospace Science and Technology*, vol. 77, pp. 595–609, 2018.
- [22] S. F. Lu, W. Zhang, and X. J. Song, “Time-varying nonlinear dynamics of a deploying piezoelectric laminated composite plate under aerodynamic force,” *Acta Mechanica Sinica*, vol. 34, no. 2, pp. 87–98, 2018.
- [23] J. A. Mitchell and J. N. Reddy, “A refined hybrid plate theory for composite laminates with piezoelectric laminae,” *International Journal of Solids and Structures*, vol. 32, no. 16, pp. 2345–2367, 1995.
- [24] S. Kapuria, “An efficient coupled theory for multilayered beams with embedded piezoelectric sensory and active layers,” *International Journal of Solids and Structures*, vol. 38, no. 50-51, pp. 9179–9199, 2001.
- [25] R. C. Batra and S. Vidoli, “Higher-order piezoelectric plate theory derived from a three-dimensional variational principle,” *AIAA Journal*, vol. 40, no. 1, pp. 91–104, 2002.
- [26] S. Lentzen and R. A. Schmidt, “Geometrically nonlinear finite element for transient analysis of piezolaminated shells,” *Thin-Walled Structures*, 2005.
- [27] S. S. Prasath and A. Arockiarajan, “Effect of interphase and thermal environment on the effective properties of Macro-Fiber Composites (MFC),” *Composites Part B*, vol. 75, pp. 327–335, 2015.
- [28] S. S. Prasath and A. Arockiarajan, “Experimental and theoretical investigation on the thermo-electro-elastic properties of Macro-Fiber Composites (MFC),” *Composite Structures*, vol. 122, pp. 8–22, 2015.
- [29] S. Q. Zhang, Y. X. Li, and R. Schmidt, “Modeling and Simulation of macro-fiber composite layered smart structures,” *Composite Structures*, vol. 126, pp. 89–100, 2015.
- [30] M. A. Kouchakzadeh, M. Rasekh, and H. Haddadpour, “Panel flutter analysis of general laminated composite plates,” *Composite Structures*, vol. 92, no. 12, pp. 2906–2915, 2010.
- [31] F.-M. Li, Z.-B. Chen, and D.-Q. Cao, “Improving the aeroelastic flutter characteristics of supersonic beams using piezoelectric material,” *Journal of Intelligent Material Systems and Structures*, vol. 22, no. 7, pp. 615–629, 2011.
- [32] S.-Y. Kuo, “Flutter of rectangular composite plates with variable fiber pacing,” *Composite Structures*, vol. 93, no. 10, pp. 2533–2540, 2011.
- [33] S. Y. Kuo, “Thermal buckling, vibration and flutter of composite laminates containing two non-uniformly distributed,” *Journal of Aeronautics, Astronautics and Aviation*, vol. 48, no. 3, pp. 173–182, 2016.
- [34] W. Zhang, L.-L. Chen, X.-Y. Guo, and L. Sun, “Nonlinear dynamical behaviors of deploying wings in subsonic air flow,” *Journal of Fluids and Structures*, vol. 74, pp. 340–355, 2017.